Lecture Notes in Physics

The Editorial Policy for Proceedings

The series Lecture Notes in Physics reports new developments in physical research and teaching – quickly, informally, and at a high level. The proceedings to be considered for publication in this series should be limited to only a few areas of research, and these should be closely related to each other. The contributions should be of a high standard and should avoid lengthy redraftings of papers already published or about to be published elsewhere. As a whole, the proceedings should aim for a balanced presentation of the theme of the conference including a description of the techniques used and enough motivation for a broad readership. It should not be assumed that the published proceedings must reflect the conference in its entirety. (A listing or abstracts of papers presented at the meeting but not included in the proceedings could be added as an appendix.)

When applying for publication in the series Lecture Notes in Physics the volume's editor(s) should submit sufficient material to enable the series editors and their referees to make a fairly accurate evaluation (e.g. a complete list of speakers and titles of papers to be presented and abstracts). If, based on this information, the proceedings are (tentatively) accepted, the volume's editor(s), whose name(s) will appear on the title pages, should select the papers suitable for publication and have them refereed (as for a journal) when appropriate. As a rule discussions will not be accepted. The series editors and Springer-Verlag will normally not interfere with the detailed editing except in fairly obvious cases or on technical matters.

Final acceptance is expressed by the series editor in charge, in consultation with Springer-Verlag only after receiving the complete manuscript. It might help to send a copy of the authors' manuscripts in advance to the editor in charge to discuss possible revisions with him. As a general rule, the series editor will confirm his tentative acceptance if the final manuscript corresponds to the original concept discussed, if the quality of the contribution meets the requirements of the series, and if the final size of the manuscript does not greatly exceed the number of pages originally agreed upon.

The manuscript should be forwarded to Springer-Verlag shortly after the meeting. In cases of extreme delay (more than six months after the conference) the series editors will check once more the timeliness of the papers. Therefore, the volume's editor(s) should establish strict deadlines, or collect the articles during the conference and have them revised on the spot. If a delay is unavoidable, one should encourage the authors to update their contributions if appropriate. The editors of proceedings are strongly advised to inform contributors about these points at an early stage.

The final manuscript should contain a table of contents and an informative introduction accessible also to readers not particularly familiar with the topic of the conference. The contributions should be in English. The volume's editor(s) should check the contributions for the correct use of language. At Springer-Verlag only the prefaces will be checked by a copy-editor for language and style. Grave linguistic or technical shortcomings may lead to the rejection of contributions by the series editors.

A conference report should not exceed a total of 500 pages. Keeping the size within this bound should be achieved by a stricter selection of articles and not by imposing an upper limit to the length of the individual papers.

Editors receive jointly 30 complimentary copies of their book. They are entitled to purchase further copies of their book at a reduced rate. As a rule no reprints of individual contributions can be supplied. No royalty is paid on Lecture Notes in Physics volumes. Commitment to publish is made by letter of interest rather than by signing a formal contract. Springer-Verlag secures the copyright for each volume.

The Production Process

The books are hardbound, and quality paper appropriate to the needs of the authors is used. Publication time is about ten weeks. More than twenty years of experience guarantee authors the best possible service. To reach the goal of rapid publication at a low price the technique of photographic reproduction from a camera-ready manuscript was chosen. This process shifts the main responsibility for the technical quality considerably from the publisher to the authors. We therefore urge all authors and editors of proceedings to observe very carefully the essentials for the preparation of camera-ready manuscripts, which we will supply on request. This applies especially to the quality of figures and halftones submitted for publication. In addition, it might be useful to look at some of the volumes already published.

As a special service, we offer free of charge LATEX and TEX macro packages to format the text according to Springer-Verlag's quality requirements. We strongly recommend that you make use of this offer, since the result will be a book of considerably improved technical quality.

To avoid mistakes and time-consuming correspondence during the production period the conference editors should request special instructions from the publisher well before the beginning of the conference. Manuscripts not meeting the technical standard of the series will have to be returned for improvement.

For further information please contact Springer-Verlag, Physics Editorial Department V, Tiergartenstrasse 17, W-6900 Heidelberg, FRG

Z. Švestka B. V. Jackson M. E. Machado (Eds.)

Eruptive Solar Flares

Proceedings of Colloquium No. 133
of the International Astronomical Union
Held at Iguazú, Argentina, 2-6 August 1991

Springer-Verlag
Berlin Heidelberg New York
London Paris Tokyo
Hong Kong Barcelona
Budapest

Editors

Zdeněk Švestka
Center for Astrophysics and Space Sciences
University of California at San Diego
La Jolla, CA 92093-0111, USA
and
SRON Utrecht, Sorbonnelaan 2
NL-3584 CA Utrecht, The Netherlands

Bernard V. Jackson
Center for Astrophysics and Space Sciences
University of California at San Diego
La Jolla, CA 92093-0111, USA

Marcos E. Machado
Department of Physics
University of Alabama in Huntsville
Huntsville, AL 35899, USA

ISBN 3-540-55246-4 Springer-Verlag Berlin Heidelberg New York
ISBN 0-387-55246-4 Springer-Verlag New York Berlin Heidelberg

Typesetting: Camera ready by author
Printing and binding: Druckhaus Beltz, Hemsbach/Bergstr.
58/3140-543210 - Printed on acid-free paper

DEDICATION

The participants unanimously agreed to dedicate these proceedings to Zdeněk Švestka, Co-Chairman of the Scientific Organizing Committee, in recognition of his fundamental contributions to the subject matter of the colloquium. Zdeněk's untiring drive to search for new clues, his youthful zest for new discoveries, his skill in organizing results in a self-consistent picture, and his ability to bring people together in campaigns, colloquia, and workshops, all serve as a model and a continuing source of inspiration to those involved in flare research.

PREFACE

IAU Colloquium 133, held at the Hotel Internacional Iguazú in the National Park of Iguazú, Argentina, 2 - 6 August 1991, had 73 registered participants from 18 countries. The program consisted of 18 invited reviews, 12 invited contributions, 24 contributed papers, and 24 posters. In addition to this program, there was a special 80-minute session called "Time Free for Bright Ideas", chaired by Einar Tandberg-Hanssen (MSFC Huntsville), which mainly concerned ideas for projects that might be realized in the late 1990s and in the first decade of the 21st century. One evening was devoted to movies on cancelling magnetic fields, filament eruptions and flares, made at the Big Bear and Udaipur Observatories (shown by Sara Martin (Caltech, Pasadena), Sylvia Livi (Porto Allegre) and Arvin Bhatnagar (Udaipur)). VLA movies were shown by Marcos Machado.

The scientific program was divided into 10 sessions, two of them in the evening, thus giving the participants more free time during daylight hours. Many informal discussions took part in the open air during the extended lunch breaks. Session 1 was concerned with the build-up and triggering of eruptive flares. Session 2 and evening session 3 centered on filament eruption, field opening and successive reconnection, and energy release and transport. In sessions 4 and 5 the flare impulsive phase and the formation of loops were discussed. Session 6 was concerned with large-scale coronal structures associated with eruptive flares in X-rays and radio waves. A discussion about mass ejections from flares in session 6 was continued in session 7. Evening session 8 was concerned with the terrestrial response to eruptive solar flares. The first two invited talks of session 9 summarized our knowledge of stellar flares while the rest of this session as well as session 10 were devoted to the presentation of plans for related observations, studies, and cooperative projects in the future. These projects included a discussion about SOLAR-A (Yohkoh, launched three weeks after this colloquium) given by its project scientist Yutaka Uchida (Tokyo). The achieved results and future prospects for the study of eruptive flares were summarized at the end of the colloquium by Peter Sturrock. The posters were divided into two sets and were briefly discussed in sessions 5 and 8.

The Scientific Organizing Committee consisted of E.W. Cliver (Boston), V. Gaizauskas (Ottawa), J.C. Hénoux (Meudon), B.V. Jackson (La Jolla, co-chairman), B.C. Low (Boulder), M.E. Machado (Buenos Aires/Huntsville), D.F. Neidig (Sacramento Peak), G. Poletto (Arcetri), E.R. Priest (St. Andrews), B.V. Somov (Moscow), R.T. Stewart (Sydney), P.A. Sturrock (Stanford), Z. Švestka (Utrecht/La Jolla, co-chairman), and S. Tsuneta (Tokyo). The Local Organizing Committee consisted of H.S. Ghielmetti (co-chairperson), A.M. Hernándes, M.E. Machado (CNIE/Huntsville), C.H. Mandrini, and M.G. Rovira (co-chairperson). With the exception of Machado, all are from IAFE, Buenos Aires.

We would like to thank the Local Organizing Committee for the excellent organization of the colloquium. Both the choice of the beautiful and extremely pleasant locale and the careful preparation of all sessions and associated activities greatly enhanced the meeting. We are greatly obliged to Marcos Machado at Huntsville for providing an efficient link to the LOC in Buenos Aires and for helping us with the editorial work.

Our thanks are also due to all the sponsors: the IAU (Commission 10), SCOSTEP, COSPAR, NASA, and CONICET.

Bernard V. Jackson and Zdeněk F. Švestka, 27 January 1992
CASS, University of California at San Diego,
Co-chairmen of the Scientific Organizing Committee of IAU Colloquium 133

Contents

3. Particle Acceleration and Radio Response

4. Flare-Associated Large-Scale Coronal Structures

5. Coronal Mass Ejections

6. Flare Stars

7. Future Projects

8. Poster Papers

Summary of the Colloquium

The following papers were presented at the Colloquium, but manuscripts were not submitted for publication in these proceedings:

Energetic Solar Flare X-Rays Observed by Ulysses and the Eruptive Phenomena in Solar Flares
S.R. Kane, K. Hurley, G. Vedrenne, J.C. Hénoux
Solar Flare Programs with the SOHO Observatory
B.H. Foing
The Hard X-Ray Spectrometer on the Argentine SAC-B Satellite
H. Ghielmetti, A.M. Hernandez, M.E. Machado, I. Nollmann, V. Mugherli, B.R. Dennis, and U. Desai
Objectives of the SIMURIS Observatory for Flare Studies
B.H. Foing, L.Dame, J.C. Vial, R. Rutten, and A. Thorne
The NASA Solar Probe Mission
B.T. Tsurutani and J.E. Randolph
Cooperative Projects (Invited)
M.E. Machado and A. Kiplinger

List of Participants

ACATTO, J. (Brazil)
ANTONINI, G. (Italy)
ANTONUCCI, E. (Italy)
BALL, L. (Australia)
BELVEDERE, G. (Italy)
BENZ, A. (Switzerland)
BHATNAGAR, A. (India)
BORNMANN, P.L. (U.S.A.)
CHIAN, A.C.L. (Brazil)
CHRISTENSEN-DALSGAARD, J. (Denmark)
CORREIA, E. (Brazil)
DENNIS, B.R. (U.S.A.)
ENOME, S. (Japan)
FALCHI, A. (Italy)
FERNANDES, F.C.R. (Brazil)
FORBES, T.G. (U.S.A.)
GAIZAUSKAS, V. (Canada)
GARCIA, H.A. (U.S.A.)
GÓMEZ, D.O. (U.S.A.)
GONZALEZ, W.D. (Brazil)
GOPALSWAMY, N. (U.S.A.)
GOSLING, J.T. (U.S.A.)
GRAETER, M. (Switzerland)
HÉNOUX, J.C. (France)
HERISTCHI, D. (France)
HERRMANN, R. (Switzerland)
HERNÁNDEZ, A. (Argentina)
HILDNER, E. (U.S.A.)
JACKSON, B.V. (U.S.A.)
KANE, S.R. (U.S.A.)
KARLICKÝ, M. (Czechoslovakia)
KAUFMANN, P. (Brazil)
KRÜGER, A. (Germany)
LINSKY, J. (U.S.A.)
LIVI, S.H.B. (Brazil)
MACHADO, M.E. (U.S.A.)
MANDRINI, C.H. (Argentina)
MARTENS, P.C.H. (U.S.A.)
MARTIN, S.F. (U.S.A.)
MAUAS, P.J.D. (Italy)
MELROSE, D.B. (Australia)
MONSIGNORI-FOSSI, B. (Italy)
MOORE, R. (U.S.A.)
MOSALAM SHALTOUT, M.A. (Egypt)
NICHOLLS, J. (Australia)
NOCI, G. (Italy)
OPHER, R. (Brazil)
PALLAVICINI, R. (Italy)
POHJOLAINEN, S. (Finland)
POLETTO, G. (Italy)
PRIEST, E.R. (United Kingdom)
RIEGER, E. (Germany)
REAMES, D.V. (U.S.A.)
ROSA, R.R. (Brazil)
ROVIRA, M.G. (Argentina)
RUST, D.M. (U.S.A.)
SCHMITT, J. (Germany)
SCHMIEDER, B. (France)
SERIO, S. (Italy)
SOLIMAN, M.A. (Egypt)
STEINOLFSON, R.S. (U.S.A.)
STEWARD, R.T. (Australia)
STOCKER, P.H. (South Africa)
STURROCK, P.A. (U.S.A.)
ŠVESTKA, Z. (USA/The Netherlands)
TANDBERG-HANSSEN, E. (U.S.A.)
TORELLI, M. (Italy)
TSURUTANI, B.T. (U.S.A.)
VAN DEN OORD, G.H.J. (The Netherlands)
VIAL, J.C. (France)
WEBB, D.F. (U.S.A.)
WU, S.T. (U.S.A.)
ZARRO, D.M. (U.S.A.)

HISTORY AND BASIC CHARACTERISTICS OF ERUPTIVE FLARES

Z. ŠVESTKA,
CASS, UCSD, CA, U.S.A. and SRON, Utrecht, The Netherlands

and

E.W. CLIVER,
Geophysics Directorate, Phillips Laboratory (USAF), Hanscom AFB, MA, U.S.A.

Abstract. We review the evolution of our knowledge and understanding of the eruptive (dynamic, two-ribbon) flare phenomenon. Starting with the first observation of a white-light flare by Carrington and Hodgson in 1859, we cover in succession the highlights: Hale's invention of the spectroheliograph in 1892 and the spectrohelioscope in 1926 started flare observations in Hα. The institution of a world-wide flare patrol brought significant advances in knowledge of flares in the 1930s and 1940s and new 'windows' were opened to observe flares at short (SID) and long (radio) wavelengths. In the 1950s and 1960s metric radio bursts were related to trapped energetic electrons and shocks, and two-ribbon flares were associated with energetic protons in space. Radio and X-ray observations gave evidence for two basic types of flare processes: an impulsive phase followed by a long-duration or gradual phase. It was found that flares were often preceded by filament activations, and growing loop prominence systems were recognized as the limb counterpart of two-ribbon disk flares. The early 1970s brought Skylab observations of coronal mass ejections (CMEs) and arcades of coronal soft X-ray loops above two-ribbon flares. In the mid-1970s, the Kopp-Pneuman reconnection model, based on configurations proposed earlier by Carmichael, Sturrock, and Hirayama, provided a framework in which the newly discovered CMEs could be related to the basic characteristics of two-ribbon flares. The 1980s brought key new results from SMM and Hinotori including images of hard X-ray flares and large-scale coronal structures associated with eruptive flares. In the conclusion, we summarize the basic characteristics of eruptive flares.

1. Introduction

We divide the history of flare research into three main periods. The first period from 1859-1934 spans the careers of Carrington and Hale. This period is notable for the relative lack of progress. The published 'record' of major flares for this 75 year interval encompasses only about 35 events, consisting of fortuitous observations of white-light flares, reports by early spectroscopists of reversals of line emission near sunspots, and, after 1892, flares observed with the Hale spectroheliograph. The spectrohelioscope developed by Hale during the 1920s was responsible for the rapid advance in the knowledge of flares that took place in the next era of flare research from 1935-1963. With the widespread use of the spectrohelioscope, the opening of new electromagnetic windows at short and long wavelengths, and the first observations of solar particles, this 'middle era' of flare research has a data survey and classification character that is well-captured by the book 'Solar Flares' by Smith and Smith (1963). The modern era, since 1963, is characterized by space observations and a trend toward synthesis indicated by the development of increasingly sophisticated and comprehensive models of the flare phenomenon.

In the following sections we will stress those aspects of flare research that apply specifically to 'eruptive flares', the topic of this Colloquium, but it should be kept in mind that the distinction

between eruptive and 'confined' or 'compact' flares (Pallavicini, Serio, and Vaiana, 1977; Švestka, 1986) is a relatively recent addition to the paradigm for understanding flares. In the concluding section we summarize the current picture of eruptive flares.

2. The Early Years of Flare Research, Carrington through Hale

The first recorded observation of a solar flare was made by R.C. Carrington in 1859 at his private observatory at Redhill, outside London. (For biographical information on Carrington, see Main (1859) and Anonymous (1875).) Carrington (1859) was engaged in his daily sunspot drawing in the forenoon on 1 September 1859 when he first noticed the flare (Figure 1). After confirming that it was not caused by stray light, he ran to find someone to verify the observation and when he returned 'within 60 seconds', he was 'mortified to find that it was already much changed and enfeebled.' The white-light emission was initially visible at points A and B and during the course of five minutes moved about 50 000 km to points C and D where it vanished as two rapidly fading dots of white light. Carrington expressed surprise that the 'conflagration' had in no way altered the appearance of the sunspot group which he had finished drawing before the occurrence. Fortunately, Carrington's observation was confirmed by Hodgson (1859), an amateur astronomer who was observing nearby. This event was almost certainly an eruptive flare based on its 'double ribbon' character (cf. Ellison, 1949) and the fact that it was followed within 18 hours by a severe geomagnetic storm. Carrington also noted a disturbance of the Kew magnetograms coincident with the flare but was reluctant to suggest a causal link between the flare and the geomagnetic activity. In fact, 78 years would pass before Bartels (1937) was able to provide the correct description of the prompt and delayed solar-terrestrial relationships manifested in this event.

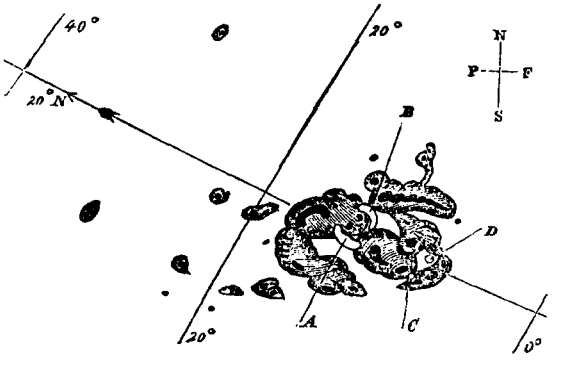

Fig. 1. The first reported flare, on 1 September 1859, observed by Carrington in white light.

Following the discovery by Janssen and Lockyer in 1868 that prominences could be viewed outside of eclipse using a spectroscope, prominence studies were the chief contributors to knowledge of eruptive solar phenomena in the 19th century. By 1871, Secchi and others had introduced a rudimentary but fundamental classification of prominences into active and quiescent types. Motions of prominences with speeds on the order of hundreds of km/s were observed above the limb through spectroscope slits (e.g., Fenyi, 1892) or deduced from Doppler shifts of spectral lines (Meadows, 1970, p. 70).

The lack of rapid progress in flare physics following Carrington's observation was due in part to the rarity of white-light flares. More to the point, the slow pace of flare research resulted from the lack of an instrument that could efficiently image flares in the narrow emission lines in which they are most prominent. Flares were occasionally observed with spectroscopes as 'brilliant reversals' in Hα when scientists placed the entrance slit over sunspot regions. Between 1869 and 1870, such reversals were reported by Secchi in Italy, Lockyer in England, and Young in the United States (Newton, 1940). In 1870, Young observed a two-ribbon flare on the disk through the widened slit of a spectroscope (Figure 2). Young thought that the flare ribbons were bright prominences observed on the disk. The invention of the spectroheliograph by G.E. Hale (1892a) and a related instrument by Deslandres made it possible for the first time to obtain images of the Sun in lines such as Hα or H and K of calcium. (For a biographical sketch of Hale, see Zirin (1968).) The basic principle of the spectroheliograph had originally been elucidated by Janssen in 1868. Two slits are used, the first isolates the part of the Sun's surface to be studied and the second isolates the spectral line forming the image. By moving the slits across a photographic plate in tandem, a monochromatic image of the entire Sun is built up.

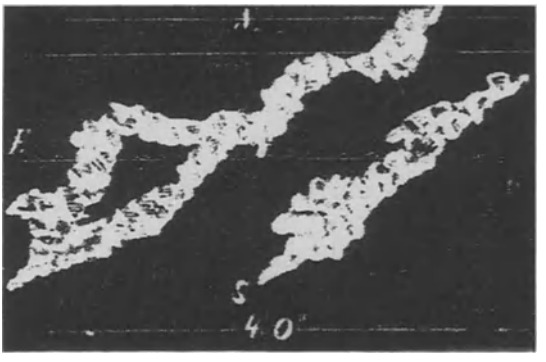

Fig. 2. Drawing by Young of a flare on 28 September 1870 observed through the widened slit of a spectroscope.

With the spectroheliograph, Hale obtained the first published photographs of a solar flare on 15 July 1892 (Figure 3). The image taken in the calcium K-line is grainy because of enlargement of the original plate (Hale, 1892b). Similar to the event reported by Carrington, the 15 July 1892 flare was observed in white light (Rudaux,1892) and was followed approximately one day later by a severe geomagnetic storm.

While the spectroheliograph represented a significant advance in solar observation, the instrument was cumbersome and not well-suited for observing rapidly changing phenomena such as flares (cf., Hale, 1926). Thus Hale developed the spectrohelioscope, an instrument that allowed the entire Sun to be scanned visually at selected wavelengths. The spectrohelioscope operated on the same principle as the spectroheliograph, except that the two slits were rapidly oscillated in tandem across the face of the Sun to give a continuous view of solar activity. The compelling nature of visual spectrohelioscopic observations is indicated by Hale's (1931) description of a large flare in January 1926 as 'the most remarkable solar phenomenon I have ever seen' - this coming after some 40 years of studying the Sun. Hale (1929) designed the spectrohelioscope to be an inexpensive instrument that could be used for patrol work and made arrangements to have the new instrument distributed to observatories around the world. At his urging, the

patrol was formalized under the auspices of the IAU and flares have been reported routinely since 1934. For the years prior to 1934, the major flare 'record' consists largely of lists compiled by Newton (1930, 12 'sudden and intense local brightenings of the Sun's surface'), Hale (1931, $\sim$ 20 'violent' solar eruptions), Newton (1940, seven cases of bright reversals of spectral lines). and Neidig and Cliver (1983, eight white-light flares). In all there are only $\sim$ 35 independent events on these lists.

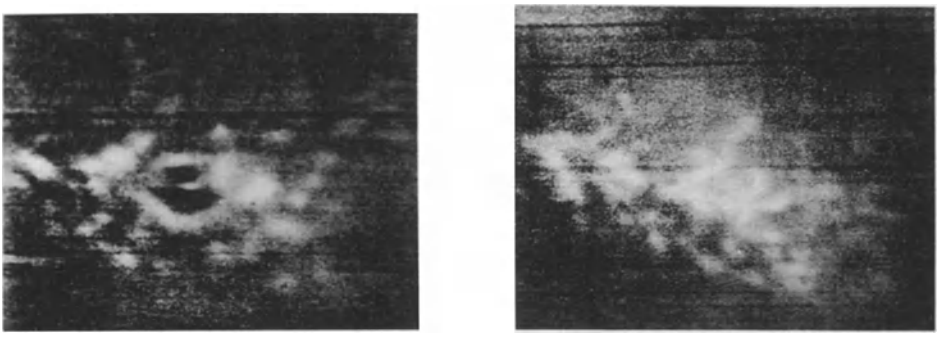

Fig. 3. The first published photographs of a flare, on 15 July 1892, taken by Hale in calcium K-line with the spectroheliograph. The left-hand frame at 1658 UT is shortly after flare onset, the right-hand frame at 1737 UT shows the maximum development.

Hale's 1931 paper entitled 'The Spectrohelioscope and Its Work, Part III. Solar Eruptions and Their Apparent Terrestrial Effects' represented a long overdue study of the connection between flares and geomagnetic storms suggested by Carrington's 1859 event. Given Hale's stature in the astronomical community, it also probably served to dispel doubts about the 'legitimacy' of solar-terrestrial studies lingering from Lord Kelvin's address to the Royal Society of London in 1892. In that address Lord Kelvin concluded that 'magnetic action of the Sun, or...hurricanes in his atmosphere' could not possibly be the source of magnetic storms at Earth (cf. Bartels, 1937; Sturrock, 1987).

3. Coming of Age as a Discipline, Systematic Observations and New Windows

Once the spectrohelioscope patrol began, knowledge of flares and their relationship with active regions and prominences advanced rapidly. McMath *et al.* (1937) reported a flare-associated ejection of prominence material with outward speed $\sim$ 700 km/s, greater than the escape velocity, that was visible to a height of 10^6 km and was followed by a 'fountain' type prominence (system of post-flare loops). Waldmeier (1938) documented the double-ribbon character of major flares and Giovanelli(1939) identified sunspot area and magnetic complexity as key variables for flare occurrence. Separation of flare ribbons, with typical speeds of 1-10 km/s, was noted by Dodson (1949) for double-ribbon flares on 8 and 10 May 1949. Direct comparisons of magnetograms with flare positions, first made by Bumba (1958) and Severny (1958), indicated that flare ribbons lie adjacent and parallel to neutral lines (cf., Ellison, McKenna, and Reid, 1961).

During the 1940s, the term 'flare' came into common usage, supplanting the previously used expression 'bright chromospheric eruption' (Richardson, 1944). While the term 'bright chromospheric eruption' is unwieldy, it retains an important aspect of certain events (mass motion) that is lost in the simpler term (cf., Dodson and Hedeman, 1968; Hudson, 1987).

In the decade following the establishment of the Hα patrol, several new 'windows' were opened to the observation of flares. In 1935, Dellinger noted that sudden disappearances of short-wave radio signals during that year occurred at intervals of approximately 54 days, twice the rotation period of the Sun, and suggested a solar origin. Within a few months, observers using Hale spectrohelioscopes confirmed this suggestion, opening up the study of flares and the ionosphere via sudden ionospheric disturbances (SIDs; Dellinger, 1937). For many years, SIDs were thought to result primarily from Lyman-α emission during flares, but rocket flight experiments in the 1950s and satellite measurements in the early 1960s showed that enhanced soft X-ray emission during flares was the principal cause of SIDs (Kreplin, Chubb, and Friedman, 1962).

A statistical study by Newton (1943) relating solar flares to geomagnetic storms gave early insights into the nature of coronal mass ejections (CMEs). Newton concluded that the semi-angle of the corpuscular stream associated with a solar flare could be as large as 45°, based on the locations of great flares that preceded intense storms. A full cone of 90° is consistent with measurements of the limb span of larger 'curved front' CMEs (Howard *et al.*, 1985). Newton obtained an average flare-to-storm delay time of slightly over a day, implying, in retrospect, peak transient wind speeds $\sim$ 1200 km/s, at the high end of *in situ* measurements of the solar wind during the past 25 years (Cliver, Feynman, and Garrett, 1990).

Appleton and Hey (1946) were the first to definitively associate enhanced radio emission with solar flares. Metric type II (Wild and McCready, 1950) bursts were discovered by Payne-Scott, Yabsley, and Bolton (1947) and attributed to disturbances (later identified with magneto-hydrodynamic shock fronts) moving through the corona with speeds $\sim$ 500-750 km/s. Type IV bursts identified by Boischot in 1957 gave evidence of outward propagating plasmoids. Apart from prominence eruptions observed in the Hα line, these 'moving' type IV bursts represent the first evidence of flare-associated mass ejections. Dodson, Hedeman, and Owren (1953) reported that major bursts at 200 MHz had an 'early' component occurring near flare onset and a second component beginning at or after the flare maximum, thereby anticipating the classification of metric radio emission into two distinct phases by Pick (1961) and Wild, Smerd, and Weiss (1963). Covington and Harvey (1958) presented evidence for two distinctive types of microwave bursts, impulsive and long-duration, and surmised that they represented thermal and nonthermal emissions, respectively. Today, the early metric component and impulsive microwave burst are identified with the flare flash phase (Ellison, 1946), and the delayed metric and long-enduring microwave emissions represent, in turn, evidence for particle acceleration and plasma heating, associated with prolonged energy release in eruptive flares.

Flare-associated 'cosmic ray' intensity increases at Earth were first reported for the flares of 28 March 1942, 7 February 1942, and 25 July 1946 (Forbush, 1946). The long durations of solar energetic particle (SEP) events, in comparison with the durations of associated flares (e.g., Meyer, Parker, and Simpson, 1956), has been problematical from the beginning of SEP observations. The traditional explanation following Reid (1964) to account for these long durations has been a brief injection of particles followed by diffusion over relatively short mean free paths, $<$0.1 AU at $\sim$ 10 MeV. A counter viewpoint is that particle acceleration in eruptive flares can occur in association with interplanetary shocks that are well-removed in space and time from the associated flare (see Reames, 1991, these Proceedings).

4. The Modern Era, Space Observations and Synthesis

In 1963, the *AAS-NASA Symposium on Solar Flares* (Hess, 1964) was a watershed meeting for the phenomenon that we call now eruptive flares. Kiepenheuer suggested that eruptive quiescent filaments should be viewed as 'soft' versions of two-ribbon flares. Kleczek arrived at

the fundamental conclusion that there is not enough plasma in the corona to condense into the loop prominences and that material must be transported from lower atmospheric layers into the loops. Avignon, Caroubalos, Martres, and Pick emphasized the close association of type IV radio bursts with two-ribbon flares. A key breakthrough at this Symposium was Petschek's model of field-line reconnection which, for the first time, made the reconnection process realistically applicable to flares. Finally, Carmichael presciently proposed the general magnetic configuration in which eruptive flares occur (Figure 4, upper left) and the relationship of eruptive flares with the yet-to-be-discovered coronal mass ejections.

Bruzek's landmark paper in 1964 established two basic tenets of the modern view of eruptive flares: (1) flare ribbons represent the chromospheric base of coronal loop prominence systems (post-flare loops), and (2) individual loops do not expand during such flares, rather the apparent growth of such systems is due to the formation of higher and higher loops while the lower ones fade in place. This fact, deduced from Hα data, was later confirmed by Skylab for loop systems observed in soft X-rays (Moore *et al.*, 1979) and by SMM in hard X-rays (Švestka *et al.*, 1987). The successive formation of higher temperature loops gave evidence that, in contrast to 'compact' flares (Pallavicini, Serio, and Vaiana, 1977), energy release in eruptive flares is not short-lived but continues for many hours.

The unique association of loop-prominence systems, type IV radio bursts (i.e. trapped accelerated electrons) and strong proton streams in space (by Ellison, McKenna, and Reid, 1961) with two-ribbon flares clearly indicated that this type of flare represented a special class of the flare phenomenon. Sturrock (1968) proposed the first quantitative model of such flares, invoking reconnection to account for particle acceleration, ejected plasma, and the formation of the two bright ribbons in the chromosphere (Figure 4, upper right).

Knowledge of ejections from flares increased substantially in the 1970s. Wave fronts generated in flares were critically summarized by Smith and Harvey (1971) and interpreted as shock waves by Uchida, Altschuler, and Newkirk (1973). During 1970 - 1973, 13 abrupt depletions of localized regions of the inner solar corona were detected by the Mark I coronameter at Mauna Loa (Hansen et al., 1974), and other coronal disturbances were observed by the NRL coronagraph on OSO-7 (as reported in Proceedings of the *IAU Symposium* **57** (Newkirk, 1974) by Brueckner (see also Tousey, 1973), and Stewart *et al.*) In 1973-1974, the coronagraph on Skylab obtained well-resolved photographs of coronal mass ejections (CMEs) (then called coronal transients, see MacQueen *et al.* in Newkirk, 1974). It was found that many CMEs are not associated with flares, but rather with eruptions of quiescent filaments (Gosling *et al.*, 1974). This gave impulse to the creation of the term *dynamic* (Švestka, 1986) or *eruptive flare* (following Priest's suggestion): it includes not only two-ribbon flares but all instabilities related to erupting filaments and any coronal configuration of a similar nature.

The above discoveries stimulated new efforts at modelling erupting flares. First Hirayama (1974) modelled the flare-associated dynamic events (Figure 4, middle), including evaporation of chromospheric gas into coronal loops. His pioneering work was followed two years later by the widely accepted Kopp and Pneuman (1976) model of field opening and sequentially reconnecting field lines (Figure 4, below). We will talk here about the K-P model, but one should not forget the earlier work of Carmichael, Sturrock, and Hirayama.

The K-P model successfully explained the successive formation of new loops, the velocity pattern of the growth of the loops and the separation of the bright ribbons, as well as the long-lasting release of energy. Sakurai's (1985) modelling of X-ray loops with the current-free approximation provided evidence that the magnetic structure of the loops had to be greatly simplified shortly before their appearance, most likely through field-line reconnection.

The original K-P model,however, also had several deficiences.

First, it did not specify any reason for the initial opening of the magnetic field structure. Only later years brought suggestions for the opening mechanism: internal, through loss of equilibrium (Martens and Kuin, 1989) or MHD instability (Sturrock, 1989; Priest and Forbes, 1990), or external, through newly emerging flux (Rust, Nakagawa, and Neupert, 1975), flux cancellation (Van Ballegooijen and Martens, 1989), or slow-mode waves (Rust and Švestka, 1979).

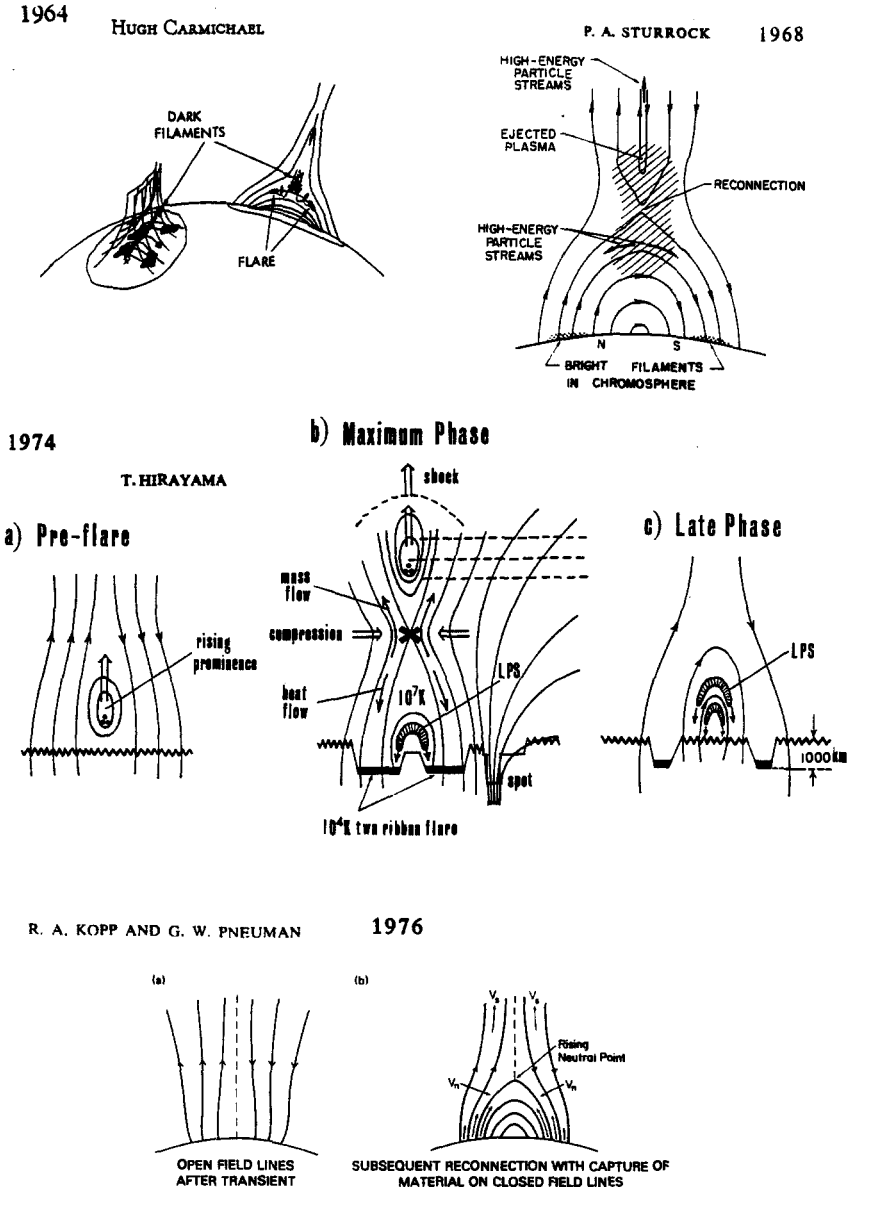

Fig. 4. The basic coronal configuration first proposed for eruptive flares by Carmichael (in Hess, 1964, *upper left*), later improved by Sturrock (1968, *upper right*), Hirayama (1974, *middle*), and eventually by Kopp and Pneuman (1976, *bottom*).

Second, the loop temperatures derived by K-P seemed high enough at the time when the model was proposed, but became too low, by almost an order of magnitude, when hard X-ray data became available. K-P supposed that a gas-dynamic shock propagates downwards from the reconnection site and heats the upflowing plasma to 3 - 4 million degrees. In 1983 Cargill and Priest showed that, in the context of the K-P model, one can heat the loops to the observed temperatures in excess of 20 million degrees by slow MHD shocks.

Third, the original K-P process failed to bring enough plasma from the chromosphere into the coronal loops to explain their observed density, at times greater than 10^{12} cm^{-3} (Heinzel and Karlický, 1987), and the total mass between 10^{16} and 10^{17} g established earlier by Kleczek (in Hess, 1964). Only improved theories of the evaporation process, proposed by Forbes and Malherbe (1986) and, in several studies, by Canfield, Fisher, and Gunkler, could keep the K-P model valid. Following Fisher (1986) one can distinguish two types of evaporation: an explosive one, if the chromosphere is heated by particle flows, and a non-explosive evaporation through conduction. The explosive evaporation occurs during the impulsive phase, whereas later on, when the 'post'-flare loops are formed, only the conductive evaporation is active, propagating at 0.2-0.4 of the sound speed. This agrees very well with evaporation speeds actually observed in a loop system by Schmieder *et al.* (1987).

Thus we conclude that the K-P model, with the modifications mentioned above, can adequately explain eruptive flare processes.

In 1982, (Švestka *et al.*, 1982a), using HXIS observations from SMM, discovered X-ray giant post-flare arches above eruptive flares. The giant arches represent the lowest and most dense parts of stationary type IV bursts and, later on, type I radio noise storms. It seems clear that the two structures in Figure 5, respectively observed by Wild (1969) at Culgoora at metric radio waves and by HXIS on SMM below 3.5 Å X-rays, are essentially the same phenomenon. Similar and probably related structures were also observed on radio waves by other authors, e.g. Gopalswamy and Kundu (1987). Kopp and Poletto (1990) demonstrated (as Sakurai did for 'post'-flare loops) that the arches can be fit by a current-free field. This implies that the arches also form through field-line reconnection, but different authors disagree so far as to where, when, and why this reconnection happens.

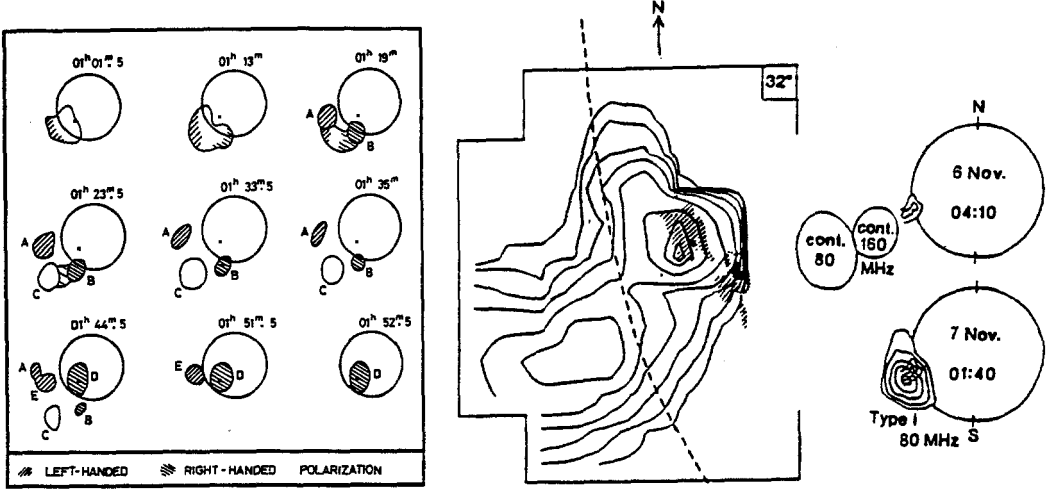

Fig. 5. *Left*: Wild's (1969) images of moving (A,B,C) and stationary (D) type IV bursts on metric radio waves. —it Middle: HXIS image of the giant arch of 6 November 1980 in 3.5 - 5.5 keV X-rays. (*Dashed curve*: solar limb.) *Right*: Type IV burst associated with this arch early on November 6 and type I noise storm above the arch on November 7 (Švestka *et al.*, 1982b).

In some eruptive flares with long-lasting X-ray bursts the X-ray spectrum progressively hardens. This was observed by ISEE-3 (Vilmer, Kane and Trottet, 1982), Hinotori (e.g. Takakura *et al.*, 1984), as well as by SMM (e.g. Cliver *et al.*, 1986). This again points to a magnetic trap above the flare site, in which the energy-dependent collisional loss of confined electrons causes the hardening (Tsuneta, 1983).

In concluding this necessarily brief review of the modern era of eruptive flare research, we mention recent studies of CME timings (e.g., Harrison *et al.*, 1990; cf., Smith and Ramsey, 1964) and size scales (Kahler *et al.*, 1989) relative to flares which, when coupled with analyses of the energy contained in flare mass motions (e.g., Webb *et al.*, 1980), indicate that the 'flare' part of 'eruptive flares' may be properly viewed as a consequence of the 'eruptive' part. The evolution of our understanding of the relationship between eruptive flares and CMEs is reviewed by Kahler (1992).

5. Conclusions

In conclusion, we want to emphasize the basic characteristics of eruptive flares as we understand them (we are aware that there is not unanimous agreement on this question, but that's one of the reasons why the Colloquium was held).

The preflare magnetic field in the Carmichel/Sturrock/Hirayama/Kopp and Pneuman configuration becomes unstable (due to an instability or an outer trigger), opens, and the open field lines subsequently reconnect. A dark filament, if present, manifests the field opening by its eruption and an associated CME may propagate into interplanetary space. The field reconnection is manifested as the sequential appearance of progressively higher flare loops formed at temperatures in excess of 20 million K, and by continuous energy release, lasting for many hours. In many events, post-flare coronal arches brighten for tens of hours in the corona following eruptive flares; these arches appear to be the lowest and densests parts of magnetic traps above the flare sites which, in their higher parts, produce moving (CME-associated) and stationary (arch-associated) type IV radio bursts; the stationary bursts gradually evolve into radio noise storms.

The consequences of the field-line opening depend very much on the strength of the involved magnetic field. In very old remnants of active regions, eruptions of quiescent filaments produce *disparitions brusques*, without any chromospheric brightenings; in somewhat stronger fields a few Hα bright patches appear, which eventually merge into two bright Hα ribbons when the field opens in an (even spotless) active region. These ribbons, parallel to the zero line, become very bright in *two-ribbon flares* which appear in fully developed regions; the most energetic of them are the *proton* or *cosmic ray flares*. Because the basic process is the same in all these phenomena, we call them collectively **eruptive flares**. All eruptive flares, from the disparitions brusques to the cosmic-ray flares, may be associated with **mass ejections** in the solar corona.

References

Anonymous: 1875, *Monthly Notices Roy. Astron. Soc.* **36**, 137.
Appleton, E.V. and Hey, J.S.: 1946, *Phil Mag.* ser. 7, **37**, 73.
Bartels, J.: 1937, *Terr. Mag. and Atmos. Elect.* **42**, 235.
Boischot, A.: 1957, *Compt. Rend. Acad. Sci. Paris* **244**, 1326.
Bruzek, A.: 1964, *Astrophys. J.* **140**, 746.
Bumba, V.: 1958, *Izv. Krymsk. Astrofiz. Obs.* **19**, 105.

Cargill, P.J. and Priest, E.R.: 1983, *Astrophys. J.* **266**, 383.
Carrington, R.C.: 1859, *Monthly Notices Roy. Astron. Soc.* **20**, 13.
Cliver, E.W., Feynman, J., and Garrett, H.B.: 1990, *J. Geophys. Res.* **95**, 17103.
Cliver, E.W., Dennis, B.R., Kiplinger, A.L., Kane, S.R., Neidig, D.F., Sheeley, N.R., Jr., and Koomen, M.J.: 1986, *Astrophys. J.* **305**, 920.
Covington, A.E. and Harvey, G.A.: 1958, *J. Roy. Astron. Soc. Canada* **52**, 161.
Dellinger, J.H.: 1935, *Phys. Rev.* **48**, 705.
Dellinger, J.H.: 1937, *Terr. Mag. and Atmos. Elect.* **42**, 49.
Dodson, H.W.: 1949, *Astrophys. J.* **110**, 382.
Dodson, H.W. and Hedeman, E.R.: 1968, *Nobel Symp.* **9**, 37.
Dodson, H.W., Hedeman, E.R., and Owren, L.: 1953, *Astrophys. J.* **118**, 169.
Ellison, M.A.: 1946, *Monthly Notices Roy. Astron. Soc.* **106**, 500.
Ellison, M.A.: 1949, *Monthly Notices Roy. Astron. Soc.* **109**, 3.
Ellison, M.A., McKenna, S.M.P., and Reid, J.H.: 1961, *Dunsink Obs. Publ.* **1**, No. 3, p. 53.
Fenyi, J.: 1892, *Astron. Astrophys.* **11**, 63.
Fisher, G.H.: 1986, *Lecture Notes in Physics* **255**, 53.
Forbes, T.G. and Malherbe, J.M.: 1986, *Astrophys. J.* **302**, L67.
Forbush, S.E.: 1946, *Phys. Rev.* **70**, 771.
Giovanelli, R.G.: 1939, *Astrophys. J.* **89**, 555.
Gopalswamy, N. and Kundu, M.R.: 1987, *Solar Phys.* **111**, 347.
Gosling, J.T., Hildner, E., MacQueen, R.M., Munro, R.H., Poland, A.I., and Ross, C.L.: 1974, *J. Geophys. Res.* **79**, 4581.
Hale, G.E.: 1892a, *Astron. Astrophys.* **11**, 407.
Hale, G.E.: 1892b, *Astron. Astrophys.* **11**, 917.
Hale, G.E.: 1926, *Proc. Nat. Acad. Sci.* **12**, 286.
Hale, G.E.: 1929, *Astrophys. J.* **70**, 265.
Hale, G.E.: 1931, *Astrophys. J.* **73**, 379.
Hansen, R.T., Garcia, C.J., Hansen, S.F., and Yasukawa, E.: 1974, *Publ. Astron. Soc. Pacific* **86**, 500.
Harrison, R.A., Hildner, E., Hundhausen, A.J., Sime, D.G., and Simnett, G.M.: 1990, *J. Geophys. Res.* **95**, 917.
Heinzel, P. and Karlický, M.: 1987, *Solar Phys.* **110**, 343.
Hess, W.N. (ed.): 1964 *AAS-NASA Symposium on the Physics of Solar Flares*, NASA-SP 50.
Hirayama, T.: 1974, *Solar Phys.* **34**, 323.
Hodgson, R. 1859, *Monthly Notices Roy. Astron. Soc.* **20**, 14.
Howard, R.A., Sheeley, N.R., Jr., Koomen, M.J., and Michels, D.J.: 1985, *J. Geophys. Res.* **90**, 8173.
Hudson, H.S.: 1987, *Solar Phys.* **113**, 1.
Kahler, S.W.: 1992, *Ann. Rev. Astron. Astrophys.* (in press).
Kahler, S.W., Sheeley, N.R., Jr., and Liggett, M.A.: 1989, *Astrophys. J.* **344**, 1026.
Kopp, R.A. and Pneuman, G.W.: 1976, *Solar Phys.* **50**, 85.
Kopp, R.A. and Poletto, G.: 1990, *Solar Phys.* **127**, 267.
Kreplin, R.W., Chubb, T.A., and Friedman, H.: 1962, *J.Geophys. Res.* **67**, 2231.
McMath, R.R., Pettit, E., Sawyer, H.E., and Brodie, J.T.: 1937, *Pub. Astron. Soc. Pacific* **49**, 305.
Main, R.: 1859, *Mem. Roy. Astron. Soc* **19**, 161.
Martens, P.C.H. and Kuin, N.P.M.: 1989, *Solar Phys.* **122**, 263.
Meadows, A.J.: 1970, *Early Solar Physics*, Pergammon Press, London.
Meyer, J.P., Parker, E.N., and Simpson, J.A.: 1956, *Phys. Rev.* **104**, 768.

Moore, R., McKenzie, D.L., Švestka, Z. Widing, K.G., and 12 coauthors: 1979, in P.A. Sturrock (ed.), *Skylab Solar Workshop II*, p. 341.
Neidig, D.F. and Cliver, E.W.: 1983, *A Catalog of Solar White Light Flares (1859 - 1982)*, AFGL-TR-83-0257.
Newkirk, G. (*ed.*): 1974, *Coronal Disturbances, IAU Symposium* **57**, Surfer's Paradise.
Newton, H.W.: 1930, *Monthly Notices Roy. Astron. Soc.* **90**, 820.
Newton, H.W.: 1940, *J. Brit. Astron. Assoc.* **50**, 273.
Newton, H.W.: 1943, *Monthly Notices Roy. Astron. Soc.* **103**, 244.
Pallavicini, R., Serio, S., and Vaiana, G.S.: 1977, *Astrophys. J.* **216**, 108.
Payne-Scott, R., Yabsley, D.E., and Bolton, J.G.: 1947, *Nature* **160**, 256.
Pick, M.: 1961, *Ann. d'Astrophys.* **24**, 183.
Priest, E.R. and Forbes, T.G.: 1990, *Solar Phys.* **126**, 319.
Reames, D.V.: 1991 (these Proceedings).
Reid, G.C.: 1964, *J. Geophys. Res.* **69**, 2659.
Richardson, R.S.: 1944, *Proc. Astron. Soc. Pacific* **56**, 156.
Rudaux, L.: 1892, *L'Astronomie* **11**, 342.
Rust, D.M. and Švestka, Z.: 1979, *Solar Phys.* **63**, 279.
Rust, D.M., Nakagawa, Y., and Neupert, W.M.: 1975, *Solar Phys.* **41**, 397.
Sakurai, T.: 1985, *Solar Phys.* **95**, 311.
Schmieder, B., Forbes, T.G., Malherbe, J.M., and Machado, M.E.: 1987, *Astrophys. J.* **317**, 956.
Severny, A.B.: 1958, *Izv. Krymsk. Astrofiz. Obs.* **20**, 22.
Smith, S.F. and Harvey, K.L.: 1971, in J. Macris (ed.), *Physics of the Solar Corona*, p. 156.
Smith, S.F. and Ramsey, H.E.: 1964, *Zs. f. Astrophys.* **60**, 1.
Smith, H.J. and Smith, E.v.P.: 1963, *Solar Flares*, The Macmillan Co., New York.
Sturrock, P.A.: 1968, *IAU Symp.* **35**, 471.
Sturrock, P.A.: 1987, *Solar Phys.* **113**, 13.
Sturrock, P.A.: 1989, *Solar Phys.* **121**, 387.
Švestka, Z.: 1986, in D.F. Neidig (ed.), *The Lower Atmosphere of Solar Flares*, p. 332.
Švestka, Z., Stewart, R.T., Hoyng, P., van Tend, W., Acton, L.W., Gabriel, A.H., Rapley, C.G., and 8 coauthors: 1982a, *Solar Phys.* **75**, 305.
Švestka, Z., Dennis, B.R., Pick, M., Raoult, A., C.G. Rapley, Stewart, R.T., and Woodgate, B.E.: 1982b, *Solar Phys.* **80**, 143.
Švestka, Z., Fontenla, J.M., Machado, M.E., Martin, S.F., Neidig, D.F., and Poletto, G.: 1987, *Solar Phys.* **108**, 237.
Takakura, T., Ohki, K., Sakurai, T., Wang, J.L., Xuan, J.Y., Li, S.C., and Zhao, R.Y.: 1984, *Solar Phys.* **94**, 359.
Tousey, R.: 1973, *Space Res.* **13**, 48.
Tsuneta, S.: 1983, Thesis, University of Tokyo.
Uchida, Y., Altschuler, M.D., and Newkirk, G.: 1973, *Solar Phys.* **28**, 495.
Van Ballegooien, A.A. and Martens, P.C.H.: 1989, *Astrophys. J.* **343**, 971.
Vilmer, N., Kane, S.R., and Trottet, G.: 1982, *Astron. Astrophys.* **108**, 306.
Waldmeier, M.: 1938, *Zs. f. Astrophys.* **16**, 276.
Webb, D.F., Cheng, C.-C., Dulk, G.A., Edberg, S.J., Martin, S.F., McKenna-Lawlor, S., and McLean, D.J.: 1979, in P.A. Sturrock (ed.), *Skylab Solar Workshop II*, p. 471.
Wild, J.P.: 1969, *Solar Phys.* **9**, 260.
Wild, J.P., and McCready, L.L.: 1950, *Australian J. Sci. Res.* A **3**, 387.
Wild, J.P., Smerd, S.F., and Weiss, A.A.: 1963, *Ann. Rev. Astron. Astrophys.* **1**, 291.
Zirin, G.E.: 1968, *Solar Phys.* **5**, 435.

1.

PREFLARE SITUATION
AND
FLARE ONSET

Related poster papers in Chapter 8:

S.F. Martin (Extended Abstract)

B. Schmieder, K.P. Dere, and J.E. Wiik

P.L. Bornmann and D. Shaw

E. Correia, P. Kaufmann, and F.M. Strauss (Extended Abstract)

A. Falchi, R. Falciani, and L.A. Smaldone (Extended Abstract)

K. Galsgaard and Å. Nordlund

BASIC MAGNETIC CONFIGURATION AND ENERGY SUPPLY PROCESSES FOR AN INTERACTING FLUX MODEL OF ERUPTIVE SOLAR FLARES

E R Priest
Mathematical and Computational Sciences Department
The University, St Andrews, KY16 9SS, Scotland, UK

Abstract

A review is given of our current understanding of: the basic magnetic configuration of a flare, including loop and arcade structures, prominence models and interactions of separate flux systems; the process of preflare energy storage in excess of potential due to photospheric motions; the conditions for flare occurrence, including shear in the corona and complexity and the roles of spot motions, flux cancellation and prominences; theories for eruption by magnetic nonequilibrium. In the course of this, the elements of a new Interacting Flux Model for flares are outlined.

1. Introduction

What is the basic magnetic configuration for a flare? How is the energy supplied? Why does the flare start? These are fundamental questions on which much progress has been made since Zdenek Svestka wrote his classic monograph on Solar Flares, in which he reviewed our knowledge comprehensively and pointed many of us in the right directions 15 years ago. The answers have been coming partly from observations and partly from MHD theory (e.g. Heyvaerts and Hagyard, 1991).

Wherever the length-scale is much larger than a mean-free path $\lambda_{mfp} = 300\ (T_c/10^6 K)^2\ (n_c/10^{17}\ m^{-3})^{-1}$ m, which is typically 300m, or even an ion gyroradius $\rho_i = 0.1\ (T/10^6 K)^{\frac{1}{2}} (B/100G)^{-1}$ m, which is typically 0.1 m, and the flow speed is much less than the speed of light (300 Mm s^{-1}), the behaviour of solar plasma is governed by the equations of magnetohydrodynamics, which describe mathematically several physical processes. The induction equation

$$\frac{\partial \mathbf{B}}{\partial t} = \nabla \times (\mathbf{v} \times \mathbf{B}) + \eta \nabla^2 \mathbf{B} \qquad (1)$$

shows how the magnetic field changes in time due to transport of magnetic field lines with the plasma and their diffusion through the plasma. The latter process only occurs effectively in narrow regions smaller than, say, 10km in width, but such regions are needed for the conversion of magnetic energy to other forms. The equation of motion

$$\rho \frac{d\mathbf{v}}{dt} = -\nabla p + \mathbf{j} \times \mathbf{B} + \rho \mathbf{g} \qquad (2)$$

describes how plasma is accelerated by the forces of pressure gradient, magnetic field and gravity, where

$$\mathbf{j} = \nabla \times \mathbf{B}/\mu \quad \text{and} \quad \mathbf{E} = \mathbf{v} \times \mathbf{B} + \mathbf{j}/\sigma \qquad (3), (4)$$

These are supplemented by equations of continuity and energy.

It should be noted that the plasma velocity ($\mathbf{v}$) and magnetic field ($\mathbf{B}$) are the primary variables, while the electric current ($\mathbf{j}$) and field ($\mathbf{E}$) are secondary and may be derived by (3) and (4) from $\mathbf{v}$ and $\mathbf{B}$ if required; they contain less information than $\mathbf{v}$ and $\mathbf{B}$ and, for

instance, say nothing about the connectivity and topology of the magnetic field. Regions of high magnetic gradient ($\nabla \times \mathbf{B}$) are regions of high current and so one can certainly talk about large-scale currents, provided it is realised that they are created by the above MHD processes rather than, as in the laboratory, being driven by electric fields.

Another point is that the MHD equations in their fullness are impossible to solve. They are three-dimensional, time-dependent and nonlinear, so that even if you were able to solve them numerically you would not be able to understand the results. We need to simplify them - to construct mathematical models in which the physical processes we want to investigate are isolated. So, for a particular model, you should ask - what are the physical assumptions, the initial and boundary conditions? Are they justifiable? The skill of the theorist is to choose assumptions that make the resulting equations both tractable and physically important.

Compare the sizes of the terms in equation (2), namely $\rho v^2/L$, p/L, $B^2/(\mu L)$ and ρg in order of magnitude. Thus, if $v^2 << c_S^2 = p/\rho$ and $v^2 << v_A^2 = B^2/(\mu\rho)$, so that the flow speed is much smaller than both the isothermal sound speed (c_S) and the Alfven speed (v_A), then equation (2) reduces to the equation of magnetohydrostatics

$$0 = -\nabla p + \mathbf{j} \times \mathbf{B} + \rho\, \mathbf{g}, \qquad (5)$$

which can in principle describe a static preflare magnetic configuration. If also the plasma beta $\beta = p/[B^2/(2\mu)] = 3.5 \times 10^{-4}\ (n/10^{15}\ m^{-3})\ (T/10^6 K)\ (B/100G)^{-2}$ is much smaller than unity, then ∇p is negligible. If the height of our structure is much smaller than the scale-height $H = 50\ (T/10^6 K)$ Mm, then gravity is negligible and the force-balance reduces to the basic equation

$$\mathbf{j} \times \mathbf{B} = \mathbf{0} \qquad (6)$$

for a force-free field where $\mathbf{j} = \nabla \times \mathbf{B}/\mu$. Using (3) it may be rewritten as

$$-\nabla (B^2/(2\mu)) + (\mathbf{B}.\nabla)\ \mathbf{B}/\mu = 0$$

representing a balance between a magnetic pressure gradient and a magnetic tension force.

Several points may be noted about equation (6), which is still three-dimensional and nonlinear and so very complicated. It implies that the electric current is parallel to the magnetic field; it is not driven by the electric field but is determined from the magnetic field physically by force-balance and boundary footpoint locations. The ratio of current to magnetic field is a function $\alpha(x,y,x)/\mu$ of position. Thus

$$\nabla \times \mathbf{B} = \alpha\, \mathbf{B} \qquad (7)$$

and the divergence of (6) gives $\mathbf{B}.\nabla\, \alpha = 0$, so that α is constant along each field line. If α takes the same value on all field lines and so is homogeneous, the curl of (7) reduces to the standard equation

$$\nabla^2 \mathbf{B} = -\alpha^2 \mathbf{B} \qquad (8)$$

for a linear force-free field; solutions to (8) are known as "constant-α" solutions.

The aims of MHD theory in tackling the solar flare phenomenon are: firstly, to describe the preflare magnetic configuration and evolution and determine why the flare begins; and, secondly, to model the process of energy release by reconnection and describe the accompanying dynamic plasma phenomena such as the eruption and mass motions. My aim is to describe progress on the first question, while Terry Forbes will describe the second in his review.

2. Basic Magnetic Configuration

It was initially realised that in the photosphere and chromosphere a flare occurs near a sunspot, a region of strong magnetic field. Later it was stressed that in particular it takes place in complex sunspot groups and near an active-region prominence. A similar refinement in understanding of the coronal part of a flare has developed: the Skylab observations showed the coronal structure to be a loop, whereas more recently SMM, VLA and NIXT results have revealed complex structures with several interacting loops. There are many ways of modelling theoretically the equilibrium configuration or parts of it, as follows.

2.1 A loop

The building blocks of the closed corona are coronal loops. The simplest way to model a loop is to neglect its curvature and regard it as a cylindrical flux tube with field components $(0, B_\phi(R), B_z(R))$ in cylindrical coordinates satisfying (6) which reduces to

$$\frac{d}{dR}\left(\frac{B^2}{2}\right) + \frac{B_\phi^2}{R} = 0. \qquad (9)$$

Alternatively, one may include curvature but regard the flux tube as thin and in equilibrium between magnetic buoyancy and magnetic tension (Parker, 1979; Browning and Priest, 1984). There is as yet no good analytical, three-dimensional model, but numerical methods have proved very useful (Sakurai, 1989; Steinolfson, 1990) and a review of flux tube equilibria has recently been given (Priest, 1990).

2.2 An arcade

There is a standard linear force-free model for a coronal arcade, namely

$$(B_x, B_y, B_z) = B_0\, e^{-\ell z}\left(\frac{\ell}{k}\cos kx, \frac{\alpha}{k}\cos kx, -\sin kx\right), \qquad (10)$$

where $\ell^2 = \alpha^2 - k^2$ and the z-axis is vertical. As α increases, so the field lines become more sheared. Alternatively, an arcade may be modelled as a cylindrically symmetric structure whose field components satisfy (9) with the z-axis horizontal. Also, numerical models for arcades have been constructed (Sturrock and Woodbury, 1967 and many articles by Wu and Klimchuk).

2.3 Prominence Models

As we shall see, a prominence occupies a central part of the preflare configuration. Prominence models may be classified as having either Normal Polarity or Inverse Polarity (Priest, 1989). The former include the Kippenhahn-Schlüter and Hood-Anzer (1990) models and the latter include the Kuperus-Raadu and Ridgway-Priest (1991) model, which is the first self-consistent, nonsingular solution of inverse polarity.

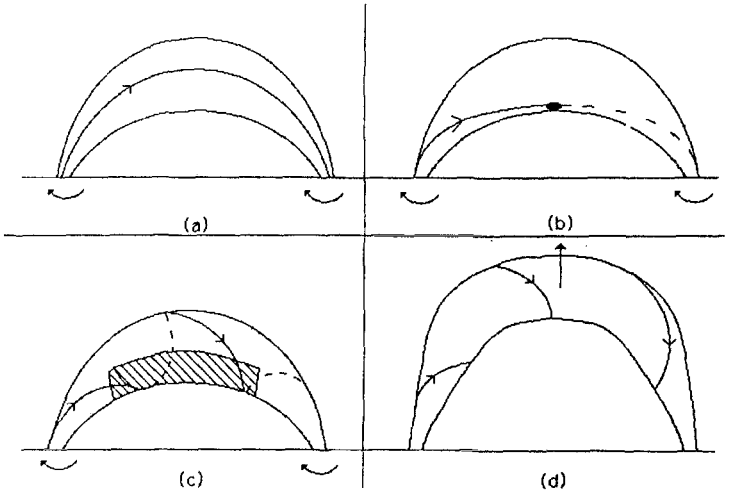

Figure 1. The Twisted Flux Tube model showing (a) an initial tube, (b) prominence formation, (c) prominence growth and (d) eruption.

The Twisted Flux Tube Model (Priest, Hood and Anzer, 1989) gave a solution for prominence plasma supported in a flux tube and suggested that, when an initial large flux tube has sufficient twist, there is a dip at its summit, and so a prominence may start to form. As the twist increases, so the prominence grows in length until eventually the twist is so large that it erupts (Figure 1). The twist can in principle be produced either by Coriolis forces twisting up the ends or by flux cancelation (Martin et al 1985; Van Ballegooijen and Martens, 1989; Ridgway and Priest, 1991), as indicated in Figure 2, although the latter process is much more likely in practice.

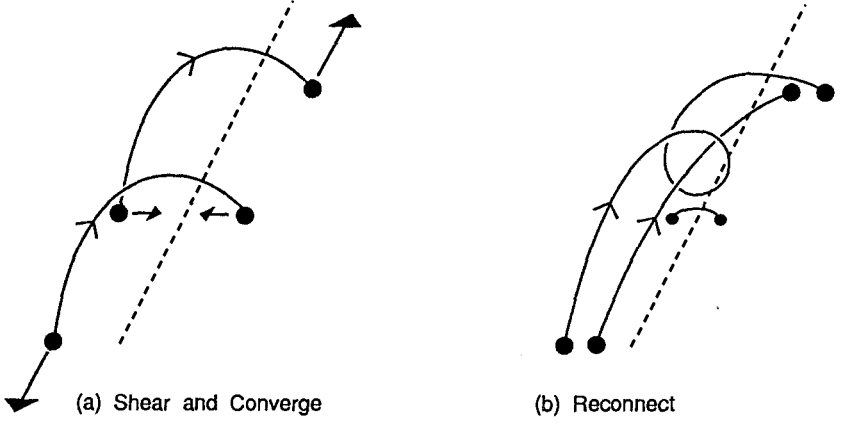

Figure 2. Formation of twist by (a) shear and convergence followed by (b) reconnection.

2.4 Interacting Flux

Two-dimensional models of the interaction between neighbouring flux systems have been presented by Priest and Raadu (1975) for two equal bipoles and by Tur and Priest (1976) for unequal bipoles and for the emergence of a bipole into an overlying field. In three dimensions an X-point becomes a separator curve and the separatrix curves (the field lines which intersect at the X-point) become separatrix surfaces separating the distinct flux systems (Figure 3), as studied by Sweet (1958), Baum et al (1979), Machado et al (1983), Gaizauskas (1989).

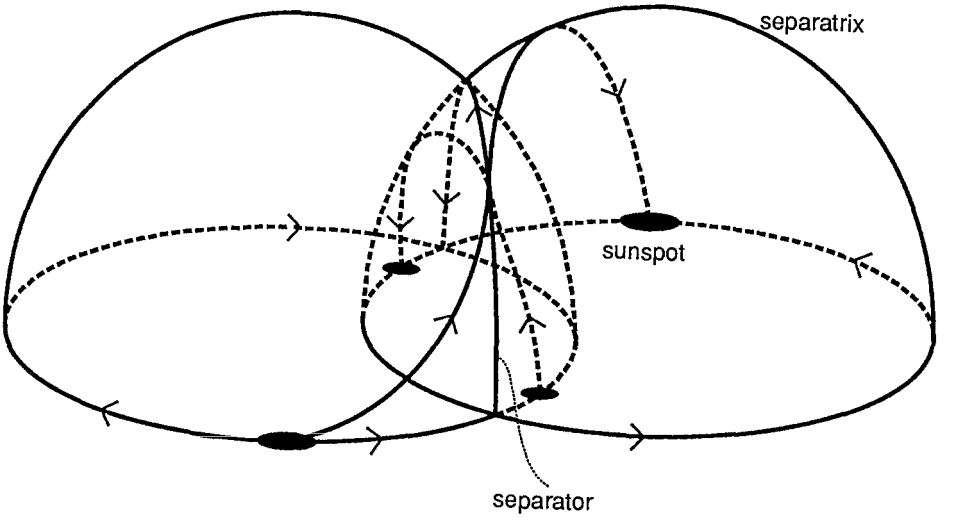

Figure 3. The topology above four sunspots.

Henoux and Somov (1987) modelled such a structure with 4 monopole sources, and Gorbachev and Somov (1988) found an example where field lines from a small region near the separator end in the Hα ribbons. Also Mandrini et al (1991) and Demoulin et al (1991) have instead modelled a flaring configuration with 4 or 17 magnetic dipoles with the flux and range as parameters, and again they find the Hα kernels are located on the separatrices - ie., the feet of the fieldlines that reconnect at the separator (Figure 4). Note that it is the MHD interaction between neighbouring flux systems that drives reconnection and therefore produces a current along the separator, rather than the tail (the current) wagging the dog (the magnetic field).

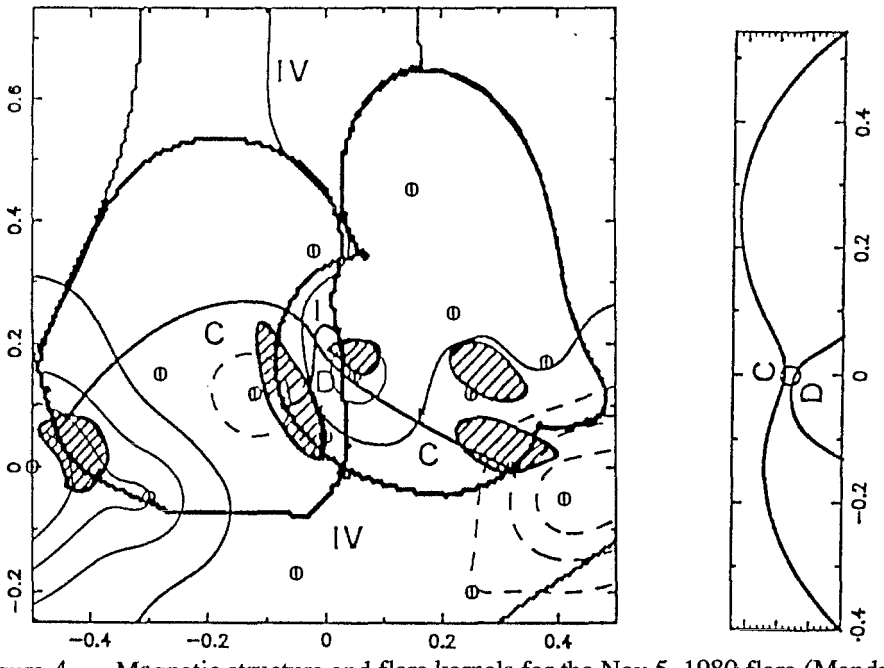

Figure 4. Magnetic structure and flare kernels for the Nov 5, 1980 flare (Mandrini et al)

3. Energy Storage

The energy for a flare is certainly of magnetic origin. It can only come from distortions away from a potential configuration. Associated with these distortions, there is free magnetic energy and currents flowing in the corona. The same is true for the MHD Turbulence Mechanism for heating the corona (Heyvaerts and Priest, 1984: 1991; Van Ballegooijen, 1986), and so maybe there is a continuity in the sequence from big flares to small flares to miniflares to microflares to nanoflares or turbulent coronal heating events. The differences could be the time to build up the free energy or the spatial coherence of the storage mechanism, with large flares having large spatial coherence or macroscopic organisation (Heyvaerts and Hagyard, 1991) on which I am focussing here.

For a given normal field component (B_n) at the photosphere, the magnetic energy is a minimum when $\nabla \times \mathbf{B} = \mathbf{0}$, so that the current vanishes and, after taking the curl, we find that $\nabla^2 \mathbf{B} = \mathbf{0}$ so that the field is a potential one. Excess energy is then stored by a change in photospheric boundary conditions, such as emerging flux (Zirin 1983), flux cancellation (Martin et al, 1985) or sunspot motions (Gestelyi et al, 1986). In general the footpoints move and B_n changes, and so at each time you need to compare the actual magnetic energy and the potential energy for the particular B_n.

The free magnetic energy is certainly sufficient for a flare. For example, if you twist up by 2π a typical loop of 500 G, length 50 Mm and width 10 Mm, you store an excess energy of 3×10^{23} J (3×10^{30} erg), sufficient for a small flare. Or if you shear an arcade of 500 G, length 100 Mm and width 40 Mm to give a shear angle of 45°, the excess energy is 6×10^{25} J (6×10^{32} erg), enough for a large flare. Also there is plenty of time to store the energy by slow photospheric footpoint motions, with evolution through equilibria. The time-scale is

the distance moved divided by the speed (say 1 km s^{-1}) and so the time to move 10^5 km and store enough energy for a large flare is about 1 day, whereas the time to move 10^4 km and give a moderate flare is 2 hours.

However, the coronal field naturally tends to reconnect and lower the energy, heating the closed corona on a time-scale τ_h ,say. Therefore, if the time (τ_p) for photospheric changes is fast ($\tau_p < \tau_h$), then the footpoint connectivity is preserved and new free energy is stored. If, on the other hand, the photospheric changes are slow ($\tau_p > \tau_h$), then the connectivity continually changes and the corona is heated by driven reconnection. τ_h is uncertain in value and depends on the magnetic configuration. In principle it could be determined observationally by comparing changes in the coronal structure with a variety of different photospheric motions. If a closed loop or arcade were heated by tearing on a time-scale $\tau_h \sim \tau_{tmi} \sim (\tau_d \tau_A)^{1/2} = (\ell^3 n^{1/2}/(B_0 \eta))$ this would give $\tau_h \sim 3 \times 10^6$ secs (≈ 5 weeks) for $B_0 = 100$ G , $T = 10^6$ K, $n = 10^{15}$ m^{-3}, $\ell = 10$ Mm, since the resulting Alfven time (τ_A) is about a second and the diffusion time (τ_d) 10^{13} secs. By contrast reconnection driven between neighbouring flux by photospheric motions would just occur on the driving time of minutes or hours, say. Thus it is much easier to store energy by twisting or shearing a closed structure.

Aly (1990) showed that for a given normal field (B_n) at the photosphere $W_{pot} < W < W_{open}$, so that the energy (W) of any 3D closed force-free field lies between the potential energy and the energy of the corresponding open field (see also Barnes and Sturrock, 1972). Therefore the open field is a state of maximum energy

$$W_{open} = \frac{1}{\mu} \int \frac{| B_z \, B_z' |}{\sqrt{[(x-x')^2 + (y-y')^2]}} \; dx \, dy \, dx' \, dy' .$$

This is at first worrying because one wonders how it it possible to open a field, but maybe an eruption only makes it partially open, or maybe there are plasmoids or knots which enable W_{open} to be exceeded. It would be useful to apply this to actual data. However, Finn and Chen (1990) find in a numerical experiment that shearing does not make their configuration approach an open field at large time. Also Aly (1990) has shown thankfully that three-dimensional force-free fields that are ideally stable and have an energy of order W_{open} (and $\alpha L \approx 1$) do exist.

The free energy in a force-free field can be calculated from vector magnetograph data (Molodensky, 1974) from the expression

$$W_{free} = \frac{1}{\mu} \int \int B_z \, [x \, (B_x - B_{x\,pot}) + y \, (B_y - B_{y\,pot})] \; dx \, dy.$$

Hofmann, for instance, (in Heyvaerts and Hagyard, 1991) found energies for 80 cases in the range 5×10^{32} to 5×10^{33} erg, but does ignore side boundaries and there are observational uncertainties (see also Sakurai, 1989; Gary et al, 1987).

The vertical current following up from the photosphere can be calculated locally from $j_z = 1/\mu \; (dB_y/dx - dB_x/dy)$ or the total current crossing a certain area follows from $I = 1/\mu \int \mathbf{B}.\mathbf{ds}$ integrated around the boundary of the region. It is found that the first flare kernels are located at peaks of j_z, ie., at regions of high magnetic shear (Hagyard, 1988; Lin

and Gaizauskas, 1987). Furthermore, the magnetic field in the corona can be calculated using extrapolation techniques from photospheric observations to give either a potential field or a linear force-free field or, very much better, a nonlinear force-free field (Sakurai, 1989; Gary et al, 1990).

However, it is important to notice that not all of the free energy is really free! When the fields reconnect, the total magnetic helicity $H = \int \mathbf{B}.\mathbf{A}\, dV$, where $\mathbf{B} = \nabla \times A$, is conserved. This is a measure of the twist and connectedness of the magnetic field, so that

$$H = H_{self} + H_{mutual}, \qquad (11)$$

where the self helicity (H_{self}) comes from the twist of each flux tube and the mutual helicity is due to the braiding of tubes around each other. Thus reconnection can actually increase the twist of a tube and so make it more unstable.

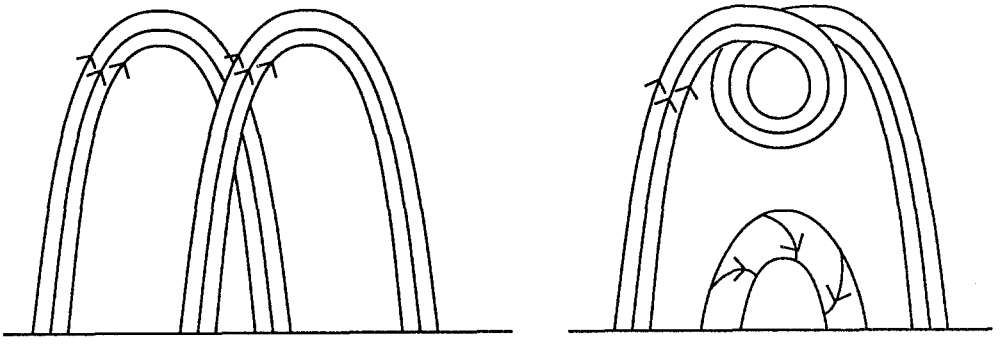

Figure 5. Conversion of mutal to self magnetic helicity.

For example, if we start with two tubes as shown in Figure 5 that are untwisted and each have magnetic flux F, they have no self helicity but a mutual helicity $H_{mutual} = 2\pi F^2$. Now suppose the tubes reconnect and so lose their mutual helicity but each become twisted by an amount T. Then the sum of their self helicities is $H_{self} = 2 T F^2$ and so conservation of total helicity implies that the twist is $T = \pi$. Indeed, this process can produce the twist that has been observed in "post"-flare loops.

The state of lowest magnetic energy with a given magnetic helicity is a linear force-free field and so the "really free" energy is

$$W_{FREE} = W - W_{lin\ fff}, \qquad (12)$$

namely the difference between the actual energy and the energy of a linear force-free field, and this is less than the free energy $W_{free} = W - W_{pot}$ in excess of potential that has been referred to so far. In view of this, it is encouraging that the observed values of W_{free} mentioned above are larger than the flare energy. Thus, I am suggesting that the energy

reduces to the energy of a linear force-free field rather than a potential field because of the need to conserve magnetic helicity. Of course some of the magnetic helicity will leave the Sun in the erupting prominence, and so Eruptive Flares and erupting prominences may serve a useful purpose in ejecting magnetic helicity from the Sun. Otherwise, in spite of cancelations of helicities of opposite sign, the magnetic helicity in the atmosphere would possibly build up indefinitely due to shearing and twisting motions in the photosphere which are preferentially of one sign in a given hemisphere.

The rate of energy supply, of increase of magnetic energy in the corona, is simply the Poynting flux through the photosphere, namely $dW_m/dt = 1/\mu \int (\mathbf{E} \times \mathbf{B})_z \, dx \, dy$ where $\mathbf{E} = -\mathbf{v} \times \mathbf{B}$ (Priest and Forbes, 1990). For a two-dimensional arcade being sheared by motions (v_y) in the y-direction along the arcade this becomes per unit length

$$\frac{dW_m}{dt} = \frac{-1}{\mu} \int v_y \, B_y \, B_z \, dx \qquad (14)$$

and so, even if B_z and v_y remain constant in time, the rate of energy increase is not constant since B_y tends to increase as the shear grows. For example, if a motion $v_y = v_0 \, x/L$ is applied to the feet of the linear force-free arcade (10), where v_0 is constant in time, the α value becomes $\alpha(t) = k \, v_0 (t/L)(1 + v_0^2 \, t^2/L^2)^{-1/2}$ and the magnetic energy per arcade becomes $W_m(t) = B_0^2 \, L^2/(\mu\pi) \, (1 + v_0^2 \, t^2/L^2)^{1/2}$ which grows at first ($t < L/v_0$) quadratically and later linearly in time. At the same time the coronal flow speeds at large heights in response to slow footpoint motions can be so high that static evolution breaks down.

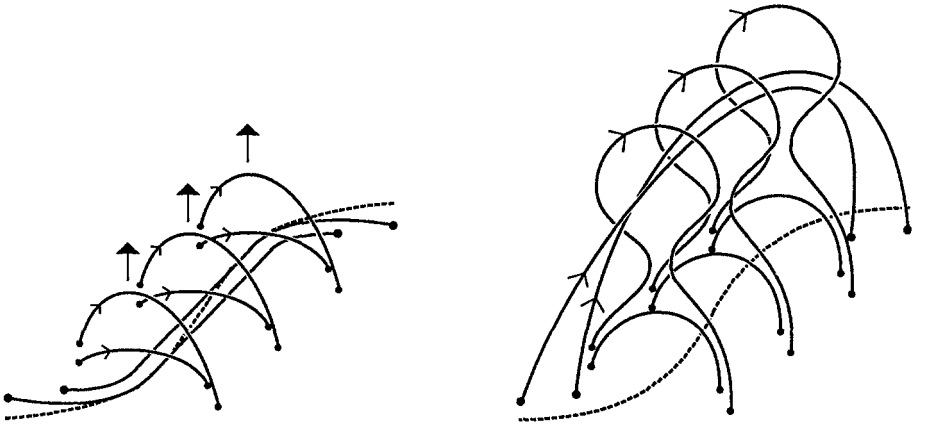

Figure 6. The overall scenario for a two-ribbon flare.

4. Conditions for Flare Occurrence

In a large flare the overall scenario (Priest, 1981; Moore, this colloquium) is that during the preflare phase a prominence and its highly sheared field rise slowly - note that by its nature such a field is nonlinear since the ambient field is essentially potential. Then at flare onset we have the impulsive phase and a rapid eruption of the prominence, which probably occur because of the start of reconnection below the rising prominence. But why does the eruption occur? Why does the flare start?

Small flares may be driven by photospheric motions with energy released in the corona at the rate of supply. There is for these flares no energy storage and only minor nonpotentiality. For large flares several necessary conditions have been proposed. The obvious one is storage of free energy in a nonpotential field, since the photospheric changes during a flare are small. Also flaring has been associated with strong magnetic gradients (Moreton and Severny, 1968).

Two important necessary conditions are "Shear in the Corona" and "Complexity". Shear before flares is often observed in the chromosphere, as shown in Hα fibrils (Tanaka and Nakagawa, 1973) and also in the photosphere, as shown in magnetograms near the polarity inversion line (Hagyard et al, 1982; Machado and Moore, 1991; Zirin and Wang, 1990; Hagyard, 1990). These are suggestive of shear in the overlying corona (but sometimes there are significant differences in orientation between Hα structures and photospheric magnetic fields (Gary et al, 1987)). An example is shown in Figure 7 in which the flare occurs at the part of the polarity inversion line where the deviation from potential is the largest.

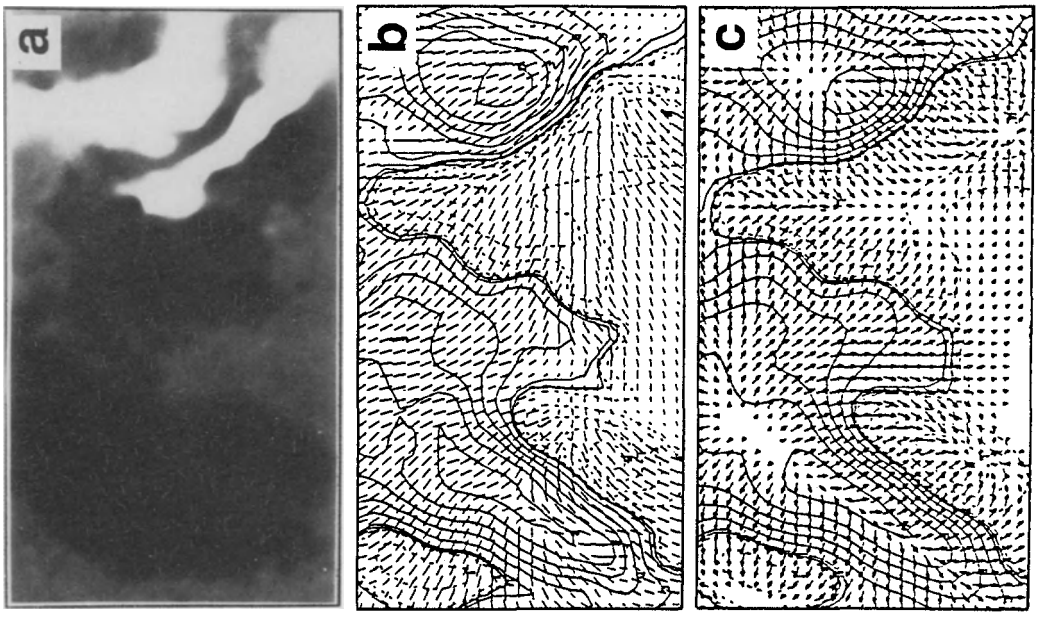

Figure 7. Hα flare, vector magnetic field and potential field (Venkatakrishnan et al).

Mona Hagyard (1990) has put forward a sufficient condition for large flares, which is very robust, even if it does not hold in every case! It has three parts, namely that (i) the shear angle ($\Delta\phi$) between the observed horizontal field and corresponding potential field be large enough ($\Delta\phi > 80°$); (ii) the field be strong enough ($B \geq 1000$ G); (iii) the spatial coherence, as measured by the distance (L) along the inversion line for these properties, be large enough ($L > 8$-10 Mm). However, this does not seem to be necessary (Heyvaerts and Hagyard, 1991), since there are some cases of weak flares with smaller fields and also one case of a large flare with no large photospheric shear. Nevertheless, the condition is reasonable, since as we shall see, a large shear tends to produce magnetic nonequilibrium, and, when L is large enough, the surrounding stabilising region cannot suppress nonequilibrium or instability. Canfield et al (1991) have confirmed Hagyard's result and have shown with their vector magnetograph that a flare occurs in a region of high shear between magnetic gradient peaks.

Sara Martin (1980) has long stressed that most major flares have a filament activation and eruption. So what is the role of an active-region or boundary prominence? Since we know that the magnetic field in a prominence has a shear angle of at least 75°, it is clear that an important role is as an indicator of high shear in the corona. But is a prominence essential to a flare, or is it just a tracer of high shear? One might expect it to be important for the eruption of a quiescent prominence where the plasma beta is of order unity but less important for an active-region prominence where the plasma has little effect on the field. Furthermore, Martin et al (1985) and Livi et al (1989) have shown the importance of flux cancellations near prominences, since they may build up the twist and therefore the free energy in a prominence, and also they find that most flares begin near the sites of flux cancellation.

Indeed, the Emerging Flux Model (Heyvaerts et al, 1977) was developed primarily to explain complexity (in the form of emerging flux) and the presence of widely separated kernels. It suggested that, after new flux emerges, a current sheet becomes turbulent when it reaches a critical height. Also, the type of flare depends on the magnetic environment, so that, if the overlying field contains no excess stored energy, no flare or at most a small one occurs, whereas if a lot of stored energy is present the emerging flux may trigger its release.

I am in the process of generalising or modernising this model to given an Interacting Flux Model with either vertically emerging flux or horizontal spot motions and several new aspects. Interacting flux is a regular part of active region evolution with impacting polarities or parasitic polarities or delta spots (Zirin, 1983) and flares often begin at remote footpoints (Machado et al, 1983; Zirin and Wang, 1990). Indeed the basic structure of a flare is now believed to be an interaction of several bipoles or multiple loops, as seen in Hα (Rust, 1968; Tang, 1985; Kurokawa, 1989; Gaizauskas, 1989 et al), in X-rays both from SMM (Machado et al, 1983; Pallavacini, 1991) and NIXT (Herant et al, 1991), and in radio images at cm and m (Kundu, 1986; Pick et al, 1990).

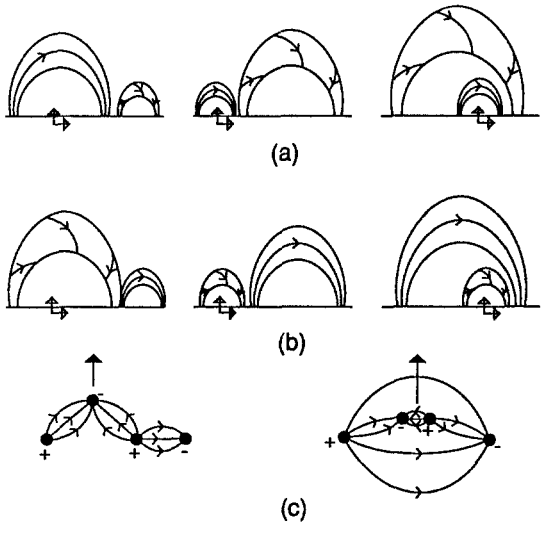

Figure 8. Secondary or Primary Roles of Interactions.

What is the role of rapid spot motions or rotations, as seen for instance in the relative motion of new and old spots (Gestelyi and Kalman, 1984; Zirin and Wang, 1990)? Sometimes to increase shear and sometimes to increase complexity. And what is the role of complexity and of the vertical or horizontal motion of one structure relative to another? It may be passive and just indicate general evolution. Or it may be secondary (Figure 8a) and trigger the release of free energy from a pregnant structure near a critical threshold. Or it may be primary in three different ways: it may produce a small flare with $\tau_p \geq \tau_h$, so that energy release is driven at τ_p; or it may itself contain the free self-energy, as indicated in Figure 8b; or it may produce free mutual energy by shearing (Figure 8c). In the latter case suppose one starts with four sunspots; then if one or two of them move rapidly, a sheared force-free field will be created as the field lines stretch out.

Why then is complexity necessary? Partly, it allows reconnection between separate structures to release excess energy that is previously stored in one or other structure. Partly, when spots move and create a force-free field, new equilibria with different connections and lower energy may become available and the flare then represents a violent transfer to a new equilibrium.

Gaizauskas and Harvey (1991) have presented an interesting example in which two spots emerged and created a beautiful delta-configuration and therefore complexity. But no flare occurred for 5 days because the overlying field was close to potential with fibrils perpendicular to the inversion line. One spot then split and separated rapidly at 300 m/s, generating high shear and the formation of a filament at the inversion line. Then several flares took place with emission at remote places, repeating at intervals of 1.5 hours. This example is entirely consistent with the interacting flux scenario I am presenting.

What can theory tell us about the possible ways in which a flare may start? In principle it seems that one just needs to solve the MHD equations $\mathbf{j} \times \mathbf{B} = \mathbf{0}$ and $\partial \mathbf{B}/\partial t = \nabla \times (\mathbf{v} \times \mathbf{B})$ for an evolution through a series of force-free equilibria due to footpoint motions. There are several possibilities for the evolution of the magnetic energy W(t) when a critical point is reached. First of all, a transcritical or pitchfork bifurcation may occur in which the equilibrium becomes linearly unstable but nonlinearly stable due to the presence of a new nearby stable equilibrium along which the evolution proceeds (Figure 9a) with no energy release. Secondly, a subcritical bifurcation may take place due to nonlinear instability or metastability, so that the system jumps down to a new equilibrium with energy release (Figure 9b). Thirdly, a state of nonequilibrium may appear with no neighbouring equilibrium, so that a catastrophe occurs with energy release (Figure 9c). It is hoped that such behaviour may show up in numerical computations. Dahlburg and Antiochos (1991) have conducted a 3D, incompressible, time-dependent, resistive experiment in which they start with a 2D arcade and twist up some of the footpoints at 0.1 v_A. The effective Lundquist number is 100, the Reynolds number 5 and the number of gridpoints 32^3. They find that the field expands and the magnetic energy increases by 50%. Then they stop twisting and hold the feet still. The field relaxes and untwists, diffusing in a thin boundary layer, but there is no sign of instability. It is remarkably stable and harder to produce a "flare" than previously realised. Perhaps they need more twist, more complexity, less diffusion or more ingenuity.

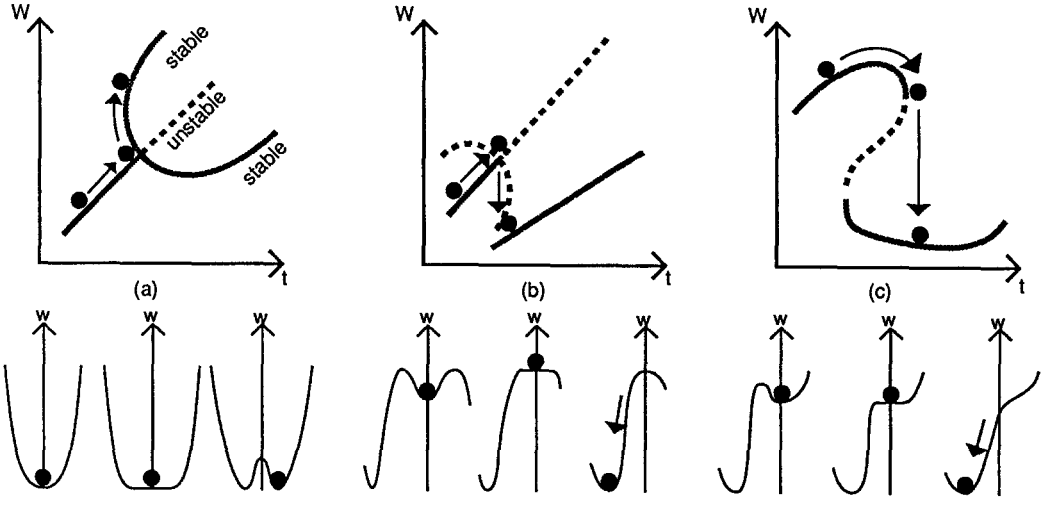

Figure 9. (a) pitch fork bifurcation (b) subcritical bifurcation (c) nonequilibrium

5. Eruption due to Magnetic Nonequilibrium

During the 1980's there have been many studies of the linear MHD stability of various structures, which have showed that it is photospheric line-tying which provides the stability and enables the field to store free energy. When a single flux tube is twisted too much it

becomes unstable (Hood and Priest, 1979; Einaudi and Van Hoven, 1983). However, a simple force-free arcade is found always to be ideally stable (Hood and Priest 1980; De Bruyne and Hood, 1989), and when resistivity is included the very slow diffusion is only replaced by rapid growth when ideal marginal stability is approached (Velli and Hood, 1989). However, when a magnetic island is present which may support a prominence, the arcade can become unstable when the prominence height or length became too large (Hood and Priest, 1980).

A numerical experiment on the shearing of a periodic set of equal arcades (Mikic et al, 1988) shows that an arcade reconnects with its neighbours and then rapidly reconnects and erupts with a plasmoid. However, when unequal arcades are sheared up, Biskamp and Welter (1989) find that the small arcade expands laterally and pinches off the arcade in a slow, rather than dynamic, manner. Thus one needs ideal instability or nonequilibrium to drive reconnection faster.

The possibility of nonequilibrium has been considered by several authors. A single curved slender flux tube in equilibrium between tension and magnetic buoyancy loses equilibrium and erupts when the separation between its footpoints is too large (Browning and Priest, 1984). Also the evolution of a magnetostatic two-dimensional arcade with a field

$$\mathbf{B} = \left(\frac{\partial A}{\partial y}, \frac{-\partial A}{\partial x}, B_z\,(A) \right) \qquad (14)$$

satisfies the Grad-Shafranov equation $\nabla^2 A = - d/dA \left(\frac{1}{2} B_z{}^2 + \mu\, p\,(A) \right)$ in which $B_y\,(x,0)$ and the footpoint displacement $d(x) = B_z \int dx/B_x$ along the y-direction is prescribed. The right-hand side of this equation gives the distortion of the field away from potential and the resulting current density. For the resulting evolution of a force-free field as the footpoint displacement is increased, Zwingmann (1987) found that there is a continuous series of equilibria with no catastrophe. He did obtain nonequilibrium when pressure gradients are included, but the resulting pressures are too high for a solar flare and Finn and Chen (1990) showed that catastrophe is absent if the entropy is changed rather than the pressure.

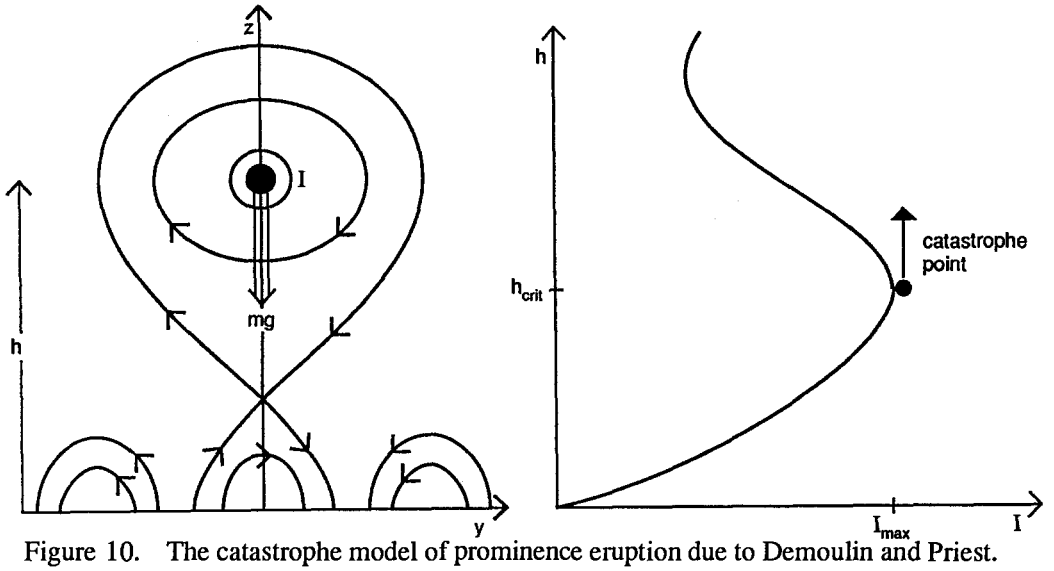

Figure 10. The catastrophe model of prominence eruption due to Demoulin and Priest.

Recently, the emphasis has shifted to include the presence of a magnetic island and a prominence. Demoulin and Priest (1988) have modelled a prominence as a filament of mass and current in a force-free field, as an extension of Amari and Aly's (1989) paper and a more detailed treatment of the Van Tend and Kuperus (1978) model. They write the field in the form (14) and solve the linear force-free equation $\nabla^2 A + \alpha^2 A = \delta(y)\,\delta(z - h)$ with the delta-function source representing the prominence at height h. The solution gives the field everywhere which is then substituted into the equation ($I B_y = mg$) for prominence equilibrium to give the height of the prominence (h) as a function of the current (I) or twist in the field (Figure 10). The result is that when the prominence twist and shear are too large, there is a catastrophe and it erupts. An interesting feature is that it only works when there is parasitic flux - ie., complexity!

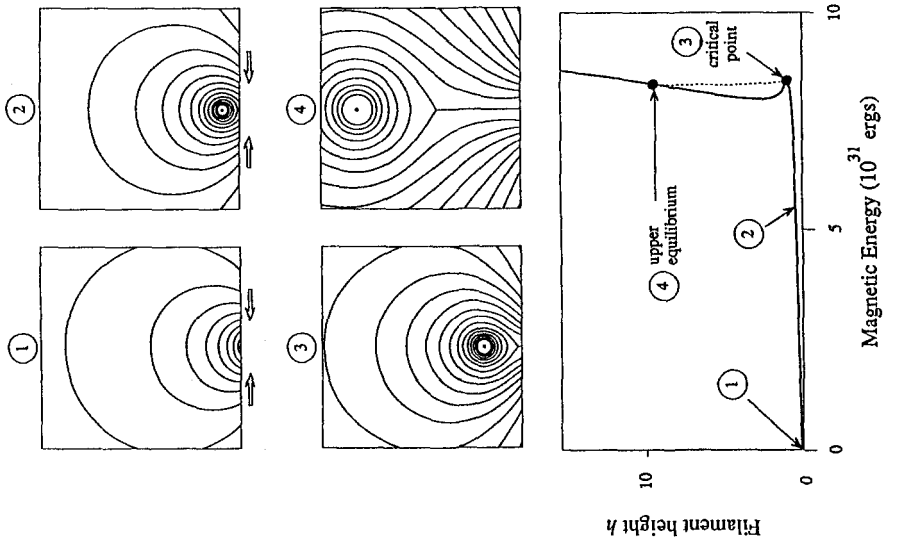

Figure 11. The catastrophe model of prominence eruption of Priest and Forbes.

This idea of a catastrophe model for prominence eruptions has been developed further by Terry Forbes and myself (Priest and Forbes, 1990; Forbes, this volume). As shown in Figure 11, first of all converging flow builds up energy and flux in a sheared arcade field, consistent with flux cancellation observations. The prominence height slowly increases (2) as the magnetic energy increases, until a catastrophe point (3) is reached. The prominence then erupts and would approach a new equilibrium at (4) in an ideal case, but the eruption drives reconnection in a current sheet below the prominence and so the eruption continues catastrophically. The consequences for energy release are described in Terry Forbes' review.

6. Conclusions

The Emerging Flux Model is being developed into an Interacting Flux Model including several new features: flux interaction may occur either by vertical (emerging) or horizontal motions; there may be different possible locations of stored energy, either in one flux system or another or in the mutual interaction between them; the magnetic helicity constraint means that the free magnetic energy is really the energy in excess of a linear force-free field; the structure that closes down is a three-dimensional one with separators and separatrix surfaces.

Partial answers to the questions posed at the beginning of my review are as follows. The magnetic configuration for a flare is a highly complex structure with interacting bipoles. The energy is supplied by sufficiently rapid changes in photospheric boundary conditions on a time-scale faster than the normal coronal heating time. Necessary conditions for the start of a flare have been deduced from observations, namely shear in the corona and complexity. High shear is indicated by the presence of a prominence and is reduced by spot motions and flux interactions. It implies the presence of free energy, while complexity eases the release of energy. MHD theory has shown that eruption in complex structures may be a magnetic catastrophe when the shear, twist and length are too large.

Acknowledgements

I am most grateful to Einar Tandberg-Hanssen and Zdenek Svestka for their pioneering work on prominence and flare observations and for the gentle, efficient and wise way they have encouraged research. I am also thankful to Peter Sturrock for his fundamental work on flare theory, on which many of the current ideas are based, and to Jean Heyvaerts and Mona Hagyard on whose review of preflare evolution I have built the present review. Finally, the kind hospitality of Marcos Machado, Marta Rovira and their colleagues has provided a memorable stay in Argentina.

References

Aly, J. J. (1990a) *Phys. Fluids B*, **2**(8), 1928.
Aly, J. J. (1990b) *Computer Phys. Commun.*, **59**, 13.
Amari, T. and Aly, J. J. (1989) *Astron. Astrophys.*, **208**, 361.
Barnes, C. W. and Sturrock, P. A. (1972) *Astrophys. J.*, **174**, 659.
Baum, P. J., Bratenahl, A., Crockett, G. and Kamin, G. (1979) *Solar Phys.*, **62**, 53.
Browning, P. K. and Priest, E. R. (1984) *Solar Phys.*, **92**, 173-188.
Biskamp, D. and Welter, H. (1989) *Solar Phys.*, **120**, 49.
Canfield, R., Beaujardiere, J. and Leka, K. (1991) *Phil. Trans. Roy. Soc.*, in press.
Dahlburg, R. and Antiochos, S. (1991) submitted.
Démoulin, P. and Priest, E. R. (1988) *Astron. Astrophys.*, **206**, 336.
Démoulin, P., Henoux, J. and Mandrini, C. (1991) submitted.
Einaudi, G. and VanHoven, G. (1983) *Solar Phys.*, **88**, 163-178.
Finn, J. and Chen. J. (1990) *Ap. J.*, **349**, 345-361.
Gaizauskas, V. (1989) *Solar Phys.*, **121**, 135.
Gaizauskas, V. and Harvey, K. (1991) in *Dynamics of Solar Flares*, (ed. B. Schmieder and E. R. Priest) p.25.

Gary, G. A., Moore, R. L., Hagyard, M. J. and Haisch, B. M. (1987) *Astrophys. J.*, **314**, 782.
Gesztelyi, L. and Kalman, B. (1986) *Adv. Space Res.* **6**, 29.
Gesztelyi, L., Karlicky, M., Farnik, F., Gerlei, O. and Valnicek, B. (1986) in *The Lower Atmosphere of Solar Flares,* D. F. Neidig, ed., Sacramento Peak, p.163.
Gorbachev. V. and Somov. B. (1988) *Solar Phys.* **117**, 77.
Hagyard, M. J. (1988) *Solar Phys.*, **115**, 107.
Hagyard, M. J. (1990) *Memorie Soc. Astron. Ital.*, in press.
Hagyard, M. J. Cumings, E., West, E. and Smith, J. (1982) *S. Phys.*, 33.
Hénoux, J. C. and Somov, B. V. (1987) *Astron. Astrophys.*, **185**, 306.
Herant, M., Pardo, F., Spiller, E. and Golub, L. (1991) *Ap. J.* in press.
Heyvaerts, J. (1990) in *Proceedings of IAU Symp 142: Basic Plasma Processes on the Sun.*, Bangalore, India, E. R. Priest and V. Krishnan, eds., p.207-214.
Heyvaerts, J. and Priest, E. R. (1984) *Astron. Astrophys.* **137**, 63-78.
Heyvaerts, J. and Priest, E. R. (1991) submitted.
Heyvaerts, J., Priest, E. R. and Rust, D. M. (1977) *Astrophy. J.* **216**, 123-137.
Heyvaerts, J. and Hagyard, M. (1991) in "Dynamics of Solar Flares" (ed., B. Schmieder and E. R. Priest) Obs. de Paris, p.1-24.
Hood, A. W. and Anzer, U. (1990) *Solar Phys.* **126**, 117.
Hood, A. W. and Priest, E. R. (1979) *Solar Phys.* **64**, 303-321.
Hood, A. W. and Priest, E. R. (1980) *Solar Phys.*, **66**, 113.
Kundu, M. (1986) *Adv. Space Res.* **6**, 53.
Kurokawa, H. (1984) *Space Sci. Rev.* **51**, 49.
Mandrini, C., Démoulin, P., Henoux. J. and Machado, M. (1991) submitted.
Lin Yuanzhang, and Gaizaukas, V. (1987) *Solar Phys.*, **109**, 81.
Livi, S. H. B., Martin, S. and Wang, H. (1989) *Solar Phys.*, **121**, 197.
Machado, M. E., Somov, B. V., Rovira, M. G. and de Jager, C. (1983) *Solar Phys.*, **85**, 157.
Machado, M. E. and Moore, R. (1991) submitted.
Martin, S. F. (1980) *Solar Phys.*, **68**, 217.
Martin, S. F., Livi, S. H. B. and Wang, J. (1985) *Australian J. Phys.*, **38**, 929.
Mikic, Z., Barnes, D. C. and Schnack, D. D. (1988) *Astrophys. J.*, **328**, 830.
Molodensky, M. M. (1974), *Solar Phys.*, **39**, 830.
Moreton, G. E., and Severny, A. B. (1986) *Solar Phys.*, **3**, 282.
Pallavacini, R. (1991) *Phil. Trans. Roy. Soc.*, in press.
Parker, E. N. (1979) *Cosmical Magnetic Fields* , Oxford Univ. Press.
Pick, M., Klein, K, Trottet, G. (1990) *Ap. J. Supp.* **73**, 165.
Priest, E. R. (1981) *Solar Flare MHD,* Gordon and Breach, London.
Priest, E. R., and Forbes, T. G. (1990) *Solar Phys.*, **126**, 319.
Priest, E. R. (1990) in *Physics of Magnetic Flux Ropes* (ed., C. Russell et al) AGU, p.1-22.
Priest, E. R. (1989) (ed.) *Dynamics and structure of quiescent solar prominences.*, D. Reidel, Holland.
Priest, E. R. and Raadu, M. (1985) *Solar Phys.*, 177-188.
Priest, E. R., Hood, A. W. and Anzer, U. (1989) *Astrophys. J.* **344**, 1010.
Ridgway, C. and Priest, E. R. (1991), submitted.
Rust, D. (1968) *IAU Symp.*, **35**, 77.
Sakurai, T. (1989a), *Solar Phys.*, **121**, 347.
Sakurai, T., (1989b), *Space Sc. Rev.*, **51**, 11.
Steinolfson, R. (1990) in *Physics of Magnetic Flux Ropes.*, (ed., C. Russell et al) AGU, p.211-218.
Sturrock, P. and Woodbury, E. (1967) in *Plasma Astrophys.*, (ed., P. Sturrock) New York, Academic, p.155

Sweet, P. A. (1958) *IAU Symp.*, **6**, 123-134.
Tanaka, K. and Nakagawa, Y. (1973) *Solar Phys.* **33**, 187.
Tur, T. and Priest, E. R. (1976) *Solar Phys.* **48**, 89-100.
Van Ballegooijen, A. (1986) *Ap. J.*, **311**, 1001.
Van Ballegooijen, A. and Martens, P. (1989) *Ap. J.* **343**, 971-984.
Van Tend, W. and Kuperus, M. (1978) *Solar Phys.*, **59**, 115.
Velli, M. and Hood, A.W. (1989) *Solar Phys.* **119**, 107.
Zirin, H. (1983) *Astrophys. J.*, **274**, 900.
Zirin, H. and Wang, H. (1990) *Solar Phys.* **125**, 45.
Zwingmann, W. (1987) *Solar Phys.*, **111**, 309.

THE ROLE OF CANCELLING MAGNETIC FIELDS IN THE BUILDUP TO ERUPTING FILAMENTS AND FLARES

Sara F. Martin
Big Bear Solar Observatory
Solar Astronomy 264-33
California Institute of Technology
Pasadena, CA, USA

Silvia H. B. Livi
Instituto de Fisica
Universidade Federal do Rio Grande do Sul
Porto Alegre, Brazil

Abstract

We present a scenario for understanding the role of cancelling magnetic fields in the build-up to eruptive solar flares. The key intermediate step in this scenario involves the formation of a filament magnetic field in the corona above a photospheric polarity inversion where cancelling magnetic fields are observed. The formation of a filament magnetic field is accomplished in several recent models by first interpreting the cancelling fields as a visible effect of a slow, steady magnetic reconnection. This reconnection results in a reconfiguring of the magnetic field; line-of-sight pairs of closely-spaced opposite-polarity fields disappear from the photosphere thereby accounting for the cancellation; simultaneously the horizontal component is increased in the corona above the polarity inversion. The new and increasing horizontal component is synonymous with the building of a magnetic field where mass can accumulate to form a filament. If the magnetic reconnection continues for a sufficient length of time, the changing equilibrium between the growing filament magnetic field and the overlying, coronal magnetic field will result in a very slow, simultaneous ascent of both the filament magnetic field and the overlying coronal magnetic field with greater motion in the outer, weaker coronal field. This upward stretching of the magnetic fields eventually results in a closer spacing of oppositely-directed coronal magnetic fields (resembling a tangential discontinuity) beneath the filament. As depicted in some flare models, magnetic reconnection then suddenly occurs in the corona beneath the filament; flare loops form in the lower part of the reconnected field and a coronal mass ejection and erupting filament comprise the upper part of the reconnected field. To illustrate the observable phases of this scenario, we describe the build-up to two simple eruptive flares in a small active region.

1.0 INTRODUCTION

In a cancelling magnetic feature, both positive and negative line-of-sight magnetic fields are observed to disappear at a common boundary. One of the earliest papers on cancelling magnetic fields suggested that a relationship might exist between these disappearing magnetic fields and the occurrence of solar flares. Martin, Livi and Wang (1985) found that all 22 of the observed 22 flares in the active region were initiated around the sites of cancelling magnetic fields. However, the relationship was believed to be an indirect one because the time-scale of cancelling fields is very much slower than the time-scale of the flares. Thus, if a physical relationship exists between the sites of disappearing magnetic fields and flares, the role of the cancelling magnetic fields was expected to be of an evolutionary nature; the cancelling magnetic fields might somehow aid in altering the magnetic field geometry in such a way that flares would be initiated above the sites of the cancelling photospheric magnetic fields.

The possibility of a physical relationship between the evolution of cancelling magnetic fields and the sporadic occurrence of flares was further analyzed by Livi et al. (1989). They verified the earlier findings of Martin et al. (1985) that flares often occur at sites where the only observable change in the magnetic field is cancellation. In addition, Livi et al. (1989) sought to understand the occurrence of flares in relation to emerging, evolving, and cancelling magnetic fields. Previous papers had already documented the association of many flares to specific evolutionary changes in the magnetic fields of active regions (Martres, Michard and Soru-Iscovici 1968); and with emerging magnetic flux regions (Rust, 1972 and 1974, Marsh, 1978; Martin et al., 1983, 1984). Following the latter findings, Livi et al. (1989, Figures 3,6 and 7) recognized that most flares associated with emerging flux occur at the boundaries where the newly emerging flux is impacting previously existing magnetic flux of opposite polarity. Their examples are consistent with the finding of Martres, Michard and Soru-Iscovici (1968); flares occurred at polarity inversions where the magnetic flux was increasing on one side of the inversion and decreasing on the other side. Livi et al. (1989) concluded that the probable common denominator in all of these associations was the disappearance of magnetic fields. In surveying the data from Big Bear Solar Observatory from Sep. 1985 through July 1988, they were also unable to find any flares which definitely were not initiated at sites where cancellation could be occurring. This led Livi et al. to hypothesize the existence of a meaningful physical association between the evolution of cancelling magnetic fields and flares although the stages in the association were not yet well-defined.

During the last 6 years, it was also recognized that filaments form at polarity inversions where magnetic fields are cancelling. (Martin et al., 1985; Martin, 1986; Hermans and Martin, 1986; Martin 1990). Martin (1990) presented the hypothesis that converging and cancelling magnetic fields were necessary conditions for the formation of filaments (prominences). Three models of filament formation now incorporate the cancelling magnetic fields as an essential observational input (van Ballegooijen and Martens, 1989; Kuijpers, 1990; Martin, this volume). The present

paper discusses how these new concepts of filament formation also lead to the eruption of filament magnetic fields and to the simultaneous occurrence of solar flares and coronal mass ejections.

2.0 AN INTERPRETATION OF CANCELLING MAGNETIC FIELDS

Although both flares and filaments occur at polarity inversions where magnetic fields are cancelling, the time-scale and spatial scales of cancelling magnetic features are much more closely related to filaments than to flares. The physical relationship between cancelling magnetic fields and filaments is not immediately obvious. The cancelling magnetic fields are observed close to the photosphere while filaments form and evolve in the corona. Cancelling fields are decreasing line-of-sight fields; filaments contain mostly horizontal fields which can be either decreasing or increasing. The rate of filament formation, however, points to the likely physical link between cancelling fields and filaments (Martin, 1990). Filaments form quickly at polarity inversions where the cancellation is relatively rapid and filaments form slowly where cancellation is also relatively slow. This finding raises the vital question: Could the horizontal field of the filaments appear at the expense of the disappearing line-of-sight fields? This is exactly what is proposed in the new generation of filament models based on cancelling magnetic fields.

All of these models propose that magnetic reconnection acts to convert line-of-sight magnetic fields into transverse magnetic fields. The disappearance of magnetic fields (cancellation) is depicted as either the upward or downward transport of magnetic field through the layer of atmosphere represented in near-photosphere magnetograms. For purposes of discussing the flare build-up, details of these models are not important. Their common significant thread is an increasing horizontal component of magnetic field in the corona, along and above the polarity inversion in the photosphere and chromosphere.

3.0 THE FLARE BUILD-UP

3.1 Hypothesized Physical Processes

Irrespective of which filament model one might favor, there are at least 3 important implications of the idea that magnetic field accumulates in the corona where filaments can form:

(1) the accumulating horizontal component of magnetic field in the corona is directly related to the amount of magnetic field that has disappeared at the photosphere;

(2) the magnetic energy content of the photosphere is reduced because the magnetic flux has disappeared; at the same time, the total energy content in the

coronal magnetic field system above the cancellation sites is increased because the resulting magnetic field configuration in and around the filament site becomes increasingly concentrated and stressed with the successive reconnections;

(3) the accumulation of filament magnetic fields in the corona is a one-way process. The filament magnetic field cannot be destroyed nor can it be retracted because of its large scale (van Ballegooijen and Martens, 1989). It also cannot initially be expelled from the sun due to line-tying. It remains beneath the overlying and surrounding magnetic fields which already exist in the corona above those polarity inversions (Martin, 1990).

Thus we identify the accumulating magnetic field along coronal filament channels as the central site of energy storage for the flare build-up.

An important property of the coronal magnetic fields is the high Alfven speed for propagating magnetic disturbances. Thus, communication takes place rapidly between all parts of a system. Every small or large change that happens in one part of the system can rapidly affect other parts of a coronal system. Consequently, small but continuous readjustments of the whole system will occur. We therefore anticipate a tendency of an outward expansion of the whole system. That change can be initially viewed as taking place in discrete steps. First the weaker, outer parts of the system expand as a consequence of the increasing inner filament fields. Then the filament magnetic field will also rise slightly in response to the outward expansion of the outer coronal field until a new equilibrium is established. However, in reality the filament magnetic field is continuously increasing and so the equilibrium state of the whole system is continuously shifting. This outward expansion eventually results in a region of oppositely directed magnetic field components beneath the rising filament. The field in that region then approximates the configuration of a tangential discontinuity. This configuration is highly favorable for magnetic reconnection to occur in the corona and hence is invoked as the starting point for some magnetic reconnection models of solar flares (review by Svestka and Cliver, 1992, these proceedings). To complete our scenario, we suggest that rapid reconnection takes place in accord with variations of the Kopp and Pneuman model (1976, Svestka, Martin and Kopp, 1981; Svestka and Cliver, 1992); flare loops form in the lower solar atmosphere; the upper part of the reconnected field is identified with the 'coronal mass ejection' and is expelled from the sun. The central part of the filament magnetic field is part of the expelled plasmoid.

3.2 Examples of the Flare Build-up

The gradual build-up to solar flares is examined with least confusion by observing the evolution of small active regions such as the one illustrated in Figures 1 and 2. The region was born between 2300 on 3 October and 1600 on 4 Oct. 1990 and was observed at Big Bear Solar Observatory (BBSO) from 4-9 Oct. 1990. In Figures 1 and 2, H-alpha center-line images are in the left column and videomagnetograms in the

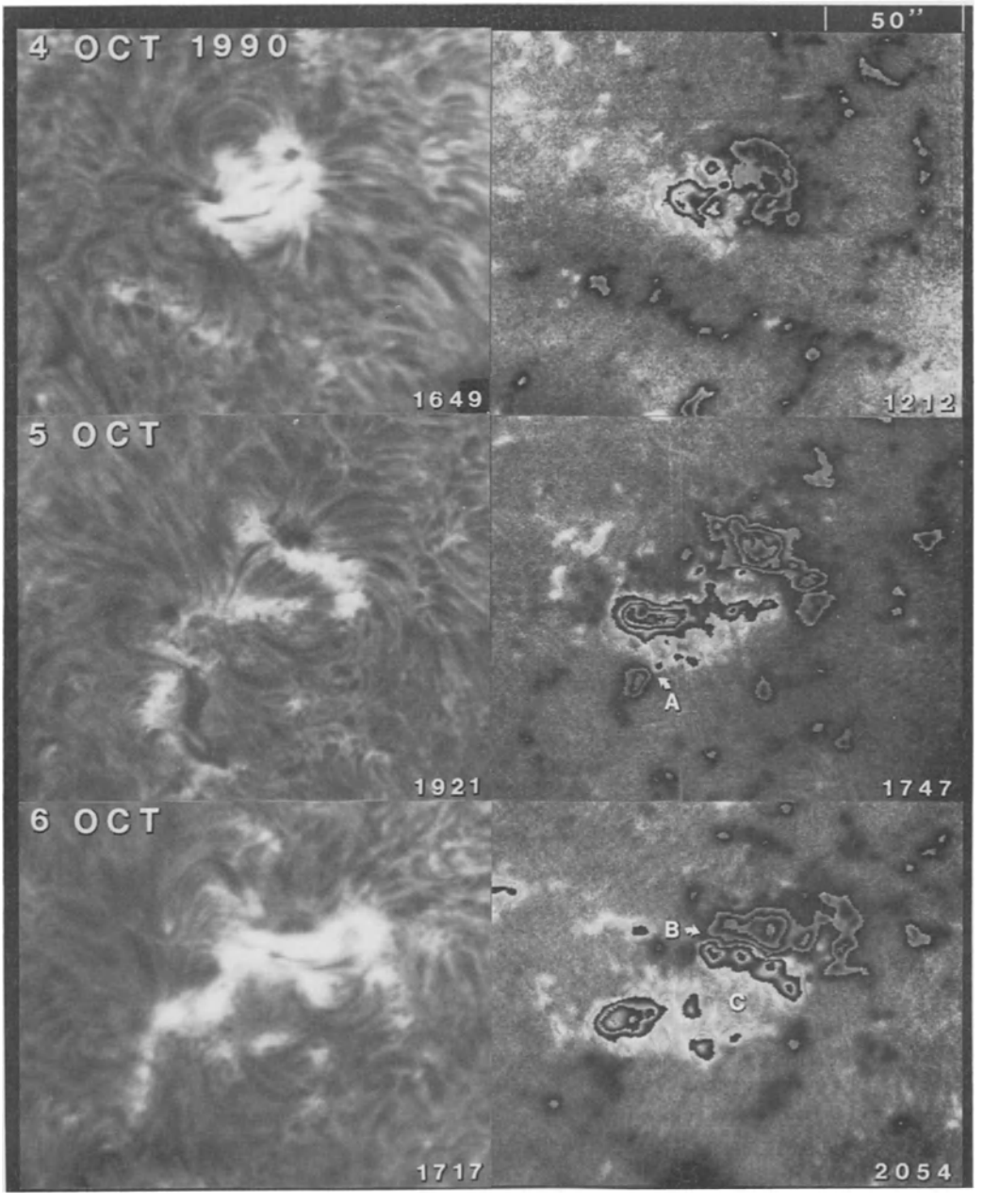

Fig. 1. The new active region, first seen on 4 Oct. 1990, has already reached its maximum magnetic flux by the morning of 5 Oct. and the intensity of the region has accordingly dropped as seen in the H-alpha images on the left. However, by 6 October, in the magnetograms on the right, a large section of the positive polarity flux (white areas and enclosed contours) reversed its direction of motion and moved into contact with the negative polarity flux (black areas and enclosed contours). The magnetic fields along this boundary are cancelling; this magnetic flux disappearance can be seen by comparing 6 Oct. with 7 Oct. in Figure 2.

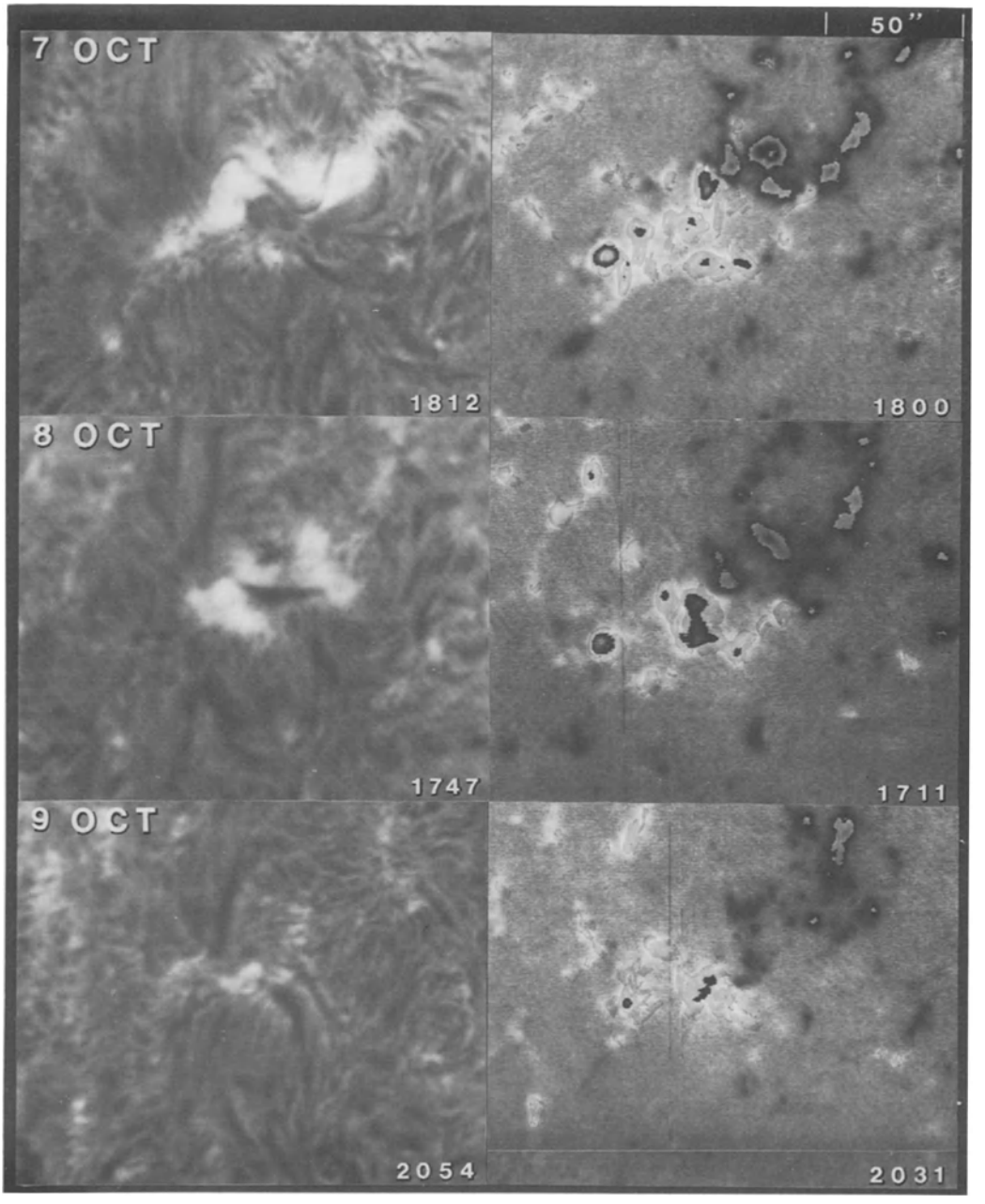

Fig. 2. The decrease in magnetic flux in the active region is seen, in the time--lapse sequences of this data, to be due to cancellation of the flux at all of the boundaries where the opposite polarities meet. At each major cancellation boundary, filaments can be seen. The redistributions of magnetic flux between 5 and 9 October appear to be related, at least in part, to the evolution of supergranules.

right column. In addition, H-alpha filtergrams at -0.6A were recorded on film continuously throughout the 4-9 October interval with wavelength scans through the H-alpha line being made about once an hour. H-alpha filtergrams were also recorded in time-lapse mode on videotape at a 2 sec interval.

During the evolution of this region, there are two polarity inversions, labelled A and B on the magnetograms in Figure 1, where cancelling magnetic fields can be seen and where filaments form. The first conspicuous site of cancellation is at the lower border of the region where the strong positive magnetic flux of the active region expands and encounters the neighboring negative polarity patch of network magnetic field at the site marked A. A filament had already formed at this site by the beginning of the observing day on 5 Oct. at 1530 UT. At that time the positive polarity flux from the active region and the negative network patch seen in Figure 1 were moving close together. Around 1800 UT, cancellation began at this site and continued throughout the rest of the observing day (which ended at 2347 UT) and was still occurring there at the beginning of the next day. The loss of flux is evident by comparing the magnetograms on 5 and 6 Oct. in Figure 1.

At 2205 UT on 5 Oct, above the cancellation site A in Figure 1, the filament existing there steadily began to appear in the blue wing (H-alpha-0.6A) as usually happens before an eruption. It rapidly became more conspicuous until about 2250, but only to the right of the cancelling site. Then it faded from view and disappeared by 2252. We attribute this disappearance to an acceleration of this section of the filament out of the passband of the filter. However, most of the filament was laterally displaced as it erupted. Consequently, the filament was continuously observable at centerline H-alpha during the rise of the flare. The flare emission began about 2259 at H-alpha center-line and at 2305 at H-alpha-0.6A. As the flare developed, additional laterally-displaced filamentary mass came into view. This structure is seen to the left of the low chromospheric part of the flare.

The second filament formed by the morning of 6 October along the main polarity inversion of the active region. In Figure 1, it is seen amidst the bright plage and at the site of the highest magnetic field gradient in the active region. It is narrow and not very dark, as is sometimes the case for filaments above sites with these characteristics. The evolution of the active region radically changed before the formation of this filament.

During 4 October, the early evolution of the region was characteristic of a simple bipolar growing flux region; the opposite polarities of the region gradually separated as the new flux emerged in the center of the region. By 5 October, the appearance of small new knots of flux had ceased. A large section of the positive polarity field reversed its direction of motion. This section then gradually moved back toward the negative polarity flux. (Positive flux is white outside of the contours and negative is black.) Small patches of positive and negative flux were cancelling during the day. During the night between 5 and 6 Oct., the entire section of positive polarity flux, above C on 6 Oct. in Figure 1, encountered the

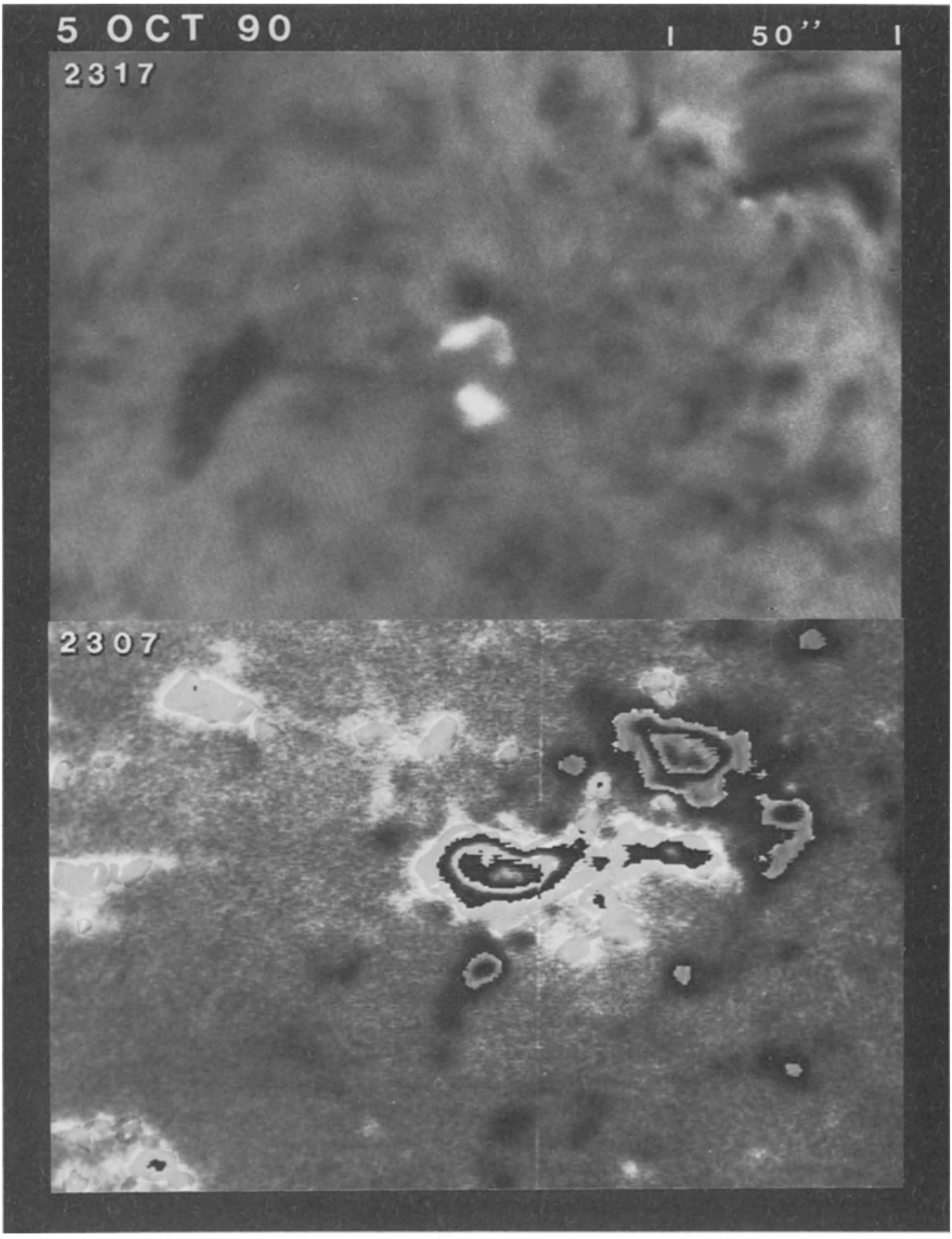

Fig. 3. The first eruptive flare is located at the lower border of the active region where the positive polarity flux of the region (white including contours) has encountered negative polarity network (black including contours). The erupting filament is seen to the left of the flare; the images are at H-alpha-0.6A.

negative polarity flux thereby forming the polarity inversion with high field gradient as seen at site B, also on Oct. 6 in Figure 1. A supergranule cell, at C, is seen in the region between the components of positive flux. It is possible that the growth of this cell forced the segment of positive flux back toward the negative flux.

By the beginning of 6 October, the filament had formed. Also, the plage around the encountering and cancelling fields was very bright, a characteristic of many areas around cancellation sites. At 1837, a classic two-ribbon flare began in concert with the abrupt disappearance of the filament mass along the polarity inversion. The flare is seen at maximum development at Ha-0.6 A in Figure 4. At the center of the H-alpha line, the emission was observed to spread over the entire active region. In addition, extensive faint emission continued to appear on the quiet sun to the east and northeast from 1858 until at least 1912 UT (lower right of the flare in Figure 4 but not seen in this image at H-alpha-0.6A).

Evidence of the erupting filament in this example is tenuous. However, from 1824 until the beginning of the flare at 1837, absorbing mass was becoming increasingly visible at H-alpha-0.6A in the east end of the filament channel. It abruptly disappeared from view at the start of the flare, probably because this mass was accelerated out of the passband of the filter. Very little lateral motion was detected during its disappearance as would be expected if the eruption occurred in the line-of-sight. Additional matter in the remainder of the filament channel also disappeared as the flare began. This is not compelling evidence of a filament eruption. However, new filament mass already began accumulating along the polarity inversion during the decay of the flare which is typical of active regions following a filament eruption. Although there was little filament mass to be expelled in this event, we still interpret it as an eruptive flare.

There is some evidence that an earlier flare, starting at 1649 along the main polarity inversion, could have been a less energetic, slow eruptive flare. The absorption along the polarity inversion was more conspicuous and exhibited a more classic preflare enhancement than the one preceding the more energetic one two hours later. The filament began to disappear rapidly in the interval from 1648 until 1652 just as the flare was beginning. This is typical for filament eruptions that are visible in the line-of-sight. Also new filament mass began to accumulate in the filament channel during the decay of the less energetic flare.

It is plausible that more eruptive flares could have occurred at this site during the BBSO night hours because more than 50% of the magnetic flux along the polarity inversion had disappeared by the morning of 7 Oct. Additionally, a filament was observed to steadily darken at H-alpha-0.6 A before the end of the observing day (2154 on 6 Oct). Many other small flares were observed at BBSO throughout 4-9 Oct. but without evidence of filament eruption.

The small active region in which the eruptive flares occurred was relatively isolated from other active regions and there were no other sites of emerging flux

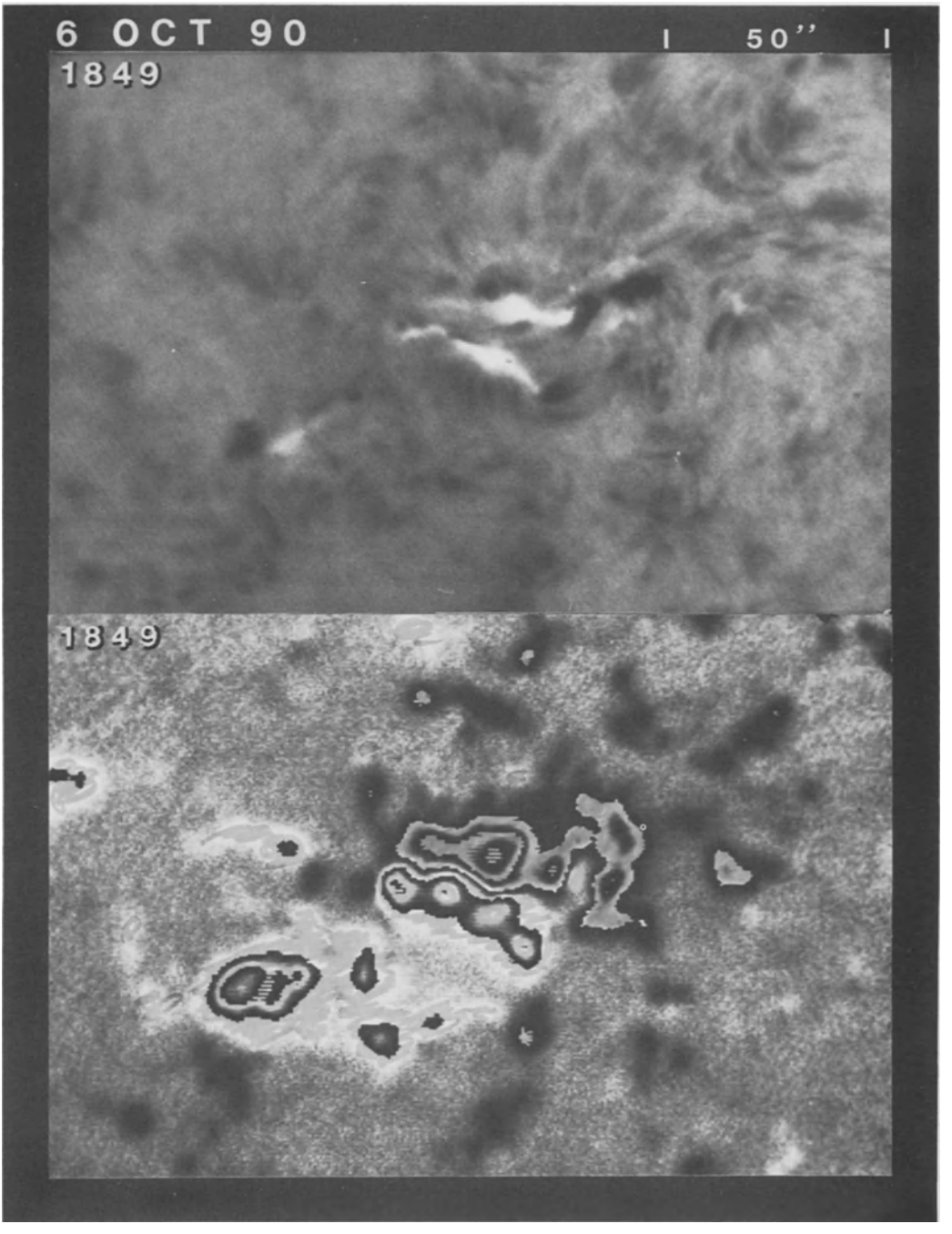

Fig. 4. The brightest emission of this second eruptive flare is in the ribbons centered around the site of rapidly cancelling magnetic fields at the site of highest magnetic field gradient seen in the magnetogram below. The erupting filament was Doppler-shifted out of the filter passband minutes before these images.

within this region at the times of the flares. Thus, we do not suspect that the formation of the filaments, their eruption, and the ensuing flares were influenced strongly by any factors other than the evolutionary changes in magnetic flux. We therefore propose that these flares are examples of the scenario of flare build-up described in the previous section.

4.0 DISCUSSION AND IMPLICATIONS OF THE CONCEPT

In the picture of the flare build-up presented here, the formation of a filament magnetic field is an essential ingredient. We place emphasis on the filament magnetic field rather than its mass because it is not evident that the mass accumlated in the coronal filament channel is significant to the eruption of the filament magnetic field. The filament mass could vary for many reasons. However, the filament magnetic field has no reason to fluctuate; in our picture, it can only increase in proportion to the cancelling fields that are observed. Further, the filament magnetic field can erupt even if there is little or no visible mass in this magnetic field. We suggest that the flare in Figure 4 illustrates this point.

The flare build-up begins with the first cancelling magnetic fields along a polarity inversion and continues either steadily or intermittently as the cancellation is observed to be either steady or intermittent. For this reason, we suggest that the rates of cancelling magnetic flux and the total quantities of cancelling magnetic flux - in relation to a surrounding system magnetic flux - will prove to be useful parameters in flare forecasting. However, this concept is presented only in its simplest form, without taking into consideration external influences or complex magnetic field geometries.

5.0 SUMMARY

The concepts presented in this paper are broad in scope and consist only of a rough outline of the stages that we conceive for the build-up to eruptive flares. Many observational and conceptual details could be added to make the picture more complete. Our primary objective here is only to formulate a concept of the flare build-up. The key stages in this build-up are:

(1) the converging flow of the photospheric footpoints of opposite polarity magnetic fields towards a common boundary (polarity inversion);

(2) the observed cancellation of magnetic flux, interpreted as a result of magnetic reconnection which concurrently leads to the disappearance of line-of-sight magnetic flux near the photosphere and to the building of a mostly horizontal filament magnetic field in the corona above the polarity inversion;

(3) the distending of the corona in a large region around and including the filament magnetic field;

(4) the onset of rapid coronal reconnection beneath the distending filament; this is synonymous with the flare 'trigger', the flare being viewed in the broad sense as all of the consequences of that secondary rapid reconnection.

In this concept of the flare build-up, there is a net transfer of energy from the photosphere into the corona where energy is stored in the magnetic fields associated with filaments and in the surrounding corona. The key signature of that transfer of energy is cancelling magnetic flux observed in near-photosphere magnetograms; that transfer is considered to be a consequence of magnetic reconnection in the low solar atmosphere. The magnetic reconnection is evidently driven by convective flows in the photosphere or by flows related to newly developing active regions.

Acknowledgements

This research was supported by the Air Force Office of Scientific Research under grant AFOSR 90-006. The authors thank V. Gaizauskas for critical reading of the manuscript.

REFERENCES

Recely, F. and Harvey, K.L.:1986, *Solar Terrestrial Predictions*, Proceedings of a Workshop, Meudon, France, 1984, (eds.) P.A. Simon, G. Heckman and M.A. Shea, Published by NOAA (Boulder, CO, USA) and Air Force Geophysics laboratory, (Bedford, MA, USA), p.204.

Hermans, L.M. and Martin, S.F.: 1986, *Coronal and Prominence Plasmas,* (ed.) A. Poland, NASA Conf. Publ. 2442, p. 369.

Kopp, R.A. and Pneuman, G.W: 1976, *Solar Phys.* 50, 85.

Kuijpers, J.: 1990, *Plasma Phenomena in the Solar Atmosphere,* 1989 Cargese workshop, eds. M.A. Dubois, F. Bely-Dubau, D. Gressillon, Les Editions de Physique, BP 112, 91944 Les Ulis Cedex, France, pp. 227-242.

Livi, S.H.B., S.F. Martin, Wang, H. and Ai, G.: 1989, *Solar Phys.* 121, 197.

Marsh, K.: 1978, *Solar Phys.* 59, 105.

Martin, S.F.: 1986, *Coronal and Prominence Plasmas,* (ed.) A. Poland, NASA Conf. Publ. 2442, p. 73.

Martin, S.F.: 1990, Lecture Notes in Physics 363, *Dynamics of Quiescent Prominences,* Springer-Verlag, p. 1.

Martin, S.F., Dezso, L., Antalova, A. Kucera, A. and Harvey, K.L.: 1983. *Adv. Space Res.* 2, 39.

Martin, S.F., Bentley, R.D, Schadee, A., Antalova, A., Kucera, A., Dezso, L., Gesztelyi, L., Harvey, K.L., Jones, H., Livi, S.H.B. and Wang, J.: 1984, *Adv. Space Res.* 4, 61.

Martin. S.F., Livi, S.H.B., and Wang, J.: 1985, *Australian J. Phys.* 38, 929.

Martres, M. J., Michard, R., Soru-Iscovici, I., and Tsap, T.: 1968, *IAU Symp. 35*, 318.

Martres, M. J., Michard, R., Soru-Iscovici, I., and Tsap, T.: 1968, *Solar Phys.* 5, 187.

Rust, D.M.: 1972, *Solar Phys.* 25, 141.

Rust, D.M.: 1974, *Flare-related Magnetic Field Dynamics*, HAO Conference held in Boulder, Colorado, p. 243.

Svestka, Z. and Cliver. E.W.: 1992, these proceedings.

Svestka, Z., Martin, S.F. and Kopp, R.A.: 1980, *Solar and Interplanetary Dynamics,* (eds) M. Dryer and E. Tandberg-Hanssen, p 217.

van Ballegooijen, A.A. and Martens, P.C.H.: 1989, *Astrophys. J.* 343, 971.

VARIATION OF THE VECTOR MAGNETIC FIELD IN AN ERUPTIVE FLARE

D. M. Rust
Johns Hopkins University Applied Physics Laboratory
Johns Hopkins Road, Laurel, Maryland, 20723 USA

G. Cauzzi
USAF Phillips Laboratory Geophysics Directorate
National Solar Observatory/Sacramento Peak
Sunspot, New Mexico 88349 USA

Summary

Observations of a 3B, M6 flare on April 2, 1991 appear to confirm earlier evidence that eruptive flares are triggered by measurable magnetic field changes. In the eight hours before the flare, the shear in the magnetic fields increased. The development that likely triggered the flare was the emergence into the active region and rapid proper motion of new flux. One of the small spots marking the negative magnetic leg of the new flux pushed into an established positive field at 0.2 km/s. Data from the JHU/APL vector magnetograph show that this motion led to the development of a sheared field. The flare started near the newly-sheared fields and spread to engulf most of the spot region. A magnetogram taken 45 min after flare onset shows possible relaxation of the sheared fields.

Introduction

We report here on observations of the vector magnetic fields in Active Region NOAA 6562 in which a two-ribbon 3B flare occurred on April 2, 1991, starting at 2251 UT. Flare maximum was at 2320 UT. The GOES X-ray classification was M6.1. On the basis of its long duration - more than 3 h - and the formation of prominent post-flare loops, we think this flare is a classic eruptive flare. H_α observations from the full-disk flare patrol at Sacramento Peak show some variation in the visibility of a thin filament between the two flare ribbons, but we cannot confirm from these films that there was a filament eruption. Nevertheless, all other indications are consistent with the usual sequence of events in an eruptive flare (Svestka 1976), including a Type IV metric radio burst lasted for ~ 3 h. The flare was responsible for a three-day proton event at Earth. The flux of 10 MeV protons peaked at 52 pfu on April 4.

We obtained vector magnetic field observations at 1452, 1815, 2215, 2335, 2347 and 2355 UT on the day of the flare and on the previous day. The observations were made with the JHU/APL vector magnetograph (VMG) at Sacramento Peak (Rust and O'Byrne 1989, 1991).

Instrumentation

The VMG has a field of view of 2.4 arcmin x 3.6 arcmin. The detector is a 384 x 576-pixel CCD array, which sets the scale at 0.375 arcsec/pixel. We inferred the vector fields from filtergrams of $I + Q$, $I - Q$, $I + U$, $I - U$, $I + V$ and $I - V$ made in the 6102 Å line of Ca I. Stokes parameters I, Q, U, and V were measured sequentially at two positions in the blue wing of the line. The JHU/APL vector magnetograph obtains images at six sequential settings of a Glan-Laser prism and a quarter-waveplate: 0°, 90°, 45° and 135°, with the waveplate out, and 0° and 90°, with the waveplate in. Filtergrams were obtained at a rate of about 30/min. Ten twelve-image sequences were taken for each pair of interleaved magnetograms. The deleterious effects of poor seeing can be alleviated with an image motion compensator (Strohbehn 1990), but it was not operating during our observations.

The narrow-band filter in the VMG is a lithium niobate ($LiNbO_3$) Fabry-Perot etalon (Burton, Leistner and Rust, 1987). It has a spectral bandwidth of 167 mÅ. The etalon is made from a 75-mm diameter wafer of crystalline, Z-cut lithium niobate polished to a thickness of 220 μm and $1/400^{th}$ wave rms flatness. Dielectric coatings on the surfaces are 93% reflecting over a 6000 - 8000 Å band, but so far, we have operated only in the 6122 Å line. The filter is tuned by application of voltage to the filter faces, which have transparent conductive coatings. The tuning parameter is 0.4 mÅ/V.

Interpretation of Stokes Measurements

We interpreted our measurements by appeal to the so-called weak field approximation (WFA) Jefferies and Mickey (1990). In the past the WFA has been applied only when the ratio of the magnetic splitting $\Delta\lambda_B$ ($= \mu_\lambda B$) to the Doppler width $\Delta\lambda_D$ of the spectral line is small. Jefferies and Mickey greatly extended the range of the WFA by carefully examining the errors entailed in letting this ratio approach and even exceed unity. They concluded that the range of WFA validity can be larger than previously thought, when magnetograph measurements are made sufficiently far into the line wings. For λ6122, where $\Delta\lambda_D$ = 116 mÅ, we can apply the WFA to all our measurements for magnetic fields < 2000 G, with < 30% error (Cauzzi, 1991).

To calibrate the VMG, we used the simple relation,

$$V = - \mu_\lambda B \cos\gamma \left(\frac{dI}{d\lambda}\right) \qquad (1)$$

where $dI/d\lambda$ is the slope of the line at the offset position $\Delta\lambda_{off}$ of the passband from line center and γ is the zenith angle of the field B.

In calibrating the VMG, we applied a voltage $\mathcal{E}_{cal}$ to the etalon. (For the Ca I line, $(B \cos\gamma)_{cal}\,(Gauss) = 13\ \mathcal{E}_{cal}$, where $\mathcal{E}_{cal}$ is expressed in volts.) To get $(B \cos\gamma)_{measured}$

from $(B \cos \gamma)_{cal} (V_{measured}/V_{cal})$, the slope of the line, $dI/d\lambda$, should be the same for both calibration and observation. This means that the calibration should be performed on the same solar scene as the observations and that the calibration step $\Delta\lambda_{cal}$ should be small. We calibrated every measurement with $\Delta\lambda_{cal}$ = 20 mÅ, which simulates a 325 G longitudinal field.

Calibration of the Q and U signals is similar to the V calibration. According to Jefferies and Mickey (1990), the Stokes Q vector is given in the WFA by

$$Q = \left(\frac{\mu_\lambda B \sin \gamma}{2}\right)^2 \left(\frac{dI}{d\lambda}\right) \left(\frac{3}{\Delta\lambda_{off}}\right) \qquad (2)$$

where, $\Delta\lambda_{off}$ is the offset of the filter passband from spectral line center and the azimuthal factor has been suppressed. Q is proportional to the square of a simulated Zeeman shift over a wide range, for appropriate choice of $\Delta\lambda_{off}$. For calibration of the Q and U signals, then, one again introduces a passband shift in the etalon, now to simulate the apparent shift $\mu_\lambda B \sin \gamma$. The calibration of Q (and U) is done with the same $\Delta\lambda_{cal}$ and $dI/d\lambda$ as the measurements. The calibration sequences constitute a separate and independent set of magnetic measurements.

Because the flare occurred at N14° E00° (heliographic coordinates), we did not need to convert from an oblique view angle, as is usually necessary before commencing interpretations.

Results

We examined the VMG data for evidence of sheared fields and moving or emerging magnetic fields. Figure 1 shows the fields and sunspots in NOAA 6562 8 h before and 45 min after flare onset. The principal features of the AR were the southwestern cluster of large spots (lower right) with positive polarity and the eastern (left) cluster of large spots, also with positive polarity. The two clusters were very different, according to our vector magnetograms. Fields in the western cluster resembled potential fields, i.e., they point radially outward from the sunspots (Figure 2). The field direction in the eastern spots was nearly parallel to the boundary between the positive spots and the surrounding negative fields (on the left). Following the terminology of Hagyard *et al.* (1984), we call the fields sheared, and one might expect a flare to begin in this region.

The flare began, or was triggered, instead, in a large emerging flux region. Arrows in Figure 1 show the two spots A and B of this EFR. These spots separated at ~ 0.2 km/s in the 8 h leading up to the flare. Spot A, with negative field, drove rapidly southwestward while increasing in size and magnetic field strength. The effect of this motion was to steepen the horizontal gradient in the longitudinal field between spot A's leading edge and the small positive spot C just visible in the image at 2335 UT. This sort of activity has been noted before in large, carefully-examined flares (e.g., Gesztelyi, *et al.* 1989, Wang *et al.* 1991; Rust, Nakagawa, and Neupert 1975; Hoyng *et al.* 1981)).

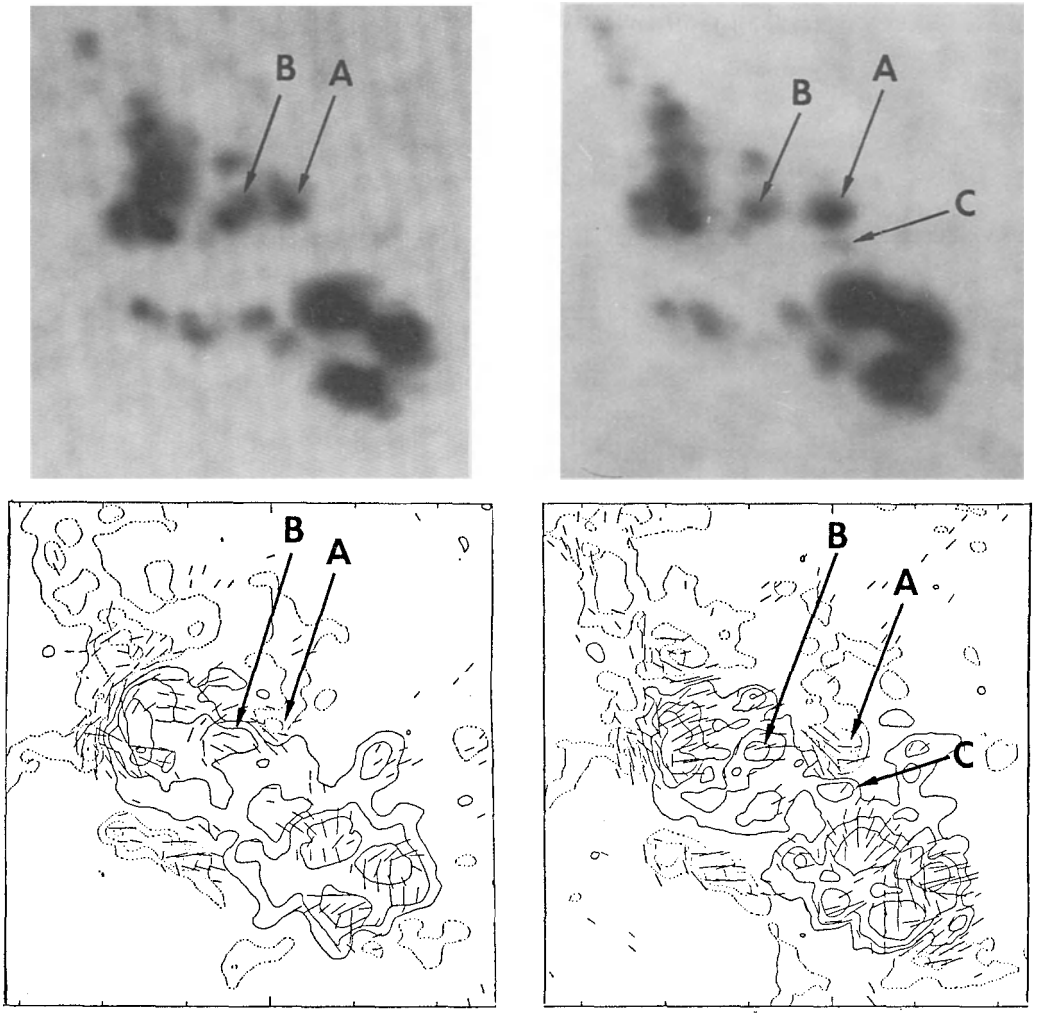

Figure 1. Filtergrams and magnetograms of AR NOAA 6562 on April 2 at 1455 UT (left) and 2330 UT (right). North is at the top, East is on the left. Arrows A and B show the EFR. The gradient in the longitudinal field steepened between A and C. Longitudinal field contours are 100, 400 and 800 G. Positive fields have solid contours, negative fields, dashed contours. Slashes represent transverse fields up to ~ 1600 G. Each image is 2.4 arcmin *x* 2.4 arcmin.

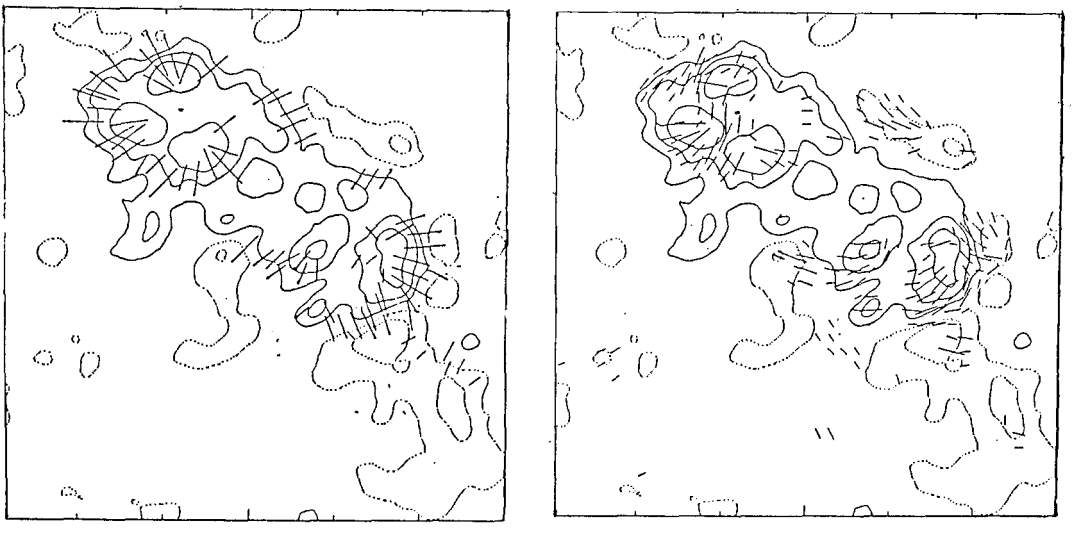

Figure 2. Comparison of the transverse component of the vector fields as measured at 1815 UT (left) and the transverse component as computed from the longitudinal fields under the assumption that no electric currents were present.

The vector magnetograms allowed us to see the effect of EFR growth and expansion on the transverse fields. Figure 3 shows, with independent magnetograms in two wavelengths, the transverse field in and near poles A and B of the EFR. These are linked by the arcade of slashes just to the left of center in the figure.

The observations at 1455 show transverse fields crossing the polarity boundary between A and C at ~ 90°. They resemble current-free fields. By 2215 UT, just 36 min before flare onset, the angle was closer to 0°. Thus, the observations show a build up of shear between A and C The lowest panels in Figure 3, taken at 2335 UT, shown a lessening of the shear.

The arrows in Figure 3 show a prominent transverse field that presented itself just before the flare, but it is not seen in any other magnetogram. It is tantalizing evidence for possible welling-up of new flux just before the flare.

High-resolution observations of the flare onset are not available, but the Sacramento Peak flare patrol images show early flare brightenings at A and C (Figure 1). Other areas in the region also brightened at about the same time. Unfortunately, the 60-s interval between exposures and the modest resolution of the images did not allow us to find the first flare kernels. We can say only that the flare may have started near the sheared region between A and C.

Conclusions

In agreement with earlier observations, e.g., Hagyard *et al.* (1984), we find that a large flare occurred near sheared fields. There were no flare ribbons near the leader spots, where the

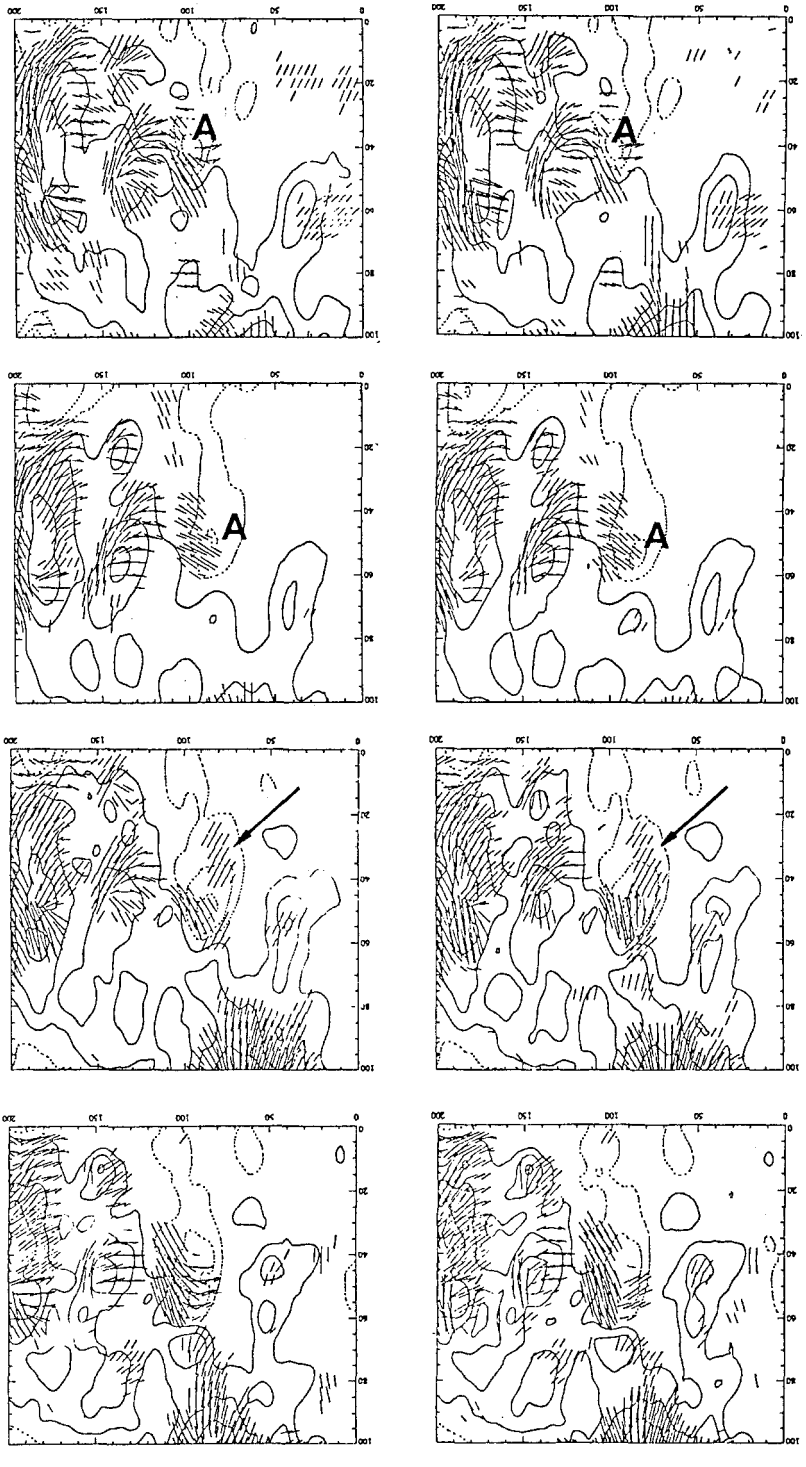

Figure 3. Two sequences of vector magnetograms in the region of the EFR. The series on the left was made with the filter at ~ 100 mÅ from line center. The sequence on the right, at 120 mÅ, was interleaved with the other, but it is an independent set of measurements. Observation times were (top to bottom) 1452, 1815, 2210 and 2335 UT.

vector fields most resembled current-free fields. However, the six magnetograms obtained before and after flare onset on April 2 have highlighted important developments that diurnal observations could not show. The April 2 data illuminate earlier classic observations of sunspot motion and flux emergence. They show that an EFR can create a sheared field in < 8 h. High-resolution H_α observations have long been interpreted in just such terms (e.g., Rust, Nakagawa and Neupert 1975), but actual transverse field measurements showing the shear were not available until now.

No large flares except the one studied here occurred in AR6562. Yet, observations on the day before the flare showed that the sheared fields seen in the northeast on April 2 were present even then, although they were weaker. Hence, we must agree with Hagyard and Rabin (1986) that strongly sheared fields may be necessary for flares, but they are not sufficient. Some "external" perturbation is required to destabilize them. We think this destabilization may be related to reconnection of the emerging flux with the established fields. Just before the flare, a strong transverse field made a sudden and brief appearance near spot A. Could this have been the real trigger of the flare? More observations are needed, but it is entirely possible that fields from below the surface could emerge in ~ 45 min and disturb the previous equilibrium.

Acknowledgements

We are grateful to Craig Gullixson for operating the vector magnetograph. This work was sponsored by the Air Force Office of Scientific Research, grant AFOSR-90-0102. G. C. held an NRC Fellowship at the USAF Phillips Laboratory during the course of this work.

References

Burton, C. H., Leistner, A. J. and Rust, D. M. 1987: *Instrumentation in Astronomy VI,* SPIE Conf. Proc. **627**, 39 - 49.

Cauzzi, G. 1991: *NSO Technical Report 1991-01*, National Solar Observatory, Sunspot, NM.

Gesztelyi, L, Karlicky, M., Farnik, F., Gerlei, O., and Valnicek, B. 1986: in *The Lower Atmosphere of Solar Flares* (D. F. Neidig, ed.), Natl Solar Obs., Sunspot, p. 163.

Hagyard, M. J., Smith, J. B., Teuber, D., and West, E. A. 1984: *Solar Phys.* **91**, 115.

Hagyard, M. J. and Rabin, D. M. 1986: *Adv. Space Res.* **6** 7.

Hoyng, P., Frost, K. J., Woodgate, B. E., and the SMM HXIS Team 1981: *Astrophys. J. Lett.* **246**, L155.

Jefferies, J. and Mickey, D. L. 1990: submitted to *Astrophys. J.*

Rust, D. M., Nakagawa, Y., and Neupert, W. 1975: *Solar Phys.* **41**, 397.

Rust, D. M. and O'Byrne, J. W. 1989: in *High Spatial Resolution Solar Observations*, D. Neidig (ed.), National Solar Observatory, Sunspot, NM, p. 378.

Rust, D. M. and O'Byrne, J. W. 1991: in *Solar Polarimetry*, L. November (ed.), National Solar Observatory, Sunspot, p. 74.

Strohbehn, K. 1990: *JHU/APL Tech. Memo. S1A-67-90*, JHU Applied Physics Laboratory, Laurel.

Svestka, Z. 1976: *Solar Flares*, Reidel, Dordrecht, p. 6.

Wang, H., Tang, F., Zirin, H., and Ai, G. 1991: *Astrophys. J.* (in press).

INTRINSICALLY HOT FLARES AND A POSSIBLE CONNECTION TO DEEP CONVECTIVE MAGNETIC FIELDS

Howard A. Garcia and Patrick S. McIntosh
NOAA Space Environment Laboratory, Boulder, Colorado

About 30 high-temperature flares (HTFs), $T_c \geq 25$ MK, observed in broadband soft x-rays, occur in each solar cycle. In the combined cycles 21 and 22, 54 of these flares have been observed. Roughly one-third of HTFs occur within about 10° of the limb; the effect of line-of-sight propagation through atmospheric layers may make them only *apparently* hot. The remainder, at smaller meridian distances, are intrinsically hot; those at super-high temperatures ($T_c \geq 30$ MK) appear to have a unique relationship to large-scale surface magnetic fields.

HTFs appear to occur only in specific types of active regions, which we have begun to study. During 1975–1991, more than 6700 active regions were classified. Of these, 35 regions were responsible for all 54 observed HTFs (i.e., about .5%); because some of these regions produced HTFs on the previous disk passage, the actual number of HTF regions is only 30 for cycles 21–22. The 13 super-hot flares (>30 MK) in cycle 21 came from only 6 regions.

Examination of Carrington longitudes for HTFs does not seem to reveal any particular active longitudes. Significant trends emerge only in the context of large-scale patterns of magnetic polarity over extended periods of time. Hα synoptic charts (McIntosh,1981; McIntosh and Wilson, 1985) presented in 10° latitude zones and stacked in a vertical time sequence show long-lived patterns of magnetic polarity, which reveal that strong active regions often form on the boundaries of large-scale magnetic structure.

Because Hα synoptic charts are constructed in time vs. heliographic longitude, it is possible to locate active regions inside charts for certain latitude zones even though the regions may belong to other latitudes. HTF regions so located share the same differential drift rate as large-scale magnetic features at 30° latitude; i.e., the actual, average latitude of HTF regions in cycle 21 was about 10°, but the sequence of those regions rotated much as did magnetic structure at 30° latitude.

Recent discoveries indicate that the Sun's convective mantle rotates differentially at nearly the surface rate and that the gradient of angular velocity at the bottom of the convection zone reverses at ~30°, where the surface rotation matches that of the rigidly rotating core. This may suggest that extremely hot flares are related to processes deep within the Sun.

McIntosh, P.S.: 1981, in *The Physics of Sunspots*, L.E. Cram and S. Thomas, eds., Sacramento Peak National Observatory, Sunspot, NM, 13.

McIntosh, P.S., and Wilson, P.R.: 1985, *Solar Physics*, **97**, 59.

INTERACTION OF LARGE-SCALE MAGNETIC STRUCTURES IN SOLAR FLARES

C.H. Mandrini*, P. Démoulin and J.C. Hénoux****

* Instituto de Astronomía y Física del Espacio, CC 67, Suc. 28, 1428 Buenos Aires, Argentina

** Observatoire de Paris, DASOP, UA326, 92195 Meudon, Principal Cedex, France

Abstract. Modelling the observed vertical magnetic field of active region (AR) NOAA 2372 by the potential field of an ensemble of magnetic dipoles, we have derived the likely location of the separatrices, surfaces that separate cells of different field line connectivities, and of the separator which is the intersection of the separatrices. The connectivity of every magnetic field line, which is defined by the dipoles located at its ends, is computed by a code that, starting from any pixel in the photospheric plane, integrates numerically the differential equation defining a line of force towards both ends of this line until one dipole is reached. This code allows us to obtain the topology of the field in three dimensions.

We have compared our results with observations of a 1B/M1 flare that developed in AR 2372 on April 6, 1980 at 20:53 UT (Lin and Gaizauskas, 1987), twenty minutes before obtaining the magnetogram. We found that four of the five off-band Hα kernels were located near or at the separatrices. These Hα kernels are connected by field lines that pass close to the separator. This indicates that the flare may have resulted from the interaction of large scale magnetic structures in the separator region. Moreover, Lin and Gaizauskas (1987) showed that the Hα flare kernels coincided with the peak values of the longitudinal electric current density. This finding and the fact that no strong current and no Hα kernel are observed at the intersection of the separator with the photosphere, lead to the conclusion that the magnetic energy released during the flare is mostly stored in an ensemble of currents flowing along lines of force. Some instability, presumably due to reconnection taking place in the separator, is likely to be the origin of the energy release and of the observed flare.

References.

Lin Yunzhang and Gaizauskas, V.: 1987, Solar Phys. **109**, 81.

This paper will be published in Astronomy and Astrophysics.

THE INTRINSIC RELATIONSHIP BETWEEN FLARES AND ERUPTION OF FILAMENT CURRENTS

S. T. Wu and Ao Ao Xu
Center for Space Plasma and Aeronomic Research
and Department of Mechanical Engineering
The University of Alabama in Huntsville
Huntsville, Alabama 35899 U.S.A.

Abstract

In this study, we have employed the data from four flares with filament eruptions given by Kahler *et al.* (1988) to deduce the filament current and total energy as functions of time according to the Kuperus-Raadu filament model (1974). From these results, we found that the impulsive phase of these four flares is at the maximum of the total energy contained in the filament, which shows that the total energy of the filament decreases at the initiation of the impulsive phase of the flare. The amount of the filament energy decreases as required by the flare energy. Further, we discovered that the importance of the X-ray flare is proportional to the rate of the increase of the total energy prior to the filament eruption. On the basis of these results, we concluded that there is an intimate relationship between the flare and eruptive filament quantitatively.

I. Introduction

It has been known that there is an intimate relationship between the impulsive phase of flares and filament eruptions. Recently, Kahler *et al.* (1988) have shown on the basis of observations that the filament eruptions are not driven by the flare plasma pressure, but instead marks an eruption of magnetic field driven by a global MHD instability of the field configuration in the region of the flare. Theoretically, a number of authors (Kuperus and Raadu, 1974; Van Trend and Kuperus, 1978; Martens, 1987; Martens and Kuin, 1989) have proposed theoretical models to describe the filament eruptions and flares. In particular, the circuit model derived by Martens and Kuin (1989) had shown that the magnetic free energy is concentrated in the currents through the filament, the underlying current sheet and the surface return current to complete a circuit.

In order to further the analysis of Kahler *et al.* (1988) quantitatively, we employed the circuit models (Kuperus and Raadu, 1974; Martens, 1987; Martens and Kuiin, 1989) to compute the evolution of the current intensity, total energy and filament speed for these four flares studied by Kahler *et al.* (1988). In our analysis, we solved the momentum and energy equations for the filament currents to obtain the physical parameters as we have mentioned. From our computed results, we note that the conclusions derived from the study of Kahler *et al.* (1988) are enhanced.

II. Analysis

The mathematical model used for this study is adopted from the theory given by Kuperus and Raadu (1974), Martens (1987) and Martens and Kuin (1989). The observed data used for this analysis are obtained from these four flares presented by Kahler *et al.* (1988), because, these four flares were selected by them with great care and exhibited general characteristics of the filament eruptions and the impulsive phase of solar flares. Furthermore, it is possible to provide all the necessary parameters to compute the current intensity, total energy, and speed of the filament ascending motion, as well as the altitude of the maximum current intensity. Using the motive equation (Kuperus, Raadu, 1974) and the total energy equation (Martens, 1987), we obtain the evolution of the current intensity and total energy of the filaments with time before and after the onset of the flare's impulsive phase. The results for the 1979 April 26 flare are shown in Fig. 1. The other three flares have similar behavior but are not shown here. These results, which are obtained for the four events, revealed the following relationship between the flares and filament eruptions.

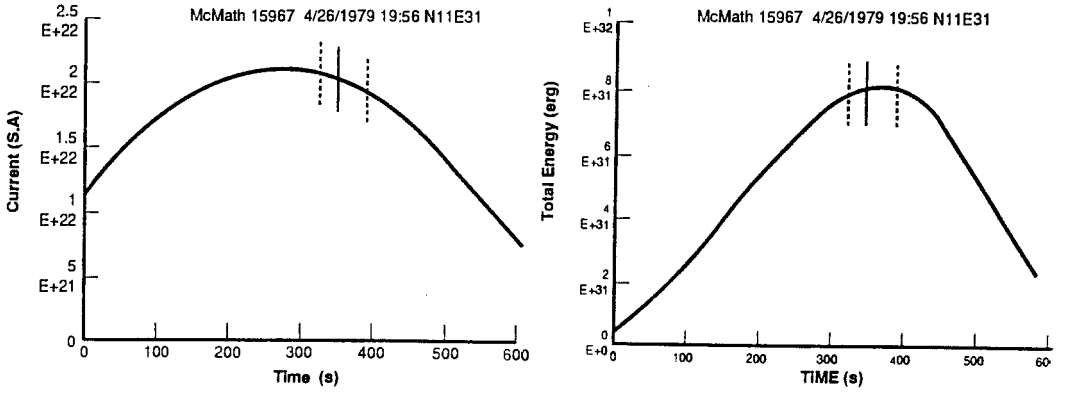

Figure 1. The evolution of the current intensity (statampers) and total energy (ergs) of the filaments for the 1979 April 26 event. The solid vertical line marks the X-ray onset of the impulsive phase. The dashed lines show the earliest and latest possible onset of the Hα flash phase as determined from the movie.

(i) The flare's impulsive phase occurs 10 -20 seconds after the maximum intensity of the filament's current,

(ii) The onset of the impulsive phase coincides with the maximum of the filament's total energy. Furthermore, we note that the total energy of the filament decreases rapidly after the onset of the impulsive phase. According to our estimate, the magnitude of the total energy of the filament decrease equals the amount of energy released from the flare.

(iii) When the impulsive phase begins, the order of magnitude of the filament's current intensity reaches the observed value (i.e. 10^{12} A).

(iv) Using the results shown in Fig. 1, we determine the mean power ($\bar{P}$) delivered to the filament before the onset of the flare's impulsive phase as shown in Table I. We

notice that the X-ray importance for three events is proportional to $\bar{P}$ except for the 1980 June 25 flare. This inconsistency may be due to the dynamical behavior of this flare as shown in Fig. 2.

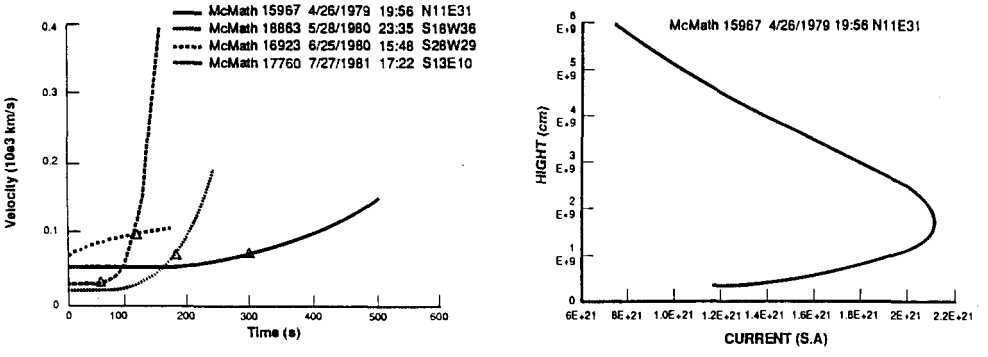

Figure 2. (a) The velocity of the filament VS time for the four observed events. and (b) The current intensity (statampers) VS height for the 1979 April 26 event.

Table I.

$\bar{P}$ of the Four Filaments and the Importance of the Relevant X-ray Events

Date of the Actions	$\bar{P}(erg \cdot s^{-1})$	Importance of the X-Ray Events
1979 Apr 26	6.3×10^{28}	C_7
1980 May 28	4.6×10^{27}	M_6
1980 Jun 25	1.5×10^{30}	M_4
1981 Jul 27	1.1×10^{30}	X_1

III. Discussion

It has been shown by Martin and Ramsey (1972) in their statistical study of 297 large flares that the motions of the filaments prior to the impulsive phase are manifestations of the early stages of filament activity. In the study described by Kahler *et al.* (1988), they suggested that all eruptive events are characterized by a rapid ($\leq$ 5 min) acceleration to a speed larger than 100 km s^{-1}, which will be accompanied by an impulsive phase. In the theoretical aspect, it has demonstrated that the circuit model (i.e. Kuperus and Raadu, 1974; Martens, 1987; Martens and Kuin, 1989; Xu and Zhang, 1991) play an important role in the description of the flare processes. Also notice that the shear and convergence motion at the photosphere may enhance the currents in the active region. When these enhanced currents of the filaments interact with the background magnetic field in the active regions, the filaments may rise. Xu and Zhang (1991) show that this ascending motion is very slow before the current intensity reaches critical value. As soon as the current intensity reaches approximately the critical value,

the ascending velocity of the filament begins to increase rapidly. This feature can be demonstrated by using the results of this study. Fig. 2a shows the velocity of the filament as a function of time for the four flares (Kahler *et al.* 1989). Fig. 2b shows the relation of the current intensity of the filament to their altitude for the 1979 April 26 event. The other events also exhibit similar features but are not shown here. From these results together with the h-t curve given by Kahler *et al.* (1988), we find that the acceleration of the filaments occur near the critical value of the current intensity. Hence, these results display the intrinsic relationship between the sudden acceleration of the filaments and the critical current intensity. To sum up, we conclude that the occurrence of the flares is due to the evolution of the filament currents.

IV. Concluding Remarks

By further analysis of the observed data of Kahler *et al.* (1988), we demonstrate quantitatively that the enhancement of the filament currents and the rapid motion of the filaments are an indication of the occurance of the flares. Once the filament current exceeds the critical value, the flare will occur. The moment of the onset of the impulse phase is consistent with the moment of the maximum filament total energy (Fig. 1). After the beginning of the impulsive phase, the filament's total energy decreases. This result shows that the flare energy is supplied by the filament. In addition, our results demonstrate that the importance of an x-ray flare is proportional to the increasing rate of the filament energy before the occurance of the flare. This may be another evidence that the flare energy is transported from the filament currents.

Acknowledgement

We would like to acknowledge Dr. E. Tandberg-Hanssen for reading the manuscript and giving valuable suggestions. The work done by S. T. Wu is supported by a NASA grant (NAGW-9) and NOAA contract (50RANR7000104).

References

Kahler, S. W., R. L. Moore, S. R. Moore and H. Zirin, 1988, *Ap. J.*, 328, 824.
Kuperus, M. and M. A. Raadu, 1974, *Astron. Astrophys.*, 31, 189.
Martin, S. F. and H. E. Ramsey, in Solar Activity Observations and Predictions, (ed. P. S. McIntosh and M. Dryer), MIT Press, Cambridge, Mass, 1972, 371.
Martens, P. C. H., 1987, *Solar Phys.*, 107, 95.
Van Trend, W. and M. Kuperus, 1978, *Solar Phys.* 59, 115.
Xu, A. A., and H. Q. Zhang, 1991, *ACTA Astron. Sinica*, (submitted)

FILAMENT ERUPTIONS, FLARING ARCHES AND ERUPTIVE FLARES

A. BHATNAGAR, A. AMBASTHA AND N. SRIVASTAVA
Udaipur Solar Observatory, Udaipur-313001 (India)

Abstract. *Several cases of erupting filaments showing distinctly their "feet" have been studied. Role of the feet and their anchorage with the photosphere in maintaining filament stability is established, apart from the footpoint separation and height criteria. Further, a homologous series of more energetic events, namely, the flaring arches and eruptive flares of March 5-7, 1991, suggest a repetitive restoration of magnetic field conditions and energy build-up within a day. High resolution H-alpha observations of these events indicate that large amount of ejected material was "siphoned out" from the chromosphere through the top of a low-lying compact emission loop within the active region.*

1. Introduction

Although filaments have been observed extensively, basic processes, such as, their formation, long life in hot coronal plasma, magnetic and velocity structures and role of the observed "feet", are not well understood. Kippenhahn and Schluter (1957) and Kuperus and Raadu (1974) have proposed prominence/filament models (for further references see: Tandberg-Hanssen 1974; Hirayama 1985; Priest 1989). Necessary conditions for formation and disruption of filaments are recently reviewed by Martin (1989a). Filaments form along channels of neutral longitudinal magnetic field, which are bounded by regions of vertical field of opposite polarity. Development of filament begins probably with the formation of footpoints connecting it to the solar interior. After it is fully formed, the number and the distance between the "feet" and the height of the filament, appear to be crucial parameters for its stability. A flare induced disturbance or reconfiguration of magnetic and/or velocity fields could trigger instabilities leading to filament eruption.

To examine the role of "feet", we have selected some typical cases of filament eruption from a large number of observations taken at the Udaipur Solar Observatory (USO). These distinctly show formation and disruption of the "feet" and their consequence on the filament eruption. "Plage filaments" in active regions also show activation and eventual eruption which may be associated or triggered by flares. Martin (1989b) has grouped various flare features into two broad classes; namely, (i) the coronal component consisting of flare loops, flaring arches, surges, erupting filaments, and (ii) the chromospheric component consisting of flare-ribbons and remote bright patches. Features of the coronal component, with the exception of surges, have not been observed or reported so often due to observational constraints. A series of homologous flaring arches and eruptive flares were observed during March 5-7, 1991 in an observationally favourable location near the SE-limb. These energetic and dynamic events are included here for a comparison with the slowly evolving filament eruption events. All observations reported here were made in H-alpha through a Razdow full disk 12.5 cm aperture telescope and small field high resolution 25 cm aperture spar telescope at USO, except for the data obtained from the Big Bear Solar Observatory (BBSO) for April 21-23, 1990. In the following, we give brief description of these events.

2. Filament Eruption Events

2.1. MAY 5-9, 1979 : A small filament appeared forming in an old decaying spotless AR McMath No. 15986 around May 4. Within 4 days, it formed into a close round shape, as seen projected on the disk (Figure 1: 09/04:34:13 UT frame). On May 9/07:33:00 UT, a subflare occurred near one of the feet of the filament which triggered its violent eruption. These observations were made in the blue wing of H-alpha line, hence upward motion of the filament was observable. It may be noted that in this case a subflare triggered a major filament eruption, while even major flares sometimes are not able to cause discernable effects on nearby filaments, as in the case of March 5-7, 1991 events discussed later. It appears that strength of the anchorage of filament feet could explain this discrepancy.

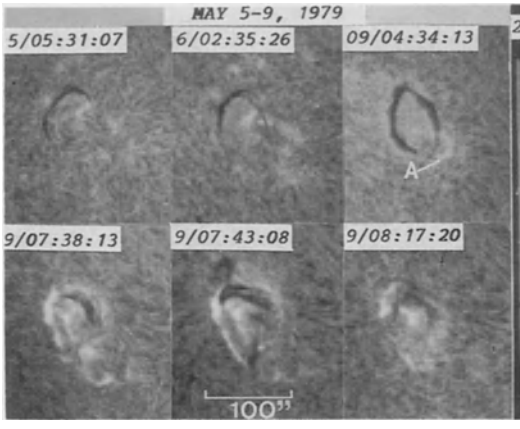

Fig. 1. Filament eruption on the disk on May 9, 1979.

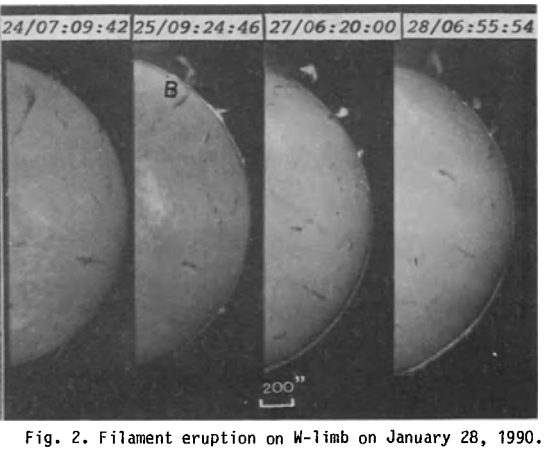

Fig. 2. Filament eruption on W-limb on January 28, 1990.

2.2. JANUARY 16-28, 1990 : Two large filaments were observed during their disk passage of January 16-28, 1990. During this period, one of them displayed some activation but did not erupt, on the other hand, the filament marked "B" remained quiescent till January 24. Subsequently, it displayed significant activation and partly lifted upward to 100,000 km from the W-limb on 25/09:24:46 UT (Figure 2). However, the main prominence body remained attached to the surface through three distinct feet and eruption was prevented perhaps due to their strong anchorage with the photosphere. On January 27, the filament was seen supported only on two feet. Between January 27-28, one more foot got disconnected, resulting in slow filament eruption with an upward speed of 9 km s^{-1}.

2.3. APRIL 11-24, 1990 : On April 10, the filament marked "B" appeared at the E-limb which showed structural variations during its disk transit. Rapid changes occurred before its eventual eruption on April 24, therefore BBSO full disk movie was obtained for April 22-23 to cover our night-time gaps. From the BBSO movie, interestingly a small "tongue" like plage brightening "F" was observed in AR Boulder No. 6022 at a distance of 145,000 km away from the filament (Figure 4: 22/16:54:07). Following this event, a pattern of brightness variation was noticed travelling down along the leg "1" during 18:56:44-19:32:04 UT. This feature, moving with a speed of 10 km s^{-1} caused brightening of its footpoint. The brightness profiles of plage "F" and footpoint "a1" show nearly identical variations but with a delay of about 5 min (Figure 3). The near simultaneity of the two phenomena suggests that this fast ejected emission feature "F" triggered the disturbance along the leg "1". The observed delay indicates that the disturbance travelled from "F" to the filament with an average speed of 480 km s^{-1}. Such travelling shock wave disturbances have been reported earlier (Ramsey and Smith 1966, Smith and Harvey 1972). Following this event on April 22, the filament displayed structural changes on April 23. One of the two feet (i.e., "2") detached from the main filament body (BBSO frame- 23/16:03:38). Thereafter, the filament erupted on April 24; initially rising slowly at a speed of 15 km s^{-1} and later with over 72 km s^{-1}, reaching up to 380,000 km above the

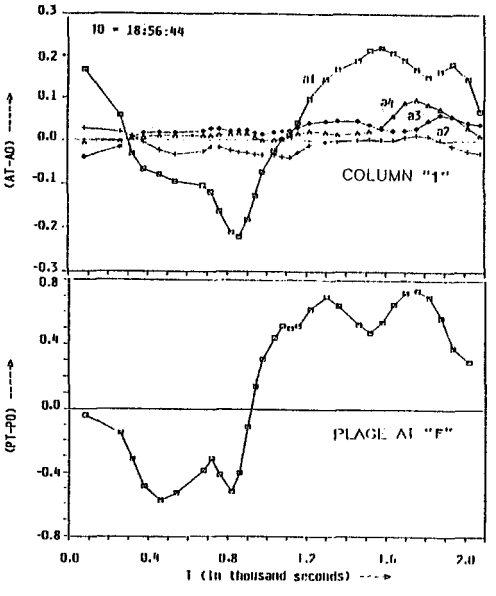

Fig. 3. Plots of brightness variation along filament leg "1" and plage "F" on April 22, 1990.

limb. This is a case of filament destabilization, possibly due to a remote disturbance, causing a distinct detachment of one of the filament feet and its eventual eruption.

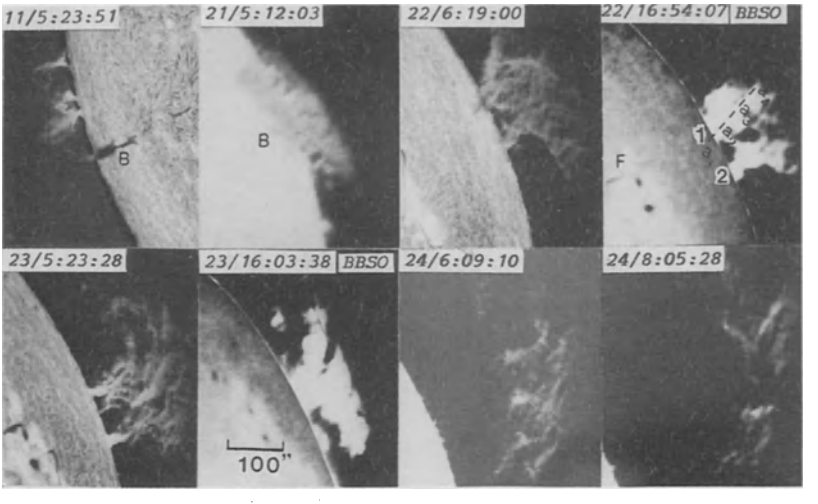

Fig. 4. Filament development, activation and eruption event of April 11-24, 1990.

2.4. MAY 2, 1990 : A moderately active prominence appeared at the E-limb on May 1 which became fully visible on May 2. Its location was just right to display the complete structure along with its anchorage through the footpoint "A" (Figure 5). Around 02/05:00:00 UT, its top portion arched towards the solar surface, finally forming two more feet at locations "B" and "C" (02/05:20:00 UT frame). Barely 15 minutes later, footpoint "B" disconnected, thereby weakening the anchorage, resulting in a mass ejection (06:12:54 UT frame). At this instant, the filament material appeared resting on "A" and "C" feet only. As the difference between the height and footpoint distance became rather too large, the filament became unstable, and foot "C" was detached. Once "C" was disconnected, the filament sprang back on the footpoint "A", resulting in a violent eruption with an average ascending speed of 100 km s^{-1} (06:36:54 & 06:42:19 UT frames). This is a classic case of filament instability initiated due to disconnection of the supporting prominence feet, which is very important for its stability.

MAY 2, 1990

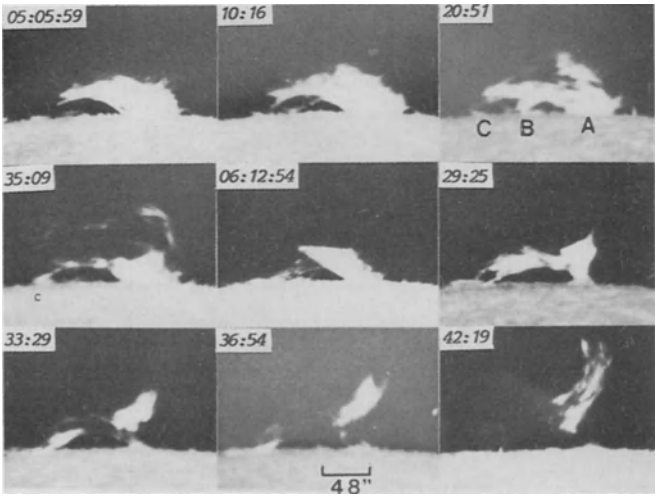

Fig. 5. Filament eruption on E-limb on May 2, 1990.

3. Flaring Arches and Eruptive Flares

Recent observations of an interesting and extremely dynamic series of homologous flaring arches and eruptive flares of March 5-7, 1991 are discussed here for a comparison with erupting filaments, however, the physical processes involved may be different:

3.1. MARCH 5, 1991 : Surge activity was seen at the SE-limb on March 4, 1991 indicating arrival of the active region Boulder No. 6538. On March 5/05:30:00 UT, an intense rapidly ascending mass, marked as "A", appeared in this region, which quickly turned into a beautiful twisted flaring arch seen connected behind the limb (Figure 6a-06:40:48 UT). This arch system reached a height of 110,000 km from the limb with a speed of 400 km s^{-1}. It is to note that even before the primary leg "A" of the arch connected to the secondary footpoint behind the limb, conspicuous increase in brightness was observed above the limb at several places around "B" (06:40:48 frame). This flaring arch activity continued for over 40 minutes. Two hours later, another very bright mass ejection ensued from the same flaring arch location (Figure 6b). Contrary to the earlier case of flaring arch event, where material was seen moving from the primary to the secondary footpoint, the mass ejection in this eruptive flare occurred almost vertically, with a speed of 110 km s^{-1}. The ejected mass reached a height of 60,000 km and then descended with a speed of about 50 km s^{-1} along the same path. The brightness and density of the material involved in the eruptive flare appeared to be several times more than in the case of flaring arch.

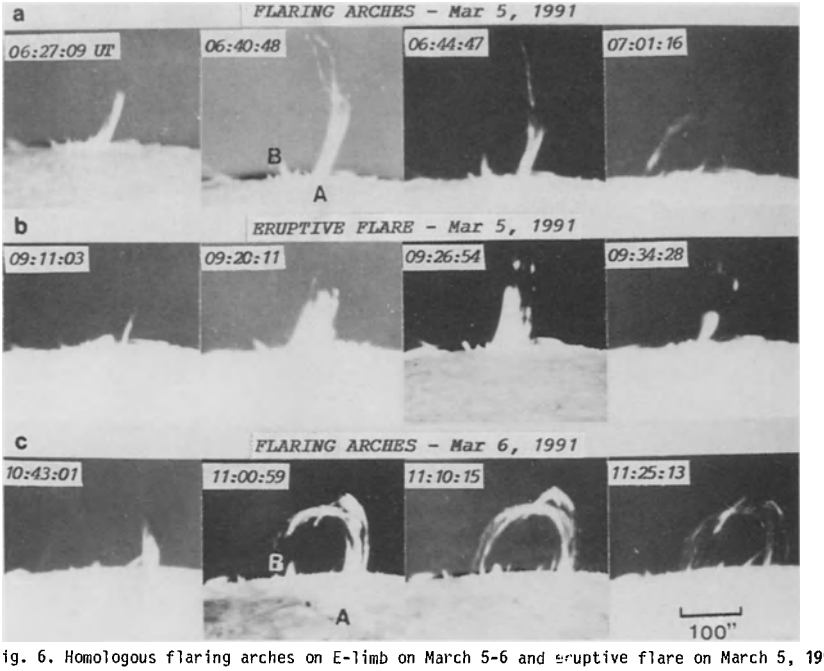

Fig. 6. Homologous flaring arches on E-limb on March 5-6 and eruptive flare on March 5, 1991.

3.2. MARCH 6, 1991 : At 10:40 UT, another set of flaring arches originated from the same region. Marked brightening was observed again at several points near "B" (Figure 6c - 11:00:59 UT) even before the arches connected to the secondary footpoints, as observed in the case of March 5 event. The duration of this event was about 45 min, beyond which observations at USO discontinued due to sunset. Hence, it is not certain whether an eruptive flare ensued after the flaring arch event in this case also.

3.3. MARCH 7, 1991 : In succession of the events of March 5 and 6, flaring arches ensued again. By this time, the active region had rotated off the E-limb, hence accurate identification of the flaring arch footpoint could be made (Figure 7a: 06:59:47-06:45:50 UT). The flaring arch was observed to rise from the top of a pre-existing dense, low-lying bright loop "A" (07:06:54 UT frame) which then bent towards a bright plage region "B" near the E-limb, slightly away from the primary footpoint. This plage "B" had brightened about 6 min before the flaring arch was even visible at the footpoint "A". In

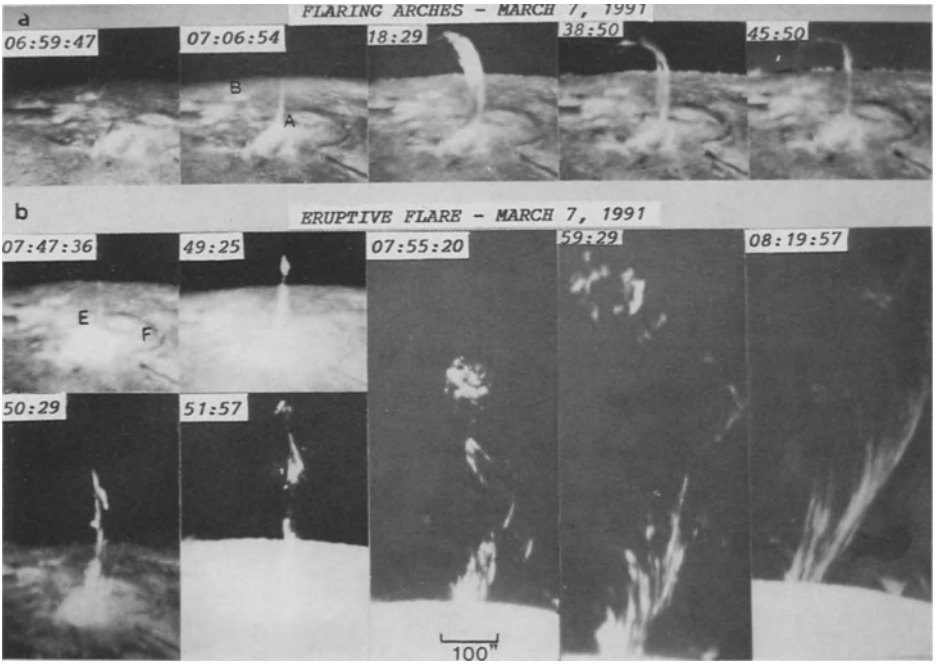

Fig. 7. Homologous flaring arch and eruptive flare on March 7, 1991.

Figure 8 is given the height versus time plot of this event, indicating that the flaring arch rose with a speed of 85 km s^{-1} and attained a maximum height of 80,000 km. From the high resolution pictures taken on March 9, it is confirmed that the flaring arch terminated on to an emerging flux region (EFR). Before the flaring arch activity completely subsided, another energetic mass ejection commenced at 07:47:10 UT from the top of the same low-lying dense bright loop "A" at "E" (Figure 7b - 07:47:36 UT). Its location was only around 20 arc-sec away from the primary footpoint of the flaring arch. This eruptive flare was an extremely energetic event, moving vertically upward with an initial speed of 500 km s^{-1} and then attaining a maximum speed over 1200 km s^{-1}. From the movie of this event, plasma blobs were seen shooting out at short intervals with enormous acceleration. The ejected material reached a height of more than 350,000 km, where its density decreased and it became too diffuse to be discernable. It may be noted that these energetic events failed to affect the stability of the neighboring long curvilinear filament F.

4. Discussion and Conclusions

From the study of the filament eruptions presented here, it appears that footpoints and their anchorage with the photosphere are crucial parameters for their stability. The anchorage of these footpoints may weaken or detach as a result of disturbances in remote active regions, a neighboring flare or emerging flux region.

Shapes and sizes of the three flaring arches observed during March 5-7, 1991 were remarkably similar. This suggests that repetitive restoration of the local magnetic field conditions and build-up of sufficient energy could occur within a day. The observed time delay of several minutes between the emergence of flaring arches and the brightening of secondary footpoints is perhaps due to the heating by particle bombardment of chromosphere along the giant x-ray arches, discovered by Svestka et al. (1982). Martin and Svestka (1988) suggested that flaring arches possess an x-ray phase which precedes H-alpha mass emission. In both cases of March 5 and 7, flaring arches were followed by very

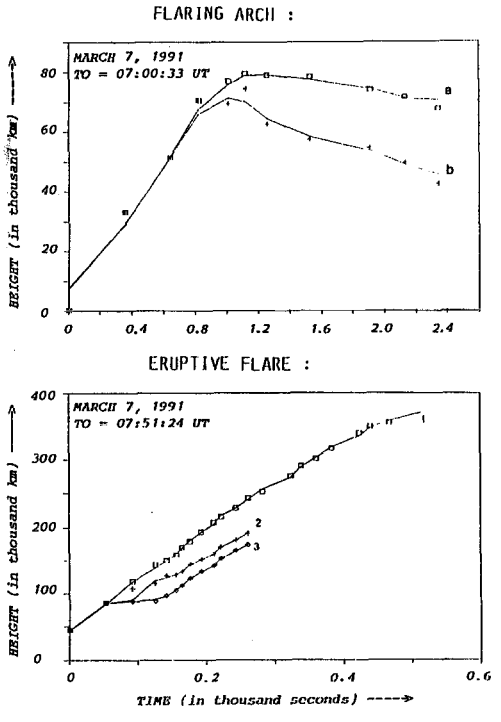

Fig. 8. Height vs time plots for flaring arch and eruptive flare on March 7, 1991.

energetic eruptive flares. An important question arises - from where could such large amount of material be supplied? At the site of the flaring arches and eruptive flares, no large scale plage or filament were seen, except for a small dense, low-lying emission loop. It does not appear probable that such a small "plage loop" could have provided the enormous material involved in the observed flaring arches and eruptive flares. It is more likely that the observed chromospheric material was "siphoned out" through the top of this loop into the corona, as indicated by a needle-like emission seen ensuing from this site. Eruptive flares were preceded by flaring arches in both the events and one is tempted to ask whether the flaring arch events initiate a "siphoning process" by suitably modifying or opening-up the magnetic field structure above the active region, so that the observed fast mass ejection could take place? Theoretical modelling of various observed phenomena related to the homologous flaring arches and eruptive flares are required to settle these questions.

References

Hirayama, T.: 1985, Sol. Phys. 100, 450.
Kippenhahn, R. and Schluter, A.: 1957, Z. Astrophys. 43, 36.
Kuperus, M. and Raadu, M.A.: 1974, Astron. Astrophys. 31, 189.
Smith, S.F. and Harvey, K. : 1972, in Physics of the Solar Corona (Ed. C.J. Macris), D. Reidel Publ. Co., pp. 156-167.
Martin, S.F. and Svestka, Z.: 1988, Sol. Phys. 116, 91.
Martin, S.F.: 1989a, in IAU Coll. No. 117 - Dynamics of Quiescent Prominences, Springer-Verlag.
Martin, S.F.: 1989b, Sol. Phys. 121, 250.
Priest, E.R.: 1989, Dynamics and Structure of Quiescent Solar Prominences, Kluwer Academic Publishers.
Ramsey, H.E. and Smith, S.F.: 1966, Astron. J. 71, 197.
Svestka, Z., Stewart, R.T. et al.: 1982, Sol. Phys. 75, 305.
Tandberg-Hanssen, E.: 1974, Solar Prominences, D. Reidel Publ. Co.

MHD Non-Equilibrium: A Numerical Experiment

Piet Martens[1], *Ming-Tsung Sun*[2], *Shi-Tsan Wu*[2]

[1] Lockheed Palo Alto Research Laboratories
Org. 91-30, Bldg. 252, 3251 Hanover Street
Palo Alto, CA 94303-1191, USA
[2] Center for Space Plasma and Aeronomical Research
The University of Alabama in Huntsville
Huntsville, AL 35899, USA

1 "Loss of Equilibrium" – Selected Results

"Loss of equilibrium" is one of the scenarios for flare onset. It assumes that in response to photospheric footpoint motions the coronal magnetic field evolves through a series of force-free equilibria up to a point where no further equilibrium exists. As continuing footpoint motions drive the field beyond this limit a dynamic rearrangement of the field sets in, resulting in a flare.

Low (1977), was the first to publish a series of force-free equilibria with such an endpoint. Many authors have since contributed to the subject, but in this short contribution we will only mention those that directly motivated the present work.

Recently Klimchuk and Sturrock (1989) have numerically analyzed Low's model sequence, and they found that when a physically meaningful experiment is conducted – i.e. when the series of equilibria is defined in terms of footpoint displacements – no "loss of equilibrium" occurs. Instead the rotational symmetry, implicitly imposed in Low's solutions, disappears, and the series of equilibria continues without symmetry beyond the threshold. Klimchuk and Sturrock therefrom conclude that for this particular force-free case ".. the concept (of "loss of equilibrium") is devoid of physical significance ..".

However, the demonstrated absence of "loss of equilibrium" in Low's solution not necessarily invalidates the concept in general. The result presented in this paper strongly suggests that "loss of equilibrium" can occur.

2 A Time Limited Series of Force-Free Equilibria

We consider a force-free magnetic arcade straddling a photospheric neutral line. The arcade has translational symmetry along the neutral line, and rotational symmetry about an axis below the surface. Our Cartesian coordinate system has z denoting the height above the photosphere, x the projected distance from the neutral line, and y the dummy coordinate along the neutral line. A parameter t denotes the depth of the symmetry axis below the photosphere.

It is convenient to work in a cylindrical coordinate system $(r,\ \varphi,\ y)$, centered at the symmetry axis $z = -t$. The radial coordinate in this system is $r^2 = (z+t)^2 + x^2$, and the partial derivatives ∂_y and ∂_φ vanish by definition. In this system, the force-free equation reduces to

$$\frac{d}{dr}(B_\varphi^2 + B_y^2) + \frac{2B_\varphi^2}{r} = 0, \tag{1}$$

with $B_r = 0$ everywhere, because the fieldlines are divergenceless.

We impose the following normal component of the magnetic flux at the photosphere:

$$B_z(z=0,t) = x\exp(-x^2). \tag{2}$$

Note that the total photospheric flux on each side of the neutral line is finite, and that the normal field is independent of the parameter t – hence only shearing photospheric motions are allowed.

The solution of Eq. (1) for the boundary condition Eq. (2) is

$$B_x = -(z+t)B_0 exp[-(x^2+z^2+2zt)/2] \tag{3}$$

$$B_y = B_0\{[1-x^2-(z+t)^2]exp(-x^2-z^2-2zt) + C^2\}^{1/2} \tag{4}$$

$$B_z = xB_0 exp[-(x^2+z^2+2zt)/2], \tag{5}$$

with B_0 an arbitrary scaling factor, and the parameter C^2 representing the axial field at infinity ($C^2 = B_y(\infty)^2/B_0^2$). We take this field to represent the overlying field of the active region of which the arcade under consideration is part.

The shear displacement along the neutral line of the photospheric footpoints of the fieldlines is given by

$$\Delta y(z=0,t) = 2\arctan(x/t)\sqrt{1-t^2-x^2+C^2\exp(x^2)}. \tag{6}$$

This shear displacement is continuous at $x = 0$, except at $t = 0$, a value which we henceforth exclude from consideration.

For a physically meaningful solution the factor under the square root in Eqs. (4) and (6) has to be nonnegative. This leads to the constraints

$$t^2 \leq C^2+1 \quad for \quad C^2 \geq 1 \tag{7}$$

$$t^2 \leq 2+2\ln(C) \quad for \quad C^2 \leq 1 \tag{8}$$

$$C^2 \geq 1/e^2. \tag{9}$$

Obviously our parameter t is intended to denote time, and the above solutions to represent a time sequence of quasistatic equilibria. We note that the quasistatic evolution can made to be as slow as one pleases by replacing t with εt. In the next section we will investigate what happens as t approaches and surpasses its upper limit. We emphasize that the sequence defined above constitutes a valid thought experiment in the sense of Klimchuk and Sturrock (1989) with the footpoint displacement everywhere finite and continuous.

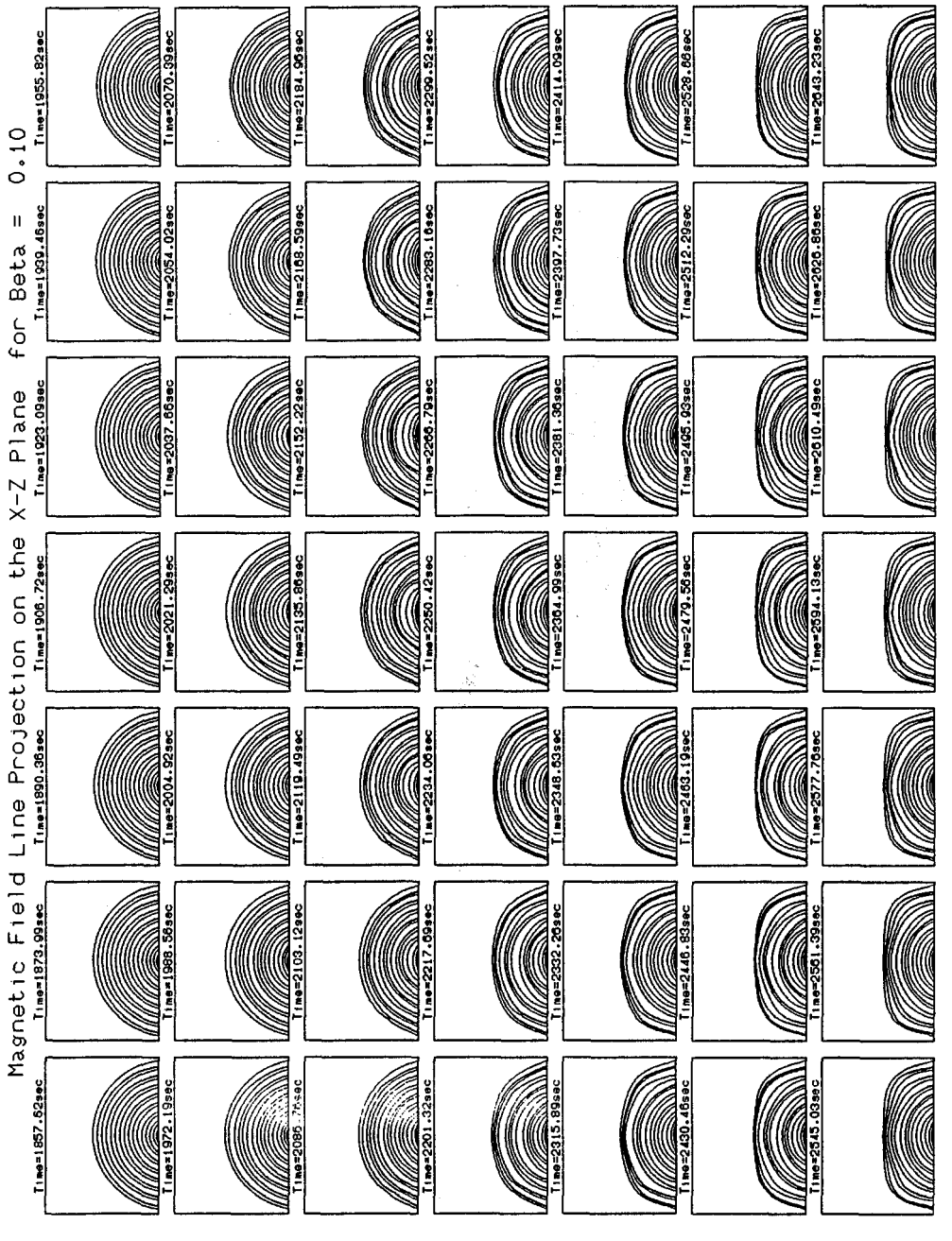

Fig. 1. Numerical simulation of the evolution of the magnetic fieldlines in projection on the $x - z$ plane.

3 Numerical Simulation

A numerical code for solving the time dependent MHD equations using a new Nimble Implicit Continuous Eulerian (NICE) integration scheme has been developed by M.T. Sun (1991). The code is very well suited to simulate solar-type MHD problems with a combination of reflecting and non-reflecting boundaries, compressibility, and large variations in plasma β. The code has successfully solved a number of test problems. Details are given in Sun (1991).

In our numerical analysis we have used the ideal, compressible, MHD equations with zero fluid viscosity and zero gravity. The ideal gas law is used, and the energy equation is adiabatic. To save computing time we have also imposed symmetry along the neutral line, $\partial_y = 0$, but not cylindrical symmetry.

In the simulation described here we used $C = 0.4$, start at $t = 0.9t_{max}$, and continue until approximately $1.3t_{max}$. The unit for the magnetic field (B_0) is 45 Gauss, the plasma β just above the neutral line is 0.1, and the plasma temperature $T = 3\times10^6 K$. This leads to realistic values for coronal pressure and density. We chose our length unit such that the physical size of the computational domain is 28,000 km in the x direction, and 12,500 km in the z direction (much smaller than the temperature scale-height, thus justifying the neglect of gravity). The grid is 36 × 25. The shear velocity scale is 1 km/sec, leading to a maximum shear velocity of 6 km/sec at one time at one point (later simulations achieved lower maximum velocities). The time unit is 5000 sec.

The results of the simulation are depicted in Figure 1. The sequence of panels with projected fieldlines shows clearly that up to about t_{max} the numerical result closely follows the analytical equilibrium sequence. After that the fieldlines start to oscillate reaching an amplitude of about 50 km/sec. This result clearly suggests that "loss of equilibrium" has occurred. Since we are using the ideal MHD equations no reconnection can take place, and an eruption is not to be expected with the infinite amount of overlying flux. Hence the observed oscillation may be the only mode of dynamic behaviour available to the field.

We cannot conclude at this point that "loss of equilibrium" has been unambiguously demonstrated, since it is possible that linear stability is simply lost as time approaches t_{max}. However, work by Cargill et al. (1986) on the stability of force-free line-tied coronal arcades has not shown instability. Cargill (1991) concludes "The bottom line is that there is strong evidence that force-free arcades are absolutely stable ..". We conclude that "loss of equilibrium" remains relevant for flares and coronal heating.

References

Cargill, P. J. 1991, private communication.

Cargill, P. J., Hood, A. W., and Migliuolo, S. 1986, *Ap. J.* **309**, 402.

Klimchuk, J. A., Sturrock, P. A. 1989, *Ap. J.* **345**, 1034.

Low, B. C. 1977, *Ap. J.* **212**, 234.

Sun, M. T. 1991, *Three-Dimensional Time-Dependent Fluid Flow Simulations: Ordinary and Magnetohydrodynamic (MHD) Fluids.* Dissertation, The University of Alabama in Huntsville.

TRIGGERING OF ERUPTIVE FLARES: DESTABILIZATION OF THE PREFLARE MAGNETIC FIELD CONFIGURATION

Ronald L. Moore
NASA Marshall Space Flight Center, Space Science Laboratory
Huntsville, AL 35812, U.S.A.

George Roumeliotis
Stanford University, Center for Space Science & Astrophysics, ERL 306
Stanford, CA 94305, U.S.A.

ABSTRACT

This paper takes the three-dimensional configuration of the magnetic field in and before eruptive flares as our main guide to how the preflare field comes to lose its stability and erupt. From observed characteristics (1) of the preflare magnetic field configuration, (2) of the onset and development of the eruption of this configuration before and during the flare, and (3) of the onset and development of the flare energy release (i.e., the heating and particle acceleration) within the erupting field, the typical erupting field configuration for two-ribbon eruptive flares is constructed. The observational centerpiece for this construction is the evidence from the Marshall Space Flight Center vector magnetograph that strong magnetic shear along the main magnetic inversion line is critical for large eruptive flares. From (a) the empirical field configuration and (b) the observation that the initial flare brightening typically stems from points where opposite-polarity flux is gradually merging and canceling at or near the main inversion line, it is argued (1) that eruptive flares are driven by the eruptive expansion of the strongly sheared core of the preflare magnetic field, (2) that this eruption is triggered by preflare slow reconnection accompanying flux cancellation in the sheared core, and (3) that in some flares the triggering reconnection and flux cancellation is between opposite-polarity strands of the extant preflare sheared core field, while in other flares it is between the sheared core field and new emerging flux.

1. INTRODUCTION

Every solar flare is either "ejective" or "confined," i.e., either does or does not produce a coronal mass ejection (Machado et al. 1988). We think that most flares, whether ejective or confined, are appropriately termed "eruptive," because we think that most flares are driven by the same kind of global eruptive instability of the magnetic field (Moore et al. 1984; Sturrock et al. 1984; Kahler et al. 1988; Moore 1988a,b, 1990). However, the "eruptive solar flares" in the title of this Colloquium are a certain type of ejective flare. Accordingly, this paper explicitly considers only "ejective" eruptive flares, although the observations and ideas about the triggering and onset of these flares probably apply just as well to "confined" eruptive flares. Moreover, while flares often involve two or more impacted, interacting bipoles (Machado et al. 1988), here we will consider only eruptive flares that occur in single-bipole field configurations, i.e., flares that involve only one major magnetic inversion line. Ejective flares of this restricted class are the two-ribbon eruptive flares that are the topic of this Colloquium.

The purpose of this paper is to give the observational basis for the present "establishment" picture of two-ribbon eruptive flares and, from that, to infer how eruptive flares are triggered. Because of the limit on the length of this paper, no actual observations are shown. Instead, with reference to representative example observations in the literature, the key findings for the magnetic field configuration, its eruption, and the onset and development of the flare in this erupting field are shown in cartoons. From these empirical results, the eruptive global magnetic instability for these flares is inferred. From the

global instability, together with observed features of the flare onset, comes the idea for the trigger, which is described with further cartoons. The inferred triggering process is slow reconnection accompanying gradual flux cancellation preceding the flare onset.

2. TYPICAL MAGNETIC FIELD CONFIGURATION BEFORE AND DURING ERUPTIVE FLARES

The typical three-dimensional form of the magnetic field before a two-ribbon eruptive flare is sketched on the left side of Figure 1 (Hirayama 1974; Heyvaerts, Priest, and Rust 1977; Moore and LaBonte 1980; Hagyard, Moore, and Emslie 1984; Sturrock et al. 1984; Moore et al. 1991). The field in the core of the bipole, i.e., the field rooted near the photospheric inversion line, is strongly sheared: these field lines closely trace the inversion line instead of going right across it as they would if the field had no shear, as would be the case if the field were in a current-free potential configuration. The shear in the bipole decreases with distance from the inversion line so that the strongly sheared core field is embedded in an arcade envelope of less-sheared closed magnetic field. Thus, the shear in the preflare bipole is markedly concentrated in a core channel running low along the inversion line.

Chromospheric images have long provided morphological evidence for the sheared core field at sites of eruptive flares. Before the flare, the photospheric magnetic inversion line is usually seen to be traced in the chromosphere by a dark filament (for example see the magnetograms and preflare Hα filtergrams for the famous [Skylab] eruptive flare of 29 July 1973 [Moore and LaBonte 1980] and for the famous [SMM] eruptive flare of 21 May 1980 [Hoyng et al. 1981]). The filament as a whole and the fibril substructure in the filament and in a channel somewhat wider than the filament (see Figure 7.6 of Martres and Bruzek [1977] and Figure 1 of Moore and Rabin [1985]) closely follow the direction of the inversion line; this is clear evidence that the field near the inversion line runs along it and hence is strong-

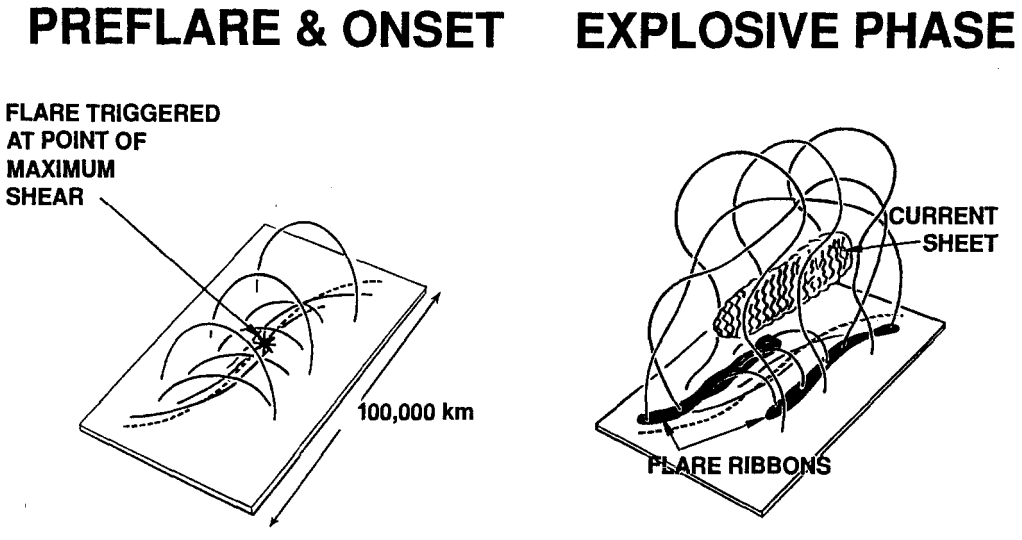

Figure 1. Magnetic field configuration of a typical two-ribbon eruptive flare; left: at and before flare onset; right: in the flare's explosive phase of peak heating and particle acceleration (from Moore et al. 1991). The core of lowest-lying strongest-sheared field shown in the preflare configuration is typically marked by a dark chromospheric filament; this provides a tracer showing that the core field begins to erupt before the explosive phase. By the peak of the explosive phase, the erupting core has greatly distended the envelope of the bipole, allowing the legs of the envelope arcade to collapse together beneath the erupted core (the double helix in this drawing) to form the current sheet and drive the heating and particle acceleration.

ly sheared (Foukal 1971). This qualitative chromospheric evidence for the core of sheared field in the preflare bipole has been confirmed and quantified by photospheric vector magnetograms. These data show that whenever (1) the field at the inversion line points along the inversion line to within 20 degrees and (2) such close alignment extends for about 10,000 km or more along the inversion line, then a large eruptive flare usually happens within a day; the first opposite points of the two chromospheric flare ribbons usually closely bracket the point of maximum shear. The vector magnetograms also confirm that the shear decreases with distance from the inversion line; the preflare photospheric field is closely aligned with the inversion line only in a channel that is roughly centered on the inversion line and that is about as wide as the overlying chromospheric filament and/or filament channel. For typical examples of these findings from vector magnetograms see Moore, Hagyard, and Davis (1987); Hagyard (1990); Hagyard, Venkatakrishnan, and Smith (1990); and Moore et al. (1991).

Soft X-ray and EUV coronal images provide further evidence that the preflare sheared core field lies within a closed-field envelope that is much less sheared than the core. Full-disk magnetograms show that most active regions are grossly bipolar: they have one main inversion line. Whether or not the bipole's core along the main inversion line is sheared enough to be marked by a chromospheric filament, coronal images show that the envelope of the bipole, the thick arcade of magnetic loops rooted well away from the core, has little shear, i.e., the envelope of coronal magnetic loops looks pretty much like a potential field (for examples of magnetograms together with coronal images showing the non-twisted, potential character of the envelope field in active regions, see Sheeley [1981] and Moore [1990]). From these observations we might expect that the envelope field still has little shear just before an eruptive flare. This expectation has been verified by a few preflare coronal images of the sites of eruptive flares (for two examples, see Moore and LaBonte [1980] and Kahler, Webb, and Moore [1981]).

Once a two-ribbon eruptive flare begins, the explosive phase of flare energy release (the phase of most powerful and most impulsive plasma heating and particle acceleration) usually ensues within several minutes and peaks within a few more minutes. The typical configuration of the magnetic field and flare at the peak of the explosive phase is sketched on the right side of Figure 1 (Hirayama 1974; Heyvaerts, Priest, and Rust 1977; Moore and LaBonte1980; Hagyard, Moore, and Emslie 1984; Sturrock et al. 1984; Moore et al. 1991). By this time in the flare, some of the sheared core field has erupted up, stretching the legs of the envelope arcade. The two chromospheric flare ribbons have formed near the inversion line and are rapidly spreading away. Hot coronal flare loops straddling the inversion line and rooted in the ribbons are being formed by reconnection at the current sheet between the two merging legs of the stretched envelope. The erupting core field often carries much of the preflare chromospheric filament with it (Tang 1986); the core eruption can thereby be traced in chromospheric movies. These movies show that by the peak of the explosive phase, in the manner of the erupting double helix in our explosive-phase cartoon in Figure 1, the erupting core field typically has arched up to a height of several times the height of the preflare filament. For example, see the filament eruption in the OSO-7 flare of 10 October 1971 shown in Roy and Tang (1975) and in Moore (1987). Other good examples are shown in Kahler et al. (1988).

3. TYPICAL ONSETS OF ERUPTIVE FLARES

This paper is intended to focus on the triggering of eruptive flares: How does the preflare field configuration lose its equilibrium so that it erupts and changes into the transient configuration of the explosive phase? For observational clues to this question, the obvious things to look at are the onset of the core eruption and the initial flare brightenings.

Most onsets of eruptive flares are covered by the following three cases: onset in the absence of emerging flux, onset with localized emerging flux (a small emerging bipole) on the main inversion line, and onset with localized emerging flux off the main inversion line but still under the envelope of the preflare bipole. In Figure 2, the configuration of the magnetic field and initial flare ribbons is shown for each of these three cases at the onset of flare brightening. The core eruption traced by the filament usually begins somewhat before any noticeable flare brightening. This early stage of the eruption at

ONSET:

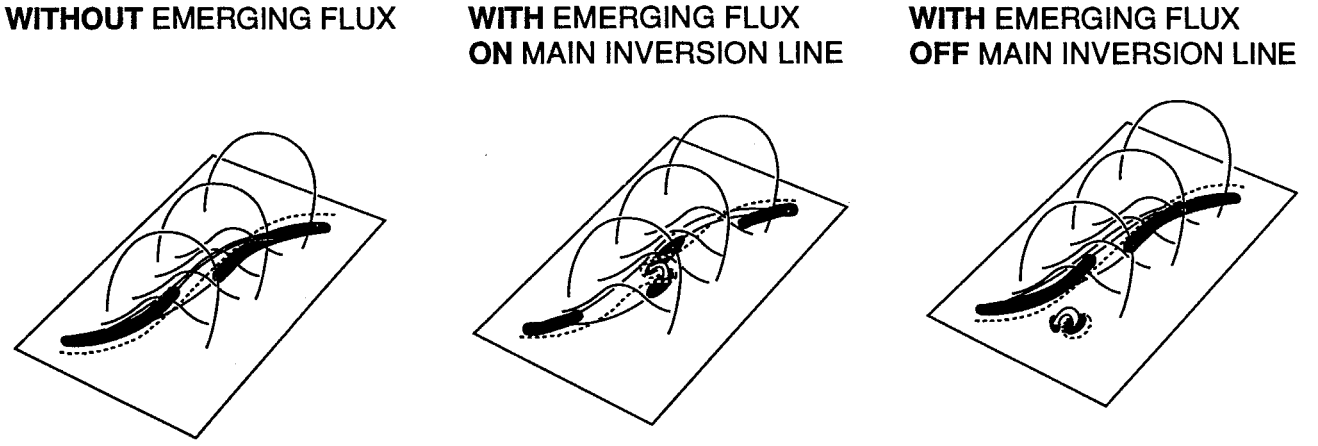

Figure 2. Typical onsets of eruptive flares; left: no emerging flux; center: emerging flux on main inversion line; right: emerging flux off main inversion line. Here, as in Figure 1, the dashed lines are magnetic inversion lines, dividing areas of opposite polarity in the photosphere; black areas are ribbons of chromospheric flare brightening. In all three cases, at flare-ribbon onset the sheared core field along and above the main inversion line has begun to erupt upward, distending the surrounding envelope field, and the initial flare ribbons along the main inversion line are tucked under the erupting core.

brightening onset is indicated in Figure 2 by the moderate upward arching and bulging of the core field in comparison to the core field in the preflare configuration in Figure 1. In the case of no emerging flux, the initial flare brightening is close against the inversion line under the erupting core. In the case of emerging flux on the main inversion line, the initial brightening is again all very near the inversion line under the erupting core; in this case, some of the initial brightening is at the place on the main inversion line where the little bipole is emerging. When the small emerging bipole in off the main inversion line, some of the initial brightening is at that location, but most of it is right along the inversion line under the erupting core. Thus, when emerging flux is present, it is usually involved in the flare onset, but with or without emerging flux, an eruptive flare begins with brightening close along the inversion line under the sheared core field that is starting to erupt.

A good example of an eruptive flare that happened without emerging flux is the SMM flare of 25 June 1980; its onset is shown in Figure 5 of Kahler et al. (1988). The preflare magnetic field configuration and evolution at this flare site was examined in detail in high-resolution images by Gaizauskas (Hagyard et al. 1986): there was no sign of emerging flux near the onset of this flare. Another eruptive flare with no noticeable emerging flux is the large SMM flare of 24/25 April 1984. For the preflare vector magnetogram and onset of this flare, see Hagyard, Venkatakrishnan, and Smith (1990) and Hagyard (1990). A good example of an eruptive flare with emerging flux on the inversion line is the SMM flare of 21 May 1980. For magnetograms showing the emerging flux, see Harvey (1983); for the flare onset (in soft X-ray emission) see Batchelor and Hindsley (1991) or Moore et al. (1991). The initial brightening in soft X-rays was a long stripe that traced the inversion line and that was brightest at the site of emerging flux (the X-ray emitting plasma was apparently on field lines rooted along the inversion line, like the field lines rooted in the flare ribbons in Figure 2). The Skylab flare of 29 July 1973 might be another example of an eruptive flare with emerging flux on its main inversion line. There was a small bipole on the inversion line at the time of the flare, but in high-resolution Hα filtergrams it did not look like an emerging bipole. More likely, it was two clumps of opposite polarity flux merging and canceling at the main inversion line. Hence, this flare is probably another example of an eruptive flare without emerging flux. In any case, after the preflare filament began to erupt, the flare ribbons turned on closely bracketing the the small bipole and then rapidly extended closely along the inversion line to attain a configuration like the flare ribbons in Figure 2. For the magnetogram and onset of this flare, see Moore and LaBonte (1981) and Moore, Horwitz, and Green (1984). Finally, a good example of an eruptive flare onset involving emerging flux off the main inversion line is that of the flare of 10 April 1980 shown in Moore et al. (1984).

4. INFERRED GLOBAL LOSS OF STABILITY FOR ERUPTIVE FLARES

Before using the observed characteristics of the onsets of eruptive flares to infer how eruptive flares are triggered, we will first infer - from the typical configuration of the field and flare before, during, and after flare onset - the overall instability that drives the field eruption and flare energy release. That is, our next step toward finding the trigger is to consider what instability is to be triggered.

The perspective sketches in the first three panels of Figure 3 reiterate our points about the preflare field configuration and the form of the erupting field and flare brightening within it during the onset and the explosive phase (= impulsive phase) of the flare energy release. The perspective sketch in the fourth panel of Figure 3 shows the configuration of the field and flare ribbons well after the explosive phase. These sketches suggest that an eruptive flare is basically a magnetic explosion that starts in the sheared core of the overall bipole. In the preflare state, because the magnetic pressure in active regions is much greater than the plasma pressure, the field is in an equilibrium configuration that is nearly force-free (e.g., Tandberg-Hanssen and Emslie 1988). That is, in the preflare configuration the pressure of the magnetic field (which tries to make the configuration explode) is confined by the tension of the magnetic field (e.g., Cowling 1957). Apparently, the global instability that results in the explosion that is an eruptive flare is a global loss of balance between the pressure and the tension: the configuration explodes when the field tension can no longer restrain the field pressure.

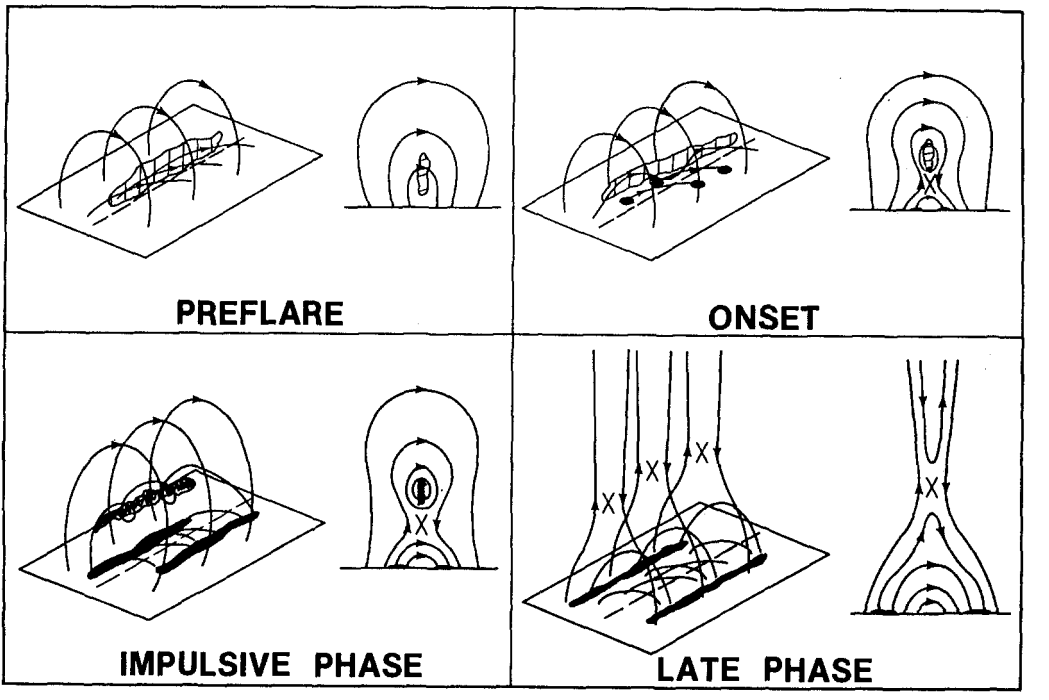

Figure 3. Progression of the field configuration, reconnection, and flare ribbons in a typical eruptive flare (from Hagyard, Moore, and Emslie 1984). In the preflare state (preflare panel), the field configuration is in force-free, magnetostatic, stable equilibrium, a balance between magnetic pressure and magnetic tension. Before the onset of flare heating (i.e., at some time after the preflare panel but before the onset panel), the core field loses its equilibrium: a loss of magnetic tension results in unbalanced magnetic pressure that causes the core field to begin to erupt. The distended field around the erupting core then collapses into the space that that the core has just vacated (onset panel); this forms a current sheet and drives fast reconnection, heating, and particle acceleration (onset, impulsive phase, and late phase panels). This reconnection further untethers the core field, providing a positive feedback that sustains the magnetic explosion (onset and impulsive phase panels). The whole process of coordinated eruption and reconnection is driven by the magnetic pressure of the unleashed core field.

The end-view sketches in Figure 3 show the reconnection that is inferred from the configuration of the field and flare ribbons and the progression of the core eruption and ribbon spreading. In the late phase, the reconnection recloses the envelope field that has been opened by the expulsion of the core field. The reconnection process supplies to the newly formed coronal loops the heat that makes them bright in soft X-ray emission and that makes their feet bright in chromospheric emission. Hence, the reconnection and flare energy release in the late phase is a consequence of the core eruption (Kopp and Pneuman 1976). As depicted in Figure 3, the reconnection in the late phase is the continuation of reconnection that begins with the onset of flare brightening. Thus, it is compatible with the observations to assume that all of the flare brightening, from its beginning, is powered through reconnection. Because the reconnection and flare energy release in the late phase seems quite obviously to be a consequence of the core eruption, and because the core eruption is already in progress at the onset of flare brightening, it is our view that all of the flare energy release and the reconnection inherent to the energy release (i.e., the reconnection depicted in Figure 3) from onset on are driven by the core eruption.

We call the reconnection depicted in Figure 3, "fast" reconnection because it has a fast driver, the core eruption. We take this fast reconnection above the inversion line to be a crucial part of the global instability that sustains the field explosion: by further unleashing the field it gives a positive feedback to the eruption (Moore and LaBonte 1981; Hagyard, Moore, and Emslie 1984; Moore, Horwitz, and Green 1984, Sturrock et al. 1984). Previous papers (e.g., Heyvaerts, Priest, and Rust 1977; Moore et al. 1991; and those papers cited in the preceding sentence) have suggested that the flare is triggered by the reconnection that accompanies the onset of flare brightening. In this paper, we depart from that view. It is our view that global stability of the field configuration is lost before onset of flare brightening and that the fast reconnection that gives this brightening is part of the global instability and is driven by the global instability; the fast reconnection at brightening onset is not the trigger of the flare, it is part of the flare. We thus conclude that the trigger must be something other than the onset of the fast reconnection; the trigger is something that happens earlier that renders the the configuration globally unstable to eruption.

5. INFERRED TRIGGER FOR ERUPTIVE FLARES: SLOW RECONNECTION

We are now ready to infer the trigger for eruptive flares. Our above discussion of the global instability that drives eruptive flares argues that the beginning of the core eruption is the beginning of the global instability. From this we infer that the trigger that we seek is the trigger of the core eruption. Our picture of the global instability also suggests that the core eruption is triggered when the magnetic pressure of the sheared core field can no longer be balanced by the magnetic tension. The tension is provided by the tying of the field to the photosphere. Hence, we infer that the triggering is the end result of a process that gradually erodes the core field's linkage to the photosphere until the confinement of the core field becomes untenable. The onset of flare brightening (which we think marks the onset of fast reconnection) is at magnetic inversion lines, often including inversion lines around emerging flux (as in Figure 2). All these considerations suggest (1) that the triggering process is located at the sites of initial flare brightening, and (2) that the triggering process is preflare gradual reconnection that accompanies preflare flux cancellation, as we will now discuss.

It is observed that when two patches of magnetic flux of opposite polarity are brought together by photospheric flows, flux cancells at the inversion line where the two patches meet (Martin and Livi, these proceedings). The cancellation is apparently accomplished by submergence of a succession of low magnetic loops formed from the merging opposite-polarity fields by reconnection at or above the photospheric inversion line (as in Figure 5 of Rabin, Moore, and Hagyard 1984). The typical sites of initial flare brightening in Figure 2 (at the inversion line in the sheared core and at inversion lines around emerging flux), are also typically sites of preflare flux cancellation (Martin and Livi, these proceedings). Cancellation reconnection is probably much slower than the reconnection in eruptive flares because its driver (photospheric flow; < 1 km/s) is much slower than the driver (core eruption; 10-100 km/s) of the reconnection in eruptive flares. Hence, we call the preflare cancellation reconnection "slow" reconnection. We think that this slow reconnection is the trigger for eruptive flares.

In Figure 4 we have sketched the operation of our proposed preflare process for triggering eruptive flares; the three cases shown correspond to the three typical cases of eruptive flare onset shown in Figure 2. In the case of no emerging flux, the triggering cancellation reconnection is on the main inversion line, in the sheared core. In this case, the core field that goes through the cancellation reconnection process loses half of its linkages to the photosphere, while its horizontal flux remains nearly unchanged. So, in this case, the flare is triggered by what may be called "tether cutting." This case of cancellation reconnection on the main inversion line has been modeled by van Ballegooijen and Martens (1989). In the case of emerging flux on the inversion line of the sheared core, the processed core field again loses half of its ties to the photosphere. So, this is again triggering by tether cutting, but driven by flux emergence rather than by photospheric flow converging on the main inversion line as required in the previous case. Finally, in the case of emerging flux off the inversion line of the core, the number of ties of the core field to the photosphere is not reduced, but the distance between the tie points is increased, which weakens the tension of the core field relative to its pressure. So, we term this process "tether weakening."

TRIGGER:
SLOW RECONNECTION IN FLUX CANCELLATION

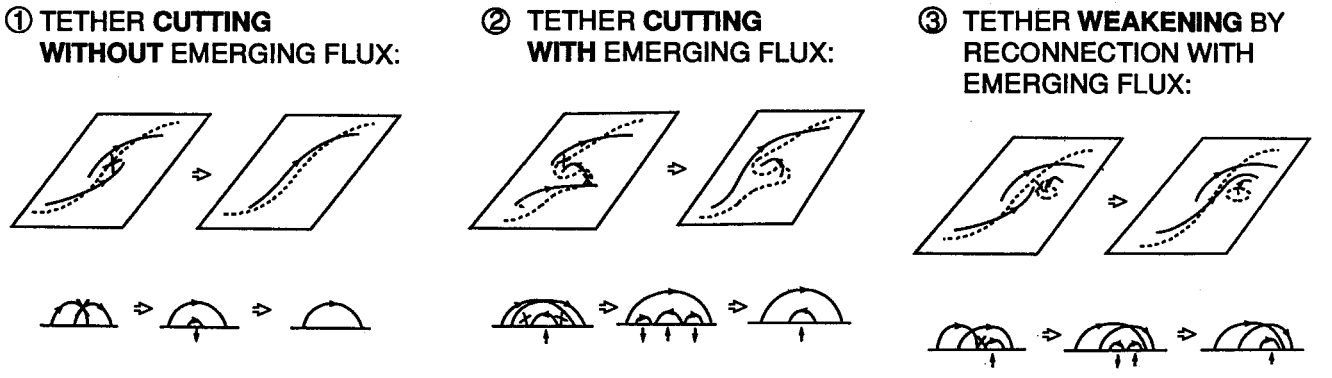

Figure 4. Inferred process for triggering typical onsets of eruptive flares; left: no emerging flux; center; emerging flux on main inversion line; right: emerging flux off main inversion line. The field lines shown are in the core of the preflare field configuration shown in Figures 1-3. The sequences of 2-D sketches below the perspective sketches show the reconnection, emergence, and submergence of field in an end view along the main inversion line. X's mark reconnection. Vertical arrows below the 2-D sketches mark flux emergence (upward arrow) and flux submergence (downward arrow).

In all cases, the preflare cancellation reconnection continues until the core field becomes so weakly tethered that it can begin to erupt and drive fast reconnection under it over the main inversion line. The trigger is that last bit of slow reconnection that renders the core field globally unstable to eruption and fast reconnection.

6. CLOSING

The main new idea of this paper is that eruptive flares are not triggered by the reconnection that happens with the initial flare brightening, but by slower reconnection that precedes the initial flare reconnection at the same sites. The flare reconnection is fast reconnection that is driven by and sustains the core eruption; the preflare triggering reconnection is much slower reconnection in flux cancellation driven by photospheric flows. We have tacitly assumed that the cancellation reconnection produces a much lower rate of magnetic energy dissipation than does the initial fast reconnection in the flare onset. Can our proposed preflare slow reconnection occur without producing more heating than observations allow? We are presently pursuing this question through a modeling study of slowly driven reconnection (Roumeliotis and Moore, in preparation).

ACKNOWLEDGEMENTS

This work was supported by NASA through the Solar Physics Branch of its Space Physics Division. The paper was improved by helpful advise from Marcos Machado. Ron Moore first heard of the idea that flares might be triggered by preflare slow reconnection in a talk given by Dan Spicer at Marshall Space Flight Center in 1985.

REFERENCES

Batchelor, D. A., and Hindsley, K. P. 1991, Solar Phys., **135**, 99.
Cowling, T. G. 1957, Magnetohydrodynamics (Interscience Publishers, Inc.: New York), p. 9.
Foukal, P. 1971, Solar Phys., **19**, 59.
Hagyard, M. J. 1990, Mem. Soc. Astron. It., **Vol. 61, No. 2**, p. 337.
Hagyard et al. 1986, in Energetic Phenomena on the Sun, ed. M. R. Kundu and B. Woodgate, NASA CP-2439 (NASA: Washington, D. C.), Ch. 1, p. 16.
Hagyard, M. J., Moore, R. L., and Emslie, A. G. 1984, Adv. Space Res., **Vol. 4, No. 7**, p. 71.
Hagyard, M. J., Venkatakrishnan, P., and Smith, J. B., Jr. 1990, Astrophys. J. Supp., **73**, 159.
Harvey, J. W. 1983, Adv. Space Res., **Vol. 2, No. 11**, p. 31.
Heyvaerts, J., Priest, E. R., and Rust, D. M. 1977, Astrophys. J., **216**, 123.
Hirayama, T. 1974, Solar Phys., **34**, 323.
Hoyng, P. et al. 1981, Astrophys. J. (Letters), **246**, L155.
Kahler, S. W., Moore, R. L., Kane, S. R., and Zirin, H. 1988, Astrophys. J., **328**, 824.
Kahler, S. W., Webb, D. F., and Moore, R. L. 1981, Solar Phys., **70**, 335.
Kopp, R. A., and Pnueman, G. W. 1976, Solar Phys., **50**, 85.
Machado, M. E., Moore, R. L., Hernandez, A. M., Rovira, M. G., Hagyard, M. J., and Smith, J. B., Jr. 1988, Astrophys. J., **326**, 425.
Martres, M. J., and Bruzek, A. 1977, in Illustrated Glossary for Solar and Solar-Terrestrial Physics, ed. A. Bruzek and C. J. Durrant (Reidel: Boston), Ch. 7, p. 53.
Moore, R. L. 1987, Solar Phys., **113**, 121.
Moore, R. L. 1988a, Astrophys. J., **324**, 1132.
Moore, R. L. 1988b, in Solar and Stellar Coronal Structure and Dynamics, ed. R. C. Altrock (National Solar Observatory: Sacramento Peak, Sunspot, New Mexico), p. 520.
Moore, R. L. 1990, Mem. Soc. Atron. It., **Vol. 61, No. 2**, p. 317.
Moore, R. L., Hagyard, M. J., and Davis, J. M. 1987, Solar Phys., **113**, 347.

Moore, R. L., Hagyard, M. J., Davis, J. M., and Porter, J. G. 1991, in Flare Physics in Solar Activity Maximum 22, ed. Y. Uchida, R. C. Canfield, T. Watanabe, and E. Hiei (Springer-Verlag: Berlin), p. 324.

Moore, R. L., Horwitz, J. L., and Green, J. L. 1984, Planet. Space Sci., **Vol. 32, No. 11**, p. 1439.

Moore, R. L., Hurford, G. J., Jones, H. P., and Kane, S. R. 1984, Astrophys. J., **276**, 379.

Moore, R. L., and LaBonte, B. J. 1980, in Solar and Interplanetary Dynamics, ed. M. Dryer and E. Tandberg-Hanssen (Reidel: Boston), p. 207.

Moore, R., and Rabin, D. 1985, Ann. Rev. Astron. Astrophys., **23**, 239.

Rabin, D., Moore, R., and Hagyard, M. J. 1984, Astrophys. J., **287**, 404.

Roy, J.-R., and Tang, F. 1975, Solar Phys., **42**, 425.

Sheeley, N. R., Jr. 1981, in Solar Active Regions, ed. F. Q. Orrall (Colo. Assoc. Univ. Press: Boulder), p. 17.

Sturrock, P. A., Kaufman, P., Moore, R. L., and Smith, D. F. 1984, Solar Phys., **94**, 341.

Tandberg-Hanssen, E., and Emslie, A. G. 1988, The Physics of Solar Flares (Cambridge University Press: Cambridge), p. 75.

Tang, F. 1986, Solar Phys., **105**, 399.

van Ballegooijen, A. A., and Martens, P. C. H. 1989, Astrophys. J., **343**, 971.

FIELD OPENING AND RECONNECTION

T.G. Forbes
Institute for the Study of Earth, Oceans, and Space,
SERB, University of New Hampshire, Durham, NH 03824, USA

ABSTRACT. During an eruptive flare a large magnetic loop or plasmoid is ejected into interplanetary space, and the closed magnetic field structure which exists prior to the flare becomes opened. One of the requirements of flare models is to explain how the field can be opened while decreasing the overall magnetic energy of the system. After the field is opened, reconnection must occur in order to restore the field to its pre-flare configuration. The strongest evidence for reconnection in flares comes from observations of the chromospheric ribbons and the coronal loops which form after the onset of a large flare. The ribbons and loops appear to propagate through the chromosphere and corona during the flare, but Doppler-shift measurements show conclusively that these apparent motions are not due to mass motions of the solar plasma. The motions can only be explained by the upward propagation of an energy source in the corona, and in the MHD-reconnection model of flares, the propagating energy source is an x-line accompanied by slow-mode shocks.

I. INTRODUCTION

One of the most important features of eruptive flares is that they eject magnetic flux into interplanetary space. Although many flares do not eject magnetic flux, those which do are of special importance for solar-terrestrial relations since the ejected flux has dramatic effects if it hits the Earth's magnetosphere. Three flare models which have been extensively investigated are the emerging-flux model (*e.g.* Heyvaerts and Priest 1976), the sheared-arcade model (*e.g.* Aly 1990), and the magnetic-flux-rope model (*e.g.* Sturrock 1989). All of these models can store and release magnetic energy efficiently provided that magnetic reconnection occurs. However, only the magnetic flux-rope model appears to provide a plausible mechanism for ejecting magnetic flux into interplanetary space.

The best evidence for reconnection during solar flares comes from observations of chromospheric ribbons and coronal loops which appear to move through the chromosphere and corona after the onset of a large flare. Doppler-shift measurements show conclusively that the motions are not due to mass motions of the solar plasma, but rather to the upward propagation of an energy source in the corona (Schmieder *et al.* 1987). In MHD reconnection model of flares, this propagating energy source is a magnetic x-line accompanied by slow-mode shocks.

Although the motion of the flare loops and ribbons shows that reconnection does indeed occur during flares, there is still little agreement as to how reconnection is initiated at the start of a flare. Clearly, some trigger mechanism must exist since flares are, by definition, an explosive-like phenomenon which involve the sudden generation of a large amount of thermal and kinetic energy. What the trigger mechanism is and how it works depends critically on how the magnetic energy is stored in the corona. Most flare models

assume that energy is stored in the corona over a period of several hours or days prior to the onset of the flare when the energy is suddenly released. The magnetic energy is stored in the corona in the form of coronal currents, and these currents generate magnetic fields which are assumed to lose equilibrium either because of an instability (resistive or ideal) or a catastrophic loss of equilibrium (Moore 1988).

Flare models which attempt to explain the behavior of large eruptive flares, must account not only for the flare ribbons and loops, but also for the occasional ejection of magnetic flux and plasma into interplanetary space. These ejections, better known as coronal mass ejections, do not always occur in association with a flare, but when they do, it is clear that the flare is a response to the overall magnetic disruption caused by the ejection (Simnett and Harrison 1985).

II. HOW TO OPEN THE FIELD WHILE RELEASING MAGNETIC ENERGY

One of the major obstacles for modelers of eruptive flares is finding a mechanism which can eject magnetic flux and plasma by decreasing the total magnetic energy stored in the coronal current system. The ejection cannot simply be a consequence of the thermal energy released in the flare since the kinetic energy associated with the ejection exceeds the energy released by heating (Canfield *et al.* 1980, Webb *et al.* 1980, Linker *et al.* 1990), and careful timing of the onset of the ejection shows that the flare starts after the ejection has already begun (Wagner *et al.* 1981, Simnett and Harrison 1985). Thus the ejection must be an integral part of the physical mechanism which releases the magnetic energy.

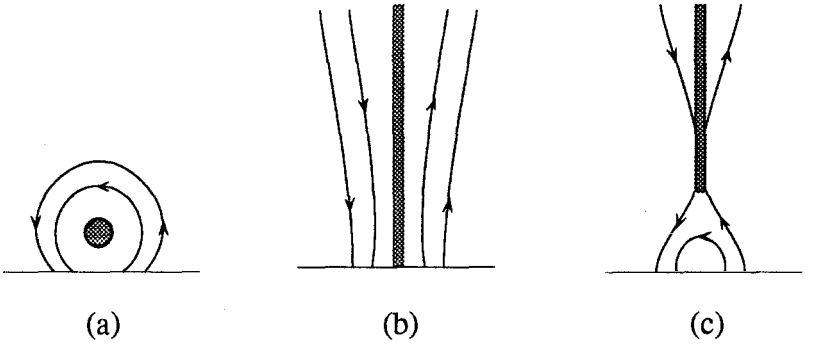

Figure 1. The three configurational stages of an eruptive flare according to Kopp and Pneuman (1976). Gray shading indicates current flow perpendicular to the plane of the figure. Work by Aly (1984, 1990) suggests that the transition form (a) to (b) is energetically impossible

During an eruption, magnetic field lines mapping from the ejected plasma to the photosphere are stretched outwards to form an extended, open field structure (Sturrock 1987, 1989). This opening of the field creates an apparent paradox since the stretching of the field lines implies that the magnetic energy of the system is increasing which is impossible if the ejection is magnetically driven (Sturrock *et al.* 1984). Barnes and Sturrock (1972) argued that this *energy paradox* does not occur because the decrease in the coronal current system, which exists prior to the eruption, releases more magnetic energy than is consumed in stretching the field lines. In other words, the magnetic energy required to

open the field should be less than the free magnetic energy stored in the corona. Following this line of thought Kopp and Pneuman (1976) proposed the scenario shown in Figure 1 for a three stage model of an eruptive flare. In the first stage (Figure 1a) prior to the eruption, there is a force-free magnetic flux rope which erupts outwards to form a fully opened magnetic field configuration (Figure 1b). Finally, in the third stage the opened configuration reconnects (Figure 1c) to form a closed, nearly current-free field. According to Barnes and Sturrock (1972) the evolution from the first stage to the second would be an ideal-MHD process occurring on the Alfvén time-scale, while the evolution from the second stage to the third would be a resistive-MHD process occurring on the slower reconnection time-scale. Thus the middle stage 2 would constitute a metastable state at an intermediate magnetic energy level as shown in Figure 2.

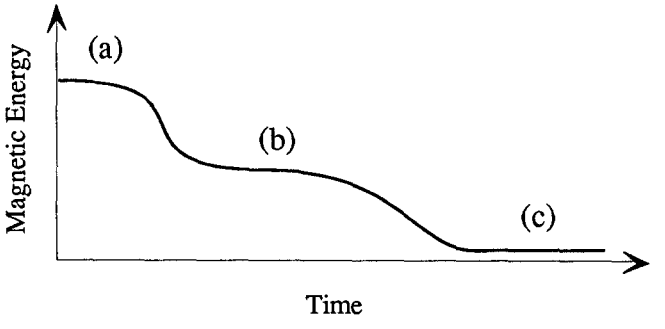

Figure 2. The levels of magnetic energy for the three configurational stage shown in Figures 1 and 2.

In 1984 J.J. Aly showed that the above scenario is likely to be energetically impossible (Aly 1984). Using quite general arguments Aly argues that the fully opened field configuration shown in Figure 1b must always have a higher magnetic energy than a corresponding force-free magnetic field as long as the field is simply connected. Aly's result caused consternation among MHD theorists because it seem to imply that an *energy paradox* does indeed exist and that eruptive flares are therefore energetically impossible. However, as Aly himself noted, there are several ways to avoid the paradox. First, the magnetic fields may not be simply connected but contain *x* and *o* points. Second, the ideal-MHD part of the eruption could extend the field to a large, but finite extent, without actually opening the field lines to infinity. Finally, the eruption might be magnetically possible if it only partly opened the magnetic field (*cf.* Wolfson and Low 1992).

Recently, P. A. Isenberg, P. Démoulin, E.R. Priest, and myself have found that it is indeed energetically possible to create an eruption by eliminating the requirement that the field be magnetically opened to infinity during the ideal-MHD transition (Démoulin and Priest 1988, Forbes and Isenberg 1991). We have constructed an MHD model which evolves through the 3 stages shown in Figure 3. During the transition from the first stage (Figure 3a) to the second stage (Figures 3b) the field is not opened but simply extended, and it is only when reconnection occurs during the transition from the second stage to the third (Figure 3c) that the ejection of a magnetic flux rope to infinity occurs. This model is essentially an MHD version of the circuit model constructed by Martens and Kuin (1989) which incorporates the diamagnetic driving force discussed by Yeh (1982, 1983).

The force which drives the filament upwards is the diamagnetic force produced by the compression of field lines between the current filament and the photosphere as shown in Figure 4. Prior to the eruption, this compression is balanced by the magnetic tension in the field lines anchored in the photosphere but passing over the top of the filament. Using a simple circuit model, Van Tend and Kuperus (1978) argued that a gradual change in either

the field holding the filament in place or the current passing through the filament can lead to a sudden loss of equilibrium.

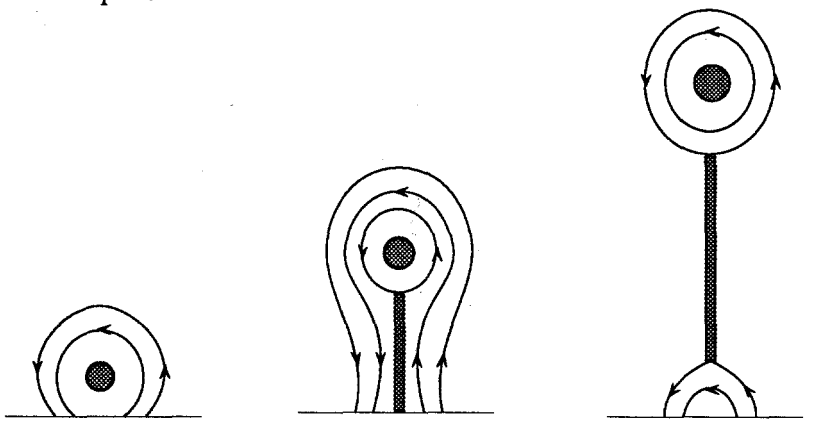

Figure 3. An alternate version of the three configurational stages which avoids the energy paradox. Here the ideal-MHD transition from (a) to (b) does not open the field to infinity.

At the present time there is no clear picture of how the current is created in the magnetic flux-rope model. One possibility is that the flux-rope is simply transported into the corona when the magnetic field emerges from the convection zone. However, it is also possible to create a flux-rope by twisting the photospheric footpoints of a pre-existing magnetic loop (Foote and Craig 1990), but there is little evidence to indicate that photospheric convection actually twists the field to the extent necessary to form an unstable flux-rope (Berger 1990).

Another alternative is to reconnect the footpoints of magnetic loops while shearing them at the same time (van Ballegooijen and Martens 1989). There is some observational evidence suggesting that such footpoint reconnection occurs in the photosphere and generates eruptive flares (Martin *et al.* 1985). However, this evidence has alternate interpretations which do not require photospheric reconnection. In any case, it is probably not necessary that the reconnection occur in the photosphere since reconnection at the a base of the corona will produce the same result (*cf.* Inhester *et al.* 1992).

The model presented in Isenberg and Forbes (1991) is based on a two-stage process. In the first stage, or storage phase, the magnetic energy of the system is slowly increased by transferring magnetic flux from the photosphere to the corona. The transfer of flux occurs quasi-statically over a time period of several days so that the system evolves through a series of equilibria. The second stage is the eruptive phase which occurs when equilibrium is lost. Immediately after the loss of equilibrium, the system evolves rapidly over a time period of a few minutes (*i.e.* a few Alfvén time-scales). Since the evolution in this stage is very rapid compared to the rate at which flux is transferred from the photosphere to the corona, no flux is transferred to the corona during the eruptive phase. This means there is no external energy input during the eruptive phase.

The models solves an idealized configuration with a force-free flux-rope (*i.e.* a current filament) and a current sheet with a variable length. To make the solution mathematically

tractable, we assume that the current sheet always remains attached to the boundary at the base and that reconnection only occurs in the sheet at the point where it intersects the boundary.

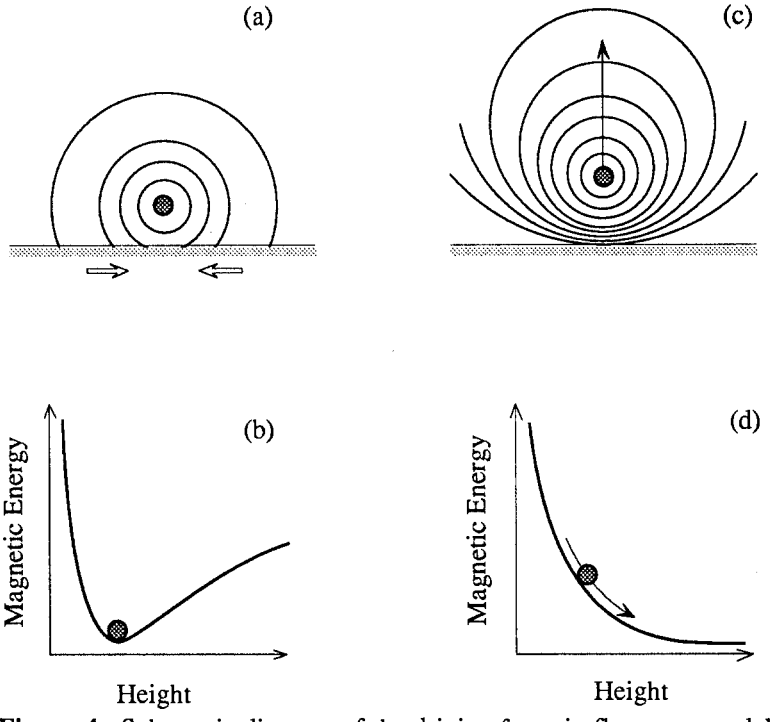

Figure 4. Schematic diagram of the driving force in flux-rope models. The shaded circle indicates the position of the magnetic flux rope or current filament.

During the quasi-static stage of the evolution, the coronal magnetic field **B** and current density **j** are determined by the magnetohydrostatic equation

$$\frac{\mathbf{j}\times\mathbf{B}}{c} = \nabla p \approx 0 \qquad (1)$$

where the current density **j** is given by Ampére's law, p is the plasma pressure, and c is the speed of light. The pressure in the corona is very small, and in general one expects the current system in the corona to be force-free except inside current sheet and very thin current filaments. Here we also consider the case where the pressure is significant within the filament since some of the numerical solutions we discuss in the next section contain such filaments.

The model assumes that all quantities are invariant in the z direction perpendicular to the x-y plane, so that the total force per unit length on the filament is

$$\mathbf{F}_{\mathrm{tot}} = \frac{1}{c}\iint_S (\mathbf{j}_\mathbf{f}\times\mathbf{B}_\mathbf{f})\,da + \frac{1}{c}\iint_S (\mathbf{j}_\mathbf{f}\times\mathbf{B}_\mathbf{e})\,da - \oint_C p\,\hat{\mathbf{n}}\,dl, \qquad (2)$$

where S is the region occupied by the filament, a is the area of S, C is the perimeter of S, l is the length of C, $\mathbf{j}_\mathbf{f}$ is the filament current density, and $\mathbf{B}_\mathbf{f}$ and $\mathbf{B}_\mathbf{e}$ are the magnetic fields due to the internal filament current and the external currents outside the filament. The region a

is assumed to be small enough to make the external field $\mathbf{B_e}$ effectively uniform within the filament. With this assumption, the condition for filament equilibria dissociates into two separate conditions – one for the internal, local equilibrium given by

$$\mathbf{j_f} \times \mathbf{B_f} = c \nabla p \approx 0 , \tag{3}$$

and one for the external, global equilibrium given by

$$\mathbf{F} = \left(I B_e^* / c \right) \hat{\mathbf{y}} = 0 , \tag{4}$$

where $\mathbf{F}$ is the external force per unit length, B_e^* is the external field evaluated at the filament, and I is the filament current. For $p = 0$ equation (3) reduces to

$$\frac{1}{8\pi} \frac{dB_\theta^2}{dr} + \frac{B_\theta^2}{4\pi r} + \frac{dB_z^2}{dr} = 0 \tag{5}$$

Conservation of mass and flux within the filament determines the distribution of current density, $\mathbf{j_f}$, and the internal equilibrium prescribed by (5) is coupled to the global equilibrium prescribed by (4) via the filament current and radius. In general, equation (5), must be solved numerically, but Parker (1974) has obtained asymptotic solutions for large expansions and contractions of the filament. Here we consider the simpler case where the filament has a constant radius R without losing any of the essential features of the model.

The analytical model assumes a photospheric boundary condition of the form

$$A(x, 0) = \frac{md}{x^2 + d^2} - \phi(t) \tag{6}$$

where m and d are constants, and $\phi(t)$ is a slowly varying function of time. The quasi-static evolution of MHD equilibria is caused by the gradual reconnection of photospheric field lines below the filament. The reconnection transfers the flux, ϕ, from the photosphere to the corona and leads to the storage of magnetic energy in the corona.

Figure 4 shows the equilibrium field configurations at four different points on the equilibrium curve in the bottom panel. Panels 1 through 3 show the quasi-static evolution along the equilibrium curve from a nearly potential configuration initially to the catastrophe-point configuration which contains a small current sheet attached to the base. Between equilibrium locations 2 and 3, a current sheet forms as more and more flux is transferred to the corona This infinitely thin current sheet represents the low β limit of a finite thickness current sheet with a magnetic null at the point where the current sheet intersects the photospheric boundary. There is no reconnection in the current sheet except at the point where it is attached to the photosphere, but because the current sheet is infinitely thin, the flux reconnected at the photosphere immediately appears at the top of the current sheet.

For a sufficiently small filament radius ($R < 10^{-3}\, d$ for the dipole case), the equilibrium curve is multiply valued as shown in the bottom panel of Figure 5. At the critical point the system undergoes an abrupt transition from the lower equilibrium at 3 to the upper equilibrium at 4. This sudden transition corresponds to a *cusp catastrophe*, one of the elementary catastrophes defined in standard catastrophe theory (*cf.* Poston and Stewart 1978).

Although the analytical solution shows that the current filament is launched upwards at the catastrophe point, it also shows that the filament does not travel very far in the absence of any reconnection. Furthermore, the magnetic energy release is relatively minor unless reconnection occurs. In order for the filament to continue to move upwards indefinitely and for significant energy to be released, substantial reconnection must occur within a few Alfvén scale-times.

III. NUMERICAL STUDIES OF FIELD LINE RECONNECTION

If reconnection occurs in the current sheet below the filament, then all the energy is released and the upward motion of the filament is unbounded, but the speed at which the current filament moves upwards depends strongly on the rate of reconnection. Observations indicate that some ejections move at a speed close to the coronal Alfvén speed, and for these coronal mass ejections the reconnection would have to be rapid enough to reconnect a significant fraction of the field within a few Alfvén time-scales. The theoretical understanding of how such rapid reconnection might occur is somewhat limited, but one attractive possibility is that the flows generated by the loss of ideal-MHD equilibrium may act to drive the reconnection rapidly (Forbes 1990).

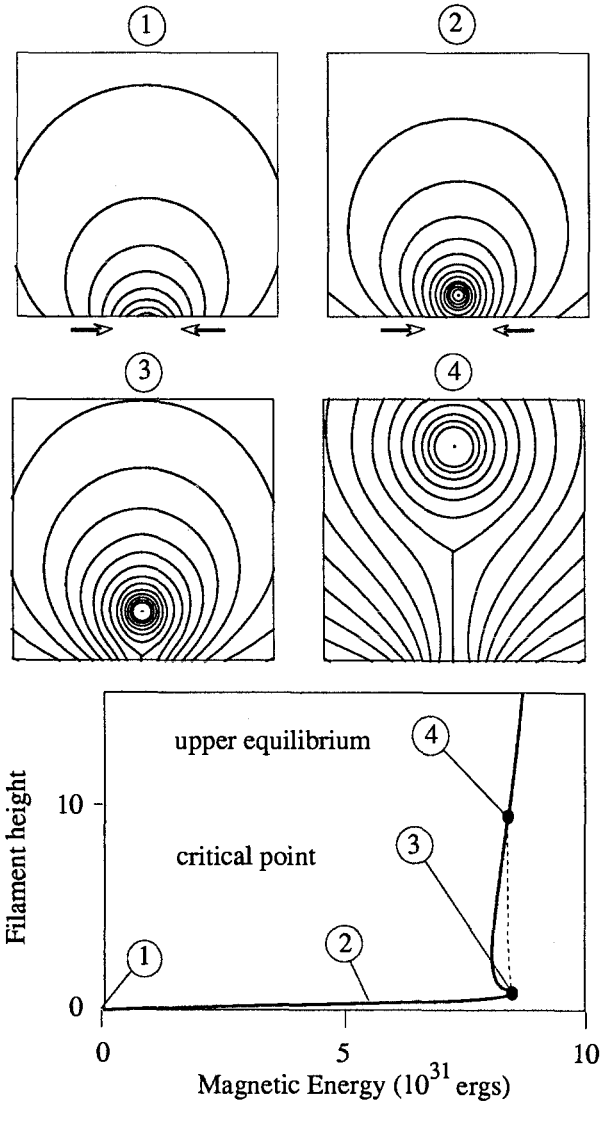

Figure 5. Equilibrium field configurations at four different points on the equilibrium curve shown in the bottom panel. Here the filament radius is $R = 10^{-5}\,d$, and the dashed curve is the expected filament trajectory when the system reaches the critical point.

Mikić *et al.* (1988) carried out the first numerical simulation of an erupting current filament in which the magnetic energy of the system decreased during the eruption. Their simulation creates a magnetic island with a current sheet below it by pinching a loop at its base, but the pinching is done indirectly by neighboring magnetic loops which expand as their footpoints are sheared (Biskamp and Welter 1989). When the current sheet becomes thin enough, it undergoes magnetic reconnection (*i.e.* it tears) and a magnetic island is ejected out the top of the numerical domain.

More recently Inhester *et al.* (1992) have carried out a simulation which forms and ejects a magnetic flux rope by shearing and converging the footpoints of an arcade of loops. In this simulation the reconnection does not take

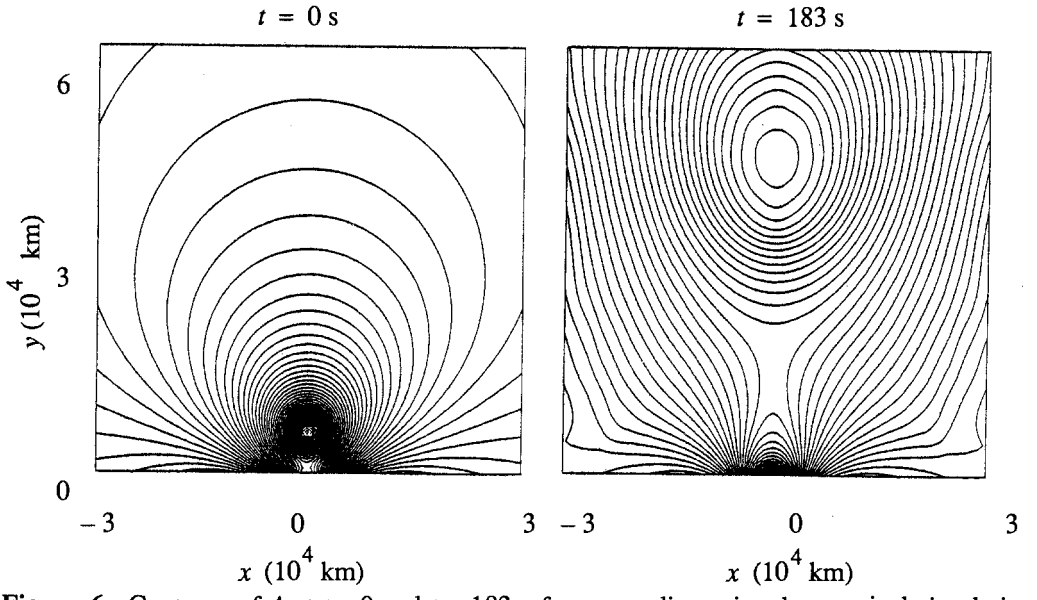

Figure 6. Contours of A at $t = 0$ and $t = 183$ s for a two dimensional numerical simulation with a quadrupole photospheric magnetic field which has a maximum field strength of 100 Gauss at the photosphere. The initial field configuration is the unstable equilibrium at the estimated location of the critical point.

place in the boundary as assumed in the analytical solutions discussed above, but instead the reconnection occurs in the coronal region above the boundary. As the footpoints of the arcade approach one another a flux rope forms simultaneously with the current sheet which tears to release the flux rope. There is no obvious loss of ideal-MHD equilibrium in this simulation since the upward motion of the flux rope occurs only in response to the tearing in the current sheet. Both the Mikić *et al.* (1988) and Inhester *et al.* (1992) show that it is not necessary for an ideal-MHD catastrophe to occur in order for an eruption to take place.

A numerical simulation of an eruption caused by a loss of magnetic equilibrium is shown in Figures 6 and 7. The simulation uses a flux-corrected transport code to solve the resistive MHD equations for a magnetic Reynolds (Lundquist) number of about 200 (Forbes 1991). In this simulation the initial magnetic field is the sum of a quadrupole background at depth d, a simple current filament centered at $y = h$, and a corresponding image filament at $y = -h$. A quadrupole is used, instead of a dipole field, because the quadrupole field gives a catastrophe even when the radius is relatively large whereas the dipole has a catastrophe only when the radius is relatively small (Démoulin *et al.* 1991). The panel labeled $t = 0.0$ in Figure 6 shows the magnetic field configuration when the filament is positioned at the catastrophe point at $h = d$. Here R, the radius of the filament, is set at 0.05 times d, and initially the plasma is at rest and has uniform entropy. The boundary conditions at the photosphere ($y = 0$) are $j = 0$, $v_x(x, 0, t) = 0$, and $v_y(x, 0, t) = 0$. The line-tying condition, $j = 0$, follows from the requirement that field lines be anchored to the base (see Forbes 1990 for further details).

Figure 7 shows the shock, filament, and x-line trajectories along with the x-line electric field as a function of time. Here the dimensionless numerical results have been rescaled in dimensional units using a length scale of 10^4 km, a maximum photospheric field

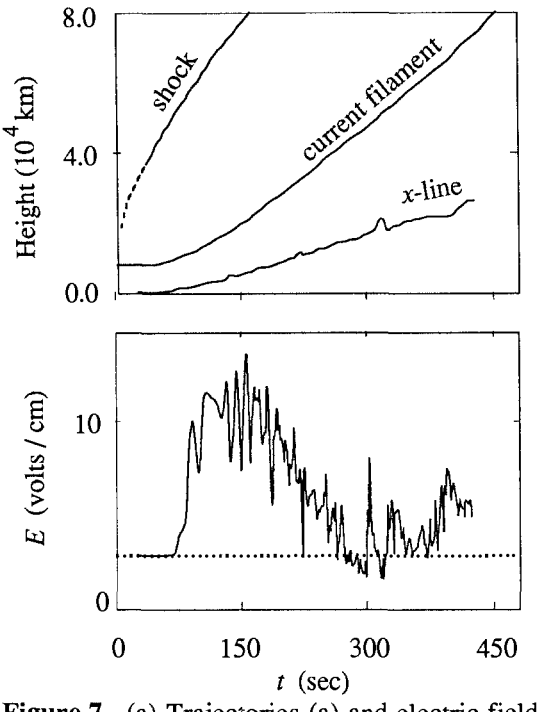

Figure 7. (a) Trajectories (a) and electric field at x-line for a numerical simulation starting at the critical point.

strength of 100 Gauss, a coronal density of 10^9 cm^{-3}, and a coronal temperature of 10^6 K. The filament is initially in equilibrium, but the equilibrium is unstable. Consequently, the filament starts to rise slowly at first, but then more rapidly later on. As the filament moves higher, rapid reconnection starts to occur at the x-line which forms below the filament. By $t \approx 400$ the filament is ejected from the top of the numerical box, and the calculation is stopped shortly afterwards. The contact of the filament with the top of the box disrupts the equilibrium of the filament, and this disruption has a definite effect on the subsequent evolution of the system. As the filament passes through the upper boundary, it starts to expand, and the expansion launches a downward traveling wave which halts the reconnection.

The electric field increases rapidly and reaches a peak value of 13 volts/cm at about t = 150 after which it slowly declines. The spiky fluctuations imposed on top of this general variation of the field are mostly due to insufficient numerical resolution inside the current sheet.

IV. CONCLUSIONS

Eruptive flares pose a challenge to theory because they require the formation of an extended magnetic field by a process which releases magnetic energy. Since extending the field acts to increase the magnetic energy, there must exist another part of the coronal magnetic field which releases more energy than the energy needed for the extension. The most plausible scenario so far suggested is the unwinding and expansion of a magnetic flux rope.

Several recent analytical studies and numerical simulations have successfully explained how a magnetic flux rope can erupt as a consequence of shearing and convergence of the footpoints of a magnetic arcade. In some cases the eruption involves a loss of ideal-MHD equilibrium, but in other cases it does not. What is essential is that rapid magnetic reconnection of the stretched field lines be able to occur, otherwise the magnetic flux rope cannot escape form the Sun. So far there is no adequate theory which explains how such rapid reconnection works.

This work was supported by the NASA Space Physics Theory program through NASA Grant NAG 5-1479 and by NSF Grant ATM-8916303 to the University of New Hampshire.

REFERENCES

Aly, J.J. 1984, *Astrophys. J.*, **283**, 349.

Aly, J.J. 1990, *Comput. Phys. Commun.*, **59**, 12.

Barnes, C.W., and Sturrock, P.A. 1972, *Astrophys. J.*, **137**, 659.

Berger, M.A. 1990, in *Physics of Magnetic Flux Ropes, AGU Monograph 58*, eds. C.T. Russell, E.R. Priest and L.C. Lee (Washington, D.C.:*Amer. Geophys. Union*), p. 251.

Biskamp, D., and Welter, H. 1989, *Solar Phys.*, **120**, 49.

Canfield, R.C., Cheng, C.-C. Dere, K.P., Dulk, G.A., McLean, D.J., Robinson, Jr., R.D., Schmahl, E. J., and Schoolman, S.A. 1980, in *Solar Flares: A Monogram from the Skylab Solar Workshop*, ed. P.A. Sturrock, (Boulder: Colorado Assoc. Univ. Press), p. 451.

Démoulin, P., and Priest, E.R. 1988, *Astron. & Astrophys.*, **206**, 336.

Démoulin, P., Priest, E.R., and Ferreira, J. 1991, *Astron. & Astrophys.*, **245**, 289.

Foote, B.J., and Craig I.J.D. 1990, *Astrophys. J.*, **350**, 437.

Forbes, T.G. 1990, *J. Geophys. Res.*, **95**, 11919 .

Forbes, T.G. 1991, *Geophys. Astrophys. Fluid Dynamics*, in press.

Forbes, T.G., and Isenberg, P.A. 1991, *Astrophys. J.*, **373**, 294.

Heyvaerts, J., and Priest, E.R. 1976, *Solar Phys.*, **47**, 223.

Inhester, B., Birn, J., and Hesse, M. 1992, *Solar Phys.*, in press.

Kopp, R. A., and Pneuman, G. W. 1976, *Solar Phys.*, **50**, 85.

Linker, J.A., Van Hoven, G., and Schnack, D.D. 1990, *J. Geophys. Res.*, **95**, 4229.

Martens, P.C.H., and Kuin, N.P.M. 1989, *Solar Phys.*, **22**, 263.

Martin, S.F., Livi, S.H.B.,and Wang, J. 1985, *Australian J. Phys.*, **38**, 929.

Mikić, Z., Barnes, D.C., and Schnack, D.D. 1988, *Astrophys. J.*, **328**, 830.

Moore, R.L. 1988, *Astrophys. J.*, **324**, 1132.

Parker, E.N. 1974, *Astrophys. J.*, **191**, 245.

Poston, T., and Stewart, I. 1978, *Catastrophe Theory and Its Applications* (San Francisco: Pitman), p. 1.

Schmieder, B., Forbes, T.G., Malherbe, J.M., and Machado, M.E. 1987, *Astrophys. J.*, **317**, 956.

Simnett, G.M., and Harrison, R.A. 1985, *Solar Phys.*, **99**, 291.

Sturrock, P.A., 1987, *Solar Phys.*, **113**, 13.

Sturrock, P.A. 1989, *Solar Phys.*, **121**, 387.

Sturrock, P.A., Kaufman, P., Moore, R.L., and Smith, D.F. 1984, *Solar Phys.*, **94**,341.

van Ballegooijen, A.A., and Martens, P.C.H. 1989, *Astrophys. J.*, **343**, 971.

Van Tend, W., and Kuperus, M. 1978, *Solar. Phys.*, **59**, 115.

Wagner, W.J., Hildner, E., House, L.L., Sawyer, C., Sheridan, K.V., and Dulk, G.A. 1981, *Astrophys. J.*, **244**, L123.

Webb, D.F., Cheng C.-C., Dulk, G.A., Edberg, S.J., Martin, S.F., McKenna, S.L., and McLean, D.J. 1980, in *Solar Flares: A Monogram from the Skylab Solar Workshop*, ed. P.A. Sturrock, (Boulder: Colorado Assoc. Univ. Press), p. 451.

Wolfson, R., and Low, B.C. 1992, *Astrophys. J.*, submitted.

Yeh, T. 1982, *Solar Phys.*, **78**, 287.

Yeh, T. 1983, *Astrophys. J.*, **264**, 630.

ENERGY RELEASE AT ALFVÉNIC FRONTS IN A FORCE-FREE MAGNETIC FLUX TUBE

Jennifer Nicholls

Research Centre for Theoretical Astrophysics,
School of Physics, University of Sydney NSW 2006
AUSTRALIA

Abstract: Melrose's model (1992) for the energy propagation into the energy release site in a solar flare in terms of Alfvénic fronts is extended to a constant-α force-free flux tube, relaxing the constraint of a uniform current profile. The important features of the model depend on α and the flux tube radius, r_0, only in the combination αr_0.

Introduction

Although simple arguments indicate that energy must flow into a flare kernel at the same time as it is dissipated, most models of solar flares ignore this. There are several exceptions, notably Raadu's current interruption model (1989). Several important features of Raadu's model have been incorporated into a model by Melrose (1991), in which Alfvénic fronts in a cylindrical flux tube (cylindrical co-ordinates r, ϕ, z) release stored magnetic energy. The energy propagates as a Poynting flux to the flare kernel where it is dissipated. Melrose neglected the magnetic field generated by the current, implying that the flux tube is not force-free. In this paper Melrose's model is generalized to a constant-α force-free flux tube.

Outline of Model

At $t = 0$ the dissipative mechanism in the flare kernel, modeled by Raadu as a double layer and by Melrose as a resistance, R_c, is turned on, marking the onset of the flare. The impulsive switching on of the dissipative region creates fronts that propagate away from the flare kernel at the Alfvén speed, as shown by Goertz and Boswell (1979) in a magnetospheric context. Associated with the Alfvén fronts is an effective impedance, which in Melrose's model is $R_A = \mu_0 v_A / 4\pi$, and whose generalization to the force-free case is discussed below. The passage of the fronts unwinds the magnetic field releasing stored energy, part of which goes into the rotational motion of the plasma. The remainder of the released energy flows as a Poynting flux to R_c.

From observations it is known that flare kernels are associated with currents flowing in the corona (e.g. Lin and Gaizauskas 1987), suggesting that the current and the power released in a flare are related. Large-scale current structures in the corona must be force-free (Parker 1979), and so must flow along the magnetic field lines. In the model of Raadu (1989) the current is partially deflected at the Alfvén fronts, thereby causing the azimuthal magnetic field, B_ϕ, for $r < r_0$, to reduce abruptly from ahead to behind the front. This reduction corresponds to a release of magnetic energy as the front passes. In Melrose's model, the deflected current flows around R_c as a singular surface current layer. The current flowing through R_c, and contributing to the dissipation, is $I_f = I_i/(1 + R_c/R_A)$, where i denotes the current ahead of the front, and f denotes that behind the front.

Force-Free Fields

The current profile is assumed to be uniform across the flux tube in Melrose's model, which means the model is valid only for $B_\phi \ll B_z$, a questionable assumption as the magnetic field lines must be highly twisted or sheared to store enough energy to power a flare. The formal solution of the force-free condition, i.e. $\mu_0 \mathbf{j} \times \mathbf{B} = 0$, is $\mu_0 \mathbf{j} = \alpha(r)\mathbf{B}$ with $\mathbf{B} \cdot \nabla\alpha(r) = 0$. Here α, which is a measure of the twist in the system, is assumed to be constant. The standard solution for a constant-α field (e.g. Parker 1979), in terms of Bessel functions, is

$$\mathbf{B} = \frac{\mu_0 \mathbf{j}}{\alpha} = AB_0 \{0,\ \mathrm{J}_1(\alpha r),\ \mathrm{J}_0(\alpha r)\},$$

where B_0 is an arbitrary magnetic field, and A is a dimensionless constant.

The edge of the flux tube is defined by the value of r_0, and the model is determined by the value of $\alpha_i r_0$. (The region outside the flux tube is of no relevance in the following discussion because the magnetic energy at $r > r_0$ does not change.) For $\alpha_i r_0 \ll 1$ the twist in the field lines is a small effect, and the region of relevance here is for $\alpha_i r_0 \approx 1$. As $\alpha_i r_0$ approaches the first zero of $\mathrm{J}_1(\alpha_i r_0)$, the model approaches a reverse field pinch (RFP), (e.g. Taylor 1974; Heyvaerts and Priest 1984); this case is discussed separately below.

Results and Interpretation

In the force-free model, the quantities of interest – the power due to the release of stored magnetic energy, the Poynting flux and the kinetic energy of the plasma – now involve integrals over r of Bessel functions:

$$\mathrm{P_{mag}} = 4\pi\bar{v}_A \frac{B_0^2}{2\mu_0} \int_0^{r_0} dr\, r \left(\mathrm{J}_0^2(\alpha_f r) + \mathrm{J}_1^2(\alpha_f r)\right)^{\frac{1}{2}} \left(A_i^2 \mathrm{J}_1^2(\alpha_i r) - A_f^2 \mathrm{J}_1^2(\alpha_f r)\right),$$

$$\mathrm{P_{kin}} = 4\pi\bar{v}_A \frac{B_0^2}{2\mu_0} \int_0^{r_0} dr\, r \left(\mathrm{J}_0^2(\alpha_f r) + \mathrm{J}_1^2(\alpha_f r)\right)^{\frac{1}{2}} \left(A_i \mathrm{J}_1(\alpha_i r) - A_f \mathrm{J}_1(\alpha_f r)\right)^2,$$

$$\mathrm{P_{Poynting}} = 8\pi\bar{v}_A \frac{B_0^2}{2\mu_0} \int_0^{r_0} dr\, r \left(\mathrm{J}_0^2(\alpha_f r) + \mathrm{J}_1^2(\alpha_f r)\right)^{\frac{1}{2}} A_f \mathrm{J}_1(\alpha_f r) \times \left(A_i \mathrm{J}_1(\alpha_i r) - A_f \mathrm{J}_1(\alpha_f r)\right),$$

where $\bar{v}_A = v_A(r=0) = A_f B_0/(\eta\mu_0)^{\frac{1}{2}}$. In practice, values are chosen for A_i, $\alpha_i r_0$, R_c and B_0 and the constraints – conservation of magnetic flux and the fact that the dissipated power is equal to the power due to the Poynting flux – give α_f and A_f.

In figures 1 and 2, $\mathrm{P_{mag}}$, $\mathrm{P_{Poynting}}$ and $\mathrm{P_{kin}}$ are plotted as a function of $\alpha_i r_0$ from zero to the first zero of $\mathrm{J}_1(\alpha_i r_0)$. In the context of solar flares the interesting region of these graphs is the central section, since at either limit the powers drop to zero. As $\alpha_i r_0 \to 0$ the original Melrose model is recovered, as can be shown analytically, so no new insights are gained from this region.

For $R_c/R_A \ll 1$, where a convenient definition of R_A for the purposes of discussion is $R_A = \mu_0\bar{v}_A/4\pi$, the magnetic field unwinds only slightly as the front passes, so only a small fraction of the released magnetic energy is used by the plasma as kinetic energy. Most of the energy goes into the Poynting flux to be dissipated at R_c, see Figure 1. Only a small fraction of the total current is deflected around R_c. As R_c/R_A is increased, the field unwinds more and more behind the front, so more energy is needed by the plasma for its rotational motion, leaving less to be dissipated. This trend continues smoothly until $R_c/R_A \gg 1$, when the magnetic field is almost completely unwound by the passage of the front. The fraction of released energy going to the kinetic energy of the plasma is now far greater than that dissipated, see Figure 2. The fraction of the current deflected around the resistive region reflects this fact and is close to unity.

The RFP is an interesting limiting case with zero net current and zero net magnetic flux. As this case is approached the solution has two different forms depending on the value of R_c/R_A. For small R_c/R_A there is no change in the system, implying that no fronts are created. For large R_c/R_A the fronts appear but propagate at negligible speed. This case is being investigated further, and may have applications in other areas of astrophysics.

To summarize, Melrose has constructed a model for energy inflow to a flare kernel using a flux tube of constant radius with a current of uniform profile across the tube. A resistance is switched on abruptly, generating Alfvénic fronts that release stored magnetic energy as they unwind the magnetic field. In this paper, where the restriction

of uniform current profile is relaxed, it is shown that the force-free model has the same qualitative results, and the important quantities depend only on the combination $\alpha_i r_0$.

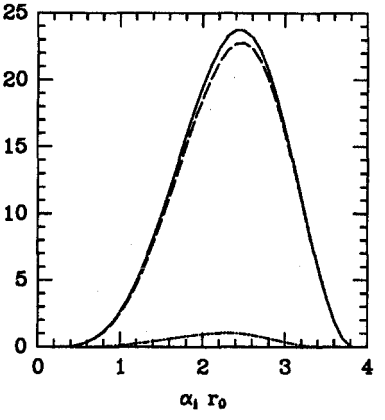

Fig. 1. For $R_c/R_A \ll 1$ the powers are plotted as a function of $\alpha_i r_0$ from zero to the first zero of $J_1(\alpha_i r_0)$. The solid line shows P_{mag}, the dashed line shows $P_{Poynting}$, and the dot-dash line indicates P_{kin}.

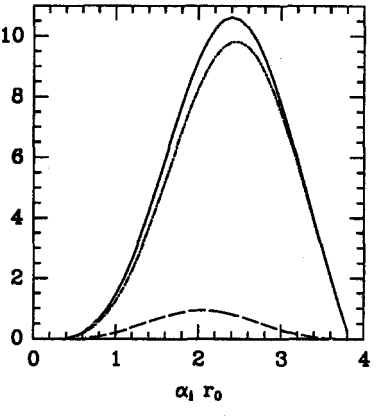

Fig. 2. As for Figure 1, except that $R_c/R_A \gg 1$.

References

Goertz, C.K., and Boswell, R.W., 1979, Magnetosphere-ionosphere coupling, *J. Geophys. Res.* **84**, 7239.

Heyvaerts, J., and Priest, E.R., 1984, Coronal heating by reconnection in DC current systems. A theory based on Taylor's hypothesis, *Astron. Astrophys.* **137**, 63.

Melrose, D.B., 1992, Energy propagation into a flare kernel during a solar flare, *Astrophys. J.* **386**.

Lin Yuanghang, and Gaizauskas, V., 1987, Coincidence between Hα flare kernels and peaks of observed longitudinal electric current densities, *Solar Phys.* **109**, 81.

Parker, E.N., 1979, *Cosmical Magnetic Fields*, Oxford University Press, p. 71.

Raadu, M.A., 1989, The physics of double layers and their role in astrophysics, *Phys. Rep.* **178**, 27.

Taylor J.B., 1986, Relaxation and magnetic reconnection in plasmas, *Rev. Mod. Phys.* **58**, 741.

2.

FLARE DEVELOPMENT

Related poster papers in Chapter 8:

V. Gaizauskas and C.R. Kerton

A.M. Hernandez, M.G. Rovira, C.H. Mandrini, and M.E. Machado

ENERGY TRANSPORT IN SOLAR FLARES: IMPLICATIONS FOR Ca XIX EMISSION

Dominic M. Zarro

Applied Research Corporation at NASA Goddard Space Flight Center
Code 602.6, Greenbelt MD 20771, U.S.A.

Abstract: Results of recent numerical calculations of the soft X-ray Ca XIX resonance line profile are reviewed. The calculations were based on three different energy transport models: nonthermal thick-target electron precipitation; thermal conduction; and electric-field acceleration. Predictions made by each of these models for the Ca XIX blueshift and nonthermal broadening are compared with observations obtained during the flare impulsive phase. Agreements and discrepancies between theory and observation are discussed.

1 Introduction

A wealth of observations of the Ca XIX soft X-ray line (λ 3.177) during solar flares has been obtained by the SOLFLEX instrument on P78-1 (Doschek et al. 1980), and by the Bent Crystal Spectrometers (BCS) on Hinotori (Tanaka et al. 1982) and the Solar Maximum Mission (SMM, Acton et al. 1980). The observations indicate large nonthermal broadenings and blue asymmetries in Ca XIX (and Fe XXV) during the flare impulsive phase. The nonthermal broadening is correlated temporally with impulsive hard X-ray (HXR) emission. The broadening reaches a maximum of $\gtrsim$ 200 km s^{-1} at the peak of the HXR emission and then decays gradually to characteristic quiescent active region values of $\lesssim$ 50 km s^{-1} (Antonucci and Dennis 1983; Fludra et al. 1989). The blue asymmetry is most pronounced during the rise phase of soft X-ray emission in disk flares. Usually, it can be approximated by an emission component that is blueshifted by 300–400 km s^{-1} from a more intense line centered at the rest wavelength (Antonucci, Gabriel, and Dennis 1984). The intensity of the blueshifted component decreases as the intensity of the stationary component increases (Karpen, Doschek, and Seely 1986), while the amplitude of the blueshift velocity tends to peak after the peak of the impulsive HXR emission (Doschek et al. 1989; Winglee et al. 1991a).

The Ca XIX blueshift observations have been interpreted as evidence for convective upflows produced by the heating and evaporation of chromospheric plasma to soft X-ray emitting temperatures (Antonucci et al. 1982; Antonucci, Gabriel, and Dennis 1984). However, the actual mechanism by which energy is transported from the initial release site to the regions where bulk motions occur is still a subject of considerable debate. Fueling this debate are the mixed results of numerical simulations based on different energy transport models. Many of these simulations predict Ca XIX line profiles that are not fully consistent with impulsive phase observations (see Doschek et al. 1986 for a review).

This paper reviews three physically different energy transport models in terms of their ability to explain the observed doppler behavior of Ca XIX emission and, by implication, the dynamics of flare plasma during the impulsive phase. In Sections 2 and 3, we describe the predictions made by the nonthermal thick-target electron and thermal conduction models of energy transport, respectively. In Section 4, we discuss the predictions made by the recently developed electric-field acceleration model. In Section 5, we summarize these predictions and outline proposed improvements to these energy transport models.

2 Nonthermal Thick-Target Electron Model

There have been several recent calculations of the Ca XIX line spectrum for a coronal loop that is heated impulsively by nonthermal thick-target electrons (Emslie and Alexander 1987; Li, Emslie, and Mariska 1989; Antonucci et al. 1991). These simulations are based on a paradigm in which accelerated high-energy electrons are injected at the loop apex and precipitate along uniform field lines to the chromospheric footpoints. As they penetrate to higher density regions, the electrons lose energy via coulomb collisions with ambient electrons and produce HXR bremsstralung radiation ($\gtrsim$ 20 keV) through interactions with ambient ions (Brown 1973; Lin and Hudson 1976).

Emslie and Alexander (1987) used the thick-target calculation results of Nagai and Emslie (1984) to compute the Ca XIX line emission from a symmetric one-dimensional loop with an input heating time profile characterized by a 30s linear rise to maximum followed by a 30s linear decay. From the distribution of temperature, density, and velocity in the loop, they derived Ca XIX profiles at heating maximum that showed a main component that was blueshifted by typically 100–200 km s^{-1} from the rest wavelength, and a second component that was blueshifted 300–500 km s^{-1}. In addition, the computed profiles exhibited line widths that were typically 200 km s^{-1} broader than the intrinsic thermal width implied by the equlibrium temperature of the loop plasma.

Mariska, Emslie, and Li (1989; hereafter MEL) extended the Nagai and Emslie (1984) simulation to a wider range of variations in peak heating flux F_c and electron spectral index δ. Their calculations included an improved treatment of the electron energy distribution in which a discontinuous step function decrease to zero electron

energy was replaced by a continuous parabolic transition below a "knee" energy E_c. Figure 1 illustrates the Ca XIX profiles computed from these simulations for different values of F_c, δ, and E_c (Li, Emslie, Mariska 1989). Each profile corresponds to the time of maximum heating and is plotted at 3s time resolution. As determined in the earlier thick-target simulations, the dominant feature in the Ca XIX spectrum is an emission component that is nonthermally broadened by $\gtrsim$200 km s^{-1} and is blueshifted by up to 400 km s^{-1}. Moreover, the nonthermal broadening of the computed profiles was discovered to be a natural consequence of the velocity dispersion along the line of sight, implying that adhoc mechanisms (such as microturbulence) are not necessary to explain nonthermal broadening during the impulsive phase.

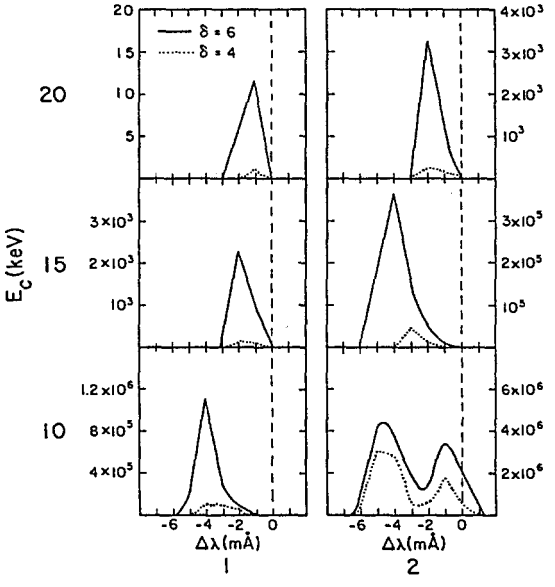

Fig. 1. Computed Ca XIX profiles for different injected electron fluxes (increasing left to right), and different "knee" energies (increasing from bottom to top). Solid lines denote $\delta = 6$; dashed lines denote $\delta = 4$. Intensity units are ergs s^{-1} Å^{-1} per square centimeter of loop cross-sectional area (from Li, Emslie, and Mariska [1989]).

Finally, Antonucci et al. (1991) applied a numerical code by Peres et al. (1987) to compute Ca XIX profiles from a thick-target heated loop. In contrast to MEL, they prescribed a heating variation in which the electron flux was switched on abruptly and maintained constant for 180s. Their assumed electron energy spectrum had a sharp low-energy cutoff at 10 keV and a considerably softer spectrum with $\delta = 8$ (cf. $\delta = 4$ and 6 in MEL). On timescales of less than $\sim$ 40s, these simulations predicted strong nonthermal broadening and an overall blueshift $\gtrsim$ 300 km s^{-1} for the Ca XIX line.

In summary, the thick-target calculations predict that, during the impulsive phase, the Ca XIX profile will show a dominant component that is blueshifted in the range 200–500 km s^{-1} and is nonthermally broadened by $\gtrsim$ 200 km s^{-1}. The blueshift and nonthermal broadening velocities are predicted also to be correlated temporally with the electron heating. The computed strength and amplitude of the blueshifted emission depend on both the intensity of the electron beam and on its spectral energy properties. In general, intense beams drive faster upflows and produce larger nonthermal broadening because of the stronger heating and evaporation they generate. On the other hand, electron beams with hard energy spectra (and/or high electron cut-off energies) tend to produce weaker blueshifted emission as the bulk of the thick-target electron energy deposition occurs deeper in the chromosphere, where evaporation is inhibited by radiative cooling processes (cf. Fisher, Canfield, and McClymont 1985).

How do the theoretical profiles predicted by the thick-target model compare with observation? McClements and Alexander (1989) addressed this question using SMM BCS Ca XIX spectra in several strong disk flares observed with 12 s time resolution. A sample of their findings is displayed in figure 2. Based on an accurate wavelength calibration derived from limb-observed flares, they could find no evidence for systematic Ca XIX blueshifts in excess of 100 km s^{-1} during the impulsive phase of hard X-ray emission. In all the examined disk flares, the Ca XIX profile during the impulsive phase exhibited a dominant nonthermally broadened stationary component with only a weaker blue-wing component at 300–400 km s^{-1}. Although the nonthermal widths of the observed profiles were consistent with computed values, the observation of a weaker blueshifted component (relative to the stationary) disagrees with the thick-target prediction.

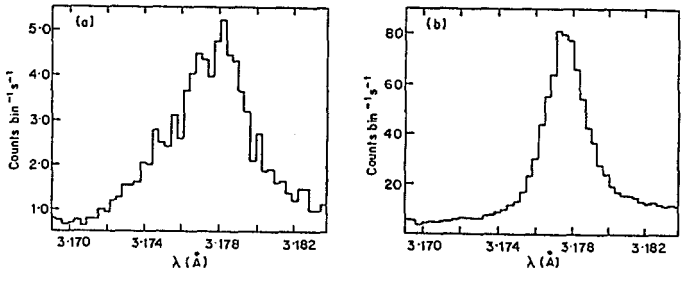

Fig. 2. Observed Ca XIX profiles during the rise phase of impulsive hard X-rays in the 1980 April 10 disk flare. The mean integration time is 12 s. The profiles show the characteristic stationary component and a blue-wing asymmetry (from McClements and Alexander [1989]).

In a single loop model, it is not expected that a stationary component of Ca XIX emission will become significant until chromospheric evaporation has had sufficient

time to enhance the density of soft X-ray emitting plasma in the loop. It is tempting to speculate that some form of preheating (which is not detectable in hard X-rays) may occur prior to the main impulsive phase. Such heating could, in principle, evaporate plasma to the point where the loop density and temperature are sufficiently high to generate stationary Ca XIX emission. Mariska and Zarro (1991) approximated the effect of preheating by injecting high-energy electrons into a loop with a high initial pressure of 50 dyne cm^{-2}. They found that, because of the greater fraction of electrons becoming thermalized in the high-density corona, the simulation could produce a stationary component earlier during the impulsive phase. Nevertheless, even with such a large pressure, they could not reproduce the absolute intensity of the stationary component observed during the early rise phase of impulsive hard X-rays.

3 Thermal Conduction Model

An initially dominant blueshifted component is also a prediction of hydrodynamic calculations in which thermal conduction is the dominant energy transport mechanism (Doschek et al. 1983; Cheng, Karpen, and Doschek 1984, Antonucci et al. 1987; Karpen et al. 1989). The source heating function in these simulations is modeled usually by adding a transient heating term to the steady heating required to maintain the preflare energy balance. Subsequent heating of the ambient plasma results in a downward-propagating conduction front that transfers energy to the chromosphere, driving evaporation and producing soft X-ray plasma (Brown, Melrose, and Spicer 1979).

Hard X-rays in the thermal model are emitted by the hot ($\gtrsim 10^8$ K) plasma behind the front and by the energetic electrons that penetrate the front (Emslie and Rust 1979). One advantage that this model has over the thick-target model is that it requires fewer high-energy electrons to produce an observed HXR flux. Thus, it is energetically more efficient than its nonthermal counterpart (Tandberg-Hanssen and Emslie 1988). However, this advantage is undermined by the fact that the depth distribution of the thermal heat source is presently quite arbitrary. By contrast, the thick-target model (and the corresponding depth-dependence of energetic electrons) is better-substantiated by a wealth of Hα, UV, and HXR observations (cf. Canfield et al. 1986).

Antonucci et al. (1987) assumed a thermal heat source that was distributed as a gaussian function of the distance along the loop. Time-dependent Ca XIX profiles were computed in the two cases of centering the source at the loop apex and at the loop footpoint. In the apex-heating case, the initial increases in plasma temperature and pressure at the loop top produced downward expansion and associated Ca XIX redshifts of typically $\lesssim 50$ km s^{-1} during the first 10s following heating turn-on. After approximately a 10–15s delay (equal to the finite propagation time of the conduction front along the loop) the Ca XIX emission became dominated by a strong blueshifted component at $\gtrsim 400$ km s^{-1}. In the base-heating case, the response of

Ca XIX matched essentially that predicted by the thick-target model with a very soft ($\delta > 7$) electron energy spectrum. In particular, a blueshifted component appeared almost instantaneously and dominated the spectrum during the initial 30s of the heating phase. The Ca XIX profiles in the base-heating case produced a better overall agreement with observation than the apex-heating case. However, as in the previous thick-target calculations, the initially strong blueshifted (and redshifted) profiles predicted by the thermal model do not appear to be supported by observations during the early impulsive phase.

Karpen et al. (1989) investigated the effects of nonlocal thermal conduction on the time-dependent behavior of Ca XIX (and Mg XIX) profiles. The classical conduction approximation is expected to break down when the mean free path of thermal electrons exceeds the temperature scale height by more than about 10%. In the latter circumstance, such as would arise under steep gradients and high energy fluxes associated with flares, the heat flux that the plasma can support becomes limited to a fraction of the total available flux of thermal energy (Karpen and DeVore 1987). This flux-limiting effect decreases the energy available for driving evaporation, leading to significant reductions in the blueshift velocity ($\sim$ factor of 2) and in the intensity of the blueshifted component relative to the classical case. Although these decreases are more consistent with observation than the classical predictions, they are still not sufficient to account for the presence of stationary Ca XIX components that always dominate the observations.

4 Electric-Field Acceleration Model

An interesting variation on the standard nonthermal and thermal transport mechanisms is provided by the electric-field acceleration model of Winglee et al. (1990b). In this model, cross-field currents in the corona are postulated to generate quasi-static parallel electric fields that accelerate electrons down to the chromosphere. These high-energy electrons heat ambient plasma by collisions and produce hard X-rays by thick-target interactions. The hard X-ray spectrum emitted by the accelerated electrons is predicted to show a double power-law, with a break energy of the order of the electric potential drop (cf. Lin and Schwartz 1987).

Test-particle simulations of this mechanism predict several important consequences for the doppler behavior of soft X-ray emission.

(1) the accelerated electrons constitute a region of downward current within which ambient plasma is bulk-heated to soft X-ray emitting temperatures. Because of the large gyro-radius of ions (compared to electrons), the electron current is closed by ions travelling perpendicular to the magnetic field. These transverse motions result in a stationary soft X-ray emission component that is nonthermally broadened;

(2) the electric field responsible for accelerating electrons downwards also accelerates ions upwards along field lines. For view-angles along the magnetic field, these upward motions produce a soft X-ray emission component that is blueshifted with a supersonic velocity determined by the energy of the potential drop;

(3) because of the larger scale lengths along the magnetic field (relative to those across field lines), the upward ion motions develop more gradually than transverse motions. Hence, the appearance of the blueshifted component is delayed with respect to the stationary component; and

(4) since transverse motions occur along the length of the potential drop, they involve a greater number of soft X-ray emitting ions than upward motions – which are confined predominantly to the collisional chromosphere. Hence, the intensity of the stationary component is greater than that of the blueshifted component.

The above predictions appear to be supported in several flares observed by SMM. Winglee et al. (1990a) examined five events that showed a double power-law HXR spectrum that steepened above ≈ 100 keV. They interpreted the double power-law as evidence for electron acceleration by DC-electric fields. After HXR maximum, the spectrum evolved into a single power-law, indicating a decrease in the electric field strength. In each event, the simultaneously observed Ca XIX spectrum exhibited a stationary resonance line that showed the greatest degree of nonthermal broadening ($\gtrsim 200$ km s^{-1}) at the peak of impulsive hard X-rays (i.e., maximum electric field strength). In the three examined disk flares, the Ca XIX profile exhibited a blue-asymmetry that could be represented by a weaker secondary emission component at blueshift velocities of 300–400 km s^{-1}. The velocity of the blueshifted component increased during the rise phase and decreased after the peak of HXR emission. The decrease in blueshift velocity coincided with the switching of the HXR spectrum from a double to a single power-law.

The observed temporal association between the HXR spectral shape and the Ca XIX nonthermal broadening and blueshift is a new result that implicates electric fields as both an energy transport mechanism and as a driver of soft X-ray plasma motions. In particular, the decrease in blueshift velocity after the peak of impulsive hard X-rays is consistent with a reduction in the strength of the electric field that is responsible for accelerating soft X-ray ions upwards.

The thick-target and thermal calculations indicate that soft X-ray nonthermal broadening can be attributed to the line-of-sight superposition of doppler-shifted profiles that are intrinsically thermally broadened. Consequently, these models predict that Ca XIX blueshift and nonthermal broadening velocities ought to be correlated temporally. The observation that Ca XIX blueshifts tend to persist longer than nonthermal broadening conflicts with this prediction. However, in the electric-field model, the observed difference in temporal behaviors is a natural consequence of the difference in acceleration length scales in the parallel and perpendicular directions to the magnetic field.

5 Summary

There have been very few detections of a dominant blueshifted soft X-ray component during the flare impulsive phase. A blueshifted Ca XIX component that was comparable in intensity to the stationary component was observed by SMM on 1980 May 21 (Antonucci et al. 1985). Similarly, an event observed by P78-1 on 1980 November 7 showed blueshifted Ca XIX (and Fe XXV) emission at flare onset with an intensity equal to the stationary component (Karpen, Doschek, and Seely 1986). Even more remarkable was an event observed by Hinotori on 1982 June 6 that showed blueshifted and redshifted Fe XXV components with equal strengths (Tanaka and Zirin 1985). However, these cases appear to be exceptions to the general result that the majority of disk flares show a strong pervasive stationary component and a weaker blueshifted component during the impulsive phase (McClements and Alexander 1989).

Of the three cited transport models, the electric-field acceleration model comes closest to explaining (at least, qualitatively) the difference in intensities of blueshifted and stationary soft X-ray components during the impulsive phase. In addition, the model is able to account for the observed difference in temporal behaviors between the Ca XIX nonthermal broadening and blueshift velocities relative to hard X-rays. A present drawback of the electric-field model is that its supporting numerical simulations have been performed assuming a small length scale that is of the order of the Debye length. The latter length is $\sim 10^{-5}$ smaller than actual loop lengths. Hence, the model has yet to mature quantitatively to the point of producing absolute flux profiles that can be compared directly with observations.

The thermal and thick-target models are capable of predicting Ca XIX spectra that can be tested quantitatively with observation. In fact, temporal integration of the computed Ca XIX profiles from both of these energy transport models produces blue-asymmetric Ca XIX profiles that are very similar in shape, width, and absolute intensity to observed profiles (cf. figure 8; Li, Emslie. and Mariska 1989). Such agreement is expected on hydrodynamic timescales – the time required for supersonic plasma to travel from the chromosphere to the loop apex. For a typical loop length of 10^9 cm and an upflow speed of $\gtrsim 300$ km s^{-1}, the hydrodynamic timescale is approximately 30s. On this timescale, the loop fills with hot plasma that becomes approximately static and emits a strong stationary Ca XIX component. Morever, as evaporation increases the pressure in the coronal loop, the pressure gradient driving the upflow reduces and the intensity of blueshifted Ca XIX emission diminishes relative to that of the stationary component.

However, on timescales shorter than the hydrodynamic time, the thick-target and thermal models predict blueshifted Ca XIX components whose intensities are generally greater than observed. It has been suggested that two-dimensional transport effects, such as would arise in a converging field geometry, may help resolve this problem. (Alexander 1990). In this scenario, the intensity of blueshifted Ca XIX emission can be reduced (relative to the uniform field case) by limiting the emission to flux tubes that have a narrower cross-sectional area ($\lesssim 10^{17}$ cm^2) at the chromo-

spheric footpoints than in the corona. Independent evidence for such small chromospheric areas has come from EUV (McClymont and Canfield 1986) and Hα redshift (Zarro and Canfield 1989) observations. A converging magnetic field has the additional effect of limiting the number flux of energetic electrons into the chromosphere via mirroring processes (LaRosa and Emslie 1988). Consequently, the blueshifted emission can be attenuated further due to the reduced energy deposition in the chromosphere. The dynamical consequences of thick-target energy transport in a converging field geometry are currently under investigation. (Mariska and Emslie, priv. comm.).

In conclusion, more theoretical and numerical work is required before the claim can be made that any of the three cited transport mechanisms are capable of explaining the observed doppler behavior of Ca XIX during the impulsive phase. Alternative transport mechanisms such as the electric-field acceleration model need to be explored further and developed to the point of predicting observable line fluxes. Alternative loop geometries such as a converging field structure or multi-loop arcades should also be considered. On the observational side, there is a pressing need for greater sensitivity at flare onset than that provided by soft X-ray spectrometers on P78-1, SMM, and Hinotori. In particular, by the time soft X-ray emission was detected by these instruments, the plasma temperature already exceeded 10^7 K. Hence, the important time during the initial heating phase was missed (Doschek 1990). With a factor of 5–10 greater sensitivity relative to the SMM BCS, the Bragg Crystal Spectrometer on the recently launched Yohkoh satellite will permit improved observations of Ca XIX (together with S XV and Fe XXV) during this critical phase.

Acknowledgements: This work was supported by NASA contract NAS5-30431 and the Lockheed Independent Research Program. The author thanks Brian Dennis for useful comments and the American Astronomical Society for providing NSF travel support to attend IAU Colloquium No. 133 on "Eruptive Solar Flares".

References

Acton, L.W. et al. (1980): Solar Phys., 65, 53
Alexander, D. (1990): Astron. Astrophys., 235, 431
Antonucci, E. et al. (1982): Solar Phys., 78, 107
Antonucci, E., Dennis, B.R. (1983): Solar Phys., 86, 67
Antonucci, E., Gabriel, A.H., Dennis, B.R. (1984): Ap.J., 287, 917
Antonucci, E., Gabriel, A.H., Dennis, B.R., Simnett, G.M. (1985): Solar Phys., 96, 129
Antonucci, E., Dodero, M.A., Peres, G., Serio, S., Rosner, R. (1987): Ap.J., 322, 522
Antonucci, E., Dodero, M.A., Peres, G., Reale, F., Serio, S., Somov, B.V. (1991): preprint
Brown, J.C. (1973): Solar Phys., 31, 143
Brown, J.C., Melrose, D.B., Spicer, D.S. (1979): Ap.J., 228, 592
Canfield, R.C. et al. (1986): "Impulsive Phase Transport", in Proc. SMM Workshop, Energetic Phenomena on the Sun, ed. by M.R. Kundu and B. Woodgate (NASA CP-2439), p. 3-1

Cheng, C.-C., Karpen, J.T., Doschek, G.A. (1984): Ap.J., 286, 787
Doschek, G.A., Feldman, U., Kreplin, R.W, Cohen, L. (1980): Ap.J., 239, 725
Doschek, G.A., Cheng, C.-C., Oran, E.S., Boris, J.P., Mariska, J.T. (1983): Ap.J., 265, 1103
Doschek, G.A. et al. (1986): "Chromospheric Explosions", in Proc. SMM Workshop, Energetic Phenomena on the Sun, ed. by M.R. Kundu and B. Woodgate (NASA CP-2439), p. 4-1
Doschek, G.A., Feldman, U., Seely, J.F., McKenzie, D.L. (1989): Ap.J., 345, 1079
Doschek, G.A. (1990): Ap. J. (Suppl.), 73, 117
Emslie, A.G., Rust, D.M. (1979): Solar Phys., 65, 271
Emslie, G.A., Alexander, D. (1987): Solar Phys., 110, 295
Fisher, G.A., Canfield, R.C., McClymont, A.N. (1985): Ap.J., 289, 414
Fludra, A., Lemen, J.R., Jakimiec, J., Bentley, R.D., Sylwester, J. (1989): Ap.J., 344, 991
Karpen, J.T., Doschek, G.A., Seely, J.F. (1986): Ap.J., 306, 327
Karpen, J.T., DeVore, C.R (1987): Ap.J., 320, 904
Karpen, J.T., C.-C. Cheng, Doschek, G.A., DeVore, C.R. (1989): Ap.J., 338, 1184
LaRosa, T.N., Emslie, G.A. (1988): Ap.J., 326, 997
Li, P., Emslie, G.A., Mariska, J.T. (1989): Ap.J., 341, 1075
Lin, R.P., Hudson, H.S. (1976): Solar Phys., 50, 153
Lin, R.P., Schwartz, R.A. (1987): Ap.J., 312, 462
Mariska, J.T., Emslie, G.A., Li, P. (1989): Ap.J., 341, 1067
Mariska, J.T. Zarro, D.M. (1991): in press
McClements, K.G., Alexander, D. (1989): Solar Phys., 123, 161
McClymont, A.N., Canfield, R.C. (1986): Ap.J., 305, 936
Nagai, F., Emslie, A.G. (1984): Ap.J., 279, 896
Peres, G., Rosner, R., Serio, Pallavicini, R. (1987): Ap.J., 312, 895
Tanaka, K., Watanabe, T., Nishi, K., Akita, K. (1982): Ap.J. (Letters), 254, L59
Tanaka, K., Zirin, H. (1985): Ap.J., 299, 1036
Tandberg-Hanssen, E., Emslie, A.G. (1988): "The Physics of Solar Flares", Cambridge University Press, Cambridge, U.K.
Winglee, R.M., Kiplinger, A.L., Zarro, D.M., Dulk, G.A., Lemen, J.R. (1991a): Ap.J., 375, 366
Winglee, R.M., Dulk, G.A., Bornmann, P.L., Brown, J.C. (1991b): Ap.J., 375, 382
Zarro, D.M., Canfield, R.C. (1989): Ap.J. (Letters), 338, L99

FLUID FLOW IN A JET AND THE CA XIX LINE PROFILES OBSERVED DURING SOLAR FLARES

P. L. Bornmann
NOAA Space Environment Laboratory, Boulder, CO, USA
and
J. R. Lemen
Lockheed Palo Alto Research Laboratory, Palo Alto, CA, USA

Two types of fluid models were considered as methods for reproducing the blueshifts and line broadening observed in soft x-ray lines during the rise of solar flares. The fluid models representing the laminar flow of material in a jet and through a pipe were used to derive the velocity at each location in the flow. These velocities were then converted to velocity distributions and convolved with a thermal Maxwellian distribution to produce theoretical line profiles. The resulting theoretical profiles were then compared with Ca XIX line profiles observed by SMM's Bent Crystal Spectrometer during the 1980 May 21 flare. Reasonable agreement was found for the jet model, while the pipe model was less successful at reproducing the observed line profiles.

The optimal values for the free parameters in the jet model were within the ranges expected for solar flare conditions. The jet was much smaller than typical flare volumes estimated from spatial images, but the resulting densities were consistent with the upper limit of densities derived using density-sensitive line ratios. This supports previous reports of small filling factors and is interpreted as evidence for a chromospheric origin for the flow. Extrapolating back in time indicates that the jet started during the time of the hard x-ray burst. Stability analysis indicates that, although the laminar jet can reproduce the observations, instabilities may cause the flow to become turbulent and that this laminar treatment is not strictly valid. In conclusion, although the observed line profiles can be explained with multiple blueshifted gaussians, results from the present work suggest that the continuous velocity distribution within a jet is a viable alternative.

This paper has been accepted for publication in the Astrophysical Journal and the initial results were reported in Bornmann (1990, Proceedings of the Max'91 Conference #3, 88–94).

Characteristics of the Impulsive Phase of Flares

(Invited Review)

A.O. Benz[1] and M.J. Aschwanden[2]

[1] Institute of Astronomy, ETH, Zürich, Switzerland
[2] NASA Goddard Space Flight Center, Greenbelt, MD 20771, USA

Summary

The impulsive phase of flares is an observational concept, characterized by spiky emissions from γ-rays to radio waves. It is generally agreed that during this time a large fraction of the original flare energy resides in energetic particles which are manifested in these emissions. Here we concentrate on recent decimeter and microwave observations that indicate a high level of fragmentation of this energy release when related to hard X-ray (HXR) flux. Recent attempts to characterize the flare and the distribution of the radio bursts in time and frequency by statistical methods are also reviewed.

1. Introduction

The impulsive phase of flares is usually defined as the time of enhanced, peaky hard X-ray emission. Many other emissions also occur and only occur in this phase including γ-ray nuclear lines produced by impinging protons, chromospheric and transition region atomic lines excited by energetic electrons, and millimeter to kilometer radio bursts. The impulsive phase thus is characterized by a multitude of manifestations of energetic particles, in particular electrons of 20–100 keV. It has been estimated (Duijveman et al. 1982) that at least 20% of the energy that is released in this phase first shows in fast electrons. Energy may also be converted before (pre-flare) and after (eruptive phenomena, CME) the impulsive phase. Nevertheless, it is energetically a clearly distinct, extremely rapid, and important phase.

2. Coherent Microwave Emissions

Flare emissions in the microwave region (> 1 GHz) have traditionally been attributed to synchrotron emission of mildly relativistic electrons (below referred to as 'gyrosynchrotron' radiation). However, since the 1960's observers have insisted that fast drifting bursts exist even in the centimeter range (> 3 GHz, e.g. Kundu 1965). In meter waves (< 0.3 GHz) narrowband emissions rapidly drifting through the spectrum are called 'type III bursts' and, in agreement with interplanetary in situ measurements,

are attributed to the leading front of electron beams. The emission process is a two-step mechanism: The beam excites electrostatic plasma waves which scatter into radio waves. Both processes are induced processes (often called coherent because many particles emit in phase). The relation between beam parameters and radio intensity is very complicated, non-linear and still mostly unknown.

The field of coherent microwave emission has developed slowly because the classical radio spectrographs registering the analog signal on film were not as successful as in the meter range for three reasons: (1) The quiet sun, the slowly varying component and the flare associated synchrotron emission are orders of magnitude stronger in the microwaves and form a strong, variable background. (2) The bursts are generally shorter, and the relative bandwidth ($\Delta\nu/\nu$) is smaller. (3) The total free-free absorption of radiation emitted near the plasma level (where $\nu \gtrsim \nu_p$, the source plasma frequency) increases with ν^2.

Single frequency measurements have given glimpses on interesting structures, in particular on short duration bursts. Spikes of a few tens of milliseconds have been found (Dröge 1976, Slottje 1978) that were later shown to be high frequency extensions of the narrowband spikes previously observed in decimeter waves (Elgarøy 1961, Dröge and Riemann 1961 and many others, cf. review by Benz 1986).

In the last decade digital techniques have revolutionized the field. Coherent emissions have been reliably identified opening up a new channel of information from active regions of the sun where the flare energy is expected to be released (densities of $10^9 - 10^{12}$ cm^{-3}, as deduced from soft X-ray observations, e.g. Strong et al. 1984). Here we concentrate on the two most important types of coherent emission: Type III bursts and narrowband spikes.

2.1. Type III Bursts

Groups of short, relatively broadband and fast drifting bursts ($\Delta\nu/\nu \gtrsim 0.1$) have been found in the decimeter region since the first (analog) spectrograph was put into operation (Young et al. 1961). Some of them — characterized by an irregular distribution of the single bursts in time and frequency — have been shown to have the same properties as metric type III bursts scaled to the higher frequency range of $0.3 - 1$ GHz (drift rate, decay time, polarization, emission mode) except their small total bandwidth (Benz et al. 1983). Therefore, they have been interpreted as electron beams causing plasma emission. The total bandwidth is then related to the magnetic field geometry and reflects its smaller scales in the lower corona. Stähli and Benz (1987) have done a similar work at 3.5 GHz and Benz et al. (1992) in the $6 - 9$ GHz range. These radiations thus are signatures of electron beams propagating in plasmas with densities varying from 10^9 to $2 \cdot 10^{11}$ cm^{-3} (assuming emission at the second harmonic of the plasma frequency).

Above 3 GHz most of the type III bursts drift to higher frequency, indicating that the electron beams propagated downward. Below roughly 1 GHz most type III bursts drift upwards (Benz et al. 1982). The corresponding densities (10^{11} cm^{-3} for 3 GHz, resp. 10^{10} cm^{-3} for 1 GHz) are within the expected range of primary energy release.

2.2 Narrowband Spikes

Narrowband spikes received attention in the late 1970's when they were also discovered in the microwaves and gave conclusive evidence (by their narrow bandwidth and high brightness temperature) for coherent emission in that frequency range. In the mean time they have become interesting for other reasons: (1) They correlate with hard X-rays of the flare. (2) They occur exclusively in the frequency range $0.3 - \gtrsim 8$ GHz. If converted to density by the assumption that $\nu \gtrsim \nu_p$, the range is about $10^9 - 10^{12}$ cm^{-3} and comparable with the density at the primary flare energy release.

Spikes have typical bandwidths (FWHP) of $1 - 2\%$. They are generally more polarized and (except the very low frequency ones) in the opposite sense than the associated metric type III bursts of the same flare. Their decay time is an order of magnitude smaller than for type III bursts at the same frequency and of the order of the thermal collision time (Güdel and Benz 1990). Harmonics in narrowband spikes are not at the frequency ratio of 1:2, but include higher numbers like 5:6 etc. (Güdel 1990).

The above properties of narrowband spikes strongly indicate a different emission mechanism than type III bursts. The high harmonics suggest gyroresonance interactions of energetic electrons with waves propagating at some finite angle to the magnetic field. The details of the emission remain unclear. Earlier maser theories based on the fundamental or second harmonic of the gyrofrequency cannot explain the observations.

We point out that narrowband spikes are less frequent than type III bursts. Spikes are usually associated with metric type III bursts, but the inverse is true only in about 10% of all cases (Benz et al. 1982). However, the above result was derived from observations with limited sensitivity (analog film recordings) and limited frequency range (≤ 1 GHz). In a majority of cases the type III bursts are far more intense than spikes.

3. Hard X-Rays

When hard X-ray emission is compared to coherent radio bursts, the different physics of the two emissions must be taken into account. The hard X-ray flux is proportional to the total energy dumped into energetic electrons (except for changes in efficiency, e.g. the few particles that escape into interplanetary space). This is not the case for coherent emissions like type III bursts or narrowband spikes, which are non-linear processes driven by anisotropic distributions in velocity space. Thus the coherent microwave radiation is a measure of gradients in velocity distributions of non-thermal particles and not of their energy. It is very sensitive to changes in the particle distribution caused for example by multiple injections. The minimum energy to produce a radio burst can be estimated from the total radiated energy and some approximate conversion factor, and it can be as small as 10^{-9} of the energy released in flares. An upper limit can only be derived from associated incoherent emissions such as hard X-rays and may be identical to their driving energy.

3.1. Correlation of HXR and Type III Bursts

Type III bursts indicate the passage of the front of an electron beam through the corona. Since the rest of the beam does not produce type III radiation, it is not surprising that type III flux generally does not well correlate in time with the hard X-ray flux. Nevertheless, occasional peak-to-peak associations have been reported (Kane 1972, Kane et al. 1982, Dennis et al. 1984, Raoult et al. 1985, Savant et al. 1990).

In general, there are many more type III bursts than hard X-ray spikes. Aschwanden et al. (1990) have compared the rate of type III bursts with the hard X-ray count rate. In this way, each radio burst is reduced to a symbol for one process (the front of an electron beam). Surprisingly, this rate correlates well with hard X-rays (Figure 1).

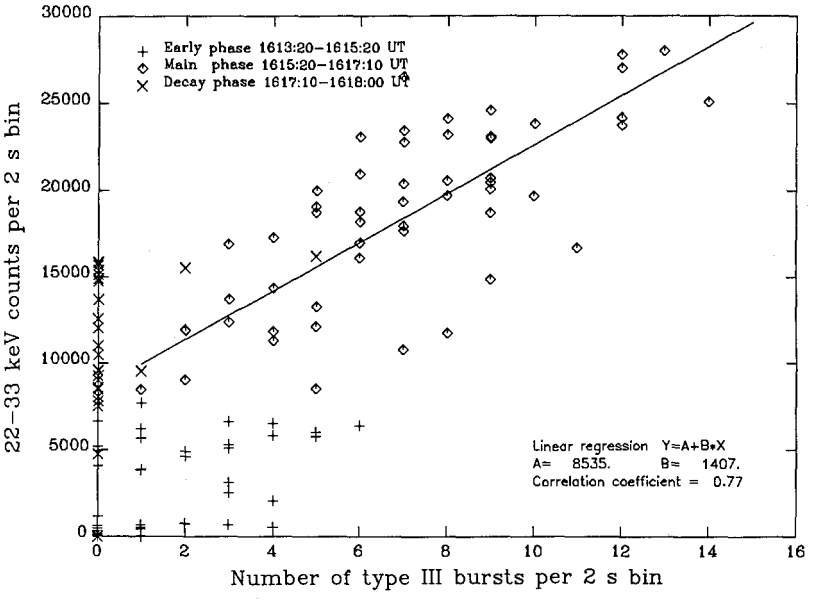

Figure 1: Correlation plot of the number of decimetric type III bursts to the HXR counts per time interval during the main phase of the flare. The regression line is for 4000 HXR counts per type III burst (from Aschwanden et al. 1990).

Figure 1 suggests that each type III burst is related to a similar number of HXR photons and thus to a similar release of energetic electrons. The correlation coefficient of 0.77 excludes any correlation by chance. The most plausible explanation is that the flare energy is released in hundreds of events of similar size. Using the thick target assumption and the value of the regression line of Figure 1, these fragments of energy are about $2 \cdot 10^{26}$ erg.

Each fragment seems to be, however, a complex event, since 80% of the type III bursts shown in Figure 1 were caused by beams going towards lower density, i.e. upwards. On the other hand, the HXR emission is generally believed to be caused by downgoing beams. In the early flare phase the energy per fragment was lower (or the

radio burst count more sensitive), and in the HXR decay phase no type III bursts occurred. A microflare 16 minutes earlier had an energy per type III burst of only 10^{24} erg.

3.2. Correlation of HXR with Narrowband Spikes

The correlation between spikes and hard X-rays can be very close and improves when the spike rate is used (and not the spike flux, Benz and Kane 1986). Güdel et al. (1991) have shown that practically all narrowband spike clusters are associated with enhanced hard X-ray emission. The duration of the spike activity is linearly correlated with the associated HXR peak. A correlation coefficient of 0.78 for 84 events corresponds to a confidence level of $> 99.9\%$. It demonstrates that the two emissions are physically related.

The correlation of spikes with hard X-rays tends to be better than that of the type III bursts. Out of 84 spike events (groups) 40 had unambiguous HXR correlation, and only 18 had better HXR correlation with type III. Figure 2 shows an example of the 26 cases with about equally good correlations between the three emissions.

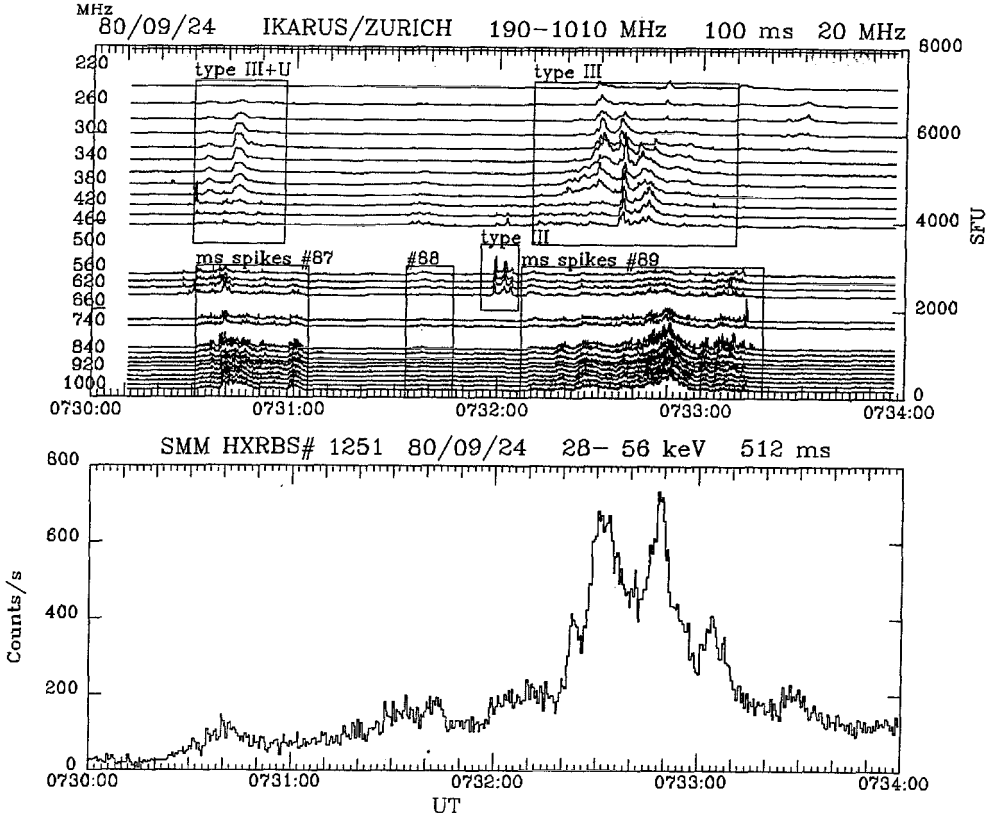

Figure 2 Radio flux (top) for several channels (frequency in MHz given at left) versus time, and hard X-ray counts for comparison. Type III and spikes (frames # 87, # 88, and # 89) are indicated (from Güdel et al. 1991).

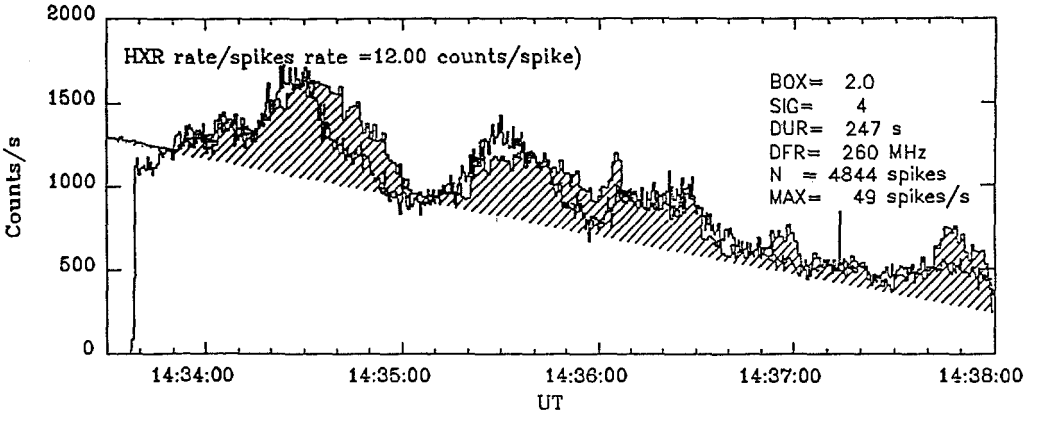

Figure 3: Correlation of spike rate (shaded) with hard X-ray count rate. A total of 4844 spikes have been counted with a maximum rate of 49 spikes/s (from Aschwanden and Guedel, 1992).

A detailed analysis of spike–HXR correlation was recently made by Aschwanden and Güdel (1992). They find close correlation between spike rate and hard X-rays in 22% of all cases, and intermittent correlation in 52% of the cases. The ratio of SMM HXRBS counts to narrowband spikes was found to be between 0.1 and 10, corresponding to an electron beam of $10^{24} - 10^{25}$ erg hitting a thick target. In Figure 3 an uncorrelated HXR background was subtracted to find a constant ratio. Surprisingly, there is an apparent delay of the spike rate in relation to the associated HXR peak. Other events showed the spikes delayed between 0 and 8 seconds. The delay tends to increase with higher HXR flux. The delay has been suggested to be caused by an increase in efficiency of radio spike production in the course of a flare (Aschwanden and Güdel, 1992). Possible parameters that may control the radio flux are the number of trapped particles, the ambient temperature etc. The situation is not very different from the interpretation of the delay between HXR and SXR.

4. Flare Fragmentation

The idealized assumption of a compact flare energy release in a single loop, commonly simplified to a delta function in space and time, stands in striking contrast to the multi-fragmented fine structures of flare-associated radio emission observed at decimetric and microwave wavelengths, and ignores theoretical requirements of beam electrodynamics and current filamentation. Recent models of flare energy release take into account the microstructure of the flaring corona, conveying the picture of a 'statistical flare' as a collective process of many micro-energy releases, characterizing the primary energy release as a 'fragmentation process', or describing the self-organization of the energy release process in terms of critical states and 'avalanche catastrophes', as known in non-linear, chaotic systems.

4.1. Observational arguments

Observational resolution of the complex spatial structure of the energy release region is still insufficient. Some support is given by the verification of multiply interacting loops during the flare energy release (Machado et al., 1988a,b), but the detection of individual reconnection events requires substantially higher sensitivity and spatial resolution in HXR and SXR imaging devices. The search for fast time structures in hard X-ray and gamma ray emission in solar flares does not reveal a richness of fine structures. In a search through 2380 flares observed by the Hard X-Ray Burst Spectrometer (HXRBS) on the Solar Maximum Mission (SMM), fast time structures (of less than 1 s) were only found in $\lesssim$ 10% of the flares (Kiplinger et al., 1983). However, fast time structures in energetic flare emission can be obscured by the high cadence of particle injections, spatial dispersion effects of particle propagation, the finite energy loss time, and by instrumental sensitivity.

A completely different picture arises from flare-associated radio observations. The flare association rate and richness of burst clusters dramatically increases in the lower corona at electron densities ($\gtrsim 10^9$ cm^{-3}) typical for flaring regions. A total of 754 type III bursts was counted in the decimetric frequency range, ($\approx 200 - 400$ MHz, Fig. 1) during the main phase of the 1980 June 27 flare (Aschwanden et al., 1990), while the simultaneously recorded hard X-ray count rate shows only about 13 significant peaks (measured with the sensitive balloon-borne 300 cm^2 phoswich HXR detector of the Univ.of Berkeley). The number and rate of electron beams causing decimetric type III bursts is believed to be a measure of individual acceleration processes, and thus a tracer of the microstructure of the flare energy release region. This is indirectly confirmed by the correlation of the radio burst rate with the flux of hard X-ray emission.

Other tracers of electron acceleration in the solar corona suggest fragmentation at even smaller scales. It is conceivable, that the observed clusters of decimetric millisecond spikes (with up to 10^4 elements) encompass the total topology of flare energy release region, where the spiky structure in frequency and time may reflect the microstructure in space and time. Benz (1985) suggested that the fragmentation of radio emission may be the result of a discontinuous energy release (beam, current, etc.) with the following properties: (i) The large scatter of spike frequencies suggests numerous microflares at many different sites, (ii) each microflare may produce a radio spike in a small volume of $\lesssim 200$ km, and (iii) a microflare has a typical energy of 10^{26} ergs.

4.2. Theoretical arguments

The picture of a highly fragmented acceleration source, which implies that solar flares are a consequence of many very small reconnection events, was already suggested by Sturrock et al. (1984), in accordance with theoretical concepts of current sheet formation (e.g. review by Parker 1989), current filamentation of runaway electrons (Holman 1985, Holman, Kundu and Kane 1989), and was demonstrated by particle-in-cell simulations (Winglee, Pritchett and Dulk 1988). Specific models for fragmented energy release in flares have been developed by studying coalescence and microscopic (kinetic) current-driven instabilities as a consequence of the tearing-mode instability

(Kliem 1990). Other scenarios employ multiple shocks forming a large number of discontinuities moving randomly in a flaring corona (Anastasiadis and Vlahos 1991). Benz and Smith (1987) proposed stochastic acceleration by lower hybrid waves as an appropriate acceleration mechanism producing the observed fragmentation features.

There is increasing evidence that a flare might consist of many small localized energy releases in a highly structured, fibrous corona, probably substantially smaller than the 'elementary flare bursts' postulated by de Jager and de Jonge (1978). There is also the question whether these 'elementary flare bursts' have a relation to the 'microflares' discovered by Lin et al. (1984), or to the 'nanoflares' postulated by Parker (1988), or generally to the process of coronal heating (Hudson 1991). The collective process of numerous microflares may not be simply a linear superposition of many independent microflares, because the close spatial location of these micro-energy releases implies mutual interactions, leading to non-linear dynamics of the postulated 'statistical flare' phenomenon.

The size distribution of solar flares follows a power law with an index of ≈ -1.8 over 5 orders of magnitude (Dennis 1985), which has been interpreted as a property of the active corona being in a scale-invariant critical state of a self-organizing, dynamical system (Lu and Hamilton 1991). The physical picture was drawn, that a solar flare might consist of avalanches of many small reconnection events, analogous to avalanches of sand grains in the models of Bak, Tang and Wiesenfeld (1987; 1988). The size of a flare is then given by the number of elementary reconnection events. Theoretical studies and simulations of such collective phenomena governed by a critical, meta-stable state in three-dimensional systems are underway to model the dynamics of "statistical flares" (Lu 1991).

The hidden order of seemingly irregular events can be investigated by statistical methods. One of them is the derivation of the fractal dimension and Lyapunov exponent of time series (Grassberger and Procaccia 1983). It can reveal whether the flaring is controlled by a few free variables or by stochastically firing independent regions. Since spikes or type III bursts can only originate from the same region if they occur at the same frequency, we can narrow down the question to the following: Do the spikes observed at one frequency originate from the same source emitting chaotic but deterministic pulses, or is each spike the result of a stochastic trigger of this source or a spatially stochastic distribution of sources, some of them having the same plasma parameters and emission frequency? Isliker (1992) has found that low fractal dimensions exist in spike clusters only for short periods. It suggests that at a given frequency one usually observes several sources, each emitting irregular pulses.

5. Conclusions

Flares seem to be fragmented on various levels characterized by different time scales: (i) HXR and synchrotron peaks with about 1 s, (ii) decimetric type III bursts (0.1 s), and (iii) narrowband spikes (0.001 s). The event rate of type III and spikes often correlate well, implying that the number of hard X-ray fluence per event is approximately constant during a flare. This surprising result suggests that the impulsive phase of a flare comprises hundreds or thousands of sub-events of similar size.

More statistical studies, particularly on the type III – HXR correlation, are needed. Very little is known about fragmentation in space. High time resolution HXR observations and spatially resolved decimetric and microwave type III and spike bursts would be interesting to compare. The spatial correlation of the coherent and HXR impulsive emissions is the ultimate goal.

References

Anastasiadis, A. and Vlahos, L. 1991, *Astron.Astrophys.*, in press.

Aschwanden, M.J., Benz, A.O., Schwartz, R.A., Lin, R.P., Pelling, R.M., and Stehling, W. 1990, *Solar Phys.* **130**, 39.

Aschwanden, M.J. and Guedel, M. 1992, *Astrophys.J.*, submitted.

Bak, P. Tang, C. and Wiesenfeld, K. 1987, *Phys.Rev.Lett.* **59**, 381.

Bak, P. Tang, C. and Wiesenfeld, K. 1988, *Phys.Rev.A.* **38**, 364.

Benz, A.O. 1985, *Solar Phys.* **96**, 357.

Benz, A.O. 1986, *Solar Phys.* **104**, 99.

Benz, A.O., Bernold, T.E.X., and Dennis, B.R.: 1983, *Astrophys.J.* 271, 355.

Benz, A.O. and Kane, S.R.: 1986, *Solar Phys.* **104**, 179.

Benz, A.O. and Smith,D.F. 1987, *Solar Phys.* **107**, 299.

Benz, A.O., Magun, A., and Su, H.: 1992, *Solar Phys.*, submitted.

Benz, A.O., Zlobec, P., and Jäggi, M.: 1982, *Astron.Astrophys.* **109**, 305.

de Jager, C. and de Jonge, G. 1978, *Solar Phys.* **58**, 127.

Dennis, B.R. 1985, *Solar Phys.* **100**, 465.

Dennis, B.R., Benz, A.O., Ranieri, M., Simnett, G.M.: 1984, *Solar Phys.* **90**, 383.

Dröge, F. and Riemann, P.: 1961, *Inf.Bull.Sol.Radio Obs.Europe* **8**, 6.

Duijveman, A., Hoyng, P., and Machado, M.E.: 1982, *Astrophys.J.* **81**, 137.

Elgarøy, Ø.: 1961, *Astrophys.Norv.* **7**, 235.

Grassberger, P. and Procaccia, I.: 1983, *Physica* **D9**, 189.

Güdel, M.: 1990, *Astron.Astrophys.* **239**, L1.

Güdel, M., Aschwanden, M.J. and Benz, A.O. 1991, *Astron.Astrophys.*, in press.

Güdel, M., and Benz, A.O.: 1990, *Astron.Astrophys.*, **231**, 202.

Holman, G.D. 1985, *Astrophys.J.* **293**, 584.

Holman, G.D., Kundu, M.R., Kane,S.R. 1989, *Astrophys.J.* **345**, 1050.

Hudson, H.S. 1991, *Solar Phys.*, submitted.

Isliker, H.: 1992, *Solar Phys.*, submitted.

Kane, S.R. 1972, *Solar Phys.* **27**, 174.

Kane, S.R. 1981, *Astrophys.J.* **247**, 1113.

Kane, S.R., Benz, A.O., and Treumann, R.A.: 1982, *Astrophys.J.* **263**, 423.

Kiplinger, A.L, Dennis, B.R., Emslie, A.G., Frost, K.J., Orwig, L.E. 1983, *Astrophys.J.* **265**, L99.

Kliem,B. 1990, in *Proc. FLARES 22 workshop*, Chantilly, France, October 16-19, (eds. B.Schmieder and E.Priest), p.119

Lu, E.T., and Hamilton, R. 1991, *Astrophys.J.*, in press.

Machado, M.E., Moore, R.L., Hernandez, A.M., Rovira, M.G., Haygard, M.J., and Smith, J.B. 1988a, *Astrophys.J.* **326**, 425.

Machado, M.E., Xiao, Y.C., Wu, S.T., Prokakis, Th., and Dialetis, D., 1988b, *Astrophys.J.* **326**, 451.

Parker, E.N. 1988 , *Astrophys.J.* **330**, 474.

Parker, E.N. 1989, *Solar Phys.* **121**, 271.

Raoult, A., Pick, M., Dennis, B.R., and Kane, S.R.: 1985, *Astrophys.J.* **299**, 1027.

Savant, H.S., Lattari, C.J.B., Benz, A.O., Dennis, B.R.: 1990, *Solar Phys.* **130**, 57.

Slottje, C.: 1978, *Nature* **275**, 520.

Stähli, M. and Benz, A.O.: 1987, *Astron.Astrophys.* **175**, 271.

Strong, K.T., Benz, A.O., Dennis, B.R., Leibacher, J.W., Mewe, R., Poland, A.I., Schrijver, J., Simnett, G., Smith, J.B.Jr., and Sylwester, J. 1984, *Solar Phys.* **91**, 325.

Sturrock, P.A., Kaufmann, P., Moore, R.L., and Smith, D.F., 1984, *Solar Phys.* **94**, 341.

Winglee, R.M., Pritchett, P., and Dulk, G.A. 1988, *Astrophys.J.* **329**, 440.

Young, C.W., Spencer, C.L., and Moreton, G.E.: 1961 *Astrophys.J.* **133**, 243.

Comparison of UV and X-Ray Solar Flare Observations and Theoretical Models

J.E. Rodriguez [1], M.G. Rovira [1], M.E. Machado [2]

and E.J. Reichmann [3]

[1]Instituto de Astronomia y Fisica del Espacio, CC 67, Suc. 28, 1428
Buenos Aires, Argentina
[2]Department of Physics, University of Alabama, Huntsville, Alabama 35899,
USA
[3]NASA/MSFC, Huntsville, Alabama, 35812, USA

Abstract: We have studied SMM Hard X-ray Imaging Spectrometer (HXIS) and Ultraviolet Spectrometer and Polarimeter (UVSP) observations of a flare on April 10, 1980, where both instruments simultaneously imaged a hard X-ray footpoint area. The UVSP recorded the emission in the NV line at 1238.8 A, with a spatial resolution of 3" and a temporal resolution of 10 seconds. While the overall footpoint area as seen in the hard X-ray images (16-30 keV) is of the order of two HXIS $(8")^2$ pixels (6×10^{17} cm^2), the UV observations show evidence of smaller scale structure ($\approx 5 \times 10^{16}$ cm^2) for individual peaks throughout the duration of the hard X-ray burst. The ultraviolet peaks are also characterized by redshifts in the line, which is formed at the 10^5 K level within the transition region.

Comparing our results with predictions by theoretical models, that compute the hydrodynamic response of the flare atmosphere to heating by non-thermal electron beams [1, 2], we find that:

a) The results are consistent with Fisher *et al.*'s assertion that the lower transition zone reaches, during individual peaks, a quasi-steady balance between conduction and radiation. Neglect of conduction effects leads to predicted NV intensities over one order of magnitude larger than observed.

b) If the observed spatial structure is interpreted as evidence of "elementary" precipitation areas, the electron energy flux in each of these is F(20 keV) $\leq 5 \times 10^{10}$ erg cm^{-2} s^{-1}.

c) There is considerable preheating in the flare region prior to the impulsive phase. Using a series of steady state models, we find that the transition zone pressure reaches values close to 10^2 dyn cm^{-2} in some of the brightest preburst areas. The mass column density at the transition zone is thus increased from its preflare value of 10^{-5} g cm^{-2} to $> 10^{-4}$ g cm^{-2}.

d) This increase in mass column, usually neglected in theoretical calculations, leads to a decrease in the predicted hard X-ray yield (16 - 30 keV) at the footpoints, due to

increased particle stopping along the flare loops, in agreement with analyses of combined HXIS and Hard X-ray Burst Spectrometer (HXRBS) observations [3].

References

1. G.H. Fisher, R.C. Canfield and A.N. McClymont: Astrophys. J., **289**, 414, (1985)
2. J.T. Mariska, A.G. Emslie and P. Li: Astrophys. J., **341**, 1067, (1989)
3. A.L. MacKinnon, J.C. Brown and J. Hayward: Solar Phys. **99**, 231, (1985)

WHITE-LIGHT FLARES

J.C. Hénoux and J. Aboudarham
Observatoire de Paris, DASOP, UA326,
92195 Meudon Principal Cedex, FRANCE.

Abstract

The observed good temporal correlation between white-light flares and hard X-ray bursts suggests that energetic electrons could be the cause of white-light flare emission. However, even if sufficient energy can be deposited in the chromosphere by electron bombardment, direct collisional heating of the photosphere requires too high a flux of electrons of a few hundred keV and does not appear plausible. We show that non-thermal effects increase the opacity of the upper photosphere and temperature minimum region. Then these regions are consequently radiatively heated both by the beam-produced flare chromospheric emission and by the quiet photospheric emission. As a consequence, a temporary decrease of the continuum intensity (negative flare) is expected. After less than 20 seconds, the radiative heating of the upper photosphere and temperature minimum region produces a white-light flare.

1. Introduction

White-light flare spectra show that they could originate from both the chromosphere and the photosphere. In many published data the Balmer discontinuity is present. However, white-light flares (WLF) without a Balmer discontinuity do exist, and they have been interpreted as due to photospheric H^- emission. The energy required from an energetic particle to reach the photosphere is significantly high. Therefore, contrary to chromospheric flares that can be easily interpreted as resulting from an energy input from the corona, white-light flares rise the problem of their origin since they imply some photospheric heating.

Hudson (1972) suggested a link between WLF and atmospheric bombardment by beams of protons or electrons. In order to penetrate deeply in the atmosphere, protons must have an energy above 100 MeV and will produce the emission of γ-ray lines. However, many of the observed WLF are not accompagnied by γ-ray emission. Direct collisional heating of the photosphere by electron bombardment requires too high a flux of electrons of a few hundred keV and does not appear plausible. Therefore none of these mechanism seems to be able to explain WLF.

However, simultaneous observations of hard X-ray and white-light emission show a very good time correlation of their impulsive phases. We showed (Aboudarham and Hénoux 1986, 1987) that non-thermal effects permit electron beams to indirectly heat the photosphere by radiation, by increasing the opacity of the temperature minimum region. This opacity enhancement could lead first to a decrease of the intensity called "negative flare" and ultimately, once the photosphere has been heated, to a white-light flare.

The causes of the chromospheric and photospheric contributions to the white-light emission are considered respectively in Sections 2 and 3. The relative variation of

intensity resulting from the bombardment of the atmosphere by beams of electrons (transient negative flares and white-light flares) is estimated in Section 4.

2. Chromospheric white-light emission

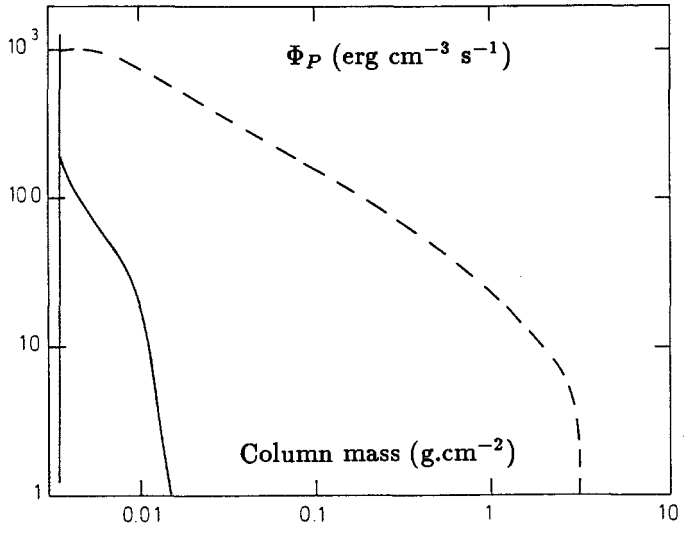

Figure.1 : Column mass dependence of the hydrogen Paschen continuum radiative losses Φ_P. Full line : model F2 (Machado et al. 1980) without any non-thermal collisional excitation and ionization. Dashed line : non-thermal processes included for a beam with an initial total energy flux $\mathcal{F}_{20}$ above 20 keV of 10^{12} erg cm^{-2} s^{-1}.

The non-thermal effects of the electrons of a beam have been ignored in most flare models. However, in an atmosphere with a low degree of ionisation degree, most of the energy lost by the electrons goes into collisional ionization and excitation of neutral hydrogen and the non-thermal excitation rates to levels 2 and 3 C_{12}^{nt} and C_{13}^{nt} and the ionization rate C_{1c}^{nt} are related to the rate of energy deposit due to collisions with hydrogen dE^H/dt by :

$$C_{1c}^{nt} \simeq 2.05\,10^{10}\frac{dE^H}{dt}, \quad C_{12}^{nt} = 1.35\,C_{1c}^{nt}, \quad C_{13}^{nt} = 0.2\,C_{1c}^{nt}.$$

The computation of the non-thermal excitation and ionization rates requires to determine the total amount of beam energy dissipated per unit volume. This was done taking into account the transfer of energy of the electrons in the solar atmosphere (Brown 1972, Emslie 1978, Chambe and Hénoux 1979). The non-thermal excitation and ionization coefficients were included in the statistical equilibrium equations that give the population of the three first levels of hydrogen (the fourth level was considered to be in LTE). The transfer equations were solved for the Lyman α, Lyman β and Balmer α lines and for the Lyman, Balmer, Paschen and Brackett continua. In the low chromosphere and below, where the temperature is less than 10^4 K, the non-termal excitation and ionization rates exceed the thermal rates. Consequently the ionization

degree is increased and the radiative losses of the chromosphere in the hydrogen recombination continua are enhanced by orders of magnitude above the values corresponding to thermal processes alone. Figure 1 shows the significant increase of the Paschen continuum emission in the case of atmospheric bombardment by a beam with an initial total energy flux $\mathcal{F}_{20}$ above 20 keV of 10^{12} erg cm^{-2} s^{-1}.

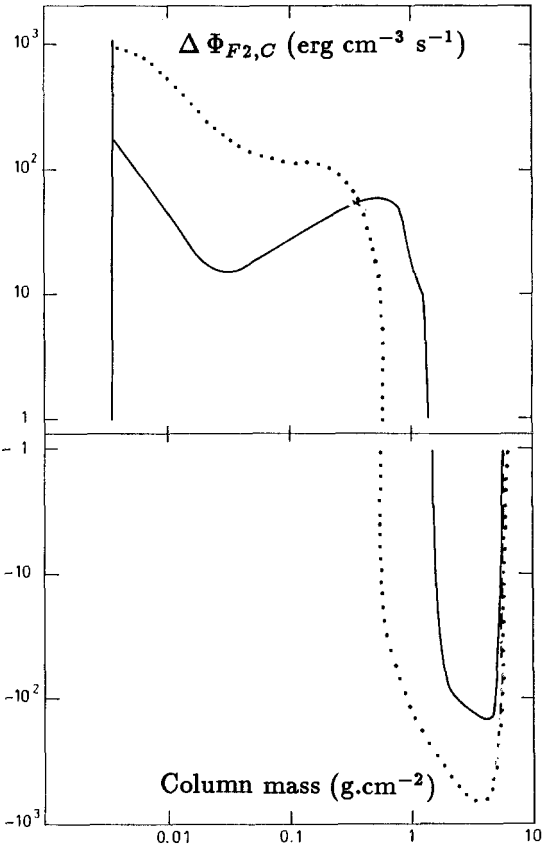

Figure 2 : Column mass dependence of $\Delta\,\Phi_{F2,C}(m)$, difference between the radiative losses of models F2 and C (Vernazza et al. 1976). Full line : non-thermal processes not included. Dotted line : non-thermal processes included ($\mathcal{F}_{20} = 10^{12}$erg cm^{-2}s^{-1}).

3. Photospheric Contribution to the White-Light Emission

In the absence of any collisional energy deposit due to particle bombardment, radiation evacuates the amount of energy deposited by any other source of energy in the atmosphere. In the temperature minimum region (TMR) and below, the main contributor to the energy losses is H^-. In the TMR and upper photosphere, non-thermal collisional ionization by an electron beam enhances significantly the degree of ionization (Aboudarham and Hénoux, 1987). In these layers the main contributor to the opacity is H^-. Since the H^- absorption coefficient is proportional to the electron number density n_e, the opacity will be increased by an electron bombardment.

One dimensional models of the TMR and upper photosphere indicate that H^- heats radiatively, rather than cools, the atmosphere (Avrett, 1980). As shown in Figure 2, an electron beam (with total energy flux $\mathcal{F}_{20}$ above 20 keV of 10^{12} erg cm^{-2} s^{-1} and power index δ=4) leads to a significant enhancement of the atmospheric radiative heating.

The temperature increase resulting from the radiative heating is not instantaneoous. At first, as discussed in Section 4.2, the opacity enhancement will reduce the net intensity by shifting downwards the level of optical depth unity. Later on, energy balance will be reached by an increase of the temperature and the white light emission will rise. This last effect is enhanced by the joint rise of the chromospheric Paschen continuum.

4. Negative and White-Light Flares

4.1 White-Light Flares

Energy balance in the TMR and upper photosphere is obtained for a temperature increase as high as 240 K at a column mass $m = 2$ g cm^{-2} for $\mathcal{F}_{20} = 10^{12}$ erg cm^{-2} s^{-1} and $\delta = 4$. Using the Machado et al (1980) F_2 flare model, modified in order to take into account this temperature increase, we computed the contrast C_λ for various values of the initial energy flux $\mathcal{F}_{20}$ in the beam. Due to the dominance of the non-thermal processes, the uncertainty on the chromospheric temperature distribution does no affect the results.

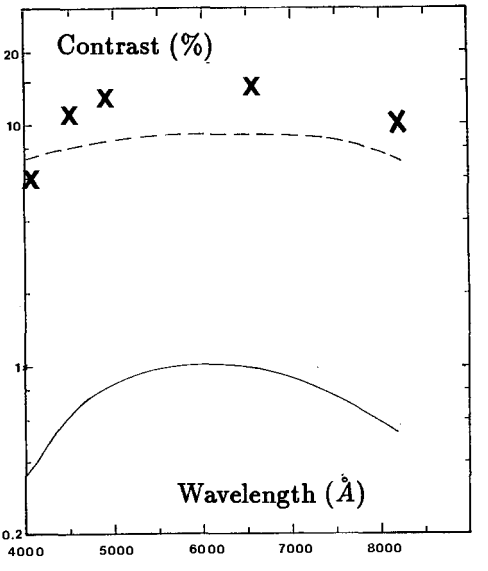

Figure 3 : Wavelength dependence of the contrast C_λ at an heliographic angle $\theta = 53^0$ ($\mathcal{F}_{20} = 10^{12}$erg cm^{-2}s^{-1}, $\delta = 4$). Crosses : data from observations made during the 24 April, 1981 flare (Neidig, 1983).

Figure 3 shows the resulting wavelength dependence of the contrast defined as $C_\lambda = (I_\lambda^F - I_\lambda^{QS})/I_\lambda^{QS}$, where I_λ^{QS} and I_λ^F are respectively the quiet-Sun intensity computed for atmospheric model C (Vernazza et al. 1976) and the intensity computed as described previously for a flaring atmosphere. The computation was done for an

heliocentric angle $\theta = 53°$ in order to compare with observations of Neidig (1983, 1988). The contrast calculated for a beam of electrons ($\delta = 4$, $\mathcal{F}_{20} = 10^{12}$ erg cm^{-2} s^{-1}) is within a factor 2 close to the observed one. A better agreement could be achieved by changing the parameters defining the beam (mainly by decreasing the power index to 3). This was not done since a more significant test would require to know both the observed white-light and hard X-ray flare spectra. However, we can state that when non-thermal effects are taken into account, the computed white-light intensities are close to the values derived from spectroscopic observations.

4.2 Negative Flares

We have seen that non-thermal ionization of hydrogen leads to two effects, i.e. i) above the TMR the radiative losses increase ii) in the TMR and in the upper photosphere, the radiative losses decrease until higher temperatures are set up. These two effects influence the radiative flux emergent at the top of the atmosphere in opposite senses and the nett observed variation of intensity depends on which of them dominates at any wavelength, position and time. This is illustrated by Figure 4 taken from Hénoux et al. (1990) (see also Aboudarham et al. 1990) that shows the wavelength dependence of the observed contrast at disk center for bombardment by electron beams carrying an initial energy that ranges from 10^{10} to 10^{12} erg cm^{-2} s^{-1}. The maximum energy flux produces a negative contrast of -5% at a wavelength of 500 nm.

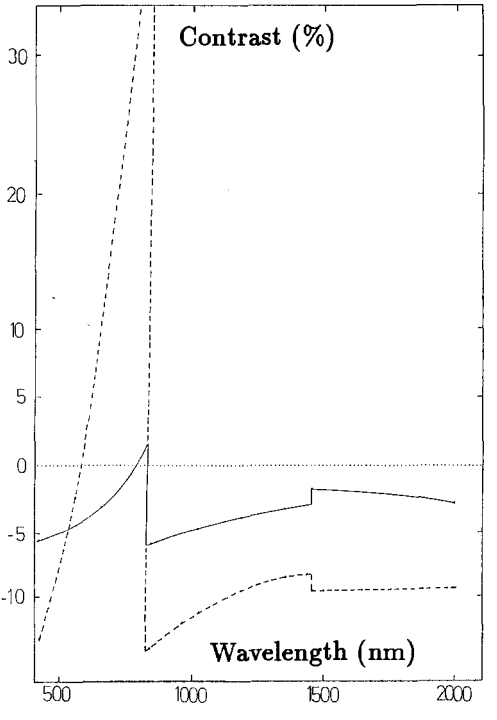

Figure 4 : Wavelength dependence of the contrast C_λ for a bombardment of the quiet-Sun atmosphere by an electron beam ($\mathcal{F}_{20} = 10^{12}$erg cm^{-2}s^{-1}, $\delta = 4$) and before the the photosphere reaches energy balance. Full line : $\theta = 0°$; dashed line : $\theta = 78°$.

Negative flares are transient phenomena. Heating of the bombarded atmosphere reduces the magnitude of the negative contrast, which at the end becomes positive. The duration $\Delta\tau$ of a negative flare depends on the wavelength and on the heliocentric angle. As observed at 2.2 μm in some dM and dMe stars, the intensity of a radiation coming from below the heated regions may be reduced during the total flare duration. To the contrary, radiation coming from chromospheric layers may not be reduced at all ($\Delta\tau = 0$). The duration of a negative flare observed in a radiation coming from the TMR an upper photosphere is $\Delta\tau = 3\mathrm{Kn}_H/(2\mathrm{dE/dt})$ and it is found to be close to 15-20 s for $\mathcal{F}_{20}=10^{12}$ erg cm^{-2} s^{-1} and $\delta=4$.

5. Conclusion

Due to non-thermal excitation and ionization processes, an electron bombardment of the solar atmosphere can produce a white-light flare. Chromospheric recombination emission, and an increase emission from a radiatively heated TMR and upper photosphere, would contribute both to the white-light emission. This does not rule out the possibility of producing white-light flares by a bombardment by protons.

Electron bombardment could also produce a transitory decrease of the intensity called negative flare. Negative flares have been observed in dM and dMe stars. They have not yet been detected on the Sun. The most appropriate wavelength to look for negative flares as a sign of non-thermal ionization processes is in the infra-red, near 2 μm.

References

Aboudarham, J. and Hénoux, J.C.:1986, Astron. Astrophys., **168**, 301
Aboudarham, J. and Hénoux, J.C.:1987, Astron. Astrophys., **174**, 270
Aboudarham, J., Hénoux, J.C., Brown, J.C., Van Den Oord, G.H.J.,
Van Driel-Gesztelyi, L and Gerlei, O.:1990, Solar Phys., **130**, 243
Avrett, E.H.:1980, in Chromospheric diagnostic and modeling, ed. by B.W. Lites, NSO, Sunspot NM
Brown, J.C.:1973, Solar Phys., **26**, 441
Chambe, G. and Hénoux, J.C.:1979, Astron. Astrophys., **80**, 123
Emslie, A.G.:1978, ApJ, **224**, 241
Hénoux, J.C., Aboudarham, J., Brown, J.C., Van Den Oord, G.H.J.,
Van Driel-Gesztelyi, L and Gerlei, O.:1990, Astron. Astroph., **233**, 577
Hudson, H.S.:1972, Solar Phys., **24**, 414
Neidig, D.F.:1983, Solar Phys., **85**, 285
Neidig, D.F.:1988, private communication
Ricchiazzi, P.J. and Canfield, R.C.:1983, ApJ, **272**, 739
Machado, M.E., Avrett, E.H., Vernazza, J.E., Noyes, R.W.:1980, ApJ, **242**, 336
Vernazza, J.E., Avrett, E.H., Loeser, R.:1976, ApJ. Supplt., **30**, 1
Vernazza, J.E., Avrett, E.H., Loeser, R.:1981, ApJ. Supplt., **45**, 635

"POST" FLARE LOOPS

Schmieder B.
Observatoire de Paris-Meudon, URA326, DASOP,
F 92195 Meudon Principal Cedex, France.

Abstract

"Post"-flare loops or cool flare loops (CFL) when observed in the Hα line are magnetic structures within an active region which are clearly a fundamental part of the flare itself and not an external phenomenon or a consequence of flares. After a two-ribbon flare the field-line reconnection gives rise to flare loops of hot temperature which shrink and become cool within few minutes to an hour. The Hα flare loops appear generally as dark loops during the gradual phase of the flare; viewed on the limb they may appear as loops in emission, reaching 50000 km. They create a system of quasi-steady arches lasting up to several hours. Large downflows are observed along the legs of the loops with deccelaration by comparing to free-fall motions. As derived from radiative transfer diagnostics, the gas pressure range of the loops is between 0.2 and 5 dyn cm^{-2} and the electron density is between 10^{10} and 10^{12} cm^{-3}.

The magnetic free energy needs to be continuously replenished from low levels during the flare. Different mechanisms may be considered, dynamical ones such as upward motion from the convection zone pushing the coronal field and twisting of the field lines, or thermal ones such as evaporation or ablation of chromospheric material. We will discuss some observational evidence supporting the Forbes and Malherbe (1986) reconnection model based on the Kopp and Pneuman configuration.

1 Morphology properties of flare loops

How beautiful is the development of Hα loops seen with a coronagraph! The geometry seems perfect, simple shapes more or less circular and well organized (observations in Wroclaw by Rompolt, in Ondřejov by Ambrož (movies) and Heinzel, in Tatranska Lomnica by Kamenický and Rušín (1990), in Australia, at Pic du Midi, at Big Bear observatory). The thickness of the loops are around 3 to 6 " (Kim 1991). The brightness of the loops is not necessary uniform along the loop, we notice the formation of knots generally at the top (Figure 1).

Cool flare loops are mainly observed using multi-wavelength filtergrams in Hα (Švestka *et al.* , 1987, Loughhead *et al.* , 1983, Hanaoka *et al.* , 1986, Kurokawa 1989). On the disk they appear in emission or in absorption (Figure 2). Reviews (Švestka 1989, Foukal 1991) related to gradual phase of eruptive flares describe the appearance of flares as the following: in large flares changes in the large-scale arrangement of the active region can typically be observed before and after the flash phase. The active filament that often lies along a magnetic neutral line rises and lifts off, then two narrow

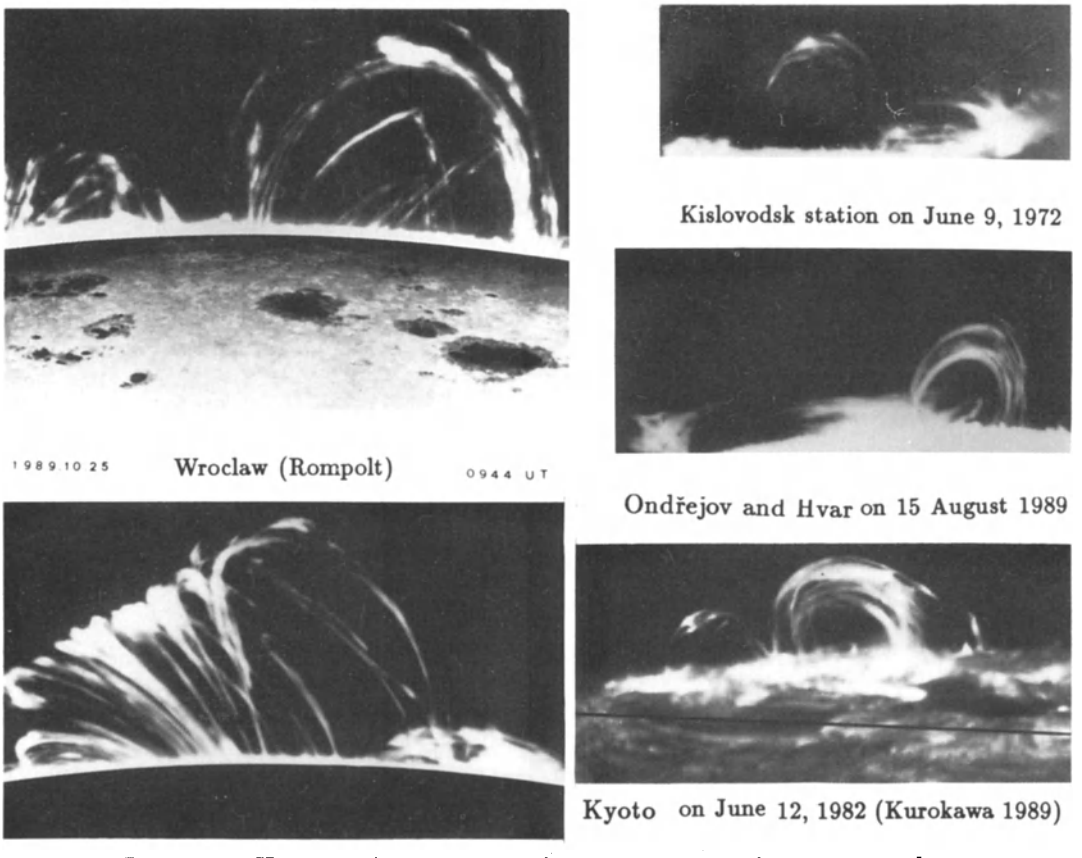

Figure 1. Hα flare loops observed at the limb with coronagraphs

ribbons appear visible in Hα one to each side of the neutral line. The flare loops are part of an arcade of loops which link the two-ribbons. Following the flare, there is magnetic reconnection approximately above the neutral line as the loops form at higher and higher altitudes. The loops observed as the event progresses align themselves more nearly perpendicular to the active region neutral line.

The filtergrams are very useful to derive morphological properties of the loops, i.e. the inclination, the shape, the altitude and the general evolution versus time. Loughhead *et al.* (1983) developed a geometrical technique based on a symmetry assumption of a loop observed on the disk, for reconstructing its true shape and for deriving its orientation with respect to the solar surface. Using this technique, Wang *et al.* (1983), Xu (1987) and Heinzel *et al.* (1991) find that flare loops have dipole or circular shapes with heights reaching 31000 to 50000 km and that they are located in planes more or less perpendicular to the solar surface.

2 Physical parameters

In order to obtain quantitative values, filtergrams are not sufficient, spectrocopic data are more suitable. Only a few are available from Chinese instruments (SSHG in Yun-

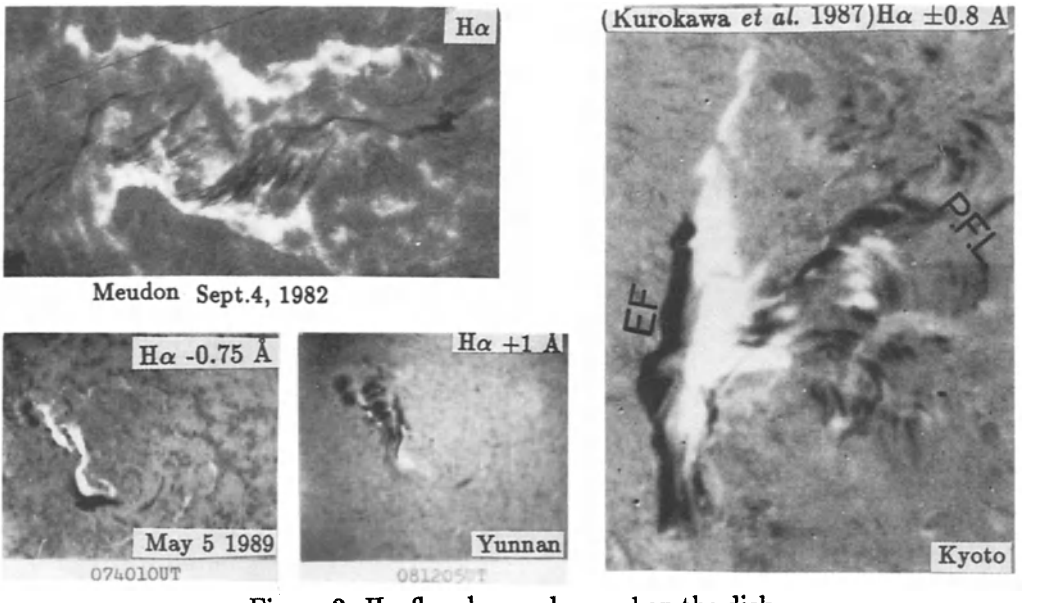

Figure 2. Hα flare loops observed on the disk

nan Observatory), from Meudon (Multi-channel Subtractive Double Pass Spectrograph MSDP) and from Moscow (Sternberg spectrograph). From Hα -profile observations, physical parameters can be derived using different technics. Based on the cloud model method we can derive the source function, the velocity, the Doppler broadening and the optical thickness (Yan *et al.* 1986, Schmieder *et al.* 1988, Mein and Mein 1989, Heinzel *et al.* 1990). Using 2 D observations with the MSDP, Heinzel *et al.* (1991) derive the variation of these parameters along a single loop.

2.1 Downflow along the loops

The determination of the flow along the loops can be computed from the observed line-of-sight velocities. Using the method of reconstructing the true shape of the loops, Loughhead and Bray (1984) computed the flow along the central axis of an active region loop (ARL) from the observed line-of-sight velocity. We emphasize the difference between ARL and CFL: along an active region loop the material is going from one footpoint to the other one (Mogilevskij *et al.* 1990, Mein and Mein 1982, Delone *et al.* 1989), while the material is going down in the both legs of cool flare loops (CFL) with an increasing velocity from zero at the top to 50-100 km s^{-1} at the footpoints (Xu 1987, Yan *et al.* 1986, Heinzel *et al.* 1991). The mechanism of formation of the ARL is similar to that of surges. The formation of the CFL will be discussed in Section 3.

2.2 MHD modeling

It is important to know if the flow corresponds to free-fall motion or if other forces are acting. The dynamical behaviour of a CFL is decribed by the following momentum-balance equation:

$$\rho d\vec{V}/dt = -\vec{\nabla}p + \vec{j} \times \vec{B} - \rho\vec{g}.$$

The plasma is accelerated or deccelerated by forces of pressure gradient $\vec{\nabla}p$, the Lorentz force and the gravity $\vec{g}$. Assuming that the flow follows the magnetic field lines and neglecting the pressure gradient, different authors (Ruždjak 1981, Gu *et al.* 1984, Xu 1987, Yan *et al.* 1986) have computed theoretical line-of-sight velocities corresponding to free-fall and have compared them to the observations. Ruždjak (1981) finds a good agreement, however we have to keep in mind that using observations at the limb the accuracy of the velocity vector is less than on the disk because the line-of-sight velocity represents the weakest component. The Chinese group concludes that the material motion is deccelerated compared to free-fall motion and other forces may be involved. Heinzel *et al.* (1991) use observations of Hα flare loops obtained with the MSDP spectrograph (Schmieder *et al.* 1988). The flow along the loop legs reaches 50 to 70 km s^{-1} at the footpoints depending on the geometry of the loop, values much too low as compared with free-fall velocity. They compute the pressure gradient and the density using non-LTE models but comparing to the observations their values can not explain the discrepancy (see section 2.3). Evolving structures or inhomogeneities may be good candidates. Kim (1991) measured recently the longitudinal magnetic field in flare loops and deduced a curve with 2 maxima, one around zero, the other one around 30 G. The field lines seem to be twisted in particular loops. Vlahos (1991) proposes that the knots in the loops correspond to small flares in his fragmentation models, but their dynamics will be more relevant to surge mechanism than to free-fall.

2.3 Electron density

Different attempts have been made to determine the electron density. Using Hα line the estimation ($Ne \cong 10^{12}$ cm^{-3}) of Zirin (1986) is based on an empirical comparison of the collisional and radiative excitation rates without any detailed computation. Hanaoka *et al.* (1986) give a value of the order of 10^{11} cm^{-3} for Hα loops, arguing that the main source of the maximum brightness continuum that they have measured on the eclipse images is the prominence-like loop material responsible for electron scattering of photospheric radiation.

Švestka *et al.* (1987) have tried to verify the electron density values proposed by Zirin by computing the expected deviations from the LTE level populations for different temperatures and densities. They have solved the non-LTE equations for a three-level plus continuum hydrogen atom model using the approach of Fontenla and Rovira (1985). The loops turn from absorption to emission at Hα ± 1 Å as soon as the gas pressure exceeds 3 dyn cm^{-2} at T = 10^4 K. This implies an electron density of 10^{12} cm^{-3} for loops visible in emission against the disc, in agreement with Zirin (Figure 3). In order to check this result they also used the broadening of Hγ and Hβ Balmer lines. Assuming that the broadening is only due to the Stark effect, the density is found to be equal to 4×10^{12} cm^{-3}. But with a turbulent velocity of 12 km s^{-1}, it could be reduced to 5×10^{11} cm^{-3} (Lin Jun *et al.* 1989,1991).

Heinzel and Karlický (1987) used the non-LTE code developed by Heinzel *et al.*

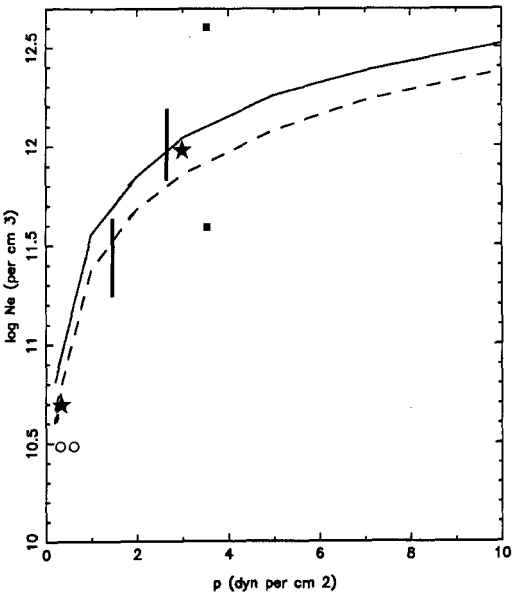

Figure 3. Variation of the electron density versus the gas pressure using non LTE models (full line: T = 8000 K, dashed line: T = 15000 K from Švestka *et al.* 1987, stars from Heinzel and Karlický 1987, circles from Heinzel *et al.* 1991), using Stark effect with and without turbulence (black squares). On the right side of the vertical bars the loops are in emission, on the left side they are in absorption.

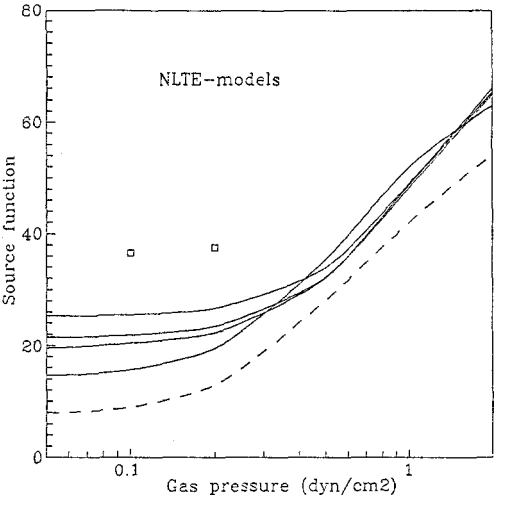

Figure 4. Variation of the source function versus the gas pressure with quiet Sun irradiation (dashed line), with enhanced incident irradiation (full lines from the bottom, v = 0, 20, 40,80 km s^{-1}), with an irradiation equal to the continuum (squares). (Heinzel *et al.* 1991).

(1987) to determine the physical conditions at the top of flare loops. They have found relatively good agreement with the previous results. The flare loops in Hα center appear in absorption against the disk for low pressure p of the order of 0.1 to 1 dyn cm^{-2}, and should be clearly visible in emission for p larger than 3 to 5 dyn cm^{-2} (Figure 3). They pointed out that we need to introduce a strong turbulence to explain loops visible in emission at Hα $\pm$ 1 Å even for a relatively high pressure equal to 5 dyn cm^{-2}. They used a three-level hydrogen atom model plus continuum and solved simultaneously the equations of radiative transfer for the lines Lα, Lβ, Hα and for the Lyman continuum, together with the equations of statistical equilibrium.

In the computation of Švestka *et al.* (1987), some effects are not included, i.e. the actual irradiance of the flaring region, the effect of soft X-rays, the effect of moving prominences on the radiation emitted. Hyder and Lites (1970) show the importance of this last effect. The atoms in the frame of prominence moving with a velocity v will see the radiation at λ_0 larger than for a stationary prominence by a factor J/J_0 with J_0 the intensity at λ_0, J at $\lambda_0(1 + v/c)$. Heinzel and Rompolt (1987) made complete computations and point out the importance of Hα Doppler brightening and Lα dimming for prominences having velocities larger than 30 km s^{-1} . This is the case of material flowing down along the legs of the loops. According to Gan and Fang (1990) the effect of soft X-rays does not seem to be important if the density is lower than 10^{11} cm^{-3}.

The irradiance from the background I_0 must be considered with attention. Recently Heinzel *et al.* (1991) have greatly improved the non-LTE modeling by using a five-level hygrogen atom model, by introducing realistic irradiation of the slab provided by the MSDP observations and by taking into account the Doppler brightening in Hα . An increase by a factor 2 of I_0 leads to an increase of the source function by a similar factor (Figure 4). Values of the electron density ($Ne \sim 3\times 10^{10}$ cm^{-3}) and of the gas pressure ($p \sim 0.18$ and 0.3 dyn cm^{-3} respectively along the loop and at a footpoint) have been determinated. This low value of Ne corresponds to Hα profiles of CFL observed in absorption, that is in good agreement with previous studies (Figure 3).

3 Formation of cool flare loops

The analysis of flare loops observed in a large range of wavelengths is important to understand the mechanism of formation of the cool loops and how energy is released during the gradual phase. Kopp and Pneuman (1976) suggested that a two-ribbon flare starts with the opening of the magnetic field lines and subsequent field-line reconnection gives rise to the flare loops. The mechanism involves energy release at the top of the loops with heating Hα bright ribbons at their footpoints. Below the reconnection point the material is compressed and condensed.

3.1 Multi-wavelength observations

Coordinated observations obtained in high-temperature lines during an eclipse (Hanaoka *et al.* 1986), in X-rays during the SMM campaign (Švestka *et al.* 1987) and in radio-wavelengths (Velusamy and Kundu 1981, Urpo *et al.* 1986) support reconnection models.

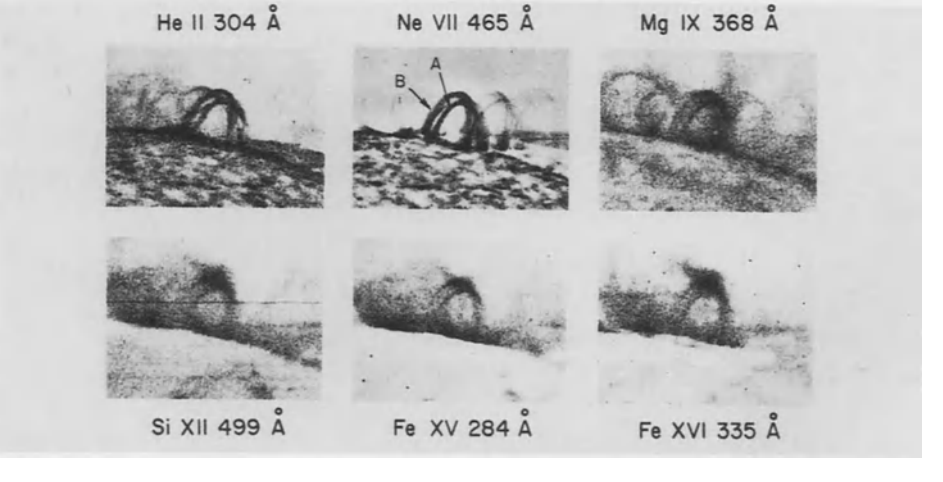

Figure 5. Flare loops as seen in different lines on August 13, 1973 (Cheng 1980). As the temperature increases, the top of the loops becomes more intense and extended than that below, indicating a high temperature reconnection point above the loops.

Hanaoka *et al.* (1986) described the relationship between cool loops (10^4 K in Hα), hot loops (10^6 K in Fe X) and hot material (8×10^6 K in Ca XV) as follows. The Hα loops are very close but slightly under two upper Fe X loops at the same instant, the rising velocity of the Hα loops is about 2 to 8 km s^{-1} . A faint loop is visible in Hα at the same altitude than a Fe X loop suggesting than a hot loop is being condensed. In the 6100 Å continuum, the images show a small helmet structure with a cusp and a streamer on the top and give evidence for the existence of open magnetic fields above the flare loops. The Ca XV emitting region is found to be suspended and compactly confined at the upper part of the loop system at the reconnection point. It is in good agreement with Skylab observations (Mac Combie and Rust 1979, Cheng 1980) showing that Fe XV and Fe XIV material were above He II loops (8×10^4 K) at 3.5 hours after the flare (Figure 5). The X-ray observations support that the CFL are formed by cooling the hot loops.

Švestka *et al.* (1987) report extensive observations obtained in a large temperature range during the SMM mission. They describe an Hα loop system appearing during the dynamic flare of 1980 Nov 6, practically at the same time (with 2 minutes delay) of the flare maximum phase (15:26 UT). The loops rise from 25 000 to 55 000 km within 90 min, which corresponds to a velocity of 5 km s^{-1}. The X-ray emission was seen much higher than the Hα loops. The altitude of the loops is successively higher in lines corresponding to increasing temperature (O VII to Fe XXV, i.e. 1.7×10^6 to 2×10^7 K). For more than 2 hours they observe the altitudes of the different temperature loops, these altitudes are aligned along two curves, one for cool material and one for hot material. In order to fit the two curves, making the assumption that the Hα loops are formed by cooling, they conclude that the hot loops cannot cool at their original altitudes. The hot loops shrink to lower heights in order to become denser and then to cool faster. Up to now we have no observational evidence of such shrinking. The hot loops are rising with a speed of 7.4 km s^{-1} the same order as the rising velocity of Hα loops.

Microwaves at 22-37 GHz were detected in the upper levels of the atmosphere at 50000 km (normally they are located around 3000 km above the photosphere). They are well correlated to the long decay events in X-rays and to the appearance of Hα flare loop system (Urpo *et al.* 1986). The authors proposed that the microwave emission originates in hot condensed regions above the flare loop system.

3.2 Mass supply

The mass in the cool Hα loop system was first estimated by Kleczek (1964) to be 10^{16} g with a typical length of 2.5×10^{10} cm, a cross section of 4×10^{17} cm^2 and an electron density 10^{11} cm^{-3}. Assuming a lifetime of 10 hours and a downflow of 50 km s^{-1}, this estimate corresponds to a replacement of the mass in the cool loop every 80 min.

A continuous resupply of mass needs to be considered. The observational evidence of reconnection is acceptable. Up to now we have found no alternative solution to explain these observations (Švestka 1989).

3.3 Additional heating

There is not enough coronal material available to provide plasma in the loops. Thus the material must evaporate from below from the chromosphere, and be heated to the observed temperatures of $2x10^7$ K at the top of the loops. Different additional heatings have been proposed, gas dynamic shock (Kopp and Pneuman 1976), global ohmic heating (Pneuman 1982), small transverse component of the magnetic field in a current sheet (Somov and Titov 1985), Alfvén waves (Lin and Zhang 1991 a b), mechanical heating (Klimchuk and Mariska (1988), slow shocks (Cargill and Priest 1983, Hick and Priest 1989), the combination of slow and fast shocks (Forbes and Malherbe 1986). The first proposed models are insufficient, the others may be considered. In particular the model of Forbes *et al.* (1989) is based on magnetic reconnection and chromospheric ablation. Very hot temperature may be achieved at the X neutral line due to slow shock heating. Hence two pairs of conduction fronts go down to chromosphere and form the flare ribbons. So ablation is expected, with an upward velocity of of less than 10 km s^{-1} above the flare ribbons. Soft X-ray emission near the reconnection site is also expected. A fast-mode perpendicular MHD shock is formed below the X-point. The radiation losses are considerably enhanced when material travels through the shock. This is in favor of a thermal instability which produces cool condensations. The evaporation over a large area could occur during time long compared with the drainage of the loops. Schmieder *et al.* (1987, 1990) have shown the possibility of such ablation of chromospheric material by analysing the Hα asymmetric profiles in the ribbons and by exhibiting large upward region in CIV line overlying bright ribbons which is unusual. In the transition region a downflow is generally observed over bright regions corresponding to faculae (Dere *et al.* 1986). The observed association of long duration of X-ray emission over the site is also a good argument in favor of evaporation process. Upflows in two-ribbon flares have been also detected by Gu *et al.* (1991). The upflows are of the order of 5 km s^{-1} in Hα and between 4 to 12 km s^{-1} in C IV line, it is impossible to detect them on filtergrams.

Uchida and Shibata (1988) suggest that the energy and mass supply to the loop top comes from below the chromosphere in the form of relaxing fronts of the magnetic field twisted in opposite sense. Although their paper specifically addresses the upflow seen around the impulsive phase, it could be equally well applied to the gradual flare situation.

Fisher *et al.* (1985) suggest that the transition region and the chomosphere are pushed downward during the impulsive phase, and that relaxation drives upflows during the later phase. Upflows of the same order as Forbes and Malherbe model are predicted.

3.4 Thermal instability and cooling time

Flaring loops which are newly formed high in the corona will cool through radiation and conduction processes. The loop will pass through the different temperature regimes, including the one characterizing Hα observations (Švestka 1989). The cooling time of such a process varies between an hour to a few minutes mainly depending on the loop density (Ne = 10^{10} - 10^{12} cm^{-3}) (Švestka 1987, Gan and Fang 1990, Lin *et al.* 1991).

4 Conclusion

"Post"-flare loops are observed during the gradual phase of two-ribbon flares. Hot loops are first formed, then shrinked and subsequently cooled to Hα temperature (10^4 K). Their observations lead to informations directly on the corona inhomogeneities, on the heating and cooling times, they are important to study the physics of magnetic structures in the corona and of course to understand the process of flares. Observations in multi-wavelengths with imaging and spectrographs are both suitable to derive the geometry, the active forces (gravity, pressure gradient, magnetic field) and finally to understand the formation of hot and cool flare loops. We hope that during the next satellite flights of Yoh-Koh and SOHO, two-ribbon flares will be observed simultaneously with ground-based telescopes.

References:

Cargill P.J., Priest E.R.: 1983, *Astrophys. J.* **266**, 383.

Cheng C.C.: 1980. *Solar Phys.* **65**, 347.

Delone A., Makarova E., Porfir'eva G., Roshina E., Yakunina G.: 1989, *Hvar Obs. Bull.* **13,1**, No. 157,

Dere K.P., Bartoe J.D.F., Brueckner G.E.: 1986, *Astrophys. J.* **305**, 947.

Fisher G.H., Canfield R.C., McClymont A.N.: 1985, *Astrophys. J.* **289**, 414.

Fontenla J.M., Rovira M.G.: 1985, *Solar Phys.* **96**, 53.

Forbes T.G., Malherbe J.M., Priest E.R.: 1989, *Solar Phys.* **120**, 285.

Forbes T.G., Malherbe J.M.: 1986, *Astrophys. J.* **302**, L67.

Foukal P.: 1991, "Solar Astrophysics ", a Wiley Interscience Publication, Jone Wiley & Sons.

Gan W.Q., Fang C.: 1990, *Astrophys. J.* **358**, 328.

Gu X.M., Ding J.P., Tang Y.H.: 1984, Scientia Sinica, XXVII, 9,973.

Gu X.M., Li Zhi, Luan TI, Li Zhi Kai, Schmieder B.: 1991, *Flares 22 workshop*, Chantilly, eds. Schmieder B. and Priest E.R., p. 141.

Hanaoka Y., Kurokawa H., Saito S.: 1986, *Solar Phys.* **105**, 133.

Heinzel P., Karlický M.: 1987, *Solar Phys.* **110**, 343.

Heinzel P., Rompolt B.: 1987, *Solar Phys.* **110**, 171.

Heinzel P., Gouttebroze P., Vial J.C: 1987, *Astron. Astrophys.* **183**, 351.

Heinzel P., Schmieder B., Mein P.: 1990, *Publ. Debrecen Obs.* **7**, 272.

Heinzel P., Schmieder B., Mein P.: 1991, *Solar Phys.*, in press.

Hick P., Priest E.R.: 1989, *Solar Phys.* **122**, 111.

Kamenický M., Rušin V.: 1990, in *Lecture Notes in Physics*, **363**, 254.

Kim I.: 1991, private communication.

Kleczek J.: 1964, in AAS-NASA Symposium on the" Physics of Solar Flares", ed. Hess W.N., NASA SP 50, 77.

Klimchuk J.A. and Mariska J.T.: 1988, *Astrophys. J.* **328**, 334.
Kopp R.A. and Pneuman G.W.: 1976, *Solar Phys.* **50**, 85.
Kurokawa, H.: 1989, *Space Sci. Rev.* **51**, 49.
Kurokawa H., Hanaoka Y., Shibata K., Uchida Y.: 1987, *Solar Phys.* **108**, 251.
Lin J., Wang Z., Zhang Z., Smartt R.N.: 1989, *Acta Astron. Sin.* **30**, 1,52.
Lin J., Zhang Z., Wang Z., Smartt R.N.: 1991, *Astron. Astrophys.* , in press.
Lin J., Zhang Z.: 1991 a, *Flares 22 workshop*, Chantilly, eds. Schmieder B., Priest E.R., p.159.
Lin J., Zhang Z.: 1991 b, *Astrophysics and Space Science*, in press.
Loughhead R.E., Wang J.L., Blows G.: 1983, *Astrophys. J.* **274**, 883.
Loughhead R.E., Bray J.R.: 1984, *Astrophys. J.* **283**, 392.
Mac Combie W.J., Rust D.M.: 1979, *Solar Phys.* **61**, 69.
Mein P., Mein N.: 1982, *Solar Phys.* **80**, 161.
Mein P., Mein N.: 1989, *Astron. Astrophys.* **203**, 162.
Mogislevskij E.I., Shilova N.S., Uvakina V.F.: 1990, *Kinem. i fisika neb.* tel 3, **6**, 41.
Moore R., Mc Kenzie D.L., Švestka Z., Widing K.G. + 12 co-authors: 1980, in P.A. Sturrock (ed), Solar Flares, Colorado Associated Uni. Press, p.341.
Pneuman G.W.: 1982, *Solar Phys.* **78**, 229.
Ruždjak V.: 1981, *Bull. Astron. Inst. Czechosl.* **32**, 144.
Schmieder B., Forbes T.G., Malherbe J.M., Machado M.: 1987, *Astrophys. J.* **317**, 956.
Schmieder B., Malherbe J.M., Simnett G.M., Forbes T.G., Tandberg-Hanssen E.: 1990, *Astrophys. J.* **356**, 720.
Schmieder B., Mein P., Forbes T.G., Malherbe J.M.: 1988, *Adv. Space Res.* **8**, No. 11,45, .
Švestka Z. : 1987, *Solar Phys.* **108**, 411.
Švestka Z., Fontenla J.M., Machado M.E., Martin S.F., Neidig D.F., Poletto G.: 1987, *Solar Phys.* **108**, 237 .
Švestka Z.: 1989, *Solar Phys.* **121**, 399.
Somov B.V., Titov V.S.: 1985, *Solar Phys.* **102**, 79.
Uchida Y., Shibata K.: 1988, *Solar Phys.* **116**, 291.
Urpo S., Teräsranta H., Pohjolainen, S.,Ruždjak V., Vršnak B., Rompolt B.: 1986,*Adv. Space Res.* **6**, No. 6, 267, .
Velusamy T., Kundu M.R.: 1981, *Astrophys. J.* **240**, L130.
Vlahos L.: 1991, *Flares 22 workshop*, Chantilly, eds. Schmieder B. and Priest E.R., p. 91.
Xu Ao Ao: 1987, *Proceedings of Irkutsk meeting*, eds. Stepanov V.E., Obridko V.N., 147.
Zirin H.: 1986, "The lower atmosphere of solar flares", ed. D.F.Neidig, Sac Peak, NM:NSO, 78.
Wang J.L., Loughhead R.E., Chen Chuan-Le: 1983, *Proceedings of Kunming Workshop* on "Solar Physics and Interplanetary Travelling Phenomena".
Yan Guo-Ying, Ding You-ji, Xu Aoao: 1986, *Acta Astron. Sin.* **3**, 26.

PLASMA PARAMETERS DERIVED FROM MSDP OBSERVATIONS OF COOL FLARE LOOPS

P. Heinzel[1], B. Schmieder[2] and P. Mein[2]

[1]Astronomical Institute, 25165 Ondrejov, Czechoslovakia
[2]Observatoire de Paris, Section de Meudon, DASOP,
F 92195 Meudon Principal Cedex, France

Abstract

MSDP observations of 16 May 1981 two-ribbon flare are used to study the physical structure and dynamical behaviour of cool flare loops. The loops have been detected in the Hα line just after the flare maximum and they appeared in absorption against the disk. Using the first-order differential cloud model (DCM1) technique, we derive empirically some basic plasma parameters at 15 points along one loop leg. The flow velocities and true heights have been reconstructed with respect to a geometrical projection. Subsequently, detailed non-LTE models of cool loops have been constructed in order to fit Hα source-function values previously derived from DCM1 analysis. It is demonstrated that this source function is rather sensitive to the radial component of the flow velocity (the so-called Doppler brightening) and to the enhanced irradiation of the loops from the underlying flare ribbons. In this way, we have been able to estimate quantitatively all plasma parameters which determine the physical structure of cool loops (i.e. the temperature, pressure, density, etc.), as well as the momentum-balance condition within the loops. For these dark loops we have arrived at relatively low gas pressures of the order of 0.1 - 0.5 dyn cm^{-2} , with corresponding electron densities around 10^{11} cm^{-3}. Pressure-gradient forces have been found to be of small importance in the momentum-balance equation. However, the classical momentum equation is not capable of explaining significant departures from a free-fall motion under the gravity force, found from our MSDP data. We propose three possible explanations to this problem.

Full version of this paper will be published in *Solar Physics*.

FLARE EVOLUTION IN THE DENSITY-TEMPERATURE DIAGRAM

S. Serio[1,2], F. Reale[1], G. Peres[3],
J. Jakimiec[4], B. Sylwester[5], and J. Sylwester[5]

1. *Introduction*

The scope of this work is to set up diagnostic tools for the X-ray flare decay phase in terms of the density-temperature (n-T) diagram. It originates from the observation of the interesting characteristics of this diagram, which were pointed out by Jakimiec *et al.* (1986, 1987) in the analysis of SMM flare data. Their basic observation was that many flares follow approximate power-law trajectories in this diagram, during their decay phase.

We have used the Palermo-Harvard hydrodynamical code to compute the evolution of flare temperature and density for a grid of confined loop flares.

The hydrodynamic code solves the conservation equations for mass, velocity and energy in a semicircular coronal loop anchored in the chromosphere, and subject to a stationary heating function, providing for steady state equilibrium, and to an impulsive heating function causing the flare (see Peres and Serio, 1984, for a complete description).

2. *Evolution of the flare in the n-T diagram*

To give an idea of how a flare develops in the n-T diagram, we show in Fig. 1 the results of the calculations for the temperature and density at the top of a model flare occurring in a loop with semilength $2 \cdot 10^9$ cm, base pressure 6 dyne cm^{-2}, subject to impulsive heating near its top of 10 erg cm^{-3} s^{-1}. Here we assume that the impulsive heating term, confined near the top of the loop, is switched on abruptly at t = 0, and switched off abruptly at t = 300 s. We see that the flare undergoes a number of fairly distinctive phases, including the initial instantaneous increase in temperature without increase in density, the evaporation phase, the maximum phase, a power-law decay phase, and an eventual thermal instability followed by the recovery to the initial conditions.

1. Istituto di Astronomia and Osservatorio Astronomico, Palermo, Italy
2. Istituto per le Applicazioni Interdisciplinari della Fisica (CNR), Palermo, Italy
3. Osservatorio Astrofisico, Catania, Italy
4. Institute of Astronomy, University of Wroclaw, Poland
5. Space Research Center, Polish Academy of Sciences, Wroclaw, Poland

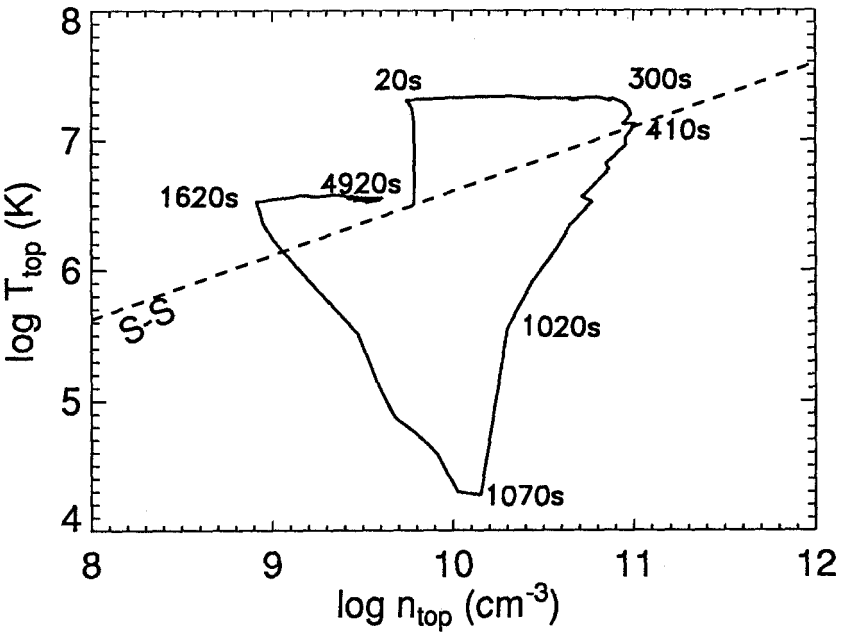

Fig.1 Density-temperature diagram for plasma located at the top of a loop of semilength 2×10^9 cm, for a flare model triggered by a constant heating (switched on abruptly at $t = 0$) lasting 300 s with an abrupt switch-off to the pre-flare value. The dashed line ($S - S$) represents the relation between the plotted parameters for steady-state conditions (RTV scaling laws).

What is most interesting here is the power-law decay phase, which lasts a sizeable fraction of the flare time, and shows a constant slope. In order to see it, let's recall that the energy conservation equations near the top of the loop, disregarding viscosity, can be written (Serio *et al.*, 1991)

$$p \frac{d}{dt} S/k = E_H(s,t) - n^2 P(T) - \frac{\partial}{\partial s} F_c \quad , \tag{1}$$

where k is Boltzman's constant, p, n and T (functions of time and of the spatial coordinate along the loop, s) are plasma pressure, density and temperature, respectively, E_H is the heating term, $P(T)$ the radiative energy losses per unit emission measure, F_c the conductive flux, and $S = k \ln(T^{5/2}/n)$ is the entropy per particle.

It is easy to see that, if we let $E_H = 0$ at the peak phase, (i.e. when $d/dt \approx 0$), the result is

$$S \sim S_o - \frac{k\, t}{\tau} \quad , \tag{2}$$

where

$$\tau = \frac{p_o}{E_H} = \frac{3.7 \cdot 10^{-4} L}{\sqrt{T_o}} \sim 120 \frac{L_9}{\sqrt{T_7}} \quad , \tag{3}$$

and the last step is based on the Rosner, Tucker, and Vaiana (1978, RTV) scaling laws on the initial (flare peak) state. We find therefore, that the entropy decays linearly, with an inverse rate given by Eq. 3. Our grid of solar models, with loops ranging in length from $5 \cdot 10^8$ to 10^{10} cm, and in maximum temperature from 10^7 to $2 \cdot 10^7$ K shows that this is indeed so, not only initially, but over a linear phase lasting from approx $1.5 - 2.0$ decay times. During the same phase, we find (Serio *et al.*, 1991) that temperature, density, and pressure follow approximately exponential decay laws, with decay times given, respectively, by

$$\tau_T \sim 1/2\tau_n \sim 3/2\tau_p \sim \tau \quad . \tag{4}$$

Although these last empirical relationships are only valid in average, it is easy to see that they will enforce power-law relationship among the thermodynamical variables during the decay phase. In particular we find

$$T \propto n^2 \quad , \tag{5}$$

which is the result we wanted to show.

Of course our result holds for an abrupt switching off of the heating. However, we can also show, by numerical calculation (Fig. 2), that if the heating is allowed to decay exponentially, the resulting trajectories in the n-T plane will still be power-laws with index intermediate between 1/2 (which is the one appropriate for steady state structures, implied by the RTV scaling law), and 2, which is characteristic for fast cooling structures (Jakimiec *et al.*, 1991).

3. *Conclusions*

From the above results the diagnostic value of the n-T diagram for the decay phase of flares. We see that the decay is bound by the $T \propto n^{1/2}$ Quasi Steady State (QSS) trajectory, when a sizeable amount of heating is being released during the decay, and by the $T \propto n^2$ trajectory when essentially no heating is deposited during the decay. In the first analysis by Jakimiec *et al.* (1986, 1987) it was apparent that most big flares during their decay evolve following the QSS trajectories, implying that the heating process is still active during the off-peak phase. We are presently carrying an extensive survey of SMM flares to study in more depth the energetics of the decay phase.

We want to point out here that the results as presented apply only to solar flares, and that we expect a dependence of the power-law index of the limiting n-T trajectory at zero heating on gravity, for flares occurring in stellar coronae. Further studies will be devoted to establishing such dependence.

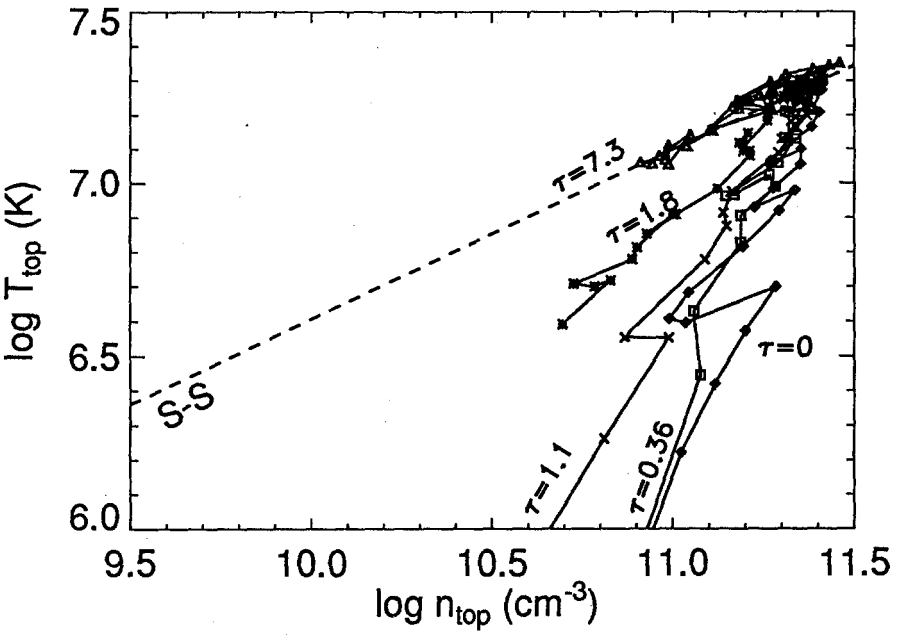

Fig.2 Density-temperature diagram illustrating the dependence of the slope of the decay phase on the e-folding decay time of the heating rate (in units of the entropy decay time defined in Eq. 3). The initial steady model is for a loop with semilength 2×10^9 cm, and temperature at the top 2×10^7 K.

ACKNOWLEDGEMENTS: This work has been supported by Agenzia Spaziale Italiana, Ministero per l'Università e la Ricerca Scientifica e Tecnologica, and by the Polish Academy of Sciences program CPBP 01.20 (Development and Exploitation of Space Research).

REFERENCES

J. Jakimiec, B. Sylwester, J. Sylwester, J.R. Lemen, R. Mewe, R.D. Bentley, G. Peres, S. Serio, and J. Schrijver, 1986, *Adv. Space Res.*, **6**, 237.

J. Jakimiec, B. Sylwester, J. Sylwester, J.R. Lemen, R. Mewe, R.D. Bentley, G. Peres, S. Serio, and J. Schrijver, 1987, in **Solar Maximum Analysis**, V.E. Stepanov and V.N. Obridko eds., VNU Science Press, Utrecht, p. 91.

J. Jakimiec, B. Sylwester, J. Sylwester, G. Peres, F. Reale, and S. Serio, 1991, *Astron. Astrophys*, in press.

G. Peres and S. Serio, 1984, *Mem. Soc. Astron. Italiana*, **55**, 749.

G. Peres, F. Reale, S. Serio, and R. Pallavicini, 1987, *Ap. J.*, **312**, 895.

F. Reale, G. Peres, S. Serio, R. Rosner, J. Schmitt, 1988, *Ap. J.*, **328**, 256.

R. Rosner, W.H. Tucker, and G.S. Vaiana, 1978, *Ap. J.*, **220**, 643.

S. Serio, F. Reale, J. Jakimiec, B. Sylwester, and J. Sylwester, 1991, *Astron. Astrophys*, **241**, 197.

The Neupert Effect: What Can It Tell us about the Impulsive and Gradual Phases of Eruptive Flares?

Brian R. Dennis, Bertrand M. Uberall, and Dominic M. Zarro

Code 682.2, Laboratory for Astronomy and Solar Physics, NASA
Goddard Space Flight Center, Greenbelt, MD 20771 USA

Abstract:

The Neupert Effect is the name given to the correlation observed in many flares between the impulsive time profile of the microwave and hard X-ray emissions and the time derivative of the soft X-ray profile. We have used data collected between 1980 and 1989 from the Hard X-Ray Burst Spectrometer (HXRBS) on the Solar Maximum Mission (SMM) and the soft X-ray detector on GOES to determine which events show this correlation and which do not. We have found that of 66 HXRBS events observed in 1980 with a peak rate of >1000 counts/s, 58 (80%) showed good correlation with peaks in the GOES time derivative plot corresponding to peaks in the HXR plots to within ±20 s. The more gradually varying X-ray events that are commonly referred to as Type C flares and that are often accompanied by eruptive flares, tend to show poorer correlation between the SXR time derivative and the HXR time profile. In several cases studied, the later, more gradually varying, peaks either did not register at all in the SXR time derivative plots or resulted in very broad peaks that, in one case on 1981 April 26, was delayed by 13 minutes.

1 Introduction

For most flares, the time integrated hard X-ray fluxes "closely match the rising portions of the soft X-ray emission curves." This simple relationship was first recognized by Neupert (1968) and is called here the Neupert effect. It is consistent with a flare model in which the hard X-rays are electron-ion bremsstrahlung produced by energetic electrons as they lose their energy in the lower corona and chromosphere, and the soft X-rays are thermal bremsstrahlung from plasma heated by those same electrons. Such a model has become known as the thick-target model (Brown 1971). In fact, the Neupert effect must exist for any flare model, provided

only that the X-rays are electron-ion bremsstrahlung and that the cooling time of the plasma is significantly longer than the impulsive peaks of hard X-ray emission. Any deviation from such a relationship can only mean that some other process is heating the soft X-ray emitting plasma besides the hard X-ray emitting electrons.

The purpose of the study reported in this paper is to determine those flares in which the temporal variations of the soft and hard X-ray emissions show this Neupert effect and those which do not. An earlier version was presented by Dennis (1991).

2 Observations

We have compared the time derivative of the soft X-ray (SXR) emission curve with the hard X-ray (HXR) emission curve of all complete events recorded with the Hard X-Ray Burst Spectrometer (HXRBS) on SMM (Orwig et al. 1980) in 1980 that have peak rates of >1000 counts/s and coincident GOES data. We have used GOES 1–8 Å Channel 1 data with 3 s time resolution and the 15-channel summed HXRBS count rates with 1 s time resolution for the comparison. In general, we find that most flares show good correlation between the soft X-ray time derivative and the hard X-ray light curve, with the peak times of the two curves agreeing to within the $\geq$3 s time resolution of the soft X-ray data.

Figure 1 illustrates the strengths and weaknesses of the technique. The general agreement between the soft X-ray time derivative shown in the middle plot and the hard X-ray time profile in the lower plot is clear in spite of the considerable scatter in the time derivative, particularly after the automatic gain change at 18:39:22 UT. This scatter is caused primarily by the digitization of the GOES data and the magnification of the uncertainties that results from taking the derivative. Nevertheless, the general trend is reliable. At least six peaks can be identified in both plots with the peak times agreeing to within ~10 s; the rise and decay times are also very similar.

Of the 66 events studied in 1980, 58 (88%) have peaks in the SXR time derivative plot within ±20 s of peaks in the HXR time profile and 53 (80%) have generally "good" correlation between the two types of plots for the duration of the burst. In 20 of these "good-correlation" events, the SXR time derivative stays high after the HXR emission decreases or a second or subsequent HXR peak results in a much larger peak in the SXR derivative than did the first peak. The greater response in SXR's could reflect a larger fraction of the released energy going to heat the plasma directly rather than to accelerate electrons.

In 8 of the 13 flares that showed "poor" correlation between the SXR time derivative and the HXR time profile, the SXR time derivative shows no peak corresponding to the initial HXR peak. In all these cases, the initial HXR peak had structure on timescales of <1 s. Such events suggest that these initial very impulsive energy releases result primarily in electron acceleration, with very little direct plasma heating, and that the secondary plasma heating from the accelerated electrons makes only a small contribution to the more gradual primary plasma

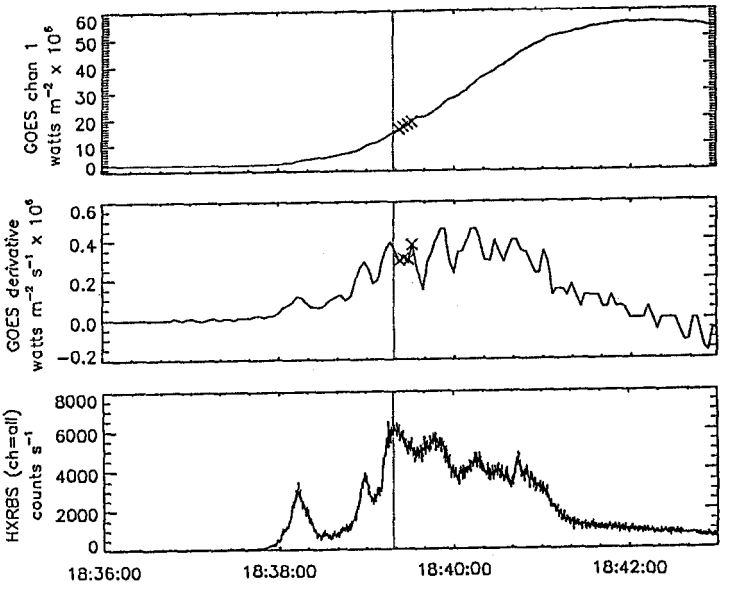

Fig. 1. Top: GOES 1–8 Å soft X-ray time profile for a flare on 1980 March 27. Note that the points marked with an X on the top and middle plots indicate the location of the GOES gain-change spike that has been removed and replaced with interpolated values. Middle: Time derivative of the top plot. Bottom: HXRBS 30–500 keV hard X-ray time profile on the same time scale. The vertical broken line through all the plots indicates the time of the HXR highest peak for comparison with the SXR plots.

heating that is taking place at the same time. The absence of such peaks in the time derivative could still be consistent with the thick-target model if one postulates that the cutoff energy of the power-law electron spectrum is much higher than the normally assumed value of ~20 keV for this flare, perhaps being as high as 50 keV. This is similar to the conclusion reached by Nitta et al. (1990), who found that the spectrum of just the impulsive component of the event on 1980 March 29 flattened at lower energies suggesting a cutoff energy as high as 50 keV. Given an E^{-5} shape of the power-law spectrum, this difference between a cutoff energy of 20 keV and 50 keV corresponds to a difference in the total energy in the energetic electrons of $2.5^5 \simeq 100$, enough perhaps to reduce the soft X-ray emission from the heated plasma to below the detectable limit of the GOES detector.

We have also studied Type C flares (Tanaka, 1983; Tsuneta, 1983) as examples of events that could be considered as "eruptive flares." These are flares in which the HXR emission is more gradually varying and is emitted for >10 minutes. For the canonical Type C flare on 1981 May 13, the gradual HXR peak at 04:15:30 UT occured at the time of the highest level of the SXR time derivative within about 1 minute but the scatter resulting from the GOES digitization at such high SXR flux levels makes any detailed comparisons impossible.

Another Type C flare reported by Cliver et al. (1986) is shown in Figure 2. This event on 1981 April 26 has a much longer duration and begins with an impulsive phase that shows the usual good correlation. The later more gradual HXR features, including the much larger peak at 11:48 UT, show no coincident features in the SXR time derivative plot. There is a broad peak in this plot at about 12:00 UT but this would imply a 12 to 13 minute delay!

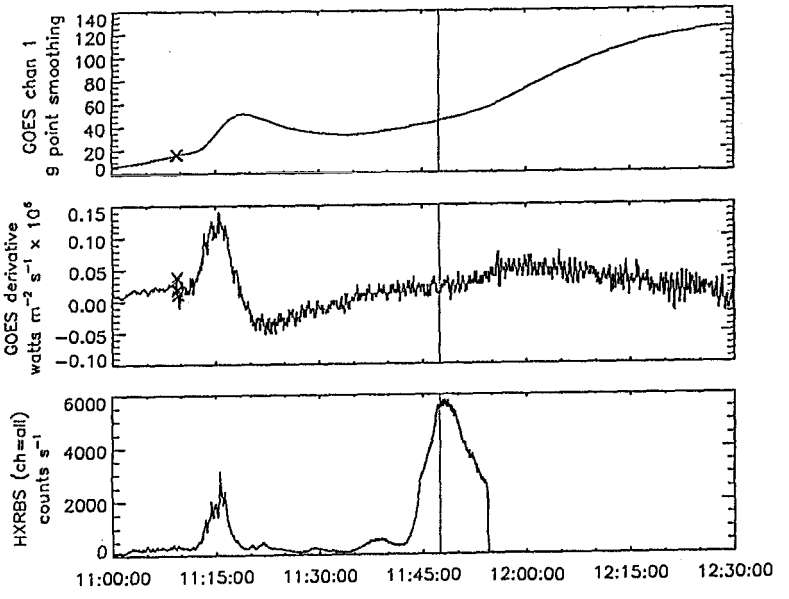

Fig. 2. Similar plots to those shown in Figure 1 for a flare on 1981 April 26.

A third long-duration event that occurred on 1981 April 10 shows little correlation between the HXR and SXR derivitive time profiles. No impulsive phase was evident and there was no obvious correlation between the two major HXR features and the SXR time derivative. The total duration of the event was similar in the HXR and SXR time derivative plots, however. The relatively poor correlations found for these non-impulsive events is the basis for the suggestion made by Feldman (1990) that there is no causal relationship between the HXR and SXR flares in these cases.

3 Conclusion

The comparison of the soft X-ray time derivative and the hard X-ray profile provides a simple but effective way of comparing the timing of the hard X-ray emission and the heating of the plasma. It is much easier to make this timing comparison than to determine the energy relationship since neither the thermal energy nor the nonthermal energy can be determined to better than an order of magnitude. In

this way, it is possible to compare the observations with the predictions of various flare models such as thermal, thick-target, and hybrid thermal/nonthermal models. Such predictions for the thick-target model are now being made by Mariska et al. (1989). Preliminary results from Emslie, Li, and Mariska (private communication) show that they do indeed agree with the observations provided that the loop cooling time is made to match the observed soft X-ray decay time, suggesting either inhibited cooling or continuous heating. Deviations from the predictions can result in refinements to the model and can contribute to the determination of the fraction of the flare energy that goes into the energetic electrons and the fraction that goes to direct heating of the ambient plasma.

We intend to pursue the comparison of soft and hard X-ray time profiles with the various model predictions using the SMM and GOES databases. We will tabulate the fraction of events for which the agreement is good and the fraction where the agreement is poor. Such a tabulation will provide a simple and potentially powerful way of classifying flares. With the availability of high quality hard X-ray data from instruments on GRO, and hard and soft X-ray observations from Yohkoh, we hope to be able to make more definitive comparisons than have been possible with the SMM and GOES data.

References

Brown, J. C.: Sol. Phys. **18** 489 (1971)

Cliver, E. W., Dennis, B. R., Kiplinger, A. L., Kane, S. R., Neidig, D. F., Sheeley, N. R. (Jr.), and Koomen, M. J.: Ap. J. **305** 920 (1986)

Dennis, B. R.: Proc. Int. Solar-A Science Workshop (Springer-Verlag), in press (1991).

Feldman, U.: Ap. J. **364** 322 (1990)

Mariska, J. T., Emslie, A. G., and Li, P.: Ap. J. **341** 1067 (1989)

Neupert, W. M.: Ap. J. Letters **153** L59 (1968)

Nitta, N., Dennis, B. R., and Kiplinger, A. L.: Ap. J. **353** 313 (1990)

Orwig, L. E., Frost, K. J., and Dennis, B. R.: Solar Phys. **65** 25 (1980)

Tanaka, K.: IAU Coll. #71, Activity in Red Dwarf Stars (P. B. Byrne and M. Rodono, eds.) p. 307 (1983)

Tsuneta, S.: in Proc. Japan - France Seminar on Active Phenomena in the Outer Atmosphere of the Sun and Stars (J. C. Pecker and Y. Uchida, eds.) p. 243 (1983)

3.

PARTICLE ACCELERATION AND RADIO RESPONSE

Related poster papers in Chapter 8:

P.J.D. Mauas and D. Gómez

P. Heinzel and M. Karlický

D. Heristchi and R. Boyer

H.S. Sawant, R.R. Rosa, J.R. Cecatto, and F.C.R. Fernandes

S. Pohjolainen, S. Urpo, H. Teräsranta, and M. Tornikoski

M. Graeter and T.A. Kucera

F. Verheest

A.C.-L. Chian and F.B. Rizzato

PARTICLE ACCELERATION IN THE IMPULSIVE PHASE OF SOLAR FLARES

D.B. Melrose
Research Centre for Theoretical Astrophysics
School of Physics, University of Sydney, NSW 2006, AUSTRALIA.

Abstract Theoretical ideas on particle acceleration in solar flares are discussed with emphasis on bulk energization of electrons during the impulsive phase. Many localized, short-lived episodes of energy release must be involved. An analogy with the acceleration of auroral electrons by multiple weak double layers (WLDs) is suggested and explored. Based on the auroral analogy a mechanism for reflecting electrons by solitary waves (SWs) in proposed. The prompt acceleration of relativistic electrons is discussed briefly.

1. Introduction

Acceleration of energetic particles in association with solar flares was originally separated into two phases (Wild, Smerd and Weiss 1963). Radio data suggest that there are many more than two phases of acceleration (e.g., Melrose and Dulk 1987), and there is unambiguous evidence for non-flare-associated acceleration, most notably in storms (e.g., Kai, Melrose and Suzuki 1985). However, it remains helpful to concentrate on two general classes of acceleration similar to the two phases as originally proposed. One class is the copious acceleration of electrons with a quasithermal distribution, especially in the impulsive phase of a flare and called "bulk energization" (Ramaty *et al.* 1980). A working definition is as follows.

> *Bulk energization* is a collisionless process, or combination of processes, that leads to a rapid increase in the mean energy of all the electrons in a given volume by a factor $\gtrsim 10$.

The argument that the process must be collisionless is that the collisional mean free path for an electron of energy E is $\propto E^2$ and exceeds the length of a typical flaring flux tube for $E \gtrsim 5\,\mathrm{keV}$, e.g., de Jager *et al.* (1987), so that collisional effect can play no role in thermalizing electrons with energy $\gtrsim 10\,\mathrm{keV}$ of relevance here. It appears that the bulk energization occurs in very many, localized, short-lived episodes of energy release. In the impulsive phase of a solar flare, timescales $\lesssim 100\,\mathrm{ms}$ are clearly present, and there is evidence for structure in the energy release on even shorter timescales (e.g., the review by Sturrock 1987).

The other class of acceleration consists of all those processes that involve suprathermal particles with a clearly nonthermal distribution. In the older classification into two phases it was thought that nonthermal particles were accelerated on a time scale longer than that of the impulsive phase, but it has since been recognized that prompt acceleration of the ions and electrons is required to account for gamma rays during the impulsive phase. The acceleration processes involved may or may not be related to the bulk energization mechanism.

In the present review emphasis is placed on processes in the impulsive phase of solar flares, and specifically the bulk energization of electrons, which has been given relatively less attention in recent reviews (cf., however, Somov 1986; Benz 1987; Melrose 1990) than other aspects of particle acceleration in solar flares (e.g., Ramaty *et al.* 1980; Ramaty and Forman 1987). In section 2 the requirements and limitations on an

acceptable bulk energization mechanism are discussed. In section 3 recent ideas on the acceleration of electrons in the terrestrial auroral zones are reviewed. A model for bulk acceleration based on the suggested auroral analogy is proposed in section 4. Prompt acceleration of relativistic electrons is discussed briefly in section 5.

2. Bulk Energization

The observational evidence relating to bulk energization in the impulsive phase of a solar flare comes mainly from hard X-ray data and from radio data on type III bursts. Hard X-ray data (e.g., Dennis 1985) are interpreted in terms of precipitating electrons emitting bremsstrahlung. Although alternative interpretations in terms of proton beams and neutral beams have not been ruled out (e.g., Brown *et al.* 1990; Martens and Young 1990), only the interpretation in terms of electrons is discussed here. The data then require that $\gtrsim 20\,\mathrm{keV}$ electrons precipitate at a rate up to about $10^{36}\,\mathrm{s}^{-1}$ (Hoyng, Brown and van Beek 1976). A substantial fraction of the primary energy released in a solar flare goes into such electrons. For example, Duijveman, Hoyng and Machado (1982) estimated that $> 20\%$ of the dissipated power goes into such electrons. The rate ($\approx 10^{36}\,\mathrm{s}^{-1}$) of precipitation and the total number of precipitating electrons required (up to $\approx 10^{39}$) are so large that the electron population needs to be resupplied by a return current drawing electrons from the chromosphere (e.g., Brown *et al.* 1990).

A small fraction (thought to be of order $\approx 10^{-3}$) of the bulk-energized electrons escape from the corona in the form of electron beams, and these produce type III radio bursts as they pass through the coronal and interplanetary plasma. Type III events can be observed *in situ* by spacecraft in the interplanetary plasma, thus providing direct information on the properties of the electrons and complementing the interpretation of the hard X-ray data (e.g., Lin 1985). Many type III events observed in the interplanetary medium are associated with storms and not with flares (e.g., Bougeret, Fainberg and Stone 1984, Suzuki and Dulk 1985). Such events are dominated by electrons of relatively low energy ($2 - 10\,\mathrm{keV}$) that could not originate from a flare site due to the prohibitive collisional losses in propagating through the lower corona (e.g., Lin 1985). It follows that bulk energization is not restricted to flares, and that it also occurs in storms where it is required to account for the electrons that produce storm type III bursts, and also presumably for the electrons that produce type I bursts. Only the flare-associated bulk energization is discussed here.

Time variations in both hard X-ray and microwave provide observational evidence that bulk energization consists of very many transient, localized episodes of energy release. Bursts of a few seconds in hard X rays were called *elementary flare bursts* by de Jager and de Jonge (1978). Elementary flare bursts may be due to energy release in individual flux tubes in a magnetic structure consisting of many intertwined flux tubes (e.g., Sturrock *et al.* 1984). The microwave data suggest that individual episodes of energy release occur on the shortest timescales ($\lesssim 100\,\mathrm{ms}$) that can be resolved (e.g., the review by Sturrock 1987). There is also a theoretical argument in favor of energy release in many localized regions based on the requirement for efficient energy dissipation. The collisional (Spitzer) resistivity is inadequate to account for coronal heating or the energy release in flares (e.g., Melrose and McClymont 1987). Alternatives include anomalous forms of resistivity (e.g., Duijveman, Hoyng and Ionson 1981) and of other transport coefficients (e.g., Papadopoulos 1985), hyperresistivity (e.g., Strauss

1988), strong double layers (e.g., Raadu 1989) and multiple WDLs (e.g., Khan 1989). In practice a high local current density is required, so that the overall current must be in the form of many thin current channels (e.g., Chiuderi 1983; Winglee, Pritchett and Dulk 1988). The filling factor of the localized energy release regions at any given time is small. Somehow all the electrons must be processed through at least one energy release region, suggesting that the plasma and energy release regions are in relative motion so that all the plasma is ultimately swept up by at least one energy release region.

Models that attribute the energy release to a single current sheet or a single double layer are unacceptable except if such single structures are interpreted as the envelopes of many small localized energy release sites. How one relates the overall energy release to the properties of the local energy release regions is a central problem in formulating any realistic model. To illustrate the difficulties, consider a current sheet of thickness ℓ and length L. Two alternative models are a plane of thickness ℓ (volume $L^2\ell$) and a cylinder of diameter ℓ (volume $\pi L\ell^2/4$). In the planar case, let J_0 be a uniform current density and let B_0 and $-B_0$ be the magnetic fields at the edges at $\pm\ell/2$, so that one has $\ell = 2B_0/\mu_0 J_0$. There is a severe constraint on the model (e.g., Chiuderi 1983): for the required anomalous resistivity the current must exceed the threshold for current instability, e.g., $J_0 > n_e e v_s$ for ion sound turbulence. Thus one requires $\ell \lesssim (2B_0/\mu_0 n_e e v_s) = 2(m_i/m_e)(v_A/V_e)(c/\omega_p)$. Inserting numerical values for the solar corona, a single current sheet with a current density at the threshold for the ion sound instability is of order 1 km thick. The inflow and outflow rates into the current sheet must be equal, implying that the inflow and outflow rates are in the ratio $v_{\rm in}/v_{\rm out} = A_{\rm out}/A_{\rm in} = \ell/L$. In the more favorable case of planar geometry, to produce the observed electron fluence of $10^{36}\,{\rm s}^{-1}$ with V_e of order $0.1c$ and $n_e = 10^{16}\,{\rm m}^{-3}$ requires $\ell L \approx 3 \times 10^{12}$ m. With $\ell \approx 1$ km this requires $L \approx 3 \times 10^9$ m, which is impossible in the solar corona. This limit on L is reduced somewhat if one takes account of inflow over a length $\gg \ell$ in a Petchek-type model, but one cannot plausibly reduce the limit to smaller than the length of a flare kernel. In the less favorable case of a cylindrical flux tube this difficulty is even further exacerbated. If one makes the plausible assumption that L exceeds ℓ by no more than an order of magnitude or so, one concludes that at any given time the dissipation must be occurring in at least of order 10^6 different current sheets.

It would be highly desirable to have a model based on reconnection in many current sheets, but no such model is available at present. A practical difficulty is in relating the (perpendicular) currents that flow in the current sheets to each other and to the global (parallel) current detected through vector magnetic field observations. The global current pattern in a reconnection model needs to be discussed critically: the current cannot close in the corona, and understanding how the current does in fact close is a prerequisite in any model that involves reconnection in many coupled current sheets. In the following discussion a model based on dissipation in multiple WDLs is described. From a formal viewpoint, a model involving dissipation of a parallel current is relatively simple to formulate because the current channels flow in parallel and the potential drops are in series along each current channel. Some of the ideas in this WDL model should apply to a model for many thin current sheets, but no such model has yet been formulated.

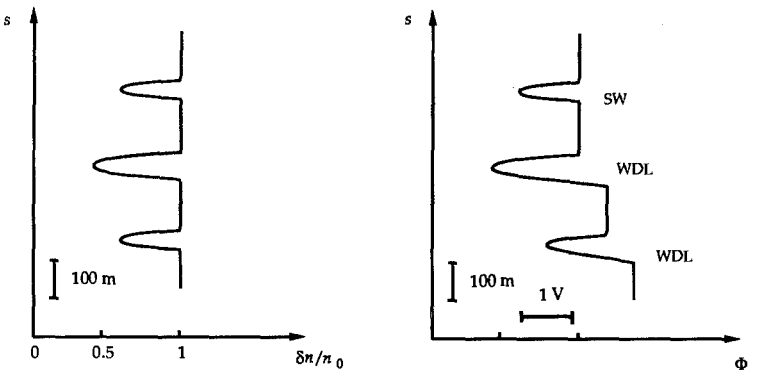

Fig. 1 A schematic description of variation of the relative density ($\delta n/n_0$) and potential (Φ) with height s as observed above the auroral zones from the Viking spacecraft; SW denotes a solitary wave, and WDL denotes a weak double layer. [After Boström *et al.* (1989) and Mälkki *et al.* (1989).]

3. Acceleration of Auroral Electrons

Acceleration of auroral electrons is probably due to multiple WDLs. Recent support for this suggestion comes from the results from the Viking spacecraft (Boström *et al.* 1989), although this interpretation is not universally accepted (e.g., Bryant 1990). Structures interpreted as WDLs and solitary waves (SW) were observed, cf. Figure 1. Associated with the WDLs there is an average electric field directed upward; the total $\Phi \approx$ few kV appears to arise from the potentials across many WDLs in series (Boström *et al.* 1988). There is only a weak upward field-aligned current associated with these structures, and the mean current density does not appear to be above the threshold for streaming instabilities (Boström *et al.* 1989). Mälkki *et al.* (1989) argued against an interpretation in terms of ion acoustic solitons and in favor of ion phase space holes (e.g., Dupree 1982; Tetreault 1988), cf. Figure 2.

An ion phase space hole is a depression in the distribution function, and so is a hole in both coordinate space and in velocity space. The hole is illustrated only in velocity space in Figure 2. An instability can cause a hole to grow when the sign of the velocity gradients of the electron and ion distributions are opposite, as illustrated in Figure 2. The instability results from electrons reflecting off the hole, transferring momentum to ions, and so driving the hole to lower velocities. This causes the hole to deepen and the potential associated with it to increase. This instability occurs under weaker conditions than required for current-driven ion-acoustic instability; specifically, it occurs for a lower current density and it does not require the ions to be much hotter than the electrons. This instability is a plausible mechanism for generating WDLs, and hence leading to an anomalous (collisionless) form of energy dissipation.

A possible model for bulk energization in solar flares could be formulated by rescaling the model for auroral electron acceleration due to WDLs formed by ion phase space holes. In the following discussion of the solar application, an important constraint is imposed by current limitation, which requires nearly equal electron fluences in opposite directions. A possibly relevant observation is that of counterstreaming auroral electrons

(Sharp *et al.* 1980), with relatively broad energy spectra and narrow angular widths 1°–10°, appear inconsistent with acceleration by a static Φ. Sharp *et al.* (1980) interpreted their data in terms of acceleration by a flickering double layer, with a flickering time (for reversal of polarity) of order the electron transit time across the double layer. An interesting feature, from the viewpoint of a possible solar analog, is that the electron fluence is large enough to depopulate the source in $\approx 10\,\mathrm{s}$, implying bulk energization, rather than the production of a runaway tail (Sharp *et al.* 1980).

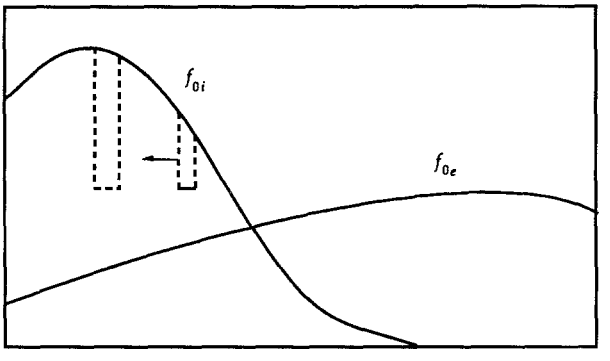

Fig. 2 An ion phase space hole that forms in the tail of the ion distribution f_{0i} grows if the electron distribution f_{0e} is an increasing function of velocity at the velocity defined by the hole. The hole drifts as indicated by the arrow. [After Tetreault (1988).]

4. A Model for Bulk Energization

The type of flare model envisaged here places emphasis on energy release in a localized flare kernel, with the energy propagating into the kernel from at least the coronal portion of a current circuit. The properties of the flare kernel can sometimes be deduced from X-ray data and from microwave spike bursts. The data suggest a range of plasma properties in flare kernels. For example, Batchelor *et al.* (1985) found $n \approx 10^{15}\,\mathrm{m}^{-3}$, $B \approx 10^{-2}\,\mathrm{T}$, $L \approx 10^{7}\,\mathrm{m}$, and de Jager *et al.* (1987) found $n \approx 10^{17}\,\mathrm{m}^{-3}$, $B \approx 0.14\,\mathrm{T}$, $L \approx 3.5 \times 10^{5}\,\mathrm{m}$ and $T \approx 5 \times 10^{8}\,\mathrm{K} \approx 50\,\mathrm{keV}$. (In storms the bulk energization occurs high in the corona, where the plasma frequency is 30–300 MHz.) The power, P, dissipated in a flare may be identified as $P = I\Phi$, where I is a current and Φ is a potential drop. Vector magnetograph data imply currents $I \approx 10^{12}\,\mathrm{A}$, and the regions of large current correlate with the positions of flare kernels (e.g., Lin and Gaizauskas 1987; Machado *et al.* 1988). The power $P \approx 10^{22}\,\mathrm{W}$ in a moderately large flare then requires a potential drop $\Phi \approx 10^{10}\,\mathrm{V}$.

There is an alternative current-driven model based on assuming $\Phi \approx 10^{5}\,\mathrm{V}$ to explain the typical energy $\approx 10^{5}\,\mathrm{eV}$ of the electrons (e.g., Lin and Schwartz 1987; Winglee *et al.* 1990). This model requires a net current $\approx 10^{17}\,\mathrm{A}$ to provide the required $P \approx 10^{22}\,\mathrm{W}$. As discussed below, no individual current can exceed about $10^{12}\,\mathrm{A}$, and hence to account for a current of $\approx 10^{17}\,\mathrm{A}$ one needs to assume that there are at least

10^5 current channels, with half flowing up and half flowing down. This alternative is not considered in detail here.

The current that can flow along a flux tube of the typical size involved in a moderate to large flare is restricted to $\lesssim 10^{12}$ A by the requirement that the magnetic field generated by the current not exceed the axial magnetic field needed to guide the current along the flux tube. A current of 10^{12} A corresponds to a net fluence of electrons (the difference in flow rate along the field line in one direction and in the opposite direction) of $\approx 10^{31}\,s^{-1}$. The argument given by Spicer (1983) and Holman (1985) that the current cannot change significantly during a flare implies that the net flow rate of electrons must remain approximately constant throughout a flare, and so remains at $\approx 10^{31}\,s^{-1}$. In contrast, the observed precipitation rate of $\gtrsim 10$ keV electrons during a flare can exceed $\approx 10^{36}\,s^{-1}$. The implication is that such a precipitation rate must be balanced by a cospatial upflow of electrons (to at least one part in 10^5) so that the net flow rate is maintained at $\approx 10^{31}\,s^{-1}$.

The model for bulk energization discussed here is based on acceleration by multiple WDLs. Such a model has the following features (e.g., Khan 1989). (1) The total current, $I_0 \approx 10^{12}$ A, consists of many thin current channels each with a current density above the threshold for triggering WDLs. The number of current channels $N_\perp$ satisfies $I_0 = N_\perp I_{DL}$, where I_{DL} is the average current flowing through each WLD. (2) The number of WLDs $N_\parallel$ along a given current channel must satisfy $\phi_0 = N_\parallel \phi_{DL}$, where $\phi_0 \approx 10^{10}$ V is the total potential drop and ϕ_{DL} is the average potential drop in individual WLDs. (3) The total power dissipated $N_\parallel N_\perp P_{DL}$ is equal to the total power $P = I_0\phi_0 \approx 10^{22}$ W released in a flare, where $P_{DL} = I_{DL}\Phi_{DL}$ is the power released in each WLD. Khan (1989) applied this model to the parameters for the flare discussed by de Jager *et al.* (1987) and found agreement for $N_\parallel \approx 10^5$ and $N_\perp \approx 10^6$. In this model the mean energy of the bulk energized electrons depends on the strength of the WDLs and the number of such WDLs that an individual electron encounters before escaping. An increase in energy by a factor of order 10 to 100, that is from $\approx 10^7$ K, to 10^8–10^9 K, seems plausible, but at present there is no detailed model for this.

An objection to any model based on acceleration by a double layer or by multiple WDLs to solar flares is that such acceleration is asymmetric in that one expects the accelerated electrons all to be propagating in the same direction, implying an unacceptably large current. The fluence of escaping electrons must be approximately equal in opposite directions along the field lines. The observations of counterstreaming electrons along the auroral field lines (Sharp *et al.* 1980) suggests that conditions exist under which this can occur. However, the interpretation of the counterstreaming auroral electrons in terms of acceleration by flickering WDLs would imply that the time-averaged potential drop is zero, and this is inconsistent with the model envisaged here which requires a potential drop of $\approx 10^{10}$ V that is quasistatic rather than flickering. (The potential drop pre-exists in a larger circuit, forms across the flare kernel when the effective resistance of the flare kernel increases suddenly during a flare; this potential cannot reverse in sign, as implied in a flickering model.) One could account for counterstreaming electrons, despite the asymmetry of the individual WDLs and of the global system itself, if the following two conditions are satisfied:

1) there is a mechanism capable of reflecting an electron beam, and

2) accelerated electrons can escape from the current channel into an interchannel region with negligible potential drop.

The second of these conditions is necessary because in a system with a uniform (across $\boldsymbol{B}$) potential drop, the energy gain of an electrons depends only on the distance it has propagated along $\boldsymbol{B}$. A possible model is one that invokes SWs to reflect the electrons, and in which the full potential drop $\approx 10^{10}$ V forms only along the current channels.

The potential required to reflect 20 keV electrons is of order 20 kV. A potential of this order is consistent with a scaling of the potentials observed in SWs in the auroral zones, where the scaling is $\phi \propto T_e$. A possible explanation of why the SWs are present arises from the limitation on the change in the current (Spicer 1983; Holman 1985). To see this suppose that the effect of one or more localized WDLs were to increase the net current faster than the circuit equation allows. Then the circuit equation requires that a potential difference develop to oppose this too rapid increase in current. (Furthermore, if the system is driven to accelerate all the ambient electrons, then the system must react to attempt to avoid a vacuum gap developing, in which case the entire potential drop would form across this gap.) A potential spike generated in this way should manifest itself in the form of a SW. The potential difference would then necessarily be large enough to limit the current by reflecting electrons. This suggests a picture in which the SWs form due to the requirement that the current be limited, and that a statistical distribution of such SWs (each of which has a short lifetime) is maintained at just the level needed to satisfy the requirement on the net current. Thus one would expect SWs to appear in association with the WLDs, as illustrated in Figure 1 for the auroral case, with their presence determined by the requirement that they reflect just enough electrons on average to maintain the net current at an approximately constant value.

A SW with peak potential ϕ_m reflects electrons with energy $\varepsilon < e\phi_m$ incident on it from either side. Consider a model in which the average separation between SWs defines an *acceleration cell.* Each cell is assumed to contain several WLDs so that the cell itself is asymmetric, tending to accelerate electrons in one direction. Each SW has a finite lifetime, and after a given SW decays there is a time delay before another SW develops to replace it. During this time electrons from the two neighboring cells are mixed but the counterstreaming continues to apply.

Electrons can escape from the current channel to which the potential drop is confined due to a relative motion of the electrons and the current channel and associated WDLs across $\boldsymbol{B}$. For example, this could be due to a perpendicular component of the electric field, which is necessarily present when a potential drop occurs along curved field lines, causing all the particles to drift across the field lines.

This suggests a model in which the electrons throughout the flare kernel are energized (a) in many current channels, (b) each of which drifts across $\boldsymbol{B}$, and (c) leaves behind counterstreaming electrons with an energy of order the potential drop across an individual cell. In this model ions would be accelerated to essentially the same energy as the electrons. Hence one would expect a copious production of ≈ 10 keV ions. These ions move much more slowly than the electrons at the same energy, and would not reach the chromosphere until long after the energetic electrons, and so their presence does not alleviate the problems associated with a return current and repopulation of the flaring flux tube (e.g., Brown *et al.* 1990)

5. Prompt Acceleration of Relativistic Electrons

Prompt acceleration of ions and of relativistic electrons is required during the impulsive phase to account for prompt gamma rays (e.g., Hudson 1985; Sakai 1990). Several alternative mechanisms for the prompt acceleration of ions seem to be viable (e.g., Melrose 1990). The prompt acceleration of relativistic electrons is more problematical. Diffusive acceleration by shock waves (e.g., Drury 1983) and by MHD waves are effective only above an appropriate threshold speed, which is $v \gtrsim v_A$ for ions, and is $v \gtrsim m_p v_A/m_e$ and $v \gtrsim (m_p/m_e)^{1/2} v_A$ for electrons resonating whistlers, respectively. The threshold condition is automatically satisfied for ions crossing a shock whose speed exceeds v_A, but this is not the case for electrons. An efficient injection mechanism is required for electrons. For example, the acceleration of relativistic electrons may be due to shock acceleration of $\approx 100\,\mathrm{keV}$ electrons produced in the impulsive phase, but one still needs to explain how the electrons are pre-accelerated to $\approx 100\,\mathrm{keV}$. Alternatively, the acceleration of relativistic electrons may due to a runaway in electric fields.

Acceleration of nonthermal electrons ($\gg 10\,\mathrm{keV}$) due to runaway in the electric fields associated with the bulk energization is a possible alternative to shock acceleration. One model (e.g., Holman 1985) involves localized regions with anomalous resistivity due to plasma turbulence generated by a current instability. The idea is to replace the Coulomb collision frequency in the standard treatment of runaway electrons by an effective collision frequency due to the plasma turbulence. With this modification, much of the theory developed for runaway acceleration in laboratory machines may be transferred to the collisionless case relevant to the solar corona. The maximum energy of the electrons in such a runaway model is $e\Phi$, where Φ is the available potential drop. Quite a different model for electron acceleration was proposed by Lotko (1986) in connection with auroral electrons. This model involves diffusive acceleration by a collection of WDLs, and so is compatible with the model for bulk energization discussed above.

Any model involving runaway acceleration should favor some electrons being accelerated to $\approx e\Phi$, where Φ is the total potential drop along the coronal flux tube. The implication that electrons with energy $\approx e\Phi \approx 10^{10}\,\mathrm{eV}$ should be favored in a model in which the net potential drop $\approx 10^{10}\,\mathrm{V}$ can be avoided if the surfaces of constant potential are not uniform across $\boldsymbol{B}$. Suppose the potential drop is confined to current channels and in any fixed location varies in both time and space as the WLDs form, drift and decay. Then an electron drifting across $\boldsymbol{B}$ gains (or loses) energy only when it passes through a WDL, leading to stochastic changes in energy. Nevertheless, $\approx 10^{10}\,\mathrm{eV}$ should be a characteristic maximum energy, and one would expect there to be observational evidence for this. Also, as discussed in connection with bulk energization, parallel acceleration is intrinsically asymmetric, and in the absence of any reflection (e.g., by magnetic mirroring) the relativistic electrons would all precipitate at one footpoint of the flux tube. For this application, it is desirable that a generalization of the theory Lotko (1986) be developed in which the WDLs are confined to narrow current channels, some pitch-angle scattering is included and magnetic mirroring is allowed. Some such theory is required to discuss these various effects quantitatively.

6. Discussion and Conclusions

Acceleration of electrons and ions in solar flares is still not adequately understood. Unresolved problems and difficulties discussed here include the following.

(1) *Bulk Energization*: A large fraction of the energy released in a solar flare is transferred to $\approx 10\,\mathrm{keV}$ electrons. The mechanism must be collisionless, and is necessarily restricted at any one time to a large number of localized sites. Possible models are based on reconnection in a large number of thin current sheets, or in multiple WDLs in a large number of current channels.

(2) *The Current Limitation*: Acceleration by multiple WDLs might be expected to produce electrons propagating in one direction. This is unacceptable for bulk energization because of a limitation on the current. A mechanism involving reflections by solitary waves is proposed here based on an analogy with auroral phenomena.

(3) *Bulk Energization in Storms*: Bulk energization seems to occur in type I–III radio storms as well as in the impulsive phase of solar flares.

(4) *Prompt Acceleration of Ions*: Gamma-ray line emission implies that energetic ions are accelerated promptly, and there are several competing theories that seem capable of accounting for this.

(5) *Prompt Acceleration of Relativistic Electrons*: Prompt acceleration of electrons to relativistic energies also seems to occur in the impulsive phase. Acceleration by the localized electric fields invoked in the bulk energization should favor the production of electrons with a characteristic maximum energy $\approx 10^{10}\,\mathrm{eV}$.

In the discussion here it is suggested that bulk acceleration might be analogous to the acceleration of auroral electrons, which appears to be due to WDLs associated with ion phase space holes. Ion phase space holes have not yet been invoked in the solar context. As indicated in Figure 2, ion phase space holes are excited when the electrons drift relative to the ions at greater than the ion thermal speed. It can occur when the ion temperature is less than the electron temperature, in which case the ion acoustic instability usually invoked in the solar context cannot occur.

In conclusion, the mechanism for bulk energization of electrons is one of the challenging theoretical problems relating to particle acceleration in the solar corona. The ideas suggested here are rather speculative and are within the framework of a model based on a current viewpoint in which the dissipation is attributed to WDLs. It is desirable that these ideas be developed quantitatively and that alternative ideas be developed within the framework of a model based on a magnetic-field viewpoint in which the dissipation is attributed to reconnection in many current sheets. It might be remarked that the current and magnetic-field viewpoints are quite different in practice, and further work needs to be done in reconciling them; in particular the global current pattern involved in reconnection models needs to be identified.

Acknowledgement I thank Lewis Ball and George Dulk for helpful comments on the manuscript.

References

Batchelor, D.A., Crannell, C.J., Wiehl, H.J., and Magun, A., 1985, *Astrophys. J.* **295**, 258.
Benz, A.O., 1987, *Solar Phys.* **111**, 1.

Boström, R., Gustafsson, G., Holback, B., Holgren, G., Koskinen, H., and Kintner, P., 1988, *Phys. Rev. Lett.* **61**, 82.
Boström, R., Holback, B., Holmgren, G., and Koskinen, H., 1989, *Physica Scripta* **33**, 523.
Bougeret, J.L., Fainberg, J., and Stone, R.G., 1984, *Astron. Astrophys.* **136**, 255.
Brown, J.C., Karlicky, M., MacKinnon, A.L., and van den Oord, G.H.J., 1990, *Astrophys. J. Suppl.* **73**, 343.
Bryant, D.A., 1990, *Physica Scripta* **T30**, 215.
Chiuderi, C., 1983, in J.O. Stenflo (ed.) *Solar and Stellar Magnetic Fields: Origins and Coronal Effects*, D. Reidel (Dordrecht), p. 113.
de Jager, C., and de Jonge, G., 1978, *Solar Phys.* **58**, 127.
de Jager, C., Kuijpers, J., Correia, E., and Kaufmann, P., 1987, *Solar Phys.* **110**, 317.
Dennis, B.R., 1985, *Solar Phys.* **100**, 465.
Drury, L.O'C., 1983, *Rep. Prog. Phys.* **46**, 973.
Duijveman, A., Hoyng, P., and Ionson, J.A., 1981, *Astrophys. J.* **245**, 721.
Duijveman, A., Hoyng, P., and Machado, M.E., 1982, *Solar Phys.* **81**, 137.
Dupree, T.H., 1982, *Phys. Fluids* **25**, 277.
Holman, G.D., 1985, *Astrophys. J.* **293**, 584.
Hoyng, P., Brown, J.C., and van Beek, H.F., 1976, *Solar Phys.* **48**, 197.
Hudson, H.S., 1985, *Solar Phys.* **100**, 515.
Kai, K., Melrose, D.B., and Suzuki, S., 1985, in D.J. McLean and N.R. Labrum (eds), *Solar Radiophysics*, Cambridge University Press, p. 415.
Khan, J.I., 1989, *Proc. Astron. Soc. Australia* **8**, 29.
Lin, R.P., 1985, *Solar Phys.* **100**, 537.
Lin, R.P., and Schwartz, R.A., 1987, *Astrophys. J.* **312**, 462.
Lin, Y., and Gaizauskas, V., 1987, *Solar Phys.* **109**, 81.
Lotko, W., 1986, *J. Geophys. Res.* **91**, 191.
Machado, M.E., Xiao,Y.C., Wu, S.T., Prokakis, Th., and Dialetis, D., 1988, *Astrophys. J.* **326**, 451.
Mälkki, A., Koskinen, H., Boström, R., and Holback, B., 1989, *Physica Scripta* **39**, 787.
Martens, P.C.H., and Young, A., 1990, *Astrophys. J. Suppl.* **73**, 333.
Melrose, D.B., 1990, *Aust. J. Phys.* **43**, 703.
Melrose, D.B., and Dulk, G.A., 1987, *Physica Scripta* **T18**, 29-38 .
Melrose, D.B., and McClymont, A.N., 1987, *Solar Phys.* **113**, 241.
Papadopoulos, K., 1985, in R.G. Stone and B.T. Tsurutani (eds) *Collisionless Shocks in the Heliosphere: A Tutorial Review*, American Geophysical Union, Washington DC, p. 59.
Raadu, M.A., 1989, *Phys. Rep.* **178**, 25.
Ramaty, R. *et al.*, 1980, in P.A. Sturrock (ed.) *Solar Flares*, Colorado Associated Press, p. 117.
Ramaty, R., and Forman, M.A., 1987, in R. Ramaty, T.L. Cline and J.F. Ormes (eds) *Essays in Space Science*, NASA Publication 2464, p. 47.
Louarn, P., Roux, A., de Feraudy, H., Le Quéau, D., André, M., and Maton, L., 1990, *J. Geophys. Res.* **95**, 5983.
Sakai, J.-I., 1990, *Astrophys. J. Suppl.* **73**, 321.
Sharp, R.D., Shelley, E.G., Johnson, R.G., and Ghielmetti, A.G., 1980, *J. Geophys. Res.* **85**, 92.
Somov, B.V., 1986, *Adv. Space Res.* **6**, 177.
Spicer, D.S., 1983, *Adv. Space Res.* **2**, 135.
Strauss, H.R., 1988, *Astrophys. J.* **326**, 412.
Sturrock, P.A., 1987, in B.R. Dennis, L.E. Orwig and A.L. Kiplinger (eds) *Rapid Fluctuations in Solar Flares*, NASA (Washington DC) p. 1.
Sturrock, P.A., Kaufmann, P., Moore, R.L., and Smith, D.F., 1984, *Solar Phys.* **94**, 341.
Suzuki, S., and Dulk, G.A., 1985, in D.J. McLean and N.R. Labrum (eds), *Solar Radiophysics*, Cambridge University Press, p. 289.
Tetreault, D., 1988, *Geophys. Res. Lett.* **15**, 164.
Wild, J.P., Smerd, S.F., and Weiss, A.A., 1963, *Ann. Rev. Astron. Astrophys.* **1**, 291.
Winglee, R.M., Kiplinger, A.L., Dulk, G.A., and Zarro, D.M., 1990, in R.M. Winglee and A.L. Kiplinger (eds) *MAX '91 Workshop #3: Max '91/SMM Solar Flares: Observations and Theory* p. 244.
Winglee, R.M., Pritchett, P.L., and Dulk, G.A., 1988, *Astrophys. J.* **329**, 440.

KINETIC DESCRIPTION OF ELECTRON BEAMS IN THE CHROMOSPHERE

D. Gómez[1] and P.J.D. Mauas[2]
1 Institute for Astronomy, University of Hawaii - U.S.A
2 Osservatorio Astrofisico di Arcetri - Italy

Introduction

Most of the work on the effects of the impact of an electron beam on the solar atmosphere has been done through a "test-particle approach", in which the energy losses for an individual particle are computed, and the results are convoluted with the initial spectrum. This approach can be very useful to study some integrated quantities (energy deposition, for instance), as has been shown by Emslie (1978) and Brown (1973), but it is inadequate to study processes in which a more complete knowledge of the distribution of the electrons in velocity space is needed (*e.g.* transition rates; see Aboudarham and Hénoux 1986; Richiazzi and Canfield 1983). And, of course, it is also unable to describe purely kinetic effects like diffusion in velocity space or the development of turbulence.

Leach and Petrosian (1981), using approximate expressions for the interaction with neutrals, derived a Fokker-Planck equation corresponding to an electron beam traversing a partially ionized plasma, and solved it for a number of particular cases. In the present study, we derived the collisional terms of the Fokker-Planck equation, including elastic and inelastic collisions with hydrogen and helium atoms. We retained the velocity-diffusion term in our calculations, and found that its smoothing action on the distribution function becomes noticeable under certain circumstances. To integrate our Fokker-Planck equation, we used a quiet-Sun model to describe the chromospheric background (Vernazza et al. 1981).

Collisional terms

An electron beam can be described through its distribution function, $f(\mathbf{r}, \mathbf{v}, t)$, whose evolution is given by the Fokker-Planck equation

$$\partial_t f + \nabla_r \cdot (\mathbf{v} f) + \frac{1}{m_e} \nabla_v \cdot (\mathbf{F} f) = - \sum_\beta \nabla_v \cdot \mathbf{j}^\beta \ , \tag{1}$$

where m_e is the electron mass, $\mathbf{F}$ represents any external force field (*e.g.* gravity) and

$$j_i^\beta = \langle \Delta v_i \rangle^\beta f - \frac{1}{2} \ \partial_k \left(\langle \Delta v_i \, \Delta v_k \rangle^\beta f \right) \ , \tag{2}$$

which describes the effect of collisions with particles of species β. Here ∂_k represents the partial derivative with respect to v_k. The brackets $\langle \Delta v_i \rangle^\beta$ and $\langle \Delta v_i \, \Delta v_k \rangle^\beta$ respectively describe the change of velocity and its second-order moment due to interactions with species β, averaged over the distribution of the corresponding target particles. For highly suprathermal electrons

$$\langle \Delta v_i \rangle^\beta = n_\beta \, v \int \Delta v_i \; d\sigma_\beta \; , \tag{3}$$

$$\langle \Delta v_i \, \Delta v_k \rangle^\beta = n_\beta \, v \int \Delta v_i \; \Delta v_k \; d\sigma_\beta \; , \tag{4}$$

where n_β and $d\sigma_\beta$ are the particle density and differential cross-section of target species β. We consider Coulomb collisions with electrons and protons, as well as elastic and inelastic collisions with hydrogen and helium atoms. Either because of the spherical symmetry of the interaction potentials involved or because of the random orientations of the atoms, the expressions for the tensors $\langle \Delta v_i \rangle^\beta$ and $\langle \Delta v_i \, \Delta v_k \rangle^\beta$ reduce to (Trubnikov 1965)

$$\langle \Delta v_i \rangle = \langle \Delta v_\parallel \rangle \; \frac{v_i}{v} \; , \tag{5}$$

$$\langle \Delta v_i \, \Delta v_k \rangle = \langle (\Delta v_\parallel)^2 \rangle \; \frac{v_i \, v_k}{v^2} + \langle (\Delta v_\perp)^2 \rangle \; \left(\delta_{ik} - \frac{v_i \, v_k}{v^2} \right) \; , \tag{6}$$

where the subscripts $\parallel$ and $\perp$ refer to the orientation with respect to $\mathbf{v}$.

The differential cross-sections for the various processes considered have been obtained from Mott and Massey (1949) and Inokuti (1971). Our results are

$$\langle \Delta v_\parallel \rangle = -\frac{2\pi e^4}{m_e^2} \; \frac{1}{v^2} \; (4\Lambda \, n_e + 2\Lambda \, n_p + (8\Lambda_{\rm H} + 2) \, n_H + (8\Lambda_{\rm He} + 2) \, 4 n_{\rm He}) \; , \tag{7}$$

$$\langle (\Delta v_\parallel)^2 \rangle = \frac{2\pi e^4}{m_e^2} \; \frac{1}{v} \; (2 \, (n_e + n_p) + 4 \, n_{\rm H} + 16 \, n_{\rm He}) \; , \tag{8}$$

$$\langle (\Delta v_\perp)^2 \rangle = \frac{2\pi e^4}{m_e^2} \; \frac{1}{v} \; ((2\Lambda - 1) \, (n_e + n_p) + 4\Lambda_{\rm H} \, n_{\rm H} + 16\Lambda_{\rm He} \, n_{\rm He}) \; , \tag{9}$$

where $\Lambda = \ln(\frac{m_e v^2 \lambda}{e^2})$ is the Coulomb logarithm ($\lambda = \sqrt{\frac{k_B T}{4\pi e^2 n_e}}$, Debye length) and the particle densities correspond to electrons, protons and neutral hydrogen and helium atoms respectively. For electron beams of 20 keV, we obtain $\Lambda \approx 21 \gg 1$. The constants $\Lambda_{\rm H}$ and $\Lambda_{\rm He}$ are $\Lambda_Z = \ln(\frac{v}{Zc\alpha_F})$, where Z=1 for hydrogen and Z=2 for helium ($\alpha_F = 1/137$, fine structure constant).

Stationary Fokker-Planck equation

The typical collision time for 20 keV electrons is 0.02 sec., much shorter than the travel time through the chromosphere. Therefore, a stationary model provides a good description of the beam-chromosphere interaction, even during the impulsive phase of solar

flares (except perhaps for particularly bursty events, Kiplinger et al. 1983). We also assume that the electron distribution function is cylindrically symmetric with respect to an axis **z**, oriented along the Sun radius. Relativistic effects are important at high velocities, but at 20 keV amount only for small corrections; a relativistic version of the present calculations can be found in Gómez and Mauas (1991). Therefore, the distribution function will be $f = f(z, v, \mu)$, where μ is the cosine of the angle between **z** and **v**. It is straightforward to show that the Fokker-Planck equation becomes

$$\mu v\ \partial_z f = \frac{1}{v^3}\left[a_\mu \partial_\mu\left((1-\mu^2)\,\partial_\mu f\right) + a_1\, v\ \partial_v f + a_2\, v^2 \partial_v(\partial_v f)\right] . \qquad (10)$$

$a_1 = v\sum_\beta\left(\langle(\Delta v_\parallel)^2\rangle^\beta - \langle(\Delta v_\perp)^2\rangle^\beta\right) - v^2\sum_\beta\langle\Delta v_\parallel\rangle^\beta$, $a_\mu = \frac{v}{2}\ \sum_\beta\langle(\Delta v_\perp)^2\rangle^\beta$ and $a_2 = \frac{v}{2}\ \sum_\beta\langle(\Delta v_\parallel)^2\rangle^\beta$ are only functions of z throughout their dependence on the particle densities:

$$a_\mu = \frac{2\pi e^4}{m_e^2}\left((\Lambda - \frac{1}{2})(n_e + n_p) + 2\Lambda_{\rm H} n_{\rm H} + 8\Lambda_{\rm He} n_{\rm He}\right) , \qquad (11)$$

$$a_1 = \frac{2\pi e^4}{m_e^2}\left((2\Lambda + 3)n_e + 3n_p + (4\Lambda_{\rm H} + \frac{13}{3})n_{\rm H} + (4\Lambda_{\rm He} + \frac{13}{3})\,4n_{\rm He}\right) , \qquad (12)$$

$$a_2 = \frac{2\pi e^4}{m_e^2}\left(n_e + n_p + 2n_{\rm H} + 8n_{\rm He}\right) . \qquad (13)$$

Results

We integrated equation (10) along z, following an explicit scheme. We iterated integrations forward and backward in z, computing the $\mu > 0$ and $\mu < 0$ electron populations, respectively. The incoming electron beam at the top of the chromosphere displays a power-law dependence on v, like $v^{-(2\delta+1)}$ (corresponding to an energy flux spectrum $E^{-\delta}$) and a gaussian profile for the pitch angle distribution, peaked at $\mu = 1$. For the background atmosphere we used the quiet-sun chromospheric model by Vernazza *et al.* (1981), as modified by Avrett (1985).

In Figure 1 we show the results of the integration, both for the complete Equation 10 and for a calculation we performed setting $a_2 = 0$ to study the effects of not considering velocity diffusion. In Figure 1-a we show the distribution function for $\mu = 1$, and in Figure 1-b $n(v) = v^2 \int f(v, \mu) d\mu$, which is the number of particles with velocity between v and $v + dv$.

As can be seen, the effect is quite important for the non-integrated distribution function, in particular at small velocities. This effect can be important when studying some angular-dependent quantities, like the polarization of the emitted radiation. For $n(v)$, on the other hand, the differences are much smaller. However, it should be pointed out that both the position of the maximum of $n(v)$, and the steepness of the rise in n at small velocities changes when considering velocity-diffusion. These changes can be of

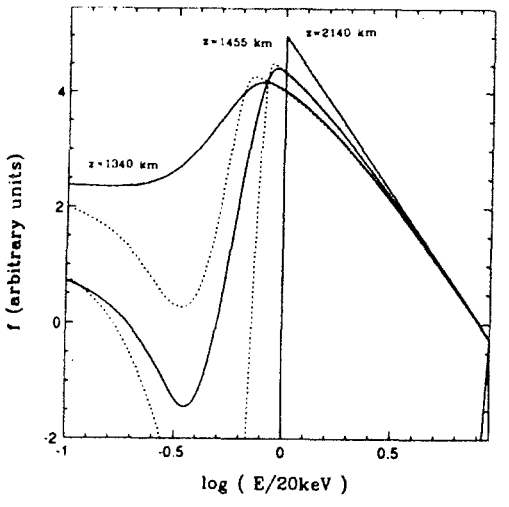

Fig. 1−a

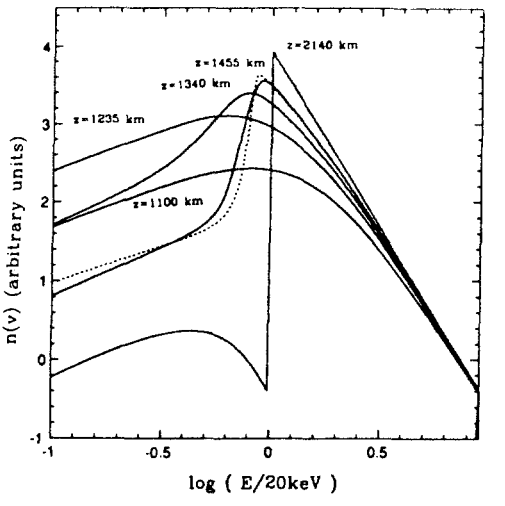

Fig. 1−b

Figure 1. Results of the calculations. *Full line*: Results obtained integrating Equation 10. *Dotted line*: Results for $a_2 = 0$. The distribution function at 2140 km is the injected one.

importance when studying the possible instabilities of the beam (see *e.g.* Emslie and Smith 1984).

References

Aboudarham, J. and Hénoux, J.C. 1986, *Astr. Ap.*, **156**, 73.

Avrett, E.H. 1985, in *Chromospheric diagnostic and modelling*, ed. B. W. Lites, (Sunspot, N.M.: National Solar Observatory), p. 67.

Brown, J.C. 1973 *Solar Phys.*, **31**, 143.

Emslie, A.G. 1978, *Ap. J.*, **224**, 241.

Emslie, A.G. and Smith, D.F. 1984, *Ap. J.*, **279**, 882.

Gómez, D. and Mauas, P.J. 1991, *Ap. J.*, submitted.

Inokuti, M. 1971, (*Rev. Modern Phys.*, **43**, 297).

Kiplinger, A.L., Dennis, B.R., Emslie, A.G., Frost, K.J., and Orwig, L.E. 1983, *Ap. J.*, **265**, L99.

Leach, J., and Petrosian, V. 1981, *Ap. J.*, **269**, 715.

Mott N., and Massey, H. 1949, *Theory of Atomic Collisions* (Oxford: Clarendon).

Richiazzi P.J. and Canfield, R.C. 1983, *Ap. J.*, **272**, 739.

Trubnikov, B. 1965, *Rev. Plasma Phys.*, **1**, 105.

Vernazza, J., Avrett, E.H., and Loeser, R. 1981, *Ap. J. Suppl.*, **45**, 635.

NUCLEAR REACTIONS IN FLARES

ERICH RIEGER

Max-Planck-Institut für extraterrestrische Physik
8046 Garching, FRG

ABSTRACT. The explosive release of energy stored in sheared magnetic fields and its subsequent transformation to a large extent into kinetic energy of charged particles is a common phenomenon occurring in plasmas throughout the universe from a place as close as the Earth's magnetosphere to objects at cosmological distances such as quasars. On this vast distance scale the Sun is of crucial importance for the understanding of these physical processes. Due to its proximity, flares can be investigated in the gamma-ray regime, which is the domain where the accelerated particles leave their fingerprints most clearly and flare-generated particles can be recorded in space and related to particular events.
In this paper we discuss the production of gamma-ray line radiation and neutrons and approach the problem of the acceleration and energy release of charged particles from the viewpoint of the observer.

1. Introduction. During powerful flares the Sun due to its closeness is the brightest gamma-ray source in the sky. At maximum phase the number of photons > 0.3 MeV recorded on Earth can be as high as 500 $(cm^2\ s)^{-1}$. Then the Sun shines out the most intense gamma-ray bursts by about a factor of ten and it dwarfs the Crab pulsar, a typical celestial gamma-ray object, by several orders of magnitude. During the big flare of 19 October 1989 a flux of 2.6 Photons $(cm^2 s)^{-1}$ was recorded by the Solar Maximum Mission (SMM) Gamma-Ray Spectrometer (GRS) in the neutron capture line at 2.223 MeV and the line fluence (time integrated flux) was close to 1000 Photons cm^{-2}. Although these fluxes are record values, it implies that during intense flares the Sun can be observed in the gamma-ray regime with high temporal resolution, which opens up the possibility to investigate the acceleration of charged particles in great detail.
In this paper a brief overview is given about nuclear reactions in the solar atmosphere by flare accelerated particles, leading to line emission, which together with bremsstrahlung from high energy electrons generate the solar flare gamma-ray spectrum. This is followed by a discussion of temporal characteristics of flares and of gamma-ray line ratios, which have implications for the problem of particle acceleration. Finally, we comment on gamma-ray line fluences as a measure of the number of interacting particles and compare this with particle fluxes measured in space. Not covered in this paper are the topics of nuclear line spectroscopy and of nuclear line positions and shapes. The reader is referred to [1-7].

2. Nuclear Line and Neutron Production. Gamma-ray lines result from the interaction of high energy particles with nuclei of the solar atmosphere. The principal mechanisms for line production are nuclear de-excitation [4, 7-10], neutron capture [11-14], positron annihilation [1, 15-17], and in a wider sense the decay of flare generated neutral pions [12].
Inelastic scattering of protons, α-particles and ions, and to a lesser degree spallation reactions of certain elements lead to excitation of nuclei to higher levels. As the life times of the excited states are 10^{-12} sec or shorter, the lines are emitted without a measurable delay and are therefore called prompt lines. For the most abundant elements the cross sections for excitation peak around 10 MeV and for spallation at somewhat higher energies ($\approx$ 20 MeV). This means that the prompt narrow lines (protons and α-particles on heavy atmospheric nuclei)

and broad lines (ions on protons and α-particles) are produced predominantly by particles (protons or ions) of relatively low kinetic energy of order 10-30 MeV.

In addition to nuclear de-excitation the interaction of accelerated ions with the solar atmosphere also leads to the production of neutrons [11, 12]. The most prolific neutron producing reaction is that of protons on ^{4}He with a threshold of about 30 MeV. These neutrons can have different fates [13]:

- They escape from the Sun (60-70 %) and those reaching Earth before decaying can be detected with suitable detectors in space [18, 19] and on the ground [20-25]. Neutrons leaving the Sun which suffer decay can be identified through their energetic decay protons, which are trapped by the interplanetary magnetic field [26-29].
- They remain at the Sun and, after thermalization, can be captured by nuclei before their decay. The reaction ^{3}He (n,p)^{3}H proceeds without the emission of radiation. The reaction ^{1}H (n, γ) ^{2}H produces the neutron capture line at 2.223 MeV. Because the capture takes place in the photosphere, the gamma-ray photons are significantly attenuated by Compton scattering if emitted parallel to the solar surface. For flares observed close to the solar limb, the 2.223 MeV line is therefore strongly weakened in comparison to nuclear de-excitation lines, which are produced at greater altitudes [14]. For flares off the limb, the 2.223 MeV line is by far the strongest one and is thus a good proxy that nuclear reactions occurred in the solar atmosphere during a flare. Contrary to the nuclear de-excitation lines, which are emitted promptly, the 2.223 MeV neutron capture line is emitted with a delay (see Figures 2 and 3). The delay results from the finite capture time of the thermalized neutrons on hydrogen and ^{3}He and depends on the density of the respective elements. A study of the time history of the line can thus yield information on the abundance of ^{3}He and the depth of the atmosphere, where these reactions occur [30-32].

Another line which is emitted with a delay (see [33], Fig. 2) is the positron annihilation line at 0.511 MeV. Positrons result from accelerated particle interactions which lead to β^+-emitting radioactive nuclei. The most prolific positron emitters are ^{11}C, ^{14}O, and ^{15}O with halflives of 20.5 min, 71 sec and 2.06 min, respectively [11, 17]. Another production mode of positrons is the prompt decay of positively charged pions created by the interaction of very high energy protons or ions with matter [12]. The energies of positrons from β^+ - and pion-decay are $\approx$ 1 MeV and 10 - 100 MeV, respectively. The slowing down and annihilation time is inversely proportional to the ambient density. For reactions to occur in the chromosphere it is short compared to the decay times of the radioactive nuclei, so that the delay observed [34] reflects the halflives of the β^+-emitters [35, 17].

Very high energy reactions also lead to the production of neutral pions which decay after 10^{-15} sec into two high energy gamma-ray photons of 68 MeV in the center of mass system. Due to the high energy of the primary charged particles ($\gtrsim$ 200 MeV) the decay spectrum is Doppler broadened around 68 MeV [12].

From the interaction of electrons with matter a continuous spectrum results extending from the energy of the most energetic electrons to almost zero. Assuming a power-law spectrum for the electrons the photon spectrum is also a power-law at energies $\gtrsim$ 300 keV [36].

3. The Solar Flare Gamma-Ray Spectrum. The solar flare gamma-ray spectrum is therefore a superposition of electron bremsstrahlung, narrow and broad line radiation and pion decay emission. In Figure 1 the count spectrum of the end phase of the big 6 March 1989 flare is shown between 0.3 and 9 MeV. Below about 1 MeV a continuum originating from electron bremsstrahlung is apparent on which the line features of the Li-Be-complex (α-α) [37], positron annihilation, and iron are superimposed.

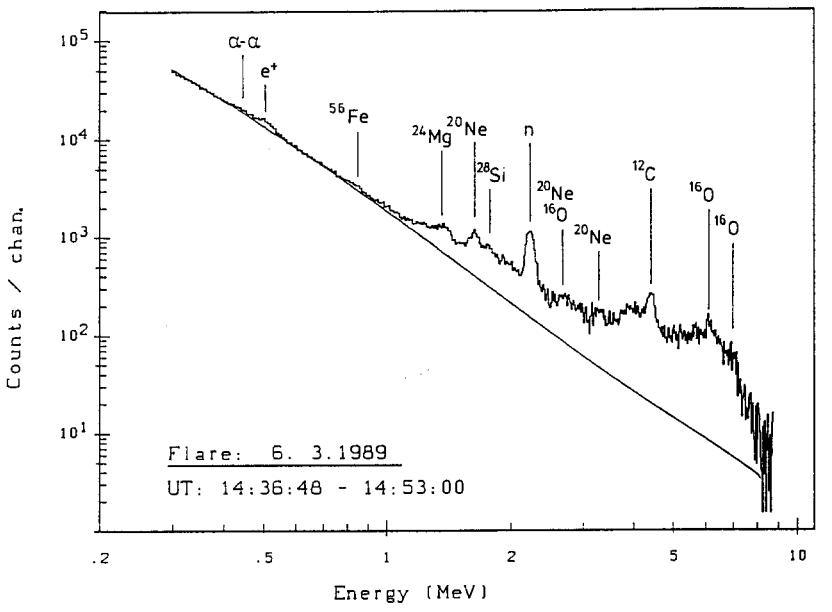

Figure 1: Count spectrum of the 6 March 1989 flare (end phase). Due to the limb near location of the flare, the neutron capture line (n) is attenuated by about a factor of 2. The shoulder-like features shortward of the ^{12}C and ^{16}O lines are instrumental. Full line: best fit power-law (< 1 MEV) in photon space transformed to count space (from [43]).

Towards higher energies lines begin to dominate the spectrum. Above 7.2 MeV a marked drop is apparent, which is due to a lack of strong nuclear lines above this limit [38]. This disparity between electron continuum and nuclear lines in different energy intervals [39, 40] is of great importance, because it facilitates the separation of the ionic from the electronic contribution. To accomplish this, the best fit power law obtained at energies below 1 MeV, as indicated by the full line in the figure, is extrapolated to higher energies [41]. The excess above this extrapolation is ascribed to nuclear interactions. It is especially prominent in the range between 4 to 7 MeV, which contains the strong lines of ^{12}C and ^{16}O. Here, for most flares investigated so far, electron bremsstrahlung contributes about 10-30 % to the overall emission (Forrest, private communication). It must be pointed out, however, that the applicaton of an unbroken power law may be an oversimplification, if the electron bremsstrahlung spectrum should flatten at MeV energies [42] suggested observationally by some rare flare events [43, 44]. In this case the ionic contribution is systematically overestimated.

4. Temporal Characteristics of Flares. The observation of the time history of flares is a powerful diagnostic tool providing insight into the phenomenon of charged particle acceleration. This was recognized since flares have been recorded with high time resolution by radio detectors (see [45, 46]). A more direct approach to electron and ion acceleration was given when the Sun could be observed at X-ray and gamma-ray energies by space born experiments (see [47, 48]). It must be kept in mind, however, that the emission time history in different energy bands is a complicated superposition of acceleration-, storage-, transport-, and energy loss processes

[49]. In this paper it is not attempted to disentangle these different phenomena (see [50 - 54]). Here we show some typical cases of flare time histories and draw qualitative conclusions about the acceleration of the parent particles.

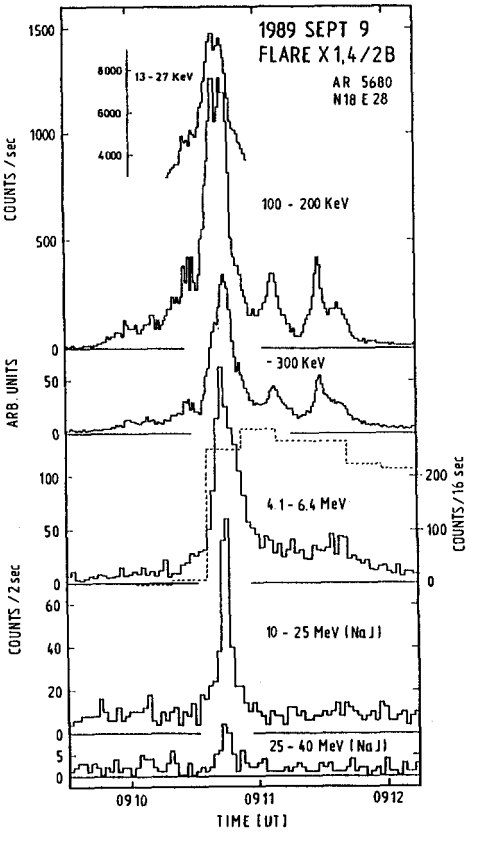

Figure 2. Time history of the 9 September 1989 flare in different energy bands. Note the impulsive appearance of the flare at all energies (GRS measurement). Dashed histogram: temporal evolution of the delayed neutron capture line.(NaI): counts of the NaI main detector only. Flare specifications are from "Preliminary Solar Geophysical Data" NOAA, Boulder, CO.

In Figure 2 and 3 impulsive and gradual events are shown, respectively. The simultaneous peaking of order 1 sec at all energies of the 9 September 1989 flare (see also [55]) indicates that the particle injection (acceleration) was rather prompt and that storage-, propagation-, and energy loss processes took a very short time. The impulsivity of the event is accentuated by the quick uprise of the neutron capture line (dashed histogram). Quite different in appearance to the impulsive 9 September 1989 flare is an episode of the 16 December 1988 gamma-ray event (Figure 3, see also [56]). Taking the time profile at medium energy X-rays as a reference for the acceleration of subrelativistic electrons [57], the peak of the emission in the nuclear energy band (4.1 - 6.4 MeV) is delayed by about 45 sec. But it is of importance to note that the emission rises simultaneously at all energies.

There is a long standing controversy about how to explain delays of peak emission between lower and higher energies. The virtues of a trap plus precipitation model or a second step (stage) model are discussed extensively in [58, 75]. In most cases, where peak delays are observed, the emission begins to rise simultaneously at all energies [59, 60]. This fact seems to favour a trap plus precipitation model. Apparently, these events occur on larger loop systems than the impulsive ones, where peak delays are hardly discernible.

Evidence that particle acceleration in solar flares can proceed in two steps or two phases comes from the temporal characteristics of the 3 June 1982 Flare [61]. This powerful event had a distinctive two-phase appearance at high photon energies (> 25 MeV): a very impulsive peak of short duration (≈ 40 sec) was followed by a more gradual emission, which lasted several minutes. This gradual peak observed at energies > 25 MeV does not stand out in the X-rays and in the nuclear energy band. Its spectrum is definitely harder than that of the impulsive burst, showing a large contribution of neutral pion decay photons [62]. The appearance of a second peak in the time history of this flare together with particle measurements after the flare [63] have been explained as evidence for a second phase acceleration by a shock-wave moving through the solar corona and creating a harder particle population than that produced during the first and impulsive phase [12]. On the other hand, it was argued that the data can be fitted on the assumption of one population of accelerated particles [64, 52, 53]. To explain the second maximum above 25 MeV, a fast rise

of plasmaturbulence is assumed to occur at the end of the impulsive phase. This increase of plasmaturbulence then leads to precipitation of impulsively created high energy protons by pitchangle scattering (see also [65]).

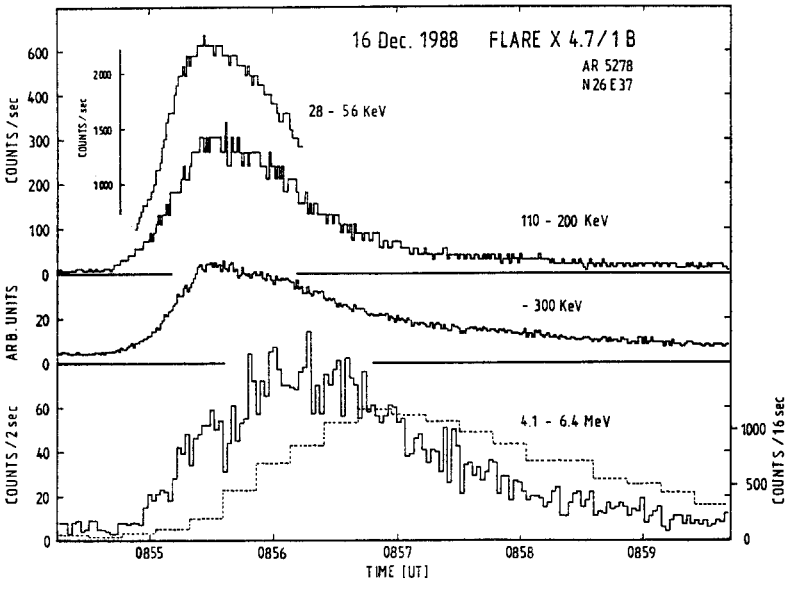

Figure 3. Time history of an episode of the 16 December 1988 flare in different energy bands. Dashed histogram: temporal evolution of the delayed neutron capture line (GRS measurement).

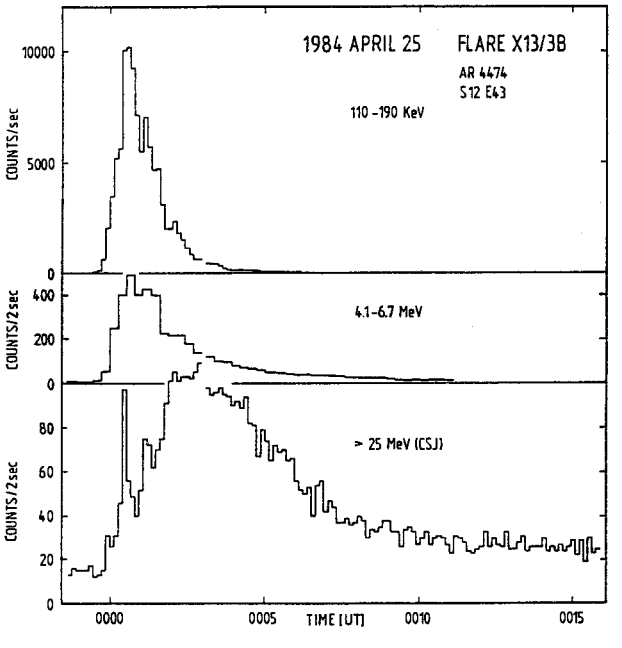

Figure 4. Time history in different energy channels of the 25 April 1984 flare (GRS measurement). (CsI): counts of the CsI back detector, only.

Concerning the temporal history, the flare of 25 April 1984 shown in Figure 4, looks almost like a twin to the event discussed above. At energies above 25 MeV an impulsive burst of about 30 sec duration is followed by an intense gradual peak, which is not apparent at lower energies. Relative to the impulsive burst the gradual peak is more pronounced in this event than in the 3 June 1982 flare, suggesting a high fluence from pion decay photons. Contrary, however, the impulsive burst does not show the spectral hardening at energies above 50 MeV, indicative of neutral pion decay photons, which makes the 3 June 1982 flare so exceptional [62, 66].

5. Nuclear Line Ratios as a Diagnostic of Accelerated Particle Spectra. If the cross sections of two lines have widely different thresholds in energy, then their flux or fluence ratio can give information about the spectrum of the high energy particles. It was already mentioned that the cross sections for the de-excitation lines of the most abundant elements of the solar atmosphere, for instance ^{12}C (4.439 MeV) and ^{16}O (6.129 MeV) are of similar energy dependence and peak around 10 MeV, if excited by protons. Their flux ratio is therefore only weakly dependent on the spectrum of the energetic particles. On the other hand, the most prolific neutron producing reaction (protons on ^{4}He) has a threshold of $\approx$ 30 MeV. Therefore, the ratio of the fluence of the de-excitation lines and the neutron yield will depend on the spectral parameters of the particles [16]. Shown in Figure 5 are calculations of the yield of the ^{12}C and ^{16}O de-excitation lines (contained in the energy range 4-7 MeV), neutrons, pions, and positrons as a function of the primary proton spectrum under the assumption that the interacting energetic protons have an isotropic distribution and that they loose all their energy in the ambient medium (thick target case) [35].

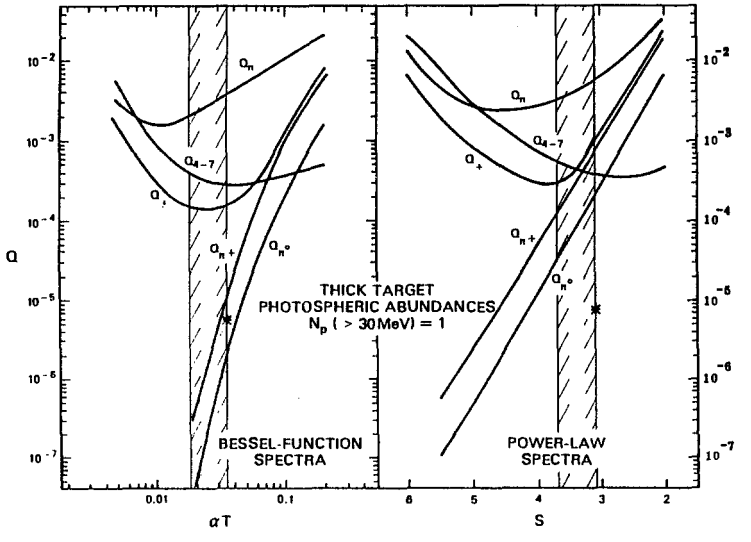

Figure 5. Neutron, 4-7 MeV nuclear gamma-ray, positron, π^+ and π° production versus the spectral parameter of a Bessel function spectrum and power-law spectrum for the primary protons (from [35]). Indicated by the dashed area is the range of the spectral parameters deduced from observations. Asterisk: π°-decay fluence of the 3 June 1982 flare impulsive phase [62, 33].

ready mentioned, only part of the neutrons produced are captured by solar atmospheric hydrogen to give deuterium, which then leads to the emission of the 2.223 MeV line [13, 14, 35]. The ratio of the 2.223 MeV and 4-7 MeV fluence is a measure of the steepness of the proton spectrum predominantly in the energy range 10-100 MeV. Shown by the dashed area in Figure 5 is the range of parameters α T (Bessel function) and s (power law) which is determined from the fluence ratio of 12 solar flares [14, 33].

It is clear that the fluence ratio of the lines mentioned does not enable us to deduce the spectral shape - Bessel function versus power law - of the energetic particles. A third and deciding point on the particle spectrum is necessary. This point is available when photons from the decay of neutral pions can be observed. The threshold for neutral pion production is above 100 MeV, so that by measuring the pion decay fluence we get information about the number of interacting protons of several hundred MeV. As up to now, however, there is only one event, the 3 June 1982 flare, which definitely showed neutral pion decay emission during the impulsive phase [62]. This pion decay fluence normalized to the 4-7 MeV fluence is inserted into Figure 5 by an asterisc at a spectral parameter value obtained from the fluence ratio of the 4-7 MeV nuclear excess and the 2.223 MeV line. It is evident that a power law spectral form of the energetic particles is ruled out. This conclusion is supported by the measurement of the arrival times of high energy neutrons at the GRS after the flare [35, 61, 67]. There is in fact no flare, for which an unbroken power law for the spectrum of the interacting primary particles is suggested by the gamma-ray measurements. A second phase is obviously needed to create such a hard spectrum.

6. Nuclear Line Fluences as a Measure of the Number of Interacting Particles and Solar Energetic Proton Events. In the previous chapter it was shown that the fluence ratio of certain nuclear lines bears information on the spectrum of the accelerated interacting particles. By using the absolute value of nuclear line fluences the number of interacting particles can be determined. As already mentioned, the energy band from 4-7 MeV which contains the strong nuclear lines of carbon and oxygen is an important measure of the interaction rate of energetic protons in flares. As can be seen in Figure 5, the yield calculations have been normalized to 1 proton with an energy of > 30 MeV. By assuming isotropic emission of the 4-7 MeV photons and negligible attenuation in the solar atmosphere, for a measured nucleonic excess photon fluence of ϕ (γ cm^{-2}), the total number of interacting protons (> 30 MeV) is obtained according to

$$\text{Np } (> 30 \text{ MeV}) = \phi \text{ (4-7 MeV)} \cdot Q^{-1}(\text{4-7 MeV}) \cdot 4\pi d^2 \qquad (1)$$

where Q(4-7 MeV) is the photon yield in the energy interval 4-7 MeV and d is the Sun-Earth distance. To determine the number of interacting protons, the spectral parameter must be known, which can be obtained as described in the previous chapter. If, on the other hand, the neutron capture line is too much attenuated in case the flare is too close to the solar limb, the 4-7 Mev fluence, by itself, is also a reliable measure of the number of interacting particles, because the 4-7 MeV yield is relatively independent on the spectral parameter within the range that flares have been observed (Figure 5). The computed number of interacting particles even depends uncritically on the assumption of their spectral shape (see [35], Table 1). From a measured excess fluence of 100 photons cm^{-2} in the energy range 4-7 MeV roughly 10^{33} Protons (> 30 MeV) interacting in the solar atmosphere can be calculated.

It is of interest to examine the relationship between the number of particles producing the gamma-ray emission (interacting particles) and those observed in interplanetary space after those flares (escaping particles). In order to minimize the influence of coronal and interplanetary transport effects only 'magnetically well connected' solar energetic proton events can be used. For these well connected events the peak flux is thought to be a reliable

energetic proton events can be used. For these well connected events the peak flux is thought to be a reliable indicator of the particle fluence injected into space [68, 69]. Investigations have yielded a surprising lack of correlation between the number of interacting and escaping particles (see [70, 71]). This is confirmed by a recent compilation of gamma-ray line events (GRL) and solar energetic proton events (SEP's) observed from February 1980 through January 1985 [72]. It is pointed out that this lack is primarily due to several large proton events for which no gamma-ray line emission was detectable. Conversely, however, GRL events are mostly associated also with SEP's. If the ratio (R) of the number of interacting to escaping protons is plotted versus the decay time of the flare soft X-ray emission, a tendency is evident in the sense that R is high ($\approx$ 100) for impulsive events and gets progressively lower for long duration events (see also [73, 1, 14]). This tendency implies that for impulsive flares the accelerated particles are effectively confined in closed (low lying) magnetic flux tubes and thus make gamma-ray lines so readily observable, whereas for long duration events the particles have easy access to open magnetic field structures. A new twist is added when the occurrence of coronal mass ejections (CME's), which represent the low energy end of accelerated particles, is correlated with GRL events [74]. It is found that after GRL events fast CME's are observed, irrespective if the flare is impulsive or gradual. On the other hand, there are fast CME's which lack an association with GRL events. It is therefore argued that CME's are not a sufficient condition for GRL events to occur, but that they can represent favourable conditions for proton acceleration through reconnection in the lower corona, which then lead to nuclear reactions resulting in gamma-ray line emission.

7. Concluding Remarks. Before the Sun was routinely observed in the gamma-ray regime by the SMM and Hinotori satellites, gamma-ray line radiation in flares was assumed to be a characteristic only of some very large and outstanding events. Since then evidence for line emission was obtained in more than 100 flares. The measurements yield new and stringent constraints on models describing the acceleration of charged particles as it is shown that ions and electrons can be accelerated to high energies in one step rather promptly. The ratio of the fluences of certain nuclear lines gives a handle to deduce spectral parameters of the primary accelerated particles. The absolute values of the line fluences are used to calculate the number of particles interacting in the solar atmosphere, which can be compared with the number of the escaping ones. In view of these capabilities one would expect the gamma-ray domain to get better notice in the literature dealing with flare phenomena.

Acknowledgements. This work was supported by the Bundesministerium für Forschung und Technologie under 010K017-ZA/WS/WRK 0275:4 in Germany.

REFERENCES

1. R. Ramaty and R.J. Murphy, Space Sci. Rev. 45, 213 (1987)
2. D.J. Forrest and R.J. Murphy, Solar Phys. 118, 123 (1988)
3. R.J. Murphy, X.-M. Hua, B. Kozlovsky, and R. Ramaty, Astrophys. J., 351, 299 (1990)
4. R.J. Murphy, G.H. Share, J.R. Letaw, and D.J. Forrest, Astrophys. J. 358, 298 (1990)
5. C. Werntz, F.L. Lang, and Y.E. Kim, Astrophys. J. Suppl. 73, 349 (1990)
6. R.J. Murphy, R. Ramaty, B. Kozlovsky, and D.V. Reames, Astrophys. J. 371, 793 (1991)
7. E. Rieger, in "Gamma-Ray Line Astrophysics", edited by Ph. Durouchoux and N. Prantzos, New York: AIP, in press 1991
8. R. Ramaty, B. Kozlovsky, and R.E. Lingenfelter, Astrophys. J. Suppl. 40, 487 (1979)
9. R. Ramaty, R.J. Murphy, B. Kozlovsky, and R.E. Lingenfelter, Solar Phys. 86, 395 (1983)
10. R.J. Murphy, "Gamma Rays and Neutrons from Solar Flares" Ph.D. thesis, Univ. of Maryland, 1985
11. R. Ramaty, B. Kozlovsky, and R.E. Lingenfelter, Space Sci. Rev. 18, 341 (1975)
12. R.J. Murphy, C.D. Dermer, and R. Ramaty, Astrophys J. Suppl. 63, 721 (1987)

13. H.T. Wang and R. Ramaty, Solar Phys. 36, 129 (1974)
14. X.-M. Hua and R.E. Lingenfelter, Solar Phys. 107, 351 (1987)
15. C.J. Crannell, G. Joyce, R. Ramaty, and C. Werntz, Astrophys. J. 210, 582 (1976)
16. R. Ramaty, in "The Physics of the Sun, Vol. II, Cap. 14, edited by P.A. Sturrock, T.E. Holzer, D. Mihalas, and R.K. Ulrich; D. Reidel Publ. Co., Dordrecht, Holland, p. 291, 1986
17. B. Kozlovsky, R.E. Lingenfelter, and R. Ramaty, Astrophys. J. 316, 801 (1987)
18. E.L. Chupp, D.J. Forrest, J.M. Ryan, J. Heslin, C. Reppin, K. Pinkau, G. Kanbach, E. Rieger, and G.H. Share, Astrophys. J. 263, L95 (1982)
19. E.L. Chupp, H. Debrunner, E. Flückiger, D.J. Forrest, F. Golliez, G. Kanbach, W.T. Vestrand, J.F. Cooper, and G.H. Share, 20th Int. Cosmic Ray Conf. Papers 3, 61 (1987)
20. H. Debrunner, E. Flückiger, E.L. Chupp, and D.J. Forrest, 18th Int. Cosmic Ray Conf. Papers 4, 75 (1983)
21. G.E. Kocharov, 18th Eur. Cosmic Ray Symp., Invited Talks,p. 51 (1983)
22. M.A. Shea, D.J. Smart, and E.O. Flückiger, 20th Int. Cosmic Ray Conf. Papers 3, 86 (1987)
23. K. Takahashi, M. Wanda, M. Yoshimori, M. Kusunose, and I. Kondo, 20th Int. Cosmic Ray Conf. Papers 3, 82 (1987)
24. A.T. Filippov, 21th Int. Cosmic Ray Conf. Papers 5, 133 (1990)
25. D.F. Smart, M.A. Shea, E.O. Flückiger, H. Debrunner, and J.E. Humble, Astrophys. J. Suppl. 73, 269 (1990)
26. P. Evenson, P.Meyer, and K.R. Pyle, Astrophys. J. 274, 875 (1983)
27. P. Evenson, R. Kroeger, and P. Meyer, 19th Int. Cosmic Ray Conf. Papers 4, 130 (1985)
28. P. Evenson, P. Kroeger, P. Meyer, D.V. Reames, Astrophys. J. Suppl. 73, 273 (1990)
29. M.A. Shea, D.J. Smart, M.S. Wilson, and E.O. Flückiger, Geophys. Res. Letters 18(5), 829 (1991)
30. G. Kanbach, K. Pinkau, C. Reppin, E. Rieger, E.L. Chupp, D.J. Forrest, J.M. Ryan, G.H. Share, and R.L. Kinzer, 17th Int. Cosmic Ray Conf. Papers 10, 9 (1981)
31. T.A. Prince, D.J. Forrest, E.L. Chupp, G. Kanbach, and G.H. Share, 18th Int. Cosmic Ray Conf. Papers 4, 79 (1983)
32. X.-M. Hua and R.E. Lingenfelter, Solar Phys. 113, 229 (1987)
33. E. Rieger, Solar Phys. 121, 323 (1989)
34. G.H. Share, E.L. Chupp, D.J. Forrest, and E. Rieger, in "Positron-Electron Pair in Astrophysics", edited by M.L. Burns, A.K. Harding, and R. Ramaty, New York: AIP, p. 15 (1983)
35. R.J. Murphy and R. Ramaty, Adv. Space Res. 4(7), 127 (1984)
36. T. Bai, 'Studies of Solar Hard X-Rays and Gamma Rays: Compton Backscatter Anisotropy, Polarization and Evidence for Two Phases of Acceleration', Ph.d. thesis, University of Maryland, 1977
37. B. Kozlovsky and R. Ramaty, Astrophys. J. 191, L43 (1974)
38. J.C. Crannell, H. Crannell, and R. Ramaty, Astrophys. J. 229, 762 (1979)
39. J.A. Ibragimov and G.E. Kocharov, Soviet Astron. Letters 3, 211 (1977)
40. R. Ramaty, B. Kozlovsky, and A.N. Suri, Astrophys. J. 214,617 (1977)
41. D.J. Forrest, in 'Positron-Electron Pairs in Astrophysics', edited by M.L. Burns, A.K. Harding, and R. Ramaty, New York: AIP, p.3 (1983)
42. F.W. Bech, R. Schlickeiser, and J. Steinacker, Solar Phys. Letters 129, 195 (1990)
43. E. Rieger and H. Marschhäuser, in 'MAX 91/SMM Solar Flares, Observations and Theory, edited by R.M. Winglee and A.L. Kiplinger, Proc. of MAX 91 Workshop No.3, Estes Park, Colorado, p. 68 (1990)
44. H. Marschhäuser, E. Rieger, and G. Kanbach, 22nd Int. Cosmic Ray Conf. Abstracts 2, SH 2.3.1, p. 463 (1991)
45. J.P. Wild, S.F. Smerd, and A.A. Weiss, Ann. Rev. Astron. Astrophys. 1, 291 (1963)
46. C. de Jager, in 'Solar Flares and Space Research', Proc. 11th Symp. Plenary Meeting COSPAR, North-Holland, Amsterdam, 419, p.1 (1969)
47. S.R. Kane, in 'Coronal Disturbances', edited by G. Newskirk Jr., IAU Symp. 57, 105 (1974)
48. E.L. Chupp, Ann. Rev. Astron. Astrophys. 22, 359 (1984)
49. J.M. Ryan, Solar Phys. 105, 365 (1986)
50. J.A. Miller and R. Ramaty, Astrophys. J. 344, 973 (1989)
51. X.-M. Hua, R. Ramaty and R.E. Lingenfelter, Astrophys. J. 341, 516 (1989)
52. V.G. Gueglenko, G.E. Kocharov, G.A. Kovaltsov, L.G. Kocharov, and N.Z. Mandzhavidze, Solar Phys. 125, 91 (1990)
53. V.G. Gueglenko, Yu.E. Efimov, G.E. Kocharov, G.A. Kovaltsov, N.Z. Mandzhavidze, M.M. Terekhov, and L.G. Kocharov, Astrophys. J. Suppl. 73, 209 (1990)
54. R. Ramaty, J.A. Miller, X.-M. Hua, and R.E. Lingenfelter, Astrophys. J. Suppl. 73, 199 (1990)
55. E.L. Chupp, H. Marschhäuser, M. Pick, G. Trottet, E. Rieger, and P.P. Dunphy, 22nd Int. Cosmic Ray Conf. Abstracts 2, SH 2.3.3, p. 465 (1991)
56. P.P. Dunphy, E.L. Chupp, and E. Rieger, 21th Int. Cosmic Ray Conf. Papers 5, 75 (1990)

57. T. Bai and R. Ramaty, Astrophys. J. 227, 1072 (1979)
58. L. Vlahos + 26 authors, in 'Energetic Phenomena on the Sun', edited by M. Kundu and B. Woodgate, NASA CP-2439, Greenbelt, Maryland, p. 2-1 (1986)
59. G.E. Kocharov, in 'The Sun and Planetary System', edited by W. Fricke and G. Teleki, D. Reidel Publ. Co., Dordrecht, Holland, p. 47 (1982)
60. E. Rieger, in 'Hinotori Symp. on Solar Flares', Inst. Space Astronautical Sciences, Tokyo, p. 246 (1982)
61. E.L. Chupp, D.J. Forrest, W.T. Vestrand, H. Debrunner, E. Flückiger, J.F. Cooper, G. Kanbach, C. Reppin, and G.H. Share, 19th Int. Cosmic Ray Conf. Papers 4, 126 (1985)
62. D.J. Forrest, W.T. Vestrand, E.L. Chupp, E. Rieger, J.F. Cooper, and G.H. Share, 19th Int. Cosmic Ray Conf. Papers 4, 146 (1985)
63. F.G. McDonald and M.A.I. van Hollebeke, Astrophys. J. 290, L67 (1985)
64. G.E. Kocharov, L.G. Kocharov, G.A. Kovaltsov, and N.Z. Mandzhavidze, Preprint 1258, Academy of Sciences of the USSR, A.F. Ioffe Physico Technical Institute, Leningrad, 1988
65. J.M. Ryan, D.J. Forrest, and W.T. Vestrand, 21th Int. Cosmic Ray Conf. Papers 5, 52 (1990)
66. E.L. Chupp, Astrophys. J. Suppl. 73, 213 (1990)
67. X.-M. Hua and R.E. Lingenfelter, Astrophys. J. 323, 779 (1987)
68. M.A.I. van Hollebeke, L.S. Ma Sung, and F.B. McDonald, Solar Phys. 41, 189 (1975)
69. M.A.I. van Hollebeke, Rev. Geophys. Space Phys. 17, 545 (1979)
70. E.W. Cliver, D.J. Forrest, R.E. McGuire, KT.T. von Rosenvinge, D.V. Reames, H.V. Cane, and S.R. Kane, 20th Int. Cosmic Ray Conf. Papers 3, 61 (1987)
71. M.-B. Kallenrode, E. Rieger, G. Wibberenz, and D.J. Forrest, 20th Int. Cosmic Ray Conf. Papers 3, 70 (1987)
72. E.W. Cliver, D.J. Forrest, H.V. Cane, D.V. Reames, R.E. McGuire, T.T. von Rosenvinge, S.R. Kane, and R.J. McDowall, Astrophys. J. 343, 953 (1989)
73. T. Bai, Astrophys. J. 308, 912 (1986)
74. E.W. Cliver, H.V. Cane, D.J. Forrest, M.J. Koomen, r.A. Howard, and C.S. Wright, Astrophys. J. 379, (1991)
75. T. Bai and P.A. Sturrock, Ann. Rev. Astron. Astrophys. 27, 421 (1989)

RADIO EMISSION OF ERUPTIVE FLARES

Marian Karlický
Astronomical Institute, Czechoslovak Academy of Sciences
251 65 Ondřejov, Czechoslovakia

Abstract

Radio spectra of some eruptive flares are described. Most of them do not conform to the classical spectrum schema. Both the type I burst chains associated with the filament activation phase of the May 16, 1981 flare, and the slow negative drift of the group of type III and U bursts in the July 12, 1982 and June 15,1991 flares illustrate the upwards expansion of complete magnetic structures. In some eruptive flares, e.g. April 24, 1985, reverse drift bursts are observed prior to the upwards expansion. In addition, narrowband dm-spikes and a variety of positively drifting features are frequently observed. These are believed to be radio signatures of localized reconnections and of the spreading of flare dissipative processes. Results of numerical simulations supporting these ideas are presented.

1. Introduction

Due to radiative processes of superthermal particles the radio bursts observed during solar flares are traces of superthermal particles from their accelerations up to their relaxations. While for the radio emission of superthermal particles on frequencies higher than 1000 MHz the gyrosynchrotron mechanism is usually considered, on lower frequencies the collective plasma processes generating radio bursts are assumed. In the later case the causes of radio emission are always the processes, in which the free energy of superthermal particles is transformed into electromagnetic waves by plasma instabilities and nonlinear effects. From such a point of view we want to analyze the radio emission of eruptive flares. Firstly, the radio spectra of some eruptive flares are presented and then the corresponding flare plasma processes are discussed.

2. Observations

Comparing the Figure 1 and the 'typical' radio spectrum of solar flares (Figure III.26, Krüger,1979) we can see that the radio spectrum

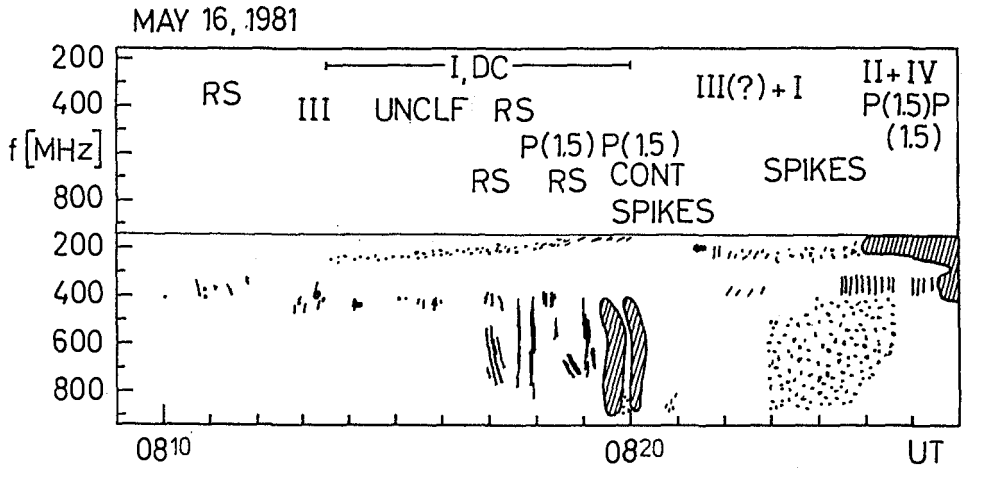

Fig.1. Radio spectrum schema of the May 16,1981 flare. In the upper part the spectrum is described.

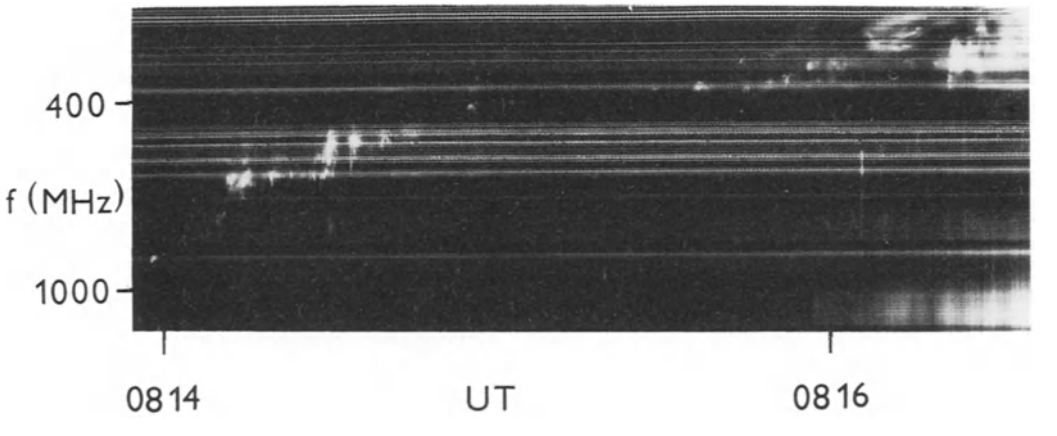

Fig.2. Radio spectrum of the June 15,1991 flare.

of the eruptive flare from May 16, 1981 differs in several aspects. Firstly, the flare starts with reverse drift bursts. Secondly, the group of broadband type III radio bursts, which is considered as a radio signature of impulsive phase, is missing. On the other hand we can see a global drift of all these bursts towards lower frequencies. This is expressed by type I negatively-drifting chains , which were observed just after Hα filament activation (Fárník et al., 1983; Karlický and Jiřička,1983)) and by the frequency drift of group of narrowband dm-spikes at 0825-0826 UT. Moreover in this phase interesting positively drifting features were observed at 0817-0821 UT. A similar sequence of radio bursts were observed during the July 12, 1982 and April 24, 1985 eruptive flares (Aurass et al.,1987). The flares start again with the reverse drift bursts, followed by a negatively drifting group of type III and U bursts. Further example of radio spectrum with the negatively drifting group of type U bursts is the radio spectrum of the June 15,1991 eruptive flare (Figure 2).

3. Interpretations

a) Global slow-negative frequency drift of radio bursts

According to the models (Van Tend and Kuperus,1978; Priest,1982; Kaastra,1985; Forbes and Isenberg,1991) the eruptive flares start due to an instability of the arcade of magnetic loops, crossing over the magnetic field neutral line. The arcade expands and the filament, which is usually carried by this arcade, is moving upwards; the filament is activeted. Assuming the plasma radiative mechanism for bursts under study and sequential acceleration of beams in such expanding arcade, we obtain just the group of type U or III bursts observed successively on lower and lower frequencies. Similar observations of the June 27, 1981 eruptive flare were described in the paper of Leblanc et al. (1983). This flare scenario also agrees with the observed type I burst chains, which are according to Spicer et al. model (1981) the radio emission from weak MHD shock, forming on the upper boundary of expanding magnetic loops.

b) Reverse drift bursts and positively drifting features

In the paper by Fárník et al. (1983) the following working hyphothesis was suggested: In a distant small flare an electron beam was accelerated. Then, propagating along the huge coronal loop, it generates on its downward path the reverse drift bursts and finally penetrates into the current system of the main flare. Here the beam, through generation of Langmuir waves, increases the electric

resistivity and thus triggers the flare. This hyphothesis is interesting not only for the interpretation of the first group of reverse drift bursts at 0750 UT of the May 16,1981 flare or for the explanation of so called sympathetic flares (Švestka,1981) but also for the flare process itself. Namely, in agreement with the paper by Norman and Smith (1978), we believe that the flare dissipative processes are spreading in the flare volume and that electron beams are the transport agents of such spreading. We suggest that some reverse drift bursts and positively drifting features can be interpreted by such processes. Numerical simulations supporting these ideas are presented in the following.

c) Narrowband dm-spikes

The observational characteristics of these spikes were described in papers by Benz (1986) and Karlický (1984,1986). Although in most cases the dm-spikes were observed during the flare impulsive phases, in eruptive flares these spikes are observed later, usually prior to the type II burst observation. In the May 16,1981 flare the group of these spikes coincides with the first peak of the hard X-ray and 6-cm radiations. There are two classes of dm-spikes models: plasma models (Kuipers et al.,1981; Tajima et al.,1990; Wentzel,1991), and models based on electron cyclotron maser (Melrose and Dulk, 1982; Winglee and Dulk,1986; Li,1986). It was suggested that the narrowband dm-spikes are the radio signatures of runaway electrons accelerated in localized reconnections (Kuijpers et al.,1981). This model is close to the microflare concept of solar flares (Vlahos,1991).

4. Numerical results supporting the presented interpretation

a) Effects of externally generated Langmuir waves in current-carrying plasmas (Karlický and Jungwirth, 1989; Jungwirth and Karlický,1989).

Among the presented ideas triggering and spreading of flare dissipative processes by electron beam belongs to the most important. The full solution of this problem is difficult, and therefore, we studied only the effects of the presence of externally (by beam) generated Langmuir waves in current-carrying plasmas. Firstly, we showed that the Zakharov equations (Zakharov, 1972), describing nonlinear interactions between Langmuir and ion-sound waves, remains formally the same also for current-carrying plasma. But the variables must be transformed. This enables us to use all known solutions of Zakharov equations also for current-carrying plasma. This analytical

base was used for the interpretation of our numerical results: The task was solved by the electrostatic particle code (Karlický,1987). The computation was made in the system with $L = \lambda = 100\lambda_D$, $m_i/m_e = 100$, with 20000 particles. In the initial state the momochromatic wave with wavelength λ and energy $w/n_e kT_e = 0.3$ was generated. Then the development of electrostatic field energy of such system for various electron-proton drift was computed. In all cases the Langmuir wave energy was absorbed in the system. This is because the modes, generated from the unstable original wave, strongly interact with the background plasma particles. Thus the plasma is heated. In the case of nonzero electron-proton drift we found some additional heating coming from electron-proton drift. That means that Langmuir waves stimulate the dissipation of current energy. In such a sence the electron beam can trigger and spread the flare dissipative processes.

b) Responce of current sheet to a time-limited enhancement of electric resistivity (Karlický, 1988)

From the macroscopic point of view the above discussed Langmuir wave effects represent anomalous resistivity. Now the question arises what happens when such processes occur in the current sheet. Firstly, similarly to the paper by Ugai (1982) we solved the set of MHD equations in the current sheet, where in one location we increased electric resistivity. At this X-point we studied the evolution of pressure, mass density, and electric current. We obtained results, which are typical for a reconnection in the current sheet. Then we interrupted the asssumed resistivity enhancement at different times. For the early interruption we found a very slow evolution of the current sheet. On the other hand, when we interrupt the resistivity enhancement in a later phase (after the plasma obtained relatively high velocities), the plasma through its inertia compresses the current sheet which leads to a fast growth of current densities. Some current threads can become unstable due to current instabilities and thus the new localized reconnections can start. Because these reconnections are the sources of new accelerated beams, the kinetic and MHD processes described here are obviously connected and form so called dissipation-spreading process in the sence of Norman and Smith's paper (1978). The presence of superthermal particles in such processes gives us a chance to observe them on radio waves.

References:

Aurass,H.,Chernov,G.P.,Karlický,M.,Kurths,J.,Mann,G.:1987,Solar Phys. 112,347.
Benz,A.O.:1986,Solar Phys.104,99.
Fárník,F.,Kaastra,J.,Kalman,B.,Karlický,M.,Slottje,C.,Valníček,B.: 1983,Solar Phys.89,355.
Forbes,T.G.,Isenberg,P.A.:1991, Astrophys.J. 273,294.
Jungwirth,K.,Karlický,M.:1989,Czech.J.Phys. B32,1285.
Kaastra,J.:1985, Solar Flares - An electrodynamic model, Thesis, Utrecht University.
Karlický,M.:1984,Solar Phys.92,329.
Karlický,M.:1986, Rapid Fluctuations in Solar Flares (eds.B.R. Dennis,L.E.Orwig), NASA Conf.Publ.2449,155.
Karlický,M.:1987,Bull.Astron.Inst.Czechosl.38,201.
Karlický,M.:1988,Bull.Astron.Inst.Czechosl.39,13.
Karlický,M.,Jiřička,K.:1983, Noise Storm Coordinated Observations (ed.E.O.Elgaroy), Rep.57,Inst.Astr.,Oslo,p.81.
Karlický,M.,Jungwirth,K.:1989,Solar Phys.124,313.
Krüger,A.:1979, Introduction to Solar Radio Astronomy and Radio Physics,D.Reidel Publ.Comp.,Dordrecht,Holland.
Kuijpers,J.,Van der Post,P.,Slottje,C.:1981, Astron.Astrophys.103,331.
Leblanc,Y.,Poquerusse,M.,Aubier,M.G.:1983, Astron.Astrophys.123,307.
Li,H.W.:1986,Solar Phys.104,131.
Melrose,D.B.,Dulk,G.A.:1982,Astrophys.J.259,844.
Norman,C.A.,Smith,R.A.:1978,Astron.Astrophys.68,145.
Priest,E.R.:1982,Fundamentals of Cosmic Physics 7,363.
Spicer,D.S.,Benz,A.O.,Huba,J.D.:1981,Astron.Astrophys.105,221.
Švestka,Z.:1981,in Solar Flare Magnetohydrodynamics (ed.E.R.Priest), Gordon and Breach Publ.Comp.,New York,47.
Tajima,T.,Benz,A.O.,Thaker,M.,Leboeuf,J.N.:1990,Astrophys.J. 353,666.
Ugai,M.:1982,Phys.Fluids 25,1027.
Van Tend,W.,Kuperus,M.:1978,Solar Phys.59,115.
Vlahos,L.:1991,Dynamics of Solar Flares (eds.B.Schmieder and E.R.Priest), Flares 22 Workshop,p.91.
Wentzel,D.G.:1991, Astroph.J. 373,285.
Winglee,R.M.,Dulk,G.A.:1986,Solar Phys.104,93.
Zakharov,V.E.:1972,Zh.Exp.Teor.Fiz.62,1745 (in Russian).

ARCSECOND DETERMINATION OF SOLAR BURST CENTERS OF EMISSION SIMULTANEOUS TO HIGH TIME RESOLUTION AND HIGH SENSITIVITY AT 48 GHZ*

J.E.R. Costa, E. Correia, P. Kaufmann
Centro de Radio-Astronomia e Aplicações Espaciais (CRAAE),
Escola Politécnica da USP, C.P. 8174,
05508 - São Paulo, SP, Brazil
and
R. Herrmann and A. Magun
Institute of Applied Physics, University of Bern,
Sidlerstrasse 5, CH-3012 Bern, Switzerland

(Extended Abstract)

A 48 GHz five-radiometer front-end and a fast data acquisition system was developed at the University of Bern and used together with the 13.7 m Itapetinga antenna to observe solar bursts. The system produces five beams overlapping by one HPBW (2 arcmin) as shown in Figure 1, and allows the spatial determination of the burst emission centers with angular accuracy of 5 to 19 arcseconds in absolute position, depending on the angular distance from baricenter, simultaneously to 1 ms time resolution and sensitivity of 0.04 s.f.u..

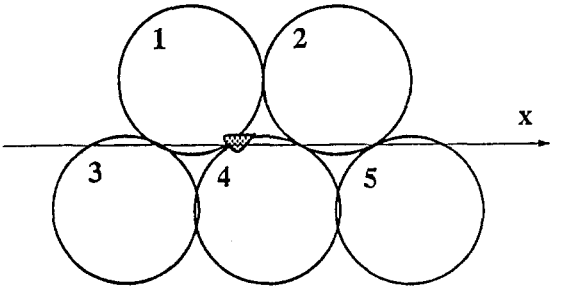

Fig. 1 - Spatial configuration of the five antenna beams. The contours are at one HPBW (2 arcminutes).

* A full version of this paper will be published elsewhere.

The system became operational late in 1989 and several solar bursts have been detected since then. All events have polarization and spectral information obtained at Bern or at OVRO, and some of them have also spatial information obtained by VLA and/or OVRO. Preliminary analysis of dynamic position behaviour of the emission centers, during impulsive events, suggests the existence of two broad classes of bursts. The first one, with 3 events, is a well localized kind of event, where the emission center remains inside an area of less than 22x22 arcsec, as the emission structures evolve in time (Figure 2). The other type, with 6 events, shows a large positional spread of the emission centers (Figure 3). Both types could be the result of a superposition of more than one source of activity, or a genuine source movement. The typical rate of emission center displacement is 10 arcsec/sec, comparable to Alfven velocities in solar plasmas, assuming movements, but can be 10 times higher in some cases. Possible limiting instrumental effects as well as the genuine physical movements of the bursting sources are discussed together with suggestions for interpretation.

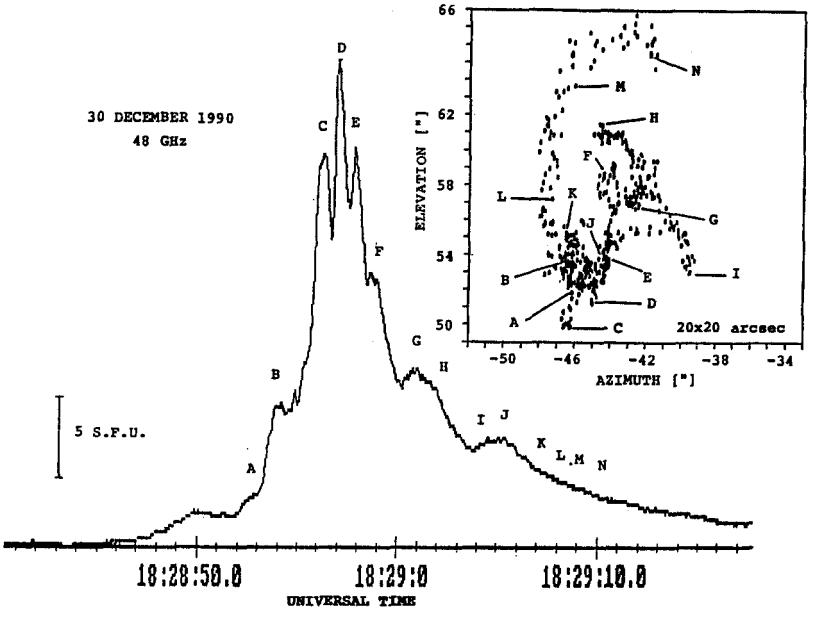

Fig. 2 - December 30, 1990 solar burst observed at Itapetinga Radio Observatory. In the box are the emission center positions relative to baricenter, at different times as marked in the event time profile. This is an example of a well localized event. The position variation stays inside an area smaller than 20 x 20 arcsec. The box scale is in arcsecs. The positions were calculated for fluxes above 3.6 s.f.u., and 32 ms time resolution.

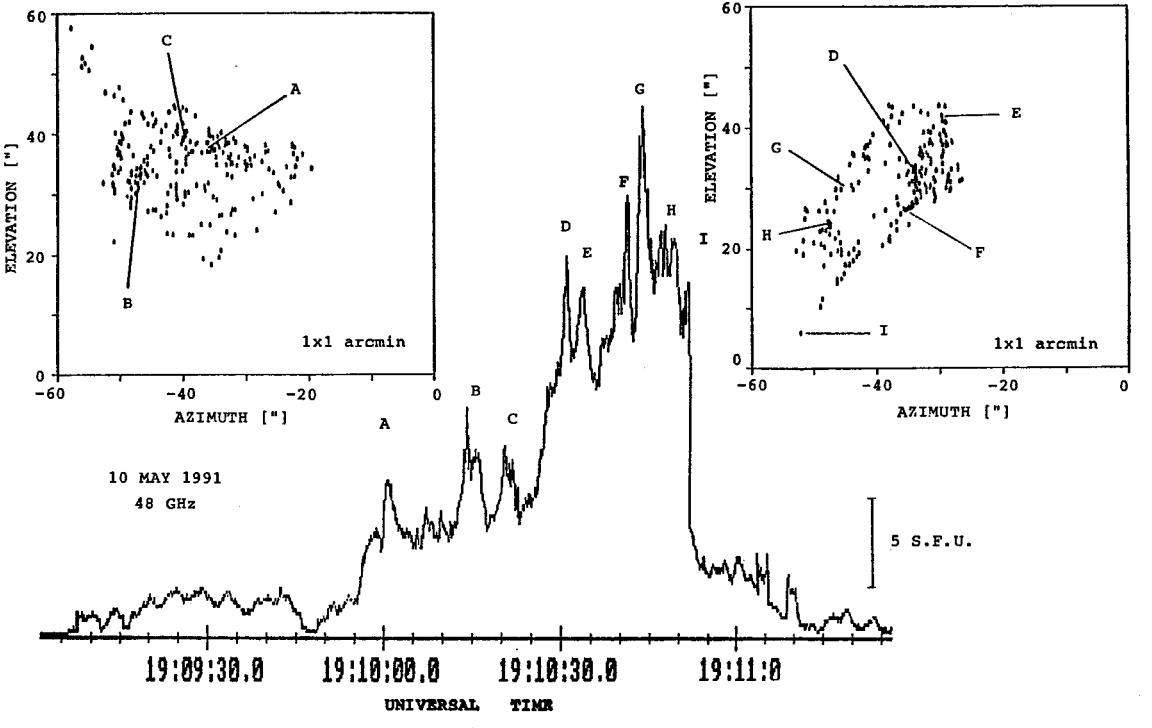

Fig. 3 - May 10, 1991 solar burst observed at Itapetinga Radio Observatory. In the boxes are the emission center positions relative to baricenter, at different times as marked in the event time profile. This example shows a kind of event with a large spread in position of the emission centers. Its area is 40x40 arcsec. The positions were calculated for fluxes above 3.6 s.f.u., and 128 ms time resolution.

TRAPPING AND ESCAPE OF THE HIGH ENERGY PARTICLES RESPONSIBLE FOR MAJOR PROTON EVENTS

Donald V. Reames
Laboratory for High Energy Astrophysics, Code 661
NASA Goddard Space Flight Center, Greenbelt, MD, 20771, USA

ABSTRACT

During the last few years, we have learned to distinguish the particle acceleration mechanisms involved in impulsive and gradual flares directly from particle observations at 1 AU. Energetic particles from impulsive flares are characterized as rich in electrons, ^{3}He, and Fe and high ionization states of Fe indicate that the material has been heated in the flare. Particles from these events are only seen from magnetically well-connected flares, and the particles reach maximum intensity in a few hours. Particles from gradual events have heavy element abundances (e.g. Fe/C) and ionization states that are near their coronal values but protons are strongly enhanced. Gradual events come from a wide longitude region and particle intensities remain high for several days, *much* longer than the associated phenomena at the Sun. Most major proton events are gradual events, but some are impulsive or have both impulsive and gradual phases. The extended evolution of the major proton events in space and time can no longer be understood in terms of slow diffusive transport of particles through the corona and interplanetary medium, since particles from the impulsive events are found to behave much differently. The observations can be understood only if the major gradual events involve a large interplanetary shock wave that accelerates particles over an extended region of longitude for a long time.

Wave-particle interactions play a major role in the trapping and acceleration of particles in large events. Streaming particles may be scattered by self-amplified waves that provide a throttling mechanism that limits the particle intensities from large events and distributes particles in time as they leak from the source region. Diffusive containment allows particle acceleration to occur on open as well as closed field lines in both impulsive and gradual events.

1. INTRODUCTION

Sometimes nature is a bit contrary. We try to study one thing and, in fact, we learn about something quite different. So it is with solar energetic particle (SEP) events. In the last few years we have focused heavily on the anomalous particle abundances associated with small impulsive solar flares (see review by Reames 1990a). These electron-, ^{3}He- and Fe-rich events provide information on the wave-particle interactions in the flare. The particles are only observed from magnetically well connected western flares and they stream outward from the flares to produce events that last only a few hours. However, it is not these events, themselves, that concerns us here, it is the revolution they have caused in our thinking about particle transport and storage that must also apply to the major proton events.

Most major proton events are different in character from impulsive-flare events (there are a few *large* impulsive-flare events with the properties described above). These events are dominated by protons, with H/He a factor of ~10 larger than the coronal value. Averaged over many events, however, the abundances of He and heavier elements are in excellent agreement with the coronal abundances. Ionic charge states are the same as those in the corona or solar wind typical of temperatures of $\sim 2 \times 10^6$ K, indicating that ambient material has been accelerated. The events are associated with gradual flares and 96% (Kahler *et al.* 1984) have

coronal mass ejections (CMEs). These particle events often last for days, remaining at peak intensity for most of this time, and they are associated with flare events at all longitudes across the visible solar disk, and sometimes beyond.

Historically, one of the most puzzling aspects of the major events is their duration. The particle intensities often peak 12-24 hours after the onset of the flare event, long after most of the flare-related phenomena at the Sun have died away. This is often explained by either storage of particles near the Sun and by slow diffusion of particles out to 1 AU with scattering mean free paths of <0.1 AU. But why do particles of the same energy from impulsive flares peak within 1-4 hours of the flare? If they come from compact flares deeper in the corona than the gradual events, why aren't they even more likely to be stored?

The large longitude span of the major events is equally problematic. If particles diffuse across field lines in the solar corona in gradual events, as has been proposed (Reid 1964; Wibberenz *et al.* 1989), why not in impulsive events? Heated Fe nuclei in +20 ionization states at energies above an MeV/amu are moving much too rapidly to capture electrons so as to reduce their ionization states to ~+13. Why aren't high charge states and enhanced abundances seen at large angles to the flare. Conversely, why aren't gradual-flare particles phenomena confined in longitude like those of impulsive flares?

Thus it is that observations in impulsive events have forced us to re-examine the physical processes of particle acceleration, containment and transport in major proton events.

2. PARTICLES FROM IMPULSIVE AND GRADUAL FLARES

One of the clearest characteristics of the particles from impulsive solar flares are the abundance enhancements. These events have enhancements in $^3He/^4He$ by factors as large as 10^4 and enhancements in Fe/C of ~10 compared with coronal values (see Reames 1990a). The Fe ions are highly ionized (+20), indicating heating to temperatures of $2x10^7$ K (Luhn *et al.* 1987). Impulsive events are also electron-rich (Cane, McGuire and von Rosenvinge 1986), they are associated with the electrons that produce type III radio bursts (Reames, von Rosenvinge and Lin 1985; Reames and Stone 1986). Electrons provide good timing information to determine flare associations of the particles, and the complete X-ray and radio properties of many events have been examined (Reames *et al.* 1988). Even though the particles are only observed from magnetically well-connected western flares (Reames, Kallenrode and Stone 1991), such flares are not rare, a recent study has examined abundances in a sample of 228 ^{3}He-rich events (Reames *et al.* 1991). Furthermore, there is now confirmation that the abundances of the energetic beam in a gamma-ray line flare show the same ^{3}He-rich, Fe-rich particle abundances inside the flare loops as those observed at 1 AU from impulsive flares (Murphy *et al.* 1991).

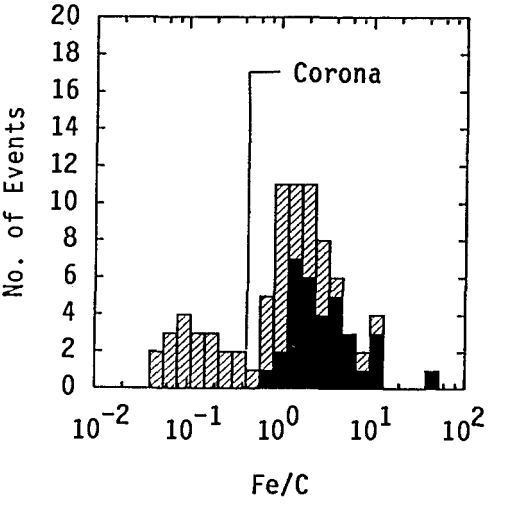

Fig. 1 Histogram of Fe/C for electron events.

A good comparison of the abundances in gradual and impulsive events is given by a recent study of electron events (Reames, Cane and von Rosenvinge 1990), where both classes are sampled. Figure 1 shows a histogram of the distribution of Fe/C for these events. The ^{3}He-rich events are identified by the blackened subset of the histogram. The distribution of this

same sample of events in flare longitude is shown in Figure 2a. Note that the Fe-rich events are clustered around W55° while the Fe-poor events are more evenly distributed in longitude. The corresponding longitude distribution of a sample of major proton events (Cane, Reames and von Rosenvinge 1991) is shown in Figure 2b. Note the even distribution of events in longitude and the generally lower values of Fe/C for the latter events. A few well-connected events in Figure 2b also have large values of Fe/C. These events usually have a strong impulsive phase and an Fe-rich population of energetic particles from this impulsive phase is seen early in the event, followed by Fe-poor particles (Reames 1990b).

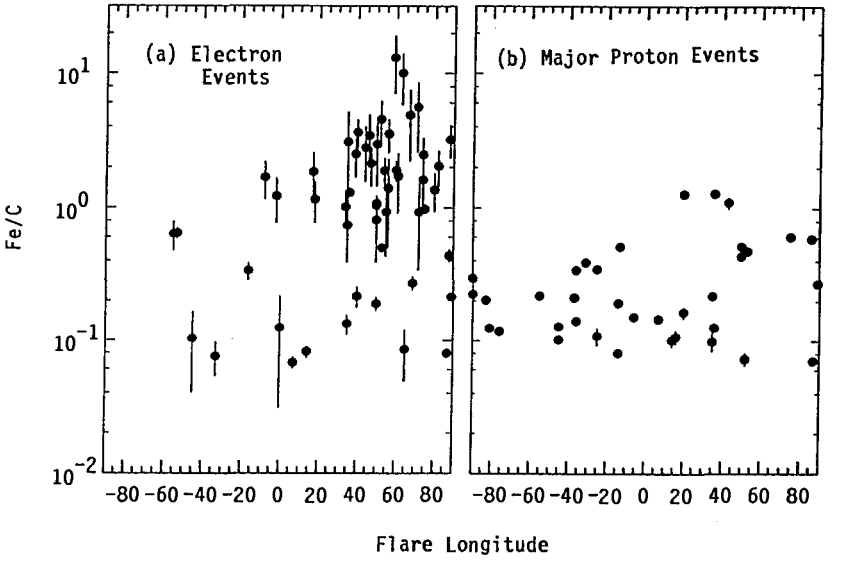

Fig. 2 Longitude distributions for electron events & major proton events.

3. TIME PROFILES

For many years studies of SEP time profiles were limited by instrument sensitivity to proton observations in large events. These slowly evolving profiles were fit to models involving impulsive injection at the Sun and slow diffusion to 1 AU (e.g. Reid 1964). The slow diffusion seemed necessary to explain why the proton events lasted days longer than the visible flares, and the models gave scattering mean free paths, λ, on the order of 0.1 AU or less (see Palmer 1982). As instrument sensitivity improved, however, we began to observe many impulsive events in which the particle transport was nearly scatter free ($\lambda \sim 1$ AU) as judged from the particle angular distributions as well as their profiles (Reames, von Rosenvinge and Lin 1985; Earl 1989; Mason *et al.* 1989).

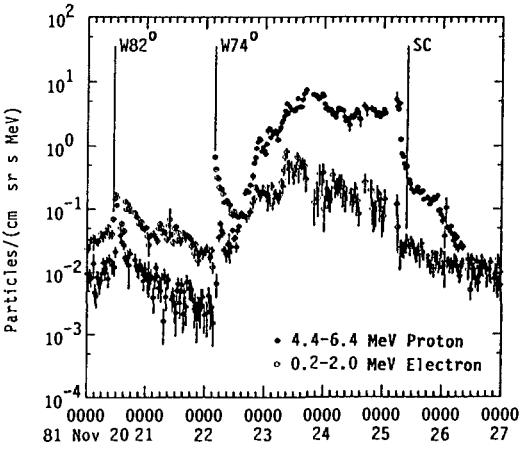

Fig. 3 Time profiles showing impulsive and gradual events.

Figure 3 shows an example of both impulsive and gradual events. Two impulsive flare

events, labeled by the flare longitudes, are dominated by electrons, but both electrons and protons peak within an hour of the flares (both events have Fe/C > 1). A large proton event begins from a W21° region a few hours after the second impulsive event and terminates near the time of passage of a shock (labeled SC), 3 days later. It is unlikely that the slow rise of the large proton event results from a sudden change in the properties of the interplanetary medium. An even more striking example of an impulsive event that occurs *during* a gradual event was shown by Mason *et al.* (1989). Recent work (Mason, Reames and Ng 1991) has shown that even classic "diffusive" profiles, observed by spacecraft at several heliospheric distances, can be fit by a slowly evolving source and rapid ($\lambda = 0.8$ AU) transport.

Very flat time profiles of MeV particles are common in major proton events. Several such profiles are shown in Figure 4 for major events selected by the presence of 135-206 MeV protons (see Reames 1990b). The 1982 June 3 event shown in the figure is best described as a large impulsive event; it has a declining profile and Fe/C=4.3 (Van Hollebeke, McDonald and Meyer 1990). The remaining events in the figure rise rapidly to a plateau in intensity, sometimes rising again to a maximum as the shock passes. The plateau region may be related to the maximum intensity of streaming particles that can emerge from the shock without producing self-amplified Alfvén waves that scatter and retard the streaming particles (Reames 1990b; Ng and Reames 1991). The flat time profiles may result from continuous acceleration by a shock wave as it propagates out to 1 AU (Lee and Ryan 1986).

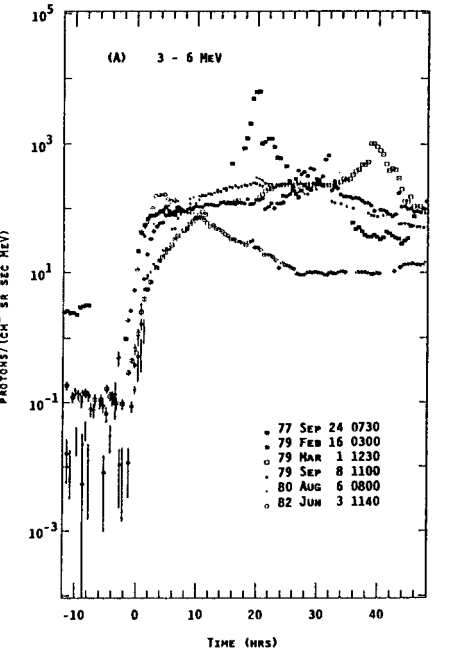

Fig. 4 Time profiles of major proton events often show an extended plateau region.

The time to maximum intensity is an important parameter when the particles are streaming outward so that this time is a property of the acceleration source. Since major proton events are virtually always accompanied by CMEs, Kahler, Reames and Sheeley (1990) plotted particle intensities as a function of the radial distance of the CME rather than a function of time. Such a plot is shown in Figure 5 for 1 MeV electrons and 175 MeV protons for 9 proton events. The events peak when the CME has propagated several solar radii above the surface and a greatly extended geometry must prevail. This late time of maximum is interpreted in terms of the evolution of the bow shock formed by the CME.

4. DISCUSSION

The studies of small impulsive flares have had a profound effect on our understanding of major proton events, namely:

(1) They have forced us to consider all events under nearly scatter-free interplanetary transport, implying long acceleration times for the major events.

(2) The longitude distribution of the impulsive events, as well as multi-spacecraft observations of them, suggests that most of the particles are confined to a narrow cone. If particles from impulsive flares are unable to diffuse freely through the corona, those from major flares should be equally constrained. We are forced to attribute the great

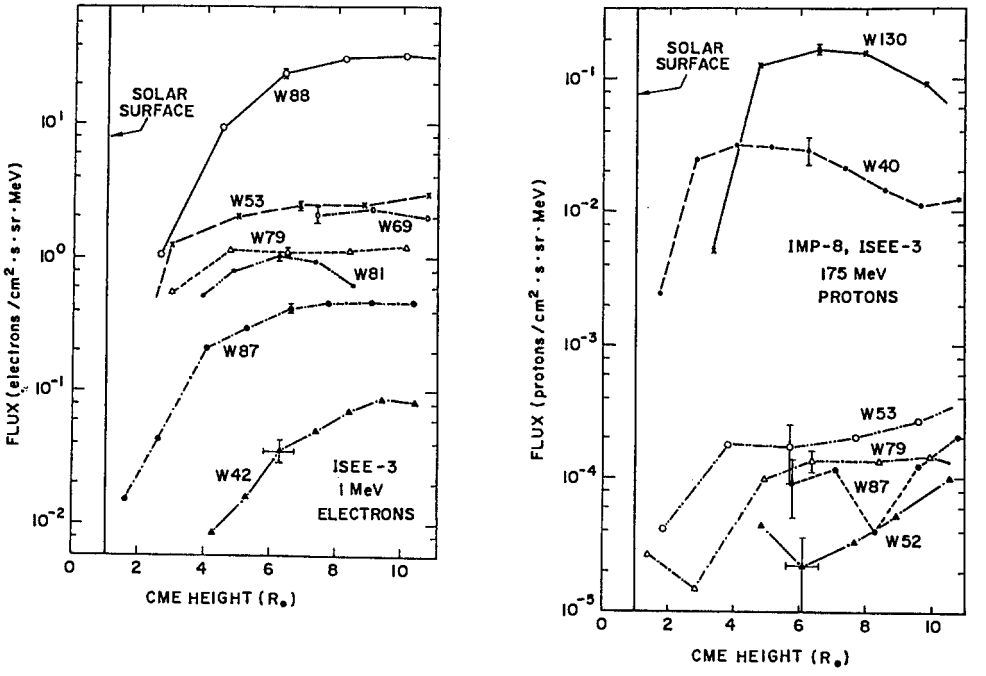

Fig. 5 Profiles of injected intensities of 1 MeV electrons (left) and 175 MeV protons (right) as a function of CME height.

longitude extent of the major events to a CME-driven shock wave that easily crosses magnetic field lines to accelerate particles throughout much of the inner heliosphere.

(3) Studies of impulsive flare events have provided a new tool, Fe/C or Fe/O, to distinguish particle acceleration modes. Within a single large well-connected event we can see an Fe-rich particle population, from the impulsive phase, early in the event followed by an Fe-poor population from the slowly evolving shock (Reames 1990b).

Meanwhile, the older paradigm, that postulated diffusive transport through the corona, has had little success during the last 25 years in identifying a mechanism that would make it easier for particles to cross field lines to spread uniformly throughout the corona than to escape the Sun. *A priori*, this model could parameterize abundance variations such as Fe/C in terms of rigidity (gyroradius) dependence in the transport, however, it is difficult to understand why multi-spacecraft observations (Wibberenz *et al.* 1989) show such a small longitude dependence in e/p where the rigidity (gyroradius) difference of the two species is a factor of ~1000. While parameters can be chosen to fit these data, a physical understanding is lacking. Transport-based models fail completely to explain the longitude-dependent observations of ^{3}He/^{4}He and of the charge state of Fe.

One of the more confusing aspects of the study of major proton events has been the varied appearance of the time profiles as a function longitude. These can be understood in terms of the large scale structure of the shock and its related driver gas moving radially outward from the Sun (Cane, Reames and von Rosenvinge 1988). For western events, the observer is only well connected to the shock early in the events, for eastern events, the peak intensity will occur after passage of the local shock when the observer is connected to the strong acceleration source near the nose of the shock. For events near central meridian, intensities may drop

near the time of shock passage as the observer enters the driver gas behind the shock. Generally speaking, the baffling array of intensity profiles can now be understood in terms of the large scale structure of the interplanetary shock.

Another lesson from small impulsive flares is that particle acceleration must occur on both open and closed field lines. In very small events with no shocks or CMEs evident, particles accelerated on closed loops have no avenue of escape; particles with gyroradii of ~ 1 cm are unlikely to escape a 10,000 km loop by scattering. Wave energy in the source can easily cause sufficient scattering, however, to effectively confine the particles on either open or closed field lines during acceleration. Particles in closed loops that leak from this diffusive containment region will eventually scatter into the loss cone to stop or interact in the denser atmosphere below, those on open field lines can stream away from the Sun. In terms of trapping, the situations for stochastic and shock acceleration are similar. In the latter case, particles are confined near the shock by self-amplified Alfvén waves generated by particles that streamed away previously (Lee 1983). Understanding wave-particle interactions has become central to our understanding of both trapping and acceleration in particle events of all sizes.

REFERENCES

Cane,H.V., McGuire,R.E., and von Rosenvinge,T.T. 1986, ApJ, 301, 448.

Cane,H.V., Reames,D.V. and von Rosenvinge,T.T. 1988, J. Geophys. Res., 93, 9555.

Cane,H.V., Reames,D.V. and von Rosenvinge,T.T. 1991, ApJ, 373, 675.

Earl,J.A., 1987, *Proc. 20th Internat. Cosmic Ray Conf.* (Moscow), 3, 198.

Kahler,S.W., Sheeley,N.R.,Jr., Howard,R.A., Koomen,M.J., Michels,D.J., McGuire,R.E., von Rosenvinge,T.T., and Reames,D.V. 1984, J. Geophys. Res., 12, 209.

Kahler,S.W., Reames,D.V. and Sheeley,N.R.,Jr. 1990, *Proc. 21st Internat. Cosmic Ray Conf.* (Adelaide), 5, 183.

Lee, M. A. 1983, J. Geophys Res., 88, 6109.

Lee,M.A., and Ryan,J.M. 1986, ApJ, 303, 829.

Luhn,A., Klecker,B., Hovestadt,D., and Möbius,E. 1987, ApJ, 317, 951.

Mason,G.M., Ng,C.K., Klecker,B., and Green,G. 1989, ApJ, 339, 529.

Mason,G.M., Reames,D.V. and Ng,C.K. 1991, *Proc. 22st Int. Cosmic Ray Conf.* (Dublin), to be published.

Murphy,R.J., Ramaty,R., Kozlovsky,B., and Reames, D.V. 1991, ApJ, 371, 793.

Ng,C.K. and Reames,D.V. 1991, *Proc. 22st Int. Cosmic Ray Conf.* (Dublin), SH 4.1.5, to be published.

Palmer,I.D. 1982, Rev. Geophys. Space Phys., 20, 335.

Reames,D.V. 1990a, ApJ Suppl. 73, 235.

Reames,D.V. 1990b, ApJ (Letters) 358, L63.

Reames,D.V., Cane,H.V., and von Rosenvinge,T.T. 1990, ApJ 357, 259.

Reames,D.V., Cane,H.V., von Rosenvinge,T.T. and Meyer,J.-P. 1991, *Proc. 22st Int. Cosmic Ray Conf.* (Dublin), SH 5.1.2, to be published.

Reames,D.V., Dennis,B.R., Stone,R.G., and Lin,R.P. 1988, ApJ 327, 998.

Reames,D.V., Kallenrode,M.-B., and Stone,R.G. 1991, ApJ, in press.

Reames,D.V. and Stone,R.G. 1986, ApJ, 308, 902.

Reames,D.V., von Rosenvinge,T.T. and Lin,R.P. 1985, ApJ, 292, 716.

Reid,G.C. 1964, J. Geophys. Res., 69, 2659.

Wibbewenz,G., Kecskemety,K., Kunow,H., Somogyi,A., Iwers,B., Logachev,Yu.I., and Stolpovskii,V.G. 1989,Solar Phys.,, 124, 353.

Van Hollebeke,M.A.I., McDonald,F.B., and Meyer,J.P. 1990, ApJ Suppl. 73, 285.

CORONAL AND INTERPLANETARY TRANSPORT OF SOLAR FLARE PROTONS FROM THE GROUND LEVEL EVENT OF 29 SEPTEMBER 1989

P.H. Stoker, PU/FRD Cosmic Ray Research Unit
Potchefstroom University for CHE, Potchefstroom 2520 SOUTH AFRICA

ABSTRACT

This behind-the-limb (assumed West 105 degrees) solar proton event was recorded by all global neutron monitors with an onset time at 1148 UT ± 2 minutes irrespective of viewing direction and cutoff rigidity. Neutron monitors with viewing directions of asymptotic longitude between 180 and 340 degrees East recorded a much faster rise time ($\sim$ 10% per minute) in count rate from onset to maximum than the $\sim$ 2% rise time between 0 to 100 degrees East, irrespective of cutoff rigidity. The exponential decay time changed from $\sim$ 40 minutes for $P_c \gtrsim 11$ GV to $\sim$ 200 minutes for $P_c \lesssim 1$ GV. These observations are compared with computations from models of coronal and interplanetary transport.

Introduction

At 1120 UT on 29 September 1989 an extremely intense solar radio emission typical of solar flare activity has been observed (Solar-Geophysical Data, 1989), with no solar H-alpha flare on the visible solar hemisphere that might be associated with an event having this intense radio emission. The solar patrol photographs (Swinson and Shea, 1990) show a behind-the-limb flare-like brightening, with loops of extraordinary long duration (> 10 hours) on the Sun's southwestern limb. These optical observations together with solar X-ray emission detected by the NOAA SMS/GOES spacecraft (Solar-Geophysical Data, 1989) with onset at 1047 UT, maximum 1133 UT, magnitude X 9.8) placed the flare at approximately 105 degrees West. The very intense and energetic solar nuclear particles that have been detected by ground-level cosmic ray neutron monitors around the globe, must have been produced by this flare.

Flare-associated solar energetic particles are usually assumed to be accelerated within the flare region, then released, subsequently propagating in the corona and lost gradually to the interplanetary magnetic field (IMF) lines for detection by spacecrafts and on Earth. Coronal transport is accepted on account of theoretical arguments and because observations have shown that particle populations were not generally able to diffuse across IMF lines. Reid (1964) and Axford (1965) postulated homogeneous isotropic two-dimensional diffusion of solar protons, released from the solar flare, between an inner reflecting boundary and an outer partially absorbing boundary surrounding the Sun in the solar corona. The particles leak through the outer boundary and move then along interplanetary magnetic field lines towards the points of observation. Axford assumed that diffusion perpendicular to the IMF lines was negligible in order to explain the initial anisotropy of an event. An irregular component of the IMF lets solar particles to propagate diffusively and accounts for the approach to isotropy.

Burlaga (1967) represented a mathematical model of solar flare particles diffusing anisotropically in the interplanetary medium without coronal diffusion. His results fit

both the increasing and decaying phases of solar flare particles recorded for many events. These early mathematical modellings of transport of particles released from solar flares have been refined since the sixties. The question still remains what the nature of the fast transport region in the solar corona is if such a region does exist, and whether the features of solar flare particles observed in interplanetary space could also be explained by rapid large-scale changes in coronal structures during a solar flare. An analysis of the features of this behind-the-limb solar cosmic ray flare event of 29 September 1989 may add new evidence on coronal acceleration and transport of near-relativistic and relativistic particles released from extremely energetic solar flares.

The rising phase

Figure 1 shows the average asymptotic viewing directions of neutron monitor stations. The geomagnetic field was very quiet from 27 through 29 September 1989, with Kp < 3, and no change in polarity of the mean solar magnetic field (Solar Geophysical Data, 1989). The IMF may therefore be the nominal Archimedean spiral with the solar flare particles arriving around the 315° East asymptotic direction.

Figure 2 shows the percentage enhanced counting rates relative to the prevailing cosmic ray counting rates for selected neutron monitors at sea level with different viewing directions in the ecliptic, plotted as a function of time. Deep River (DR), looking into the nominal IMF direction, did record a fast increase of counting rate (9% per minute) but Hobart (HO) recorded a faster increase (12% per minute). Sanae (SA) and Kerguellen (KE) with opposite viewing directions to Hobart and Deep Rivier respectively, show a slower rise of 2% per minute. This initial anisotropy becomes isotropic after about 2 hours. The nearest integral values of the percentage increases per minute in counting rates during the fast rising phase of the ground level enhancements (GLE) are displayed in Figure 3 for all stations with cutoff rigidity $\lesssim$ 10 GV. The underlined digits are the percentage increases per minute recorded by stations at mountain altitudes. From this Figure it follows that stations with viewing directions north of 25° S asymptotic latitude and between 180° and 340° E asymptotic longitude (band AB in Figure 4) have observed the fast rise in counting rates and have therefore been exposed directly to solar

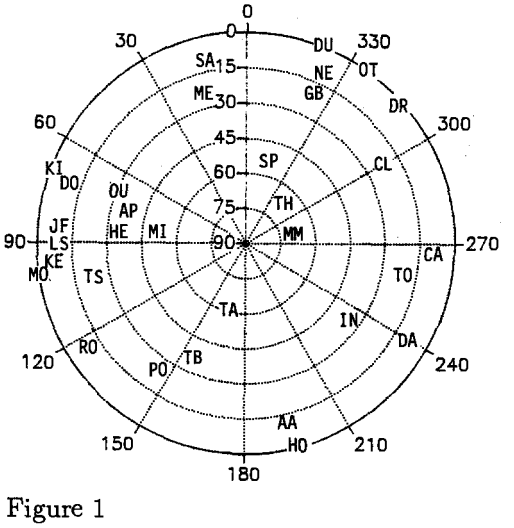

Figure 1

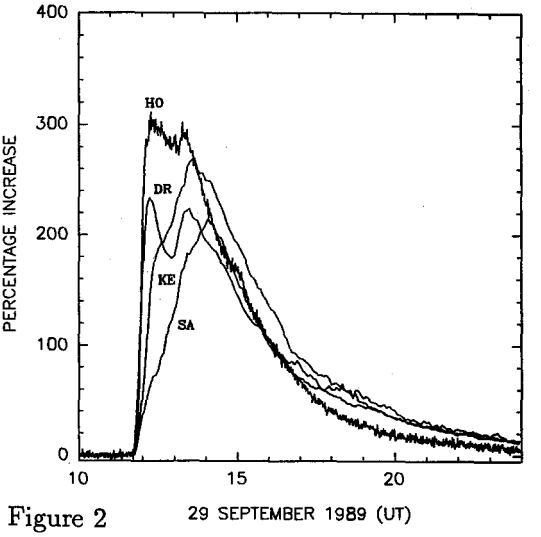

Figure 2

cosmic rays guided by the pervailing IMF. Stations with opposite viewing directions (band BC in Figure 4) experienced a much slower ($\sim$ 2% per minute) rise in neutron monitor counting rates. The rises of stations at high (3-10 GV) are similar to the rises at low ($<$ 3 GV) cutoff rigidities irrespective of the altitude of the station.

In Figure 4 percentage counting rates are plotted for neutron monitor enhancements $\leq$ 50% as a function of time for all neutron monitors with small time data of $\leq$ 5 minutes. Two broad bands appear: the one band, AB, are neutron monitors with fast rise times (see Figure 3) and the other band, BC, stations with opposite viewing directions. Potchefstroom and Samarkand fall in between (at B), while the south viewing stations Terre Adelie and Mirny, together with Sanae show further delays and slower increases. Three high-cutoff neutron monitors (Tokyo, Mount Norikura and Mexico) can be seen attaining their maximum intensities of less than 50% at $\sim$ 1200 UT. The

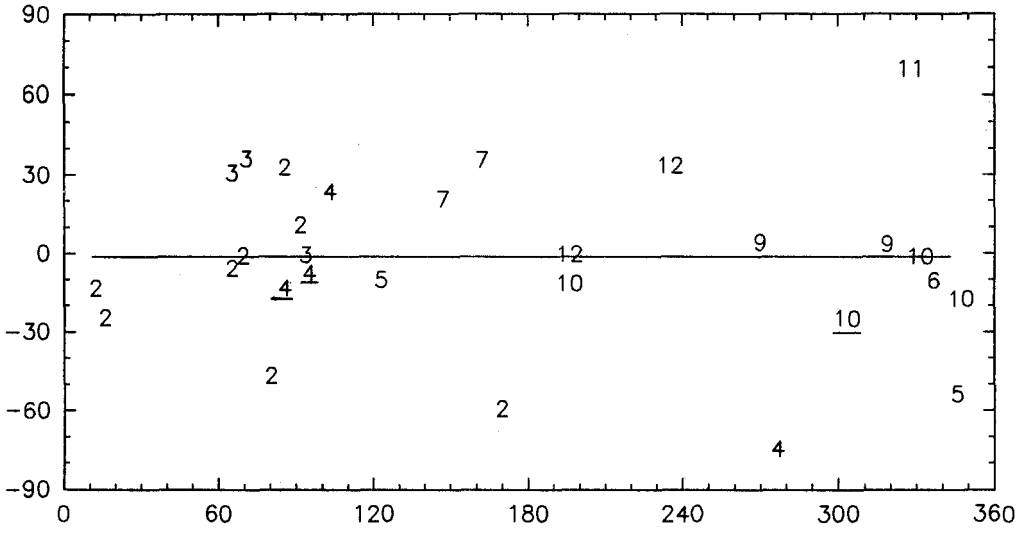

Figure 3

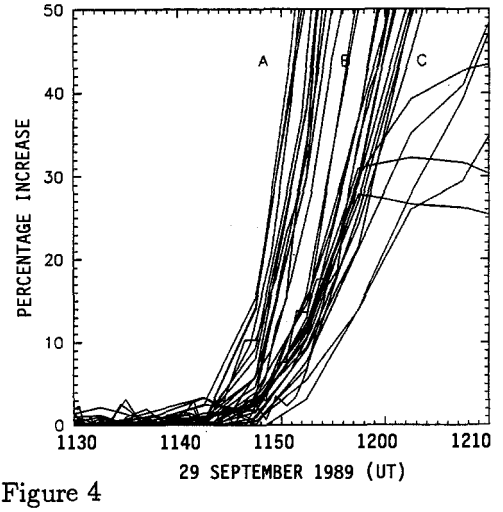

Figure 4

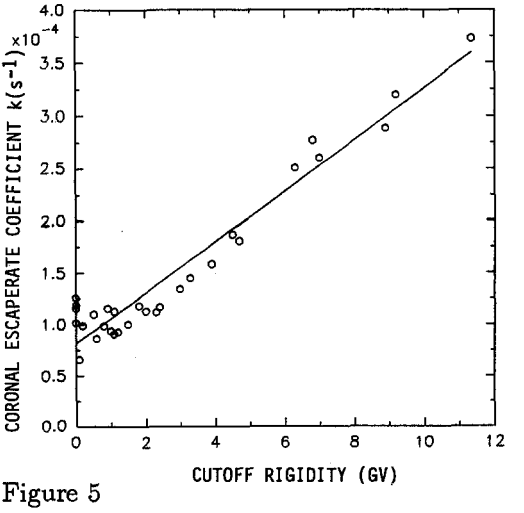

Figure 5

onset time of all the monitors appears to be at about 1148 ± 2 minutes. The second band BC is due to a slower initial rise of enhancements than recorded by the first (AB) set of monitors. This effect may be due to higher rigidity particles of several GV arriving first and settled then to a softer spectrum constant in time. The two-band structure together with the evidence in Figure 3 suggest that the particles were not transported in a diffusive interplanetary magnetic field with a gross-scale Archimedean configuration, but in an IMF with twisted IMF tubes of force in order to guide the particles to the two opposite viewing directional regions of Figure 3.

The decay phase

At later times the dependence described by the Reid (1964) equation changes to a linear variation in the logarithm of the counting rate with time. All the neutron monitor recordings show this linear relationship. Linear regression fittings to these slopes yield the coronal escape coefficients k. These coefficients have been plotted as a function of cutoff rigidity at the stations in Figure 5 illustrating clearly an energy dependence of k. The slope of the plot yields a change in the escape rate with cutoff rigidity of $0.28 \times 10^{-4} s^{-1} GV^{-1}$. On the other hand, both the rising and decaying phases can also be described by Burlaga's model without assuming coronal transport and escape. This model predicts that the counting rate due to solar flare protons is proportional to $(1/t)^{5/2} \exp(g/t)$, with t the time from escape. Applying this model to all the neutron monitor enhancements, the instance of escape from the solar flare is 1133±5 UT.

Conclusions

1. A structure of two twisted IMF tubes of force can explain the rising phase of the ground level enhancements.
2. The rise in counting rate did not depend on cutoff rigidity or on station altitude suggesting a time-independent release and transport of sub-relativistic and relativistic protons from the solar flare.
3. The escape rate coefficient, k, from the Reid model of coronal transport is a linearly increasing function of rigidity.
4. The instance of escape from the flare region is 1133±5 UT.
5. Both the simple Reid-Axford equations for coronal transport and Burlaga's mathematical model provide a good mathematical description of both the rising and decaying phases of the GLE's of 29 September 1989, notwithstanding that solar energetic particles of $\sim$ 1 GeV have been released extensively from the solar coronal region for several hours, and higher energy particles for a shorter time period. The alternative description that the particles have been accelerated over a large portion of the corona by large scale shock waves before released into the interplanetary medium without steady state coronal transport cannot be ruled out.

References

Axford, W.I., 1965, Planet. Space Sci. **13**, 1301-1309.
Burlaga, L.F., 1967, J. Geophys. Res. **72**, 4449-4466.
Reid, G.C., 1964. J. Geophys. Res. **69**, 2659-2667.
Solar Geophysical Data, NOAA, 1989, No. 542, part I and no. 543, part I.
Swinson, D.B., and M.A. Shea, 1990, Geophys. Res. Letters, **17**, 1073-1075.

HIGH ENERGETIC SOLAR PROTON FLARES OF 19 TO 29 OCTOBER 1989

M.A. Mosalam Shaltout
National Research Institute of Astronomy and Geophysics
Helwan - Cairo - Egypt

Abstract : The evolution of solar flare activity was followed by the method of cumulative summation curves according to observed H-alpha flares and X-ray bursts (measured on satellites) in the active region No. 5747 during one rotation when the energetic solar flares of 19 October 1989 occurred. It was found that the steep trend of increased activity sets on several tens of hours prior to the occurrence of the energetic flare, which could be used, together with other methods, for forecasts of major flares.

1. Introduction

The significant proton event which started on 19 October 1989 at 1305 UT, was commensurate in total fluence to the great proton event of August 1972. High solar activity persisted through 19 October as the solar region 5747 (coordinates lat. 27°S, long. 209°, CMD 7°E) of spot class DKC and area 1160 msh produced an energetic solar flare of X-ray emission level X13 and Hα importance 4B at 1258UT. This event was associated with major radio bursts.

Satellite altitude proton enhancements at greater than 10 Mev and 100 Mev occurred in the wake of the X13/4B flare. The greater than 10 Mev event began on 19 October at 1305 UT and reached a maximum of 73000 pfu on 20 October at 1600 UT. The event continued on 21 and 22 October. The greater than 100 Mev event began at 1710 UT on 19 October, peaked at 680 pfu at 1530 UT on 20 October, and ended at 2200 UT on 20 October. A ground-level event was observed on 19 October with increases over cosmic ray background of 45 percent. A polar cap absorption PCA began at 1315 UT on 19 October.

19 October saw geomagnetic field activity at quiet to active levels at middle latitudes field ranged from quiet to major storm levels. The field increased to severe storm level near 9 UT on 20 October as a result of the X13/4B flare of 19 October. Thereafter, field activity declined to active to minor storm level as the flare effects began to subside.

The development of the activity in the region where the proton flare occurred on 19 October 1989, is represented with the help of the method of summation curves like with some of the proton regions in the past [Krivsky (1975), and Mosalam Shaltout (1989)]. This method which shows the trends in the release of energy of active regions for flare and X-ray bursts, can be used to characterize typical intervals in the active region development, which often display the same trend of development over a number of days. The method can also be used as one of the ways of forecasting the occurrence of flares with emissions of energetic particles. If a steep trend, e.g., of the flare parameter F (H-alpha index) or X (X-ray index), is in evidence, one may expect a proton flare to occur one or a few days later.

2. Data treatment

The used data have been obtained from "Solar-Geophysical Data", Prompt Reports No. 543 and 544, published by NOAA, Boulder, Colorado, U.S.A.

The flare parameter F represents solar flares inclusive sub-flares observed in H-alpha in the world station network (Solar-Geophysical Data), defined by the daily summation of area of solar flares in millionths of the solar disk (MSD) which occurred in the investigated active region. The parameter X is defined as the daily summation of the peak flux of the X-ray bursts in the 1-8A° band in Wm^{-2} released in the investigated active region, as observed by the GEOS satellite (Solar-Geophysical Data).

East-west solar scans at 10.7 cm are taken daily at the Algonquin Radio Observatory of the National Research Council of Canada. Also, east-west strip scans of the sun at 21 cm are made available by Fleurs Radio Observatory of Sydney, Australia. The data of the both are available at "Solar-Geophysical Data". The daily solar radio flux produced by the solar region 5747 at 10.7 cm and 21 cm wavelength was estimated, from the east-west strip scans of the sun, for each day of the period 13-28 October, 1989. In an analogy to the method of Tanaka and Kakinuma (1964) for solar proton flare prediction, based on the ratio of solar radio flux of the proton flare productive active region at 3 cm to that of 8 cm wavelength the author adopted a similar method, based on the ratio of the solar radio emission of the active regions at 10.7 cm to that at 21 cm wavelength, for which data are available from 'Solar-Geophysical Data". According to Tanaka and Kakinuma (1964), the ratio is increasing a few days before the major flare occurrence.

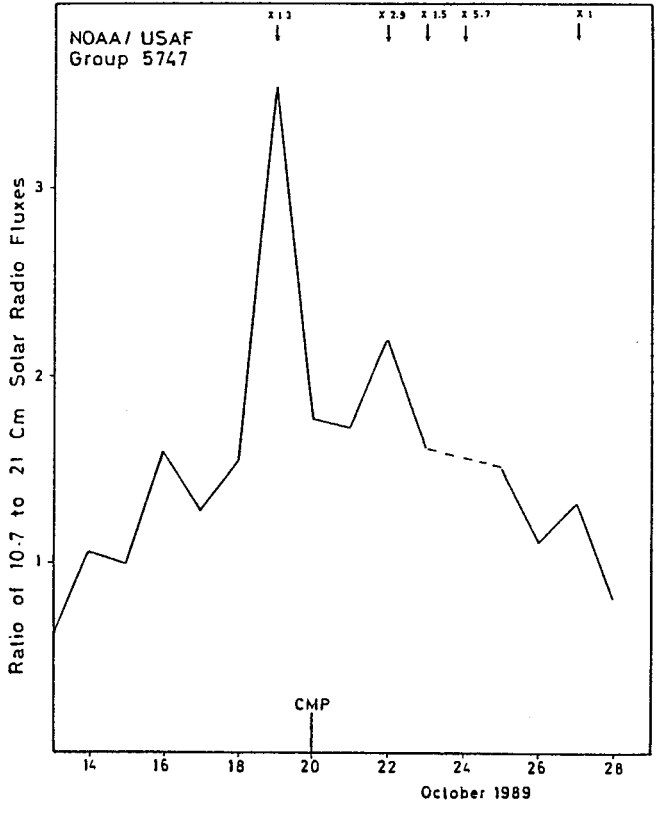

Fig. 2. Ratio of 10.7 to 21 cm solar radio fluxes for the active region No. 5747 during its crossing over the solar disk in the period 13-28 October, 1989.

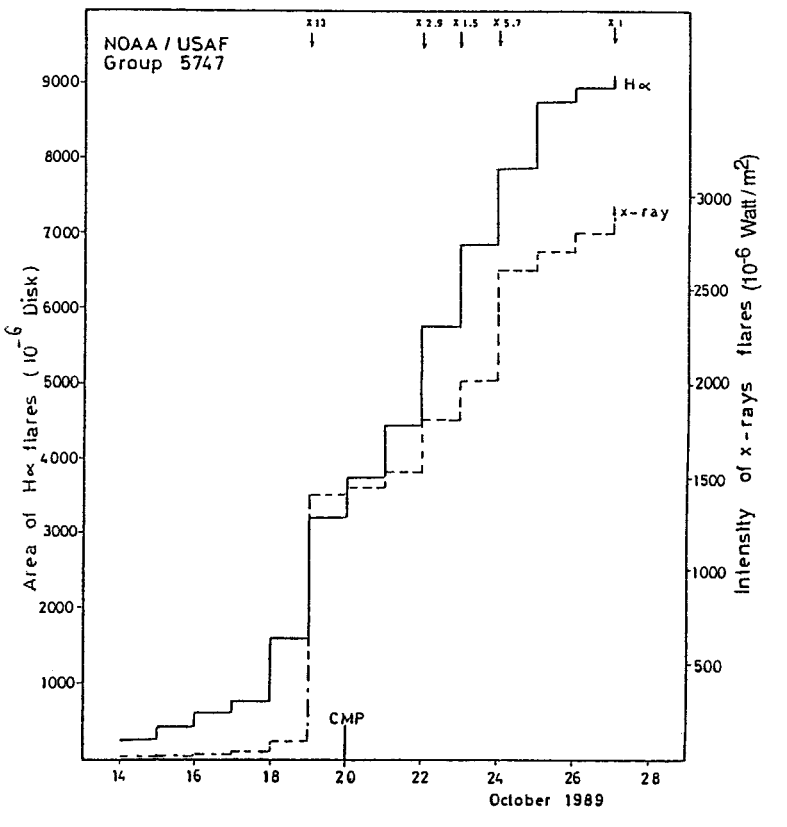

Fig. 1. Cumulative summation curves of F (____) and X (- -) for the observed H-alpha flares and X-ray bursts in the active region No. 5747 during one rotation in October 1989.

3. Results

The daily values of the flare parameter F and X of the studied active region were processed in the form of cumulative summation curves (Figure 1). The curve of F became more steep than that of X on 18 October, one day before the onset of the 19 October 1989 energetic flare.

Both the curves of F and X became more steep after 19 October, before the occurrence of a series of other energetic flares on 22, 23, 24 and 27 October 1989.

The changes of these trends are related to the development of the active region and to th type of spot groups, as well as to the configuration of magnetic fields. Also, the changes in the trends are correlated with the heating in the coronal condensations (Krüger, 1969).

Figure 2 shows the ratio of 10.7 to 21 cm solar radio fluxes for the studied active region during its crossing of the solar disk in the period 13-28 October. It is noticed that there is an increasing trend in the ratio from 13 to 19 October, 1989, before the occurrence of the energetic solar proton flare of 19 October. Also, after the ratio decrease on 20 and 21 October, it increased again on 22 October, before the occurrence of the energetic flare of 22 October.

4. Conclusion

The results show an increase in the trend of the flare activity (according to flare in H-alpha as well as according to X-ray bursts) several tens of hours prior to the occurrnece of a high energetic solar flares which could be used together with other methods (similar to that in Figure 2), for forecasting major and high-energy particle events.

References

Krivsky, L. : 1975, Bulletin of the Astronomical Institute of Czechoslovakia, Vol. 26, No. 4, 203.

Krüger, A. : 1969, Annals IQSY 3, 70.

Mosalam Shaltout, M.A. : 1989, Proceedings of the Seventh National Radio Sciences Conference, Feb. 20-22, 1990, R3, Military Technical College, Cairo-Egypt.

Tanaka, H., Kakinuma, T. : 1964, Rep. Ionos. Space Res. Japan 18, 32.

4.

FLARE-ASSOCIATED LARGE-SCALE CORONAL STRUCTURES

No related poster papers in Chapter 8.

LARGE-SCALE QUASI-STATIONARY X-RAY CORONAL STRUCTURES ASSOCIATED WITH ERUPTIVE SOLAR FLARES

R. A. Kopp* and G. Poletto**
* Los Alamos National Laboratory, Los Alamos, NM 87545
** Osservatorio Astrofisico di Arcetri, Largo Enrico Fermi, 5, 50125 Firenze, Italy

Abstract. About ten years ago the Hard X-Ray Imaging Spectrometer aboard the Solar Maximum Mission detected for the first time large, faint coronal structures associated with dynamic flares. These have come to be known as "giant arches". Notwithstanding their extreme faintness, the energy content of these giant structures is of the order of 1-10% of the total energy released by large flares ($\simeq 10^{32}$ erg), thus representing a non-negligible term in the global flare energy balance. Analogously, their mass content ($\simeq 10^{15}$ g) is quite similar to that inferred for post-flare loops and coronal mass ejections.

In spite of their obvious relevance, little is known about these giant features. Only about ten such arches have been identified to date, and the observations have both insufficient spatial resolution and inadequate time coverage. As a consequence, it is hard even to define their "typical" behavior and to ascertain their basic characteristics.

Because of these difficulties, we still lack a generally accepted flare scenario which accounts for the presence of such structures. After reviewing the observational properties of giant arches we will describe the hypotheses advanced thus far to explain their origin, evolution and energy supply. Uncertainties in the interpretations will be emphasized and alternative models proposed, in an attempt to define future observations which may allow us to understand the role of arches in the flare process and to make full use of the new information they provide.

1. Introduction.

On 21 May, 1980, at $\simeq$ 20:50 UT, a two-ribbon (2-R) flare of importance 2B occurred in AR 2456, at a longitude and latitude of approximately 10° west and 10° south. The Solar Maximum Mission observed the event during two successive orbits and, once more, about 6 hours after the flare onset. Data taken during the first orbits showed the usual "post-flare" loops: it was hoped that an extended data set, providing evidence for the late-time growth of the post-flare arcade, could be collected through the subsequent observations. At that time such data were, and still are, rather scanty; moreover, they were all taken in soft X-rays, while the Hard X-Ray Spectrometer (HXIS) had the capability of operating at higher energies.

However, the late time images showed, rather than high post-flare loops bridging over the photospheric neutral line, an unexpected feature, which seemed to extend *along* the neutral line. Svestka et al. (1982a), who first studied this structure, referred to it as a "giant arch", pointing to its enormous dimension. This has become the accepted

name for all structures with similar characteristics subsequently observed in association with dynamic flares. The May 21/22 giant arch was so weak that it showed up only in long time integrations of HXIS images, taken in the two lowest channels (i.e., between 3.5 and 8.0 keV). Nevertheless, although steadily declining in brightness, it remained visible for about 10 hours, at an apparently constant altitude.

Large loops, with a size comparable to the May arch, had been observed in the past, for instance by Skylab. However, these loops linked different active regions, which was not the case for the May feature. Moreover, its presence at a time close to a two-ribbon event and in the same area, suggested that the arch might be an as yet undetected component of the 2-R flare scenario. With a temperature of $\simeq 7 \times 10^6$ K and an emission measure on the order of 10^{48} cm^{-3}, it had, due to its enormous volume, a mass content ($\simeq 10^{15}$ gr) comparable to that of a typical filament or mass ejection and, in spite of its weakness, a non-negligible energy content - more than 10^{30} ergs at the time of maximum brightness (Hick and Svestka, 1985) - which accounted for about 10% of the total flare energy (De Jager and Svestka, 1985): if giant arches were really an essential aspect of dynamic flares, their role should not be overlooked.

These characteristics made giant arches a quite interesting phenomenon and prompted a search for other examples of this class of structure. Thus far, however, only a few have been detected and their behavior is still not well defined. In the following, after first reviewing the available observations of giant arches, we will discuss in Section 3 the different interpretations that have been advanced to explain their origin, lifetime, and energy supply. In section 4 the diverse scenarios will be confronted, for the purpose of identifying what we know, what we still don't know, and which observations might, in the future, allow us to understand fully these elusive features.

2. Observations of giant arches.

A second detection of giant arches occurred on November 6, 1980. At 03:29 UT a two-ribbon flare of importance 2B occurred in Active Region 2779, close to the eastern solar limb. Unfortunately, at the time of the flare SMM was not observing this active region and a re-pointing occurred only about 3 hours later. At that time a large X-ray emitting feature extending beyond the solar limb and clearly not totally covered by the HXIS Coarse Field of View (CFOV), was imaged in the lowest HXIS energy channels (Svestka et al., 1982b). Its size and association with a 2-R flare were reminiscent of the May arch. However, in contrast to that case, the limb position of the November structure made it possible to measure its height at different times: it turned out not to be stationary, as its brightness maximum, still steadily declining with time, was located at increasingly larger altitudes.

Later in the day, as well as during the next day, additional 2-R flares occurred in AR 2779: giant structures altogether similar to the previous ones, albeit somewhat fainter, were associated with each event. A total of 4 giant arch events were observed by HXIS over these two days. Their striking similarities suggested that, in addition

to the formation of new arches, the pre-existing emission features might have been re-energized, thus justifying the name of "revivals" adopted for these repetitive events. Therefore the meager sample of X-ray giant arches included now a few more cases, but, at the same time, supposedly consisted of two classes of features: primary giant arches and "revivals" of this -hypothetical- structure. However, as we will discuss shortly, the observational evidence for this classification is rather scanty. Marginal evidence for another primary candidate, on June 4, 1980, has been found by Hick and Svestka (1987), still from HXIS data.

A few years later, in the period 20/23 January, 1985, a further set of 4 arches was identified in SMM Flat Crystal Spectrometer (FCS) data. The first arch was observed about 5 hours after the onset of a 1B two-ribbon flare. The second and third structures, associated with dynamic flares, and the last one, for which no parent event was detected, have been considered by Hick et al. (1987) as revivals of the primary arch. HXIS and FCS have now provided data for 10 giant arches. At present, all the information about giant arches has been derived by analyzing these 10 events.

It is not surprising, with such a small data set, to see that many questions, which must be answered by observations, are still open. The "conventional" view for giant arches assumes that they form at the time of 2-R events and that they, unaffected by other kinds of flares, may revive at the time of further dynamic events. Also, we speak of a "primary" event when we refer to the first appearance of an arch, which is assumed to be stationary, while successive arch formations, or "revivals", imply also the presence of upward moving structures. Eventually, these will meet the previous structure, which supposedly keeps its identity at the time of revivals. Although data are consistent with this scenario, they are largely incomplete and allow also for alternative interpretations.

We would like to point out that hardly any of the available data refers unquestionably to the *first* time an arch forms. Moreover, none of the hypothetical primary arches has been imaged at times close to the onset of the parent flare. In the case of the observations of the June and November events, the existence of a primary arch has only been hypothesized. FCS images of the January 1985 event, where a primary is supposedly observed, start only about 5 hours after the onset of the associated flare, thus providing no evidence for the initial phases of the arch. In the May event, observations were initiated a couple of hours after the associated flare. Moreover, both these latter cases refer to structures located close to the disk center, at a position which makes the detection of upward radial motions quite difficult. In conclusion, since there is no uncontroversial evidence for the presence of an arch at the time of the flare onset and since arches fade with time, at least to the extent that HXIS cannot image them any longer, it is *likely* that they first form at the time of a 2-R flare event (i.e., there was no pre-existing bright loop), but this statement, as well as the lack of motion of primary arches, should be substantiated by further observations.

The situation is not much better when talking about "revived" arches. In this case, we should in principle have the capability to ascertain whether the previous structure is still present at the time of formation of a revived arch, or whether it disappears.

However, at the time of occurrence of a flare, weak structures are washed out by the overwhelming brightness of the flare itself, making the detectability of arches quite difficult. Altogether, data show that, shortly before an arch revival, the decaying remnants of the original arch may still be present, but there is *no* uncontroversial evidence about the simultaneous presence of the old and revived structures.

Finally, a main characteristic of these features needs to be especially emphasized. Out of 10 arches observed so far, 9 have been associated with 2-R flares. However, no flare seems to be associated with the tenth event. Obviously, there is a strong relationship between the appearance of giant arches and two-ribbon flares, but the presence of an event which does not confirm this association is puzzling and should not be overlooked.

3. The origin and energy supply of giant arches.

3.1. Primary arches.

As we mentioned in the previous section, we deem it likely that giant arches originate - as a rule - at the time of 2-R events and do not represent pre-existing emission features which are energized by the flare. Although more data are needed to confirm this hypothesis, there is no evidence, that we are aware of, for such large structures prior to HXIS observations and their progressive fading with time seems to substantiate our view. Therefore, even if we can't rule out the possibility of an extremely faint arch, undetectable by our present instrumentation, whose structure persists throughout the flare process, giant arches seem to represent a by-product of 2-R flares, and we should be able to find a compelling reason for their occurrence in the underlying flare process. In fact, the two models advanced so far to explain the origin of giant arches rely on the Kopp-Pneuman interpretation (1976) of 2-R flares to account for these large structures. Nevertheless, they invoke different mechanisms to explain their presence.

In the first model, proposed by Svestka et al. (1982a), giant arches represent the upper disconnected parts of the usual "post-flare" loops created by a reconnection process. Pointing to the shear of field lines before a flare and to the magnetic field simplification which follows the flare, these authors suggested that reconnection between the nearest disconnected field lines might create two kinds of structures. Below the reconnection site, the usual post-flare arcade would form; above the reconnection site, the upper portion of the reconnecting fields would create elliptical loops, topologically interconnected along the neutral line to form a spiral system, observable as an arch. The resulting configuration would be quite similar to that suggested by Anzer and Pneuman (1982) to model the initial stage of a coronal transient. Svestka et al.'s model provided a qualitative explanation of why giant arches are associated with 2-R events and why they are oriented normally to the post-flare loops.

Further support for this interpretation came from Hick and Priest (1989), who showed that the slow-shock mechanism responsible for the heating of post-flare loops (Cargill and Priest, 1982; Cargill and Priest, 1983) might be operating in giant arches

as well. Although they based their analysis only on order-of-magnitude estimates of a number of poorly known physical parameters (the length of slow shocks, the reconnection speed, the magnetic field orientation with respect to the slow shocks, and so on), and although they focused mainly on the May 21/22 event, the resulting overall scenario which emerges from Svestka et al.'s and Hick and Priest's works is appealing. A single process accounts for the rising post-flare arcade and the giant arches, as well as for the heating of both structures.

However, an alternative view was proposed by Poletto and Kopp (1988) and Kopp and Poletto (1990), who suggested that giant arches might be large loops created by magnetic reconnection occurring far above the flare site, but still within the normal 2-R. flare framework. In contrast to the post-flare loops, arches would not represent a direct linkage across the neutral line, but would connect to more peripheral areas, far from that part of the neutral line over which the lower lying post-flare arcade forms. Thus, an arch may be topologically quite distinct from this latter structure, in contrast to the previous model where it surmounts directly the region occupied by the post-flare loops.

In order to verify this hypothesis, Kopp and Poletto, assuming that reconnection would create potential structures, evaluated in the current-free approximation the three-dimensional topology of the coronal field in the regions where the events of May and November 1980 occurred. In both cases, they were able to show that a number of projected fieldline shapes agreed pretty well with the giant arch shapes. *Per se* this result is not conclusive, as a chance coincidence between computed field lines and fuzzy structures observed with a resolution of only 32″ cannot be ruled out. However, the technique used to simulate the November arches had the capability of predicting the location of the arch's footpoints: this prediction was confirmed by independent observations, lending support to the above scenario.

The predictive technique used by Kopp and Poletto (1990) took advantage of the limb position of the November events: as we mentioned in Section 2, on November 6/7 the HXIS arches projected above the solar limb and their true height, h, could be easily determined. The top of any arch necessarily lies along the neutral line, since at that point $B_r = 0$. Therefore, evaluating the neutral line position at the altitude h and integrating *downwards* from this level to the photosphere, it is possible to check whether the computed field lines project onto the observed arch shape and whether any activity is observed at the predicted footpoints. In fact, independently of these calculations, Martin, Svestka and Bhatnagar (1989) had previously correlated the Hα brightness fluctuations of a small plage at the eastern border of NOAA 2779 with that of the HXIS arch and had suggested that this plage represented one of its footpoints. This turned out to coincide precisely with the location predicted by the magnetic modeling. Moreover, they were able to identify also the second Hα footpoint of the arch by examining the area where, according to Kopp and Poletto's results, it should be located. Because this latter footpoint area was peripheral (with respect to the flare position) and rather diffuse, it had not been examined by Martin, Svestka and Bhatnagar in their original search for the arch footpoints.

The arch energy, in Kopp and Poletto's scenario, is provided by reconnection. The decrease of differential magnetic energy with increasing height of the neutral line should therefore cause arches reaching greater heights to have lower thermal energy densities. Although it was not possible to check quantitatively this hypothesis, an approximate evaluation of the energy released by reconnection at a couple of heights proved it to be large enough to provide for the energy requirements of arches forming at those altitudes. In conclusion, this model, as also the one of Svestka et al. (1982a), interprets giant arches as by-products of the reconnection process, but the topology of the reconnected structures is quite different. The two models differ even more in their interpretation of revivals.

3.2. Arch revivals.

In Kopp and Poletto's model, primary and revivals form in the same way: there is no difference between these structures. This implies that the static nature of the May 21 structure is, according to these authors, only coincidental: the positional shift of progressively higher structures would not have been apparent because the active region was located close to the disk center. We will come back to this point in the next section when comparing the two scenarios.

Svestka's (1984) and Hick and Svestka's (1987) interpretation of revivals takes as a focal point - notwithstanding the elusiveness of observations in this respect - the presence of the primary structure at the time a dynamic flare triggers the formation of a new arch. The old arch supposedly acts as an obstacle to this rising structure, hindering its ascent. Eventually, a further reconnection phenomenon is thought to occur when the old and new arches "meet".

This latter scenario is partially based on an analysis of the "moving thermal disturbances" which these authors identified in both the November and the June events. Temperature maps in the HXIS FFOV (Fine Field of View) showed that the region of maximum temperature (in excess of 2.1×10^7 K) shifted outward with time, with a propagation speed of 6-8 km s^{-1}. After leaving the FFOV, the disturbance possibly kept propagating outwards: the region of maximum temperature observed in the CFOV was also rising with time, continuing with the same speed the apparent motion detected in the FFOV.

It is interesting to note that such a disturbance was not detected when analyzing HXIS observations of a confined flare which had occurred on the same day. Consequently Hick and Svestka (1987) associated their thermal disturbances with dynamic events and assumed that they are a signature of the imminent revival of an arch structure. In their opinion, the thermal disturbance is part of the revived arch, in its earliest phase of development. Its ascent is dictated by reconnection and occurs at about the reconnection speed. Taking the latter, as usual, from the rate of growth of the post-flare arcade, this turned out to be about the same as the thermal wave speed. Later on, however, the thermal disturbance did not slow down - in contrast to the late time

behavior of the post-flare loops. This anomalous behavior was ascribed to the merging of the old and new structures.

4. How can we distinguish between different scenarios?

The two models described above comprise rather different interpretations of the same basic observational data. From the event analyses which have been performed thus far, it has not been possible to determine which, if either, scenario is the physically correct one. Evidently greater scrutiny of existing, as well as future, observations will be required to provide criteria capable of making a unique choice between models. In the following we attempt to identify several of these key factors.

a) The first problem we have to consider is related to the origin of these large structures: *do giant arches comprise the helical upper loops formed via reconnection as envisaged by Anzer and Pneuman (1982), or do they represent topologically simpler reconnected loops rooted in the photosphere?* Recently Poletto and Svestka (1991) may have found a clue to the answer to this question. If arches are the upper disconnected parts of loops, they cannot show up before post-flare loops form: the appearance of an arch *before* a post-flare loop arcade develops would force us to identify arches with entire loops, attached to the solar surface, rather than with the detached upper part of a growing arcade. Such a case has been detected in the analysis of HXIS short accumulation images obtained during the early phase of formation of the arch which followed the 2-R flare at 14:45 UT on November 6. This flare was anomalous, in that the post-flare arcade developed more than half an hour after the flare onset; yet, minutes after flare onset an arch was formed, and its rise could be followed at times when the underlying flare had the appearance of a confined event. This behavior can be interpreted as resulting from the opening of only a high set of field lines. The same explanation holds for the arch observed on 22 January 1985, for which no accompanying chromospheric activity was detected; also for this event any interpretation within the framework of the Hick-Svestka model would be difficult. On the other hand, if arches represent recently reconnected large-scale structures, occasionally they should appear independently of 2-R events when only weak high-lying features get disrupted. A thorough search of data would be required to identify further events of this kind. Observations are also badly needed of arch "revivals", to ascertain whether the old arch is really still present at the time a new one is being formed (a case which could hardly be explained by the Kopp-Poletto reconnection model). Finally, we need to understand the temporal relationship between the formations of an arch and of the associated post-flare loops: do we need to invoke an approximate time coincidence between two independent disruptive events (an unlikely circumstance) or do the two phenomena occur in succession as the result of a common underlying process?

b) *Is there any uncontroversial evidence for a two-category classification of giant arches?* From the observational point, we have already stressed the need for an unambiguous detection of the first time an arch forms. However, Kopp and Poletto's model implicitly assumes no difference between giant arches: a possible weak point in this interpretation is the apparent lack of an upward rise of the May 21 feature (a "primary

arch"). We have argued that projection effects may account for this behavior; nevertheless, it seems to remain a critical point. This model also does not explicitly mention the thermal disturbances which heavily enter in Hick and Svestka's interpretation. However, an alternative view to these latter authors' model might be that it is the upward motion of the thermal disturbance, rather than that of the top of the post-flare arcade, that reflects the systematic rise of the reconnection region. In this case we can summarize the sequence of phenomena which occur at increasingly high levels, as envisaged in the two models, as follows:

Hick and Svestka	*Kopp and Poletto*
old arch	- - - - - -
thermal disturbance≐new arch	thermal disturbance≐reconn. region
reconnection region (just above PFL tops)	giant arch
PFL's (post-flare loops)	PFL's

Both scenarios look somewhat hypothetical and suffer from the lack of a quantitative treatment of data. Since Hick and Svestka's model has already been illustrated, we will spend a few words to justify the role of the thermal disturbance within Kopp and Poletto's reconnection scenario. Previously, in both models the post-flare loop rise was assumed to trace the ascent of the reconnection region into the corona; i.e., the upward velocity of the neutral line was equated to the observed rate of formation of increasingly high loops. As a consequence, the reconnection speed was found to decrease with height, because the growth rate of high post-flare loops is less than that of low loops. However, the first signature of the release of energy via reconnection should appear as a temperature increase of the ambient plasma. Thus the height of the thermal disturbance at any time should give a much better indication of the location at which reconnection is occurring than does the height of the post-flare loop system. Only later on, after a newly formed loop has become filled with evaporated plasma and it has radiatively cooled below, say, 10^5 K, should it become visible in Hα as a post-flare loop. In this hypothesis, the time delay between the magnetic energy release and the first appearance of a loop increases with height because of the greater loop length, which results in a lower loop density and correspondingly longer radiative and conductive cooling times. Qualitatively, this effect is observed; moreover, further support for this picture comes from the absence of thermal disturbances associated with a confined flare (see Sec. 3.2). However, a definitive proof of this hypothesis will be reached only through a simulation of the whole process. On the other hand, Hick and Svestka's scenario will be strengthened if future observations demonstrate the absence of thermal disturbances at the time of formation of primary arches. Finally we note that, if the motion of the thermal disturbance really images the height vs. time history of the reconnection region, the neutral line rises upward at an apparently constant speed (at least for heights $\geq$ 60000 km; we do not have observations at lower altitudes), significantly modifying previous estimates of the reconnection rate.

c) *What is the source of the arch energy supply?* We cannot answer this question before first resolving question *a*. There are, however, a number of candidates. But it should be pointed out that, whichever process one envisages, it must provide energy to the arch more-or-less continuously for several hours after the flare. The observed arch lifetimes are simply too long to allow otherwise: simulations that assume the arch is simply a pre-existing loop which is heated by a sudden energy release at the time of the flare, show that cooling by radiation and conduction will occur on a much shorter time scale than the observed arch durations (Kopp and Poletto, 1991, unpublished results). Achterberg and Kuijpers (1984), in an attempt to overcome this difficulty, identified the energy source of the May 21 arch as energetic electrons traveling across the magnetic field and diffusing into the X-ray arch from the flaring loop system. However, it has not yet been proven that high energy electrons ($E \geq 100$ keV) are available in a number and for a long enough time to account for the characteristics of the May 21 structure. On the other hand, for a definitive test of the idea (Poletto and Kopp, 1988) that arches form via sequential reconnections at ever-greater heights, we need better data on the thermal energy of arches formed at various heights. Only through detailed comparisons of such data with magnetogram-based calculations of stored coronal magnetic energy, might one hope to determine if the total energy released during a given arch event can be quantitatively explained by the hypothesized reconnection process.

d) *Are there still alternative scenarios to be considered?* There seems to be at least one picture which has not yet been fully explored, namely that which involves the relationship between X-ray giant arches and filament eruptions/Coronal Mass Ejections (CME). The well-known associations between 2-R flares and giant arches and between 2-R flares and CME's suggest the possibility of a connection between arches and CME's. The approximate equivalence between the arch mass content and the mass of filaments/CME, already mentioned in the Introduction, may further hint to this connection. We know little, on the observational side, about the occurrence of CME's at the time of the 10 giant arches that have been detected thus far. A mass ejection was associated with the May 21 event (McCabe et al., 1986), although this seems to be a somewhat anomalous event: the filament did not erupt and kept essentially the same position it had before the flare. Indirect evidence points to the existence of a large mass ejection at the time of the first flare in the sequence of November events. Is it possible that coronal arches are part of a scenario which includes the upward distention of magnetic field lines, the formation of post-flare loops, and an ensuing coronal transient? Alternatively, might giant arches simply account for that part of the mass of a coronal transient which was trapped on large coronal magnetic loops - these having managed, by virtue of their specific topology relative to the disruption, to remain intact throughout the event?

We have already pointed out how the original interpretation of Svestka et al. (1982a) was quite similar to Anzer and Pneuman's (1982) picture of coronal transients. The apparent lack of motion of the May 21 arch made it difficult to understand how that structure could be explained on the basis of a model which attempted to reproduce the upward motion of a transient. However, Van Tend and Kuperus (1978) suggested a model for filament eruptions which allows for the possibility of a secondary equilibrium

position, tentatively identified with the arch position. Is the May 21 arch a structure which failed to become a transient? On the other hand, we know that, at the time of a CME, loops can be seen expanding out through the corona: may giant arches be structures filling in the gap between the smaller size active region loops and the expanding CME loops? Although these possibilities have been recognized, they are barely mentioned in the literature (Simnett and Forbes, 1991). When future X-ray data of higher sensitivity and spatial resolution provide us with more information on giant arches (in particular, on the unsettled question of the reality of a twofold arch classification), it should be possible to formulate a realistic description of these elusive features within the broader dynamic-flare scenario.

5. Acknowledgments.

We would like to thank Z. Svestka for several useful exchanges regarding HXIS arch observations and data analyses during the preparation of this review. R. A. Kopp gratefully acknowledges support from the Italian Space Agency (ASI) and the Ministero dell'Università e Ricerca Scientifica (MURST). The work of G. Poletto was supported by the Italian Space Agency (ASI).

References.

Achterberg, A. and Kuijpers, J.: 1984, *Astron. Astrophys.*, **130**, 111.
Anzer, U. and Pneuman, G. W.: 1982, *Solar Phys.*, **79**, 129.
Cargill, P. J. and Priest, E. R.: 1982, *Solar Phys.*, **76**, 357.
Cargill, P. J. and Priest, E. R.: 1983, *Astrophys. J.*, **266** , 383.
De Jager, C. and Svestka, Z.: 1985, *Solar Phys.*, **100**, 435.
Hick, P. and Priest, E.R.: 1989, *Solar Phys.*,**122**, 111.
Hick, P. and Svestka, Z.: 1985, *Solar Phys.*, **102**, 147.
Hick, P. and Svestka, Z.: 1987, *Solar Phys.*, **108**, 315.
Hick, P., Svestka, Z., Smith, K.L., and Strong, K.T.: 1987, *Solar Phys.*, **114**, 329.
Kopp, R. A. and Pneuman, G. W.: 1976, *Solar Phys.*, **50**, 85.
Kopp, R.A. and Poletto, G.: 1990, *Solar Phys.*, **127**, 267.
McCabe, M. K., Svestka, Z., Howard, R. A., Jackson, B. V., Sheeley, N. R.: 1986, *Solar Physics*, **103**, 399.
Martin, S.F., Svestka, Z., and Bhatnagar, A.: 1989, *Solar Phys.*, **124**, 339.
Poletto, G. and Kopp, R.A.: 1988, *Solar Phys.*, **116**, 163.
Poletto, G. and Svestka, Z.: 1991, *Solar Phys.*, submitted.
Simnett, G. M., Forbes, T. G.: 1991, in *Dynamics of Solar Flares*, Proc. Flares 22 Workshop, B. Schmieder and E. Priest, Eds., 121.
Svestka, Z.: 1984, *Solar Phys.*, **94**, 171.
Svestka, Z., Stewart, R., Hoyng, P., Van Tend, W., Acton, L.W., Gabriel, A.H., Rapley, C.G., and 8 co-authors: 1982a, *Solar Phys.*, **75**, 305.
Svestka, Z., Dennis, B.R., Pick, M., Raoult, A., Rapley, C.G., Stewart, R.T., and Woodgate, B.E.: 1982b, *Solar Phys.*, **80**, 143.
Van Tend, W. and Kuperus, M.: 1978, *Solar Phys.*, **59**, 115. vfill

Large Scale Structures Associated with Eruptive Flares and Radio Waves

N. Gopalswamy and M. R. Kundu

Astronomy Program, University of Maryland, College Park, MD 20742

Abstract: We review some recent results obtained from 2-dimensional imaging observations of the Sun using the Clark Lake multifrequency radioheliograph. The radioheliograph produced images of the Sun's corona on a daily basis at several frequencies within the range 20–125 MHz during the period 1982–87. Using these images both large scale structures as well as transient phenomena such as bursts have been studied. In this paper we discuss the nature of radio emission associated with eruptive filaments and CMEs. It is possible to trace the structure of magnetic fields in the corona based on the multifrequency observations of moving type IV bursts at meter and decameter wavelengths. We illustrate this by discussing specific events. We discuss a rare case of the detection of thermal radio emission in association with a fast CME. We estimate the CME mass using spatially resolved radio data.

1 Introduction

Both stationary and dynamic structures in the upper corona can be studied using spatially resolved meter-dekameter wave observations. Manifestations of the dynamic structures such as filament eruptions, coronal mass ejections (CMEs) and flares are observed at these wavelengths. Some of these manifestations are observed as moving type IV and type II bursts produced respectively by plasmoids or magnetic arches and shock waves and some are observed as type III and type V bursts produced by energetic electron streams. The dynamic structures are usually observed by the nonthermal radiation they emit. Also inferred from their nonthermal emission are certain high coronal loops emitting stationary continua such as flare continua, stationary type IV bursts and storm radiation. Other stationary structures seen in radio are coronal holes and coronal streamers which emit thermal radiation. Mass ejections are occasionally observed through thermal emission if no nonthermal particles are trapped in the ejecta. These observations are important for two reasons: to understand the association of CMEs with nonthermal radio bursts and to estimate the mass of CMEs by an independent method (Gopalswamy and kundu, 1991). Multifrequency imaging observations are needed

to understand the structure of these magnetic loops or arches. Arch shapes have been inferred from single or two frequency imaging observtions for flare continuum (e.g., Robinson, 1985; Gopalswamy and Kundu 1987a), and moving type IV bursts (e.g.,Stewart, 1985). From Clark Lake imaging observations at three or four frequencies, we studied a number of these structures which are reviewed in this paper.

2 Magnetic Field Structure in Moving type IV Bursts

2.1 A Moving Magnetic Arch

On November 3, 1986 a fast (600 kms^{-1}) moving type IV burst was observed at three frequencies: 73.8, 50 and 38.5 MHz, in association with a coronal mass ejection (observed by the SMM-C/P instrument), preceded by type III bursts and followed by stationary type IV and type II bursts (Gopalswamy and Kundu, 1989b). The moving type IV burst was seen up to a height of 4.5 $R_\odot$ from the Sun center at 38.5 MHz and had two sources at each frequency. In Fig.1, we have connected the centroids of each source at three frequencies at different times during the evolution. The centroids seem to lie dispersed on the two legs of a large arch that moves out in time. Initially, the separation between the legs of the arch is small, and it increases with time. Closing of the arches at the top was arbitrary because we had observations only at three frequencies. In the last part of Fig.1, we have sketched the arch through the sources from $\sim$ 20:06 to 20:19 UT, the last time the moving source was seen. The type II burst started around 19:46 UT at 50 MHz, at a height of 2.3 $R_\odot$. The CME loop top was at a height of 2.4 $R_\odot$ at 19:39 UT itself. Since the estimated speed of the CME was 750 kms^{-1}, the CME leading edge is expected at a height of 2.8 $R_\odot$. Hence the type II location is $\sim$ 0.5 $R_\odot$ behind the CME, suggesting that the type II shock was not piston driven by the CME. We have illustrated this point using other events elsewhere (Gopalswamy and Kundu 1987, Kundu et al 1989, Gopalswamy 1990). Assuming that the type II shock was a blast wave generated at the time of the flare at 19:21 UT (when the type III bursts occurred), the type II speed was estimated to be 650 kms^{-1}. Immediately after the type II burst, both the components of the type IV brightened. This can be interpreted as a fresh injection of nonthermal electrons into the arch producing moving type IV burst as the shock front passes through the arch.

2.2 Multiple Moving Structures

Two moving type IV bursts and a stationary continuum source were observed on January 16, 1986. In contrast with the November 3, 1986 event, the sources had little dispersion with frequency in the radial direction. The loop structures seen in Fig.2 have been obtained by joining the loci of 50 MHz centroids and closing the loop at the top (arbitrary). Note that the two components in the first pair move with different speeds while the components in the second pair move with nearly the same speed. The speed difference suggests that the two arches may not be in the same plane. The small arch sketched in Fig.2b is due to the flare continuum.

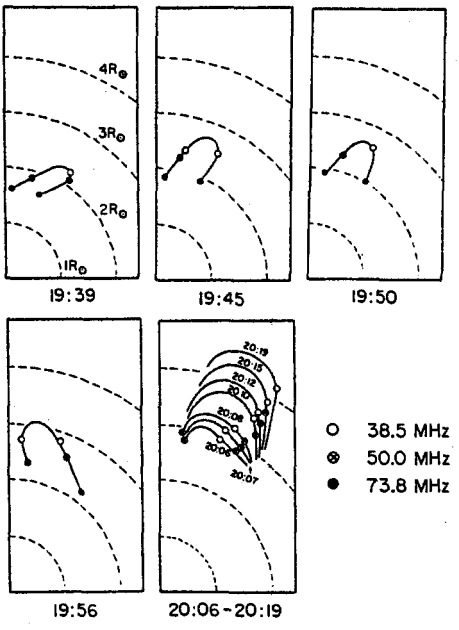

Fig. 1. moving arch of Nov. 3 1986. Sun-center is at the lower left corner of each box.

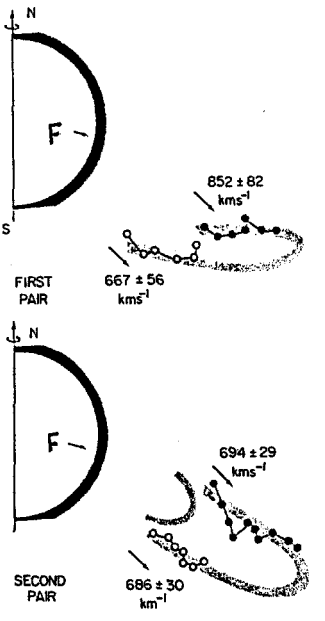

Fig. 2. Moving arches of Jan. 16, 1986. The arrow marks denote the location $H-\alpha$ flare loops.

It is not clear if the sources represent two legs of a huge arch or just two pairs of plasmoids. If it is a loop structure, then it is similar to the 1986 Nov 03 event, except for the absence of frequency dispersion. This may be due to a peculiar distribution of density in the loop. If the sources represent a pair of plasmoids, then it is tempting to identify with the sequence of plasmoids obtained as solutions to interacting arcades which are laterally restricted (Biskamp and Welter, 1989). It is interesting to note that the sources did not show any lateral motion. If we consider one such source as a plasmoid then the radio emission can be explained as a Razin-suppressed gyrosynchrotron emission from mildly relativistic ($\sim$ 100 keV) electrons with a number density of 10^2– $10^5 cm^{-3}$ in a 2 G magnetic field (Gopalswamy and Kundu, 1990).

3 A Slowly Moving Plasmoid

Extremely slow filament disintegrations are known to associated with noise storm radiation (Kundu et al 1989; Kundu and Gopalswamy, 1990). Here we discuss a filament eruption accompanied by a slowly moving type IV burst. The filament eruption event of February 2, 1986 was well observed so that useful comparison can be made with radio and optical observations. A filament situated to the east of AR4711 ($S10E49$) became active since 18:24 UT and the upper part started lifting around 19:19 UT. The leading edge of the filament acquired a steady speed at 19:32 UT and completely disappeared at 19:52 UT. Starting from $\sim$ 19:30 UT,

the filament activity was accompanied by a C level GOES flare and a microwave GRF. Radio emission at meter-dekameter wavelengths started immediately after the filament disappearance. The radio emission consisted of a continuum and a moving type IV burst, the latter separating and moving away from the former as an isolated source. The projected source position of the moving type IV burst was very close to the location where the filament was last seen. The height-time plot of the filament and the moving type IV are shown in Fig.3. The speed of the moving type IV was nearly the same as that of the leading edge of the rising filament (140 kms^{-1}) Superposition of the centroids of 73.8 and 50 MHz moving type IV sources, on the February 2,1986 Mauna Loa Observatory (MLO) K-Coronameter map showed that the moving radio source was located in the vicinity of the brightness enhancement (Gopalswamy and Kundu, 1989b). The 50% brightness contour of the 73.8 MHz overlaps with the coronal enhancement. As only one map per day was available from MLO for this period, motion of the coronal enhancement could not be studied. It is also possible that the plasmoid is very dense and the 73.8 MHz radiation emerges from the peripheries of the enhancement. The presence of enhanced material at the time and height of the moving type IV burst suggests the possibility of an accompanying CME. We interpret the moving type IV burst as the radio emission from a plasmoid formed out of the heated filament material by reconnection; nonthermal particles accelerated during reconnection got trapped in the plasmoid and produced the observed radiation through gyrosynchrotron process.

4 Thermal Emission Associated with CMEs

If there are no nonthermal particles generated during a CME event, then the only radio signature possible is the enhanced thermal emission due to the denser coronal material contained in the CME, since thermal bremsstrahlung depends on thermal electron density (Sheridan et al, 1978). This event was considered as a support to the SKYLAB era conclusion (Gosling et al 1976) that slow CMEs are not associated with nonthermal radio emission (Dulk, 1980). However there is increasing evidence that slow CMEs are indeed accompanied by type II and/or moving type IV bursts (Kundu, 1987; Kundu et al, 1989; Gopalswamy, 1990). Our investigation of spatially resolved radio data from Clark Lake and simultaneously obtained SMM-C/P data suggests that the CME speed does not determine the CME-radio burst association. There are at least half a dozen events where CMEs with speeds less than 400 kms^{-1} are associated with type II and/or moving type IV bursts (see Table 1).

The 1986 Feb 16 CME is another evidence that the CME speed may be unimportant in the question of whether the radio emission would be thermal or nonthermal. It was a relatively fast CME (450 kms^{-1}). Since the activity center (AR4713) was $\sim 20°$behind the limb, the deprojected speed was slightly higher (475 kms^{-1}). No type II or moving type IV burst was observed but the CME was seen clearly in thermal emission. In spite of relatively poor resolution at radio wavelengths (4

Table 1. Slow CMEs associated with type II/type IV bursts

Event date	Radio emission	CME speed	References
Jun 27 1984	type II, type IV	350 km/s	Gopalswamy & Kundu 1987
Nov 12 1984	type II	150 km/s	St. Cyr 1991
Feb 17 1985	type II, type IV	240 km/s	Kundu et al 1989
Feb 22 1985	type II	160 km/s	St. Cyr & Webb 1991
Feb 2 1986	type IV	140 km/s	Gopalswamy & Kundu 1989
Nov 6 1986	type IV	85 km/s	Gopalswamy & Kundu 1990

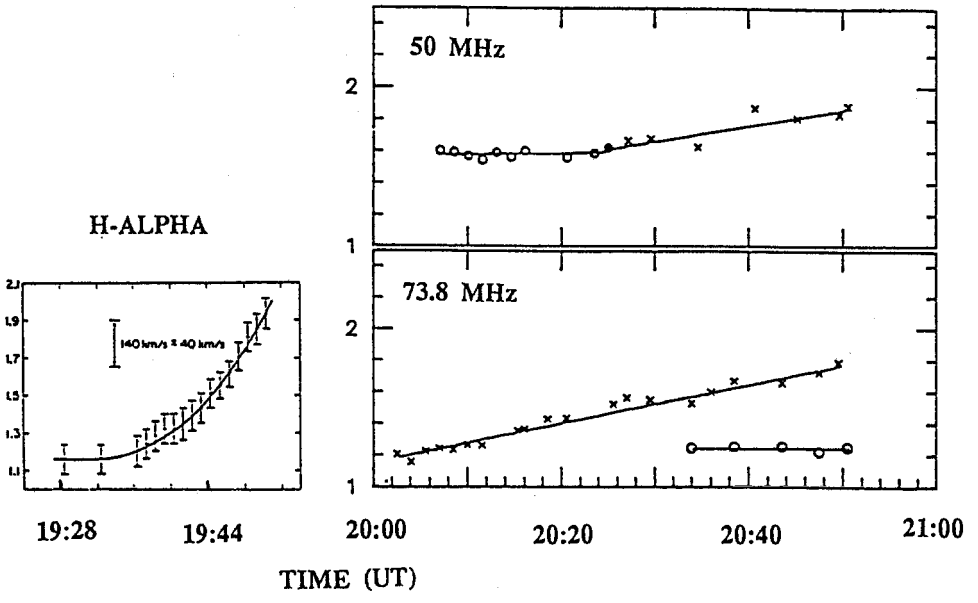

Fig. 3. Height-time plot of the moving type IV burst and the erupting filament on Feb 2 1986. The vertical scale for filament (left) is distance from the sunspot in units of $10^5 km$; forthe plasmoid it is from sun center in units of $R_\odot$. Open circles and crosses correspond to continuum and moving type IV respectively.

arcmin compared to 13 arcsec in white light), the structures in the CME have excellent correspondence in white light and radio. The CME could be seen in the difference image as the excess emission between 19:36 and 20:26 UT (Fig. 4). Using the optically thin bremsstrahlung formulae we could estimate the excess mass in the CME (see Gopalswamy and Kundu, 1991) to be a few times $10^{15} g$ which is in the general range of masses known for many other CMEs (Hildner, 1977; Poland et al, 1981; Howard et al, 1984; Jackson, 1985).

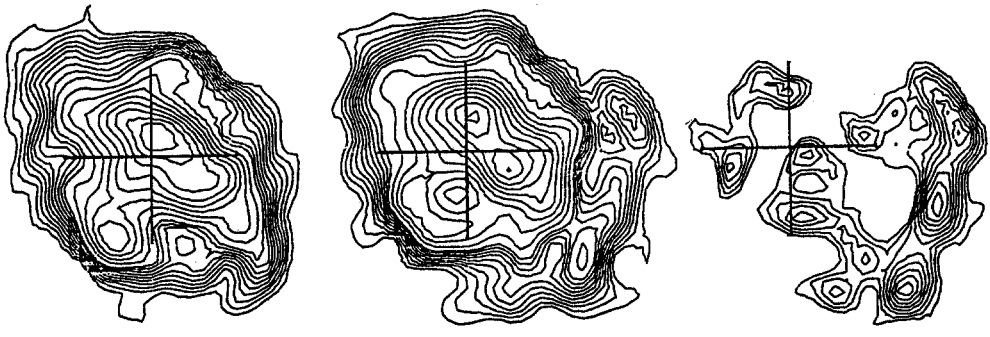

Fig. 4. Contour maps (left: 19:55 UT) before, (middle: 20:29 UT) during and the subtracted image (middle – left) of the Feb. 16 1986 CME. The central cross represents the extent of the optical disk. The contours are in units of 1000 K at 10–100 in steps of 10 and 100–300 in steps of 20. The bright sources in the difference map may be due to variability in quiet Sun peaks or a result of ionospheric shift between the two maps used in the subtraction process.

5 Conclusions

The Clark Lake multifrequency radioheliograph has been extremely useful in studying a wide variety of eruptive structures in the corona which can trap energetic electrons to produce nonthermal radio emission. On one occasion, we observed two pairs of moving sources. An isolated moving type IV source was observed at the time and location of the filament disappearence; the filament and the type IV had the same speed suggesting that the plasmoid might have formed out of the heated filament material. Our observations lead to the conclusion that the association of moving type IV bursts with CMEs depends on the availability of nonthermal particles and the ability of the instrument to detect these emissions. The speed of the CME does not seem to play a crucial role in its being associated with radio emission. A fast CME was observed in purely thermal emission, with no accompanying type II and/or moving type IV burst. We derived the mass of the CME from radio observations and the results are in the range of mass estimates obtained from white light observations.

This research was supported by NASA grants NAG-W1541 and by NSF grant ATM 87–17157.

References

Biskamp, D. and and Welter, H. (1989): Solar Phys. **120**, 49

Dulk, G. A.(1980): in Radio Physics of the Sun, ed. by Mr. Kundu and T. E. Gergely, (D. Reidel, Dordrecht) p. 419

Gopalswamy, N. (1990): in Basic Plasma Processes on the Sun, ed. by E. R. Priest and V. Krishan, (IAU Colloquium 142) p.495

Gopalswamy, N. and Kundu, M. R. (1987a): Solar Phys. **111**, 347

Gopalswamy, N. and Kundu, M. R. (1987b): Solar Phys. **114**, 347

Gopalswamy, N. and Kundu, M. R. (1989a): Solar Phys. **122**, 91

Gopalswamy, N. and Kundu, M. R. (1989b): Solar Phys. **122**, 145

Gopalswamy, N. and Kundu, M. R. (1990): Solar Phys. **128**, 377

Gopalswamy, N. and Kundu, M. R. (1991): Astrophys. J. Lett. (submitted)

Gosling, J. T., Hildner, E. MacQueen, R.M., Munro, R. H., Poland, A. I., and Ross, C. L. (1976): Solar Phys. **48**, 389

Hildner, E. (1977): in Study of Interplanetary Travelling Phenomena, ed. by M. A. Shea, D. F. Smart and S. T. Wu (D. Reidel, Dordrecht), p. 6

Howard, R. A., Sheely, N. R., Koomen, M. J. and Michels, D. J. (1984): Adv. Space Res. **4**, 307

Jackson, B. V. (1985): Solar Phys. **100**, 563

Kundu, M. R. (1987): Solar Phys. **111**, 53

Kundu, M. R. and Gopalswamy, N. (1990): Solar Phys. **129**, 133.

Kundu, M. R., Gopalswamy, N. White, S. M., Cargill, P., Schmahl, E. J., and Hildner, E. (1989): Astrophys. J. **347**, 505

Kundu, M. R., Schmahl, E. J., and Fu, J. Q. (1989): astrophys. J. **336**, 1078

Poland, A. I., Howard, R. A., Kooman, M. J., Michels, D. J., and Sheeley, N. R. (1981): Solar Phys. **69**, 169

Robinson, R. D. (1985): in Solar radiophysics, ed. by D. J. McLean and N. R. Labrum, (Cambridge University Press, cambridge), p. 385

Sheridan, K. V., Jackson, B. V., McLean, D. J., and Dulk, G. A. (1978): Proc. Astron. Soc. Aust. **3**, 249

St. Cyr, C. ; St. Cyr and Webb, D. F. (1991): Private communications

Stewart, R. T. (1985): in Solar radiophysics, ed. by D. J. McLean and N. R. Labrum, (Cambridge University Press, cambridge), p. 361

Coronal Millimeter Sources Associated with Eruptive Flares

Albrecht Krüger[1] and Seppo Urpo[2]

[1]Zentralinstitut für Astrophysik, Rosa-Luxemburg-Str. 17a,
D - O1591 Potsdam, Germany

[2]Helsinki University of Technology, Otakaari 5a,
SF-02150 Espoo, Finland

Abstract: Sporadically occurring coronal millimeter wave sources (CMMSs) detected as off-limb brightenings corresponding to a height of the order 10^5 km above the photosphere attract much interest. The lifetime of the phenomenon is several hours and it can be interpreted as a special kind of long-duration post-flare (and inter-flare) emission at coronal altitudes. There is a relationship to other solar radio phenomena, e.g. GRF-microwave bursts and noise storms, as well as to longduration events (LDEs) in soft X-rays, coronal hard X-ray arches, and coronal mass ejections (CMEs). The main results obtained until now on CMMSs are comprehensively summarized for the first time and new aspects included. The relevant emission process(es) have been analysed considering the whole microwave range. Open questions and implications for the study of eruptive flare dynamics and coronal structures by a new diagnostic tool are discussed. Finally, prospects of further investigations have been considered.

1. Introduction

Usually solar millimeter-waves originate at heights of less than few thousand km above the photosphere. This concerns mainly the quiet Sun, the S-component, and perhaps a number of minor burst events which is documented by solar maps and model calculations (cf. Urpo, Hildebrandt and Krüger, 1987). Occasionally, however, after inspection of a sufficiently large number of observations, the detection of off-limb sources reveals the unusual existence of mm-wave radiation at much greater source heights, i.e. of several tens of thousands km above the photosphere. These sources are related to flares and microwave bursts but are lasting significantly longer than normal impulsive flare/burst events (Urpo, Krüger, and Hildebrandt, 1986a). Millimeter radiation related to an Hα prominence and extending up to a height of 200000 km was already noted by Kundu (1972). Independently, Urpo et al. (1983, 1985, 1986a) detected the phenomenon of coronal millimetre wave sources (CMMSs) at the Metsähovi radio maps, which subsequently led to more systematical studies of the properties of the phenomenon (Urpo et al., 1986b, 1989; Krüger et al., 1989). It was shown that CMMSs are likely to be related to flares starting up to several hours prior to the accidental mm-wave observation and therefore forming a special group of long-living post-flare events or a "super-gradual" burst-like background of a flare- rich solar active region. The present report summarizes the outcome of recent studies on the CMMSs and encloses results from latest observations.

2. Observations

Most information presently available on CMMSs stems from solar maps of the Metsähovi Radio Research Station of the Helsinki University of Technology (Urpo, Pohjolainen, and Teräsranta, 1987 - 1991). The observations are made with a 14m parabolic antenna located in a radome. The main observing frequencies are 37 and 22 GHz (8.1 and 13.5 mm wavelength) corresponding to a spatial resolution of 2.4 and 4.0 arc minutes, respectively. Single observations of coronal millimeter wave sources of different nature have been obtained also at other stations, e.g. Hiraiso, La Posta, Itapetinga, Haystack and Katsiveli. The CMMSs are observed as off-limb brightenings in solar isophote maps at a fixed frequency (Figure 1). In general the off-limb sources observed fall into different classes comprising (i) immediate burst sources, (ii) post-burst sources, and (iii) erupting (quiescent) filaments (cf. Zodi et al., 1988). Up to now a total of about 80 cases of CMMSs selected from more than 2000 solar mm-wave maps obtained at different stations is available for a study.

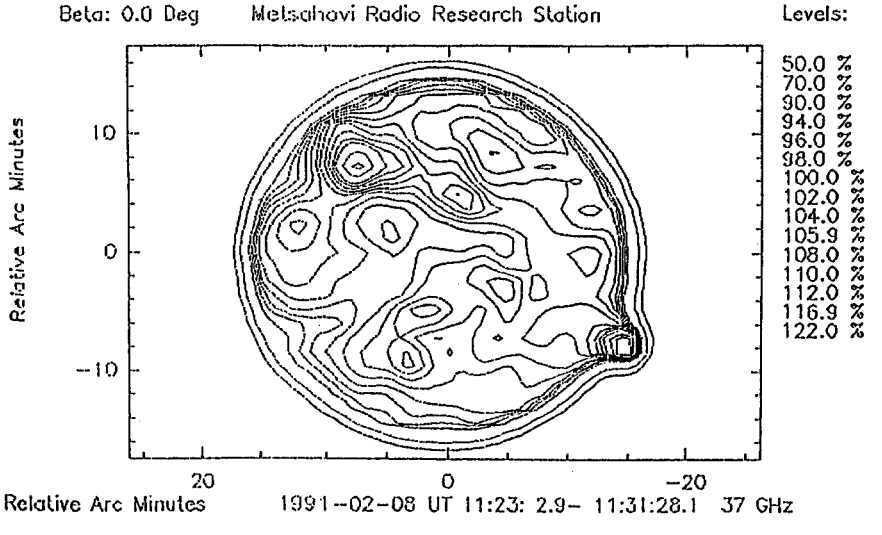

Figure 1. mm-wave off-limb source on 8 February 1991. Subflare activity and a LDE of > 10 h duration started more than 5 hours prior to the mm-wave observation.

3. Association with Hα-Flares and Time Characteristics of CMMSs

Comparisons with flare reports show that most of the CMMSs are related to optical flares (and associated X-ray and radio bursts) starting up to some hours earlier in the

same active region. Cases of missing association with visible Hα-flares can be attributed to behind-limb events. It can be concluded that most CMMSs form a special kind of post-flare emission which is also seen in Hα and other spectral ranges (e.g., LDEs). In several cases mm-wave observations are also available during the main phase of flares. Therefore we split up our discussion on the mm-wave signatures of solar limb events into two parts, viz. on main-burst and post-burst sources.

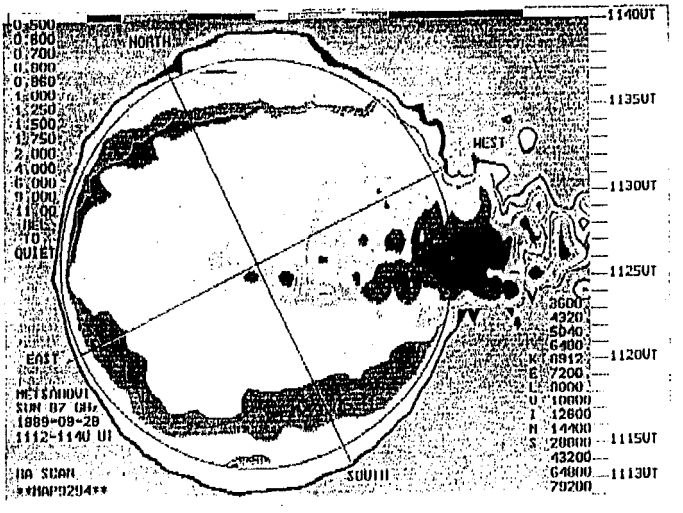

Figure 2. The large limb event on 29 September 1989 seen on a radio map recorded at 87 GHz (3.4 mm wavelength). The time of horizontal scans across the Sun is marked at the left margin of the Figure.

3.1 mm-wave radiation during the main phase of solar flares

Since (unlike Hα) no permanent patrol of the Sun at mm-waves is available, images of well documented mm-wave bursts are comparativeley rare. In the following we show examples of CMMSs of different behaviour.

(a) The outstanding eruptive limb event of 29 September 1989

One of the most spectacular events seen at mm-waves occurred on 29.09.89 at 11:20 UT. Figure 2 shows the burst source on a map taken at 87 GHz (3.4 mm wavelength) during its main phase. The parent active region was one day after the W-limb passage so that the burst source detectable at heights > 9000 km was full in view of the observation (Urpo et al., 1990). The event was associated with a strong LDE-X-ray burst (X 9.8) and a GLE/particle event with proton energies up to 610-850 MeV. If the radiation pattern is not totally due to side lobes (as the authors believe), there would be first evidence of 3 mm- radiation at source heights greater than 300000 km possibly implying optically thin bremsstrahlung

consistent with an extended source of optically thin Coulomb bremsstrahlung of a relatively cool ($T \sim 10^6$ K) and dense ($N_e \approx 10^9\ cm^{-3}$) plasma.

(b) The limb event of 4 April 1990

The development of a limb event at 37 GHz was observed in a sequence of solar maps. The event belongs to a subflare at N22E72 starting at 13:15 UT (Solar-Geophysical Data) and reaches a height of more than 70000 km at 13:17 UT with a further slower increase until 13:29 UT. The lifetime of this event, however, is only of the order of two hours quite in accordance with the soft X-ray burst emission accompanied. Next day again an off- limb source has been observed in the same region which was due to repeated flare activity.

3.2 Long lasting CMMSs

Observations after the main phase of flares verify the existence of long lasting off-limb sources at mm-waves. The following features can be remarked:

- Long lasting (for several hours) CMMSs differ from main-phase burst sources by smaller brightness, in the average.
- Long lasting CMMSs must not be necessarily related to very strong flare events occurring a short time before.
- Sometimes CMMSs can be detected before the onset of a flare in the same region.
- Long lasting CMMSs typically occur in big active regions with a complicated magnetic field topology.

The time history of CMMSs has been studied statistically by Urpo et al. (1986b, 1989). Superimposed on a large scattering of brightness temperatures and source heights measured, there is indicated an (exponential) decrease of the brightness temperatures with time after the preceding flare start (or maximum). The source height is expected to grow rapidly during the initial flare phase and then remains approximately constant.

4. Relation to Microwave Bursts and the Spectrum of CMMSs

It is evident that CMMSs appear to be related to gradual microwave and/or impulsive (including complex) bursts which start up to a few hours prior to the time of the mm-wave observation. The lifetime of CMMSs is much greater than that of these bursts as measured by patrol radio telescopes. Initially the coronal mm-wave emission was interpreted in accordance to Hα-observations by optically thick bremsstrahlung at $T_b \sim 10^4$ K. However, a correction of the measured brightness spectrum for source sizes smaller than the half power beam width of the radio telescopes used are in favour of a thermal optically thin bremsstrahlung spectrum the extension of which is also observed towards longer wavelengths (Borovik et al., 1989). The spectrum of a CMMS observed on 22 September 1980 at the large radio telescope RATAN 600 at cm-waves indicates that possible ways of interpretation depending on the extrapolation of the spectrum into the dm-range are yet open: Model calculations show different possibilities of high-temperature gyromagnetic emission and low- or medium-temperature bremsstrahlung depending on different source parameters. In essence, the the analysis of the microwave spectrum favours the interpretation by an inhomogeneous source composition. Cold

prominence-like matter may be responsible for radiation at frequencies f > 37 GHz while hotter components generate the spectrum at the longer microwaves.

5. Association with X-Rays, CMEs, and Noise Storms

The relations between CMMSs and X-ray bursts and CMEs have been studied by Krüger et al. (1989). There was found an association between CMMSs and LDE-soft X-ray bursts which is closer than the association with type II/IV bursts and proton flares: Although only a part of the CMMSs (about 40%) was found to be associated with LDEs within a time interval of < 5 hours, the association grew up to 95 % when this time interval was enlarged.
Since there is a good correlation between LDEs and coronal mass ejections (CMEs), also CMMSs and CMEs are related to each other, although both phenomena may belong to different dynamic processes.
There are indications that almost all active regions producing CMMSs also generate radio noise storms observable during their disk passage on the Sun (Böhme and Krüger, 1989; Krüger et al., 1991b).
Like noise storms, LDEs, and hard X-ray arches, the CMMSs indicate the presence of far reaching coronal arch systems forming the legs of CMEs. It is important to note that in conjunction with LDEs the HXIS instrument aboard the SMM satellite detected extended X-ray arch-like structures lasting for some 10 hours after huge two-ribbon flares with a source temperature $\geq 2\times10^7$ K forming the base of a noise storm developing from a type IVmB burst (Švestka, 1984a). Also revivals of such coronal X-ray arches have been observed (Švestka, 1984b). This phenomenon is quite analogeous to the renewed occurrence of CMMSs in the same region observed in several cases. But in contrast to HXR, the mm-radiation is more effective at lower temperatures (as far as bremsstahlung is concerned) and thus, in principle, would be also capable to trace cooler regions which are not visible in X-rays at all. The question arises whether CMMSs, LDEs, and HXR-arches together originate at deeper levels with a fast rise of their source region (with speeds of 100 or 1000 km/s) up to 50000-200000 km height and remaining there or being renewed without ascending source motion from below. In any case the energy supply must be provided even during the inter-flare periods in order to maintain the emission. A scenario for the first type of development was given by Hick and Švestka (1987).

6. Conclusions

The conclusions can be summarized as follows:

- Coronal mm-wave sources (CMMSs) are observed as off-limb brightening in solar isophote maps.
- CMMSs are connected with (1) Hα flares and microwave bursts, (2) long living super-gradual post-flare emission, (3) filament eruptions.
- CMMSs are rarely observed and typically indicate extended flare-rich active regione and/or complexes of activity.

- CMMSs are closely related to LDEs and HXR-arch structures as well as to radio noise storms.
- CMMSs are likely to indicate far reaching magnetic field structures which may form the legs of CMEs.
- CMMSs are also related (like filament eruptions and CMEs) to dynamic flare processes, however, the physical link between long lasting confined sources and explosively dynamic processes is not yet understood.
- CMMSs are in favour of an inhomogeneous source structure signifying (1) cold, optically thick plasma preferably at short mm-wavelengths and (2) hotter optically thin plasma at longer mm- and cm-waves.
- Future tasks involve observations with better spatial resolution and a more systematic coverage of CMMSs in time and spectrum including both Stokes parameters I and V.

References

Böhme, A., Krüger, A.: 1989, in: R.B. Teplitskaya (ed.), *Solar Magnetic Fields and Corona*, Novosibirsk, p. 313.

Borovik, V.N. and 6 coauthors: 1989, *Solar Phys.* **124** , 157.

Hick, P., Švestka, Z.: 1987, *Solar Phys.* **108**, 315.

Krüger, A., Hildebrandt, J., Urpo, S., Pohjolainen, s.: 1989, *Adv. Space Res.* **9**, (4)47-(4)51.

Krüger, A. and 7 coauthors: 1991a, *Solar Phys.* **134**, 171.

Krüger, A., Böhme, A., Hildebrandt, J., Urpo, S.: 1991b, *Contribution to Solar Wind Seven*, 16.-21.09.1991, Goslar, Germany.

Kundu, M.R.: 1972, *Solar Phys.* **25**, 108.

Solar-Geophysical Data, NOAA, US Dept. of Commerce, Boulder, USA, 1979-1991.

Švestka, Z.: 1984a, *Mem. S.A.It.* **55**, 725.

Švestka, Z.: 1984b, *Solar Phys.* **94**, 171.

Urpo, S., Teräsranta, H., Rompolt, B., Garczyńska, I.: 1983, *Report to the XIth General Assembly of URSI*, Helsinki.

Urpo, S., Teräsranta, H., Ruzdjak, V., Vrsnak, B. Rompolt, B., Kren, G.: 1985, *Hvar Obs. Bull.* **9**, 25.

Urpo, S., Krüger, A., Hildebrandt, J.: 1986a, *Astron. Astrophys.* **163**, 340.

Urpo. S., Teräsranta, H., Pohjolainen S., Ruzdjak, V., Vrsnak, B., Rompolt, B.: 1986b, *Adv. Space Res. 6*, 267.

Urpo, S., Hildebrandt, J., Krüger, A.: 1987, *Solar Phys.* **112**, 119.

Urpo, S., Pohjolainen, s., Teräsranta, H.: 1987-1991, Helsinki Univ. of Technology, Metsähovi Radio Res. Station, *Reports*, Series A, 1 - 6.

Urpo, S., Teräsranta, H., Krüger, A., Hildebrandt, J., Ruzdjak, V. : 1989. *Astron. Nachr.* **310**, 423.

Urpo, S., Tornikowski, M., Teräsranta, H., Krüger, A.: 1989, *Contr. to XXVIII COSPAR* (S9), The Hague, Netherlands.

Zodi, A.M. and 5 coauthors: 1988, *Solar Phys.* **116**, 83.

ON THE ASSOCIATION BETWEEN LARGE SCALE X-RAY BRIGHTENINGS AND SOLAR FLARES

C.H. Mandrini* and M.E. Machado**
* Instituto de Astronomía y Física del Espacio, CC 67, Suc. 28, 1428 Buenos Aires, Argentina
** Department of Physics, University of Alabama, Huntsville, 35899 Alabama, USA

Abstract. We have studied SMM Hard X-ray Imaging Spectrometer (HXIS) observations of large scale brightenings (LSBs) associated with confined flares that developed in complex active regions. These structures have sizes ($> 10^{10} cm$) similar to the so-called "giant arches", that were discovered in HXIS images hours after the onset of two-ribbon flares.

We have analyzed seven events, four observed after flares that took place in active region (AR) 2372 (NOAA number) during April 7 and 8, 1980 and three from AR 2779 during November 11 and 12, 1980. Both ARs have the same magnetic configuration, two main spots with a reverse polarity region in between; in this type of configuration four topologically distinct sets of field lines are present. The three-dimensional field topology of AR 2372 was derived, using magnetograph data from April 6, in one of our recent works. This computations show the presence of a separator above the intermediate bipolar region and lines of force joining the main leading and trailing spots over it. These lines would correspond to the large loops observed in X-rays. Thus, these large scale features appear as pre-existing magnetic structures, whose brightening can be due to heating by internal energy dissipation or by energy leakage at the separator region. In some of our examples we were able to study simultaneously the temporal evolution of the flare and large loops parameters, we found that the LSBs temperature reaches its maximum during, or slightly after, the impulsive phase in hard X-rays and the emission measure some tens of minutes later; in all cases the LSB maximum temperature is higher than the flare's. We demonstrated that this can be due to the injection of suprathermal particles that are accelerated at the separator region. We have observed other characteristics in these large features, like a temperature stratification in the April LSBs and a growth with time in the November events.

Our findings concerning confined flares and LSBs have led us to propose an alternative scenario for the origin of giant arches. In this view giant arches appear as the result of the sequential energization, due to reconnection, of a conglomerate of pre-existing large scale loops.

This paper has been submitted for publication to Solar Physics.

A GIANT POST-FLARE CORONAL ARCH OBSERVED BY SKYLAB

Zdeněk Švestka

Center for Astrophysics and Space Sciences, University of California at San Diego, La Jolla, California, USA, and SRON Utrecht, The Netherlands

and

Stanislava Šimberová

Astronomical Institute of Czechoslovak Academy of Sciences, Ondřejov, Czechoslovakia

Abstract. The limb event of 13 August 1973, observed by Skylab in soft X-rays, exhibited typical characteristics of the giant post-flare arches observed by HXIS and FCS on board SMM in the 1980s. We present here examples of the processed Skylab images which yield 4 times better angular resolution than the SMM experiments and thus, for the first time, make it possible to distinguish the real fine structure of a giant post-flare arch.

1. Introduction

After the detection of 10 giant post-flare arches in SMM data (see, e.g., Hick, 1988, p. 15), observed either in X-ray continuum below 3.5 Å or in X-ray lines of Mg XI (9.2 Å) and O VIII (20.0 Å), it became obvious that these structures should also have been observed by Skylab soft X-ray telescopes which imaged the Sun in similar energy bands: 2 - 54 Å in the S-054, and 8 - 47 Å in the S-056 experiment. Until recently, however, any search for such structures was unsuccessful, due to the high background of scattered light which did not allow long enough exposure times, and which also does not allow accumulation of images which made these relatively weak structures recognizable in projection on the solar disk in the SMM data (where the background noise was very low).

However, there is one conspicuous event in Skylab data which was observed on the limb, where the background does not have this disturbing effect, and which appears to be essentially the same phenomenon as the giant post-flare arches observed by the SMM. This event occurred on 13 August 1973 and was first detected by Tandberg-Hanssen *et al.* (1975) who considered it to be a coronal condensation. Later on, Vorpahl, Tandberg-Hanssen, and Smith (1977) and MacCombie and Rust (1979) classified it as a long-duration X-ray event and included it among other eruptive flares with growing systems of loops. However, the event actually has all characteristics of the giant post-flare arches detected by the SMM, as has been demonstrated by Švestka (1991).

2. Characteristics of the Arch

We will mention here the three most essential characteristics which strongly indicate that the event on 13 August 1973 was a giant post-flare coronal arch (see Švestka, 1991, for more extensive evidence):

(1) According to Vorpahl, Tandberg-Hanssen, and Smith (1977), the Skylab feature reached an altitude of 180 000 km. This is an altitude typical for giant arches (cf. Švestka, 1984), but much higher than (post-)flare loops in eruptive flares (e.g., Moore *et al.*, 1980).

(2) The top of the Skylab structure was rising with a very low speed of about 0.55 km/s which was rather constant for 10 hours (MacCombie and Rust, 1979). While flare loops have higher speeds early in their development, and the speed of their growth is gradually decreasing, giant arches show a wide spectrum of speeds, from less than 0.5 km/s (Hick and Švestka, 1985) to more than 8 km/s (Švestka, 1984) and the speed in all observed cases was found to be constant.

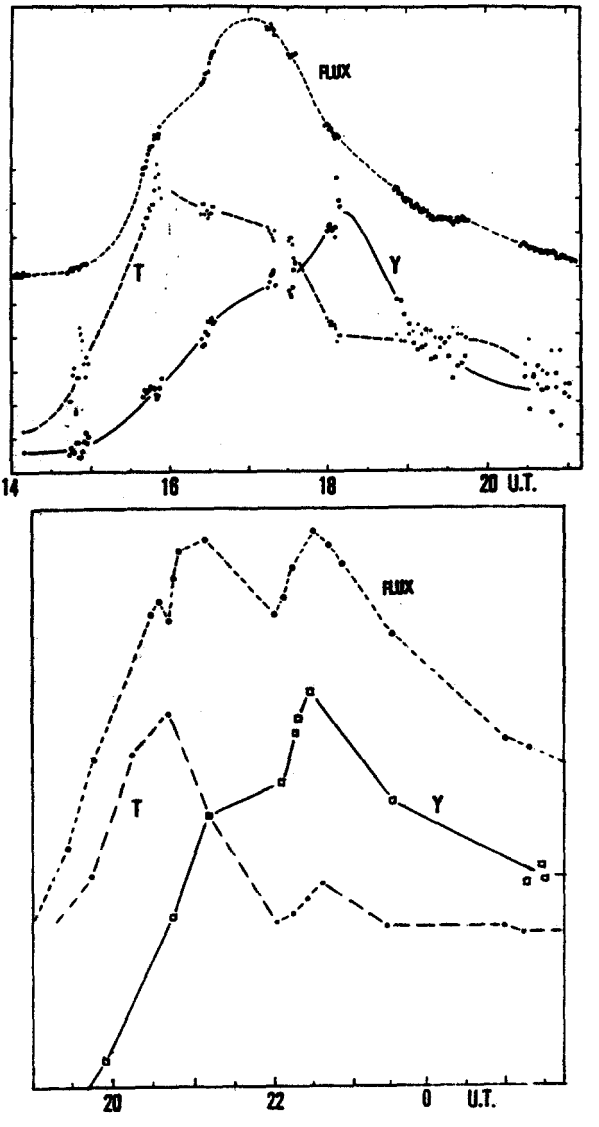

Fig. 1. *Above*: Time development of flux, temperature (T), and emission measure (Y) in the giant post-flare arch observed by HXIS on board SMM in 3.5 - 8.0 keV X-rays on 6 November 1980 (after Švestka, 1984). *Below*: time development of flux, temperature, and density (emission measure) in the limb structure of 13 August 1973 observed on Skylab in 8 - 16 Å X-rays (after Vorpahl, Tandberg-Hanssen, and Smith, 1977).

(3) Figure 1 compares the time evolution of this Skylab feature (after Vorpahl, Tandberg-Hanssen, and Smith, 1977) with that of the well-studied giant arch of 6 November 1980 (after Švestka, 1984). The behavior is almost exactly the same: maximum temperature is reached less than 1 hour after the arch onset, maximum brightness about 2.5 hours after onset, and maximum emission measure still one hour later. Apart from the double maximum in brightness, the two sets of curves presented in Figure 2 are astonishingly identical. Note, for a comparison, that (post)-flare loops reach maximum temperature in their onset phase and maximum emission measure only a few tens of minutes later (cf., e.g., Figure 5 in Švestka et al., 1982).

Thus there can be little doubt that this was a giant post-flare arch according to the SMM definition (cf., e.g., Svestka, 1984).

3. Processing of 2 - 17Å Images

All the giant arches seen by HXIS were observed with spatial resolution of 0.5 arc min. The arches observed by FCS also had spatial resolution of the same order, because we had to "smooth" 4 pixels to get enough counts for a statistically significant analysis (cf. Hick *et al.*, 1987). *Thus this Skylab event offers a unique opportunity to analyze a giant post-flare arch with spatial resolution improved by a factor four or better* (nominally, the angular resolution of X-ray telescopes on Skylab at the solar limb was 5 arc sec).

We have begun to process the X-ray images of the arch, obtained by the S-054 Skylab experiment, using filters 1 (2 - 17 Å) and 3 (2 - 54 Å). Digitized original images of the event are available on magnetic tapes kindly provided by David Batchelor at NASA GSFC, but unfortunately, due to several unfavorable circumstances, we have been unable to read and process these tapes so far. Therefore, for this presentation, we had to use 16 years old second-generation photographic copies of the event, of much lower quality than Batchelor's data, and available only for filter 1. We have digitized these plan film copies and processed them using a method of local optimization of density in the subimages of 33 x 33 pixels with a linear transformation of density. The results are shown in Figure 2.

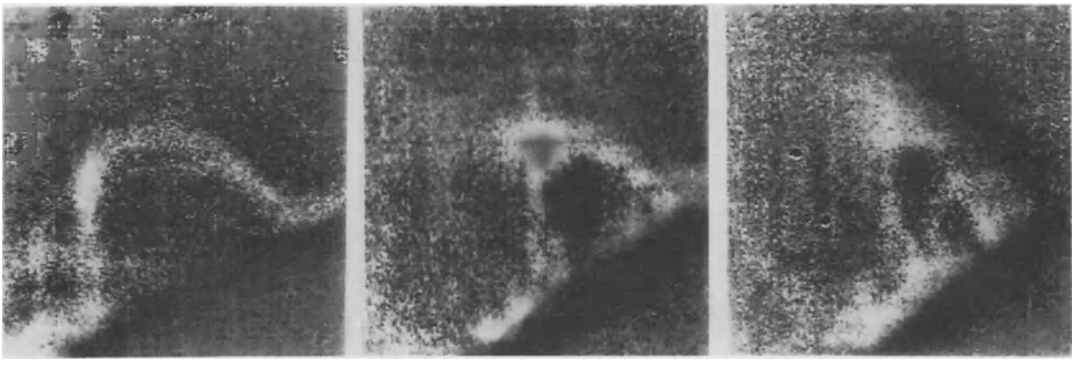

Fig. 2. Processed images of the event using 64 s exposures through filter 1 (2 - 17 Å). *Left*: situation 2 hour before the event, at 17:43 UT on August 13. *Middle*: near the maximum brightness of the event, at 21:43 UT on August 13. *Right*: more than 11 hours after the onset of the event, at 07:06 UT on August 14.

The images clearly demonstrate that the post-flare giant arches, seen before on SMM as unresolved clouds, consist of well-defined individual loops. The first image shows that high coronal structures existed in the corona above the active region prior to the post-flare giant arch appearance. This is in agreement with SMM observations in November 1980 (Švestka, 1984) and January 1985 (Hick *et al.*, 1987) when the post-flare arches were classified as revivals of preexisting coronal formations. However, the second image, near the event maximum, shows that the brightest arch component is not identical with the brightest component prior to the event. Thus, other loops have apparently been formed or brightened in the post-flare arch.

The second image also shows that the brightness maximum was at the top of the imaged loop(s). This is in agreement with SMM observations of the giant arch of 21/22 May 1980, when the maximum brightness also was located near the top of the arch (Hick and Švestka, 1985). Already MacCombie and Rust (1979) detected this maximum at the top of the August 1973 structure and considered it for the typical brightening at the top of post-flare loops. In post-flare loops, this top brightening indicates loop formation through a reconnection process (following Kopp and Pneuman's (1976) model) and the same conclusion can be drawn here for the arch. Thus these observations support the interpretation of giant arches by Poletto and Kopp (1988; see the discussion in Section 5 of Poletto and Švestka, 1990) who suppose that new arch loops are successively formed in the high corona through field-line reconnection following the flare.

The last image in Figure 2 shows the situation during the arch decay. We see here quite different loops and the highest one still shows maximum brightness at its top. It is of interest that the loop footpoints get, at least in the projection, move progressively closer to each other during the arch development. This indicates changing shear in the arch structure; however, more images have to be processed to fully understand this effect.

We hope that much more information can be obtained after we process the original images on the GSFC tapes and, in particular, when we process images from the 2 - 54 Å energy band and use images with various exposure times. These results should appear in one of *Solar Physics* 1992 issues.

References

Hick, P.: 1988, *Interpretation of Energetic Phenomena in the Solar Corona*, Thesis, University Utrecht.

Hick, P. and Švestka, Z.: 1985, *Solar Phys.* **102**, 147.

Hick, P., Švestka, Z., Smith, K.L., and Strong, K.T.: 1987, *Solar Phys.* **114**, 329.

Kopp, R.A. and Pneuman, G.W.: 1976, *Solar. Phys.* **50**, 85.

MacCombie, W.J. and Rust, D.M.: 1979, *Solar. Phys.* **61**, 69.

Moore, R.L., McKenzie, D.L., Švestka, Z., Widing, K.G., and 12 co-authors: 1979, in P.A. Sturrock (ed.), *Solar Flares*, Proceedings of Skylab Workshop, p. 341.

Poletto, G. and Kopp, R.A.: 1988, *Solar Phys.* **116**, 163.

Poletto, G. and Švestka, Z.: 1990, *Solar Phys.* **129**, 363.

Švestka, Z.: 1984, *Solar Phys.* **94**, 171.

Švestka, Z.: 1991, *Solar Phys.* **135**, 419.

Švestka, Z., Dodson-Prince, H.W., Martin, S.F., Mohler, O.C., Moore, R.L., Nolte, J.T., and Petrasso, R.D.: 1982, *Solar Phys.* **78**, 271.

Tandberg-Hanssen, E. and 8 co-authors: 1975, *Bull.AAS* **7**, No.3, Part 1, p. 444.

Vorpahl, J.A., Tandberg-Hanssen, E., and Smith, J.B.: 1977, *Astrophys. J.* **212**, 550.

5.

CORONAL MASS EJECTIONS

Related poster papers in Chapter 8:

W.P. Guo, J.F. Wang, B.X. Liang, and S.T. Wu

J.T. Gosling, D.J. McComas, and J.L. Phillips

A.L. Clúa de Gonzalez, W.D. Gonzalez, S.L.G. Dutra, and B.T. Tsurutani

CHARACTERISTICS OF CORONAL MASS EJECTIONS

Ernest Hildner
NOAA Space Environment Laboratory
325 Broadway, Boulder, Colorado 80303 USA

Abstract: Coronal mass ejections (CMEs) are important and beautiful solar phenomena. Their frequency of occurrence, locations, speeds, and sizes are presented, measured over a significant fraction of a solar cycle. As yet, there is no consensus model which adequately explains these measurements, in part because the initiation and evolution of CMEs appear extremely complex and intractable.

INTRODUCTION

This paper presents information about the appearance, frequency, locations, speeds, and sizes of coronal mass ejections, as observed in the fields-of-view of orbiting coronagraphs. Presentation of these characteristics is intended to set the stage for the coronal mass ejection (CME) papers which follow.

The paper concludes with comments about the general characteristics of the initiation of coronal mass ejections and the models which attempt to describe these initiations.

For more information about CMEs than is contained in this volume, the reader is referred to three references to the literature by Harrison [1], Hundhausen [2], and Kahler [3].

A white light image obtained with an orbiting coronagraph captures a pattern of brightness. The brightness arises from Thomson scattering of photospheric light by the coronal electrons. Both the flux and the average polarization of the photons arriving at the coronagraph can be measured, but for the purposes of this paper polarization measurements are ignored. Because every free electron in the corona participates in Thomson scattering, coronagraph images reveal the presence of all the ionized material in the corona. That is, the brightness in an individual pixel of a coronagraph image depends solely upon the integral of the density of coronal electrons along the line-of-sight. The brightness contribution of any electron along the line-of-sight is weighted according to the distance of closest approach of that line-of-sight to the Sun and to the location of the electron along the line-of-sight light scattered by dust . Though ignored here, there are also contributions to the brightness in an individual pixel due to the F-corona and light scattered within the coronagraph. For thorough explanations of the K-coronal weighting functions and the F-coronal contribution, the reader is referred to the presentations by Billings [4] and Saito [5]. In what follows, we assume that the F-coronal and instrumentally scattered light contributions do not influence our interpretations, either because they have been subtracted from the images, or they are sufficiently faint to be ignored. While this is an adequate approximation for what is reported here this assumption is often not true for other studies.

Lacking space for a comprehensive review, Solar Maximum Mission (SMM) coronagraph observations are emphasized in what follows. The SMM coronagraph data started in 1980 and ended in 1989; though interrupted from late 1980 until 1984, this is the longest observed run of any orbiting coronagraph. Throughout this period, observations were of good quality, were taken routinely, and were available at fairly high cadence. SOLWIND observations--which extend to greater height in the corona--have their own stories to tell about the characteristics of CMEs farther from the Sun.

CME Appearance. Recently, Hundhausen [2] has described the three-part structure shown by many CMEs. The three parts consist of a bright erupting prominence at the bottom, surrounded by a dark coronal cavity, in turn surrounded by a bright arc of denser coronal material. In some coronal mass ejections an erupting prominence is not seen, but the other two components of the CME are almost always present. Rarely, we see CMEs that lack the coronal cavity; that is, they seem to be filled with brightly emitting denser material. Typically, the prominence does not move outward as rapidly as the outer parts and radial stretching of the C

CME results. The outer arch of the CME is smooth and nearly structureless, whereas there is a much more "knotty" structure in the prominence. Typically, as the outer arch of a CME rises, the legs remain rooted at their initial position angles. As the arch moves higher, the legs become approximately radial at these position angles and eventually fade away.

STATISTICAL PROPERTIES

Observations from orbiting coronagraphs span more than one solar cycle. OSO-7 and Skylab in the early 70's monitored a portion of solar cycle 19, the SOLWIND coronagraph monitored the rise of solar cycle 21, and overlapped in 1980 with the SMM coronagraph. The Solar Maximum Mission (SMM) coronagraph observed the corona in 1980 and then again from 1984 until 1989.

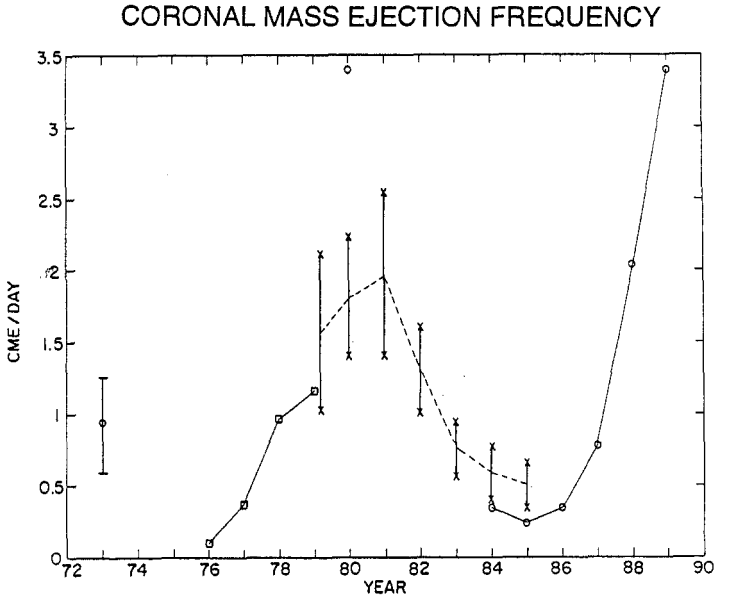

Figure 1. Annual Average CME rate. Observations from Skylab (in 1973), Helios (□), SOLWIND (X), and SMM (o) span 16 years. To estimate the entire production of CMEs, the observed production rates have been corrected for visibility and duty cycle effects. See text from Webb [6].

Frequency of Occurrence. Figure 1 shows the number of CMEs occurring per day. In years when observations were available from more than one orbiting instrument, agreement is rather good, except for 1980 when there is a 50 percent discrepancy between SOLWIND and SMM observations. To estimate the total number of CMEs per day emitted from the entire Sun averaged over a year, Webb [6] has applied the following correction to the number of CMEs actually observed. First, the number of CMEs observed above the solar limbs is doubled, to account for ejections which presumably left the Sun in the earthward and anti-earthward directions; then these numbers are increased to account for the duty cycle of the experiment during the year.

The number of CMEs emitted per day by the Sun appears to vary approximately in phase with the solar cycle. Although there are some difficulties in comparing occurrence rates obtained with different instruments, due to particular instrumental effects, we can infer significant variations from the SMM observations alone. Figure 1 shows that CME rates fell about a factor of 10 from the maximum of solar cycle 21 to the minimum separating solar cycle 21 and 22, and then rose to the earlier value at the maximum of solar cycle 22. The average number of CMEs per day appeared to be the same in 1980 and 1989 when the average

sunspot numbers in both those years were about 155; however, in years when the average monthly sunspot number was 33 to 38, the CME occurrence rate varied by a factor of 3 from about 0.3 to about 0.9 per day.

Figure 2, also from Webb [6], compares CME rates (corrected as for Fig. 1) to sunspot numbers.

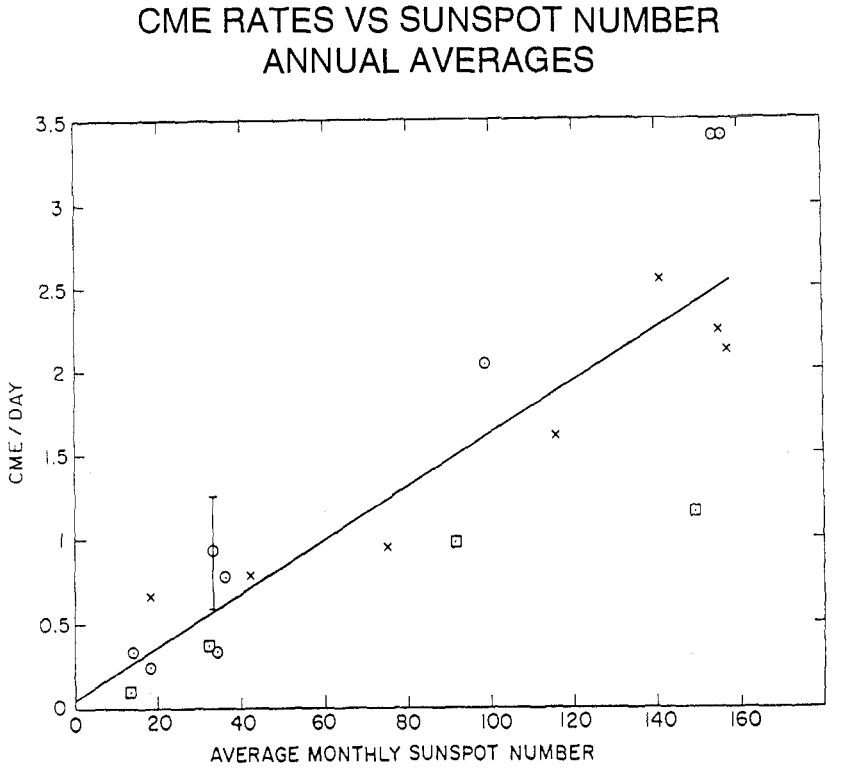

Figure 2. Variations of CME rates with sunspot numbers, annual averages. The annual average CME rates of Figure 1 are here plotted against their appropriate annual average monthly sunspot number. Data symbols are as in Fig. 1 f. From Webb [6].

Locations. For many, but not all, coronal mass ejections, it is possible to delineate the position of the northern and southern edges. For a given CME, the position angles of these two edges, $\phi 1$ and $\phi 2$ (measured counterclockwise in the plane of the sky from 0^{o} at solar north) can be averaged--$(\phi 1 + \phi 2)/2$--to give the position angle--or, equivalently, the apparent latitude--of the "center" of the CME. Figure 3 shows SMM observations of CME locations in 7 years. The top panel of the figure shows that in 1980, at solar cycle maximum, CMEs were observed over both north and south poles, and the distribution of latitudes of CME centers was quite flat. The distribution of apparent latitudes of CMEs shrinks toward the equator as solar minimum (1986) is approached and then rapidly reoccupies a broad range of latitudes in the years of rising solar cycle.

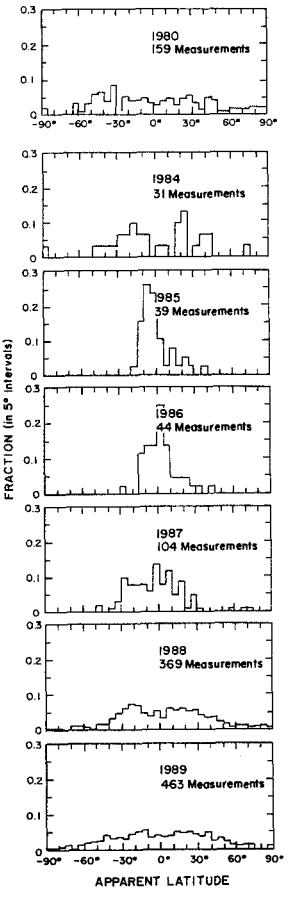

Figure 3. Apparent central latitudes of 1209 CMEs observed from SMM, year by year. From Hundhausen [7].

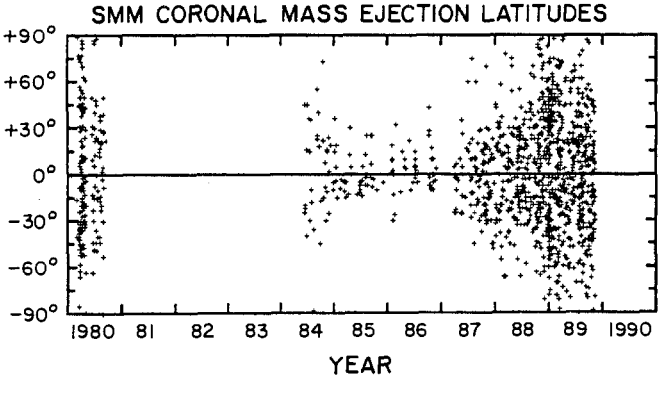

Figure 4. Locations of apparent central latitudes, using same data as in Figure 3. From Hundhausen [7].

Figure 4 presents the locations of CMEs during the solar cycle in the familiar "butterfly diagram" format. Hundhausen [7] has pointed out that Figure 4 closely resembles a similar-format figure showing the locations of prominences, but differs markedly from a similar-format figure showing the locations of active regions. He asserts that this comparison confirms that CMEs are physically better connected with large, closed, coronal magnetic structures than with small-scale, intense, active region, magnetic structures.

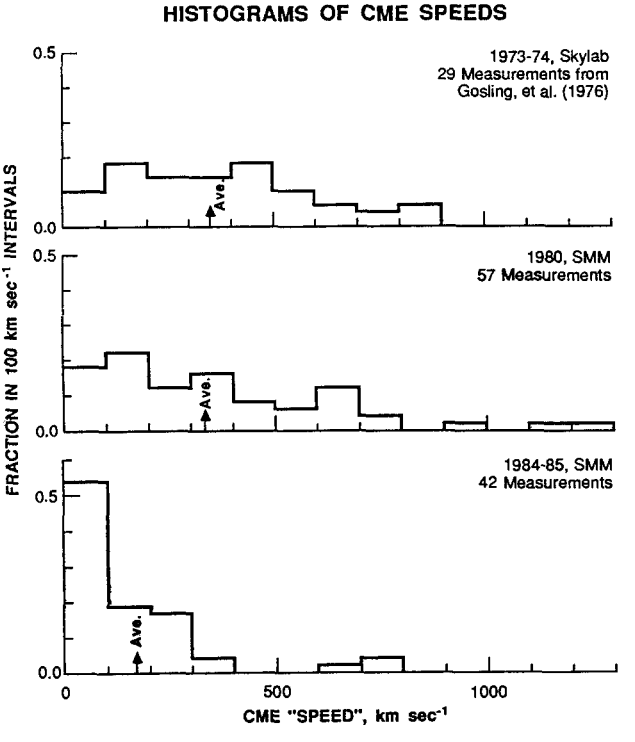

Figure 5. CME speeds in three epochs. From Hundhausen [8].

Speeds. Many, but not all, coronal mass ejections have features which can be identified in successive images. From the projected heights of a feature at various times it is possible to derive speeds for the CMEs. It is conventional not to correct the measured speeds for projection effects, even though not all CMEs arise in the plane of the sky. Typically, CME speeds are nearly constant and accelerations or decelerations are mild, especially at heights of a few solar radii. Figure 5 shows CME speeds measured at three epochs of the solar cycle. The Skylab and SMM observations were taken with similar instruments and reduced in similar ways. The top panel shows data from a 9-month interval approximately five years after solar maximum. In this period, speeds ranged from $\lesssim$100 to $\lesssim$900 km s^{-1} and average about 350 km s^{-1}. In 1980, at solar maximum, CME speeds ranged up to 1300 km s^{-1}, but generally the distribution of speeds was similar to that in 1973-1974. The bottom panel, for 1984-1985, approximately 5 years after solar maximum, as in the top panel, shows a strikingly different distribution of measured speeds; there were many more slow than fast events, and few speeds exceeded 400 km s^{-1}. Those CMEs were traveling outward at speeds less than the Alfvén speed and less than the sound. It is obvious that these CMEs cannot be "pistons" driving shocks. It is

also interesting to note that CMEs do not slow in a ballistic fashion as they rise. Although many CMEs progress outward at low heights at speeds well below the local ballistic escape speed, eventually the CMEs' constant speeds exceed the lower speed of escape from greater heights.

There is no obvious, systematic difference in appearance between fast and slow CMEs. That is, it is not possible to tell from a single snapshot of a CME whether it is fast or slow.

Sizes. In contrast to the previously discussed properties of CME characteristics, the sizes of CMEs, their angular widths, do not appear to vary appreciably with phase in the solar cycle. Here, we take the angular width or size of a CME to be the difference between the position angles of the two edges, $[\phi 2 - \phi 1]$. Figure 6 shows the distribution of angular widths of CMEs measured with the SMM coronagraph in each of seven years. Although the distributions are smoother in years of numerous observations, their shapes do not differ greatly from year to year. The annual average size of a CME varies only a few degrees from 45^{o} during the solar cycle.

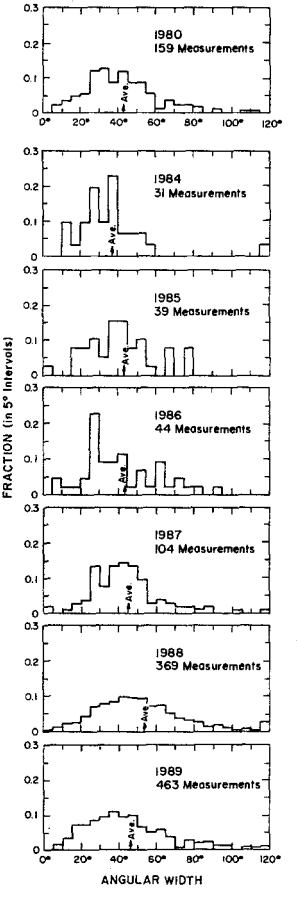

Figure 6. Angular widths of 1209 CMEs observed from SMM, year by year. Annual average values are shown by arrows. From Hundhausen [7].

Obviously, an event spanning 45° covers a much larger range of position angles than the typical active region. This observation reinforces the idea that coronal mass ejections are associated with large-scale coronal magnetic configurations rather than with active region scale configurations.

Models. Even a modest discussion of the various CME models which have been proposed is beyond the scope of this paper. For brevity, it is convenient to consider categories of models. Harrison [1] suggested that there are four categories of CME models. (a) A stable magnetic configuration is disrupted by a large-amplitude perturbation. (b) An initially stable configuration evolves to a metastable state, which is then disrupted in response to a small perturbation. (c) An initially stable configuration evolves incrementally in response to small changes at the boundary until the next small boundary change imposes an abrupt loss of equilibrium. (d) An equilibrium magnetic configuration exhibits large-amplitude, rapid evolution in response to incremental, slow changes in boundary conditions.

Harrison gives an extensive discussion of proposed CME models in the context of these four categories. We note that Harrison's categories (b) and (c) seem to differ only very subtly, if at all. In Harrison's category (a) models, the CME is initiated by a flare; however, many CMEs are initiated without a flare being present.

Regrettably, no model in any of these four categories is completely satisfactory to explain coronal mass ejections. Physically unrealistic simplifications abound (for example: solving a 2-D problem when most solar magnetic configurations are intrinsically 3-D, assuming dynamic structures are permeated by force-free fields; or considering a series of static equilibria to represent dynamical phenomena), because the realistic problem is intractable.

CONCLUDING COMMENTS

Enough coronagraph observations have accumulated that we may be confident about the salient characteristics of coronal mass ejections. (A noteworthy exception is the magnetic field in and around CMEs.) As yet, there is no consensus on the mechanisms which initiate and drive these beautiful objects, despite diligent effort on the part of many theorists.

The triple coronagraph on the SOHO mission, to be launched in 1994, promises to extend the range of heights over which individual CMEs are observed. In conjunction with the emission line measurements made by the other instruments aboard SOHO, we can look forward to a better understanding of a CME's history--and its make-up. We will have more information abut CMEs' internal density, temperature, and velocity structure than we have ever had before.

ACKNOWLEDGEMENTS

In this review I have drawn heavily upon the work of Richard Harrison and Art Hundhausen. I am deeply grateful to them for making their papers available to me in advance of publication. Stephen Kahler gave helpful comments on this paper.

REFERENCES

1. Harrison, R.A.: Phil. Trans. Roy. Soc. A, in press (1991).
2. Hundhausen, A.J.: in Proc. Sixth Intl. Solar Wind Conf., NCAR Tech. Note, Boulder, TN-306, Vol. 1, 181, (1988).
3. Kahler, S.W.: Rev. Geophys. 25, 663, (1987).
4. Billings, D.W.: *A Guide to the Solar Corona*, Academic Press, New York, (1966).
5. Saito, K.: Ann. Tokyo Astron. Obsvy., Second Series XII, 53, (1970).
6. Webb, D.F.: Adv. Space Res. 11, (1) 37, (1991).
7. Hundhausen, A.J., J. Geophys. Res., submitted, (1991).
8. Hundhausen, A.J.: Personal Communication, (1990).

The Solar Sources of Coronal Mass Ejections

David F. Webb

Institute for Space Research, Boston College,
Newton Center, MA, U.S.A., 02159

Abstract: Despite nearly two decades of observations and study of coronal mass ejections (CMEs), the question of the physical and phenomenological origins of CMEs remains unanswered. This question has been addressed in several different types of studies, each having important limitations. These include statistical analyses of the probabilities of association with CMEs of certain kinds of solar activity near CME onset, studies of the timing and location of activity associated with individual events, and hybrid studies combining these methods. These studies suggest significant levels of association between CMEs and such near-surface activity as eruptive prominences, optical and X-ray flares, and gradual microwave and metric type II and IV radio bursts. The highest frequencies of association are between CMEs and prominence eruptions and long-enduring X-ray events. This relationship appears strong enough to suggest that prominence- related ejections may form a separate physical class of CMEs. On the other hand, about half of all CMEs appear to have no "good" associations. I review the results of studies of CME origins, including recent results on the timing and location of CMEs and related activity.

1 Introduction

Much has been learned about coronal mass ejections (CMEs) since they were first extensively studied during Skylab. Although only a fraction of all observed coronal activity, CMEs are of interest because they involve discrete ejections of mass and magnetic fields into the solar wind. However, we still lack a good understanding of the origins of CMEs at or near the surface, and how they are driven through the corona. In this paper I review results pertaining to the first question.

CMEs are best observed near the limb of the sun in Thomson- scattered white light by coronagraphs. In order to observe subtle coronal structures, coronagraphs must occult the photosphere and bright inner corona below about 1.5 R_0. These instrumental considerations place fundamental limitations on how well we can determine the initiation process of CMEs. Data sets from three orbiting coronagraphs have governed the studies of CMEs. The first High Altitude Observatory (HAO) coronagraph was successfully flown during the Skylab missions in 1973–1974 and observed nearly 100 CMEs. The Solwind coronagraph, built by the Naval Research Laboratory, was flown on the P78-1 satellite and observed more than 1200 CMEs between March, 1979 and September, 1985. The HAO coronagraph-polarimeter (C/P) on the Solar Maximum Mission (SMM) satellite obtained observations of over 1300 CMEs during 1980 and after its repair, from June 1984 until SMM's reentry in December 1989.

The coronagraph observations have been complemented by additional CME observations in the inner and distant corona. The ground-based HAO K-coronameter at Mauna Loa Solar Observatory (MLSO), Hawaii observes over an altitude range of 1.2–2.2 R_0, while a prominence monitor simultaneously records disk and limb Hα images.

These observations were made during most of the SMM mission, from August 1980 to the present. From 1975 through about 1982 observations of CMEs in the interplanetary medium were obtained by the zodiacal light photometers on the Helios spacecraft. With this instrument CMEs could be observed from 0.3 to 1.1 AU and even from within the CME itself.

To try to better understand their origins, the CME observations are usually compared with spaceborne and ground- based data of other kinds of near-surface activity thought to be related. These have included data in EUV and hard and soft X-rays from the Skylab, SMM, Solrad and GOES satellites, spatially resolved microwave and metric radio burst data from radio observatories such as Culgoora, Clark Lake and Nancay, swept frequency burst data, and optical observations of flares and prominence eruptions from worldwide observatories, recently including the USAF SOON network. Some theoretical models of CMEs have also addressed their initiation, but only in ad hoc ways.

In the next section I review general results from previous CME association studies, and in Sections 3 and 4 the timing, spatial scales and locations of activity related to CMEs for flares and erupting prominences (EPs), respectively. Recent results placing CMEs in the context of large-scale coronal structures are described in Section 5 and the main points summarized in the last section. The relation of CMEs to theoretical models, shock waves, interplanetary phenomena, and metric radio bursts are addressed elsewhere in these proceedings (also see reviews such as [1]).

2 Review of CME Association Studies

The Skylab mission provided the first large data base of CME events which could be compared with other solar phenomena to search for spatial and temporal associations. Gosling et al. [2] and Munro et al. [3] carried out the first surveys associating the ~ 75 major Skylab CMEs viewed in the middle corona with near-surface activity, and found good associations with EPs, Hα flares, X-ray events, and type II and IV radio bursts. Webb and Hundhausen [4] found that about 2/3 of the SMM CMEs with measured speeds observed during activity maximum in 1980 could be well associated with these same kinds of solar activity. In addition, they found that most of the associated soft X-ray events were of long duration (LDEs). For both epochs the CMEs were most commonly associated with EPs (about 80% of the associated CMEs) and soft X-ray events; EPs were about twice as likely to be associated than were Hα flares or metric radio bursts. Harrison [5] and St. Cyr and Webb [6] performed similar studies with SMM data covering the epoch around solar minimum, 1984–1986, and got similar results. However, [6] found that a lower fraction of CMEs had apparent associations, likely an effect of the lower average speeds of the CMEs during this period. Table 1 [6] summarizes the key results and demonstrates that the distribution of the various forms of activity related to CMEs does not change over the solar cycle.

Other results also reveal an important role for prominences in the origin of CMEs. Bright cores of material, presumed to be the remnants of Hα prominences, have been seen in about $\frac{1}{3}$ [4] to $\frac{1}{2}$ [6] of all SMM mass ejections. Although the brightest of

these structures match well with Hα-emitting material lower in the corona, most of this material becomes nearly fully ionized as it moves outward [7]. On the other hand, occasionally some of the prominence material can survive unheated to 1 AU as evidenced by enhanced He^+ events.

A prominence is also a key part of the classic picture of a CME as a three-part event. In this picture the pre-event structures, consisting of the prominence, overlying coronal cavity and ambient corona, erupt to become the bright core, intervening dark shell or cavity, and outer loop of the CME in coronagraph images. It is important to note that most CMEs form below the field of view of a coronagraph, even below that of the K-coronameter which restricts the height of formation to below 1.2 R_0. However, eruptions of pre-existing streamers, the so-called streamer blowout events, clearly involve the expulsion of coronal material and mass previously in the coronagraph field.

The association studies show that, not only are EPs the most common activity associated with CMEs but nearly all single associations are EPs. Even when CME-associated, flares are usually accompanied by cool eruptive material. Wilson and Hildner [8] found that about half of the magnetic clouds, considered to be signatures of CMEs at 1 AU, defined by Klein and Burlaga [9] could be associated with filament disappearances back at the sun. Cane et al. [10] and Heras et al. [11] found a number of cases where interplanetary shocks, which are associated with CMEs, and energetic particle events arose from isolated EPs. Despite the lack of accompanying flares, these events resulted in very energetic interplanetary phenomena. Finally, the 1 AU in-situ signatures of disturbances following flares and large, isolated filament disappearances exhibit distinct differences, suggesting that such EPs form a separate class of CMEs [12].

There may also be two classes of CMEs in terms of their kinematical properties or energetics. Using K-coronameter observations, [13] found a clear difference between flare- and prominence-associated CMEs. Flare-associated CMEs exhibited higher speeds with little evidence of acceleration, while prominence-associated CMEs were slower and displayed substantial acceleration in the low corona. MacQueen and Fisher suggested that flare-associated CMEs are produced in impulsive accelerations acting over small spatial (0.2 R_0) and temporal ($\leq$ 10 min.) regimes, while prominence-associated CMEs are subjected to significant accelerations over extended distances and times. However, one problem with this simple picture is that because of the limited time cadence of coronagraph observations, accelerations cannot be determined accurately for faster CMEs; they could have accelerations similar to prominence-associated CMEs. In addition, because many CMEs are associated with both prominences and flares [4, 6], there is ambiguity about the way [13] made their flare and prominence associations. A contrary view is that of [14] and others who suggest that there exists a broad spectrum of CME sources ranging from large flares in complex active regions to eruptions of isolated quiescent prominences. These events would then differ only by degree, and would not be separate classes as suggested by [13].

There is evidence that the latitude distributions of CMEs track prominences and EPs more closely than flares over the solar cycle [15, 4, 48]. For example, the CME/prominence distributions are both flatter and more extended in latitude near activity maximum than minimum, unlike sunspot groups (i.e, active regions/flares). Recently, Hundhausen [48] has shown that during the entire SMM period the latitude/time plot of all SMM CMEs more closely resembled that of streamers and prominences than of sunspots

(the "butterfly" diagram) or active regions. But the annualized occurrence frequencies of CMEs and all related activity tracers tend to track the activity cycle [16].

To conclude this section, I emphasize the following caveats which apply to CME association studies [17, 4, 18]: 1) Because of the Thomson-scattering process, coronagraphs are most sensitive to CME material near the plane of the sky, i.e., the solar limb, leading to ambiguities in the longitude of the source region of the CME. 2) Coronagraphs occult the inner corona wherein most CMEs are formed. Therefore, a large extrapolation of the height/time trajectory backward in time and space to the limb at 1 R_0 is usually necessary. 3) The height vs time trajectories are not always well determined because of insufficient data points and/or inaccurate measurements of the subtle fronts of CMEs. 4) The most significant acceleration of a CME occurs low in the corona where it is poorly observed, leading to large uncertainties in the onset time. Those using statistical association methods assume no CME acceleration (i.e., constant speed) in calculating the extrapolated onset time for a CME at the solar limb. 5) The altitude at which the CME is formed and initiated is usually not known and may not lie at 1 R_0. Finally, the statistical studies tend to show that only 40–60% of all CMEs have "good" associations. A priori, this might be expected since half of the CMEs could be associated with unobservable surface activity over the limb. However, the low coronal activity considered related to CMEs (EPs, X-ray LDEs, metric radio bursts) should be visible for some distance over the limb. In addition, slower CMEs tend to be unassociated [6], and some likely frontside CMEs have no associated activity. Wagner [19] claimed that a large fraction ($\geq$ 30%) of CMEs comprise a separate class which leave no detectable near-surface signature, but the evidence for the existence of such a class is not compelling [e.g., 4].

3 Relationship of Flares to CMEs

CME Precursors and Timing: Flares A currently popular paradigm is that the activation of coronal magnetic fields leading to a CME begins well before the appearance of any surface activity in the form of flares or EPs. If so then CME models based on pressure or thermal drivers cannot be applicable because the required overpressure from the flare or EP is not available to drive the CME and, to compensate, the CME onset would have to occur during the flare. This would require unrealistic acceleration profiles or high starting heights for the CME, neither of which is observed. Some of the energy released during a CME could drive precursor activity, and there is some evidence of precursor activity tens of min. to hours before the onset of surface activity and even before CME onset.

Jackson and colleagues described evidence for two kinds of coronal precursors occurring before the onset of Skylab CMEs. The first were called "forerunners", large, faint regions of enhanced brightness that were found to rim the CMEs [20]. The outer boundaries of the forerunners maintained a constant offset of 1–2 R_0 from the CME. If real, they are significant because the volume of corona encompassed by the forerunner is much larger than that of the following CME. Moreover they imply that the onset of the material ejection begins much higher in the corona and at an earlier time than previously thought. Jackson [21] noted that in some events forerunner material was ac-

tually in motion prior to the associated surface activity. However, using Solwind data, [22] concluded that forerunners were either an artifact of the contouring process used or, at least, were structures not separate from the CME itself. This controversy remains today; there have been no published results using the SMM data. Hopefully, CME data from the SOHO coronagraph will be able to resolve this issue.

A second type of precursor was reported by [23]. Culgoora type III radio bursts showed significant temporal clustering an average of 6 hrs. before Skylab CMEs were detected. Culgoora radioheliograph positional data revealed that these same type IIIs clustered spatially at the limb within 20° of the centroid of the CME. Jackson (priv. comm.) plans to compare 5 years of the Culgoora data with Solwind and SMM CME data to confirm the previous study.

Data nearer the time of CME onset indicate the existence of precursor activity before some, but not all CMEs. An early assessment of SMM flare-associated CMEs [24] indicated that their departure times preceded flare onsets. Recently, Harrison [25, 26] has found that CME onsets precede any subsequent associated Hα or X-ray flares by an average of 17 min. He associates CME onsets with precursor X-ray arches having large scale sizes of $\sim 10^5$ km. and connecting two active regions. This result, which applies only to flare (in active regions)- associated CMEs, is based on only 3–7 cases with coincident SMM X-ray burst images and C/P CME observations. In addition, nearly all X-ray flares observed by the SMM HXIS instrument were preceded by weak soft X-ray bursts [27]. However, other recent results [28, 26] using SMM XRP and GOES X-ray data do not show such a clear pattern. Precursors are often not found in the same active region related to the CME and associated main flare, and the locations of these flares with respect to the centroid of the CME vary. In summary, there is some evidence that weak soft X-ray emission may accompany CME onsets, but this result should be considered tentative.

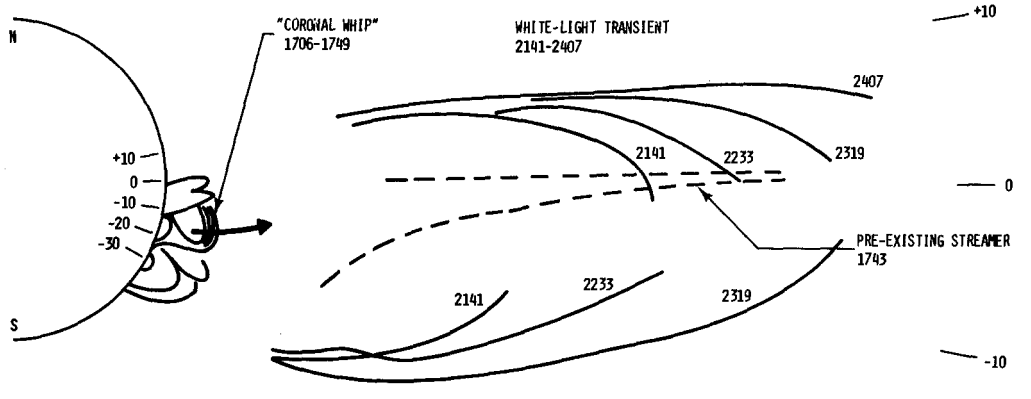

Fig. 1. Composite drawing showing leading edges of Skylab white light CME loops (times in UT) erupting from X-ray arch in low corona [29].

Harrison was not the first to associate a precursor X-ray arch with the onset of a CME. Rust and Hildner [29] identified a faint, expanding soft X-ray arch at the limb on 13 August 1973 as the source of the leading loops of a CME seen later in the outer corona (Figure 1). The X-ray arch had the same mass and acceleration as the subsequent white light loop. Like Harrison's events, this X-ray arch was a separate precursor event to a

large LDE that occurred in the same active region with a peak flux 2 hrs. later. Data from Yohkoh and SOHO should help answer if such expanding X-ray arches are the early stage of CMEs.

CMEs and Durations of X-ray Flares It is logical to assume that the opening of large-scale coronal fields in a CME should result in some signature of heating in the low corona. The Skylab and SMM data suggest that this is the case, but definitive evidence is lacking. Perhaps the best Skylab evidence for such heating were the soft X-ray LDEs and their associated microwave gradual rise and fall signatures. Sheeley et al.'s [30] observations of $\geq$ 4.5 hr. Solrad LDEs suggested that all such LDEs are accompanied by CMEs and most LDEs are associated with disappearing filaments. Webb et al. [31] examined the fainter LDEs outside of active regions and found them to be associated with a pre-existing filament cavity within which a filament disappeared, leading to a filling-in and probably heating of the cavity. Many of these events had flux levels well below that of the Solrad whole-sun X-ray detector. Kahler [32] found that LDEs consist of arcades of high loops which he argued were the X-ray analogs of Hα post-flare loop prominence systems (LPS).

Pallavicini et al. [33] surveyed Skylab X-ray limb-flares and concluded that all flares consisted of two classes: confined, compact flares with small volumes, low heights and short durations (tens of min.), and those with large volumes, high heights, and long durations (hours). The second class was well associated with CMEs, but the first class was not. These results suggested that when CMEs are associated with flares, those flares should be LDEs. Overall, these Skylab studies and the reconnection model involving LPS/LDE flares [34, 14] led to the concept of two classes of flares which persists to this day [35].

The relationship between CMEs and X-ray flare events was investigated further by [36] using Solwind and GOES data. They found that the probability that a CME would be associated with an X-ray flare increased with the duration of the X-ray event. For events with durations $\geq$ 6 hrs., all X-ray flares were associated with CMEs. Surprisingly, their plot of CME/X-ray association was a smoothly increasing function of X-ray duration with no cutoff at short durations. That CMEs are associated with a wide range of X-ray burst durations has been confirmed in subsequent studies [4, 37, 26].

Since short-duration flares are supposed to be confined and non-eruptive, it is of interest to study the CMEs associated with such flares. Kahler et al. [37] did so and found that such short- duration flares are compact and their associated CMEs tend to be narrow. Figure 2 shows this, as well as an apparent trend for longer X-ray durations with increasing CME angular widths. This implies a correlation between the spatial scale sizes of CMEs and their associated flares.

CMEs and the Energetics of X-ray Flares Hundhausen and Sime (priv. comm.) have studied about 30 CMEs for which high quality HAO MLSO coronameter and SMM C/P data exists (most during the rise to maximum period in 1988-1989). This combined data set is important for learning about the origins and kinematics of CMEs because it extends the height interval over which CMEs can be studied from near the surface (1.2 R_0) to 6 R_0, minimizing the spatial and temporal extrapolations needed for comparison with other activity. Using such data sets, Hundhausen (priv. comm.) finds no clear relation between the energetic scale of a CME, such as its size, mass or energy, and

that of any associated X-ray events. In addition, even very fast, energetic CMEs may or may not be accompanied by LDEs in a whole- sun detector, even when the solar background flux is low. Figure 3 shows examples of the height/time plots of two similar fast, energetic SMM/MLSO CMEs, both with large EPs at the limb extending onto the disk. One was associated with an energetic (M3 level) LDE and the other with no X-ray event above the background (C6 level). Also, even in the case of the associated LDE, the CME and prominence appeared to be in motion several min. before X-ray onset. In this and several other cases, the CME initiations could be directly observed within the field of view of the instruments and the launch times determined to uncertainties of a few min. Even for fast events, the CME onsets tend to occur several min. before that of any associated X-ray emissions. Hundhausen also finds that the widths and speeds of SMM CMEs are not dependent on latitude, implying that flare-associated CMEs (from active regions) are not qualitatively different from those accompanying isolated high-latitude filament eruptions. Thus, these recent results support the idea that flares, when they occur, play only a secondary role as a byproduct of the CME process.

TABLE 1 - Results of Association Studies

	1973–74 Skylab [3]	1980 SMM [4]	1984–86 SMM [6]
No. of CMEs with Measured Speeds	40*	58	73
Average CME Speed (km/s)	470	340	237
No. of CMEs with Associations	34 (85%)*	38 (66%)	34 (47%)
Distribution of Associations			
Erupting Prominences	31 (91%)	26 (68%)	26 (76%)
X-ray Events	16 (47%)	29 (76%)	25 (74%)
Hα Flares	13 (38%)	14 (37%)	9 (26%)
Radio II, IV Bursts	14 (41%)	12 (32%)	7 (21%)

* See [4] for discussion of Skylab CME speed measurements and associations.

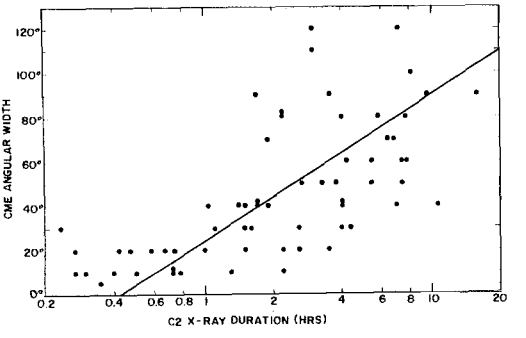

Fig. 2. Angular widths of Solwind CMEs vs duration of associated 1-8Å GOES X-ray flares. Line is least-squares fit [37].

Locations of CMEs and Flares Harrison and colleagues have studied the detailed positions and timings of X-ray flares associated with CMEs. Their scenario places the sources of flare-associated CMEs in large X-ray arches connecting different active regions. When the CME reaches a sufficient height, a flare may be triggered in one footpoint of the arch. Thus, this flare should be positioned near one leg rather than the center of the angle subtended by the CME span. A comparison of the positions of 48 flares with the angular extents of their associated CMEs was interpreted by [25] as showing a strong tendency for the flares to occur near one leg of the CME (Figure 4a). However, there are problems with this apparently straightforward result. Harrison plots his histograms of the number of CME flares vs the parameter, α, relating the limb location of the flare to the CME span. If these angles are replotted in terms of a more physically meaningful equal-angle parameter (R), then Harrison's distribution

can not be statistically distinguished from a random one, even for the smallest R, i.e., flares nearest one CME leg. Recently, [37] found the locations of flares associated with Solwind CMEs over the same time period broadly distributed with regard to the CME spans (Figure 4b). In addition, [28, 26] have found relatively flat distributions of α (replotted in Figures 4c and 4d as R) for CME flares during the recent solar minimum.

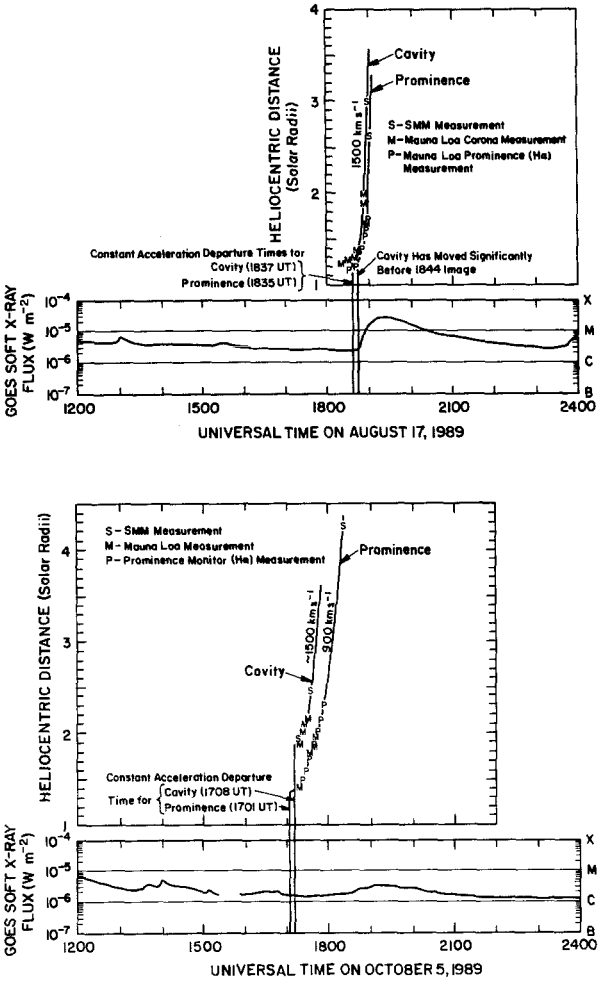

Fig. 3. Height/time plots of two fast, energetic CME/EPs, one associated with an energetic (M3) X-ray LDE (top) and the other with no X-ray event above background. Courtesy A. Hundhausen.

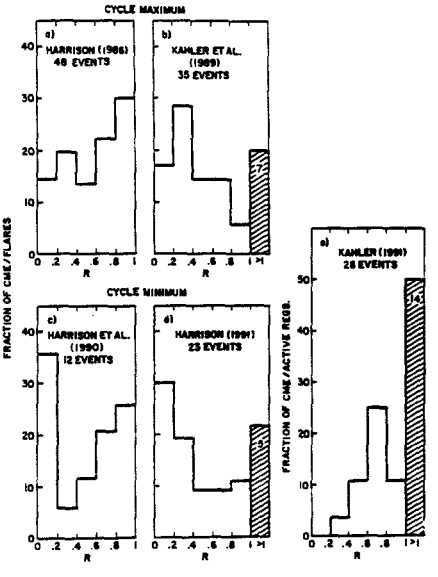

Fig. 4. Histograms of percentage of CME-associated flares vs distance parameter, R, the angular displacement of flare site to CME centroid at limb. (a) and (b): data during activity maximum; (c) and (d): data during minimum. (E) relates location of new- cycle active regions to CMEs.

These researchers emphasize the fact that the characteristic angular sizes of CMEs exceed those of any associated Hα flares and active regions by factors of 3–10. Kahler

et al. [38] also found that the Hα impulsive phase brightening of four well-studied flares was much smaller than the sizes of associated erupting filaments. To summarize, CME flares and active regions are much smaller than and can lie anywhere under the span of the accompanying CME.

Interesting new results suggest that there are systematic offsets between CMEs and any underlying flares and the active regions in which they occur. Harrison et al. [28] found that the flare active regions associated with SMM CMEs in 1985–1986 lay systematically equatorward, but not at the legs of the CMEs. Kahler [39] compared the locations of high-latitude, new-cycle active regions associated with SMM CMEs during 1986–1987. He found that the CMEs extended between new-cycle regions across the equator and, therefore, that these regions nearly always lay on the high-latitude, or poleward side of the center of the CMEs and at their legs (Figure 4e). A major difference in these two studies was that Harrison et al. [28] examined only low-latitude, old-cycle regions at activity minimum, whereas Kahler [39] studied only high-latitude, new-cycle regions.

Good correlations have been found by [40, 41, 39, 16] between the occurrence rates of CMEs and that of sunspot numbers (i.e., active regions) over different phases of the cycle. However, [42] found no such correlation in terms of longitude quadrants using the 1980 SMM data, and he suggested that the large-scale coronal field plays the key role in CME production. Taken together, these results suggest that if, at the start of a cycle, CMEs are directly connected to active regions, the large-scale structures from which the CMEs arise become decoupled from the strong surface fields or don't share the same migration patterns as the cycle evolves.

4 Relationship of Prominences and CMEs

Locations of CMEs and Prominences As reviewed earlier, the association studies have consistently revealed a closer association between CMEs and prominences and their eruptions than with flare phenomena, including the observation of prominence material within the CME itself. One reason that this relationship is only now becoming clear is that, historically, EPs have been more poorly observed and reported compared to flare activity. Like flares, recent results reveal evidence of systematic latitude offsets between CMEs and their associated filaments or prominences, and that these offsets vary with the cycle. Based on comparisons of MLSO K-coronameter and prominence-monitor data, Sime (priv. comm.) reports that prominences tend to be systematically offset either equatorward or poleward of their associated CMEs at different phases of the cycle. During the rise of the present cycle in 1987$\sim$1989, the prominences tended to lay poleward of the CMEs, in agreement with the result [39] for active regions. Since prominences and active regions lie on or over the inversion line of the surface magnetic field polarity, these results suggest that CMEs do not radially overlie the inversion lines associated with the strongest surface field. Instead CMEs may be more intimately connected to the large-scale coronal loops observed in X-ray and metric radio images to interconnect active regions.

My colleagues and I are using HeI λ 10830 and SMM CME data to better understand the disparity in size scales between CMEs and their lower atmosphere manifestations,

and to search for the boundaries of the fields opened during the CME. Harvey et al. [43] found that He double-ribbon events were a good ground-based proxy for the soft X-ray signatures associated with filament eruptions on the disk. We have compared the size scales and angular positions of SMM CMEs with their associated He double-ribbon events from 1984–1989. In agreement with Sime's results, we find that these He events were also systematically offset poleward from the CMEs. In addition, despite the fact that the He events represent probably the largest surface manifestation of activity associated with CMEs, the CME spans still significantly exceed the projected widths of the double ribbons, and the projected spatial overlap at the limb between the two phenomena is poor. We are in the process of extending this study to include Skylab X-ray and white light data and Solwind CMEs from 1979– 1984.

CME Precursors and Timing: Erupting Prominences It is well known that various kinds of filament activity precede the eruption of the filament itself by tens of min. Since EPs are the most common activity associated with CMEs and appear as bright cores within many CMEs [4], pre-eruptive filament activity should be considered a form of CME precursor. Kahler et al. [38] found that the eruption of four Hα filaments began before the onset of associated flare impulsive phases and showed no new acceleration attributable to the impulsive phase. Therefore, these EPs, and by analogy the CMEs associated with them, were driven independently of the flare and its impulsive phase.

I am not aware of any comprehensive studies comparing the timing and acceleration profiles of EPs associated with CMEs. The ideal data set for this comparison is probably the MLSO K- coronameter, Hα prominence-monitor and SMM coronagraph suite of instruments mentioned earlier. As illustrated by Figure 3, Hundhausen (priv. comm.) has compiled a number of cases with such data which typically show both the CME and prominence in motion many min. before any associated flare onset. However, it is not clear if the time resolution of these data is sufficient to determine whether the prominence motion begins before the white light ejection.

CMEs and Late-Phase Phenomena Loop prominence systems (LPS) are extensive loop arcades which overlie the magnetic inversion line for some hours following major flares. The loop footpoints form the flare double ribbons, a key signature of eruptive flares. Kopp and Pneuman [34] proposed that an LPS forms due to magnetic reconnection of oppositely directed field lines, and the Skylab observations indicated that LDEs were the lower coronal signature of LPSs. Thus, each newly formed loop is first observable in hotter coronal lines [30, 32], then later in cooler lines, such as Hα, as it cools. As with other flare phenomena, the angular size of an associated CME is much larger than that of the LPS. Thus, if reconnection is a common process in the corona following CMEs, LPSs may only denote the areas where this process is occurring in the strongest fields. Regardless, LPSs, LDEs and other late-phase phenomena appear to be the best indicator of reconnection continuing in the low corona for hours following a CME. Another type of late-phase event, the gradual hard X-ray burst, is also closely associated with CMEs and major flares [44]. These events follow the onsets of CMEs by 5–60 min. and are characterized by a hardening of the E $\geq$ 30 keV X-ray spectrum and a large ratio of microwave to hard X-ray fluxes. They have been interpreted in terms of acceleration and trapping of electrons via reconnection in an LPS following a CME.

5 CMEs and Pre-existing Coronal Structures

We need to address the important question: What are the ambient coronal structures from which CMEs arise and with which CMEs interact? I have presented evidence for precursor activity, such as forerunners and X-ray arches, occurring in large-scale coronal structures tens of min. to hours before CME onset. These results need to be confirmed and extended with better data.

Some of the most massive and energetic CMEs are the so-called streamer blowout events, one of which was well described by [45]. In such events, a pre-existing streamer typically increases in brightness for one to several days before erupting as a CME (Figure 5). Following the CME, the helmet streamer is gone, often replaced by a thin ray. These events appear on white light synoptic charts as "bugles", portions of the streamer belt which brighten and widen with time until they disappear during a CME [48].

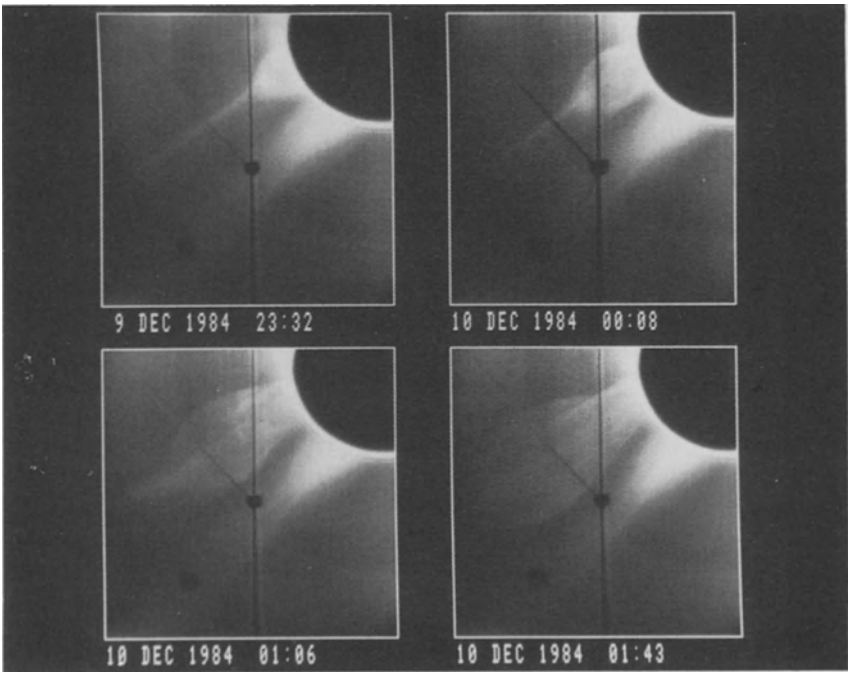

Fig. 5. Time development of one type of CME, the eruption of a pre-existing helmet streamer on 9/10 December 1984. Courtesy A. Hundhausen.

Hundhausen and Kahler (priv. comm.) have made preliminary studies comparing the locations of SMM CMEs and streamers and concluded that 75–80% of all CMEs can be associated with pre- existing streamers. Using MLSO coronameter data, [46] showed that the CME occurrence rate is inversely correlated with the evolutionary timescale of the bright coronal structure, basically streamers. This result also suggests that CMEs are physically related to streamers since they occur most frequently when the streamers are evolving most rapidly, such as around maximum. Finally, during

the 1987–1989 rise in the solar cycle, the sunspot latitudes moved equatorward (the familiar "butterfly" pattern) while the latitudes of the coronal helmet streamers moved poleward. Hundhausen [48] finds that the SMM CME latitudes tracked the helmet streamer latitudes more closely than those of the sunspots.

It is unclear what relation, if any, CMEs have to the coronal giant arches, first observed in the 1980 SMM HXIS images. These large ($\geq 10^5$ km) structures lie over active regions and appear to brighten in association with double-ribbon flares. Since these features appear to be quasi-stationary and long- lived, it is difficult to understand how they can be associated with flares normally related to CMEs. At least two different interpretations of the arches have been suggested [47]. See the papers by Poletto and others elsewhere in these proceedings for further discussion of these features.

6 Summary and Conclusions

The wide acceptance of the Kopp-Pneuman type of reconnection model as a description of the late phase of a EP-flare following a CME now appears to have been premature. Such a scenario seemed to provide an excellent explanation for the Skylab-era X-ray and EUV observations of LPSs, LDEs and other late-phase phenomena. However, with the analyses of CME data obtained over the last decade, it is becoming increasingly apparent that we still lack a physical understanding of the origin of CMEs and their source regions, a relationship more complex than previously thought. The accumulated evidence is leading us toward a view wherein the stability and evolution of the large-scale coronal magnetic fields appear to play a key role in the initiation of CMEs, and the observable surface manifestations of this activity can be diverse, subtle or non-existent.

The results of the statistical studies associating CMEs and near-surface activity indicate that the most commonly associated events are EPs and X-ray events, especially long-enduring bursts. Such LDEs and LPSs provide evidence of continuing reconnection in the lower atmosphere long after the CME has departed. Observable optical flares and related phenomena do not frequently accompany CMEs. But about half of all CMEs have no "good" associations at all. Undoubtedly, some of these null associations are due to the spatial and temporal limitations inherent in statistical methods utilizing coronagraph data, but an unknown fraction of CMEs do appear to have null associations. In addition, there appears to be no good correlation between the size and energy of a given CME and the occurrence of, or size and energy of any near-surface activity.

Following Skylab, much of the research involving flares and CMEs has utilized data at X-ray wavelengths which are sensitive to heating effects in the low corona. The overall results suggest that, when associated with a CME, the main flare onset trails the CME launch by many min. The evidence for X-ray activity at the location and time of CME onset remains sketchy. The flare and active region scale sizes are 3–10 times smaller than CME scales, and the flare can occur anywhere under the span of the associated CME. The impulsive phase appears to be part of the confined flare and has little influence on the eruptive material in the form of the EP and CME. Associated CME flares can have varying durations, although the majority of well-associated flares have long durations of tens of min. to hours.

Studies have consistently shown a close association between CMEs and EPs, in-

cluding the observation of prominence material within the CME. The high degree of correspondence between these events, which are frequently associated with the double-ribbon, LPS phenomenon, suggests that CMEs and EPs form at least one physical class of event. On the other hand, many CMEs do not have accompanying EPs, although observational sensitivity to Hα-emitting material may play a role. As with flares, when associated the observable portions of EPs are often not centered under the CME span and their size scales and spatial overlaps are not well matched.

The important question of what ambient coronal structures CMEs arise from and are influenced by is only now being addressed. Most, but not all CMEs appear to occur in pre-existing white light streamers. The CME occurrence rate is proportional to the evolutionary time scale of bright coronal structures such as streamers. The CME rate tracks that of the sunspot cycle and other related activity tracers, but the latitude/time distribution of CMEs matches that of streamers much better than that of sunspots, the zones where flares occur. There is some evidence for precursor activity occurring in large-scale coronal structures prior to the onset of CMEs or of associated flare activity, but more careful study of this aspect is needed.

Finally, there is new intriguing evidence for systematic latitude offsets between CMEs and their associated EPs and flares and active regions, and the nature of these offsets may vary with the solar cycle. These results suggest that CMEs do not radially overlie the inversion lines associated with the strongest surface field, but are displaced equatorward or poleward at different phases of the cycle. This shift may imply that CMEs arise in large-scale coronal structures akin to the high loops and arcades known to interconnect active region complexes and other large- scale coronal structures, such as the arcades bounding coronal holes. I thank S. Kahler for the use of review material, A. Hundhausen and J. Burkepile for unpublished data, and E. Cliver, E. Hildner and B. Jackson for helpful comments. This work was supported at Boston College by the AF Phillips Laboratory, GPS under contract AF19628-90-K-0006.

References

1. Kahler, S.: Rev. Geophys. **25**, 663, (1987)
2. Gosling, J.T., Hildner, E., MacQueen, R.M., Munro, R.H., Poland, A.I., and Ross, C.L.: Solar Phys. **48**, 389, (1976)
3. Munro, R.H., Gosling, J.T., Hildner, E., MacQueen, R.M., Poland, A.I., and Ross, C.L.: Solar Phys. **61**, 201, (1979)
4. Webb, D.F., and Hundhausen, A.J.: Solar Phys. **108**, 383, (1987)
5. Harrison, R.A.: Solar Phys. **126**, 185, (1990)
6. St. Cyr, O.C. and Webb, D.F.: Solar Phys., in press, (1991)
7. Illing, R.M.E., and Athay, R.G.: Solar Phys. **105**, 173, (1986)
8. Wilson, R.M. and Hildner, E.: J. Geophys. Res. **91**, 5867, (1986)
9. Klein, L.W. and Burlaga, L.F.: J. Geophys. Res. **87**, 613, (1982)
10. Cane, H.V., Kahler, S.W., and Sheeley, N.R., Jr.: J. Geophys. Res. **91**, 13321, (1986)
11. Heras, A.M., Sanahuja, B., Domingo, V., and Joselyn, J.A.: Astron. Astrophys. **197**, 297, (1988)
12. Wright, C.S.: Solar-Terrestrial Predictions, R.J. Thompson et al., eds., (1)658, (1990)
13. MacQueen, R.M., and Fisher, R.R.: Solar Phys. **89**, 89, (1983)
14. Anzer, U., and Pneuman, G.W.: Solar Phys. **79**, 129, (1982)
15. Webb, D.F.: in Solar-Terrestrial Physics, M.R. Kundu et al., eds. (Insdoc, New Delhi, India) 283, (1986)
16. Webb, D.F.: Adv. Space Res. **11**, (1)37, (1991)

17. MacQueen, R.M.: Solar Phys. **95**, 359, (1985)
18. Harrison, R.A., and Sime, D.G.: Astron. Astrophys. **208**, 274, (1989)
19. Wagner, W.J.: Ann. Rev. Astron. Astrophys. **22**, 267, (1984)
20. Jackson, B.V. and Hildner E.: Solar Phys. **60**, 155, (1978)
21. Jackson, B.V.: Solar Phys. **73**, 133, (1981)
22. Karpen, J.T. and Howard, R.A.: J. Geophys. Res. **92**, 7227, (1987)
23. Jackson, B.V., Sheridan, K.V., Dulk, G.A., and McLean, D.J.: Proc. Aust. Soc. Astron. **3**, 241, (1978)
24. Wagner, W.J.: Adv. Space Res. **2**, 203, (1983)
25. Harrison, R.A.: Astron. Astrophys. **162**, 283, (1986)
26. Harrison, R.A.: Adv. Space Res. **11**, (1)25, (1991)
27. Tappin, S.J.: Astron. Astrophys. Suppl. Ser. **87**, 277, (1991)
28. Harrison, R.A., Hildner, E., Hundhausen, A.J., Sime, D.G., and Simnett, G.M.: J. Geophys. Res. **95**, 917, (1990)
29. Rust, D.M. and Hildner, E.: Solar Phys. **48**, 381, (1976)
30. Sheeley, N.R., Jr. and 12 coauthors: Solar Phys. **45**, 377, (1975)
31. Webb, D.F., Krieger, A.S., and Rust, D.M.: Solar Phys. **48**, 159, (1976)
32. Kahler, S.: Astrophys. J. **214**, 891, (1977)
33. Pallavicini, R., Serio, S., and Vaiana, G.S.: Astrophys. J. **216**, 108, (1977)
34. Kopp, R.A., and Pneuman, G.W.: Solar Phys. **50**, 85, (1976)
35. Svestka, Z.: in The Lower Atmospheres of Solar Flares, D.F. Neidig, ed. (NSO, Sunspot, NM), 332, (1986)
36. Sheeley, N.R., Jr., Howard, R.A., Koomen, M.J., and Michels, D.J.: Astrophys. J. **272**, 349, (1983)
37. Kahler, S.W., Sheeley, N.R., Jr., and Liggett, M.: Astrophys. J. **344**, 1026, (1989)
38. Kahler, S.W., Moore, R.L., Kane, S.R., and Zirin, H.: Astrophys. J. **328**, 824, (1988)
39. Kahler, S.: Astrophys. J. **378**, 398, (1991)
40. Hildner, E., Gosling, J.T., MacQueen, R.M., Munro, R.H., Poland, A.I., and Ross, C.L.: Solar Phys. **48**, 127, (1976)
41. Howard, R.A., Sheeley, N.R., Jr., Michels, D.J., and Koomen, M.J.: in The Sun and the Heliosphere in Three Dimensions, R.G. Marsden, ed. (Reidel, Dordrecht, Holland) 107, (1986)
42. Sime, D.G.: in Proc. ESA Workshop on Future Missions in Solar, Heliospheric & Space Plasma Physics, ESA SP-235, 23, (1985)
43. Harvey, K.L., Sheeley, N.R., Jr., and J.W. Harvey: Solar- Terrestrial Predictions, P.A. Simon et al., eds., 198, (1986)
44. Cliver, E.W., Dennis, B.R., Kiplinger, A.L., Kane, S.R., Neidig, D.F., Sheeley, N.R., Jr., and Koomen, M.J.: Astrophys. J. **305**, 920, (1986)
45. Illing, R.M.E., and Hundhausen, A.J.: J. Geophys. Res. **91**, 10951, (1986)
46. Sime, D.G.: J. Geophys. Res. **94**, 151, (1989)
47. Poletto, G., and Svestka, Z.: Solar Phys. **129**, 363, (1990)
48. Hundhausen, A.J.: J. Geophys. Res., submitted, (1992)

Remote Sensing Observations of Mass Ejections and Shocks in Interplanetary Space

B.V. Jackson

Center for Astrophysics and Space Sciences,
University of California at San Diego, La Jolla, CA 92093, USA

Abstract: It has long been known that disturbances can propagate from Sun to Earth with periods of a few days following large solar flares. These disturbances involve a significant portion of the lower solar corona and the energy of the flare. Several techniques have been used to remotely detect and follow different structures as they propagate outward from the Sun. These techniques include interplanetary scintillation (IPS), kilometric radio and HELIOS photometer observations. Structures in the interplanetary medium can generally be classed as those which propagate outward from the Sun and those which co-rotate with approximately the solar rotation rate. In this review I will concentrate on ejecta and shocks known to be associated with large solar flares observed on the surface of the Sun and their manifestations using various observational techniques. The observational techniques most commonly used are each sensitive to a specific type of structure and more sensitive at one portion of the interplanetary medium than another. Because of the different techniques used, there can often be misinterpretation of the data. In addition, none of the remote sensing observations has complete spatial or temporal coverage. Thus, both the basic physics as well as the spatial and temporal evolution of mass ejections can be confused as these events propagate through the interplanetary medium. Examples of the data related to mass ejections from each of these techniques are shown and interpreted. We expect that future observations will more accurately describe the structures present as their basic physics becomes better known.

1 Introduction

The outermost parts of the solar atmosphere - the corona and solar wind - experience dramatic perturbations in the form of flare-related disturbances. These disturbances extend to the magnetosphere of Earth and to Earth itself. They are observable in a wide variety of phenomena, ranging from type II metric radio bursts to interplanetary scintillation (IPS) observations. In the past, remote-sensing observations of the origins of these disturbances on the Sun have been restricted to coronal emission-line observations and the meter-wave radio band, but since the 1970's we have seen the addition of powerful new tools for observation: sensitive coronagraphs, both in space and at terrestrial observatories; low-frequency radio telescopes; space-borne kilometric wave radio receivers; interplanetary scintillation data; and the HELIOS photometer observations.

2 Near the Solar Surface

2.1 Coronagraph Observations

Near the Sun, coronal mass ejections (CMEs) (Figure 1) mark the location and the approximate coronal involvement of eruptive solar flares. The speed and masses of these ejecta can be shown [1] to involve a significant and in some instances a major portion of the energy released in a flare. To date H_α instrumentation and coronagraph techniques which image the ejection in white light, directly view the outward motion of this mass in the lower corona from 1 - 10R_S.

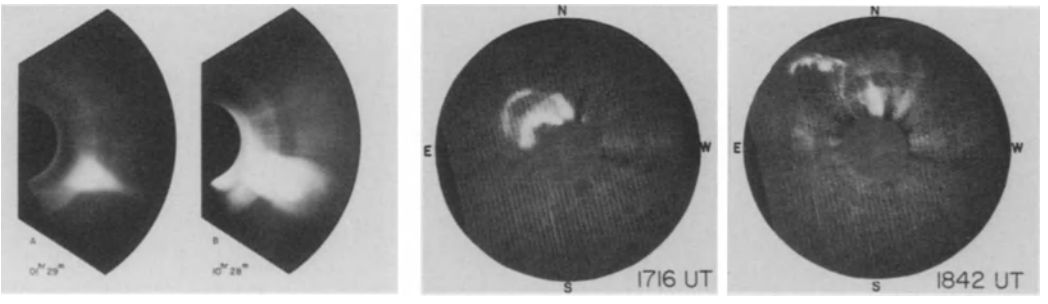

Fig. 1. Examples of coronal mass ejections. **(a)** the 21 January 1974 CME as observed by the Skylab coronagraph. The outer edge of the field-of-view extends to 6R_S. **(b)** the 24 May 1979 CME as observed by the SOLWIND coronagraph. The outer edge of the field-of-view extends to 8R_S in these images.

One of the most extensive data bases of CMEs accumulated in the past comes from the SOLWIND coronagraph [2]. Using a fairly crude ($\sim$ factor of two) mass estimation technique, Howard *et al.* [3] were able to determine individual masses for nearly 1000 CMEs. These mass estimates are plotted as in [4] as numbers of events per unit mass interval (Figure 2). The total CME mass over the observing time interval (1010 days from 28 May 1979 through December 1981) is obtained simply by integrating the exponential curve of Figure 2 and is 3.66×10^{18} g or 4.19×10^{10} g s^{-1}. To obtain the total mass from CMEs, a coronagraph duty cycle of 66.5% [3] for the total 3-year time interval needs to be included. In addition, a visibility factor which concludes that 1.5 times as many CMEs are present as observed by SOLWIND, and an out-of-the-plane increase of mass by a factor of two is also present. A further increase is necessary from the acknowledgement and corresponding observations [5] that perhaps as much of the CME mass in a typical event continues to flow outward from below the coronagraph occulting disk as is observed above it in a single image. Thus, I estimate that the total mass from all mass ejections in the solar wind is approximately $(4.19\times10^{10}/0.665)\times1.5\times2.0\times2.0$ $= 3.78\times10^{11}$ g s^{-1}. I note that the latter three factors in the preceding calculations are relatively uncertain. Their values were chosen to provide a realistic upper limit to the total CME mass.

The above calculations show that there is a finite upper limit to the total CME mass flux, which falls significantly below the total solar wind mass flux. The total solar wind mass flux over the same time interval (measured in the ecliptic at Earth as 3×10^8 n_p cm^{-2} s^{-1} where each proton is associated with 1.94×10^{-24} g of material [6]) can be determined by assuming the flux constant with heliographic latitude. The total mass flux over the entire heliosphere is 1.64×10^{12} g s^{-1}. The CME mass derived above is therefore 23% of the total solar wind mass at times of solar maximum.

The shape of the curve in Figure 2 is in itself interesting. The least massive CMEs do not fill the exponential curve. This could be due to many factors, but is probably partly a selection effect caused by the fact that the least massive CMEs are not as completely observed by the SOLWIND coronagraph. The mass represented by the area between the exponential curve and the data points for the low mass CMEs amounts to no more than 5% of the total, ie., an insignificant fraction of the total mass. There is no evidence that the smallest mass CMEs increase in number so that they rise in mass above the exponential curve, and thus no evidence that the total mass of the solar wind is made up of very small mass ejections. The fact that the numbers of mass ejections follow an exponential rather than power-law or some other curve over nearly a decade of CME masses may also provide significant clues to their production.

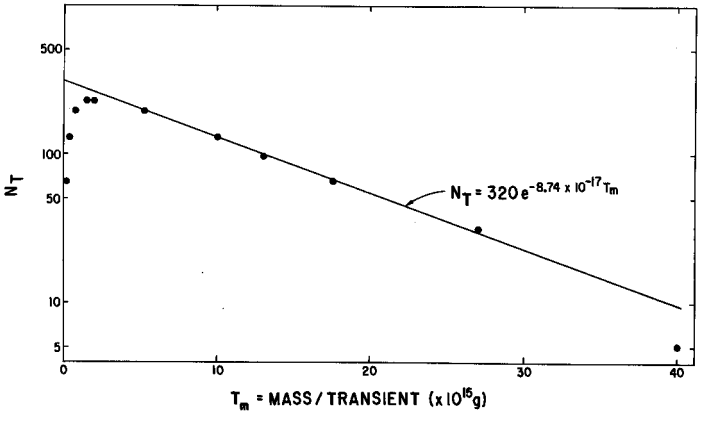

Fig. 2. Number of mass ejections per unit mass interval for the CMEs observed from the SOLWIND coronagraph from 28 May 1979 through 1982.

Not all CMEs can be associated with H_α or X-ray flares observed on the solar surface. Because coronagraph-observed CMEs are best observed on the solar limb, at best an association can be found only for the CMEs whose surface manifestations correspond to features on the side of the Sun towards Earth [7]. Even taking this into account, the presence of a CME does not imply the presence of a classical H_α two-ribbon flare with an associated X-ray brightening on the the solar surface or vice versa [8, 9]. Thus, the total solar wind mass from these flare-associated CMEs will be somewhat less than the fraction determined above. I presume, however, that the presence of a CME near the solar surface implies the opening of magnetic field structures on the Sun with an

associated outward expulsion of material in the form of ejected mass. Since an opening of magnetic field with an expulsion of mass into the heliosphere is the definition of an eruptive flare, for the purposes of this conference I will adopt this as the definition of an eruptive flare. Using this definition, the heliospheric effects associated with eruptive flares are directly related to the results of Figure 2.

2.2 Radio Signatures

Shock waves thought to be highlighted by the type II metric radiation associated with them, can be observed to move outward in the lower corona associated with some flares. An example of a metric type II burst dynamic spectrum is shown in Figure 3.

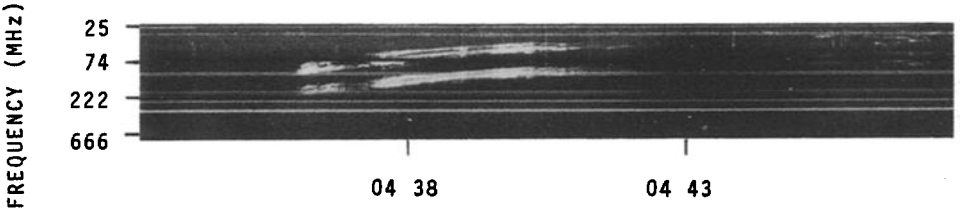

Fig. 3. Dynamic spectrum of a metric type II radio burst as observed by the Culgoora radio spectrograph on 9 October 1969.

The mass ejections associated with type II radiation are commonly those with the highest speeds [10]. While large, bright surface H_α flares, type II radio bursts implying fast coronal shocks, and mass ejections are indicative of a common phenomena, the presence of such features is not at all in one-to-one correspondence. Furthermore, the location of type II radiation relative to CMEs in the lower corona often does not coincide with the top or fastest portion of the CME (reviewed in [11]). Figure 4 gives an example from SMM of the location of a CME and the corresponding type II metric radiation. Clearly the type II radiation is not present in conjunction with the outer portion of the CME and in this case, the type II radiation appears to arise from two distinct locations to either side of the CME [12]. Modeling of the shock response to CMEs [13] has shown that the formation of a fast shock can be highly dependent on the magnetic field direction and plasma density relative to the propagation direction of the shock.

Moving type IV metric radiation has been shown to be associated with mass ejections and their outward motion (less rapid than type II radiation for events on the solar limb) and is considered indicative of an outward-moving plasmoid of material somehow associated with mass ejections [14]. It has been suggested that these events are evidence for a closed or confining magnetic field topology [15] associated with an expulsion of mass. However, these events are even less commonly associated with CMEs than are type II radiation, and although some good correspondences with coronagraph CMEs have been shown [16], it is not at all certain what radiation process or CME topology is necessary for the radiation to occur.

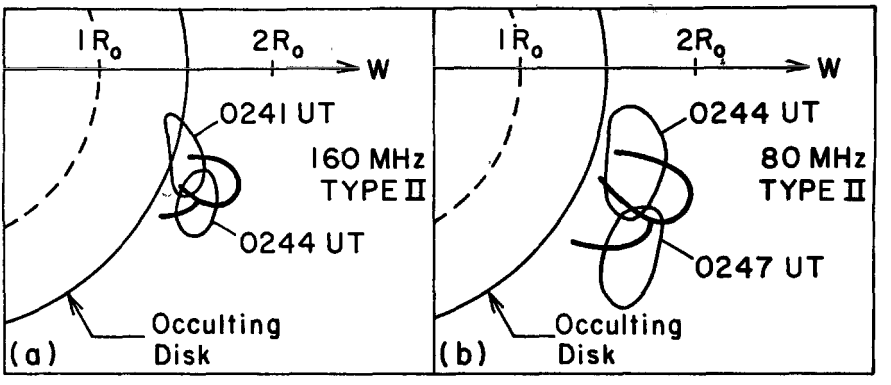

Fig. 4. Schematic diagrams of a CME at two times (**a**) 024410 UT and (**b**) 024730 UT, and comparisons with the 160 and 80 MHz type II burst positions (from [12])

2.3 Indirect Radio Probes

Beyond the region normally viewed by a coronagraph and metric radiation sensors there is a region of the heliosphere from approximately 10 to 20 R_S that has been little-observed by any technique. Two experiments which have probed this region deserve mention, however. These are Faraday rotation measurements [17] and scintillation measurements [18, 19]. Both techniques usually require the fortuitous placement of a spacecraft behind the Sun. Several mass ejections have been observed by the Faraday rotation technique [17]. Significant in the observations is the fact that while a simple loop of current-carrying plasma should show first a one-way directed and then an oppositely-directed excursion of the response from the ambient, perhaps only one of the CMEs does. Thus, an explanation of all CMEs as current driven loops is not valid. Scintillation observations in the same height range can provide extremely high signal to noise detection of the onset of solar disturbances. These data have been mapped to both CMEs observed by the SOLWIND coronagraph and solar surface flares [20]. Significant in these measurements are the short times often observed for the propagation of a CME to heights many solar radii above the Sun following its surface or near-surface manifestation. Two scenarios present themselves from this aspect of the data – either some events have been accelerated to extremely high speed very close to the Sun or else the event actually extends outward to a greater height at its onset than is evident from usual observations near the solar surface. In addition, the scintillation observations are most clearly associated with shocks observed *in situ* at the HELIOS spacecraft [21] and not with the density enhancement often associated with a CME.

3 Interplanetary Distances

The HELIOS photometer data were first identified as a valid source of information for mapping mass ejections by [22] in 1982. Since then, the HELIOS photometers have been used to image the interplanetary medium from 20 R_S out to 1 AU [6, 23]. Before this, the only other way to remotely sense disturbances in the inner heliosphere was by kilometric radio radiation from space and by interplanetary scintillation techniques.

3.1 HELIOS Photometer Observations

The HELIOS spacecraft, the first of which was launched into heliocentric orbit in 1974, had on board three sensitive zodiacal-light photometers for the study of the zodiacal-light distribution. These photometers swept the celestial sphere at 16°, 31° and 90° ecliptic latitude to obtain data fixed with respect to the solar direction, with a sample interval of about five hours. The two spacecraft were placed in heliocentric orbits with perihelia of about 0.3 AU.

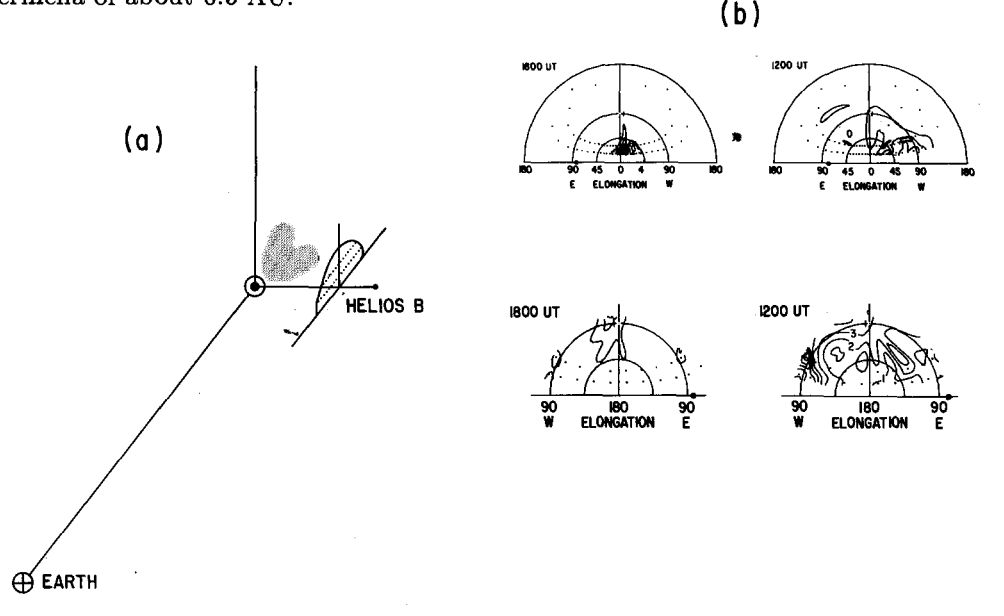

Fig. 5. HELIOS 2 view of the 7 May 1979 CME. (a) Schematic of the Earth, Sun and HELIOS 2 at the time of the ejection. (b) HELIOS 2 images of the mass ejection over 18 hours from 1800 UT 8 May and 1200 UT 9 May. The upper images look toward the Sun, the lower images look anti-solar (from [26]).

Figure 5, showing contour images constructed from the data, is an example of the type of information available from the HELIOS spacecraft photometers. The masses and mass ejection shapes obtained from these observations indicate that the material of a mass ejection observed in the lower corona moves coherently outward into the interplanetary medium. Mass estimates of coronal mass ejections observed by HELIOS are generally approximately twice those determined by the SOLWIND coronagraph for

the same events. We interpret this difference [5, 24] as due primarily to the inability of a coronagraph to measure the total mass of an ejection at any given instant.

The orbits of the HELIOS spacecraft can give them a perspective view of mass ejections that are 90° orthogonal to that from Earth. The shapes of three of these CMEs that appeared as loop-like mass ejections as observed by Earth-based coronagraphs were measured as they moved past the HELIOS photometers in order to determine their edge-on thicknesses. The extents of these CMEs as obtained from the HELIOS data was nearly the same as in the coronagraph view [24] for each event studied. From this, the implication is that mass ejections (even those of loop-like appearance) have considerable thicknesses as they move outward into the interplanetary medium.

The mass ejection of 7 May 1979 was followed in a comprehensive analysis from near the solar surface to the farthest extent that can be observed by HELIOS [25]. Observations of this mass ejection from the Wroclaw observatory show the H_α manifestations and the position of the associated loop-like eruptive limb prominence near the solar surface. This ejection accelerated after passing through the SOLWIND field of view (above $\sim 8.0 R_S$) and when it was observed later by HELIOS above $20 R_S$. The ejection had two major prongs of material that were traveling at a speed of about 500 km s^{-1} as measured from the outward motion observed in HELIOS data. The analysis also includes UCSD IPS measurements [26] which show an enhancement of speed and the scintillation level during passage of the excess mass. IPS observations measure the speed of the small-scale density inhomogeneties ($\sim$200km) within the ejection perpendicular to the line-of-sight to 3C48 [25]. The small-scale speed enhancement to about 500 km s^{-1} for two days following the event compare favorably with the speed of bulk motion obtained from HELIOS data.

3.2 Kilometric Radio Observations

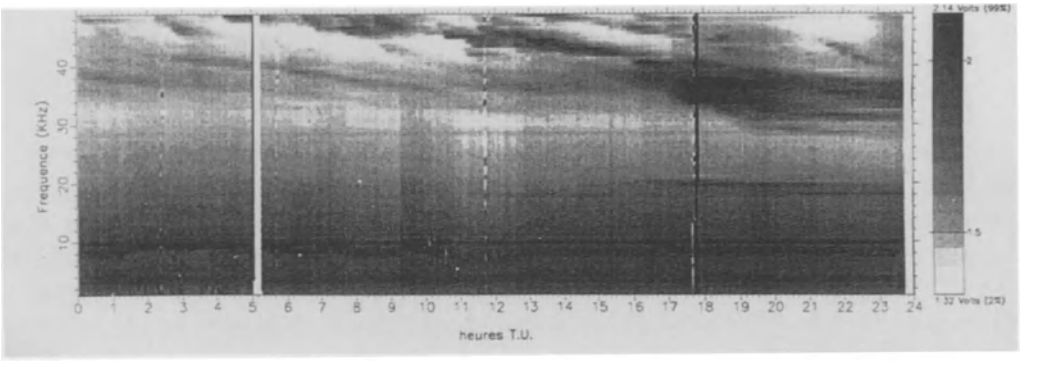

Fig. 6. Dynamic spectrum of a type II kilometric radio burst on 21 January 1991 as observed from the Ulysses spacecraft.

Kilometric type II radio bursts often appear as the interplanetary counterpart of their lower metric cousins. Figure 6 is the presentation of the dynamic spectrum of one such burst as observed from the Ulysses spacecraft in 1991 [27]. These remotely-sensed

features can in some instances be associated with the most massive and highest speed CMEs observed earlier in the corona by coronagraphs [28]. Unfortunately, very few simultaneous observations of mass ejections and kilometric type II radiation of the same event exist. The actual location of the burst centroid(s) relative to a mass ejection observed in the interplanetary medium is thus only a matter of speculation. I suspect that most of the positional qualifiers for lower coronal shocks and their placement relative to CMEs behave in a similar manner when dealing with the formation of kilometric type II radiation.

To date, five density enhancements behind shocks observed *in situ* have also been measured by the HELIOS spacecraft photometers [29]. As expected from kilometric radio observations and *in situ* density measurements, brightness increases observed by HELIOS indicate that interplanetary shocks are fairly extensive heliospheric features.

3.3 Interplanetary Scintillation Observations

IPS has been used since 1962 [30] to observe the interplanetary medium. The technique usually relies on measuring the rapidly fluctuating intensity level from point-like radio sources. Whether a single-site array is used or a multiple one where velocities can be measured [26], the technique relies on the presence of density inhomogeneties in the interplanetary medium to move across the line-of-sight to the source. The presence of the disturbance is indicated by either an enhancement of the scintillation level [31], an increase of the IPS-determined speed [32] or both [33].

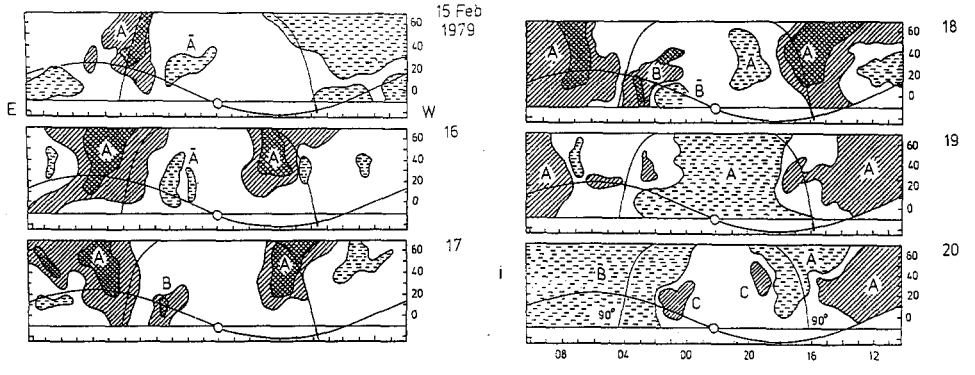

Fig. 7. Schematic of 81.5 MHz IPS data as observed by the Cambridge, England IPS array in February 1979. Sky maps in right ascension and declination show regions of increased (positive) and decreased IPS levels relative to average values which change on a daily basis (from [34]).

An example of the analysis from the Cambridge group using February 1979 data [34] is shown in Figure 7. Many different IPS disturbances are observed in the data each day. Over a 24-hour time interval it is possible to determine an approximate size and shape of the structures that move past Earth. These features, presumably modified significantly by their passage through the interplanetary medium on the way to 1 AU, are generally classified into structures that are either co-rotating or cut off from the

Sun. Some of these structures certainly are remnants of mass ejections as discussed in [35] or even [31]. *In situ* measurements *e.g.*, [34] can help to elucidate the differences between these two forms of disturbances.

Unfortunately, although these observations measure disturbances in the solar wind, they do not have a straightforward interpretation as mass unless the scintillation level enhancement is proportional to a line-of-sight density enhancement. While this proportionality has been determined in several ways [36, 37], with different results, the technique works well at 81.5 MHz only beyond approximately 50° (>0.75 AU) from the Sun. At this solar distance, most mass ejections have evolved significantly [38], so that the extent of an event is difficult to discern given the signal to noise present in the observations.

4 Conclusions

Near the solar surface, the observations of the corona at the approximate time of a flare show that a significant fraction of the flare energy is manifest in the outward motion of mass. As this material moves outward into the interplanetary medium it is observed remotely by a variety of techniques. The HELIOS photometer technique generally probes only the heliosphere inside 1 AU using Thomson scattering of sunlight from electrons along the line-of-sight. The second technique using kilometric radio observations relies on the ability of a high speed disturbance to excite the local plasma frequency or its harmonic as it passes a given portion of the interplanetary medium. The third technique (IPS) measures the relative enhancements in small-scale density inhomogeneties along the line-of-sight. The shapes and speeds of different structures evolve somewhat as they move outward through the heliosphere, and since none of the techniques that trace the events overlap well temporally or spatially there are usually ambiguities in the observations. Thus, none of the techniques is complete in itself, and all must operate in conjunction with additional information to describe the heliospheric aftermath of flares in a complete fashion.

Acknowledgements: I am grateful for the many helpful comments and encouragement from my colleagues during the course of this review. My work has been supported by grants NASA NAGW-2002 and AFOSR-91-0091 to the University of California at San Diego.

References

1. D.M. Rust, E. Hildner, and 11 co-authors, in Solar Flares, A Monograph from Skylab Solar Workshop II, P.A. Sturrock, ed. (Colorado Associated Press), (1980)
2. N.R. Sheeley, Jr., D.J. Michels, R.A. Howard, M.J. Koomen, Astrophys. J., **237**, L99, (1980)
3. R.A. Howard, N.R. Sheeley, Jr., M.J. Koomen, D.J. Michels, J. Geophys. Res., **90**, 8173, (1985)

4. B.V. Jackson, R.A. Howard, M.J. Koomen, D.J. Michels and N.R. Sheeley, Jr., BAAS, **17**, 636, (1985)
5. B.V. Jackson, Solar Phys. **100**, 563, (1985)
6. R. Schwenn, in Physics of the Inner Heliosphere, R. Schwenn and E. Marsch, eds. (Springer-Verlag, Berlin - Heidelberg - New York), (1990)
7. R.H. Munro, J.T. Gosling, E. Hildner, R.M. MacQueen, A.I. Poland and C.L. Ross, Solar Phys., **61**, 201, (1979)
8. D.F. Webb and A.J. Hundhausen, Solar Phys., **108**, 383, (1987)
9. N.R. Sheeley, Jr., R.A. Howard, M.J. Koomen and D.J. Michels, Astrophys. J., **272**, 349, (1983)
10. J.T. Gosling, E. Hildner, R.M. MacQueen, R.H. Munro, A.I. Poland and C.L. Ross, Solar Phys., **48**, 389, (1976)
11. W.J. Wagner, Adv. Space Res., **2**, 203, (1983)
12. D.E. Gary, G.A. Dulk, L. House, R. Illing, C. Sawyer, W.J. Wagner, D.J. McLean and E. Hildner, Astron. Astrophys., **134**, 222, (1984)
13. R.S. Steinolfson, Solar Phys., **94**, 193, (1984)
14. J.P. Wild, Proc. Astron. Soc. Australia, **1**, 365, (1970)
15. G.A. Dulk, Solar Phys., **32**, 491, (1973)
16. R.T. Stewart, G.A. Dulk, K.V. Sheridan, L.L. House, W.J. Wagner, C. Sawyer and R. Illing, Astron. Astrophys., **116**, 217, (1982)
17. M.K. Bird, H. Volland, R.A. Howard, M.J. Koomen, D.J. Michels, N.R. Sheeley, Jr., J.W. Armstrong, B.L. Seidel, C.T. Stelzried and R. Woo, Solar Phys., **98**, 341, (1985)
18. R. Woo, Astrophys. J., **219**, 727, (1978)
19. R. Woo, J. Geophys. Res., **93**, 3919, (1988)
20. R. Woo, J.W. Armstrong, N.R. Sheeley, Jr., R.A. Howard, D.J. Michels and M.J. Koomen, J. Geophys. Res., **90**, 154, (1985)
21. R. Woo, private communication (presentation at the Solar Wind 7 conference in Goslar, Germany, September, 1991), (1991)
22. I. Richter, C. Leinert and B. Planck, Astron. Astrophys., **110**, 115, (1982)
23. B.V. Jackson and C. Leinert, J. Geophys. Res., **90**, 10759, (1985)
24. B.V. Jackson, R.A. Howard, N.R. Sheeley, Jr., D.J. Michels, M.J. Koomen and R.M.E. Illing, J. Geophys. Res., **90**, 5075, (1985)
25. B.V. Jackson, B. Rompolt and Z. Svestka, Solar Phys., **115**, 327, (1988)
26. W.A. Coles and J.J. Kaufman, Radio Science, **13**, 591, (1978)
27. R.G. Stone and 26 co-authors, ESA Special Publication, **SP-1050**, (1983)
28. H.V. Cane, N.R. Sheeley, Jr. and R.A. Howard, J. Geophys. Res., **92**, 9869, (1987)
29. B.V. Jackson, Adv. Space Res., **6**, 307, (1986)
30. A. Hewish, P.F. Scott and D. Wills, Nature, **203**, 1214, (1964)
31. A. Hewish and S. Bravo, Solar Phys., **106**, 185, (1986)
32. T. Watanabe and T. Kakinuma, Adv. Space Res., **4**, 331, (1984)
33. B.V. Jackson, in Proc. of the Maynooth, Ireland Symposium on Solar/Interplanetary Intervals, M.A. Shea, D.F. Smart and S.M.P. McKenna-Lawlor eds., 169, (1984)
34. K.W. Behannon, L.F. Burlaga and A. Hewish, in press in J. Geophys. Res., (1991)
35. B.J. Rickett, Solar Phys., **43**, 237, (1975)
36. S.J. Tappin, Planet. Space Sci., **35**, 271, (1987)
37. R.D. Zwickl, private communication (Presentation at the SEIIM conference held in Colorado Springs, Colorado, 1988), (1988)
38. N.R. Sheeley, Jr., R.A. Howard, M.J. Koomen, D.J. Michels, R. Schwenn, K.H. Muhlhauser and H. Rosenbauer, J. Geophys. Res., **90**, 163, (1985)

IN SITU OBSERVATIONS OF CORONAL MASS EJECTIONS IN INTERPLANETARY SPACE

J. T. Gosling
Los Alamos National Laboratory
MS D438, Los Alamos NM 87545 USA

Abstract. Coronal mass ejections, CMEs, in the solar wind at 1 AU generally have distinct plasma and field signatures by which they can be distinguished from the ordinary solar wind. These include one or more of the following: helium abundance enhancements, ion and electron temperature depressions, unusual ionization states, strong magnetic fields, low plasma beta, low magnetic field variance, coherent field rotations, counterstreaming (along the field) energetic protons, and counterstreaming suprathermal electrons. The most reliable of these appears to be counterstreaming electrons, which indicates that CMEs at 1 AU typically are closed field structures either rooted at both ends in the Sun or entirely disconnected from it as plasmoids. About 1/3 of all CMEs have sufficiently high speeds to produce transient interplanetary shock disturbances at 1 AU; the remainder simply ride along with the solar wind. The frequency of occurrence of CMEs in the ecliptic plane, as distinguished by the counterstreaming electron signature, varies roughly in phase and amplitude with the 11-yr solar activity cycle. Near solar maximum they account for ~ 15% of all solar wind measurements, while near solar minimum they account for less than 1% of all the measurements. All but one of the 37 largest geomagnetic storms near the last solar maximum were associated with Earth-passage of interplanetary disturbances driven by fast CMEs; that is, CMEs are the prime link between solar and geomagnetic activity. However, more than half of all earthward directed CMEs are relatively ineffective in a geomagnetic sense.

The leading edges of coronal mass ejections, CMEs, have outward speeds at distances of several solar radii above the photosphere ranging from less that 50 km s^{-1} to greater than 1200 km s^{-1} [1,2]. When the speed difference between the leading edge of a CME and the ambient solar wind ahead exceeds the characteristic speed with which small amplitude pressure waves propagate, a shock should form ahead of the CME. At 1 AU typical solar wind bulk flow speeds are of the order of 400 km s^{-1} while the sound and Alfven speeds typically are each of the order of 50 km s^{-1} [3]. Thus CMEs with speeds in excess of ~500 km s^{-1} should usually

drive shock wave disturbances in the solar wind, while slower ones should not. In fact, a nearly one-to-one correlation exists between large, fast CMEs detected by satellite coronagraphs and transient shock wave disturbances in the solar wind observed at roughly the same solar longitudes [4]. Transient interplanetary shocks thus serve as useful fiducials for searching for plasma and/or field anomalies by which one might uniquely identify CMEs in the solar wind. As illustrated in Figure 1a, an offset is expected between an interplanetary shock and the CME that drives it.

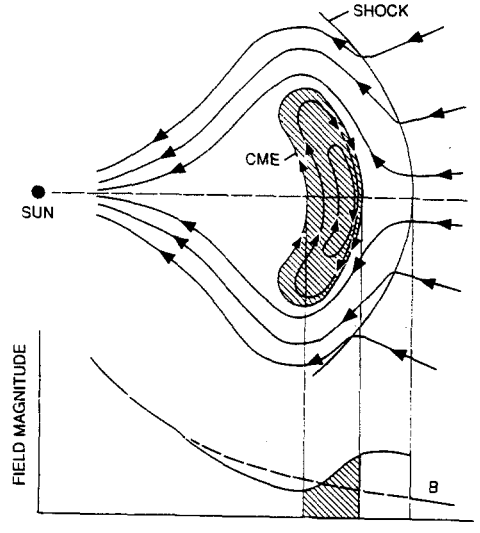

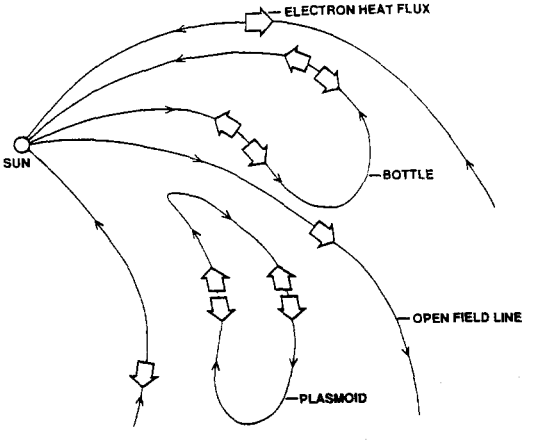

Fig. 1a (Left). A meridional cut through a hypothetical interplanetary shock wave disturbance driven by a fast CME as well as the corresponding radial variation of magnetic field strength along the centerline of the disturbance. Compression, driven by the relative motion between the CME and the ambient solar wind ahead, produces strong magnetic fields in a broad region extending sunward from the shock to well within the leading portion of the CME itself. The ambient magnetic field drapes about the CME [5] because CMEs generally originate in closed field regions in the corona not previously participating in the solar wind expansion. Note, particularly, that the shock and the CME are separated by an extended region of shocked ambient plasma. Adapted from [6].

Fig. 1b (Right). A sketch illustrating possible origins of counterstreaming halo electrons in the solar wind. Adapted from [7].

Figure 2a displays selected solar wind plasma data from the Los Alamos plasma experiments on IMPs 7 and 8 for an interplanetary shock disturbance observed in July 1977. Discontinuous increases in the proton density, temperature, and bulk flow speed near the start of the day on July 29 signal passage of the shock. Approximately 12 hours later a sudden and large increase in the abundance of He^{++} and a large decrease in proton temperature occurred. Such variations are often observed a number of hours after shock passage [8,9], and were the first anomalies identifying CMEs recognized in solar wind data. (Interestingly, this recognition predated the first good observations of CMEs by the OSO 7 and Skylab coronagraphs.) Note that the

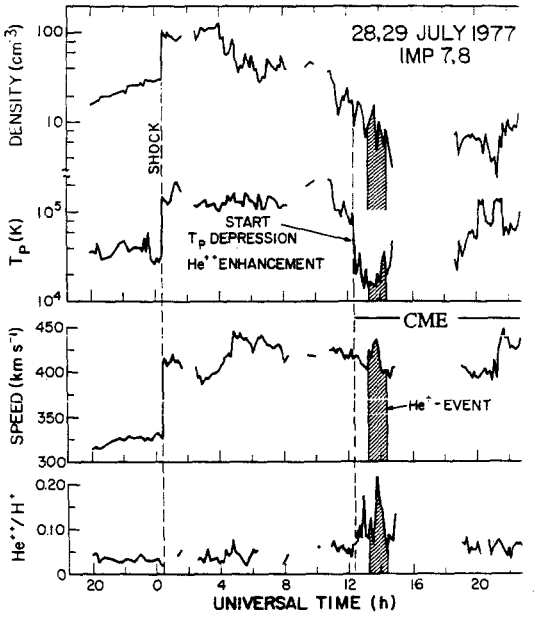

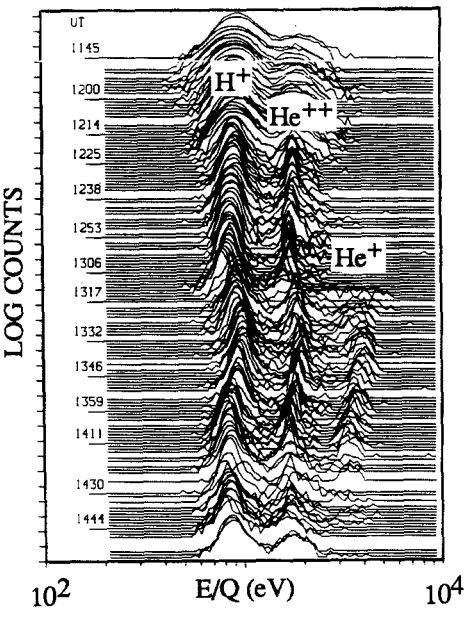

Fig. 2a (Left). Solar wind plasma measurements encompassing a shock wave disturbance on July 28, 29, 1977. From [10].

Fig. 2b (Right). A time series of 1-dimensional solar wind E/q spectra obtained within the CME on July 29, 1977. Tic marks on the left-hand vertical scale denote factors of 10 differences in counts. Adapted from [10].

plasma identified as the CME in this event had a higher speed than the ambient plasma ahead of the shock, as would be expected if it were the cause of the shock. On the other hand, this plasma had a lower density than the ambient even though one of the things that characterizes CMEs in coronagraph observations is a high density. Examination of a large number of solar wind shock disturbance events reveals that CMEs in the solar wind at 1 AU typically do not have particularly high densities when compared to the surrounding solar wind. This suggests that CMEs experience greater expansion in transit to 1 AU than do typical solar wind plasma volume elements.

Figure 2b, which displays a vertically stacked time series of E/q spectra obtained by the IMP instrumentation, provides a more detailed examination of the July 29, 1977 CME, the onset of which is obvious at 1224 UT. The most remarkable aspect of the data is the sudden appearance within the CME at 1314 UT of a large spectral peak at an E/q value of 4.0 times that of the H^+ peak. This third peak was caused by He^+, which has an m/q value of four times that of H^+. Normally He^+ is quite rare in the solar wind, virtually all of the helium present being doubly ionized owing to the million degree temperature of the solar corona from which the solar wind

arises. The exceptionally large He^+/He^{++} abundance (~0.3) measured for ~1 hr within the interior of the July 29,1977 CME indicates a somewhat cooler origin for that particular volume of plasma. We, in fact, believe that that volume originated in a solar filament. However, the special nature of this particular observation cannot be overemphasized. This is by far the largest He^+ enhancement yet observed, although smaller He^+ enhancements have been detected in several other events [11,12]. Usually the helium within filament material ejected into the solar wind must become almost completely ionized as it passes outward through the corona.

Over the years a variety of plasma and field signatures have been identified, in addition to those above, that qualify as unusual compared to the normal solar wind but that are often observed a number of hours after passage of interplanetary shocks. Presumably they serve to identify at least portions of the CMEs driving the shocks. The most prominent of these signatures according to [7] are (1) helium abundance enhancements, (2) ion and electron temperature depressions, (3) unusual ionization states, (4) strong magnetic fields, (5) low plasma beta, (6) low magnetic field variance, (7) coherent field rotations, (8) counterstreaming energetic protons, and (9) counterstreaming suprathermal electrons. Most, but not all, of these characteristics are also found about equally often elsewhere in the solar wind where it is assumed that they serve to identify those CMEs with speeds that are too low to produce shock disturbances. It is worth emphasizing that relatively few CMEs at 1 AU exhibit all of these characteristics [13]. Further, some of these features are more commonly observed than are others. Our experience is that a counterstreaming flux of suprathermal electrons above ~ 80 eV is the most reliable signature of a CME in the solar wind at 1 AU. The following paragraph helps explain why the counterstreaming electron signature is so reliable.

Solar wind electrons above ~80 eV are commonly referred to as the "halo" population to distinguish them from the thermal electron population at lower energies. These electrons carry the solar wind electron heat flux, and are usually narrowly beamed along the interplanetary magnetic field in a direction pointed outward away from the Sun. As illustrated in Figure 1b, a unidirectional beam of halo electrons normally arises because field lines in the solar wind usually are "open" and are effectively connected to a hot source (the solar corona) at only one end. Counterstreaming of these electrons is usually taken to indicate that a field line is connected to a hot source of electrons at both ends. Thus, the counterstreaming halo electron events, which we associate with CMEs in interplanetary space, are commonly interpreted in terms of "closed" field structures such as the connected loop or disconnected plasmoid drawn in the figure. The closed field topology suggested by counterstreaming electron events is consistent with coronagraph observations, which indicate that CMEs generally originate in closed field regions in the solar corona not previously participating in the solar wind expansion [14]. Indeed, it is precisely because CMEs generally originate in closed field regions and because the halo electrons are so sensitive to field topology that counterstreaming electrons are such a reliable signature of CMEs.

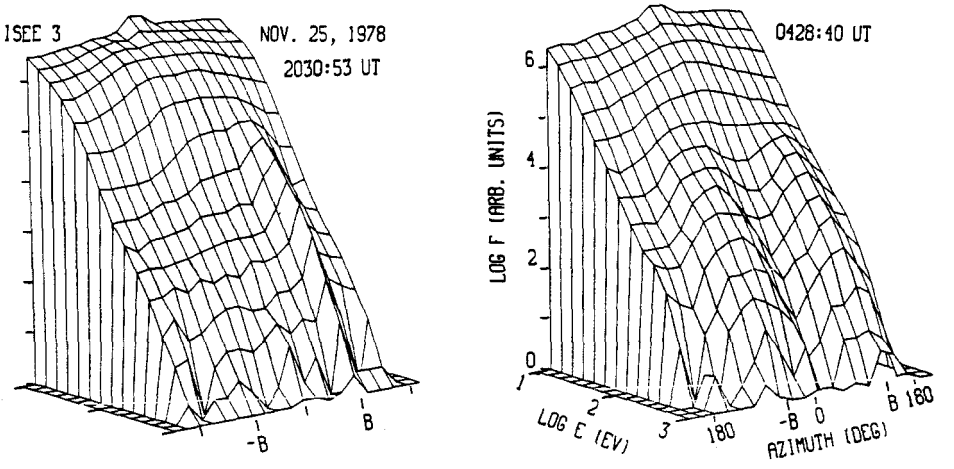

Fig. 3. Solar wind electron distributions within the normal solar wind (left) and within a CME (right). An azimuth of 0 deg corresponds to flow away from the Sun. The small blip at the lowest energy is an artifact. Adapted from [15].

Figure 3, which displays 3-dimensional views of 2-dimensional solar wind electron distributions measured by Los Alamos plasma instrumentation on ISEE 3, illustrates how counterstreaming electron events can be recognized in solar wind data. The electron distribution on the left is representative of what is normally observed in the solar wind, and contains an enhancement at energies above ~ 80 eV in the direction pointed outward away from the Sun along the interplanetary magnetic field. By way of contrast, the distribution on the right, obtained within a counterstreaming event, contains enhancements at these energies in the directions both parallel and antiparallel to the field.

We have scanned color-coded plots of electron angular distributions similar to those previously shown [7,15] in order to identify the counterstreaming electron events in the ISEE 3 / ICE plasma data that we associate with CMEs (ISEE 3 was renamed ICE in December 1983 after it was redirected toward an encounter with comet Giacobini-Zinner). At least 286 counterstreaming events have been identified in the interval extending from launch in August 1978 through December 1990. The average event duration was ~18 hours, corresponding to a radial thickness of about 0.2 AU. Approximately 1/3 of the events had sufficiently high speeds relative to the ambient solar wind to drive interplanetary shocks at 1 AU. The other events had no obvious associations with interplanetary shocks.

Figure 4a shows selected plasma and field data from ISEE 3 for a transient shock disturbance driven by a fast CME (identified by the counterstreaming signature). Note that the leading portion of the CME had a higher speed than that of the ambient wind ahead of the shock. The shock was, of course, a result of the interaction between the CME and the slower solar wind

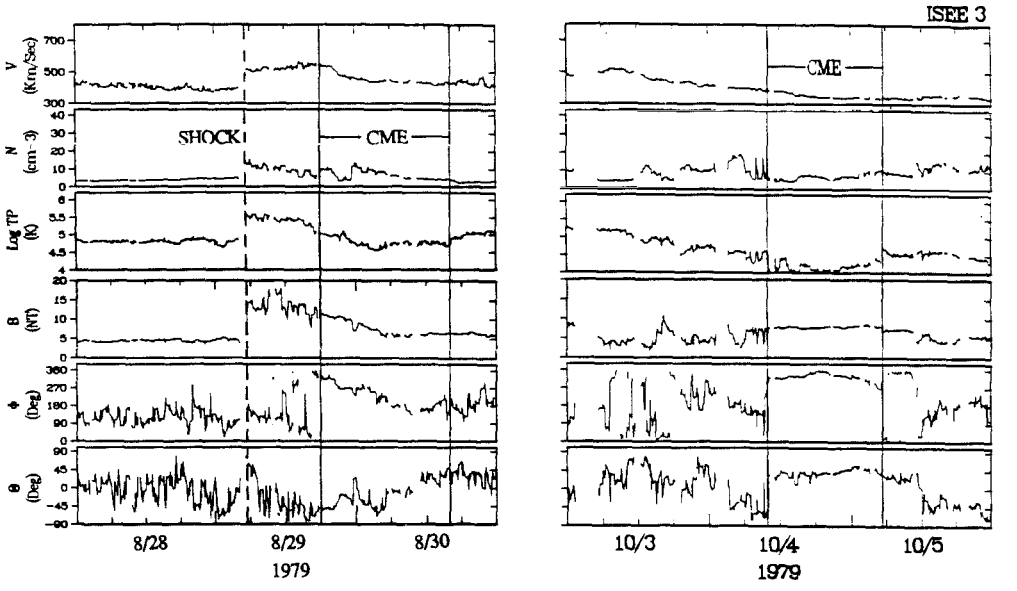

Fig. 4a (Left). Selected solar wind plasma and field measurements encompassing a shock wave disturbance driven by a fast CME. Adapted from [15].

Fig. 4b (Right). Selected solar wind plasma and field measurements encompassing a slow CME. Adapted from [15].

ahead. This interaction both accelerated the ambient wind and decelerated the CME, and the resulting compression produced a region of enhanced density, proton temperature, and field strength extending rearward from the shock into the leading portion of the CME itself. By way of contrast, Figure 4b shows selected plasma and field measurements encompassing a counterstreaming event that was not shock associated. Note that the bulk flow within the counterstreaming event was less than or comparable to that of the ambient solar wind ahead, which explains the lack of a shock association. In addition, it is clear that the counterstreaming event was a distinct plasma and field entity, distinguished by low plasma density, low proton temperature, moderately strong and steady magnetic field, low plasma beta, and field rotations at either end. This event illustrates that the magnetic field tends to be somewhat elevated within CMEs in the solar wind at 1 AU even when there is no evidence for compression in interplanetary space. However, interplanetary compression is primarily responsible for the very strong fields commonly observed within shock events.

Although CMEs in interplanetary space, as distinguished by the counterstreaming electron signature, are usually distinct plasma and field entities such as the ones illustrated in Figure 4, in most respects they do not usually differ greatly from the ordinary solar wind. On a statistical basis, when compared with the entire body of solar wind data, the characteristics of these events that stand out the most are stronger field strengths, lower proton and electron

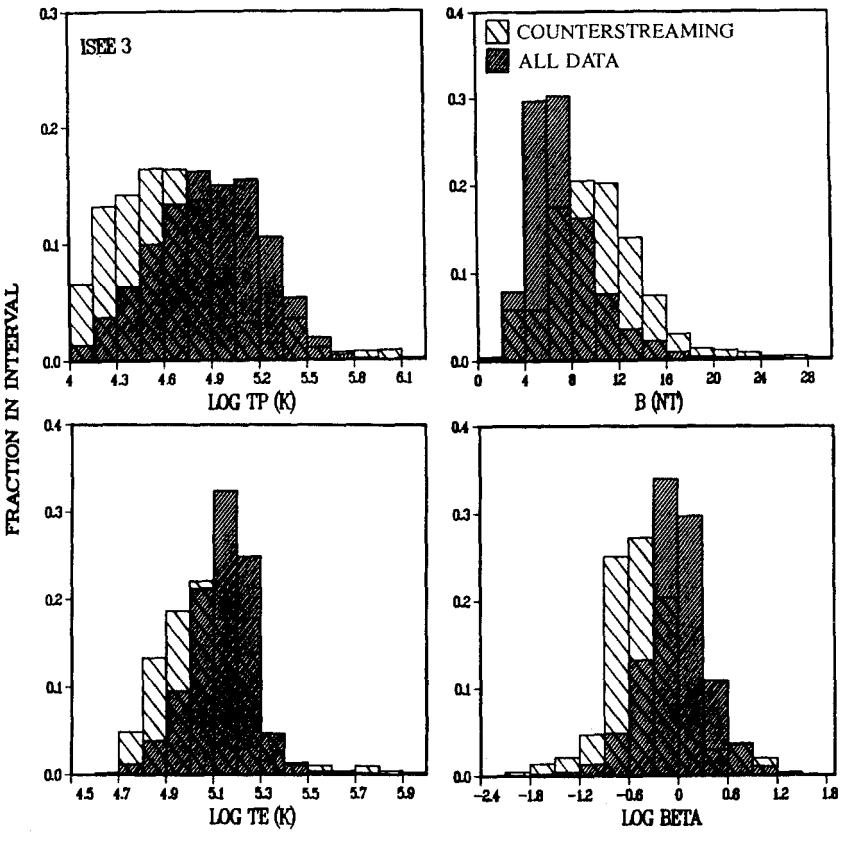

Fig. 5. Histograms of the relative frequency of occurrence of different values of proton and electron temperature (left) and magnetic field magnitude and plasma beta (right) within counterstreaming events and for the entire solar wind data set from August 1978 through December 1979. Adapted from [15].

temperatures, and lower plasma beta. This is illustrated by the plots shown in Figure 5, which compare the frequency of occurrence of these quantities in counterstreaming electron events with those for all of the ISEE 3 solar wind data for the 1978-1979 interval. As we have already noted, these events are usually not distinguished by abnormal plasma densities despite the fact that density is apparently one of the distinguishing traits of CMEs in coronagraph observations.

Analysis of coronagraph observations reveals that the occurrence rate of CMEs tends to track the solar activity cycle, as measured by (say) sunspot numbers [16]. From the coronagraph observations Kahler [17] has estimated that CMEs contribute ~ 10% of the solar wind mass flux in the ecliptic plane at solar activity maximum and ~ 1% near solar minimum. One test of the reliability of using counterstreaming electron events as signatures of CMEs in the solar wind at 1 AU would be to see if counterstreaming events exhibit a similar variation over the solar cycle. Figure 6a shows the percentage of the available solar wind electron data from ISEE 3 / ICE for which counterstreaming was observed on an annual basis from 1978 through 1990. For the

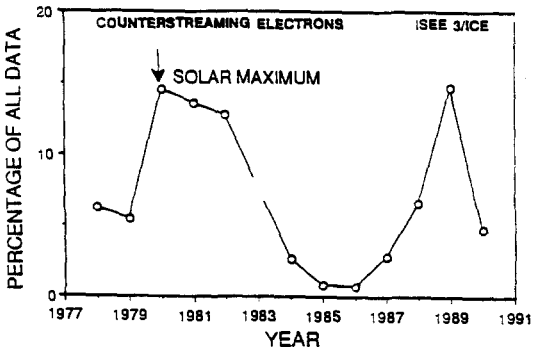

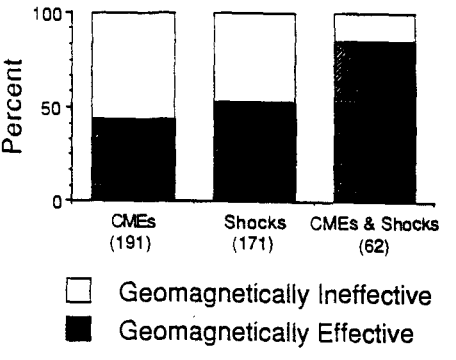

Fig. 6a (Left). Counterstreaming solar wind halo electron observations by ISEE 3 / ICE as a percentage of all the solar wind electron data, plotted on an annual basis. The counterstreaming percentages vary roughly in phase and amplitude with the 11-yr solar activity cycle as measured by sunspot numbers. Adapted from [18].

Fig. 6b (Right). Bar graph indicating the geomagnetic effectiveness of CMEs, shock disturbances, and shock/CME events passing Earth in the interval from August 1978 through October 1982 at the last solar maximum. The numbers in parentheses indicate the number of interplanetary events in each category. The different types of events are not mutually exclusive. From [6].

most part, the annual variation in counterstreaming percentage varied smoothly as a function of the phase of the ~11-yr sunspot cycle. Near solar activity maximums in 1980 and 1989 counterstreaming events accounted for ~14.7% of the available solar wind measurements. By way of contrast, near solar minimum in 1986 counterstreaming events accounted for only 0.7% of the available solar wind data. These percentages are comparable to Kahler's estimates noted above, although his estimates are for mass flux rather than for the percentage of time that CMEs pass a spacecraft at 1 AU. Yearly estimates of the numbers of CME events expected at a single point in the ecliptic plane (such as, for example, at ISEE 3 / ICE or at Earth) derived from both coronagraph observations andthe ISEE 3 / ICE electron measurements are also in reasonable agreement [18]. The number of CMEs/yr at a single point in the ecliptic plane varies from about 70 events/yr at solar maximum to about 5-10 events/yr at solar minimum. Taken together, these results provide further strong evidence that CMEs in the solar wind at 1 AU, including the many slow ones which do not produce transient interplanetary shocks, can usually be identified by the counterstreaming signature.

Finally, the high flow speeds and strong magnetic fields (often with strong southward components) associated with interplanetary disturbances driven by fast CMEs suggests that such events should often be quite effective in stimulating geomagnetic activity. Indeed, recent work with the ISEE 3 data indicates that fast CMEs are the crucial links between solar activity and large, nonrecurrent geomagnetic storms. For example, it has been shown [6,19] that all but

one of the 37 largest geomagnetic storms in the August 1978 - October 1982 interval spanning the last solar maximum were associated with Earth-passage of solar wind disturbances driven by fast CMEs (as identified by the counterstreaming electron signature).

On the other hand, many CMEs and CME-driven interplanetary disturbances passing the Earth were relatively ineffective in stimulating major geomagnetic activity. One commonly-used measure of geomagnetic activity is the K_p index, which ranges from 0_o up to 9_o in 28 logarithmic steps. In what follows we have assumed that interplanetary events are geomagnetically effective only if they produce a geomagnetic disturbance with $K_p > 4_+$. Figure 6b shows that only 44% of all CMEs and 53% of all transient shock disturbances (which we assume were driven by CMEs whether or not the CME itself was actually encountered directly), but 85% of all events in which the Earth encountered both a shock and the CME driving it in the 1978 - 1982 era were geomagnetically effective in this sense. Further analysis reveals that the geomagnetic effectiveness of these events was directly related to the associated flow speed, magnetic field magnitude, and strength of the southward field component. We have suggested [6] that the initial speed of a CME relative to the ambient solar wind ahead is ultimately probably the most important factor in determining if an earthward directed CME will be geomagnetically effective. A substantial speed differential appears to be essential for producing strong magnetic fields in interplanetary space via compression, and a large southward field component, the most important element in coupling solar wind energy to the Earth's magnetosphere, is more likely when the total field is strong.

Acknowledgment. This work was performed under the auspices of the U.S. Department of Energy with NASA support under S-04039-D. I thank the meeting organizers and NASA for travel support to the colloquium.

REFERENCES

1. J. T. Gosling, E. Hildner, R. M. MacQueen, R. H. Munro, A. I. Poland, and C. L. Ross, The speeds of coronal mass ejection events, *Solar Phys., 48*, 389, 1976.

2. R. Howard, N. R. Sheeley, M. J. Koomen, and D. J. Michels, Coronal mass ejections: 1979-1981, *J. Geophys. Res., 90*, 8173, 1985.

3. W. C. Feldman, J. R. Asbridge, S. J. Bame, and J. T. Gosling, Plasma and magnetic fields from the Sun, in *The Solar Output and Its Variation*, edited by O. R. White, Colorado Assoc. Univ. Press, Bounder, CO, p. 351, 1977.

4. N. R. Sheeley, R. A. Howard, M. J. Koomen, D. J. Michels, R. Schwenn, K.-H. Muhlhauser, and H. Rosenbauer, Coronal mass ejections and interplanetary shocks, *J. Geophys. Res., 90*, 163, 1985.

5. J. T. Gosling and D. J. McComas, Field line draping about fast coronal mass ejecta: A source of strong out-of-the-ecliptic magnetic fields, *Geophys. Res. Lett., 14*, 355, 1987.

6. J. T. Gosling, D. J. McComas, J. L. Phillips, and S. J. Bame, Geomagnetic activity associated with Earth passage of interplanetary shock disturbances and coronal mass ejections, *J. Geophys. Res.*, *96*, 731, 1991.

7. J. T. Gosling, Coronal mass ejections and magnetic flux ropes in interplanetary space, in *Physics of Magnetic Flux Ropes*, edited by C. T. Russell, E. R. Priest, and L. C. Lee, Geophysical Monograph 58, Amer. Geophys. Union, p. 343, 1990.

8. J. Hirshberg, S. J. Bame, and D. E., Robbins, Solar flares and solar wind helium enrichments: July 1965-July 1967, *Solar Phys.*, *23*, 467, 1972.

9. J. T. Gosling, V. Pizzo, and S. J. Bame, Anomalously low proton temperatures in the solar wind following interplanetary shock waves: Evidence for magnetic bottles?, *J. Geophys. Res.*, *78*, 2001, 1973.

10. J. T. Gosling, J. R. Asbridge, S. J. Bame, W. C. Feldman, and R. D. Zwickl, Observations of large fluxes of He^+ in the solar wind following an interplanetary shock, *J. Geophys. Res.*, *85*, 3431, 1980.

11. R. Schwenn, H. Rosenbauer, and K.-H. Muhlhauser, Singly ionized helium in the driver gas of an interplanetary shock wave, *Geophys. Res. Lett.*, *7*, 201, 1980.

12. R. D. Zwickl, J. R. Asbridge, S. J. Bame, W. C. Feldman, and J. T. Gosling, He^+ and other unusual ions in the solar wind: A systematic search covering 1972-1980, *J. Geophys. Res.*, *87*, 7379, 1982.

13. R. D. Zwickl, J. R. Asbridge, S. J. Bame, W. C. Feldman, J. T. Gosling, and E. J. Smith, Plasma properties of driver gas following interplanetary shocks observed by ISEE 3, in *Solar Wind 5*, NASA Conf. Publ., CP-2280, edited by M. Neugebauer, p. 711, 1983.

14. A. J. Hundhausen, The origin and propagation of coronal mass ejections, in *Proceedings of the Sixth International Solar Wind Conference*, edited by V. Pizzo, T. E. Holzer, and D. G. Sime, NCAR/TN-306+Proc, Boulder, CO, p. 181, 1988.

15. J. T. Gosling, D. N. Baker, S. J. Bame, W. C. Feldman, R. D. Zwickl, and E. J. Smith, Bidirectional solar wind electron heat flux events, *J. Geophys. Res.*, *92*, 8519, 1987.

16. D. F. Webb, The solar cycle variation of the rates of CMEs and related activity, *Adv. Space Res.*, *11*, (1)37, 1991.

17. S. Kahler, Observations of coronal mass ejections near the Sun, in *Proceedings of the Sixth International Solar Wind Conference*, edited by V. Pizzo, T. E. Holzer, and D. G. Sime, Tech. Note 306+Proc, p. 215, Natl. Cent. for Atmos. Res., Boulder, CO, 1988.

18. J. T. Gosling, D. J. McComas, J. L. Phillips, and S. J. Bame, Counterstreaming solar wind halo electron events: Solar cycle variations, *J. Geophys. Res.*, submitted, 1991.

19. J. T. Gosling, S. J. Bame, D. J. McComas, and J. L. Phillips, Coronal mass ejections and large geomagnetic storms, *Geophys. Res. Lett.*, *17*, 901, 1990.

Meter-Decameter Radio Emission Associated with a Coronal Mass Ejection

M. R. Kundu and N. Gopalswamy

Astronomy Program, University of Maryland, College Park, MD 20742

Abstract: A study of meter-dekameter radio emission associated with the 1986 Feb 10 coronal Mass ejection event is presented here. The event was accompanied by a major flare (optical importance 1B and X-ray importance C9.6), preceded by a filament disappearance. Changes in the intensity of a pre-existing noise storm was observed during the onset of the flare. A flare continuum, a moving type IV, and a type II occurred during the event. The event was also associated with a strong hard X-ray burst. The speeds of moving type IV burst and CME were of the same order of $1600\,kms^{-1}$, while the type II shock speed was $1900\,kms^{-1}$. The positional data indicate that the moving type IV burst and the inferred type II shock had different trajectories. The moving type IV burst was confined to one leg of the CME while the type II shock was far ahead of the CME leading edge. We discuss the inferred relation among different entities such as the CME, type II shock, type IV plasmoid and the erupting filament.

1 Introduction

The origin of shocks producing coronal type II bursts has been controversial. The super-Alfvenic motion of coronal mass ejection (CME) through the corona and flare explosion have been proposed as sources of the type II shocks. From our earlier observations (Kundu et al 1989; Gopalswamy and Kundu, 1987; Gopalswamy, 1990) we have shown that only the shocks from flare explosion seems to be consistent with the temporal and spatial association between a CME and the associated Type II burst, as was first pointed out by Wagner and MacQueen (1983). Our observations are not consistent with the SKYLAB era conclusions that only high speed CMEs are ssociated with type II and /or moving type IV bursts (Gosling et al 1976; Dulk, 1990). There is no evidence for a piston driven shock in the set of simultaneous radio and white light observations available so far. In this paper we report on a fast CME event associated with a type II and a moving type IV burst. The present observation provides further evidence that the coronal type II bursts are produced by flare explosions.

2 Radio Observations

Several types of meter-decameter radio bursts were observed on February 10 1986 by the Clark lake multifrequency radioheliograph: noise storm, flare continuum (FC), a type II burst and a moving type IV burst which accompanied a major flare. The noise storm was already in progress when the flare (optical 1B, X-ray C9.1 occurred in AR 4713. The Swept Frequency Interferometer Records (Courtesy: Sgt. Lutz, World Data Center) showed that the type II burst started at $\sim$ 72 MHz when the FC was seen at lower frequencies. After about 20:27 UT, the FC, the type II and the moving type IV were in progress simultaneously, so it is difficult to see them on the record. However, on the radio maps, the different types could be identified. The type II disappeared $\sim$20:27 UT and the flare continuum took over again. The moving type IV was present for a short while along with the stationary FC. At 73.8 MHz, the type II centroid was at a height of $1.38R_{\odot}$ at 20:24:16.7 UT. The type II was located in the same position angle as the CME that followed. The moving type IV sources at 50 and 38.5 MHz were nearly at the same location. The best fit to the observed height time plot of the moving type IV gives a speed of $\sim 1600 \pm 170\, kms^{-1}$ (Gopalswamy and Kundu, 1990). From its appearance, the moving type IV seems to be an "isolated source" variety.

3 White Light Observations

Both the Mauna Loa K-coronameter and the Coronagraph/Polarimeter (C/P) aboard SMM satellite were operational on this day and several images of the corona were produced. Two coronal mass ejections (CME) were observed from above the west limb in C/P images. The first one occurred during the period 12:14–15:51 UT near the equator (position angle 275°) and had a speed of $390 \pm 50\, kms^{-1}$. The second CME occurred approximately in the same location during 20:43 - 21:40 UT. Although C/P images were available since 19:09 UT, only 20:43 UT image showed a faint CME at position angle of 272°. At 21:40 UT, the mass ejection had moved beyond the field of view. We estimate the CME speed based on the three images at 20:31, 20:43 and 21:40 UT. The leading edge of the CME at its apex ($PA 272°$) was at a height of $3R_{\odot}$ at 20:43 UT. It had gone beyond the field of view ($> 6.0R_{\odot}$) at 21:40 UT. This indicates a CME speed of at least $750\, kms^{-1}$. Since no CME was seen at $1.5R_{\odot}$ (the occulting height) at 20:31 UT, this means that the CME was somewhere between 1 and $1.5R_{\odot}$ at this time. If we take the extreme case of $1.0R_{\odot}$, the CME must have traveled with a speed of $\sim 1820\, kms^{-1}$ in order to reach a height of $3.0R_{\odot}$ at 20:43 UT. Taking the other limit of $1.5R_{\odot}$ at 20:31 UT, the CME speed would be $1365\, kms^{-1}$. Thus, the CME speed is expected to be between these two limits, $1365 - 1820\, kms^{-1}$, implying an onset time within the interval 20:26-20:31 UT, assuming a constant speed. Any acceleration will imply an earlier onset. Allowing for an initial height of the erupting CME structure will place the CME speed above $1365\, kms^{-1}$. For purposes of our discussion, we shall use the average value of $1600\, kms^{-1}$.

4 Discussions and Conclusions

The relative location of the CME, the moving type IV and the type II burst are shown in Fig.1 at various times. The moving type IV burst was detected in the radioheliogram at $\sim$ 20:32:39 UT at a height of $1.62R_{\odot}$. Since the height - time plot of the moving type IV was well determined (Gopalswamy and Kundu 1990) we can get its extrapolated location at the time of the nearest C/P image (20:31:02 UT) as $1.40R_{\odot}$. This is clearly below the C/P occulting disk.

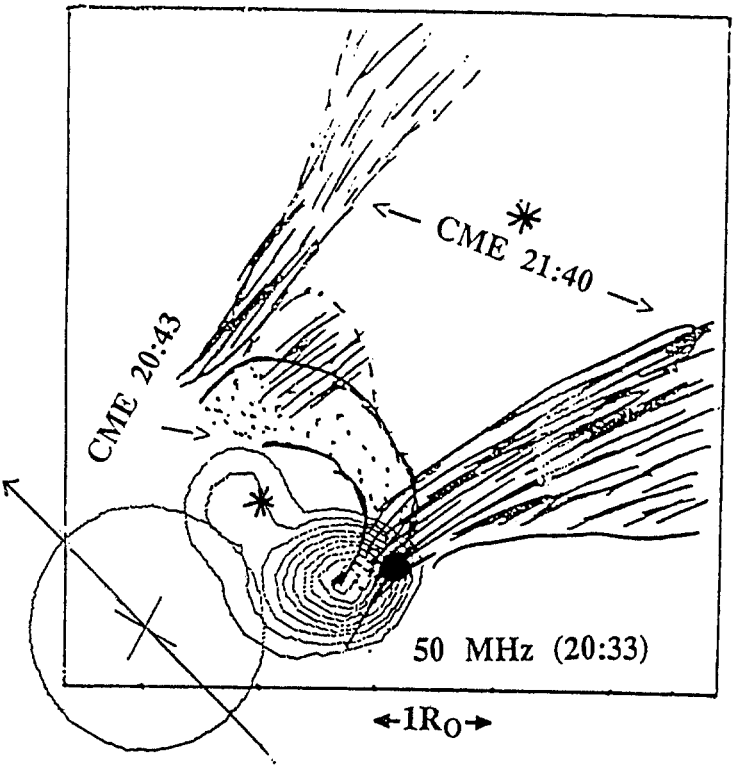

Fig. 1. Superposition of the centroids of type II burst locations and and contour map (at 20:33 UT) of moving type IV bursts (50 MHz). The CME is sketched from the 20:43 and 21:40 UT C/P images. The asteriks radially below and above the 20:43 UT CME correspond to the observed (20:24:16 UT) and extrapolated (20:43) type II centroids. The filled circle is the centroid of moving type IV at 20:37 UT. The arrow points to solar north and the big circle is the optical disk.

At 20:43:47 UT, when the CME was first detected, the plasmoid had the same height as the CME. Therefore, we conclude that the CME and the plasmoid moved with approximately the same speed. Further, the location of the plasmoid just

below the occulting disk at 20:31:02 UT is consistent with our speed estimate for the CME. From the time of arrival of the type II burst at various frequencies, we can estimate the type II shock speed as $\sim$ 1900 kms^{-1}. From this we can extrapolate the location of the shock at 20:43:47 UT as $4.6R_{\odot}$, while the CME leading edge was at $3.0R_{\odot}$. Although the type II burst location is ahead of the CME leading edge as expected for a piston driven shock, we argue that the shock may not be driven by the CME. Since the CME has a high speed, we expect a fast mode shock to form at the 'stand-off' distance. This distance is expected to be much smaller than the characteristic dimension of the piston (see e.g., Hundhausen, 1988). The thickness of the CME at the position angle of the type II shock was $\sim$ $0.5R_{\odot}$ which is 3 times smaller than the distance at which the shock was located. The type II was first observed at a height of $1.38R_{\odot}$ at 20:24:17 UT. Extrapolating the locations of Moving type IV and the CME to this time, we find that they probably were not ejected yet or were under the process of slow acceleration. Hence we conlude that the realtive positions of type II, moving type IV and the CME are not consistent with a shock piston driven by the coronal mass ejection. On the other hand, the shock speed is consistent with the blast wave scenario where the shock originated at the flare explosion at $\sim$ 20:22 UT (time of hard X-ray peak) and arrived at the 73.8 MHz plasma level at 20:24:17 UT with a speed of $\sim 1900\, kms^{-1}$ as obtained from radio observations.

This research was supported by NASA grants NAG-W1541 and by NSF grant ATM 87-17157.

References

Dulk, G. A.(1980): in Radio Physics of the Sun, ed. by Mr. Kundu and T. E. Gergely, (D. Reidel, Dordrecht) p. 419

Gopalswamy, N. (1990): in Basic Plasma Processes on the Sun, ed. by E. R. Priest and V. Krishan, (IAU Colloquium 142) p.495

Gopalswamy, N. and Kundu, M. R. (1987): Solar Phys. **114**, 347

Gopalswamy, N. and Kundu, M. R. (1990): Astrophys. J. Lett.**365** , L31

Gosling, J. T., Hildner, E. MacQueen, R.M., Munro, R. H., Poland, A. I., and Ross, C. L. (1976): Solar Phys. **48**, 389

Kundu, M. R., Gopalswamy, N. White, S. M., Cargill, P., Schmahl, E. J., and Hildner, E. (1989): Astrophys. J. **347**, 505

MODELS OF NORMAL AND INVERSE POLARITY FILAMENT ERUPTIONS AND CORONAL MASS EJECTIONS

Dean F. Smith*
Berkeley Research Associates, P.O. Box 241, Berkeley, CA 94701

Ernest Hildner
NOAA Space Environment Laboratory, R/E/SE, 325 Broadway, Boulder, CO 80303

and
Richard S. Steinolfson
Department of Space Sciences, Southwest Research Institute, San Antonio, TX 78228

An important problem in contemporary solar research is the relation between flares, filament eruptions, and coronal mass ejections (CMEs). Suppose that we take the viewpoint that flares, filament eruptions, and CMEs are all different aspects of the destabilization of a global magnetic configuration. In this case, to be successful a flare and filament eruption model such as that of Martens and Kuin (1989; hereafter MK) should not lead to predictions that contradict CME observations.

We recount some observational properties. Hundhausen (1988) and Kahler (1988) note that CME structure often has three parts: a bright loop of enhanced density (1) encloses a dark region of depleted material (2) containing a bright core (3). They relate these satellite coronagraph observations to ground-based coronagraph and coronameter observations, and show that the bright loop is the initial overlying corona, the dark region is the prominence cavity, and the bright core is the erupting prominence. The basis of this association can be seen clearly in Figure 4 of Illing and Hundhausen (1985) which leads to the following inference.

Since the difference in velocities between the bright loop's leading and trailing edges is much smaller than the difference in velocities between the loop's trailing edge and the bright core, the loop's transverse dimension (its thickness) increases much more slowly than does the depleted region or cavity dimension. Kahler (1988) states that the three-component model fits many, but not all observed CMEs. To explain the large fraction of CMEs that do exhibit this structure, a successful theory must not lead to more compression of material immediately above the prominence or filament than in the region of the bright loop.

This requirement was compared with predictions for the MK flare-filament eruption model as extended by us. The field lines in this model with the values of the filament current and background dipole field as in MK are shown in Figure 1 for two different filament heights, H. Like MK, our results are zero-conductivity or infinite time plots; they assume that magnetic field evolution dominates compression or other effects, appropriate for a low beta coronal plasma. They are static equilibria and do not include dynamic effects. We shall be careful to clarify the effect of dynamics on our arguments. Suppose that we identify the innermost

*Work performed as a NRC Senior Research Associate at NOAA/SEL, Boulder, CO.

dotted flux tubes in Figure 1a,b with the prominence cavity or dark region and the outermost dotted flux tubes in the same figures with flux tubes of the initial overlying corona or bright loop. In going from Figure 1a to Figure 1b, is there any tendency for these flux tubes to "evolve" in a manner consistent with observations? As the filament height is increased, these flux tubes expand at almost the same rate (confirmed quantitatively by computing flux tube cross-sectional areas (Smith, Hildner, and Kuin 1991; hereafter SHK)).

This behavior of a succession of static equilibria does not agree with the observations noted above. For a background field given by the more realistic streamer model of Low (1986), disagreement only increases. If successive static equilibria adequately model a rising filament below a streamer, the field lines immediately above the filament are compressed as they push into the field lines of the streamer. We note that dynamics would only make this situation worse since there are forces on the current in the filament pushing it outward in the MK model. The MK model belongs to the class of Inverse polarity models (Priest 1989; Leroy 1989), so named because in the plane transverse to the photospheric neutral line the field lines under the filament run in the opposite direction to the field lines at the photosphere, i.e., there is a neutral point underneath the filament. Thus the MK model and, by generalization, the whole class of Inverse polarity models are not useful for modelling CMEs accompanied by erupting filaments.

Thus we examine Normal polarity configurations (Priest 1989; Leroy 1989), so named because in the plane transverse to the photospheric neutral line the field lines in the filament run in the same direction as the field lines at the photosphere (as in the Kippenhahn and Schlüter (1957) model). This kind of model is easily obtained from the MK model by reversing

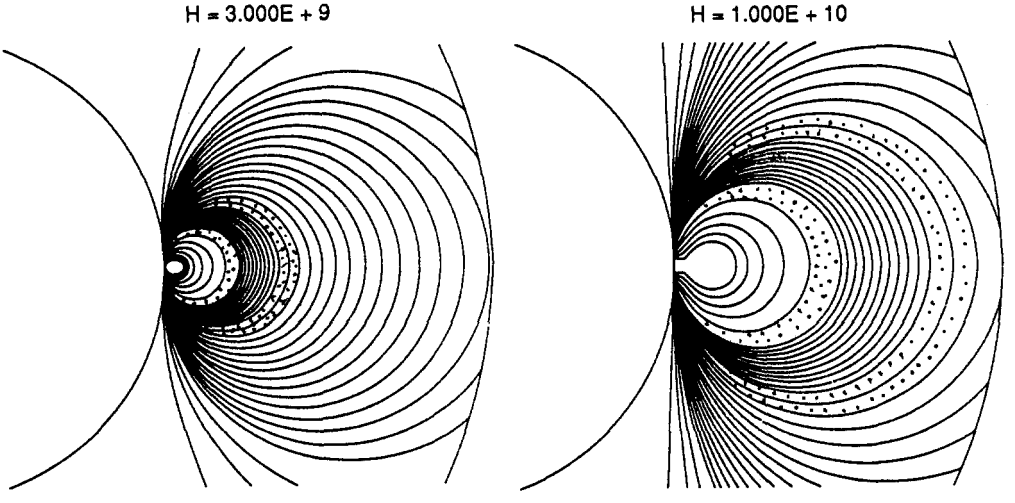

Fig. 1. a) A polar plot of the field lines in the MK model for a filament height $H = 3 \times 10^9$ cm. The filament is located at the center of the oval that just touches the Sun. The dotted flux tubes are discussed in the text.
b) The same as a) for $H = 1 \times 10^{10}$ cm. The filament is located at the center of the oval whose straight field line extensions touch the surface of the Sun.

the directions of the filament and mirror currents. An example of a Normal polarity configuration static equilibrium is shown in Figure 4 of SHK for a background field of the Low (1986) streamer model. There are now two neutral points above the filament: an X-type neutral point above the filament and a higher X-type neutral point between the field lines above the filament and the field lines around the streamer current sheet.

However, this zero-conductivity configuration prompts many questions. In a corona of finite conductivity, when current begins to flow in the filament, how long does it take for the field lines to distort, pass through, and arrive underneath the filament? What is the dynamic evolution of a realistic coronal streamer in which such a filament is embedded? We are using a two-dimensional (2D) magnetohydrodynamic (MHD) simulation to answer these questions. Some preliminary results are shown in Figure 2. First, a streamer configuration relaxes for 30 hours to a quasi-steady state. Then, the filament current and the mirror current are ramped up linearly over 30 minutes and allowed to relax.

The equations solved are the continuity, momentum, and polytropic energy equations. The polytropic energy equation is very useful for producing a solution as in Figure 2a with all transitions (sonic, Alfvénic) properly treated. However, it forces us to resort to some ruses for treating the forces that must be handled in the filament eruption problem. In particular, suppose that we simply increase the density by a factor ~100 in the region of the filament. In marching the grid this naturally leads to large, unphysical velocity outflows from the region of the filament; i.e., the equations try to smooth out this density inhomogeneity. Instead, we artificially "load" mass onto the filament by increasing the gravity G at the point of the filament. Figure 2 has $\Delta G = 24$ for an initial density $n_0 = 10^{10}$ cm^{-3} at the surface. The region of enhanced G is convected with the filament in the velocity field which subsequently results. The current in the filament is such that when it is at its starting height of 10^5 km, the field due to it at the photosphere is 0.7 G where the pre-existing streamer field is 2.3 G.

The perturbation produced by the filament and mirror currents gives rise to a global perturbation of the magnetic field, and thus is capable of producing volume body forces as in the 2½-D simulation of Steinolfson (1991). Figure 2 shows simulation results for three hours after the filament current commences. Since this is an MHD simulation, the main variables are the density, velocity, and magnetic field **B**. The current cannot be specified directly. Rather, the magnetic field increase in each time step due to the increasing filament and mirror currents is added to the previous magnetic field for 30 minutes. Then the configuration is allowed to relax and the filament and mirror currents decrease.

Figure 2 shows that an arch forms with a density ~3 times the pre-event density; the arch has "legs" reminiscent of CME photographs. There is a relatively low-density region between this arch and the position (just below the low-density region) where the filament would be if it were simply convected outward with the flow. The match of these preliminary results with observations is very promising, but only an analysis of the energetics involved will justify the additional effort of a 3D simulation to confirm it. Thus far, we cannot tell if the CME draws its energy from the energy put into the perturbation or from energy previously stored in the initial streamer configuration. It is argued by one of us (Hildner 1992) that only the latter case would lead to a viable CME model.

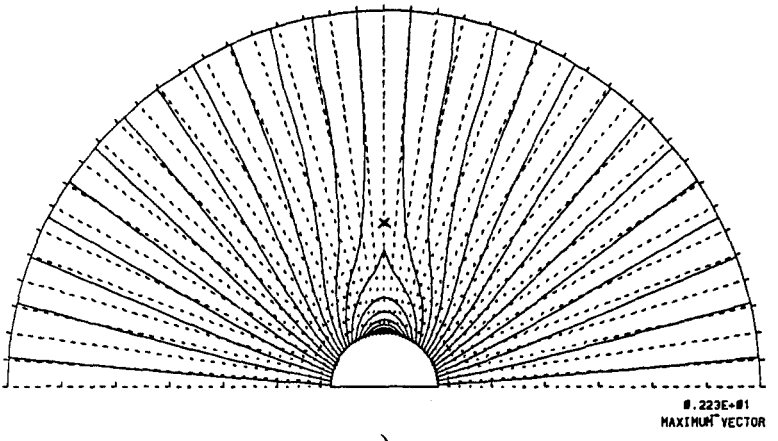

a)

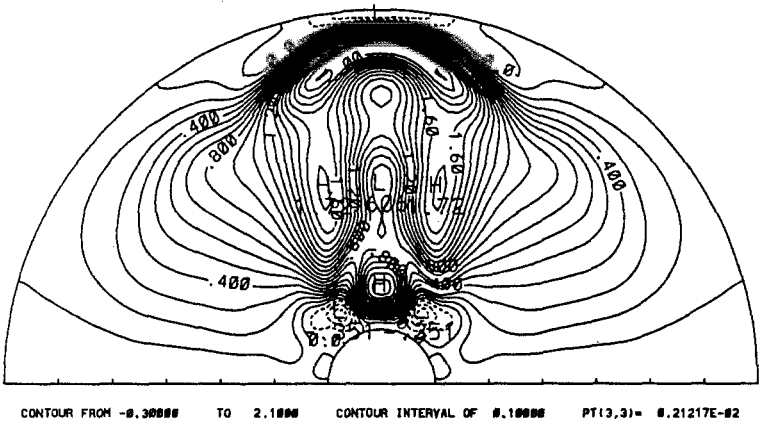

b)

Fig. 2. a) Magnetic field (solid) and velocity lines of the MHD simulation after 3 hours. The filament position is indicated by the x.
b) $n/n_{streamer} - 1$ of the MHD simulation after 3 hours where n is the density and $n_{streamer}$ is the density of the initial streamer at zero time.

Hildner, E.: 1992, this volume.
Hundhausen, A. J.: 1988, Proc. 6th Intern. SOLWIND Conf., NCAR TN-306, Boulder, CO.
Illing, R. M. E., and Hundhausen, A. J.: 1985, *J. Geophys. Res.* **90**, 275.
Kahler, S.: 1988, Proc. 6th Intern. SOLWIND Conf., NCAR TN-306, Boulder, CO.
Kippenhahn, R. and Schülter, A.: 1957, *Z. Astrophysik* **43**, 36.
Leroy, J. L.: 1989, in *Structure and Dynamics of Quiescent Solar Prominences* (E. R. Priest, ed.), Kluwer, Dordrecht, p. 77.
Low, B. V.: 1986, *Astrophys. J.* **310**, 953.
Martens, P. C. H., and Kuin, N. P. M.: 1989, *Solar Phys.* **122**, 263 (MK)
Priest, E. R.: 1989, in *Structure and Dynamics of Quiescent Solar Prominences* (E. R. Priest, ed.), Kluwer, Dordrecht, p. 1.
Smith, D. F., Hildner, E., and Kuin, N. P. M.: 1991, *Solar Phys.*, in press (SHK).
Steinolfson, R. S.: 1991, *Astrophys. J.*, in press.

MHD SHOCKS AND SIMPLE WAVES IN CMES

Richard S. Steinolfson
Southwest Research Institute
6220 Culebra Road
San Antonio, TX 78228

Extended Abstract

Previous studies have shown how the various types of MHD shocks (slow, intermediate, and fast) may form near the leading edge of coronal mass ejections in relatively simple geometric (2-D, Cartesian) models. These models also neglect the important contribution of the outflow velocity and the current sheet since they do not incorporate a coronal streamer configuration in the initial state. It is shown that some of these previous results remain true for a model with a more realistic spherical geometry (2-D and 3-D) and when the CME propagates through a streamer. However, there are several important differences. Some are of a more detailed character such as the slow shock becoming a perpendicular shock at the center of the current sheet rather than a gas dynamic shock and being less noticeably concave upward. One very important difference is that (except for possibly the very fastest disturbances), the results indicate that fast MHD shocks probably do *not* form within the field of view of most coronagraphs. This is true despite the fact that the disturbance speed greatly exceeds the fast mode speed. This apparent anomaly occurs due to the formation of fast simple expansion waves ahead of the central part of the disturbance which modify the initial corona such that either a slow or intermediate shock forms. The leading fast simple waves become compressive at the flanks of the disturbance but have not steepened into shocks. The three-dimensional simulations also provide information on the global CME structure as well as the anticipated reduction in observed brightness as the CME occurs further from the limb. For the results given here the CME is shaped more like a radially expanding arcade than a bubble. The CME brightness is reduced by 30% as the CME moves from the limb to 45° away from it. The peak brightness in a polar view is about 65% less than the maximum in a meridional projection. These results are discussed in more detail in: R. S. Steinolfson, "The three-dimensional structure of coronal mass ejections," *J. Geophys. Res.* (in press) 1992.

Terrestrial Response To Eruptive Solar Flares: Geomagnetic Storms

Walter D. Gonzalez
Instituto Nacional de Pesquisas Espaciais, Sao Jose dos Campos, Sao Paulo, Brazil

Bruce T. Tsurutani
Jet Propulsion Laboratory, California Institute of Technology, Pasadena, California, USA

Abstract

During the interval of August 1978 – December 1979, 56 unambiguous fast forward shocks were identified using magnetic field and plasma data collected by the ISEE-3 spacecraft. Because this interval is at a solar maximum we assume the streams causing these shocks are associated with coronal mass ejections and eruptive solar flares. For these shocks we shall describe the shock- storm relationship for the level of intense storms ($Dst < -100$ nT). Then, we will discuss the interplanetary structures that are associated with the large-amplitude and long-duration negative B_z fields,which are found in the sheath field and/or driver gas regions of the shock and are thought to be the main cause of the intense storms.

We will also present for the solar physicist a summary of the interplanetary/magnetosphere coupling functions, based on the magnetopause reconnection process. We will end by giving an overview of the long-term evolution of geomagnetic storms such as those associated with the seasonal and solar cycle distributions.

1. Introduction

Because the emphasis of this review is to discuss the origin of geomagnetic storms in eruptive flares and, since the latter are claimed to be closely associated with coronal mass ejections (Z. Svestka, private communication) and fast forward shocks to them (*e.g.* Sheeley *et al.*, 1985), we reduce our task to the study of the association of geomagnetic storms with interplanetary shocks.

Recent studies by Gonzalez and Tsurutani (1987), Tsurutani *et al.* (1988, 1991) and Gosling *et al.* (1991) indicate that the category of storms having the largest association with interplanetary shocks are the most intense ones. This level of storm intensity can be expressed by the storm index threshold $Dst < -100$ nT. Gonzalez and Tsurutani (1987), Tsurutani *et al.* (1988, 1991) and Gonzalez *et al.* (1989) have shown that the main interplanetary feature associated with intense storms, accompanying the shocks, is the presence of a large-amplitude (< -10 nT), long-duration (> 3 hours) and negative B_z component of the IMF. Thus this review also concentrates on the origin of this type

of B_z fields and on its quantitative interaction with the magnetosphere which leads to the development of the storms.

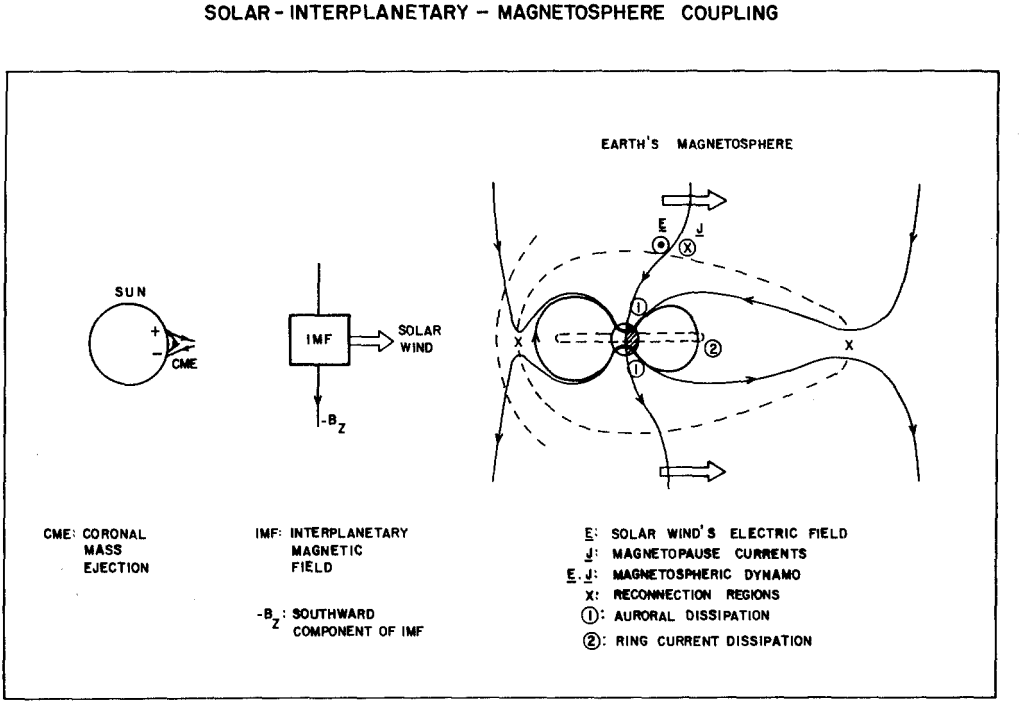

Figure 1. Schematic of the solar-interplanetary-magnetosphere coupling during solar maximum years at which a coronal mass ejection (CME) is the most important solar source for the interplanetary and magnetospheric disturbances.

Figure 1 shows schematically the solar-interplanetary-magnetosphere coupling for eruptive flares. At the sun the main ingredient is the CME, whereas at the interplanetary medium the main responsible feature for the development of the storm is the presence of a southward IMF carried by the solar wind. At the magnetosphere this southward field reconnects with the geomagnetic field leading to an effective momentum and energy transfer via a magnetospheric dynamo. In this figure two of the most important dissipation regions within the magnetosphere are indicated, the auroral and the ring current regions. The former refers to the substorm process, for which the level of intensity is monitored by the auroral electrojet index AE, and the latter refers to the storm process itself with its intensity monitored by the storm index Dst.

2. Interplanetary Shocks and Magnetic Storms

The ISEE-3 satellite, situated in a halo orbit around the L_1 libration point (at approximately 240 earth radii in front of the earth), measured 56 unambiguous fast forward shocks during the interval of August 16, 1978 to December 28, 1979 (*e.g.* Tsurutani and Lin, 1985). From these 56 shocks it was reported by Gonzalez and Tsurutani

(1987) that only nine preceded (within typical time lags) the occurrence of an intense geomagnetic storm (Dst < -100nT). Thus from the predictive point of view one can say that about 14% of the interplanetary shocks during solar maximum are expected to lead to the development of intense storms.

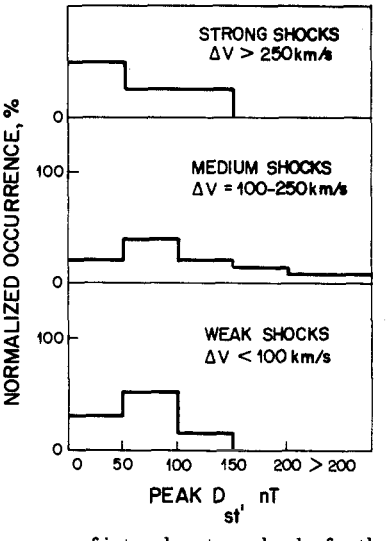

Figure 2. Normalized occurrence of interplanetary shocks for the interval August 1978–December 1979, observed by ISEE-3, as a function of the storm intensity (given by peak Dst). They are shown for three selected shock-strength intervals (strong, medium and weak). Taken from Gonzalez and Tsurutani, 1987.

On the other hand, since nine of the intense storms that occurred within this studied interval were associated with shocks, one can also say that during solar maximum 90 % of the intense storms are expected to be associated with fast forward shocks within 1 AU. A similar conclusion was arrived at by Gosling *et al.* (1991).

With respect to any influence of the shock's strength in the intensity of the resulting storm, it has long been known (*e.g.* Akasofu and Chapman, 1963) that there is no association at all. Figure 2 (taken from Gonzalez and Tsurutani, 1987) illustrates this point where it is shown that both weak and strong shocks have equal chances to lead to magnetic storms of any intensity.

3. Sources of Southward IMF Fields for Intense Storms

Gonzalez and Tsurutani (1987) reported that all ten intense storms (Dst < -100 nT) that occurred during the ISEE-3 studied interval had associated with them large-amplitude (< -10 nT), long-duration (> 3 hours) negative B_z fields in the interplanetary medium.

Figure 3 shows one example of such an association for the day August 28, 1978. This figure illustrates the fast forward shock event that was observed at 02:00 UT of day 27, the compressed (and heated) sheath field region lasting to approximately 18:25

UT of day 27 and also a driver gas region lasting to approximately 12:00 UT of day 28. In this case, the $-B_z$ event is associated with the driver gas for which a magnetic cloud (with rotation in the B_y component) was observed (Gonzalez *et al.*, 1990*a*).

Figure 3 also shows the occurrence of a high-intensity, long-duration and continuous auroral activity (HILDCAA) event as shown by the horizontal bar in the AE panel. Tsurutani and Gonzalez (1987) and Tsurutani *et al.* (1990) associated these HILDCAA events with the simultaneous occurrence of large amplitude Alfvenic fluctuations and argued that magnetic reconnection between the southward field of these fluctuations and the geomagnetic field is responsible for the magnetospheric energization.

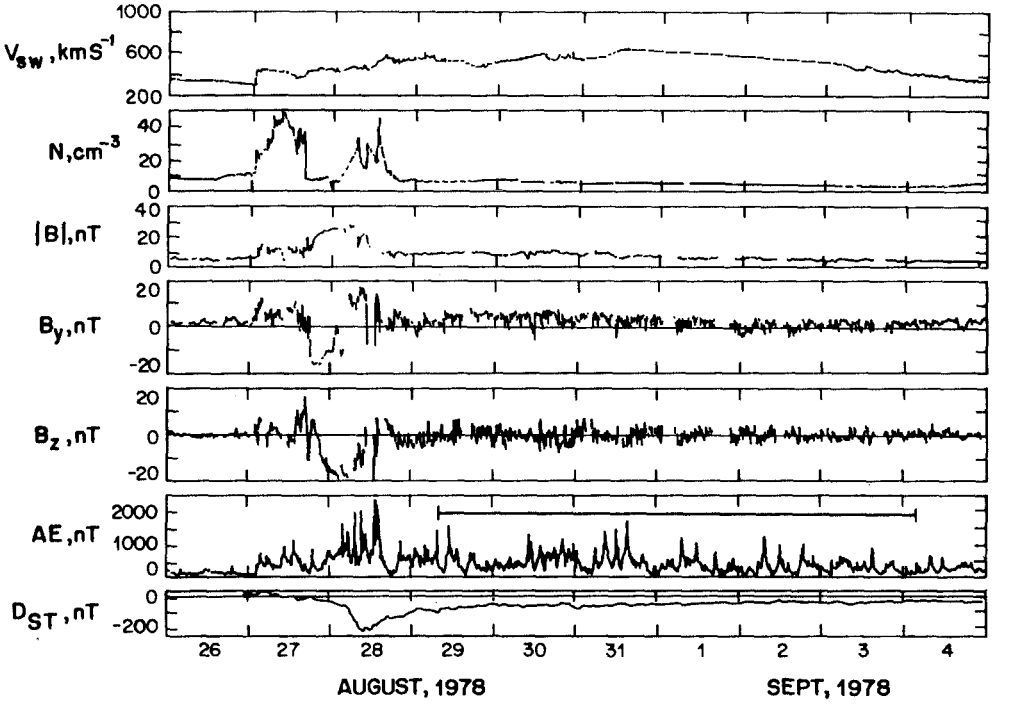

Figure 3. Example of a shock (02:00 UT August 27), sheath and driver gas fields associated with the intense storm of August 28 (peak $Dst = -220$ nT). They were followed by a HILDCAA event (shown by a horizontal bar on the AE panel)

Tsurutani *et al.* (1988) studied the interplanetary structures associated with the $-B_z$ events responsible for the 10 intense storms of the Gonzalez and Tsurutani (1987) study. Figure 4 is an updated version of those structures. They are divided in two groups: those that belong to the sheath region of the shock and those encountered within the driver gas region. About half of the 10 events belong to each of these two groups and can be associated with any of the suggested possibilities. Because the suggested structures are self explanatory, we shall not extend our discussion on this matter.

SHEATH FIELDS

a) Shocked Southward fields
Tsurutani *et al.*, 1988

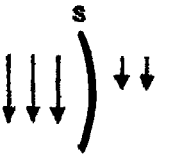

b) Shocked heliographic current sheets
Tsurutani *et al.*, 1984

c) Turbulence, waves and discontinuities

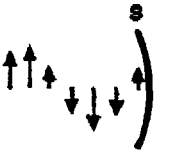

d) Draped magnetic fields
Zwan and Wolf, 1976

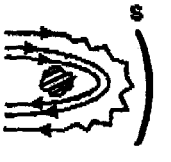

McComas *et al.*, 1989

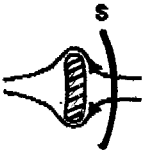

DRIVER GAS FIELDS

e) Magnetic clouds
Klein and Burlaga, 1982

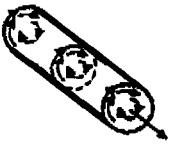

Fluxropes
Marubashi, 1986

Magnetic tongues
Gold, 1962

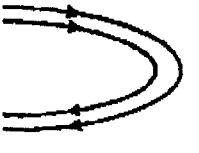

Figure 4. The various interplanetary features that involve large-amplitude, long-duration negative B_z fields for the 10 intense storms (Dst < -100 nT) of August 1978 – December 1979. They are grouped into two broad categories: Sheath fields and Driver gas fields.

4. Solar Wind-Magnetosphere Coupling Functions

Magnetic field reconnection between the southward directed IMF and the geomagnetic field (Dungey, 1961) is the most acceptable mechanism for the energy transfer responsible for the auroral and ring current energization processes. Since early work (Arnoldy, 1971; Tsurutani and Meng, 1972) it is known that a simple correlation between IMF $-B_z$ and magnetospheric dissipation parameters, such as the auroral index AE, give fairly high correlation values due to the fact that the B_z parameter is the main ingredient of the reconnection energy-transfer mechanism. More complex functions associated with the electric field transfer and with the energy transfer of magnetopause reconnection were later introduced (Gonzalez *et al.*, 1989 and references therein). Table 1 is a summary of the most commonly used coupling functions. In this Table, v and ρ are the solar wind speed and density, respectively; B_T is the transverse (to the Sun-Earth line) component of the IMF vector, $B_T = (B_z^2 + B_y^2)^{\frac{1}{2}}$ in solar magnetospheric coordinates; B is the IMF amplitude and θ is the angle between $\underline{B_T}$ and the geomagnetic field vector taken at the magnetopause; and L_o is a constant scale-length factor (equal to 7 earth radii). Gonzalez (1990*a*) showed that most of these functions can be derived as particular cases of more general expressions for the electric field and energy transfer at the magnetopause due to large-scale reconnection.

5. Seasonal and Solar Cycle Distributions of Intense Storms

It is known that geomagnetic activity has a seasonal variability with maxima at

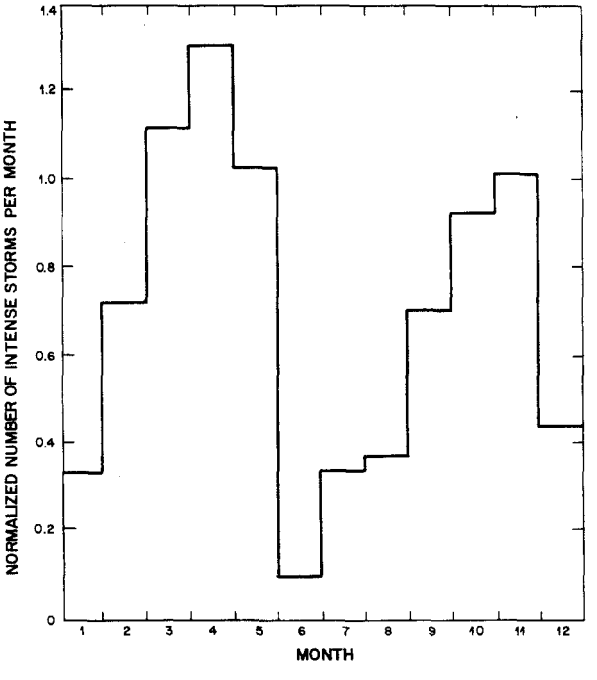

Figure 5. Seasonal distribution of intense storms (Dst < -100 nT) for the interval 1975–1986. The normalized number of these storms per month is given.

TABLE 1

MOST COMMONLY USED COUPLING FUNCTIONS FOR THE SOLAR WIND–MAGNETOSPHERE INTERACTION

(a) Electric field related		(b) Power related		(c) Simple expressions	
VB_z	Rostoker et al. (1972) Burton et al. (1975)	$\varepsilon = VL_o^2B^2\sin^4(\theta/2)$	Perreault and Akasofu (1978)	B_z	Arnoldy (1971) Tsurutani and Meng (1972)
VB_T	Doyle and Burke (1983)	$(\rho V^2)^{1/2}VB_z$	Murayama (1986) Gonzalez et al. (1989)	B_zV^2, BV^2	Murayama and Hakamada (1975) Crooker et al. (1977) Baker et al. (1981) Holzer and Slavin (1982)
$VB_T\sin(\theta/2)$	Gonzalez and Mozer (1974) Doyle and Burke (1983)	$(\rho V^2)^{-1/3}VB_T^2\sin^4(\theta/2)$	Vasyliunas et al. (1982) Gonzalez et al. (1989)	B_z^2V, B^2V	Holzer and Slavin (1982) Baker et al. (1981)
$VB_T\sin^2(\theta/2)$	Kan and Lee (1979) Gonzalez and Gonzalez (1981) Reiff et al. (1981) Wygant et al. (1983) Doyle and Burke (1983)	$(\rho V^2)^{1/6}VB_T\sin^4(\theta/2)$	Vasyliunas et al. (1982) Bargatze et al. (1986) Gonzalez et al. (1989)		
$VB_T\sin^4(\theta/2)$	Wygant et al. (1983) Doyle and Burke (1983)				

the two equinoxes (*e.g.* Russell and McPherron, 1973). However it is not clear if such variability is also distinguishable for intense storms. This expectation is confirmed by the distribution shown in Figure 5. It refers to the intense storms ($Dst < -100$ nT) that occurred within the 1975–1986 interval. However it remains to be seen if the mechanisms suggested for the seasonal variability of geomagnetic activity in general (*e. g.* Russell and McPherron,1973 ; Murayama,1974) are or are not applicable to the category of intense storms (Clua de Gonzalez *et al.*, 1991).

Gonzalez *et al.* (1990*b*) studied the solar-cycle distribution of intense storms for the interval 1880–1985 using the geomagnetic indices aa (1880–1964) and *Dst* (1965–1985). They showed that intense storms tend to occur within the solar cycle with a dual-peak distribution. On the average the first peak tends to occur close to solar maximum and the second peak about two years after solar maximum. These authors also showed that a similar dual-peak distribution occurred during the 1970–1981 interval for the yearly number of large negative B_z events with amplitudes $< -10\ nT$ and duration > 3 hours, supporting the association described in Section 3. However the exact nature of this dual-peak distribution still needs to be studied.

Conclusion

In this brief review some aspects of intense geomagnetic storms have been presented with the aim of suggesting further research within the framework of the solar-interplanetary-magnetosphere coupling. This review refers to solar maximum years within which the CMEs and the eruptive solar flares are more abundant.

Acknowledgments

The authors have benefitted from discussions with A.L. Clua de Gonzalez and O. Mendes, Jr. We thank the organizers of the *Eruptive Solar Flares Colloquium* of the 1991 IAU Meeting, Dr. B.V. Jackson and Dr. Z. Svestka, for giving us the opportunity to present this review. This work was partially supported by the *Fundo Nacional de Desenvolvimento Cientifico e Tecnologico* of Brazil and by the *Jet Propulsion Laboratory, California Institute of Technology*, under contract with NASA.

References

Akasofu, S.-I., and S. Chapman, The development of the main phase of magnetic storms, *J. Geophys. Res.*, 68, 125, 1963.

Arnoldy, R.L., Signature in interplanetary medium for substorms, *J. Geophys. Res.*, 76, 5189, 1971.

Baker, D.N., E.W. Hones, Jr., J.B. Payne, and W.C. Feldman, A high-time resolution study of interplanetary parameter correlations with AE, *Geophys. Res. Lett.*, 8, 179, 1981.

Bargatze, L.F., D.N. Baker, and R.L. McPherron, Solar wind-magnetosphere energy input functions, in *Solar Wind Magnetosphere Coupling.* (Edited by Y. Kamide and J.A. Slavin), pp. 101–109, Terra Scientific, Tokyo, Japan, 1986.

Burton, R.K., R.L. McPherron, and C.T. Russell, An empirical relationship between interplanetary conditions and Dst, *J. Geophys. Res.*, 80, 4204, 1975.

Clua de Gonzalez, A.L., W.D. Gonzalez, S.L.G. Dutra, B.T. Tsurutani, Periodic variation in the geomagnetic activity: A study based on the Ap index, *J. Geophys. Res.*, submitted, 1991.

Crooker, N.U., J. Feynman, and J.T. Gosling, On the high correlation between long-term averages of solar wind speed and geomagnetic activity, *J. Geophys. Res.*, 83, 1933, 1977.,

Doyle, M.A., and W.J. Burke, S3-2 measurements of the polar cap potential, *J. Geophys. Res.*, 88, 9125, 1983.

Dungey, J.W., Interplanetary magnetic field and the auroral zones, *Phys. Rev. Lett.*, 6, 47, 1961.

Gold, T., Magnetic storms, *Space Sci. Rev.*, 1, 100, 1962.

Gonzalez, W.D., A unified view of solar wind-magnetosphere coupling functions, *Planet. Space Sci.* 38, 627, 1990.

Gonzalez, W.D., and F.S. Mozer, A quantitative model for the potential resulting from reconnection with an arbitrary interplanetary magnetic field, *J. Geophys. Res.*, 79, 4186, 1974.

Gonzalez, W.D., and A.L.C. Gonzalez, Solar wind energy and electric field transfer to the Earth's magnetosphere via magnetopause reconnection, *Geophys. Res. Lett.*, 8, 265, 1981.

Gonzalez, W.D., and B.T. Tsurutani, Criteria of interplanetary parameters causing intense magnetic storms ($Dst < -100$ nT), *Planet. Space Sci.*, 35, 1101, 1987.

Gonzalez, W.D., B.T. Tsurutani, A.L.C. Gonzalez, E.J. Smith, F. Tang, and S.J. Akasofu, Solar wind-magnetosphere coupling during intense magnetic storms (1978–1979), *J. Geophys. Res.*, 94, 8835, 1989.

Gonzalez, W.D., L.C. Lee, and B.T. Tsurutani, Comment on the polarity of magnetic clouds, *J. Geophys. Res.*, 95, 17267, 1990a.

Gonzalez, W.D., A.L.C. Gonzalez, and B.T. Tsurutani, Dual-Peak solar cycle distribution of intense geomagnetic storms, *Planet. Space Sci.*, 38, 181, 1990b.

Gosling, J.T., D.J. McComas, T.L. Phillips, and S.J. Bame, Geomagnetic activity associated with Earth passage of interplanetary shock disturbances and coronal mass ejections, *J. Geophys. Res.*, 96, 7831, 1991.

Holzer, R.E., and J.A. Slavin, An evaluation of three predictors of geomagnetic activity, *J. Geophys. Res.*, 87, 2558, 1982.

Kan, J.R., and L.C. Lee, Energy coupling functions and solar wind-magnetosphere dynamo, *Geophys. Res. Lett.*, 6, 577, 1979.

Klein, L.W., and L.F. Burlaga, Magnetic clouds at 1AU, *J. Geophys. Res.*, 87, 613, 1982.

Marubashi, K., Structure of the interplanetary magnetic clouds and their solar origins, *Adv. Space Res.*, 6(6), 335, 1986.

McComas, D.J., J.T. Gosling, S.J. Bame, E.J. Smith, and H.V. Cane, A test of magnetic field draping induced B_z perturbations ahead of fast coronal mass ejecta, *J. Geophys. Res.*, 94, 1465, 1989.

Murayama, T., Origin of the semiannual variation of geomagnetic Kp indices, *J. Geophys. Res.*, 79, 297, 1974.

Murayama, T., and K. Hakamada, Effects of solar wind parameters on the development of magnetospheric substorms, *Planet. Space Sci.*, 23, 75, 1975.

Murayama, T., Coupling between solar wind and the Dst index, in Solar Wind-Magnetosphere Coupling Edited by Y. Kamide and J.A. Slavin, pp. 119–126, *Terra Scientific*, Tokyo- Japan, 1986.

Perreault, P. and S.I. Akasofu, A study of geomagnetic storms, *Geophys. J. R. Astron. Sci.*, 54, 547, 1978.

Reiff, P.H., R.W. Spiro, and T.W. Hill, Dependence of polar cap potential drop on interplanetary parameters, *J. Geophys. Res.*, 86, 7639, 1981.

Rostoker, G., L. Lam, and W.D. Hume, Response time of the magnetosphere to the interplanetary electric field, *Can. J. Phys.*, 50, 544, 1972.

Russell, C.T. and R.L. McPherron, Semiannual variation of geomagnetic activity, *J. Geophys. Res.*, 78, 92, 1973.

Sheeley, N.R., Jr., R.A. Howard, M.J. Koomon, D.J. Michels, R. Schwennn, K.H. Muhlauser, and H. Rosenbauer, Coronal mass ejections and interplanetary shocks, *J. Geophys. Res.*, 90, 163, 1985.

Tsurutani, B.T., and C.I. Meng, Interplanetary magnetic field variations and substorm activity, *J. Geophys.* Res., 77, 2964, 1972.

Tsurutani, B.T., C.T. Russell, J.H. King, R.D. Zwickl, and R.P. Lin, A kinky heliospheric current sheet: cause of CDAW 6 substorms, *Geophys. Res. Lett.*, 11, 339, 1984.

Tsurutani, B.T. and R.P. Lin, Acceleration of $>$ 47 KeV ions and $>$ 2 KeV electrons by interplanetary shocks at 1 AU, *J. Geophys. Res.*, 90, 1, 1985.

Tsurutani, B.T. and W.D. Gonzalez, The cause of high-intensity long-duration continuous AE activity (HILDCAAs): interplanetary Alfven wave trains, *Planet. Space Sci.*, 35, 405, 1987.

Tsurutani, B.T., W.D. Gonzalez, F. Tang, S.I. Akasofu, and E.J. Smith, Origin of interplanetary southward magnetic fields responsible for major magnetic storms near solar maximum (1978–1979), *J. Geophys. Res.*, 93, 8519, 1988.

Tsurutani, B.T., T. Gould, B. Goldstein, W.D. Gonzalez, and M. Sugiura, Interplanetary Alfven waves and auroral (substorm) activity IMP-8, *J. Geophys. Res.*, 95, 2241, 1990.

Tsurutani, B.T., W.D. Gonzalez, F. Tang, and Y. Te Lee, Superstorms, *Geophys. Res. Lett.*, in press, 1991.

Vasyliunas, V.H., J.R.Kan, G.L. Siscoe, and S.I. Akasofu, Scaling relations governing magnetosphere energy transfer, *Planet. Space Sci.*, 30, 359, 1982.

Wygant, J.R., R.B. Torbert, and F.S. Mozer, Comparison of S3-3 polar cap potential drops with the interplanetary magnetic field and models of magnetopause reconnection, *J. Geophys. Res.*, 85, 5727, 1983.

Zwan, B.J., and R.A. Wolf, Depletion of solar wind plasma near a planetary boundary, *J. Geophys. Res.*, 81, 1636, 1976.

6.

FLARE STARS

Related poster paper in Chapter 8:

P.J.D. Mauas, A. Falchi, and R. Falciani

STELLAR FLARES: CONFINED OR ERUPTIVE EVENTS ?

R. Pallavicini
Osservatorio Astrofisico di Arcetri
Largo Fermi 5, 50125 Florence, Italy

Abstract. Observations in different spectral bands have shown the existence of many similarities between solar and stellar flares, in spite of the far larger energies that are typically involved in the latter. The analogy may go as far as to include the occurrence on stars of both confined and eruptive flares similar to those observed on the Sun. The observational evidence for the existence of stellar eruptive flares is reviewed and it is shown that the data are still inconclusive in this respect. Models of stellar flares as either confined or eruptive magnetic structures are also discussed and it is concluded that models are unable at present to discriminate between the two cases.

1. Introduction

To talk about stellar flares in a meeting that has specifically been devoted to the study of *eruptive* solar flares might suggest that phenomena of this type are also observed on other stars. This is not the case. It must be emphasized from the very beginning that the observational evidence for the existence of stellar analogues of eruptive flares is only marginal at best. There are a few indications of their possible occurrence, but none of them can be regarded as definitive. However, in spite of the limited observational evidence, there have been some theoretical efforts aiming at modeling stellar flares as either analogues of confined solar flares or as eruptive two-ribbon flares. This is the topic that will be discussed in this paper. Before doing that, however, it may be appropriate to give some general information on stellar flares for those who are not too familiar with the subject. Only afterwards, I will present the (limited) observational evidence we have for the occurrence of eruptive flares on stars, and finally I will discuss the modelling of stellar flares as both confined and eruptive events. The main purpose of this discussion will be to see whether the two cases can be distinguished on the basis of a comparison between observations and theoretical models.

Impulsive flare-like brightenings similar to solar flares have been observed on many different types of stars (Pettersen 1989). These include classical UV Ceti-type flare stars, RS CVn and Algol-type binaries, pre-main sequence stars (both classical T-Tauri and weak-lined T-Tauri stars), and a few other individual objects (e.g. X-ray flares have been reported for the G0 V star π^1 UMa and for the A-type visual binary Castor A+B; Landini *et al.* 1986, Pallavicini *et al.* 1990a). Not all these flares share the same observational characteristics. Those which show the greatest analogy to solar flares are observed from late-K and M dwarfs with Balmer lines in emission (dKe-dMe stars) and, more specifically, from a subclass of them, the so called UV Ceti-type flare stars. As has been discussed in several recent review papers (*e.g.* Haisch and Rodonò 1989, Haisch *et al.* 1991, Pettersen 1991, Pallavicini 1991a,b, and references therein), there are many similarities between solar flares and flares on UV Ceti-type stars, but there are

also significant differences. First and most important, the energy involved may be orders of magnitude larger than in the largest solar flares. If energy is derived from the same mechanisms thought to be responsible for solar flares (*i.e.* dissipation of magnetic energy in stressed non-potential configurations), this implies that much larger volumes or larger magnetic fields, or both, must be involved in stellar flares.

In this paper I will not address the (yet unsolved) question whether the differences observed between solar and stellar flares are due to the different physical environments in which the same basic processes occur, or rather if the basic mechanisms themselves are different in the solar and stellar case. I will simply chose the first alternative, *i.e.* I will work within the framework of the solar analogy. If this is the case, the large energies involved in stellar flares (which may be up to $\approx 10^{35}$ *erg* in a flare on a dMe star, and up to two orders of magnitude more in flares of RS CVn binaries and pre-main sequence objects) require volumes that are much larger than those of typical solar flares, unless magnetic fields as high as $\approx 10^4$ *gauss* or higher exist on stars (cf. Pallavicini 1991b). For the largest flares on RS CVn and Algol-type binaries, and on pre main-sequence objects, it is hard to escape the conclusion that the flare typical sizes must be very large and even comparable to the stellar radius. However, to take this as evidence that stellar flares, at least those with long durations and large energies, must be necessarily of the *eruptive* type (as they are on the Sun) is a conclusion which may not be sufficiently justified, given our ignorance of the basic physical processes responsible for stellar flares.

2. Stellar flares: observational background

Stellar flares, like solar flares, are extremely complex phenomena that involve all atmospheric layers, from the photosphere to the corona, throughout the various phases of the flare process. Coordinated multiwavelength observations are required if we want to grasp the essential physics involved. The need for this was realized long time ago in solar physics, but only recently these observations have become possible also in the stellar case (Kahler *et al.* 1982, Doyle *et al.* 1988, Rodonò *et al.* 1989, Hawley and Pettersen 1991). Until recently, flares on UV Ceti-type stars had been observed almost exclusively in broad-band optical continuum radiation. This is in striking contrast to the case of the Sun, for which the *white-light* flare was until a few years ago a very rare phenomenon observed only during the most intense events (Neidig 1989).

With the development of more sensitive techniques for ground-based observations, and the opening of the space to stellar observations, other diagnostics have become accessible for stellar flares (see reviews by Byrne 1989, Foing 1989, Bastian 1990, Butler 1991, Linsky 1991, Bookbinder 1991, and references therein). These include high resolution spectroscopy of optical lines, ultraviolet line and continuum emission, soft X-rays at energies ≤ 10 *keV*, and radio continuum emission (including the possibility of obtaining radio dynamic spectra). Although this has considerably reduced the gap between solar and stellar observations, and has contributed enormously to our understanding of stellar flares, there are still many other diagnostics that are totally unaccessible in the stellar case. For instance, we do not have any *direct* information on the spatial structure of stellar flares, and we have no measurements of hard X-rays and particle emission. Our knowledge of mass motions in stellar flares is also quite limited, since high spectral resolution has to compete with lack of photons in time-resolved flare observations. These limitations have important consequences for establishing the existence or not of *confined* and *eruptive* flares on other stars.

When observed in optical broad-band emission, a typical flare on a UV Ceti-type star appears as a rather short-lived impulsive brightening of up to several magnitudes (Rodonò *et al.* 1989, Hawley and Pettersen 1991). The duration of the brightening may range from less than a second to a few tens of minutes, and the time profile is often (at least for the longer and more intense flares) rather complex, with multiple peaks occurring in rapid succession (Fig. 1).

This is somewhat similar to what is observed for hard X-ray flares on the Sun. The latter are correlated temporally with white-light solar flares, which occur as rapid brightenings in small localized regions on the Sun. If the same occurs for stars, the continuum optical emission of stellar flares could be used as a proxy for hard X-rays, and hence for obtaining information about the initial energy release and particle acceleration process. Although this assumption is often made and is not contradicted by the observational evidence, it must be taken with some caution since it relies only on the solar analogy and on our present understanding of *solar* flare processes.

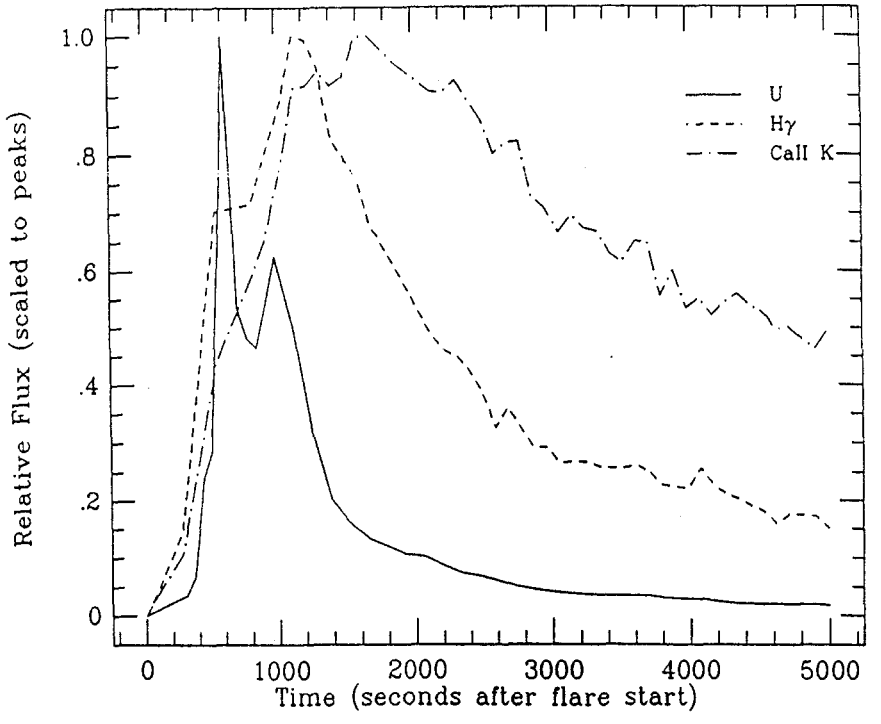

Figure 1. Light curves of a large flare on AD Leo in optical U-band continuum emission, in Hγ and in the Ca II K line. All fluxes have been normalized to their peak value (adapted from Hawley and Pettersen 1991).

Flare optical line emission (in the Hydrogen Balmer lines and the H and K lines of Ca II) show a completely different behaviour, again in analogy with the solar case. Line emission, in fact, is typically more gradual, peaks later and lasts longer than the optical continuum (Fig. 1). This is similar to the behaviour of Hα in relation to white-light emission in solar flares. Ca II emission is further delayed with respect to the Balmer lines. Moreover, the Balmer lines are usually broadened during the impulsive phase of stellar flares, and the broadening decreases rapidly as the continuum emission declines. Ca II lines, on the contrary, show little or no broadening and this suggests that the Balmer lines are largely broadened by the Stark effect, to which the Ca II lines are much less sensitive.

Observations obtained recently by Rodonò *et al.* (1989) show the presence of *negative* stellar flares at 2.2 μ. No similar phenomenon has yet been observed for solar flares, although lack of adequate monitoring at infrared wavelengths may at least partially be responsible for that. Negative stellar flares have occasionally been observed also at optical wavelengths, particularly

in the red I band. There is no simple explanation for this effect. One possibility is that enhanced ionization by non-thermal particles increases H^- opacity (Hénoux *et al.* 1990).

X-ray observations of stellar flares with imaging telescopes on satellites such as *Einstein*, *EXOSAT* and now *ROSAT* have provided much useful information on the high-temperature coronal part of stellar flares (Haisch 1983, Pallavicini *et al.* 1990b, Linsky 1991). Soft X-ray emission in UV Ceti-type flare stars show typically a gradual development, more similar to that of optical line emission than to continuum emission. Temperatures derived from X-ray observations of stellar flares are in the range $(2-4) \times 10^7$ K, similar to typical coronal temperatures of solar flares. The emission measures, however, are often orders of magnitude larger than in solar flares, with typical values ranging from 10^{51} to 10^{53} cm^{-3}. As shown by the extensive observations obtained by *EXOSAT*, the X-ray light curves of flares on UV Ceti-type stars show a remarkable similarity to those of soft X-ray flares on the Sun, and also the temperatures are similar. Thus, only the energies and emission measures involved may be larger in the stellar case.

The X-ray observations allow us to make some further considerations about flares on RS CVn and Algol-type binaries and on pre-main sequence (PMS) stars. While flares on the latter stars have occasionally been observed in optical continuum radiation, as they are for UV Ceti-type stars, it it much more difficult to detect optical continuum flares from RS CVn binaries, since these stars are typically hotter and brighter. As a matter of fact, the only detection of an optical flare from an RS CVn star has been reported at this conference by Foing *et al.* (for the star HR 1099). On the contrary, flares are commonly observed from RS CVn and Algol-type binaries at X-ray, UV and radio wavelengths. The flares seen at X-ray wavelengths are typically much stronger and longer lived than flares on UV Ceti-type stars, and also the coronal temperatures are often higher. This could suggest that flares on RS CVn binaries are fundamentally different from flares on dMe stars and on the Sun (Mullan 1989, Pallavicini and Tagliaferri 1989). Flares with energies of up to 10^{36} *erg* in X-rays (and at least one order of magnitude more over the entire electromagnetic spectrum) have been reported for these stars (cf. Linsky 1991).

Although energetically unimportant, radio emission is another useful diagnostics of the physical conditions in stellar flares. Stellar radio emission is reviewed elsewhere in this volume (see paper by R. Stewart) and therefore will not be discussed here. I simply call attention to the fact that radio emission, at least potentially, can be very important for addressing the question of whether *eruptive* flares exist on stars. The large radio emitting regions detected with VLBI techniques in some RS CVn binaries and PMS objects (Mutel *et al.* 1985, Phillips *et al.* 1991) suggest injections of non-thermal electrons in large magnetic structures. It is not yet clear, however, whether these radio emitting regions are produced by flare-associated global disruptions of the magnetic configuration or rather indicate the existence of an extended magnetosphere (possibly involving interconnecting loops in binary systems) around RS CVn and PMS stars.

3. Do eruptive stellar flares exist ?

The existence of stellar analogues of solar eruptive (2-ribbon) flares has been suggested several times in the literature. In most, probably all cases, these are just suggestions, *i.e.* one of the possible interpretations of the available data. To my knowledge, in no case the observational evidence is so strong as to prove definitely that eruptive stellar flares do exist. However, the data do not contradict such a possibility, and the existence of eruptive stellar flares appear not only as possible but even as likely. In this section, I will summarize the main arguments that have been presented in favor of eruptive flares on stars.

By using a large sample of *EXOSAT* observations of flares on UV Ceti-type stars, Pallavicini *et al.* (1990b) suggested the existence of two classes of stellar flares similar to solar compact

and two-ribbon flares. This suggestion was based only on morphological differences (*i.e.* the duration and intensity of the flare) and on the analogy with similar phenomena observed on the Sun (Pallavicini *et al.* 1977). By the same token, the long-duration flares typically seen in RS CVn and Algol-type systems should all be of the 2-ribbon type (*e.g.* White *et al.* 1986) However, while on the Sun spatially resolved observations show that longer flares usually involve larger structures and the reconnection of a disrupted magnetic configuration, there is no direct proof that the same also occurs for stars. The larger energies do suggest larger structures, but the long time evolution could also be produced by a gradual release of energy in a confined structure, without involving a global disruption of the magnetic configuration.

Haisch *et al.* (1983) went a step further in their analysis of a long duration X-ray flare on Prox Cen observed with *Einstein*. Spectral analysis of time resolved data at different phases throughout the event revealed a temporary increase of the hydrogen column density during a 4 minutes interval immediately following the peak of the event. While the *Einstein* IPC data were consistent with virtually no absorption at all other times ($N_H \approx 10^{18} - 10^{19}\ cm^{-2}$), the hydrogen column density increased to $N_H \approx 10^{20}\ cm^{-2}$ during that short-time interval. This was interpreted as evidence for obscuration of the X-ray flare by a cloud of cool absorbing material as coud be produced by the eruption of a filament at the time of the flare. The long duration of the X-ray event (more than 2 hours) was consistent with this interpretation, assuming again that stellar flares are scaled-up versions of solar flares.

Obscuration by cool prominence material was also suggested by Giampapa *et al.* (1982) as a possible cause of an intensity dip observed in the U band just before a flare on EQ Peg. As mentioned above, *negative* flares are often observed in the red *I* band, but are very rare at shorter wavelengths. Negative flares are more commonly interpreted as due to an increase of H^- opacity as a consequence of increased ionization in the lower atmospheric layers. Thus, although we cannot exclude the interpretation of Giampapa *et al.* for the rare U-band negative flare observed on EQ Peg, other interpretations are also possible.

Houdebine *et al.* (1990) have reported a large blue-shifted component in Hγ observations of a flare on AD Leo. The blue-shifted component lasts only a few minutes in the early flare phases, and the maximum inferred velocities decrease from nearly 6,000 $Km\ s^{-1}$ to less than 4,000 $Km\ s^{-1}$ during a 3 min interval. If interpreted as a prominence eruption or a coronal mass ejection, a mass of $\approx 7.7 \times 10^{17}\ gr$ and a kinetic energy of $\approx 5 \times 10^{34}\ erg$ are derived for this event. These values are both much larger than those typically observed in solar coronal mass ejections. Collier Cameron and Robinson (1989a,b) have provided evidence that corotating clouds of cool Hα material exist in the corona of the PMS star AB Dor. However, it is unclear whether these clouds are associated with transient flare-like events or are more stable prominence-like structures.

Finally, Simon *et al.* (1980) reported the presence of a red-asymmetry in Mg II *h* and *k* line observations obtained with *IUE* during a flare from the RS CVn binary UX Ari. The red asymmetry indicated the presence of material moving at a speed of 475 $Km\ s^{-1}$ away from the observer. A possible interpretation of the data is that reconnection occurred between two different systems of loops, one anchored on the G5 V component of the binary and the other on the K0 IV component. Field line reconnection, and transfer of mass from the K0 subgiant to the G5 dwarf through the reconnection point could explain the observed red asymmetry. Although attractive, the suggested scenario is highly speculative, as admitted by the authors.

4. Modelling of confined stellar flares

Since the observations do not appear to be able to discriminate between compact and eruptive stellar flares (except in a very crude way), we may ask whether theoretical models can allow some further steps forward. A comprehensive flare model that treats all atmospheric levels from

the photosphere to the corona, taking into account all relevant physical processes, does not yet exist (see, however, a first attempt in this direction by Hawley and Fisher 1991). The models that have been developed so far are either for the optical thick lower atmospheric layers (with the purpose of modelling optical flares), or for the optically-thin coronal part (with the purpose of modelling X-ray flares). In this paper, I will not discuss the first class of models (for which I refer to Pallavicini 1991a,b) and I will restrict myself to coronal models. These can be roughly subdivided into two groups: a) hydrodynamic models of magnetically confined structures; b) reconnection models in open to closed magnetic configurations. The first type of models, which is more relevant for *confined* flares, will be discussed in this section; reconnection models, which are more pertinent to *eruptive* flares, will be discussed in the next section.

A first attempt to model stellar X-ray flares as a result of hydrodynamic processes in a magnetically confined coronal structure was made by Reale *et al.* (1988) using the Palermo-Harvard hydrocode (Pallavicini *et al.* 1983, Peres 1989). The flare they chose for modelling is the same long-duration event on Prox Cen that Haisch *et al.* (1983) interpreted as a stellar analogue of a solar two-ribbon flare. The reasons for this apparently odd choice is that the Prox Cen flare was one of the very few sufficiently strong events that were observed by *Einstein* for their entire duration; the others were interrupted by the frequent data gaps due to the low orbit of the *Einstein* satellite. However, Reale *et al.* did not attempt to model the entire flare, but modelled only the central portion around the peak, while neglecting completely the slowly declining tail of the event.

By assuming a circularly symmetric loop of length L, and a localized heating at the top of the loop, they tried to reproduce the observed light curve of the flare in the *Einstein* IPC band. The heating was assumed to be constant thoughout the flare rise phase and to stop abruptly after 700 *sec.* The loop length was treated as a free parameter, searching for the value that gives the best fit to the flare light curve. Since they limited the number of possible free parameters by chosing a particular form of the heating function, the decay of the flare is determined almost uniquely by the loop length, longer loops producing more gradual decays. The best fit is obtained with a loop with $L = 1.4 \times 10^{10}$ *cm.* When compared to the Sun, this is a much longer loop than for typical confined solar flares. Note that the radius of Prox Cen is only $0.14 R_{\odot}$ and the inferred length of the flaring loop is in fact comparable to the stellar radius. By contrast, most *confined* flares on the Sun have loop lengths of the order of $\approx 0.1 R_{\odot}$ or less.

Does the large loop inferred by Reale *et al.* (1988) indicate that stellar flares, even of relatively small intensity (the flare on Prox Cen had a total X-ray energy of only 2×10^{31} *erg* and an emission measure of $\approx 1 \times 10^{51}$ cm^{-3}) require much larger structures, relative to the stellar radius, than confined solar flares ? And secondly, is the good agreement found between observations and model (at least for the first part of the decay phase) sufficient proof that the flare on Prox Cen was indeed compact and with no appreciable energy deposition during the decay ?

In order to answer some of these questions, Cheng and Pallavicini (1991) have carried out extensive modelling of flares on dMe stars using the NRL hydrocode that solves numerically the full set of mass, energy and momentum equations for a two-fluid plasma (Cheng *et al.* 1983). Rather than trying to fit a particularly well observed event, they have built a grid of different models by changing loop length, preflare conditions, flare heating rate, and spatial and temporal dependence of the heating function. By exploring the parameter space, it is thus possible to get better insights into the flare process, and to test how sensitive the models are to the assumed input parameters.

The basic hydrodynamic results are similar to those obtained by applying the same codes to the solar case (Pallavicini *et al.* 1983; Cheng *et al.* 1983, 1985; Peres *et al.* 1987). The major difference is due to the higher gravity and smaller pressure scale height of dMe stars (which have typically surface gravities 2 to 4 times larger than the Sun). If energy is deposited at the loop apex, a high temperature region forms there. Energy is rapidly conducted down toward the

loop footpoints and the transition region between the chromosphere and the corona steepens and moves downwards. If the energy conducted to the chromosphere is larger than can be radiated away, a high pressure region forms at the top of the chromosphere. The heated chromospheric material expands upwards at velocities of several hundred $Km\ s^{-1}$ filling the coronal portion of the loop (*chromospheric evaporation*), while at the same time the high pressure region acts like a piston compressing the underlying chromospheric material. The compressed region that forms at the loop footpoints could in principle be responsible for the optical flare and even for white-light flares (as has been suggested for the Sun by Cheng *et al.* 1983 and for dMe stars by Livshits *et al.* 1981). However, because of the larger gravity and smaller pressure scale height of dMe stars, the compression region encounters a very steep density gradient that limits the amplitude and time duration of the compressed region. It seems unlikely therefore that this compressed region can contribute significantly to the optical flare in dMe stars.

The subsequent evolution of the flare during the decay phase depends critically on whether energy is deposited during the decay phase or not. If the heating is switched off abruptly, the plasma cools rapidly and a thermal instability occurs which leads to rapid condensation of the coronal plasma to temperatures of $\approx 10^5 K$ and to large downflows. The final state is entirely different from the initial one. On the contrary, if energy deposition is continued during the decay phase (*e.g.* by means of a slowly decaying heating function) the plasma gradually cools down to the preflare conditions, and no catastrophic instability occurs. In any case, the way energy is deposited during the flare (both the heating rate and the heating time dependence) is fundamental for determining the time profile and physical parameters (temperature, density, bulk velocity) of the flare. Conclusions based on a prescribed form of the heating rate cannot be claimed to be unique.

As shown by Cheng and Pallavicini (1991), X-ray light curves predicted by their code are in good agreement with typical light curves observed by *EXOSAT* for flares on dMe stars. For the longest X-ray flares observed by *EXOSAT*, practical limits on computer time have prevented so far to check whether these flares can be reproduced by means of confined flare models. Extrapolations based on the grid of models of Cheng and Pallavicini, as well as the results of Reale *et al.* (1988) for Prox Cen, suggest that this should be possible through a suitable choice of the loop length and the heating function. Thus, it seems difficult to determine the nature (either confined or eruptive) of a stellar flare by simply matching observed and predicted X-ray light curves.

The results of Cheng and Pallavicini (1991) are summarized in Fig. 2 which shows a comparison of predicted and observed emission measures and total X-ray energies for flares observed by *EXOSAT* and for 4 of the 10 different models run by them. Models 3 and 9 are both for a small loop with $L = 2 \times 10^9\ cm$, but the total energy released in model 9 is one order of magnitude larger than in model 3. Models 5 and 8, instead, are for a large loop (with $L = 8 \times 10^9\ cm$), and again differ one from the other by one order of magnitude in the energy input. The energy deposited in models 9 and 5 is about the same, but the two models differ in the loop length. As can be seen from the figure, small X-ray flares with energies of the order of $\approx 10^{31}\ erg$ and emission measures of the order of $\approx 10^{51}\ cm^{-3}$ (similar to the Prox Cen flare discussed above) can be reproduced by a small loop (model 3), without the need of the large loop, comparable to the stellar radius, required by Reale *et al.* Only very large flares (with X-ray energies of the order of $\approx 10^{34}\ erg$ and emission measure of $\approx 10^{53}\ cm^{-3}$) require large loops (model 8), unless unrealistically high magnetic fields are invoked to provide for both energy release and confinement. Intermediate size flares (with energies of the order of $\approx 10^{32}\ erg$ and emission measures of $\approx 10^{52}\ cm^{-3}$ can be reproduced equally well with both a small loop (model 9) and a large loop (model 5). Without other constraints it is not possible to choose between the two cases by simply fitting the observed X-ray light curve.

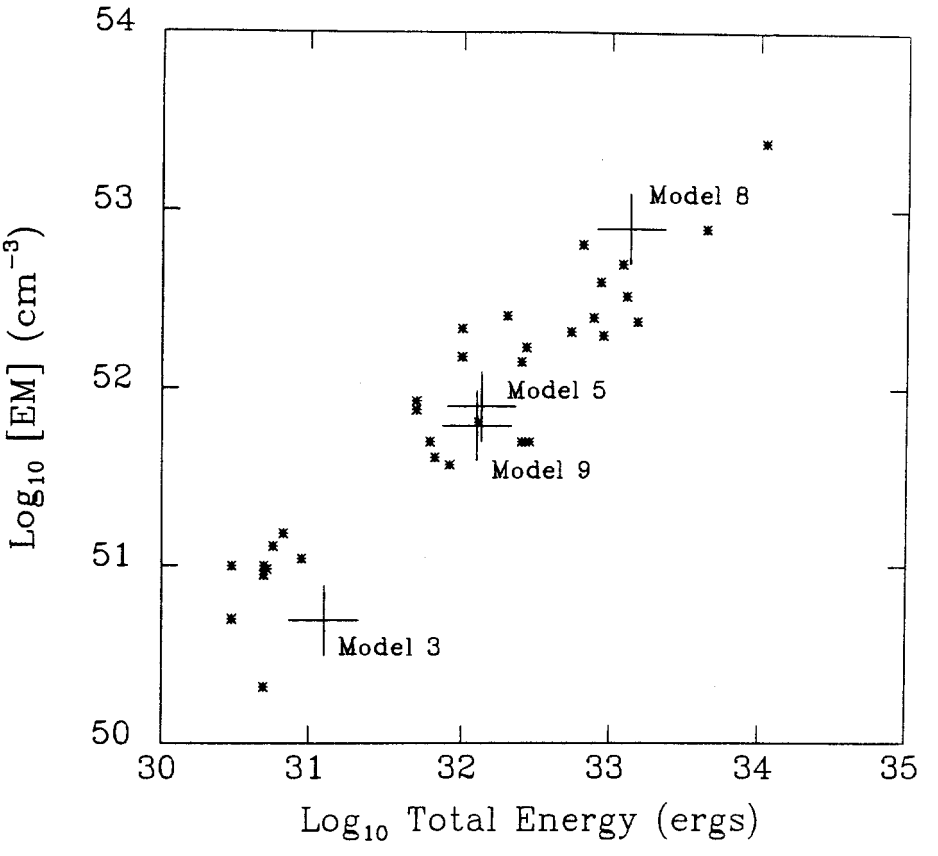

Figure 2. Comparison of observed and computed emission measures and total energies for X-ray flares on dMe stars. The observational data are from *EXOSAT*, the computed data are the results of hydrodynamic simulations of confined flares (from Cheng and Pallavicini 1991).

5. Modelling of eruptive stellar flares

If the identification of long-duration X-ray events with stellar analogues of solar erupting flares is correct (Pallavicini *et al.* 1990b), the modelling of such events by means of magnetically confined closed structures (as has been done by Reale *et al.* 1988 for the flare on Prox Cen and by Hawley and Fisher 1991 for a long-duration flare on AD Leo) may not be correct. Rather, models that involve reconnection in open to closed magnetic configurations should be more appropriate, as believed to be the case for solar two-ribbon flares (Kopp and Pneuman 1976, Kopp and Poletto 1984).

In the classical Kopp and Pneuman model of solar two-ribbon flares, a magnetic configuration is disrupted by an unspecified mechanism: the open field lines, under the action of an unbalanced Lorentz force, relax back to a closed lower-energy configuration and energy is released gradually by magnetic reconnection as the fields lines reconnect at progressively higher altitudes during the flare decay. Application of this model to stellar conditions has been made by Poletto *et al.* (1988) and Poletto (1989) for long-duration flares on dMe stars and by van den Oord and Mewe (1989) for a large flare on Algol. Here, I will follow the analytical formulation

of Poletto *et al.* (1988) which is useful to illustrate the main points (see also Pallavicini *et al.* 1988).

The assumed magnetic field configuration is two-dimensional with a radial (non-potential) magnetic field at heights $h > R_1$ (where R_1 is the height of the reconnection point) and a potential field at heights $h \leq R_1$. The latter is expressed in terms of a single lobe of a Legendre polynomial of degree n, i.e. $P_n(\theta)$ where θ is the colatitude. The degree n is a measure of the extent in latitude of the flare region, larger values of n corresponding to smaller regions. To simulate the formation of loops at increasing heights during the flare decay, the reconnection point R_1 is set to progressively higher altitudes, thus modelling a time-dependent process. The rate at which magnetic energy is released as reconnection leads from the initially open to a closed (potential) configuration is given by:

$$\frac{dE}{dt} = A(n,\theta_o)\ R_\star^3\ B_m^2\ \frac{y^{2n}[y^{(2n+1)}-1]}{[n+(n+1)y^{(2n+1)}]^3}\ \frac{dy}{dt} \tag{1}$$

where $R_\star$ is the radius of the star and $A(n,\theta_o)$ is a function which depends on the degree n of the Legendre polynomial and on the central heliographic colatitude θ_o of the region. B_m is the maximum field strength at photospheric level in the flare region, y is the height of the reconnection point expressed in terms of the stellar radius and dy/dt is its upward velocity. As suggested by the solar case, this can be expressed as

$$y(t) = \frac{R_1}{R_\star} = 1 + (\frac{h_m}{R_\star})[1 - \exp(-t/t_o)] \tag{2}$$

where h_m is the maximum height reached by the reconnection point during its upward movement and t_o is the time constant of the process. For simplicity, it is assumed that the flare region is centered at the equator, that its longitudinal extent is ≈ 1.5 times its extent in latitude (as suggested by solar flares), and that h_m is comparable to the latitudinal extent.

Poletto *et al.* (1988) and Poletto (1989) showed that eq. (1) was capable of reproducing the observed X-ray light curve of a long duration flare on EQ Peg, as well as of the flare from Prox Cen that we have repeatedly mentioned above. However, they also showed that the model is unable to uniquely determine the physical parameters of the flaring region (size, magnetic field, density). The basic problem is well illustrated in Fig. 3 where we plot, as a function of time, the energy release rate given by Eq. (1) (normalized to the stellar radius and to the maximum photospheric field B_m), for various values of the degree n and the time constant t_o.

As shown by Fig. 3, the shape of the curve of the energy release rate vs. time depends almost exclusively on the parameter t_o, i.e. on the time constant of the upward movement of the reconnection point, which is an unknown quantity in the stellar case. On the contrary, the absolute values of the energy release rate depends on both the degree n (i.e. on the size of the region) and the photospheric magnetic field B_m. As expected, the energy released will be higher for larger regions and/or higher magnetic fields. Thus, while fitting an observed X-ray light curve with Eq. (1) allows the time constant t_o to be uniquely determined, in no way we can disentangle the flare size and the magnetic field strength. In order to do so, additional constraints are required, such as an independent estimate of the field strength in the flare region or a determination of the flare coronal density from the ratio of density sensitive lines. Neither measurement is feasible at the present time. Thus, while the model is consistent with the interpretation of long duration flares as analogues of eruptive solar flares, this is by no means a proof that open magnetic structures and reconnection are involved in long duration stellar flares. Moreover, the inability of the model to uniquely determine the flare parameters greatly reduces its usefulness in interpreting stellar flare data.

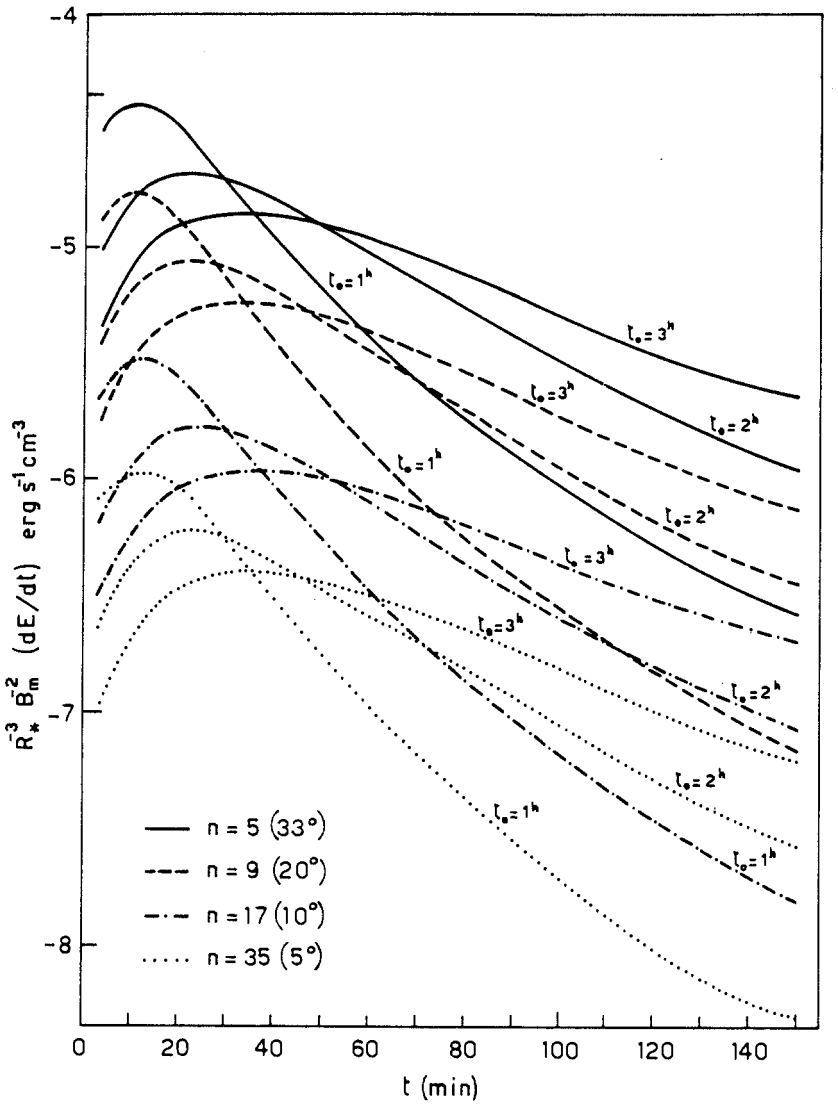

Figure 3. Magnetic energy release *vs.* time predicted by the reconnection model of eruptive stellar flares (Eq. 1). The different curves refer to different sizes of the flare region and to different upward velocities of the reconnection point (as given by Eq. 2). The energy release has been scaled to the stellar radius and to the maximum photospheric magnetic field in the region (from Poletto, Pallavicini and Kopp 1988).

6. Conclusion

In this paper, we have seen that the observational evidence for the existence of eruptive stellar flares, similar to solar 2-ribbon flares, is only marginal at present. There are several lines of evidence that suggest their possible occurrence, but none can be considered as definite. We have also seen that models are unable to distinguish between confined and eruptive flares, because:

a) different classes of models can reproduce the same data (as shown by the flare on Prox Cen); b) for any given class of models, the solution is not unique (given the large number of free parameters than enter the models). If any progress has to be made in this area, there is urgent need of better observational constraints. In particular, observations of flare mass motions at X-ray and optical wavelengths, with high sensitivity and spectral resolution, would be invaluable to address the question whether eruptive flares do exist on stars.

References

Bastian, T.S.: 1990, *Solar Phys.* **130**, 265.

Bookbinder, J.A.: 1991, in *Stellar Flares* (B.R. Pettersen ed.), *Memorie Soc. Astron. It.* **62**, in press.

Butler, C.J.: 1991, in *Stellar Flares* (B.R. Pettersen ed.), *Memorie Soc. Astron. It.* **62**, in press.

Byrne, P.B.: 1989, *Solar Phys.* **121**, 61.

Cheng, C.-C., Karpen, J.T., and Doschek, G.A.: 1985, *Astrophys. J.*, **286**, 787.

Cheng, C.-C., Oran, E.S., Doschek, G.A., Boris, J.P., and Mariska, J.T.: 1983, *Astrophys. J.* **265**, 1090.

Cheng, C.-C., and Pallavicini, R.: 1991, *Astrophys. J.* **381**, 234.

Collier Cameron, A., and Robinson, R.D.: 1989a, *Montly Not. Roy. Astron. Soc.* **236**, 57.

Collier Cameron, A., and Robinson, R.D.: 1989b, *Montly Not. Roy. Astron. Soc.* **238**, 657.

Doyle, J.G., Butler, C.J., Byrne, P.B., and van den Oord, G.H.J.: 1988, *Astrophys. J.* **193**, 229.

Foing, B.H.: 1989, *Solar Phys.* **121**, 117.

Giampapa, M.S., Africano, J.L., Klimke, A., Parks, J., Quigley, R.J., Robinson, R.D., and Worden, S.P.: 1982, *Astrophys. J. Letters* **252**, L39.

Haisch, B.M.: 1983, in *Activity in Red-dwarf Stars* (P.B. Byrne and M. Rodonò eds.), Dordrecht: Reidel, p. 255.

Haisch, B.M., Linsky, J.L., Bornmann, P.L., Stencel, R.E., Antiochos, S.K., Golub, L., and Vaiana, G.S.: 1983, *Astrophys. J.* **267**, 280.

Haisch, B.M., and Rodonò, M. (eds.): 1989, *Solar and Stellar Flares*, Dordrecht: Kluwer.

Haisch, B.M., Strong, K.T., and Rodonò, M.: 1991, *Ann. Rev. Astron. Astrophys.* **29**, in press.

Hawley, S.L., and Fisher, G.H.: 1991, *Astrophys. J.*, in press.

Hawley, S.L., and Pettersen, B.R.: 1991, *Astrophys. J.* **378**, 725.

Hénoux, J.-C., Aboudarham, J., Brown, J.C., van den Oord, G.H.J., van Driel-Gesztelyi, L., and Gerlei, O.: 1990, *Astron. Astrophys.* **233**, 577.

Houdebine, E.R., Foing, B.H., and Rodonò, M.: 1990, *Astron. Astrophys.* **238**, 249.

Kahler, SD., and other 30 authors: 1982, *Astrophys. J.* **252**, 239.

Kopp, R.A., and Pneuman, G.W.: 1976, *Solar Phys.*, **50**, 85.

Kopp, R.A., and Poletto, G.: 1984, *Solar Phys.* **93**, 351.

Landini, M., Monsignori-Fossi, B.C., Pallavicini, R., and Piro, L.: 1986, *Astron. Astrophys.* **157**, 217.

Linsky, J.L.: 1991, in *Stellar Flares* (B.R. Pettersen ed.), *Memorie Soc. Astron. It.* **62**, in press.

Livshits, M.A., Badalyan, O.G., Kosovichev, A.G., and Katsova, M.M.: 1981, *Solar Phys.* **73**, 269.

Mullan, D.J.: 1989, *Solar Phys.* **121**, 239.

Mutel, R.L., Lestrade, J.F., Preston, R.A., and Phillips, R.B.: 1985, *Astrophys. J.* **254**, 641.

Neidig, D.F.: 1989, *Solar Phys.* **121**, 261.

Pallavicini, R.: 1991a, in *Basic Plasma Processes on the Sun* (E. Priest and V. Krishan eds.), Dordrecht: Kluwer, p. 77.

Pallavicini, R.: 1991b, in *The Sun: A Laboratory for Astrophysics* (J.C. Brown and J. Schmeltz eds.), Dordrecht: Kluwer, in press.

Pallavicini, R., Peres, G., Serio, S., Vaiana, G.S., Acton, L., Leibacher, J., and Rosner, R.: 1983, *Astrophys. J.* **270**, 270.

Pallavicini, R., Poletto, G., and Kopp, R.A.: 1988, in *Activity in Cool Star Envelopes* (O. Havnes *et al.* eds.), Dordrecht: Kluwer , p. 171.

Pallavicini, R., Serio, S., and Vaiana, G.S.: 1977, *Astrophys. J.* **216**, 108.

Pallavicini, R., and Tagliaferri, G.: 1989, in *Solar and and Stellar Flares - Poster Papers* (B.M. Haisch and M. Rodonò eds.), Catania: Astrophysical Observatory, p. 17.

Pallavicini, R., Tagliaferri, G., Pollock, A.M.T., Schmitt, J.H.M.M., and Rosso, C.: 1990a, *Astron. Astrophys.* **227**, 483.

Pallavicini, R., Tagliaferri, G., and Stella, L.: 1990b, *Astron. Astrophys.* **228**, 403.

Peres, G.: 1989, *Solar Phys.* **121**, 289.

Peres, G., Reale, F., Serio, S., and Pallavicini, R.: 1987, *Astrophys. J.* **312**, 895.

Pettersen. B.R.: 1989, *Solar Phys.* **121**, 299.

Pettersen, B.R. (ed.): 1991, *Stellar Flares*, Florence: Società Astronomica Italiana, in press.

Poletto, G.: 1989, *Solar Phys.* **121**, 313.

Poletto, G., Pallavicini, R., and Kopp, R.A.: 1988, *Astron. Astrophys.* **201**, 93.

Phillips, R.B., Lonsdale, C.J., and Feigelson, E.D.: 1991, *Astrophys. J.*, in press.

Reale, F., Peres, G., Serio, S., Rosner, R., and Schmitt, J.H.M.M.: 1988, *Astrophys. J.* **328**, 256.

Rodonò, M.: 1989, in *Solar and Stellar Flares - Poster Papers* (B.M. Haisch and M. Rodonò eds.), Catania: Astrophysical Observatory, p. 53.

Simon, T., Linsky, J.L., and Schiffer, F.H.III: 1980, *Astrophys. J.* **239**, 911.

van den Oord, G.H.J., and Mewe, R.: 1989, *Astron. Astrophys.* **213**, 245.

White, N.E., Culhane, J.L., Parmar, A.N., Kellet, B.J., Kahn, S., van den Oord, G.H.J., and Kuijpers, J.: 1986, *Astrophys. J.* **301**, 262.

Radio Flare Emission from Late-Type Stars

R.T. Stewart

Australia Telescope National Facility, CSIRO, PO Box 76, Epping, NSW 2121, Australia

Abstract: A brief review is presented of recent progress in understanding the nature of several varieties of radio flare emission from late-type stars.

Introduction

A number of comprehensive reviews on stellar radio emission have appeared over the past few years (see Dulk 1985, Kuijpers 1989 and Bastian 1990). In this short review, I will restrict discussion to radio flares from late-type stars only. Such stars include G and K subgiants in RSCVn and Algol binaries, single (possibly FK Coma) K subgiants and giants, PMS G and K dwarfs and DMe flare stars. All of these flare stars are characterised by rapid rotation plus active chromospheres and coronae.

Observational Limitations

It is important to realise the severe limitations imposed on observations of stellar radio flares by their large distances. For example, the most intense solar bursts recorded at centimetre wavelengths have luminosities of about 5×10^{12} (erg s^{-1} Hz^{-1}). If placed at the distance of the nearest star such bursts would not be detected by the most sensitive radio telescopes. Indeed, the only reason we detect radio flares from other stars is because they are extremely luminous. (It is somewhat paradoxical that the strongest radio star in the sky produces the least energetic flares.) Radio flares from rapidly rotating dwarf and giant stars have luminosities up to 10^4 and 10^6 times solar flares (Fig 1). Another point worth remembering is that most stellar radio observations are restricted to small fractional bandwidths and to microwave frequencies. Consequently, we do not see anything like the variety

and complexity of solar bursts (see Bastian 1990 for examples of complex decimetre dynamic spectra from dMe flare stars).

Again, because of the scarcity of stellar radio observations, a number of authors have, in my opinion, mistaken slowly varying enhanced radiation from dMe flare stars for "quiescent emission", despite the fact that this weak radiation is not always present and that it has been observed to vary by factors of 20 or more (see White *et al.* 1989 for examples). This is not simply a question of semantics. It is important not to confuse flare-related bursts with persistent emission caused by quasi-continuous acceleration of electrons. I think it likely that most examples of quiescent radio emission observed to date from late-type stars are caused by low-level flaring. Sometimes the flares may be eruptive and of long duration, as in the slowly varying burst from EQ Peg A which followed the largest X-ray flare yet observed from a dMe star (Kundu *et al.* 1988).

(a) Energetic Flares

The predominant type of radio-flare emission observed at centimetre wavelengths from RSCVn and Algol binaries and from PMS dwarfs (such as AB Dor) and FK Coma giants (such as HD32918 and FK Coma Berenices), is found to be gyro-synchrotron radiation from mildly relativistic electrons (which are accelerated during flares and trapped in strong magnetic fields low in the stellar corona). Near the flare maximum the radio source is optically thick (due to self-absorption by the energetic electrons) and the spectrum shows a remarkable similarity to that of an intense solar microwave burst (Stewart *et al.* 1988). Below the turnover frequency the spectral index α (defined as $S \propto \nu^{\alpha}$ is between 0.7 and 1.2, rather than the 2.5 expected from an optically thick uniform synchrotron source. This characteristic property of intense solar and stellar flare bursts can be explained by a magnetic dipole model (Nelson and Stewart 1979) containing mildly relativistic electrons emitting gyro-synchrotron radiation from optically thick shells which increase in size with decreasing frequency. (The shells where the optical depth is unity are very thin, arising from the rapid decrease of emissivity and absorption with height.)

The dipole model has been applied to stellar microwave flares by Stewart *et al.* (1988) to explain a relationship between peak radio-flare luminosity L and rotation (Fig.1). It predicts that the scale size of the magnetic (dipole) field ($B \leq 3000G$) on late-type stars increases with equatorial surface velocity v.

From Eq.(16) of Stewart *et al.*

$$R_{\star}(v)/R_{\circ} \propto v^{1\pm0.2} \tag{1}$$

where $R_{\star}$, $R_{\circ}$ are stellar and solar radii.

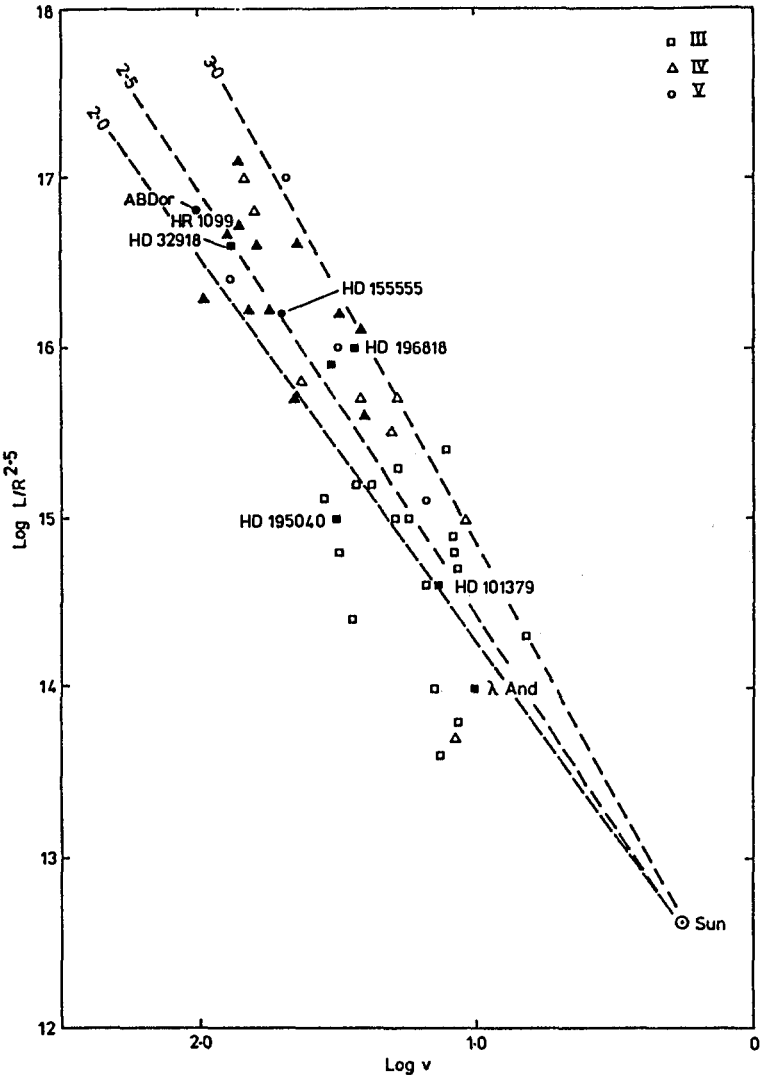

Fig. 1. Plot of 8.4 GHz peak luminosity scaled by $(R_\star/R_\odot)^{2.5}$ versus the equatorial surface velocity v for 51 late-type stars. Figures on the dashed lines indicate slopes.

This prediction can be tested on several well-known stars. For the active RsCVn binary HR1099 where v= 75 km s^{-1} we expect from Eq.(1) that

$$0.2 \leq R_\star/R_\odot \leq 0.8 \qquad (2)$$

a value consistent with VLBI measurements at 8 GHz of the angular size of an intense flare from HR1099, where the estimated source size was about 75% of the diameter of the K subgiant (Lestrade *et al.* 1984). For the single PMS K star AB Dor, Slee *et al.* (1986) and Lim (1991) estimated a source

size of the order of half the diameter of the star from an apparent$\approx$ 50% rotational modulation effect during periods of flaring. Substituting v= 100 km s^{-1} into Eq.(1) gives

$$0.2 \leq R_{\star}/R_{\circ} \leq 1.0 \qquad (3)$$

Marcy and Bruning (1984) argue that the absence of Zeeman broadening of the spectral lines from Λ Andromeda gives an upper limit of 8% for the filling factor for a strong magnetic field (B= 2000 G). Substituting v= 10 km s^{-1} into Eq.(1) gives $R_{\star}/R_{\circ}$ ranging from 4% to 8%, consistent with the upper limit of Marcy and Bruning.

Note that the Stewart *et al.* model does not require the electron energies nor the surface magnetic induction to increase with stellar rotation. The model only requires the total energy (number of energetic electrons) for flares from late-type stars to increase in proportion to the volume of the magnetic trap. This raises problems for flare theories which already have difficulties explaining the rate and efficiency of acceleration of solar flare particles (see Melrose, these proceedings).

(b) Slowly Varying Events

The dipole model has been extended recently by White *et al.* (1989) to include optically thick and thin gyro-synchrotron radiation from a non-uniform distribution of source electrons. For reasonable parameters for dMe flare stars the spectral index α can flatten or even become negative (when the source is completely optically thin). One might expect an optically thin source to arise during times of low-level flaring when a continuous supply of energetic electrons can escape outwards along magnetic field lines to higher and higher levels in the corona, where the magnetic induction is lower and the source region becomes more extended. This scenario may apply to the halo sources observed in RSCVn binaries by VLBI. Here the source size may be several stellar radii in extent, comparable with heights expected for closed magnetic field lines in helmet streamers (see Morris *et al.* 1990). The large-scale magnetic fields where the electrons are trapped can to a first approximation, be considered as a global dipole where the optically thin source will become moderately circularly polarized. Low-level polarised emission is often observed from RSCVn binaries with the sense of circular polarisation reversing between 1.4 and 5 GHz (Mutel *et al.* 1987).

For some dMe stars there is evidence also that low-level enhanced radiation is due to optically thin gyro-synchrotron emission. One such example is AT Mic. Observations (from Large *et al.* 1989) are reproduced in Fig.2 and show a slowly varying emission with a negative spectral index ($\alpha \leq -1.0$) between 0.84 and 1.5 GHz.

From Eq.(8) of White *et al.* (1989) for optically thin gyro-synchrotron emission

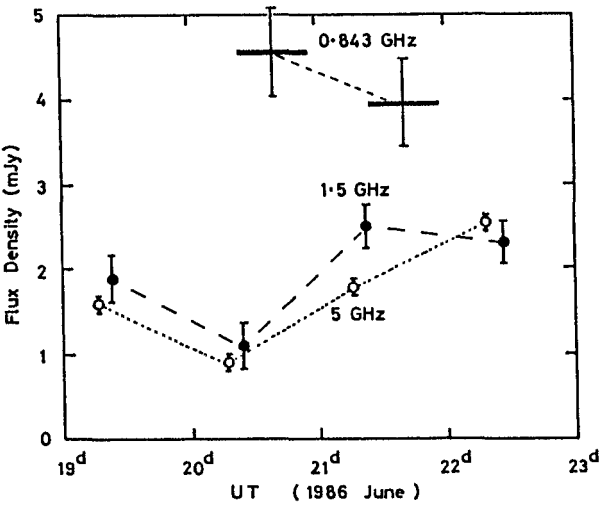

Fig. 2. Flux densities of AT Mic measured in 1986 June. The vertical bars represent 1σ uncertainties. The 12-hour duration of the Molonglo synthesis telescope (MOST) measurement is indicated by the horizontal bars. The VLA 30-minute observations at 1.5 and 5 GHz are plotted with a slight horizontal separation for clarity.

$$S(\mathrm{mJy}) = 10^{1.62-0.17\delta}[\mathrm{m} + \mathrm{n}(-0.2 + 0.9\delta) - 3]^{-1} \mathrm{N_5 B_3^{-0.2+0.9\delta} r_9^3 d_{pc}^{-2}} \quad (4)$$

Assuming a power law distribution of electrons, the observed spectral index corresponds to an energy spectral index $\delta = 3$. For a uniform (m = 0) density distribution ($N_5 = 10^5$ cm^{-1}), a surface field B = 1000 G, and a distance d= 8.2 pc, Eq.(4) gives a flux density S = 4 mJy at 1 GHz for a dipole scale size of $r_9 = 10^{10}$ cm, corresponding to a source size of $\approx$ 1.0 stellar radii. VLBI measurements at 1.667 GHz of a radio flare from YZ CMi (Benz and Alef 1991) show it to be 80% circularly polarized and associated with a source size of 1.7 stellar diameters. This may be another example of optically thin gyro-synchrotron emission.

(c) Coherent Bursts

The gyro-synchrotron bursts described above are characterised by being broadband, showing a moderate degree of circular polarization, and having a spectral index $\alpha \leq 1$. There is another type of emission at microwaves which is highly polarized, narrowband, and often impulsive. It occurs from both dMe stars and RSCVn binaries but is more common from the former. Light-travel-time arguments indicate that the burst brightness temperatures are too high for incoherent emission. The most likely coherent

emission processes produce radiation at once or twice the electron cyclotron frequency or at twice the upper hybrid frequency, although there are other ways of generating coherent emission in a plasma (see Kuijpers 1989 for details). If the emission does occur at twice the cyclotron frequency then the frequencies at which these bursts are observed, usually between 1 GHz and 5 GHz, give a measure of the maximum magnetic induction in the source region B $\approx$ 1000 G.

Summary

Stellar radio flares show many resemblances to solar flares but are much more energetic. Both incoherent and coherent emission processes occur but the most useful for modelling the stellar atmospheres at present are the intense gyro-synchrotron bursts. A relationship between radio-flare luminosity and rotation indicates that the strong magnetic field regions on the stellar photosphere, which extend into the stellar corona where the radio emission occurs increase in size with rotational velocity. Equipment sensitivity restricts our detailed knowledge of stellar flares to a level comparable to that of solar flares about 20 years ago.

Bastian, T.S. (1990): Solar Phys. **130**, 265.
Benz, A.G., Alef, W. (1991): Astron. Astrophys. in press.
Dulk, G.A. (1985): Ann. Rev. Astron. Astrophys. **23**, 169.
Kuijpers, J. (1989): Solar Phys. **121**, 163.
Kundu, M.R., Pallavicini, R., White, S.M., Jackson, P.D. (1988): Astron. Astrophys. **195**, 159.
Large, M.I., Beasley, A.J., Stewart, R.T., Vaughan, A.E. (1989): Proc. Astron. Soc. Aust. **8**, 123.
Lestrade, J.F., Mutel, R.L., Phillips. R.B., Webber, J.C., Niell, A.E., Preston, R.A. (1984): Astrophys. J. Lett. **282**, L23.
Lim, J. (1991): PhD Thesis, Macquarie University, Australia.
Marcy, G.W., Bruning, D.H. (1984): Astrophys. J. **281**, 286.
Melrose, D.B. These proceedings.
Morris, D.H., Mutel, R.L., Su.B. (1990): Astrophys. J. **362**, 299.
Mutel, R.L., Morris, D.H., Doiron, D.J., Lestrade,J.F. (1987): Astron. J. **93**, 1220.
Nelson, G.J., Stewart, R.T. (1979): Proc. Astron. Soc. Aust. **3**, 392.
Slee, O.B., Nelson, G.J., Innis, J.L., Stewart, R.T.,Vaughan, A.E., Wright, A.E. (1986): Proc. Astron. Soc. Aust. **6**, 312.
Stewart, R.T., Innis, J.L., Slee, O.B., Nelson, G.J., Wright, A.E. (1988): Astron. J. **96**, 371.
White, S.M., Kundu, M.R., Jackson, P.D. (1989): Astron. Astrophys. **225**, 112.

7.

FUTURE PROJECTS

No related poster papers in Chapter 8.

THE SOLAR-A MISSION EXPERIMENTS AND THE TARGETS

(Short Summary of the Talk)

Yutaka UCHIDA[1] and Yoshiaki OGAWARA[2]

[1]Department of Astronomy, University of Tokyo
[2]Institute of Space and Astronautical Science

1. Introduction

This paper is a short summary of the talk presented at the conference. Additional information can be found in reviews given elsewhere by the authors (Uchida and Ogawara, 1991, Ogawara et al., 1991). Because data from the successfully launched satellite are becoming available at the time of writing, we present this summary for record and reference.

2. The Solar-A Mission

The Solar-A project* is a Japanese high energy solar physics project operated by ISAS (= Institute of Space and Astronautical Science, with collaborations of the National Astronomical Observatory [NAO], University of Tokyo [UT], Kyoto University [KU], Nagoya University [NU], Rikkyo University [RU], etc..) with international collaboration of US scientists supported by NASA (Lockheed Palo Alto Research Laboratory [LPARL], Stanford University [SU], University of California at Berkeley [UCB], and University of Hawaii [UH]), and UK scientists supported by SERC (Mullard Space Science Laboratory of University of London [MSSL], and related institutes). Overviews about the satellite and its payload can be found in Ogawara et al. (1991).

The experiments on board Solar-A consist of (i) HXT, a Fourier synthesis hard X-ray imager (constructed by UT-NAO-ISAS) producing hard X-ray images with high time resolution, (ii) SXT, a soft X-ray telescope with a grazing incidence hyperboloid-hyperboloid mirror combined with a CCD detector, (constructed by LPARL-UT-NAO-ISAS) having much better temporal and spatial resolution, higher sensitivity, and reduced scattering, as compared with the Skylab soft X-ray telescope, (iii) BCS, a high sensitivity Bragg crystal spectrometer (constructed by MSSL(RAL,NRL,NIST)-NAO) covering resonance lines of S XV, Ca XIX, Fe XXV, and Fe XXVI, and (iv) WBS, a

* The satellite was successfully launched on August 30, 1991 from the Kagoshima Space Center, and renamed Yohkoh according to the ISAS system for the successfully launched satellite. "Solar-A" in the following should read as "Yohkoh" wherever it appears.

wide-band spectrometer (constructed by RU-ISAS-NAO) covering the spectral range from soft X-rays to gamma-rays. HXT and SXT are co-aligned, and have a built-in white light telescope sensing their positions. More detailed descriptions of each experiment and the parameters such as spatial and temporal resolutions etc. can be found in the *Solar-A Special Issue*, part of *Solar Physics* **136**, 1 - 110 (Nov. 1991).

3. Scientific Objectives and Merits of Solar-A

The scientific objective of the Solar-A mission is to investigate solar high energy phenomena with this *coordinated* set of instruments by providing greatly improved sensitivity, and spatial and temporal resolution, as compared with their predecessors. HXT will help in solving various problems related to the rapid, impulsive phase of solar flares, which have never before been imaged with such high resolution (spatial, as well as temporal). Also, the high spatial and temporal resolution of SXT will be valuable in determining the morphology of flares and their development over time. The wide dynamic range due to the low scattering mirror, together with the high sensitivity CCD and fast rotating shutter-filter system controlled by the on-board CPU, will be essential in observing a wide range of objects, from dark pre-flare loop structures to the brightest parts in strong flares. Since the most likely flare mechanism is thought to be related to the magnetic field, the knowledge about the pre-flare loop shapes and their change with time, which represent the configuration of the magnetic field and its changes, will be vital in pursuing the origin of flares.

The information about the temperature, as well as of the velocity, derived from the spectrometers of BCS will contribute to deciding the physical state and motion of the flaring plasma. Although BCS is spatially non-resolving, the presence of time correlations between BCS and SXT brightenings may allow us to identify the BCS sources and obtain information about the mass supply to the flaring regions. Temperature information, together with morphological information, can also be obtained from SXT, using different filter-shutter combinations. On the other hand, information about accelerated particles, both electrons and ions, derived from the spectral information provided by WBS, support the imaging observations of HXT.

The white light aspect telescope, which is co-aligned with the hard- and soft X-ray telescopes, will solve the difficulties encountered in the past in the accurate inter-alignment of the X-ray images and images of ground-based observations. This is especially important for the hard X-ray images in which previously no landmarks other than the flares could be seen. This will dramatically increase the reliability of the physical interpretations based on these hard- and soft X-ray images.

4. Targets of Observations of Solar-A

Targets for the soft X-ray observations with SXT and BCS are the regions heated to very high temperatures. For the hard X-ray observations with HXT and WBS these are locations where high energy particles are emitting bremsstrahlung in their interaction with ions.

Hot plasma and high energy particles are produced, probably much more easily than has been thought, in violent dynamical processes in magnetic fields. Dissipation of

large amounts of energy in the rarefied plasma in the corona or transition zone on a short time scale will produce a region of very high temperature when the cooling time scale is much longer than the time scale of energy liberation. A violent disturbance in the magnetic field seems to inevitably produce high energy particles. Thus, several different categories of processes producing X-ray flares are possible. However, if X-ray emitting, high temperature regions are present in the corona, the footpoints of these regions will be heated and optical flares will result in more or less similar ways, constrained by the properties of the magnetic field (e.g. in the two footpoints of a loop structure).

The targets of interest may be:

(A) Development of Active Regions:

(a) Possible differences in the X-ray loop configurations above "young and active", small spot groups and "established", large spot groups may be revealed. It is possible that the former are brighter and show more twists, indicating the presence of stronger electric currents flowing along the magnetic field lines.

(b) What happens to the active region X-ray loops when two active regions come together and form a δ-type spot group which is intrinsically flare active? Do current-sheet type "barriers" form, preventing smooth reconnections on separatrix surfaces, and do these "barriers" disappear, allowing reconnection, when a flare occurs?

(c) How are the mass and energy supplied to the active region loops? There is a possibility that weaker versions of loop flares discussed by Uchida and Shibata (1988) may be taking place in active region loops. The so-called active region loops may not be stationary, but may be an ensemble of loops appearing and disappearing, giving a similar outlook of the region statistically.

(B) Flare Related Phenomena:

(a) What happens immediately before the flare starts? This is of special interest since the pre-flare coronal loop structures will be visible by SXT, and since the X-ray loops represent magnetic connections which should change if, for example, magnetic reconnections occur.

(b) When and where are the mass and energy injected into the flare loops? Does not the dynamical process, seen as high temperature, large blue-shifted components in Ca and Fe lines, that occurs in some cases before the impulsive phase, represent the mass injection process into the flaring loops (Uchida and Shibata, 1988)?

(c) Do simple loop flares and large arcade flares have a mechanism in common, or are they different? Since it seems that a large arcade flare starts from similar brightenings separated by the field reversal line, a large arcade flare is thought to consist of many loop flares. It seems, however, that a single loop flare does not show the same opening up-closing down process of the flux tube, as is supposed to happen in an arcade flare (Švestka and Schadee, 1983)

(d) When and where does electron acceleration occur? Although the location of the particle dumping will be seen clearly by HXT, a more careful approach is necessary to pinpoint the acceleration region of particles. A thin-target source prior to the dumping of the accelerated particles should be sought and traced. It is more difficult spatially

and temporally to pin down where the ions are accelerated. Time-coincidence of the brightening of a certain point in the image with the enhancement in the WBS gamma-ray spectra may enable us to make a statement about this, though not firmly.

(e) Detection of white light flares: the time-lapse subtraction of the pictures taken by the white light aspect telescope will improve the detectability of white light flares.

(f) Detection of flare ejecta corresponding to sprays in Hα, flare blasts (MHD shock waves) corresponding to type II burst shocks and Moreton waves, and plasmoids corresponding to the moving type IV radio bursts, may be possible using SXT and HXT, intentionally looking at the dark background corona while a flare is in progress.

(C) Dynamical Phenomena Not Necessarily Related to Flares

(a) A search for the X-ray counterpart of Brueckner's jets in EUV, or surges in Hα can be made by SXT.

(b) The X-ray counterpart of disappearances of quiescent filaments, related to low energy two ribbon flares in Hα, will be observable with SXT. Whether or not these filament disappearances actually open up the above-lying magnetic fields and reclose them causing low energy two-ribbon flares should be examined.

(c) Coronal mass ejections will be one of the most attractive targets of SXT. SXT will be able to see the early launching phase of this mass ejecting process, and can tell whether the start of this is really earlier than the start of the related flare as Harrison (1986) claimed, or, to the contrary, starts from high up in the corona at a later time.

(D) Solar Cycle-Associated Activities

(a) X-ray bright points and their solar-cycle variations will form topics which are interesting from the point of view of magnetic behavior of the sun as a whole.

(b) Observation of the whole-sun X-ray images over a long period will give us very important information about the overall solar activity.

(E) Quiet Sun Features

(a) Formation and evolution of quiet coronal loops may be studied by a long exposure, global image of SXT. The quiet coronal loops must also show formation and decay, and we should be able to pin these processes down.

(b) Coronal holes are so-to-speak the "negative picture" of the quiet coronal region, and therefore, the behavior of the coronal holes can be studied as long as the faint coronal loops are seen as expected.

(c) Five-minute oscillations of the sun, and possibly, the variation of the solar irradiance, will be observable by the white light aspect telescope. However, continuous data sequences of the entire surface are not guaranteed because the priority of the Yohkoh observations is given to flares and other X-ray emitting sources.

5. Schemes of Collaboration of the Solar-A Team with the Outside Scientists

We regard the Yohkoh collaboration with other ground-based observatories very vital, and would like to add some relevant information about our scheme of collaboration with outside scientists.

Data: To do justice to the hard-working team members, the rights for the preferential use of the data are given to the team members for the first two years after the launch, and 6 months thereafter for the newly acquired data. Then, the data is open to the solar research community through NSSDC. Collaborative research, either through coordinated observations or on a personal basis with the members, is encouraged as described below.

Team Organization: A Steering Committee, called the Solar-A Science Committee decides important matters concerning this Japan-US-UK trilateral project.(Contact address: Yohkoh Science Committee, Institute for Space and Astronautical Science, Sagamihara, Kanagawa, 129 Japan. Chairman of the Committee: Y.Uchida, [yuchida@solar.stanford.edu]).

Collaboration with Outside Scientists: Coordinated observations with ground-based observatories can be arranged by contacting the above Committee well ahead of time, after January, 1992. Collaboration on a personal basis is also acceptable with a report to the above Committee from the research counterpart inside the Team. NASA plans a Guest Investigator program starting two years after the launch.

Newsletters: The Solar-A Team plans to publish a Newsletter providing the solar research community with some information like the list of flares Yohkoh observed, the predicted time of Yohkoh observation in the next week, etc. This Newsletter will be posted on an Email Bulletin Board set up at a workstation in ISAS. Details will be announced through Solarmail as soon as circumstance allows.

References

Harrison, R.A., 1986, *Astron. Astrophys.*, **162**, 283.

Ogawara,Y., Takano,T., Kato,T., Kosugi,T., Tsuneta,S., Watanabe,T., Kondo,I., and Uchida,Y., 1991, *Solar Phys. Special Issue*, in press.

Švestka,Z., and Schadee,A.,1983, *Solar Phys.*, **86**, 267.

Uchida,Y., and Ogawara,Y., 1991, in *Physics of Solar Flares*, eds. L.Culhane and C.Jordan, (Publ. Royal Soc.), in press.

Uchida,Y., and Shibata,K.,1988, *Solar Phys.*, **116**, 291.

Nobeyama Radioheliograph

Shinzo Enome

Nobeyama Radio Observatory Minamisaku, Nagano, 384-13 Japan

Abstract: A new dedicated radioheliograph, or a tee-shaped interferometer, is under construction at Nobeyama by the solar radio astronomy group during fiscal years 1990 and 1991. It will be used to obtain images of active region magnetic fields during solar flares by observing microwave radiation through the mechanism of gyro-synchrotron emission. The observation frequency is 17 GHz, the spatial and time resolutions are 10 arcsec and 50 msec, respectively. It is scheduled to be completed by March 1992, the end of the fiscal year 1991 and to go into full-scale routine observations in the summer of 1992. The major performance characteristics, the current status of construction and expected programs of observations are briefly described.

1 Objectives

The primary objective of the Nobeyama Radioheliograph will be the observation of the magnetic field geometry of flaring regions on the Sun, allowing the identification of different configurations (such as single loop or multi-loop geometries), the location of the acceleration site (near the loop top or loop footpoint), and determination of the coincidence or displacement of microwave sources with respect to X-ray sources or H-alpha kernels. Observations of the birth and evolution of active regions, another objective to be pursued by the Nobeyama Radioheliograph, will give us new insight into energy build-up and pre-flare activities. The Nobeyama Radioheliograph will further make it possible to discriminate low-contrast or faint structures on the solar disk such as dark filaments, bright points, coronal holes, and other large-scale structures. It is essential that all these observations are conducted by a dedicated machine to achieve unprecedented uniform sampling of every form of solar activity with high spatial and temporal resolutions of 10 arcsec and 50 msec, respectively.

2 Requirements, Design and Performance

In order to realize the above objectives, requirements for the new instrument, which will determine the performance of the total system, have been formulated, constrained by technical feasibility and design goals. Since these issues have been discussed elsewhere (Enome, 1991) in some detail, we will restrict ourself to brief descriptions here.

The requirements are summarized as follows:

1) The Nobeyama Radioheliograph is a dedicated instrument for solar observations. Since the Sun is the best-known variable star, it is imperative to continuously monitor its variabilities and activities with an instrument devoted specifically to this purpose.

2) The Nobeyama Radioheliograph is to have full-Sun field of view, is an important performance element for a dedicated instrument.

3) The frequency of observations is selected to be 17 GHz. This is based on 15 years of experience at Nobeyama, which guarantees us a satisfactory noise environment and spectral characteristics of solar bursts in the optically thin domain at this frequency for most cases (Kosugi et al., 1988). In order to obtain spectral information and high spatial resolution for bursts, simultaneous observations at 34 GHz are prepared using a frequency-selective surface for the subreflectors. This technique has been shown feasible very recently by our group and is now ready for installation. (Irimajiri and Takano, 1991).

4) The new instrument should achieve the best possible performance, within various limitations, with respect to space-time resolution, position accuracy, image quality and polarization capability. It is also extremely important to have the radioheliograph system equipped with a high-speed computer system, which will enable us to obtain well-processed radio images of Sun within a reasonable time after the observations are made, i.e., in quasi-real-time.

The major characteristics of the Nobeyama Radioheliograph are summarized below.

Array Configuration: A Tee-Shaped Array
Observing Frequency: 17 GHz (and 34 GHz in preparation)
Bandwidth: 40 MHz
Antenna Diameter: 80 cm
Number of Antennas: 84
Fundamental Antenna Spacing: 1.528 m
Maximum Baseline Lengths: 488.96 m (EW) and 220.03 m (NS)
Field of View: 40 arcmin
Spatial Resolution: 10 arcsec
Image Quality: 100:1 (Snap Shot) 1000:1 (Synth. Mode)
Sensitivity: 10 msfu (Snap Shot)
Observation Time: 6 hours/day

Overall Phase Stability: 5 degree/6 hours

A brief remark should be made about the phase stability of the interferometer. Element antennas are arranged in a configuration of a superposition of multiple grating arrays of harmonic spacings with ample redundancies. This enables us to deduce complex phase errors of individual antennas using a self-calibration technique applied to regular solar observations (Nakajima et al., 1980). To achieve the desired results, we must pay careful attention to phase stability of the system in the front end receivers and in the transmission lines.

3 Current Status and Schedule

Currently (October, 1991), we are in the final stage of the second fiscal year. The overall schedule of construction of the system follows the time table planned initially. The observation building will be completed shortly, followed by the installation of the intermediate frequency receivers, the back end receivers or digital correlator sub-system, and in early December the computer sub-system, which will be tuned as individual sub-systems by the end of December, 1991. Adjustment of the total system will start in early January, 1992, in order to obtain correlation outputs within a period of three months. If the number of correlations is large enough, it will be possible to obtain a radio image of the Sun, or at least, a quasi-image of the Sun by the end of March, 1992.

4 Observation Programs

Several months of preparations of the software system are required to ensure full-scale routine observations after we obtain correlation outputs. It is planned, therefore, to start cooperative observations in August with the solar observation satellite Yohkoh (or SOLAR-A), which will give us an enormous amount of high quality data for solar flares and active regions.

Joint and open use of the Nobeyama Radioheliograph or its data sets is being considered with domestic and foreign members of the solar physics community.

5 Concluding Remarks

About one year ago, or in November last year, we held a Nobeyama symposium on the Radioheliograph to introduce the design, performance and plan for the system and a schedule to bring together sixty participants among which we intend to invite more than a dozen scientists from abroad. We are now planning to propose a second Nobeyama symposium to convene in the autumn of 1993, just before or after the General Assembly of URSI to be held in Kyoto, Japan.

References

Enome, S., 1991, Nobeyama Radioheliograph, Solar Physics, "Special Issue on SOLAR-A Science Meeting in October, 1990", in press.

Irimajiri, Y. and Takano, T., 1991, Frequency Selective Surfaces for Radio Astronomy, Experimental Astronomy, in press.

Kosugi, T., Dennis, B.R., and Kai, K., 1988, Energetic Electrons in Impulsive and Extended Solar Flares as Deduced from Flux Correlations between Hard X-Rays and Microwaves, Astrophys. J., 324, 1118-1131.

Nakajima, H., Sekiguchi, H., Aiba, S., Shiomi, Y., Kuwabara, T., Sawa, M., Hirabayashi, H., Kosuch, t., and Kai, K., 1980, A New 17 GHz Solar Radio Interferometer at Nobeyama, Publ. Astron. Soc. Japan, 32, 639-650.

Decimeter High Resolution Solar Radio Spectroscope

H.S. Sawant, J.R.A. Sobral, J.A.C.F. Neri, F.C.R. Fernandes,
R.R. Rosa, J.R. Cecatto and D. Martinazzo
Instituto Nacional de Pesquisas Espaciais - INPE, Divisão de Astrofísica
São José dos Campos, SP, Brasil

High sensitivity (8 - 0.8 s.f.u.), high time (100 msec), frequency (300 - 3000) KHz resolution decimeter spectroscope operating at present in the frequency range of (1600 $\pm$ 50) MHz has been put into operation in São José dos Campos at the National Space Research Institute, Brazil. Finally, this spectroscope will be operated over a frequency range of (200 - 2500) MHz. However, in high resolution mode, it will be operating over a frequency range of ($f_s \pm \Delta f$), (Δf will be selected in the range of (50 - 500) MHz or as desirable), where f_s is the frequency selected in the entire range of band. At the same time, the entire frequency band will be monitored with low resolution mode. Initial observations of this spectroscope at (1600 $\pm$ 50) MHz, the details of spectroscope and future development plans (up to 1992) are presented.

Introduction:

The Space Science Division of INPE has initiated a programme of the development programme of a Decimetric (200 - 2500) MHz Spectroscope to operate in high time frequency resolution mode using a 9 meter diameter parabolic polar-mounted antenna in São José dos Campos, Brazil (Sawant and Rosa, 1990). To our knowledge, the only digital spectroscope covering wide frequency range (100 - 3000) MHz is operating at present in the northern hemishpere with high time frequency resolution (Benz et al, 1991 and references therein). The spectroscope described here will have higher sensitivity and digital coverage for about fifty frequencies in the selected band of frequencies for observations.

Instrumentation:

Fig 1 shows the schematic diagram of the present operating system. The antenna was mounted in late 1990. In the month of Dec. 1990 and Jan. 1991 the antenna was tested for its electrical characteristics in a solar transient mode in various elevations using the Sun itself as a radio source.

Fig 2a shows the observed half power beam width in horizontal polarization, at 1.6 GHz, which is of the order of 1.5°, which is little more than expected (1.25°). This is because of the finite size of the Sun. This leads to the estimation of the antenna gain of about 42 db. Fig 2b shows the first solar bursts observed by this telescope immediately after the solar transient on 11th Jan., 1991 and this was associated with type II, III GG, RS radio bursts (SGD number 559, Part I, 1991).

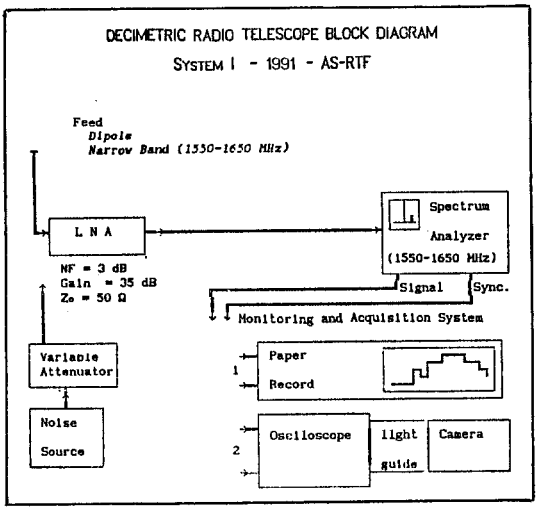

Figura 1

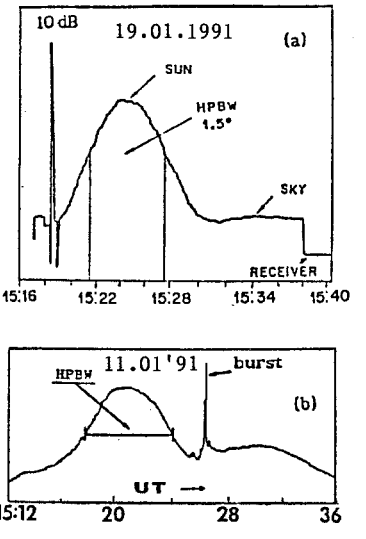

Figura 2

Fig 1. Block diagram of the high time and frequency resolution spectroscope operating in the band of (1650 $\pm$ 50) MHz.

Fig 2a. Half power beam width of a 9 meter diameter antenna at 1.6 GHz. 2b. First solar burst observed at 1.6 GHz with this radiometer immediately after solar transient.

Noise figure of the amplifier is 3 db. Gain of the total system is 120 db and dynamic range is of the order of 30 db. Table I shows the minimum detectable flux for various combinations of time and frequency resolutions. So far we have observed with this system for about 300 hours. Real observed interference in this frequency range lasted only a total of 15 minutes at satellite frequencies around 1.6 GHz. Various types of bursts showing frequency and time structures to the limit of our resolutions have been observed and are under detailed investigations. Fig 3 shows the dynamic spectra of the solar activity observed on 29th May, 1991 and associated patrol record. Some of these bursts have shown high frequency drift rates.

Table I

		Sensitivity (s.f.u.)					
Band of Observation (MHz)	± 50	~ 50.6	~ 16.8	~ 5.0	~ 1.6	100	Time Resolution (msec)
		~ 35.8	~ 11.8	~ 3.6	~ 1.2	200	
Freq. Resolution (KHz)		100	300	1000	3000		

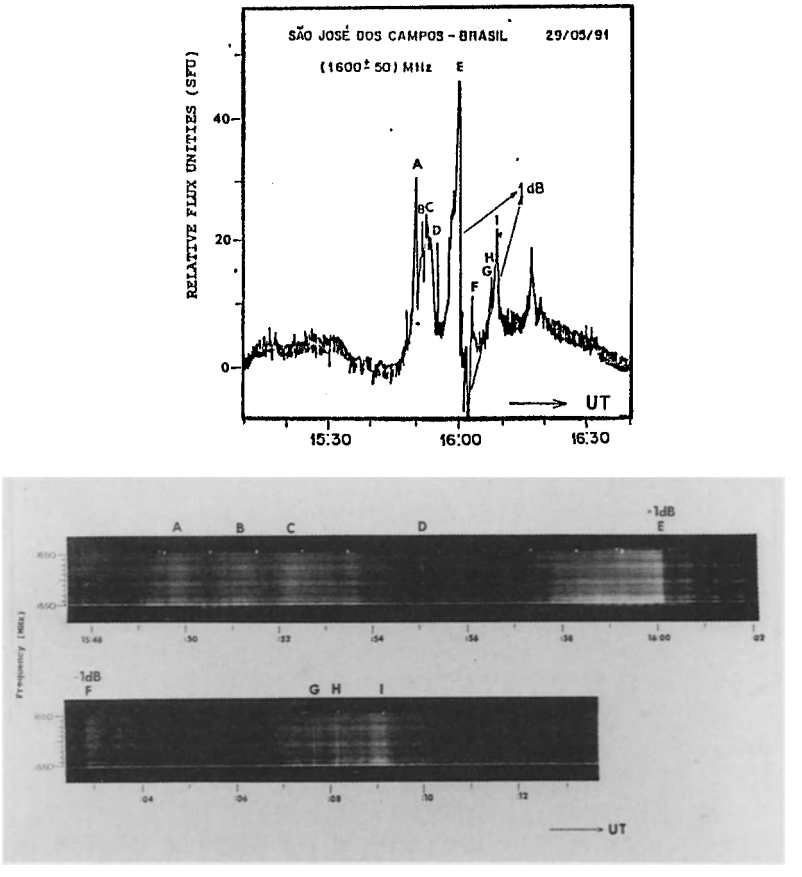

Fig 3a. Dynamic spectra of solar bursts observed on May 29th, 1991. The bursts indicated by letters D and G, each lasting 2 sec, show positive drift rates. The bursts indicated by letters A, B, C, E, F, H and I are of longer duration, 5 sec. Between the points marked E and F, the attenuation was 1 db mode.

Future Plans:

Fig 4 shows the block diagram of the system that will be put into operation in 1992. It will be operating over a band of (50 - 500) MHz with time resolution of (25 - 100) msec and frequency resolution of (1000 - 3000) KHz, at any selected center frequency, preferably above 1000 MHz, almost simultaneously in right and left hand circular polarization. Recording will be done on the film and at least 50 frequencies will be digitized, since structures in frequency of less than 10 MHz are rarely observed above 1000 MHz (Benz, personal communication). Finally, two systems will be put into operation, one operating over entire band with conventional patrol mode resolutions and another with a high resolution mode system as described in this report.

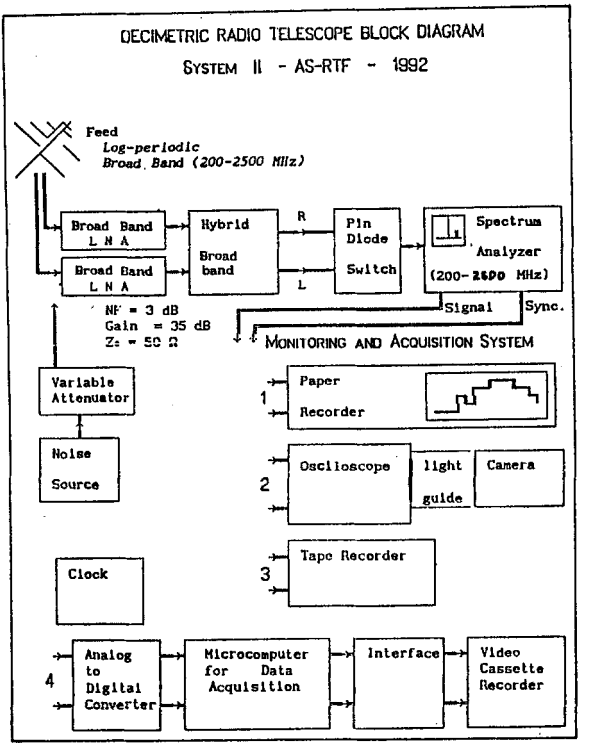

Fig 4. Block diagram of the high time resolution spectroscope and polarimeter that will be put into operation in 1992.

References:

Benz, A.O.; Güdel, M.; Isliker, H.; Miszkowiez, S. and Stehling, W. "A Broadband Spectrometer for Decimetric and Microwave Radio Bursts First Results", submitted to Solar Physics, 1991.

Sawant, H.S.; Rosa, R.R. "High sensitivity, high frequency and high time resolution decimetric spectroscope". Revista Mexicana de Astronomia y Astrofisica, vol. 21, pg. 651, 1990.

Sawant, H.S.; Sobral, J.H.A.; Neri, J.A.C.F.; Fernandes, F.C.R.; Rosa, R.R.; Cecatto, J.R.; Martinazzo, D. "High Sensitivity, High Frequency and High Time Resolution Decimeter Solar Radio Spectroscope. Published in the proceedings of the 43rd. Annual Metting of SBPC, UFRJ, pg. 689, R.Janeiro, July 14 - 19 , 1991.

Solar Geophysical Data, number 559, Part I, pg. 124, March 1991.

Considerations of a Solar Mass Ejection Imager in a Low-Earth Orbit

B.V. Jackson [1], D.F. Webb [2], R.C. Altrock [3] and R. Gold [4]

[1]Center for Astrophysics and Space Sciences,
University of California at San Diego, La Jolla, CA 92093, USA
[2]Institute for Space Research, Boston College,
Newton Center, MA 02159 USA
[3]Phillips Laboratory/PHS, National Solar Observatory/Sacramento Peak,
NOAO, Sunspot, NM 88349 USA
[4]Johns Hopkins University, Applied Physics Laboratory,
Johns Hopkins Road, Laurel MD 20707 USA

Abstract: We are designing an imager capable of observing the Thomson scattering signal from transient, diffuse features in the heliosphere[1]. The imager is expected to trace these features, which include coronal mass ejections, co-rotating structures and shock waves, to elongations greater than 90° from the Sun from a spacecraft in an ≈800 km Earth orbit. The predecessor of this instrument was the zodiacal-light photometer experiment on the HELIOS spacecraft which demonstrated the capability of remotely imaging transient heliospheric structures [2]. The HELIOS photometers have shown it possible to image mass ejections, co-rotating structures and the density enhancements behind shock waves. The second-generation imager we are designing, would have far higher spatial resolution enabling us to make a more complete description of these features from the Sun to 1 AU. In addition, an imager at Earth could allow up to three days warning of the arrival of a solar mass ejection.

1 Signal Levels and Number of Photons

Because the signal levels present from the features to be measured are small compared to the solar brightness, the Solar Mass Ejection Imager (SMEI) must be designed carefully to eliminate unwanted stray light and other sources of unwanted brightness. Table 1 estimates the signal levels expected for various phenomena at 1 AU. The brightnesses of coronal mass ejections (CMEs) and streamers were derived from features traced outward from the Naval Research Laboratory (NRL) SOLWIND coronagraph to the HELIOS photometer field. For CME brightnesses the assumption is that the CME in question moves outward from ~0.3 to 1 AU at constant velocity and without dispersion. Shock brightnesses were estimated from the *in situ* plasma density enhancements behind shocks observed from the HELIOS spacecraft [3] and assumed to be viewed at 60° and

90° from the Sun-spacecraft line. A more complete description of these calculations is given in [4]. Signal levels in the following table are given in terms of "S10 units" which are equivalent to the flux of one tenth magnitude star per square degree.

TABLE 1 Signal Levels Expected at 1 AU

Feature	Elongation (degrees)	Signal Intensity (S10)	Signal Duration (days)
Bright CME	60	3	1.5
	90	2	1.5
Bright streamer	60	2	1
	90	1	1
Bright shock	90	1-2	0.5
Major unidentified in-situ fluctuation	60	3	2
	90	2	2
Comet shock	20	3-10	0.1

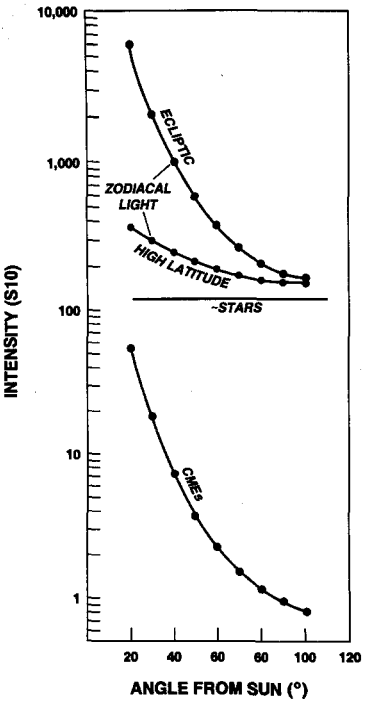

Fig. 1. The brightness of various signals that will be observed by the imager versus elongation at 1 AU.

The Thomson-scattered coronal light must be detected in the presence of background diffuse light from many sources: scattered light from bright sources such as the Sun, Moon, or Earth; the zodiacal light and Gegenschein; and the stars, either individually as bright point sources or collectively as a contribution to the diffuse sky brightness. Figure 1 is a plot of estimates of the brightness contributions from these signals to be observed from an Earth-orbiting SMEI at different angular distances (elongations) from the Sun.

The ultimate limit of diffuse-light sensitivity should be set by photon counting statistics; this limit depends upon the optics and scanning configuration, spectral bandpass, and total detector efficiency. The total detected photon count N can be approximated as in [5] by

$$\log N = 6.65 - 0.4 m_V + 2 log D + log(\Delta t) \quad (1)$$

where m_V is the equivalent stellar visual magnitude, D the aperture (diameter) in cm, and Δt the integration time in seconds. The background sky brightness varies roughly over the range 100-6000 S10 units between the darkest sky and the ecliptic plane at solar elongations $\geq 20°$. If we presume that $D = 1.43$ cm (the size of a one-half inch square

aperture as in a design for the WIND spacecraft [6]) and $\Delta t = 1$ s, then from equation (1) we obtain 920 photons available per given 1° square degree brightness of 1.0 S10 unit ($m_V = 10$). Detector bandpasses and instrument quantum efficiencies further limit the number of photons which can be detected.

In general, the signal-to-noise ratio of the instrument will be limited by integration times, viewed area of sky, and the size of the aperture. If the spacecraft gathers only a tiny fraction of the necessary counts to detect a signal in the darker areas of sky on a single pass, then we conclude that we must count photons with our detectors. The WIND imager design intended to use photon-counting image intensifiers to do this. The limit of the signal to noise for a stable photon-counting instrument is purely statistical; how many detected photons are necessary to measure the signal above the far brighter zodiacal light background. If longer times are spent on any given section of sky, such as with a slowly rotating low-Earth orbiter, then many signal photons can be present in each pixel. It then becomes possible to use a CCD detector that integrates the incoming photons to build up a sufficient signal above a statistical noise readout level as well as detect the signal above the zodiacal-light background.

2 The Preferred Spacecraft and Orbital Configuration

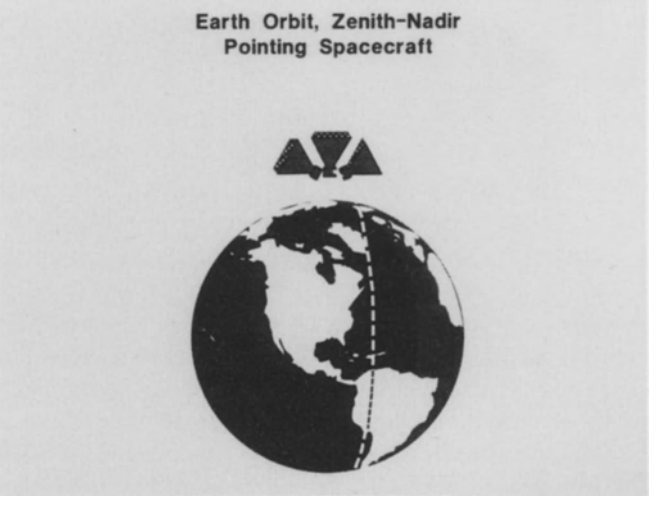

Fig. 2. Orbit of a typical Sun-synchronous satellite (9am – 9pm). The spacecraft orbit is circular at ≈800 km above the surface of the Earth and maintains its relation with respect to the Sun-Earth line.

Although the Solar Mass Ejection Imager instrument could be designed for successful operation on nearly any spacecraft, one of the simplest and most effective configurations would be on a near-Earth orbiting zenith-nadir pointing spacecraft. From such an orbit, the brightest objects to be eliminated from the instrument view are 1) the Sun, 2) the Earth, and 3) the Moon. From low-Earth orbit the Earth can be nearly as bright as the Sun and covers nearly 180° of the sky. Figure 2 gives a schematic of the SMEI

instrumentation in a typical polar Sun-synchronous orbit. Although the most simple orbit for the imager would be a terminator orbit (a 6am – 6pm one), we depict a 9am – 9pm orbit, more typical of DMSP-type orbits. Figure 3 gives one layout of the proposed instrumentation for the mass ejection imager front end to be operated in an ≈800 km orbit.

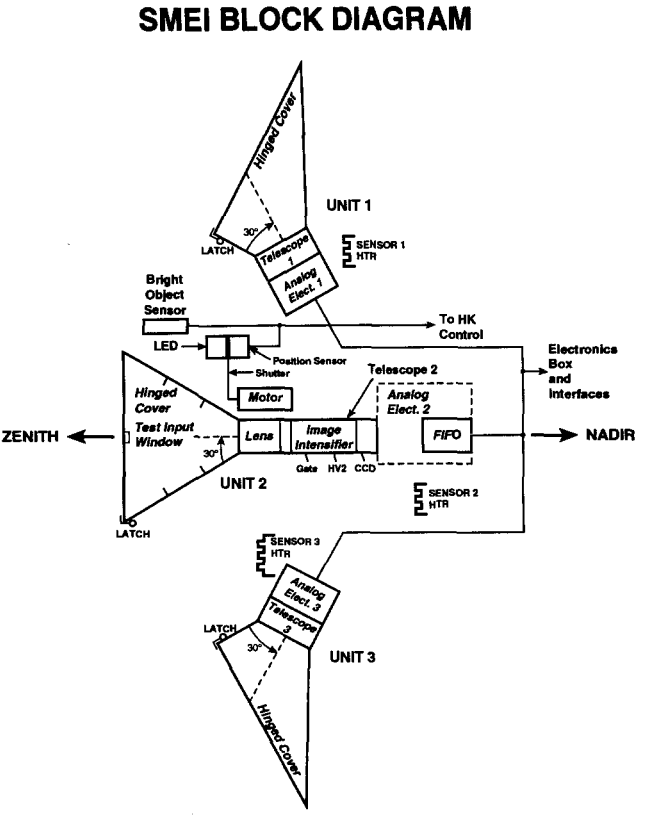

Fig. 3. Schematic of the proposed spacecraft Solar Mass Ejection Imager front end; baffles, optics and electronics.

3 Background Signals from Zodiacal Light, Stars and Other Sources of Low-Level Light

Low-level sources of light from the cosmos such as zodiacal light and the Milky Way are generally brighter than the variable Thomson scattering signal we wish to detect. We must be able to subtract these signals from the background, or at least keep them constant from orbit to orbit. The zodiacal light appears to be unchanging and smoothly varying from the HELIOS deep-space orbit to levels near the lower levels of brightness

to be viewed by the imager. By determining the pointing direction for each pixel it will be possible to remove this unwanted source of background light either by means of a lookup table, a mathematical algorithm, or by assuming an unchanged value from previous orbits. Stars can be dealt with in the same way. However, because stars are point sources of light, the positions of each pixel boundary will necessarily need to be accurately known (within $\sim 0.1°$) to eliminate their brightnesses from the record.

3.1 Zodiacal Light and the Gegenschein

The Zodiacal Light brightness approximately follows the plane of the ecliptic (Figure 1). In principle, this source of background light should present no problem for the imager as long as its signal, which is far brighter than the Thomson scattering signal, does not statistically overwhelm the faint signal we wish to detect, or saturate the imager.

We are extremely fortunate that the HELIOS spacecraft has provided a working model for the Solar Mass Ejection Imager. A hypothetical small percent variation in the zodiacal cloud at the spatial or temporal scales of features we wish to detect might mask their signal. This is not the case for the HELIOS spacecraft to approximately 1 S10 unit. We presume that at the spatial and temporal scales of heliospheric brightness changes the zodiacal cloud remains smooth and temporally non-varying even below this level. Gegenschein light, thought to be due to backscatter from the zodiacal cloud, is present in the direction opposite the Sun and should not interfere with a sunward-looking imager.

3.2 Starlight

Starlight in general is present as discrete sources of light. However, the brightnesses of stars are comparable to 119 S10 units in all directions [7] (Figure 1). There is approximately one 8th magnitude star in every square degree. Certain portions of the sky are brighter than others and may present certain problems for the imager. These include the Milky Way and other large diffuse objects such as M31 and the large and small Magellanic Clouds. Some imager pixels may contain a bright or variable star that overwhelms the Thomson scattering signal at that solar elongation. These "bad" pixels will need to be identified and removed from the record on each orbit. If the option is available to transmit all the data to the ground, as is presumed possible from most low-Earth orbiters, then the on-board spacecraft electronics becomes simpler to construct than for spacecraft in high orbits. The necessary algorithms, if needed, can be developed and adjusted once the data are on the ground.

3.3 Auroral Light and the Geocorona

Light from aurora on rare occasions has been reported as high as 1000 km above the surface of the Earth [8]. Auroral light intensities vary greatly with geomagnetic latitude and solar activity, so that at times these emissions could be visible from the mass ejection imager. To determine the extent to which auroral intensities could be present, we note that measurements of the brightest aurorae from the ground at the zenith can be $\sim 4 \times 10^3$ rayleighs for the H_β and similar wavelength lines at geomagnetic latitudes of $\sim 65°$ [9]. One S10 unit equals 0.0036 rayleighs $Å^{-1}$ [7]. For the solar mass ejection

imager which is sensitive over ~3000Å, 1 S10 unit $\approx 0.0036 \times 3000 = 10.8$ R. Thus, one auroral line within the wavelength range of the instrument could be as bright as 370 S10 units, and total brightnesses from the many spectral lines of brightest aurorae of several thousand S10 units when observed from the ground. However, we expect this light to be negligible above 800 km. This is because to first order the brightness of auroral light will decrease with molecular density. The integrated fraction of molecules above 800 km relative to that over a 20 km column from 120 to 140 km (the height of normal auroral formation) is $\sim 10^{-4}$ [9]. Following this argument, to be brighter than 1 S10 unit above 800 km, an aurora would have to be as bright as 10^4 S10 units when observed from the ground. Typical brightnesses of the brightest aurorae above 800 km should thus seldom become greater than 1 S10 unit. If such aurorae exist over time intervals short relative to successive orbital passes of the spacecraft, they could interfere with the operation of the mass ejection imager, but only in the darkest parts of the heliosphere at very specific positions relative to Earth's geomagnetic equator.

The geocorona has been detected at various wavelengths, but especially in hydrogen Lyman radiation as a glow in the direction towards the Sun [10]. Typical brightnesses of the geocorona in Balmer α emission (6563Å) are known to be as great as 20 rayleighs or as bright as ~2.0 S10 units. The brightness fall-off with height above the surface of the Earth is unlike aurorae in that the geocorona is brightest at heights of $>10^3$ km. This emission, if included in the imager bandpass, could contribute a background comparable to the signal photons observed by the solar mass ejection imager at 90° elongation and greater. However, the geocorona to first order remains approximately constant relative to solar elongation and is brightest towards and to the west of the Sun [11]. The relative invariability of the geocorona at a given solar elongation on the time scales of mass ejections implies that this source of brightness should pose no problem for an Earth-based imager, especially if Balmer α is not included significantly in the instrument bandpass.

3.4 Ram Glow and Other Spacecraft-Produced Illumination

Ram Glow is a low-level light source which forms a comet-like halo and tail near a spacecraft in low-Earth orbit. The glow is caused by many different sources [12] including: 1) a concentration of the ambient gasses which peak in the ram direction, 2) outgassing from the spacecraft, 3) leakage, 4) venting and 5) thruster firings. In visible light from low-Earth orbit some of the constituent molecular glows are significantly above the ~100 S10 unit zodiacal light background at 90° elongation. The amounts of this glow vary from spacecraft to spacecraft. Extrapolating from Shuttle measurements, at heights below 400 km the glow rivals or can be greater than the background zodiacal light. If the source of this light were to vary, it could cause significant problems for the imager at these heights. With the possible exception of sources on the vehicle such as emissions from other experiments, these sources of light extrapolate to well below the level that could cause a detrimental effect on the imager at the 800 km orbit.

4 Conclusions

We envision a imager capable of tracing solar mass ejections and other heliospheric features from near the Sun out to the orbit of the Earth. Such instrumentation would have the capability of forecasting the arrival at Earth of these features in real time. Results from the HELIOS spacecraft have demonstrated that such instrumentation is feasible, and they also give limits on the signal to noise required for such instrumentation. Although several instrument designs are possible depending on the type of spacecraft and its orbit, most of our preliminary designs depend upon the rotation of the spacecraft to scan the sky. Such an instrument will compile an image in a plane parallel to the spacecraft rotation axis. In the case of an instrument in Earth orbit on a nadir-pointing vehicle, this rotation is provided by the orbital motion.

References

1. B. Jackson, R. Gold and R. Altrock: Adv. Space Res., **11**, 377, (1991)
2. B.V. Jackson: Yosemite 1988 Conference on Outstanding Problems in Solar System Plasma Physics: Theory and Instrumentation, Yosemite National Park, California, February 2-5, 1988, (1989)
3. B.V. Jackson: Adv. Space Res., **6**, 307, (1986)
4. B.V. Jackson: AFGL-TR-88-0195, (1988)
5. B.V. Jackson, H.S. Hudson, J.D. Nichols and R.E. Gold: Yosemite 1988 Conference on Outstanding Problems in Solar System Plasma Physics: Theory and Instrumentation, Yosemite National Park, California, February 2-5, 1988, (1989)
6. B.V. Jackson, H.D. Zink and R.E. Gold: JHU/APL SDO 8416, Report to the USAF and NASA, (1987)
7. C.W. Allen: Astrophysical Quantities (Athlone, London, England) (1964)
8. George Carruthers: private communication (1991)
9. A.V. Jones: Aurora, ed. by B.M. McCormac (Reidel, Dordrecht, Holland) (1974)
10. R.R. Meier and P. Mange: Planet. Space Sci., **21**, 309, (1973)
11. D.E. Anderson, Jr., R.R.Meier, R.R. Hodges, Jr. and B.A. Tinsley: J. Geophys. Res. **92**, 7619, (1987)
12. D.G. Torr: NASA Conference Publication **3002**, (1988)

8.

POSTER PAPERS

AN OBSERVATIONAL-CONCEPTUAL MODEL OF THE FORMATION OF FILAMENTS

(Extended Abstract)

Sara F. Martin

Big Bear Solar Observatory, Solar Astronomy 264-33 California Institute of Technology
Pasadena, CA, USA

Examples of the formation of filaments are analyzed from high resolution H-alpha filtergrams from the Big Bear Solar Observatory, the U.S. National Observatory at Sacramento Peak, the Ottawa River Solar Observatory and the Udaipur Solar Observatory along with line-of-sight magnetograms from the Big Bear Solar Observatory and the U.S. National Observatory at Kitt Peak.

It is deduced that the magnetic field in the environment of filaments has a rotational configuration that requires depiction in three dimensions and looks like a 'rotational discontinuity' (Spreiter and Alksne, 1969, *Reviews of Geophys.* **7**, 11), a magnetic field geometry that is also commonly observed in the plasmas of the interplanetary medium at some interfaces between oppositely-directed magnetic fields. Evidence for this magnetic field configuration in the environment of filaments comes from the asymmetric rosettes and patterns of the fibrils adjacent to the filaments, from the direction of the structure within and under the filaments, and from the deduced direction of the magnetic fields adjacent to the filaments as they are forming. The directions of motion of the magnetic fields adjacent to the filaments reveal that the assymetry of the rosettes and direction of the fibrils is not due to the flow pattern of the photospheric magnetic fields adjacent to the filaments. Instead, the asymmetry of the rosettes and patterns of the fibrils are related to the local direction of the magnetic fields in and around the filaments as previously interpreted by Foukal (1971, *Solar Phys.* **19**, 59). Immediately adjacent to filaments, the magnetic field lines from the rosettes are inclined from vertical in planes approximately parallel to the sides of the filaments; they are also inclined in opposite directions from vertical on the two sides of the filaments. In general, the inclinations of the field lines around and in filaments are: (1) in the same general direction as the fibrils that appear to stream from the core of the rosettes or adjacent plage, (2) greatest adjacent to the filaments, decreasing with increasing distance from the sides of the filaments, and (3) 90 degrees (horizontal) in the filament channel. Recognition of this pattern of inclined magnetic fields in the environment of a filament as being like a 'rotational discontinuity' brings new information for consideration in modelling the formation of filaments.

The formation of the filaments coincides with the observed convergence, encounter, and cancellation of knots of magnetic flux of opposite polarity in a polarity inversion. It is hypothesized that the horizontal magnetic fields in the coronal part of the polarity inversion increase simultaneously with the cancellation observed in the line-of-sight magnetograms. It is further hypothesized that these changing magnetic fields occur simultaneously due to a slow type of magnetic field reconnection whose point of initiation is at or near the photospheric/chromospheric interface and between the oppositely-inclined and opposite polarity magnetic fields which have converged together from the two sides of the filament channel. This proposed configuration of reconnection would result in the conversion of pairs of oppositely-directed field lines into single, nearly horizontal field lines which rise into the corona, coming to equilibrium as additional field

lines in the horizontal, coronal region of the polarity inversion (which would correspond to the middle of a rotational discontinuity). Mass concurrently accumulating in the horizontal part of the polarity inversion, eventually reaches a density and temperature which allows it to be detected as a filament. By means of the proposed reconnection, magnetic and kinetic energy are extracted from regions close to the photospheric-chromospheric interface and stored in the chromospheric and coronal parts of the polarity inversion. The energy stored within the coronal part of the polarity inversion is then available for subsequent release in dynamic coronal events.

This research was supported by the U.S. Air Force Office of Scientific Research under grant AFOSR 90-0006.

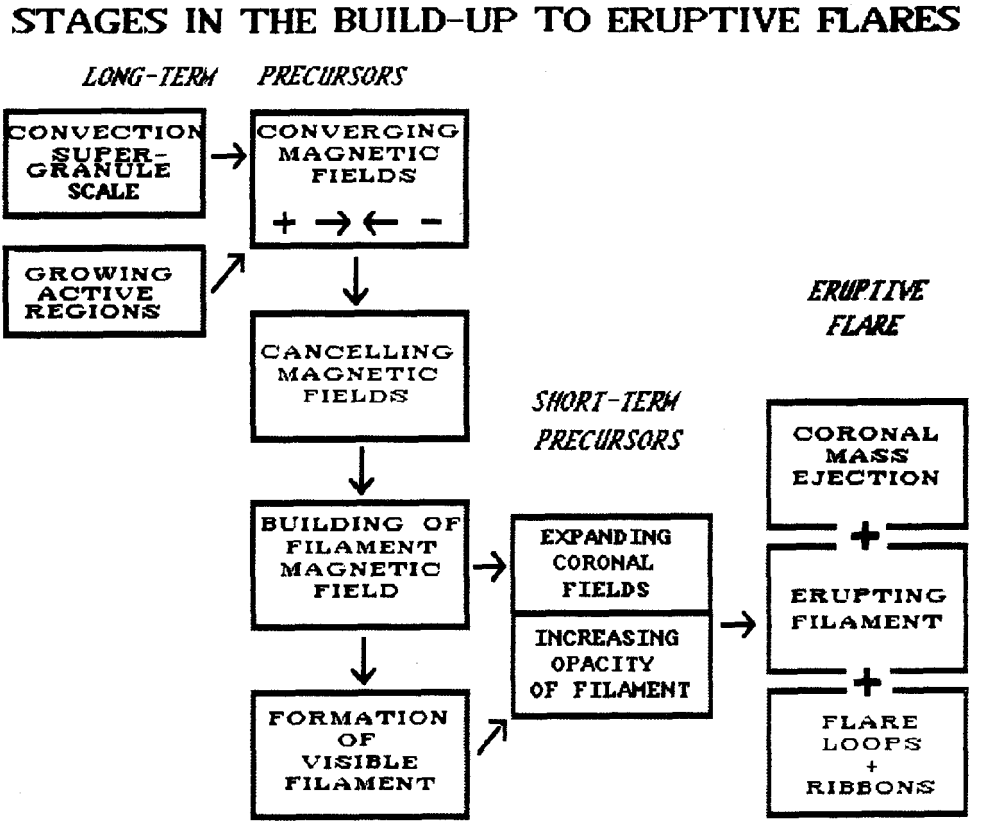

DYNAMICS IN THE PROMINENCE-CORONA TRANSITION REGION FROM HRTS SPECTRA

Schmieder B.[1], Dere K.P.[2], Wiik J.E.[1,3]

[1]Observatoire de Meudon, DASOP, F-92195 Meudon Principal Cedex, France
[2] NRL, Washington DC-20375, USA
[3] Institute of Theoretical Astrophysics, Pb 1029 Blindern, N-0315 Oslo 3, Norway

Abstract

Line profiles of UV emission lines between 1206Å and 1670Å observed in two prominences with the *High Resolution Telescope and Spectrograph* (HRTS) are analysed. Spectral lines in this region of the solar spectrum such as C I, Fe II, Si IV and C IV, provide information on plasmas in the 10 000 K to 200 000 K range. In the active prominence observed with HRTS-1 a good correlation is found between the intensities and velocities of different lines formed over a range of temperatures. On the contrary, poor cross correlation between the velocities observed in plasmas of cold temperatures indicates the presence of different structures in the SL2 prominence. Microturbulent velocities from 0 to 25km s^{-1} are found in both prominences.

1 Introduction

Prominence environements have been under investigations the last couple of decades. A large amount of data has been available for this purpose from the many rocket flights and the shuttle mission carrying the *High Resolution Telescope and Spectrograph* (HRTS) instrument. Its spectral range covers UV emission lines between 1206Å and 1670Å corresponding to plasmas of temperatures in the 10 000 K to 200 000 K range.

We examine data obtained during the first rocket flight of the instrument (HRTS-1) in 1975 and during operations aboard the Spacelab-2 mission (SL2) in 1985. The interaction of the cold prominence plasma with its hotter surroundings is still an unknown problem which concerns the problem of formation of prominences. The HRTS-1 and SL2 data are appropriate for studying the prominence-corona transition region where the temperature rises from 10^4-10^6 K.

We use the wavelength moments of the profiles (Dere *et al.*, 1984) to determine the variation of line-of-sight velocity and micro-turbulence with height and temperature in the prominences. Hα observations made at Meudon provide the topology of the prominences and are used as reference for the SL2 slit pointings (Figure 1).

2 Prominence line-of-sight and non-thermal velocities

2.1 HRTS-1, Active Prominence

The presence of emission lines from C IV, N V and O IV ($1.0\text{-}1.5 \cdot 10^5 K$) indicates a hot transition region around the prominence. We find a good correlation between the intensities, the velocities and the width of lines of different temperatures (Figures 2a and b). Thus, we see the same structures in the different lines. We estimate the structures diameters to a FWHM of $\sim 1.5''$. For the lines formed at T around $10^5 K$ we

Figure 1: Hα image of the quiescent prominence observed with SL2. Some slit pointings are indicated. Meudon Observatory.

find an average micro-turbulent velocity of 20km s^{-1}, in good agreement with previous results (Vial *et al.* 1980). For lines formed at temperatures above $10^5 K$ lower values are derived (Table 1, Figure 4). Similar results have been obtained for these lines before in quiet and active regions although there is a possibility that it may be due to the generally low intensity of these hotter lines. The maximum micro-turbulence as well as the line-of-sight velocities occur near the top of the prominence.

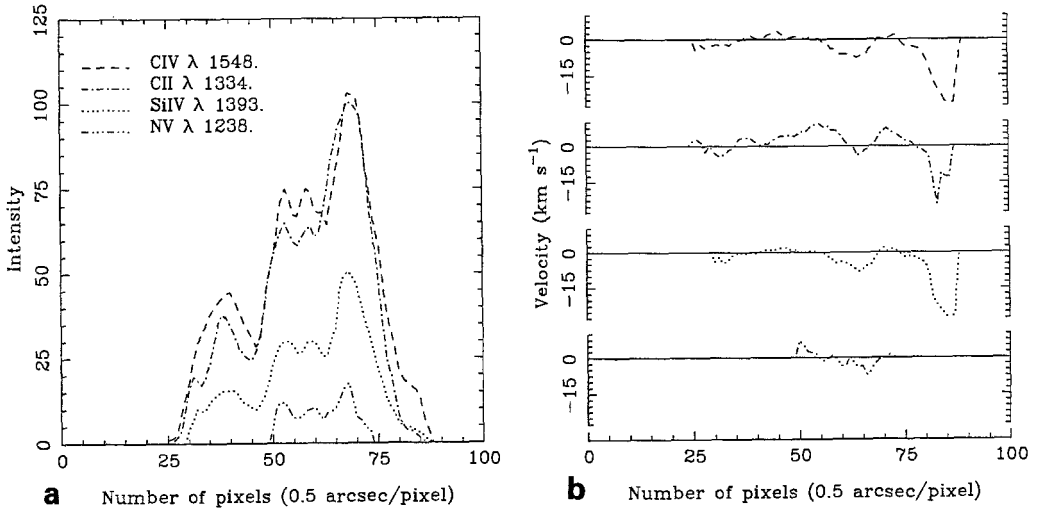

Figure 2: a) Intensity and b) velocity versus height (HRTS-1)

2.2 SL2, Quiescent Prominence

We have examined the behaviour of two lines (Si II, C IV) in several slit pointings, N, out of 17 available. Three of these are presented: foot (position 5), bright point (position 7), and arch (position 9). We find good correlation between the intensities of Si II and C IV, but poor correlation between the velocities of these lines (Figures 3a-d). Cross correlations between the velocities observed in plasmas of different temperatures indicate the presence of different structures. The non-thermal velocities are low in all parts of the prominence, less than 10km s^{-1}, except in the bright point observed in C IV near the limb in position 7 (Table 2). This bright point could be the signature of reconnection. An enhanced intensity at this location is also visible in other lines. We find a line-of-sight velocity less than 10km s^{-1} in the arch and in the footpoints.

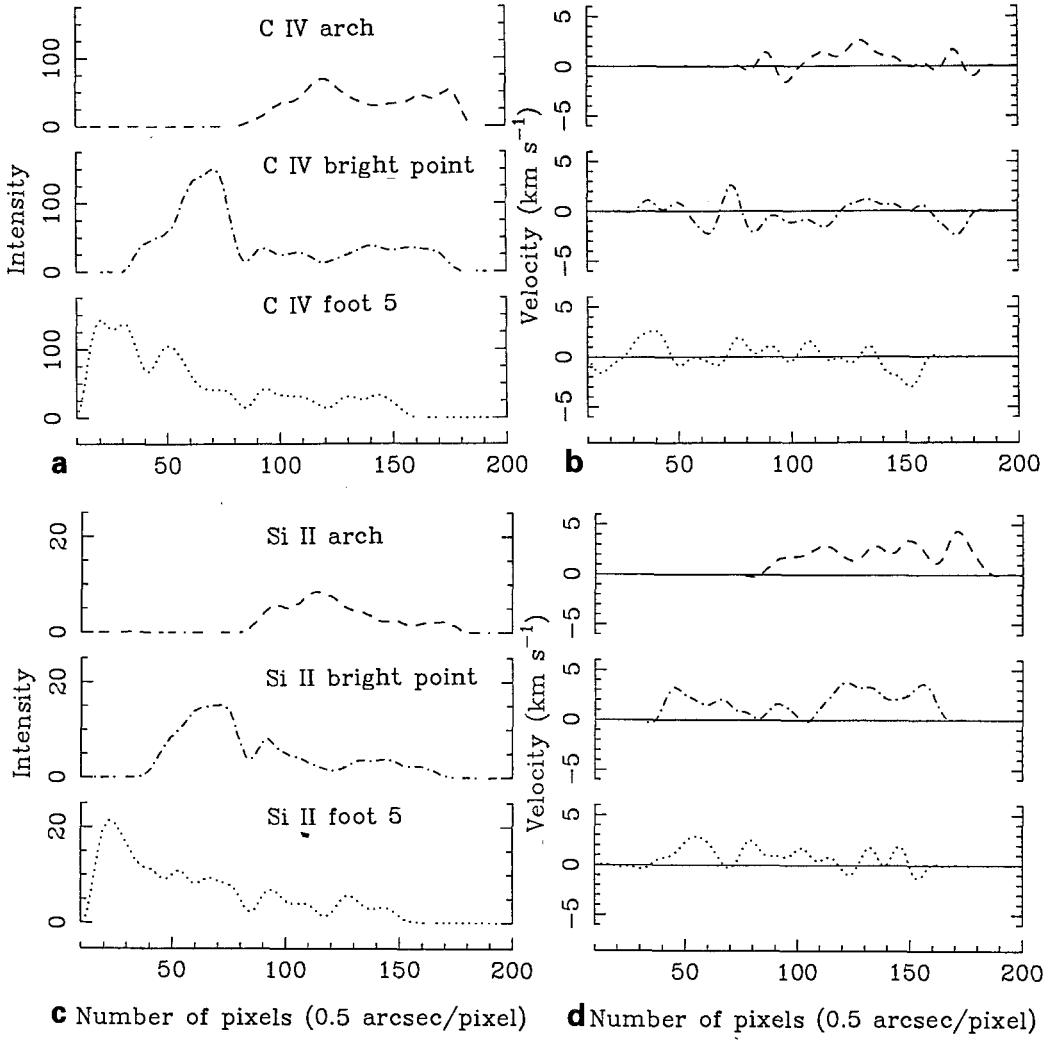

Figure 3: SL2 a and b) C IV (λ1548Å) intensity (a) and velocity (b) versus height. c and d) Si II (added λ1526 and 1533Å) intensity (c) and velocity (d) versus height.

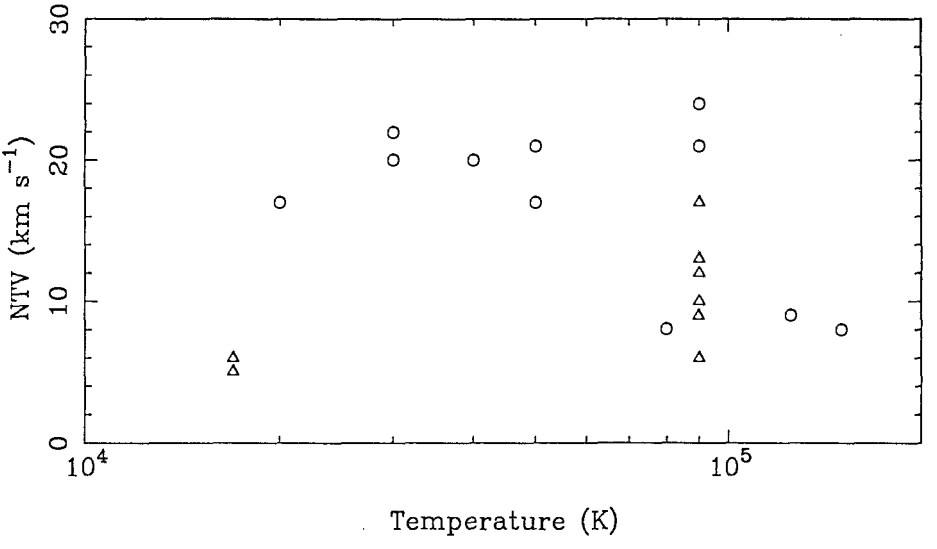

Figure 4: NTVs versus temperature (circles HRTS-1; triangles SL2)

Ion	Å	Temp. *K*	NTV *km s*$^{-1}$	
Fe II	1442.	$2 \cdot 10^4$	17	±10
C II	1334.	$3 \cdot 10^4$	20	±4
C II	1335.		22	±5
Si III	1206.	$4 \cdot 10^4$	20	±4
Si IV	1393.	$5 \cdot 10^4$	21	±5
Si IV	1402.		17	±5
O III	1666.	$8 \cdot 10^4$	8	±4
C IV	1548.	$9 \cdot 10^4$	24	±6
C IV	1550.		21	±5
O IV	1401.	$13 \cdot 10^4$	9	±4
N V	1238.	$15 \cdot 10^4$	8	±5

Table 1 HRTS-1; Observed NTV

Ion	N	Temp. *K*	NTV *km s*$^{-1}$	
Si II	5	$2 \cdot 10^4$	5	±2
	7		6	±2
	9		0	
	14		5	±3
	16		5	±2
C IV	5	$9 \cdot 10^4$	7	±3
	7		17	±6
	9		6	±3
	14		9	±4
	16		12	±6

Table 2 SL2; Observed NTV

3 Conclusion

The behaviour of these two prominences is different related to their temperatures and their velocities. This implies that their physical conditions are certainly different. Before making any general conclusion on the prominence-corona transition region, we need to know the topology of the observed prominences and their general evolution. Good spatial and spectral resolution are required.

References

Dere KP, Bartoe JDF, Brueckner GE: 1984, *Astrophys. J.* **281**, 870
Vial JC, Lemaire P, Artzner G, Gouttebroze P: 1980, *Solar Phys.* **68**, 187

ACTIVE REGION CLASSIFICATIONS, COMPLEXITY, AND FLARE RATES

P. L. Bornmann and D. Shaw
NOAA Space Environment Laboratory, Boulder, CO, USA

The McIntosh active region classifications (McIntosh 1990 and references therein), which are reported for each active region on the solar disk, are used by the NOAA Space Environment Laboratory to forecast solar flares. These forecasts are based on the average number of flares produced per day for each of the original 63 classifications, as compiled by Kildahl (1980). Because these forecasts currently require an estimate of each region's evolution over the next several days, the TELSAR (Tracking and EvoLution of Solar Active Regions) project was started to provide statistical information on the evolution of active regions through the McIntosh classification system. The first results of this project (Bornmann *et al.* 1991) traced the evolution of over 1000 active regions, and derived statistics on flare rates expected on each of the 7 days following a reported classification. Subsequent investigations of the data seemed to indicate that the existing classification system forms a grid of classes that is finer than can be accurately assigned by Air Force's Solar Optical Observing Network (SOON) and other observing sites that report these classifications. In this paper we report the initial results of an investigation of the various classification decisions used by the McIntosh classification system. In particular, the relative importances of these classification decisions are related to the average flare rates of the classes.

One of the primary goals of the TELSAR project was to combine the reported sequences of McIntosh active region classifications, and thereby to piece together the complete evolution of typical active regions. Some of the initial TELSAR results were not completely satisfying. A large number of unique evolutionary sequences were found, as well as numerous sequences that seemed to oscillate between neighboring classes. In addition, for each observing day the various observing sites often reported classifications that differed by one classification parameter. Taken together, these initial results seemed to indicate that the differences between many classes were difficult to determine. This could then explain the excess "noise" in the data, if it is caused by classifications that only slightly "missed the target."

The McIntosh active region classifications consist of three parameters that are derived from a number of sunspot properties observed in white light (Solar Geophysical Data 1972; McIntosh 1990; the operational Air Force Reports; see also the schematic of the classification

Table 1. Initial and Weighted Complexity Indices

Decision	Classes*	Initial Weight	Regression Weight	
Penumbra on largest spot?				
No	Aww, Bww	0	0.0	
Yes	Hww, Cww, Dww, Eww, Fww	1	0.008	+/– 0.002
Size of largest spot?				
Small	wXw, wRw, wSw, wAw	0	0.0	
Large	wHw, wKw	1	0.193	+/– 0.004
Group length?				
Unipolar	Aww, Hww	0	0.0	
Small	Bww, Cww, Dww	1	0.0	
Medium	Eww	2	0.412	+/– 0.006
Large	Fww	3	1.375	+/– 0.015
Interior spot distribution?				
Unipolar	wwX	0	0.0	
Open	wwO	1	–0.008	+/– 0.002
Intermediate	wwI	2	0.065	+/– 0.003
Compact	wwC	3	0.611	+/– 0.009
Shape of largest spot?				
Symmetric or not specified	wXw, wRw, wSw, wHw	0	0.0	
Asymmetric	wAw, wKw	1	0.079	+/– 0.003
Penumbra at both ends of group?				
No	Aww, Hww, Bww, Cww	0	0.0	
Yes	Dww, Eww, Fww	1	0.011	+/– 0.003
Additive Normalization Constant		0	0.018	+/– 0.002

* where "w" denotes wildcard or place holder

decisions in Bornmann *et al.* 1991). These parameters are not always independent, and in some cases the relative importance, or ordering, within a single parameter is not well established. Therefore, we have identified six classification decisions, listed in Table 1, that are incorporated in the McIntosh classifications. These decisions were then compared with average daily rate of M flares (Kildahl 1980). Because some classes were rarely observed and therefore have large statistical errors, only those classes observed more than 20 times in Kildahl's 8-year study were used for the following comparisons.

Two complexity indices were derived from these six classification decisions: the initial index and the weighted index. The initial complexity index was derived from the simple sum of the somewhat arbitrarily assigned integral weights for each classification decision, as indicated in Table 1. This index is essentially a measure of the number of indications that the region is well developed. It can be visualized as a rough measure of the class' distance

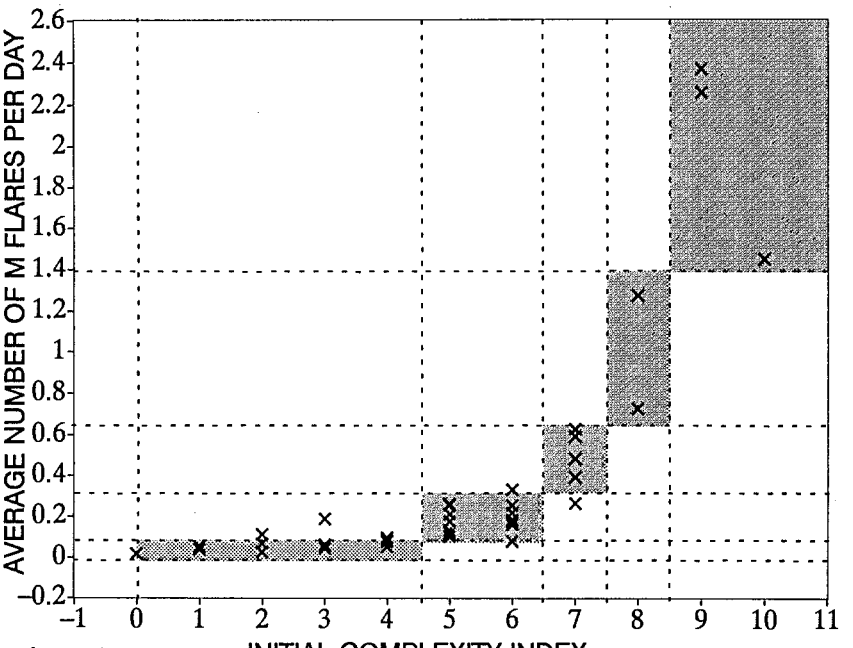

Figure 1.

from the "origin," or location of the simplest class, in the three-dimensional McIntosh classification space. When compared with the M flare rate, this index showed a significant nonlinear correlation, as shown in Figure 1. From Figure 1 we conclude that the probability of a flare increases with the number of indications of a region's development or with the distance of the class from the origin of the classification system.

Because of the correlations found between the flare rate and this initial complexity index, a multiple regression analysis was used to develop an improved, weighted complexity index. (Neidig *et al.* 1984 examined the importance of the three classification parameters as a group, but did not derive weights for individual parameters.) The multiple regression against the M flare rate was used to derive the optimal weights for each of the six classification decisions. Similar to the initial complexity index, the weighted complexity index was defined as the sum of the normalization constant plus the corresponding weight of each of the classification decisions, as listed in Table 1. This weighted complexity index shows a strong linear correlation with M flare rate ($R = 0.885$), as can be seen in Figure 2.

The weighting factors derived from the multiple regression analysis can be interpreted as the relative importance for M flare production of each of the classification decisions. Of the six classification decisions considered here, three dominated the correlation with flare rate. The group length was most important for flare production, followed by the occurrence of a compact distribution of spots within the group. Of somewhat less importance was the size of the largest spot. These three classification decisions may be related to the strength of the magnetic field and the degree of magnetic shear within the region.

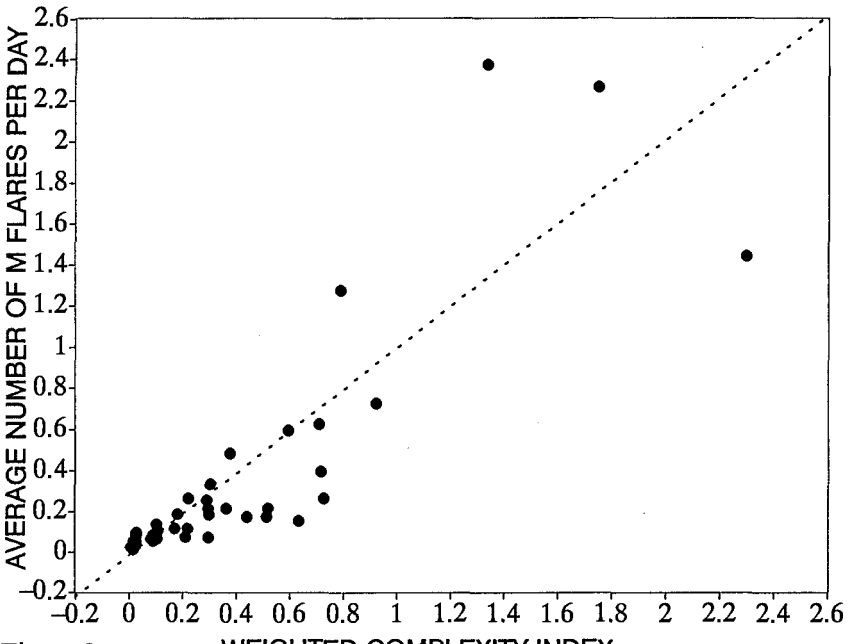

Figure 2.

Three other classification decisions were less significant for producing flares. Taken together, these three decisions affected the average flare rate by only 0.1 flares per day. These were the asymmetry of the largest spot, the existence of penumbrae at both ends of the group, and the existence of penumbra on the largest spot. The lack of strong weights for these three decisions may indicate either a lack of strong physical relationship with flare production, or it may reflect the numerous improper classifications that result from the inability to accurately determine these particular classification parameters.

Much of the software for the initial TELSAR project was written by Darren Kalmbach and David Kulhanek, as part of their senior computer science project at the University of Colorado.

References:

Air Force's Air Weather Service Pamphlets, "Solar Optical Observing" (*e. g.* 1981: 105–60; 1988: 105–10).

Bornmann, P. L., Kalmbach, D., Kulhanek, D., and Casale, A., "A Study of the Evolution of Solar Active Regions for Improving Solar Flare Forecasts", *Proceedings of the Solar Terrestrial Predictions Workshop* held October 1989, vol. 1, p. 301, 1991.

Kildahl, K. J. N., "Frequency of Class M and X Flares by Sunspot Class (1969–1976)", *Solar-Terrestrial Predictions Proceedings*, vol. 3, Donnelly, R. (ed), p. 166, 1980.

McIntosh, P. S., "The Classification of Sunspot Groups", *Solar Physics,* **125**, 251, 1990.

Neidig, D. F., Wiborg, P. H., Seagraves, P. H., Hirman, J. W., and Flowers, W. E., "Objective Forecasts for Solar Flares using Multivariate Discriminant Analysis", *Proceedings of the Solar Terrestrial Predictions Workshop*, p. 300, 1984.

Solar Geophysical Data, "Descriptive Text", 1972 and more recent editions.

COMPACT SOURCES OF SUPRATHERMAL MICROWAVE EMISSION DETECTED IN QUIESCENT ACTIVE REGIONS DURING LUNAR OCCULTATIONS

E. Correia, P. Kaufmann and F.M. Strauss*
Centro de Rádio Astronomia e Aplicações Espaciais,
Escola Politécnica da Universidade de São Paulo,
C.P. 8174, 05508 São Paulo, Brazil.
*In memorian, 1942-1981.

ABSTRACT

Solar quiescent active regions are known to exhibit radio emission from discrete structures. The knowledge of their dimensions and brightness temperatures is essential for understanding the physics of quiescent confined plasma regions. Solar eclipses of 10 August 1980 and 28 January 1990, observed with high sensitivity (0.01 s.f.u.) and high time resolution (30 ms) at 22 GHz, allowed the unprecedented opportunity to identify Fresnel diffraction effects during lunar occultations of active regions. The present results indicate the presence of quiescent discrete sources smaller than one arcsecond in one dimension that can be associated to the compact sources of suprathermal microwave emission. Assuming symmetrical sources, their brightness temperatures were larger than 2×10^7 K and 8×10^7 K, for the 1980 and 1990 observations, respectively. From energetic point of view the results give new information about confinement of plasmas in active regions.

(A full version of this paper was submitted to Solar Physics)

VELOCITY FIELD IN THE 13 JUNE 1980 FLARE AREA

A. Falchi[1], R. Falciani[2], and L.A. Smaldone[3]
[1] Osservatorio Astrofisico di Arcetri - L.go E. Fermi 5 - 50125 Firenze (Italy)
[2] Dip. di Astronomia dell'Università- L.go E. Fermi 5 - 50125 Firenze (Italy)
[3] Dip. di Scienze Fisiche dell'Università - Pad. 19-20 Mostra d'Oltremare
80125 Napoli (Italy)

The 13 June 1980 flare area was observed at NSO - Sacramento Peak Observatory, simultaneously with the Universal Spectrograph (USG) and with the Universal Birefringent Filter (UBF) in parallel with the Zeiss H_α filter. We consider the flare emission obtained with the spectrograph in the H_β, H_γ, H_δ, Ca II-K and $Na - D_2$ lines to detect possible asymmetry in their profiles. An emission in the red wing of the considered Balmer lines and of the Ca II-K line is evident but no asymmetry is seen in the $Na - D_2$ line. This red emission is assumed to be the signature of downward motions; we obtained from the Balmer lines a velocity of $\sim 30. \pm 2$ km sec^{-1} and from the Ca II-K line a velocity of $\sim 20. \pm 2$ km sec^{-1}. We compare the $Na - D_2$ line profiles, obtained with the USG and with the UBF in the same area of the flare, and we find that a red emission is present in the UBF line at the seeing spatial resolution of ≈ 2 arcsec. The downward velocity obtained from this line is 10 ± 4 km sec^{-1}.

A characteristic blue asymmetry, indicative of coronal upflows, is present in the Ca XIX spectrum obtained with the Bent Crystal Spectrometer (BCS) on the Solar Maximum Mission (SMM). This is qualitatively consistent with the generally accepted scenario of a chromospheric evaporation sufficiently rapid to drive both coronal upflows and chromospheric downflows. The velocities obtained from chromospheric lines are compared with the ones predicted by numerical simulations of gas dynamics in flare loops (Fisher 1986, 1989). The results show that the chromospheric condensation, predicted to be moving downwards with constant velocity within the condensation, probably has a velocity gradient and that the layers ahead of it seem to be affected by the motion of the condensation.

We point out that the velocity field values deduced from different spectral signatures, originated in different physical conditions within the flare atmosphere, may represent a very important tool to improve the reliability of the proposed dynamic models. However since our results are based only on observations for one flare, it seems to us that what is needed is a higher number of observations, with the highest possible time resolution, allowing the determination of the velocity field in various spectral features. We also stress the importance of having high spatial resolution (at the seeing limit) since the spatial inhomogeneity in the physical conditions of the flare kernels may represent a new sort of information for understanding solar flares.

Deformation of magnetic null points

K. Galsgaard and Å. Nordlund

Copenhagen University Observatory
Øster Voldgade 3, 1350 Copenhagen K
Denmark

1 Introduction

Magnetograms from plage regions show that the vertical component of the magnetic field has a self-similar horizontal distribution with a fractal dimension of around 1.5 (Tarbell et al. 1990). Both the spatial distribution and the temporal displacements of identifiable magnetic features are consistent with random walk of the magnetic field in the labyrinth of paths between convection cells on the solar surface (Schrijver et al., 1991). Both observations and numerical calculations show that the distribution of granules follows a power law (Stein and Nordlund, 1990), and the chaotic time evolution of the granulation pattern probably is the ultimate cause of the random walk. The fractal surface distribution of the magnetic field must continue into the upper atmosphere, which is likely to be pervaded by a self-similar three-dimensional web of magnetic field.

X-ray observation of flares by the Solar Maximum Mission show that the peak flare energy follows a power law distribution over 3.5 orders of magnitude in energy (B. Dennis, 1985). Radio observations show that the initial phase of flares is composed of many small scale millisecond events (See Benz and Aschwanden, these proceedings). Based on numerical experiments, Lu and Hamilton (1991) suggest that the power law distributions occur because the magnetic field is in a self organized critical state (Bak, Chen & Wiesenfeld, 1988). This means that the field evolves on the edge of an unstable situation, where infinitesimal disturbances may trigger events of arbitrary size within the power law distribution, and that flare events are composed of a huge number of small events with physical sizes near the shortest length scale in the field.

These ideas suggest that the field topology in the solar atmosphere has an intermittent structure, down to the smallest length scales. The evolution of such magnetic fields must be characterized by a complex dynamic response to deformations. One way to obtain an understanding of the dynamic behavior is by investigating topological building blocks of complex fields and study how they react to simple deformations. Here we argue that the existence of 3D magnetic null points may lead to local instabilities. Complex fields with null points on different length scales may lead to non-linear large scale disruptions of the field topology, through the evolution of many small scale events.

2 Deformation formalism

The induction and continuity equations determine the evolution of the magnetic field and the mass density. Combining these we get an equation for the Lagrangian time derivative of the ratio between the magnetic field and the gas density (Moffatt, 1978; Parker 1979).

$$\frac{D\frac{\mathbf{B}}{\rho}}{Dt} = \left(\frac{\mathbf{B}}{\rho}\cdot\nabla\right)\mathbf{u}. \tag{1}$$

Solving this equation is equivalent to making a spatial transformation of the vector function $\mathbf{F} = (\mathbf{B}/\rho)$ (Parker 1979), with a solution at time t given by

$$\mathbf{F}(\mathbf{r}',t) = \frac{\partial \mathbf{r}'}{\partial \mathbf{r}}\mathbf{F}(\mathbf{r},0) = \underline{\underline{\mathbf{G}}}(\mathbf{r},t)\mathbf{F}(\mathbf{r},0). \tag{2}$$

Here $\mathbf{r}'$ is the new position at time t of the material from position $\mathbf{r}$ at time 0. This position may be found by integration of the velocity as a function of time. If the velocity field is divergence free, the density of a volume element is conserved. In this case Eq (1) becomes an equation for the magnetic field alone

$$\mathbf{B}'(\mathbf{r}') = \underline{\underline{\mathbf{G}}}(\mathbf{r})\mathbf{B}(\mathbf{r}). \tag{3}$$

The current in the deformed system is obtainable from the derivative matrix of the magnetic field,

$$\frac{\partial B_i'}{\partial r_j} = \sum_{lk}\left(G_{ik}\frac{\partial B_k}{\partial r_l} + \frac{\partial G_{ik}}{\partial r_l}B_k\right)G_{lj}^{-1} \tag{4}$$

The first term is the normal linear coordinate transformation of a matrix, while the last term only contributes when the deformation is non-linear.

3 Deformations

The topology of a first order 3D null point is determined by the eigenvalues of the magnetic derivative matrix, with two main classes corresponding to real and complex eigenvalues. Here we show an example of a deformation of an initially force free null point with real eigenvalues; one negative and two positive. This gives a situation where the field lines approach the null point along the eigenvector direction belonging to the negative eigenvalue and spread out over a separator surface spanned by the two other eigenvectors (Green 1988), as illustrated in the upper left panel of Figure 1.

The magnetic field in the example is a constant α force free field with $\alpha = -\frac{\pi}{4}$, defined by three pairs of complex wavevectors and vector potentials. This field has eight null points per 3D period (in a box spanned by the wavevectors). One

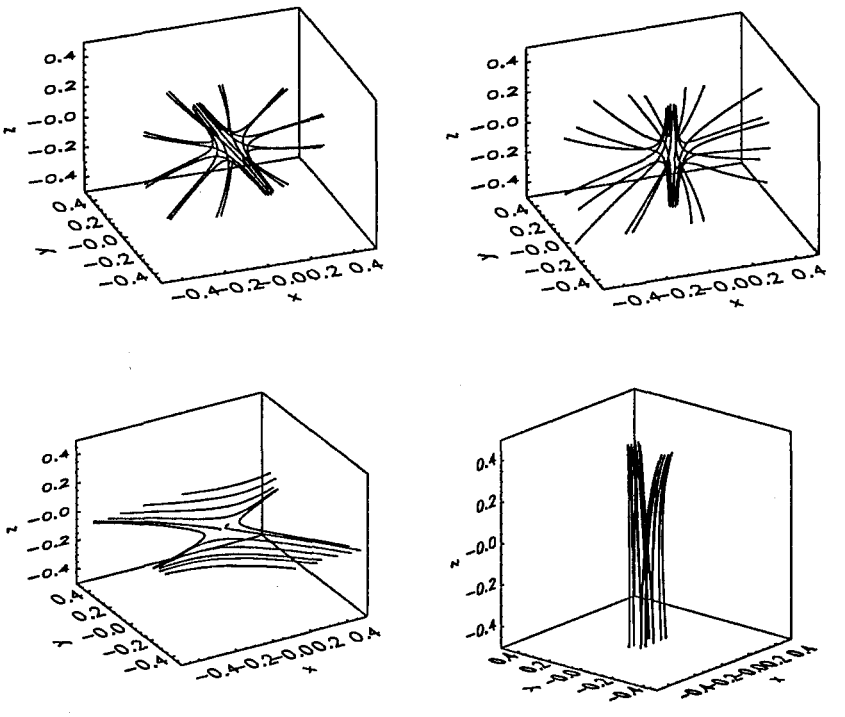

Fig. 1. The upper left panel shows the original magnetic and current field topology, illustrated by field line traces. The traces start from a number of points around the main axis and are followed in both directions. The upper right panel shows the magnetic field after the shear deformation. The lower two panels show the Lorentz force (left) and the current (right) after the deformation.

null point is at the origin with its main axis in the y direction and the separator plane coinciding with the xz plane.

$$\begin{aligned}
\mathbf{k}_1 &= \tfrac{\pi}{4}\left[\left(0,\tfrac{1}{\sqrt{2}}\right),\left(0,\tfrac{1}{\sqrt{3}}\right),\left(0,\tfrac{1}{\sqrt{6}}\right)\right], & \mathbf{A}_1 &= \left[\left(\tfrac{1}{\sqrt{2}},\tfrac{1}{\sqrt{2}}\right),\left(0,\tfrac{-2}{\sqrt{3}}\right),\left(\tfrac{-3}{\sqrt{6}},\tfrac{1}{\sqrt{6}}\right)\right] \\
\mathbf{k}_2 &= \tfrac{\pi}{4}\left[\left(0,\tfrac{-1}{\sqrt{2}}\right),\left(0,\tfrac{1}{\sqrt{3}}\right),\left(0,\tfrac{1}{\sqrt{6}}\right)\right], & \mathbf{A}_2 &= \left[\left(\tfrac{1}{\sqrt{2}},\tfrac{-1}{\sqrt{2}}\right),\left(0,\tfrac{-2}{\sqrt{3}}\right),\left(\tfrac{2}{\sqrt{6}},\tfrac{1}{\sqrt{6}}\right)\right] \\
\mathbf{k}_3 &= \tfrac{\pi}{4}\left[(0,0),\left(0,\tfrac{1}{\sqrt{3}}\right),\left(0,\tfrac{-2}{\sqrt{6}}\right)\right], & \mathbf{A}_3 &= \left[\left(\tfrac{-2}{\sqrt{2}},0\right),\left(0,\tfrac{-2}{\sqrt{3}}\right),\left(0,\tfrac{-2}{\sqrt{6}}\right)\right]
\end{aligned} \tag{5}$$

$$\mathbf{B} = \mathrm{Re}\left(\sum_{i=1,3} \mathbf{k}_i \times \mathbf{A}_i e^{(\mathbf{k}_i \cdot \mathbf{r})}\right) \tag{6}$$

The deformation that we use is a shear deformation where the change in position is determined by

$$\delta x = a \sin\left(\frac{\pi}{4\sqrt{3}} y\right). \tag{7}$$

The linear transformation $\underline{\underline{G}}$ corresponding to this deformation changes the magnetic field by adding a part of the magnetic fields y component to the x component; $B_x \rightarrow B_x + B_y \frac{\pi}{4\sqrt{3}} a \cos(\frac{\pi}{4\sqrt{3}} y)$. As a result of the transformation, the magnetic null points main axis is turned clock-wise around the origin in the (x, y) plane.

The force that arises from the deformation separates space around the null point into two regions (and their mirror images), according to the net balance of magnetic tension and pressure forces. One region consists of the volume between the separator plane and the tilted main axis, extending into the third direction to form a wedge. A net tension force tries to drag the field lines out of this region. The second region is outside the two tension wedges. Here a net magnetic pressure gradient force tries to press the main axis closer to the plane. The net deformation work (integrated over the deformation) is positive (works *against* the deformation), showing that the initial configuration is dynamically stable.

4 Conclusion

The example shows that the periodic 3D null point system is globally stable with respect to a simple shear deformation. Other examples show that some complex fields contain regions which are locally unstable. The size of these regions depend on the relative orientation of the symmetry axes of the field and the deformation. When complicated magnetic fields are stressed by external deformations they are likely to reach states where they become locally unstable. When a sufficient number of local volumes become unstable it may be possible to get larger scale instabilities, corresponding to the slides of a sandpile in a self organized critical state (Bak, Chen & Wiesenfeld, 1988).

References

Bak, P., Chen, K., Wiesenfeld, K.: 1988, *Physical Review A*, **38**, 364

Lu, E.T. and Hamilton, R.J.: 1991, *Ap. J. Letters* **380**, L89

Dennis, B.R.: 1985, *Solar Phys.* **100**, 465

Green, J.M.: 1989, *J. Geophys. Res.* **93**, 8583

Moffatt, H.K.: 1978, *Magnetic Field Generation in Electrically Conducting Fluids*, Cambridge Monographs on Mechanics and Applied Mathematics

Parker, E.N.: 1979, Cosmical Magnetic Fields, Oxford: Clarendon Press

Schrijver, C.J., Zwaan, C., Balke, A.C., Tarbell, T.D., Lawrence, J.K.: 1991, *Letter to Astronomy Astrophys.* (in press)

Stein, R.F. and Nordlund, Å.: 1990, Proceedings of the Heidelberg Conference on "Mechanisms of Chromospheric and Coronal Heating", Heidelberg, Germany 5-8 June, p.386

Tarbell, T., Ferguson, S., Frank, Z., Shine, R., Title, A., Topka, K., Scharmer, G. : 1990a, Solar Photosphere: Structure, Convection and Magnetic Fields, J.O.Stenflo (ed.), IAU Symp. 138, Kluwer Acad. Publ., Dordrecht, p. 147

This article was processed using the LaTeX macro package with ICM style

THE X12 LIMB FLARE AND SPRAY OF 01 JUNE 1991

V. Gaizauskas and C. R. Kerton
Herzberg Institute of Astrophysics
National Research Council of Canada
Ottawa, Canada K1A 0R6

Introduction

Preliminary results are presented from Hα observations of part of a large spray ejected when a flare classed as X12 in soft X-ray emission erupted just beyond the eastern limb around 15:00 UT on 01 June 1991 (*Solar Geophysical Data*, 1991). The Hα-scanning photoheliograph of the Ottawa River Solar Observatory picked up the spray and limb flare about 30 minutes later. Images on a scale of 15"/mm were photographed from 15:33 to 16:08 UT over a field of view of 4' x 5' every 2.5 s on 35 mm film. Between successive exposures the wavelength setting of a 0.25 A Zeiss filter was shifted one step at a time over the range ± 1.0 A in a repeating cycle of 12 steps. The spatial relationship of the spray to the flare is shown in Figure 1.

The Spray

The large speed ($\geq$ 300 km s^{-1}) and breadth typical of sprays (Smith , 1968) pose a challenge for interpreting observations made with a limited field of view and in a narrow wavelength band. Only part of the entire structure can be encompassed at one time in our fixed field. And only those sub-structures in the spray with low velocities in the line of sight are seen at any setting of our narrow pass-band - the rest are Doppler-shifted well beyond the ± 1 A total displacement in our scanning cycle. We nevertheless take advantage of our large image scale, narrow pass-band, and high time resolution to point out some previously unobserved aspects of a spray.

The most striking property of this spray is the sharp contrast between a main part consisting of many regularly curved streamers and a turbulent zone restricted to the south side of the main part. The clumps and knots of plasma that typify sprays lies within that second zone. Even though all fine structures in the spray change rapidly during a half-hour, the basic differentation persists between the large zone of regular streamers and the narrower disordered one to the south.

The moving knots of matter in the turbulent zone follow a trajectory which, nearly straight at higher altitudes, curves strongly to become more horizontal near the solar surface and passes over the activated filament near the central part of Figure 1.

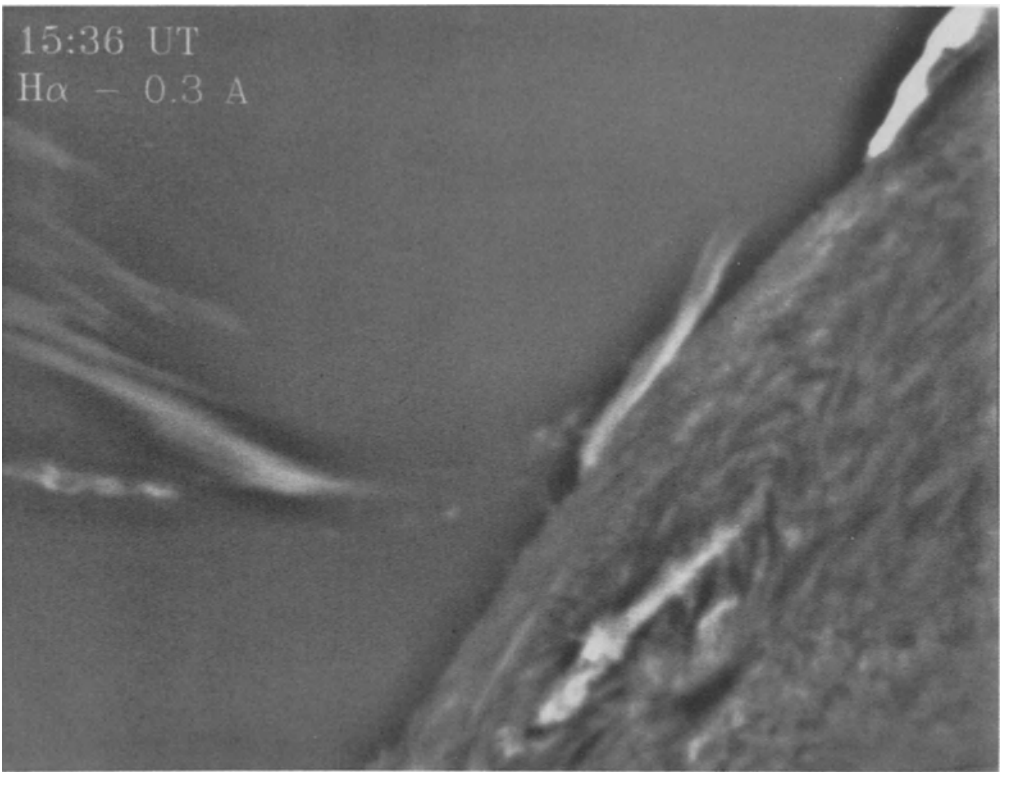

Fig.1: Computer-enhanced image of northeastern limb of the Sun in a 4' x 5' field enclosing the spray (left and centre), X12 flare (extreme top and left), and an activated filament (centre). The dark edging along the solar limb is an artifact of of the enhancing process. Orientation : east (left), north (top).

We do not witness a single knot proceeding along the entire length of that trajectory. Knots usually appear near the switchover from a horizontal to a more radial path, and elongate as they move outwards. In one instance a small cluster of knots moving at nearly 200 km s^{-1} transforms into a well-defined helicoid (Figure 2), 2 x 10^4 km long, which unravels in about 100 s.

We know that a large activity complex is approaching the eastern limb beyond the activated filament. A much smaller active region occupies the foreground of the same image. A long-lived coronal hole is located just north of the flare.We propose therefore that the spray is ejecting matter into a mound of magnetic field lines encasing the approaching activity complex. The outermost field lines of that mound probably merge with the radially-directed field of the nearby coronal hole. We interpret the narrow zone of persistent turbulent activity on the southern side of the spray as a polarity boundary in the large-scale magnetic field between the approaching activity complex and existing patterns on the visible face of the Sun. We infer from our images that the energy release responsible for the spray originates close to the surface but beyond the limb. The passage of shocks from that site along a polarity boundary would promote growth of a variety of instabilities along its length - the tearing mode, leading to the creation of magnetic

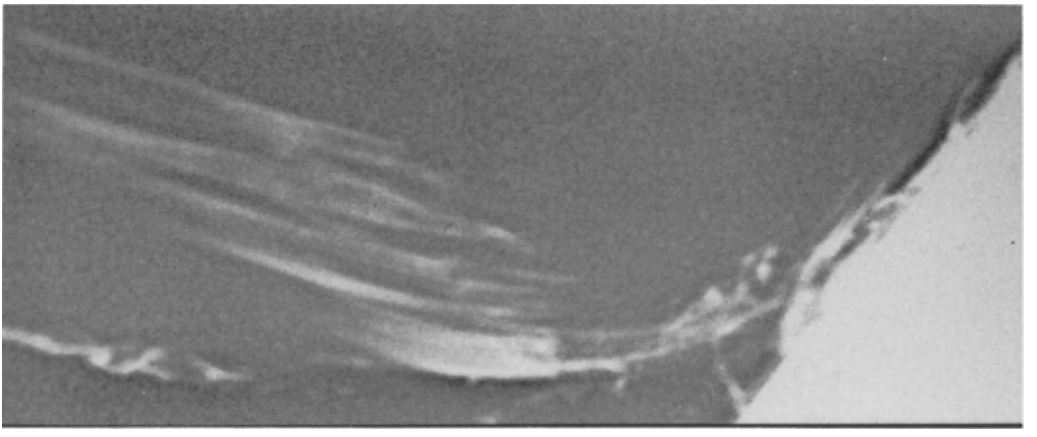

Fig.2: Computer-enhanced image of the spray in the blue wing (Hα–1 A) at 15:36 UT. A helicoid with pitch of at least 2π is clearly visible near the lower left corner. The size of the image (oriented as in Figure 1) is 250" x 100".

islands which might be manifested as the moving knots; the kink mode, becoming manifest as an unravelling helicoid.

The Limb Flare

The flare loops were inadvertantly cut off in one corner of the field of view (they were not yet visible when the spray was first sighted visually). They were observed at the early stage for only 35 min (Figure 3) in which time they changed drastically. We estimate that the topmost structure we observed was rising faster than 10 km s^{-1}. Their greatest height attained in our clipped field of view is at least 3.5 x 10^4 km .

But our most startling finding was the equally fast growth of dark matter which obscures most of the brilliant flare loops viewed in the red wing of Hα throughout our observing period. Initially almost no dark matter obscures the loops seen in the centre of the line (Figure 3, 15:33 UT). Dark arches subsequently form; they are most easily seen in the core of the line but are overwhelmed by more diffuse structures at more remote wavelengths. Our scan was limited to the range Hα ±1.0 A, but the rapid and continuing increase of absortpion with each step in wavelength makes it clear that we were still far from the wavelength of maximum absorption at the limit of our scan. The blue-wing images at the later times show some fine-scale structures running transverse to the general orientation of the growing dark arches. Lowered absorption in the core of the line compared to the wings indicates that no matter was at rest near the flare.

We conclude that in the declining stage of this huge flare cool matter was being forced under pressure from the lower atmosphere to coronal heights, not in a single structure or cloud, but as a combination: cloud and field-aligned structures. Our limited scan in wavelength precludes any estimate of the line-of-sight velocities for any of these components. The absorption is always

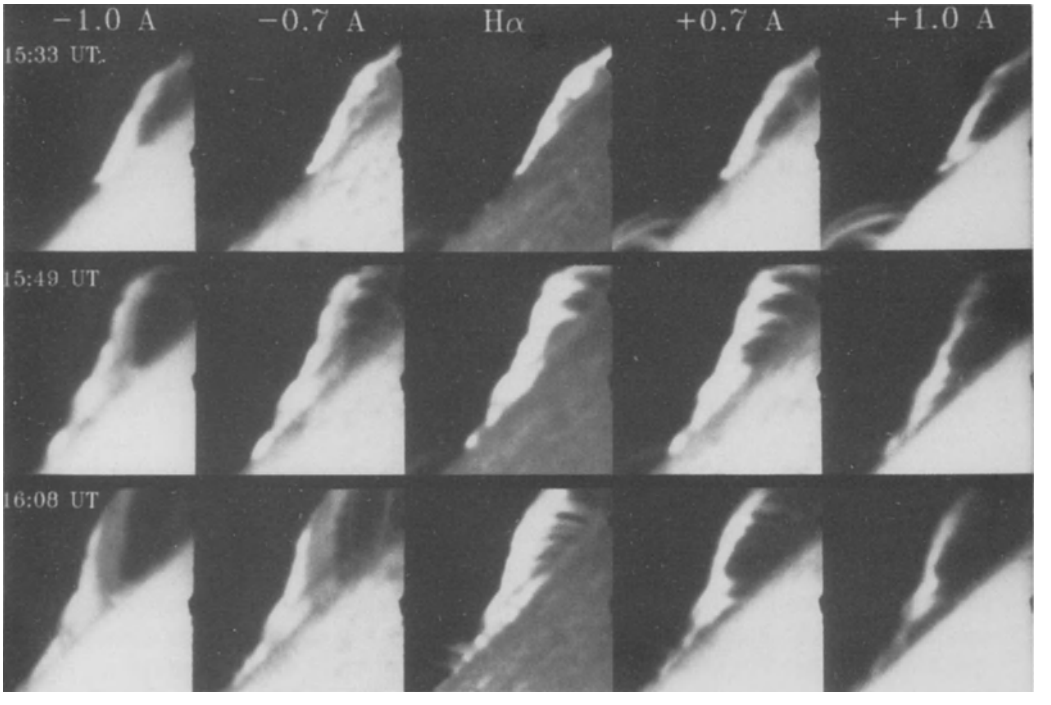

Fig.3: Rising bright loops of X12 limb flare partially obscured by absorbing matter. Each column represents a different offset in wavelength from the centre of Hα. Each row represents a different time. Orientation as in Figure 1. Size of each panel is 85" x 85".

more dominant in the red wing. Thus an expansion of cool matter towards the more remote flare prevails in this complex flow pattern and adds a new puzzle to the existing ones concerning the decay phase of flares.

Acknowledgments

We are indebted to the National Research Council of Canada for the appointment of C.R. Kerton to a Student Assistant position in the 1991 Summer Employment Program of the NRCC.

References

Smith, E. v. P.: 1968, *Nobel Symp.* **9**, 137.
Solar Geophysical Data : 1991, Nos. 563 and 564, Part 1.

ANALYSIS OF X-RAY FLARES OBSERVED BY THE SMM SPACECRAFT

A.M. Hernandez*, M.G. Rovira*, C.H. Mandrini* and M.E. Machado**
* Instituto de Astronomía y Física del Espacio, CC 67, Suc. 28, 1428 Buenos Aires, Argentina
** Dept. of Physics, University of Alabama in Hunstville, USA

Abstract. We show preliminary results of a study of hard and soft X-ray emission correlations in solar flares, using total fluxes as well as image information provided by the SMM spacecraft.

1. Introduction

In order to try and improve our understanding of X-ray signatures of solar flares, in terms of the interplay between the intervening processes of energy release, transport and dissipation, we have started a comparative study of hard and soft X-ray emission output in events observed by the HXIS instrument on the SMM spacecraft. This paper gives preliminary results from a subset of the total number of events that are currently being analyzed on a statistical basis.

2. Relationship Between Hard and Soft X-Rays

In Table I we list 19 X-ray events, which were observed in 1980 by HXIS and by the SMM Hard X-Ray Burst Spectrometer (HXRBS). The list comprises events in a wide range of X-ray intensities including some of the brightest flares recorded by HXIS, down to some of the weakest events detected by HXRBS in hard X-rays.

As representative of the soft X-ray emission output we took the spatially integrated light curves (counts/s) of emission in the HXIS bands 1 plus 2 (3.5 to 8.0 keV hereinafter SXR). For the hard X-rays, we considered: (a) 16 to 30 keV records from the HXIS imaging data (HXR); (b) 22 to 30 kev records the HXIS High Energy Monitor (HEM), which had no spatial resolution but higher sensitivity than the imaging data; (c)> 25 keV full Sun emission recorded by the HXRBS (HXRBS). For each of these we measured peak counting rates, the slopes during the rise phase of the emission and total duration. Due to low sensitivity, the HXR duration is the most uncertain parameter in the HXIS data analysis, followed by the HXR slope in the weakest events.

The correlation between various pairs of these parameters is plotted in Figure 1. In spite of good overall correspondence, the plots also show considerable scatter when looking at individual events. The calculated correlation coefficients range from 0.70 for the SXR slope vs HXR slope, to 0.96 for the SXR vs HEM counting rates. From this, we infer that a causal relationship between processes that lead to HXR and SXR emission is apparent from the data, as shown by other studies (see e.g. Tandberg-Hanssen and Emslie, 1988 for a review; Dennis, these proceedings), but we also find it worthwhile to investigate the causes of the observed scatter, which is far larger than statistical uncertainties in the brightest events.

3. Discussion

In order to understand the implications of analyses such as the one in the previous section, one has to keep in mind that there is no such a thing as a "standard" solar flare (Martens and Kuin, 1989; from a quotation by H. Dodson-Prince). Understanding why different flares "look different"

is thus important, to learn about the sometimes subtle interplay between radiation signatures and energy transport and dissipation processes.

TABLE I.
Peak Counting Rates

Date UT	SXR/HXIS (c/s)	HEM/HXIS(c/s)	HXRBS(c/s)
Apr 7 1:10	1538	2.4	600
Apr 8 3:07	2061	24.0	3800
Apr 13 4:09	635	5.7	800
Apr 13 8:43	33	4.6	2000
May 8 13:44	467	3.2	440
May 9 7:14	3194	52.8	10800
May 21 20:55	3576	66.4	14300
July 14 8:25	3363	30.0	5332
July 20 19:27	744	19.0	2624
Nov 1 19:22	511	10.4	1004
Nov 2 2:11	225	2.0	–
Nov 5 22:35	1902	14.5	12730
Nov 10 8:14	667	4.1	341
Nov 11 6:32	335	4.7	526
Nov 11 17:25	627	11.7	3694
Nov 11 20:54	1306	11.9	894
Nov 11 23:48	261	2.8	388
Nov 12 2:51	795	8.7	968
Nov 12 17:00	548	9.1	600

Looking at Figure 1, we see first an excellent correspondence between HEM and HXRBS measurements. This is not surprising, since both overlap within the 25 - 30 keV energy range, where a major contribution to the HXRBS recorded emission resides. Such a clear correspondence is not seen in the HXR vs HXRBS comparison, with HXR extending down to 16 keV. Two flares in particular, May 21 and July 14, show significant and oppositely directed changes in their location within the diagram. Similar scatter and changes are seen in the SXR vs HXRBS and SXR vs HXR plots. One event, May 9, stands out quite clearly in all plots wich involve d(SXR)/dt, while considerable scatter and/or lack of correlation is observed in the SXR vs d(HXR)/dt and d(SXR)/dt vs d(HXR)/dt plots.

On the other hand, particular characteristics of flares that we have singled out are:

a) The May 21 flare is a long duration eruptive event (de Jager and Svestka, 1985). b) The May 9 flare is the most compact X-ray event in our selected list of HXIS flares (Machado, 1983; Machado et al., 1988). c) The July 14 event is a composite compact plus eruptive event, with the X-ray lightcurve dominated by the short-lived compact source which occurred in high density

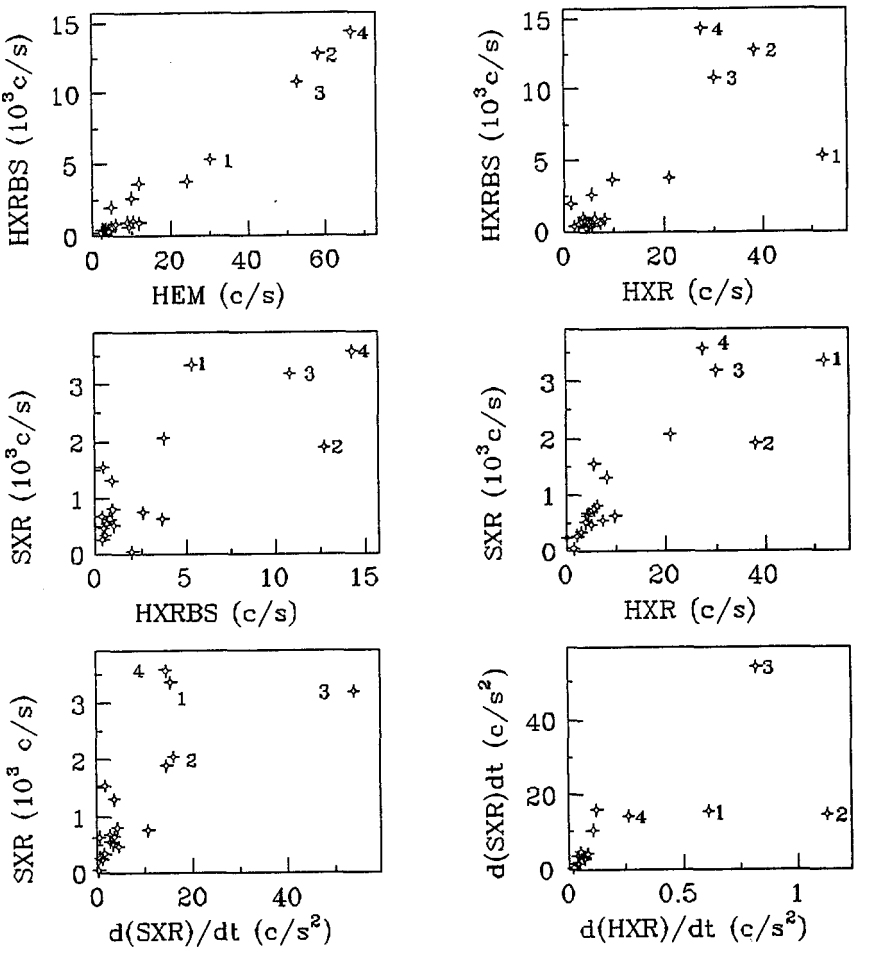

Figure 1. Various correlations between observational quantities. 1) Jul 14 flare, 2) Nov 5 flare, 3) May 9 flare, and 4) May 21 flare.

($>10^{11}$ cm^{-3}) low-lying loops (Machado et al., 1985, 1988). d) The November 5 flare is also rather concentrated, but occurred right after (7 minutes) another weaker event with similar morphology and location. This flare thus occurred during the decay of the prior event, which was still bright in SXRs (Duijveman et al., 1982) e) Both the April 7 (01 UT) and April 8 events are multiple loop flares which extend over the whole active region (Machado et al., 1983). However, the one on April 7 is a long duration, weak, flare in hard X-rays, while the April 8 event is more concentrated in X-ray images and shows a more impulsive HXR burst of shorter duration.

Combining the results of the correlation study with these particular characteristics of individual events, we can now extract some preliminary conclusions. The risetime of soft X-ray

emission relates more to the sizescale of the event than any other factor like e.g. burst impulsiveness, as notably shown by the May 9 event. This, combined with the behavior of similarly compact events occurring in dense preflare regions (e.g. July 14, November 5), confirms that chromospheric evaporation plays an important role in SXR flare development. Also, in dense events, a substantial fraction of the emission observed at around 20 keV may be thermal. This is apparent from the changes observed in the comparison of HXRBS/HEM and HXRBS/HXR plots, particularly in the case of the July 14 event. Results by Machado et al. (1985) and Li and Emslie (1990), have shown that even in nonthermal hard X-ray burst models beam heating can create hot plasma that contributes to the observed output at such energies. According to Li and Emslie (1990), it is plausible that all flares show such "thermal contamination" to some, extent, but only in dense flares it becomes obvious to studies such as ours. Finally, the behavior of the April 7 (01 UT) event, which shows relatively high SXR peak value in all correlations, shows that duration is more important, again in relative terms, than impulsivity or hard X-ray peak intensity. As already noted, this event showed a long duration weak hard X-ray burst, again signaling a causal relationship between processes leading to HXR and SXR emission. A similar behavior, in terms of the importance of overall burst duration, is implied by the May 21 data, but the strength of the correlation is somewhat masked in this flare, by the fact that it also showed the strongest HXR peak in our list of events.

References.

de Jager, C., and Svestka, Z.: 1985, Solar Phys., **100**, 435.
Dennis, B.R., Uberral, B.M., and Zarro, D.M., these Proceedings.
Duijveman,A, Hoying, P., and Machado, M.E.:1982, Solar Phys., **81**, 137.
Li, P., and Emslie, A.G.:1990, Solar Phys., **129**, 113.
Machado, M.E.: 1983, Solar Phys., **89**, 133.
Machado, M.E., et al.: 1983, Solar Phys., **85**, 157.
Machado, M.E., Rovira, M.G., and Sneibrun, C.: 1985, Solar Phys. **99**, 189 .
Machado, M.E. et al.: 1988, Ap.J., **326**, 451 (Paper II).
Martens, P.C.H., and Kuin, N.P.M. : 1989, Solar Phys., **122**, 263.
Tandberg-Hansenn, E. and Emslie, A.G.: 1988, The Physics of Solar Flares, Cambridge Univ. Press., Cambridge.

DISTRIBUTION FUNCTION FOR ELECTRON BEAMS IN THE CHROMOSPHERE

P.J.D. Mauas[1], and D. Gómez[2]
1 Osservatorio Astrofisico di Arcetri - Italy
2 Institute for Astronomy, University of Hawaii - U.S.A

Introduction

The interaction of electron beams with the solar atmosphere during flares has been studied for several years. Flare-associated hard X-rays, microwave and H_α emission are generally explained as the consequence of this interaction, as well as the heating of at least part of the chromosphere. Electron beams have also been proposed to explain the continuum emission in white-light flares (*e.g.* Hénoux and Aboudarham, these proceedings).

On the other hand, non-thermal excitation and ionization of neutral hydrogen in the chromosphere by these accelerated electrons can be the cause of a number of effects usually attributed to the chromospheric heating (see *e.g.* Mauas and Machado 1986). Therefore, semiempirical models can overestimate the heating by neglecting the enhancement in the radiation produced by non-thermal processes (Aboudarham and Hénoux 1986, 1987).

In a previous work (Gómez and Mauas, these proceedings, hereinafter GM), we formulate the Fokker-Planck equation for an electron beam incident on the solar chromosphere, including the effect of collisions with electrons, protons and neutral hydrogen and helium. In the present work we present the results of the integration of that equation, and the calculation of the energy deposition and non-thermal collision rates for a beam incident on a quiet-Sun atmosphere.

Results

In this work we integrate the Fokker-Planck equation for a stationary beam with no magnetic trapping, as expressed by GM. As the underlying atmosphere we used the quiet-Sun model C by Vernazza *et al.* (1981), as modified by Avrett (1985). For the input beam we assumed the distribution function

$$f(v,\theta,z=0) = f_0 \left(\frac{v}{v_0}\right)^{-\eta} e^{-\theta^2/\alpha} \quad .$$

Here v_0 is the cutoff velocity (we used the velocity corresponding to a cutoff energy of 20 keV), $\eta = 2.\delta + 1$, where $\delta = 5$ is the spectral index for the energy flux, and $\alpha = 0.3$. For $v < v_0$ we assumed $f(z = 0) = 0$. This assumption has little effect on the main features of the solution. The normalization constant f_0 corresponds to an input energy flux of 10^9 erg cm^{-2} s^{-1} (Machado, Emslie and Brown 1978). Details on the numerical code are given in Mauas and Gómez (1991).

Once the distribution function at each height is known, it is straightforward to compute the energy deposition. The results are presented in Figure 1, comparing them with the results obtained with a test-particle approach, like the one by Emslie (1978). Note that the expression in Emslie (1978) diverges for low column mass, and should be corrected as in Duijveman *et al.*. (1983). It can be seen in Figure 1 that, due to the inclusion in our calculations of an angular dispersion in the incident beam, the energy deposition is somewhat smoother than for the test-particle approach, though the main characteristics remain the same.

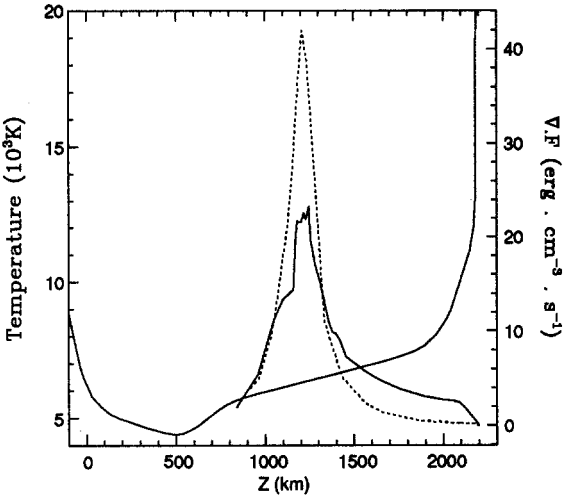

Figure 1. Energy deposition. As a reference, the atmospheric model is shown. *Full line*: Fokker-Planck treatment. *Dotted line*: Test particle aproach.

In Figure 2 we show the non-thermal collision rates, obtained from the computed distribution functions. In all cases, they were computed using Born-approximated cross-sections (Mott and Massey 1949), and integrating them with the computed distribution function. For comparison, we include the thermal rates, obtained from the expresion given by Vernazza *et al.* (1981). As can be seen, the non-thermal rates for excitacion

of the Lyman lines and the Lyman continuum can be orders of magnitude larger than the thermal ones, and this effect can be of great importance when studying the chromospheric response to the flare. This is not true for the H_α excitation rate, due to the fact that the thermal rate is much larger in this case.

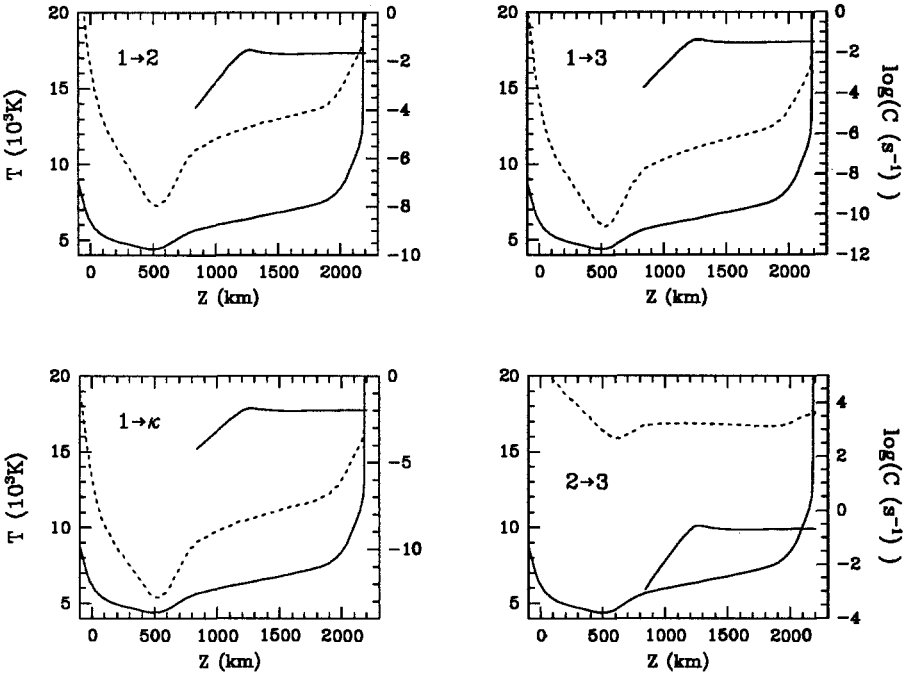

Figure 2. The collision rates obtained from the computed distribution function, compared with the thermal ones. The levels involved are indicated inside each panel (κ denotes the continuum). As a reference, the atmospheric model is shown. *Full line*: Non-thermal rate. *Dotted line*: Thermal rate.

Discussion

Note that the excitation rate is almost constant from the injection level to the region where the energy is deposited. This is due to the fact that the fraction of the energy lost by the beam due to inelastic processes is so small that the distribution function remains almost unchanged. On the other hand, the energy deposition peaks very sharply at a column mass depending on the position of the energy cutoff.

To investigate the effect of an abrupt energy cutoff, we made some runs with a different distribution function at injection. Instead of assuming $f(z = 0) = 0$ for $v < v_0$, we

assumed a quadratic distribution function up to 20 keV. The main characteristics of the solution remain the same.

Thus, the effect of the precipitation of an electron beam on the chromosphere has two components. In the high chromosphere the signature of the beam can be found in the collisional excitation and ionization rates, while in the mid-chromosphere an abrupt deposition of energy takes place. To study the response of the chromosphere to the flare and its spectral signatures, a self-consistent model is required, including the effects not only of an enhanced temperature, but also of the non-thermal effects of the electron beam.

References

Avrett, E.H. 1985, in *Chromospheric diagnostic and modelling*, ed. B. W. Lites, (Sunspot, N.M.: National Solar Observatory), p. 67.

Aboudarham, J., and Hénoux, J.C. 1986, *Astr. Ap.*, **156**, 73.

Aboudarham, J., and Hénoux, J.C. 1987, *Astr. Ap.*, **174**, 270.

Duijveman, A., Somov, B.V., and Spektor, A.R. 1983, *Solar Phys.*, **88**, 257.

Emslie, A.G. 1978, *Ap. J.*, **224**, 241.

Machado, M.E., Emslie, A.G., and Brown, J.C. 1978, *Solar Phys.*, **58**, 363.

Mauas, P.J., and Gómez, D. 1991, in preparation.

Mauas, P.J., and Machado, M.E. 1986, in *The Lower Atmosphere of Solar Flares* (Sunspot, NM: National Solar Observatory), p. 192.

Mott, N., and Massey, H. 1949, *Theory of Atomic Collisions* (2nd. ed., Oxford: Clarendon).

Vernazza, J., Avrett, E.H., and Loeser, R. 1981, *Ap. J. Suppl.*, **45**, 635.

SUB-SECOND VARIATIONS OF HXR AND H-ALPHA FLARE EMISSION

P. Heinzel and M. Karlický

Astronomical Institute
25165 Ondřejov, Czechoslovakia

Abstract

For a series of electron beam pulses, we have computed the time-dependent chromospheric heating and the corresponding hard X-ray (HXR) flux. Moreover, by solving the time-dependent NLTE problem for hydrogen, we theoretically predict the Hα-line intensity variations on sub-second time scales. Both HXR-fluxes and Hα wing intensities do exhibit a spiky behaviour, consistent with short pulse-beam heating. However, the spikes in Hα are unexpectedly 'inverse', i.e. the line intensity *decreases* during the beam heating. They correlate rather well with HXR emission peaks computed for 24 keV channel. We compare our theoretical results with recent observations of Kiplinger et al. (1991).

1. Pulse-Beam Heating of the Solar Atmosphere

Starting from commonly accepted hypothesis that high-energy electron beams heat the solar atmosphere during the impulsive phase of a flare, Karlický (1990) and Karlický and Hénoux (1991) have constructed a series of new hydrodynamical flare models. They use a particle representation of the electron beam, thus accounting for the finite travel time of electrons and the general form of the beam distribution function. Such a particle approach also allows direct evaluation of the HXR radiation, which is not possible with a hydrodynamical code alone. A response of the solar atmosphere is modelized using the standard set of 1D hydrodynamical equations which describe the vertical structure of the flare. An initial model at t=0 is that of Vernazza et al. (1981) and for t>0 the depth-dependent temporal variations of the kinetic temperature T(t), electron density $n_e(t)$ and other parameters are obtained. While Karlický (1990) has presented the solution only for one short-duration beam pulse, in this paper we demonstrate the

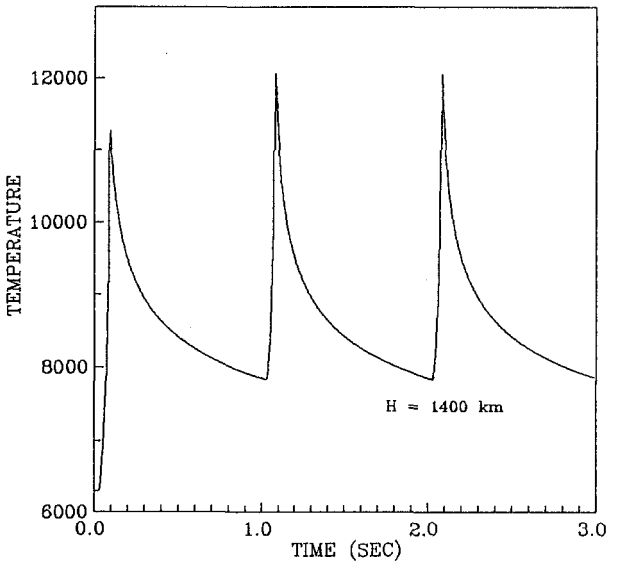

Fig. 1
Temporal profile of the kinetic temperature for three beam pulses, each lasting approximately 0.1 sec. H=1400 km is the chromospheric height where the heating was computed.

behaviour of a series of three subsequent identical pulses each of them lasting 1 sec. On this scale, 0.1 sec interval corresponds to a heating time (the beam is switched-on) and 0.9 sec is the cooling period (relaxation). In Fig. 1 we show the temperature profiles for such three pulses at the chromospheric height H=1400.

2. Hα Response to Pulse Beam Heating

As a next step, Heinzel (1991a,b) has developed the NLTE code for solving time-dependent hydrogen rate equations for a three-level model atom with continuum. Since the time-step is typically less than 10^{-2} sec (an adaptive time mesh is used in all simulations), several simplifications have been necessary in order to make the code reasonably fast. Net radiative brackets in the rate equations have been replaced by escape probability functions for Hα and Lyman continuum . Both Lyman lines are put into detailed radiative balance in the region where Hα is formed. Subordinate continua are optically

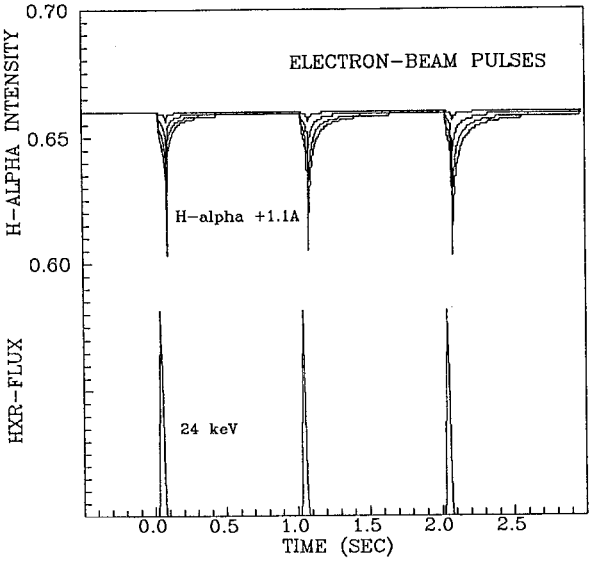

Fig. 2
Temporal variations of HXR flux (24 keV, arbitrary units) and the corresponding Hα + 1.1Å intensity (normalized to disk-center continuum intensity). Lower Hα intensities correspond to thicker emitting layers (from 100 km to 1500 km).

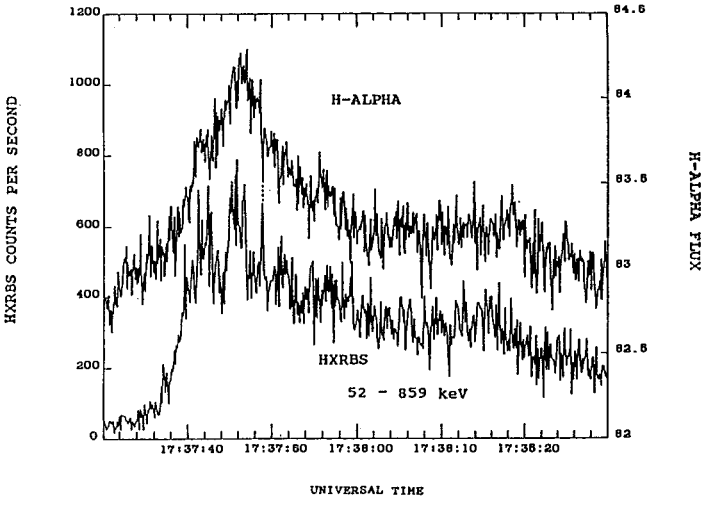

Fig. 3
Hα and HXRBS observations of 30 June 1989 flare taken from Kiplinger et al. (1991). Hα flux is integrated from two brightest flare kernels. An example of the inverse Hα spike (hump), well correlated with HXR emission peak, is indicated by a dotted line.

thin with their radiative rates fixed by the photospheric radiation fields. Numerical solution of such NLTE rate equations was performed at selected depths, in this case for H=1400 km where the Hα line wings are supposed to be formed (for further details see Heinzel, 1991b). As the input for this NLTE code we have used only the temporal profile T(t) as shown in Fig. 1. The corresponding electron densities $n_e(t)$ are then consistently evaluated by the NLTE code. Therefore, we don't use $n_e(t)$ previously evaluated by Karlický 's hybrid code because this code incorporates, as a first approximation, simplified ionization formula of Brown (1973).

3. Results

For a series of three electron-beam pulses, we have evaluated the temporal profiles of HXR-fluxes for 24 keV channel and the Hα-wing intensity at Hα + 1.1Å (Fig. 2). We have found rather good correlation between HXR and Hα , but the Hα wings exhibit 'inverse' spikes (humps) rather than expected emission peaks. This is due to a higher rate of the second-level population as compared to that for third level (i.e. during the heating process). A comparison of these theoretical results with Hα and HXRBS/SMM data recently presented by Kiplinger et al. (1991) (see Fig. 3) indicates that the predicted sub-second spikes may be of real importance during the impulsive phase of solar flares. Therefore, we propose to conduct coordinated Hα and hard X-ray observations with sub-second temporal resolution, possibly at different sites in order to exclude the effects of seeing and instrumental noise. Statistically significant correlation between Hα-humps and HXR-spikes would support the model of the pulse-beam heated chromosphere.

References

Brown, J.C.: 1973, *Solar Phys.* 31, 143.

Heinzel, P.: 1991a, in *'Dynamics of Solar Flares'*, Flares 22 Workshop, eds. B. Schmieder and E.R. Priest, Observatoire de Paris, DASOP, 69.

Heinzel, P.: 1991b, *Solar Phys.*, in press.

Karlický, M.: 1990, *Solar Phys.* 130, 347.

Karlický, M. and Hénoux, J.-C.: 1991, *Bull. Astron. Inst. Czechosl.* 42, 22.

Kiplinger, A.L., Labow, G., and Orwig, L.E.: 1991, in *Max '91 Workshop # 3*, eds. R.M. Winglee and A.L. Kiplinger, University of Colorado, Boulder. 210.

Vernazza, J.E., Avrett, E.H., and Loeser, R.: 1981, *Astrophys. J. Suppl.* 45, 635.

THE ROLE OF PROTONS IN SOLAR FLARES

HERISTCHI, D. and BOYER, R.
URA 326, DASOP, Observatoire de Paris, Section de Meudon
MEUDON, FRANCE

The main sources of evidence for the presence of high energy protons and other nuclei in the solar atmosphere during flares are the recorded nuclear γ-ray lines and neutrons (Chupp 1987; Dennis 1988). The interaction of high-energy protons with the ambient electrons can produce the observed continuous $X-$ray and $\gamma-$ray radiation. This process of production has been discarded by several authors because of the number of protons needed to produce X-rays this way. Emslie and Brown (1985) have pointed out that, in a thick target, a proton produces about 1836 times more photons in the low-energy range than an electron having the same velocity. This is due to the fact that the energy loss rate of the two particles is approximately the same when they are travelling at the same velocity. These authors then find a discrepancy of three orders of magnitude. In their work, however, the interaction of fast protons with ambient electrons is assumed to be strictly equivalent to the interaction of fast electrons with ambient protons.

The "proton-electron bremsstrahlung" interaction has been thoroughly investigated (Heristchi 1986, 1987) and its main characteristics were found to differ considerably from electron-proton bremsstrahlung. A model of solar X-ray production is therefore proposed that easily explains the global characteristics of X-rays and $\gamma-$rays from solar flares. A high-energy proton spectrum is posited in the solar atmosphere, with protons spiraling in an ambient magnetic field, assumed to lie perpendicular to the solar surface, and having a nearly horizontal fan-beam distribution. The X-ray spectrum from such a distribution can be calculated easily, for thick target production. An example of the expected spectrum is given in Figure 1, where a curve labeled 90° concerns a limb event and 0° a disk-center event. Note that for limb events there is an extensive spectrum through a large range of energy. With a proton spectrum limited to 8 GeV, the photon spectrum extends to about 80 MeV, while the corresponding energy of electrons having the same velocity as the protons is only 4.3 MeV. Some expected characteristics of solar flares predicted by our model are shown in this figure. In the low energy range of the X-ray spectrum ($0.01 - 0.1\,MeV$), there is a small amount of directivity in the radiation. This verifies the measured low directivity of flare emission by "spectroscopic" observations from two spacecraft (Kane *et al.* 1980). An extensive spectrum over a large energy range is predicted for events on or near the limb. The $\gamma-$ray

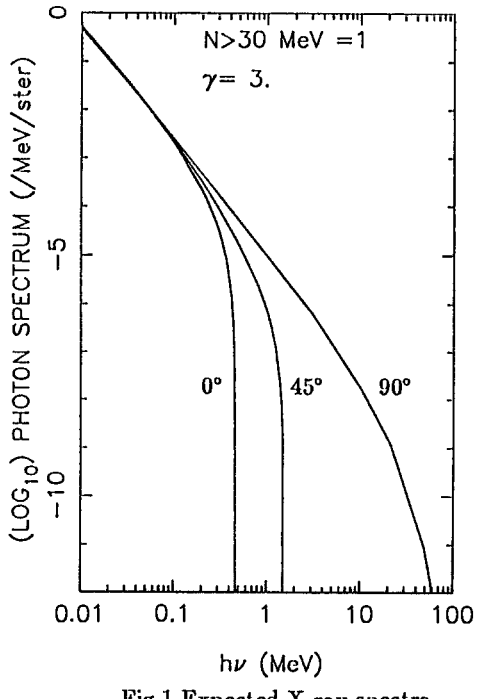

Fig.1 Expected X-ray spectra

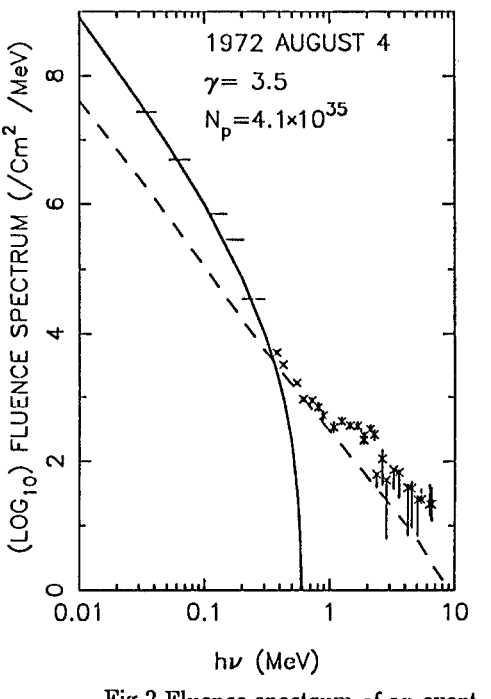

Fig.2 Fluence spectrum of an event

continuum with energies of more than $10\,MeV$ is detected only from near-limb events (Rieger *et al.* 1983). The role of secondary or knock-on electrons is also considered. In the low-energy range, these electrons produce X-rays with an intensity significantly lower than that of the proton-electron bremsstrahlung ($\approx 5\%$, Emslie and Brown 1985). For disk events where the X-ray spectrum from protons is limited, X-rays from knock-on electrons are the principal source of radiation in the high-energy range. For such an event, then, we predict a spectrum with a break at approximately $0.1\,MeV$ and a second change of spectrum at $0.3 - 0.4\,MeV$. An example of such a spectrum is given in Figure 2. We show that there is good agreement between the theoretical curve and the measured data.

We have shown that the proton model can explain many aspects of the observed characteristics of the solar flares. As mentioned above, certain quantitative questions concerning the number of protons have been used to discard this model, despite what it has accomplished.

Figure 3 shows an example of the fluence spectrum of an X-ray event, compared with the expected X-ray spectrum from proton-electron bremsstrahlung. In Figure 4 the proton spectrum needed for X-ray production (B) is compared with that obtained (R) from neutron measurement

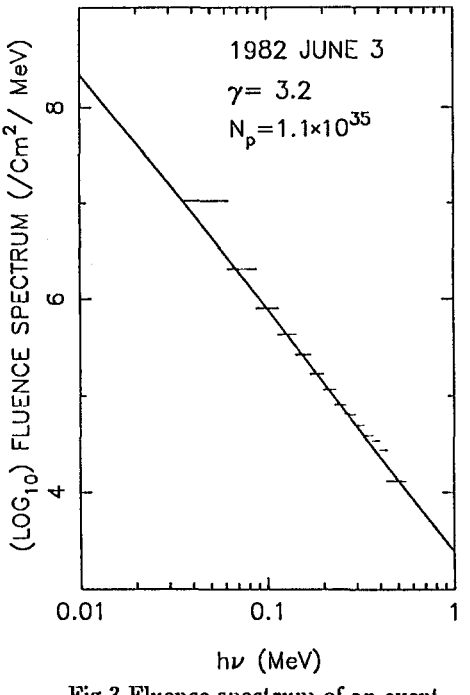

Fig.3 Fluence spectrum of an event

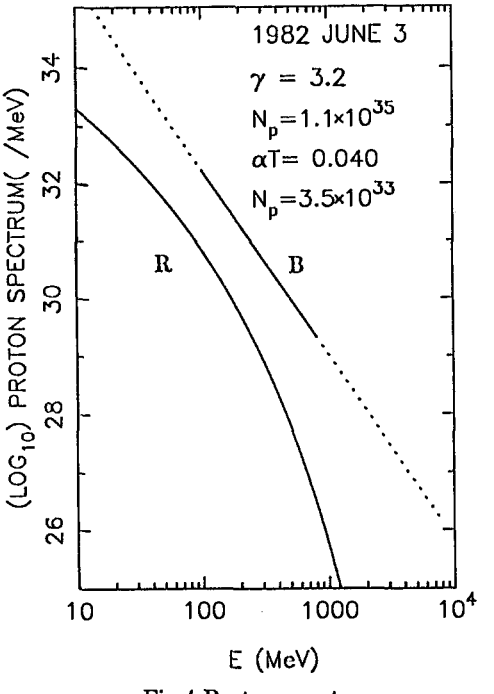

Fig.4 Proton spectra

(Ramaty and Murphy 1987). We see that the discrepancy is on the whole of one order of magnitude. Such a discrepancy can be explained easily by considering the differential cross section for neutron production.

The characteristics of solar high energy radiations and of the particles detected in interplanetary space can be very useful in understanding the solar flare mechanism. It is generally accepted that, in interplanetary space, the electron-to-proton ratio varies greatly from event to event (Lin 1974). For the solar atmosphere, the relation between the number of protons and that of electrons is well known (continuum > 300KeV X-ray intensity, Forrest 1983). There is also a lack of correlation (Cliver *et al.* 1989) between the proton number in space and in the Sun (γ–ray line intensity). There are three different possible explanations for these facts: 1) particles in the solar atmosphere and space come from two distinct sources, each having its own acceleration mechanism; 2) there is a single acceleration, and only a non-significant part of particles goes into space; 3) the X-rays

come from proton interaction with the ambient electrons, in which case one part of the protons goes through the solar atmosphere and produces X-rays, γ–ray lines, while the other part of the protons and all the electrons go into space.

Examining the other experimentally established characteristics of flares gives us some help in choosing between these three possibilities. For instance the ^{3}He abundance, which varies from event to event, is sometimes very high and cannot be easily explained by the first hypothesis, nor can the presence of partially ionised ^{4}He in space. Then the second hypothesis can be discarded, since by direct comparison we know that sometimes the proton number in interplanetary space is higher than in the solar atmosphere (Ramaty and Murphy 1987).

The third hypothesis explains the electron-to-proton ratio easily and offers a solution for the ^{3}He abundance, its variations, and the partially ionised ions. To explain the particle separation (protons in the solar atmosphere and space, electrons only in space) a closed magnetic structure (closed relative to the solar atmosphere) is needed. A part of protons that have high magnetic rigidity can leave this magnetic structure and interact with the solar atmosphere, while electrons and the rest of the protons are trapped in this magnetic structure and go with it into space. To carry out this scenario, a low density plasmoïd was proposed that originates deep in the photosphere and rises under magnetic and buoyancy forces (Heristchi *et al.* 1989)

This rapid examination of certain aspects of high-energy phenomena during flares shows that our model can easily explain many aspects of energy transport in the solar atmosphere.

Chupp, E. L. 1987, Physica Scripta, T18, 5.
Cliver, E. W. *et al.* 1989, Ap. J., 343, 953.
Dennis, B. R. 1988, Solar Phys., 118, 49.
Emslie, A. G., and Brown, J. C. 1985, Ap. J., 295, 648.
Forrest, D. J. 1983, in *Positron-Electron Pairs in Astrophysics*, ed. M. L. Burns, A. K. Harding, and R. Ramaty (New York : AIP), p. 3.
Heristchi, D. 1986, Ap. J., 311, 474.
Heristchi, D. 1987, Ap. J., 323, 391.
Heristchi, D., Raadu, M. A., Vial, J.-C., and Malherbe, J.-M., 1989, *Solar and Stellar Flares.* I.A.U. Collo. No. 104, Poster Papers, eds. B. M. Haisch and M. Rodono, p. 321.
Kane, S. R., Anderson, K. A., Evans, W. D., Klebesadel, R. W., and Laros, J. G. 1980, Ap. J. (Letters), 239, L85.
Lin, R. P. 1974, Space Sci. Rev., 16, 189.
Ramaty, R., Murphy, R. J. 1987, Space Sci. Rev., 45, 213.
Rieger, E., Reppin, C., Kanbach, G., Forrest, D. J., Chupp, E. L., and Share, G. H. 1983, *Proc. 18th Internat. Cosmic Ray Conf.*, 10, 338.

HIGH SPECTRAL RESOLUTION OF MM-WAVELENGTH (23 - 18 GHz) SOLAR BURSTS

H.S.Sawant, R.R.Rosa, J.R.Cecatto, F.C.R.Fernandes
Instituto Nacional de Pesquisas Espaciais - INPE
Astrophysics Division
P.O.Box 515, CEP 12201 S.J.Campos, SP, Brasil

Extended Abstract:

Variable frequency mm-wavelength, (23-18 GHz) radiometer, with frequency resolution of 1 GHz and variable time, (16-0.6) sec, resolution, in conjunction with a 13.7 m antenna, located in Itapetinga, São Paulo, Brazil, has been put into operation since 1988 for investigations of spectra of active region, before and after the flare and that of the burst components. Solar observations are carried out quarterly for about 15 to 21 days.

So far, 20 groups of the microwave bursts, mostly associated with SF flares, have been observed. Most of these bursts are weak (Fig. 1). More interesting are those low level (< 5 s.f.u.) spiky bursts of duration of the order of 1 sec superimposed on gradual bursts of the duration of 10 sec (Fig. 2). Spike bursts exhibit nearly symmetrical rise and fall time. In some cases fall time is little longer than rise time. At 90 GHz similar bursts have been also observed (Gopalswamy N., personal communication). We define "simple solar microwave bursts" as exhibiting one peak and total duration lasting less than five seconds. These bursts are investigated in search of possible response to single ejection of energetic electrons (~300 keV).

Available high spectral resolution data showed that all frequencies peaked simultaneously within the time resolution. Also, most of the observed bursts did not show obvious frequency fine structures to the limit of our frequency resolution.

Some of the above bursts are investigated jointly with X - rays obtained from HXRBS data and microwave data obtained from OWENS VALLEY, for better understanding of time evolution of particle acceleration.

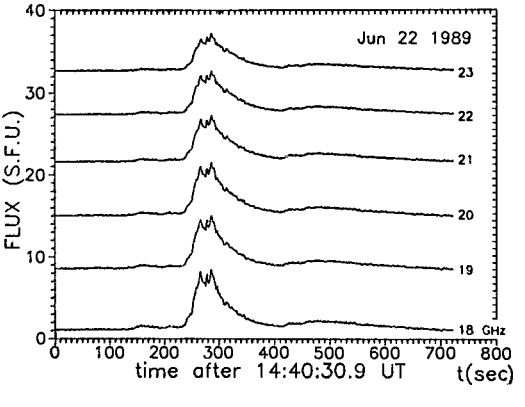

Fig.1 - Observed high spectral weak microwave burst in June 22 1989.

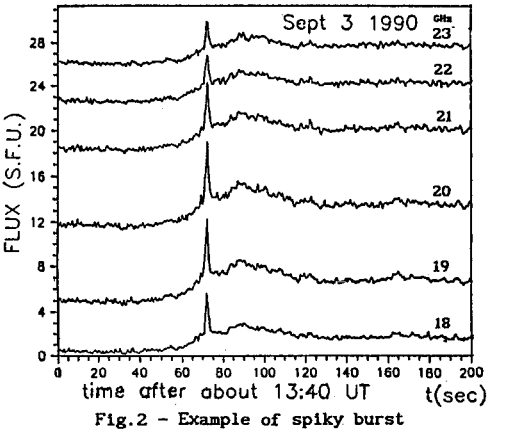

Fig.2 - Example of spiky burst superimposed on gradual one, in September 3 1990.

Microwave flare characteristics in 8 and 3 mm Metsähovi measurements compared with optical and H-alpha data

S. Pohjolainen, S. Urpo, H. Teräsranta, M. Tornikoski

Metsähovi Radio Research Station
Helsinki University of Technology
02150 Espoo, Finland

Abstract: In 1989-1990 several microwave bursts were detected at 37 and 90 GHz (8 and 3 mm wavelengths, respectively) during solar mapping or source tracking at the Metsähovi Radio Research Station, Finland. Nine of the events are analysed and discussed in this paper.

1 Observations

Microwave bursts recorded in mapping mode on June 20, June 21, and September 29 in 1989, and April 3, April 4, April 5, May 13, May 15, and May 28 in 1990 were chosen to analyse the positions, rise and fall times, intensities and area sizes of the bursts. They were also compared with the Solar Geophysical Data information on H-alpha, prominence and filament features occuring at the same time. One solar map of each day is presented in Figure 1. In Figure 2 are the intensity profiles of the nine bursts. The levels are relative to the quiet Sun (level 1.0 representing the brightness temperature 7800 K at 37 GHz and 7200 K at 90 GHz).

On September 29, 1989, a large area of enhanced brightness temperature was visible as far as 0.5 $r_\odot$ outside the solar limb. On April 3-5, 1990 the active region 6007 produced a large burst each day. The burst area on the first day was estimated to be 5-10 degrees behind the limb. The activity came down to normal level in one hours time. The bursts on April 4 and 5 had similar basic structure (rise and fall), although the one on April 4 had two intensity peaks. The time between these maximums was around 5 minutes. The assembled data on microwave bursts is presented in Table 1.

2 Conclusions

In comparing the information on microwave bursts and the data available on H_α flares, active prominences and filaments, we find that the microwave bursts correlate well with H_α flares but are connected with very different types of prominence and filament structure, see Table 2. Although we must have in mind that the sample here is too small to draw any tenable conclusions. We also know from experience that if the comparison is done with the original optical data, more features correlating with microwave bursts can be found.

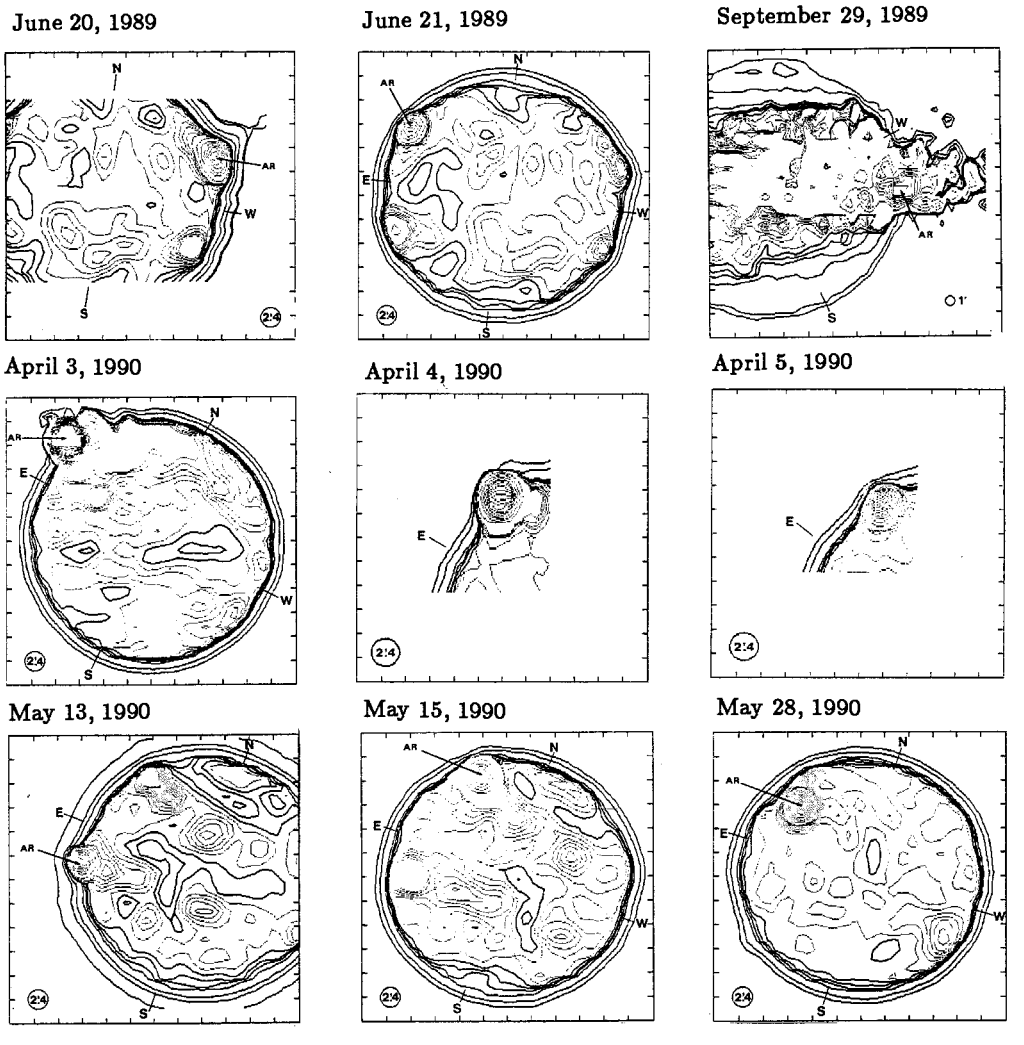

Fig. 1. Solar maps measured at Metsähovi:
June 20, 1989 at 15.14-15.23 UT (37 GHz)
June 21, 1989 at 12.12-12.40 UT (37 GHz)
Sept. 29, 1989 at 11.12-11.40 UT (90 GHz)
April 3, 1990 at 08.03-08.32 UT (37 GHz)
April 4, 1990 at 13.23-13.26 UT (37 GHz)
April 5, 1990 at 13.51-13.55 UT (37 GHz)
May 13, 1990 at 12.44-12.53 UT (37 GHz)
May 15, 1990 at 13.07-13.16 UT (37 Ghz)
May 28, 1990 at 05.01-05.29 UT (37 GHz).
The beam size is 2.4 arc min at 37 GHz and 1.0 arc min at 90 GHz. The darker lines represent levels below the estimated quiet Sun level. The analysed active regions are marked AR in the maps.

Fig. 2. (next page) Intensity profiles of the nine bursts, time (hours) versus relative intensity. The intensity value from each map is marked with an x.

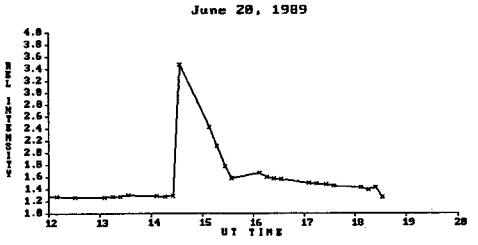
June 20, 1989
UT TIME

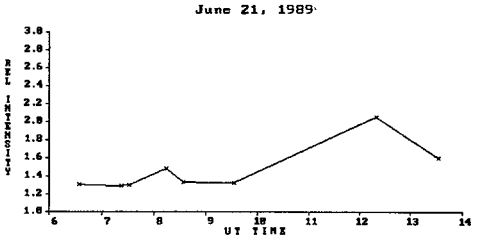
June 21, 1989
UT TIME

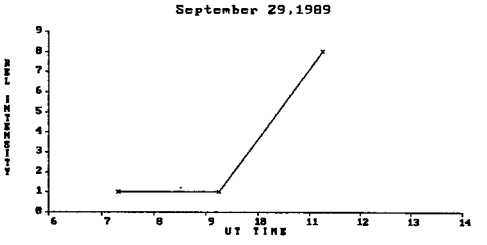
September 29,1989
UT TIME

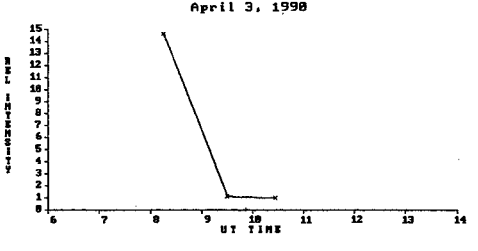
April 3, 1990
UT TIME

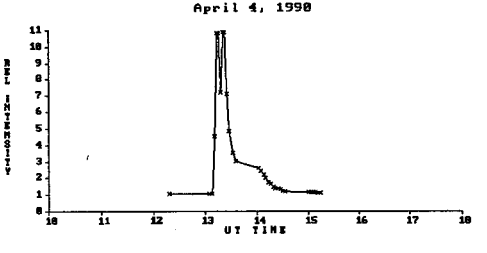
April 4, 1990
UT TIME

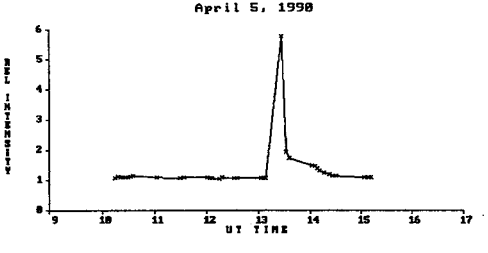
April 5, 1990
UT TIME

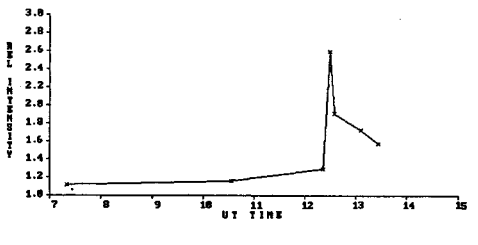
May 13, 1990
UT TIME

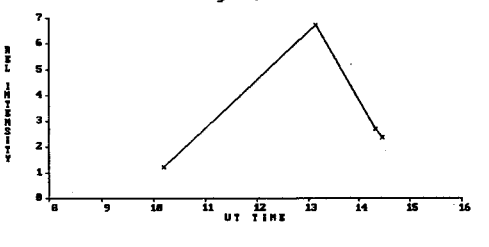
May 15, 1990
UT TIME

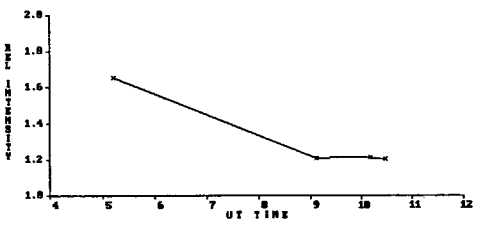
May 28, 1990
UT TIME

Table 1. Data on nine microwave flares measured during solar mapping at Metsähovi in 1989-1990.

Day	Time (UT)			Lat	CMD	W_s^2	Relative	Flux	Frequency	beam	NOAA/
	Start	Measured Maximum	End	center approx.	center approx.		intensity			size	USAF
ddmmyy						(arc²min)		(sfu)	(GHz)	(arc min)	Region
20.6.1989	14.55	15.01	18.50	N24	W75	1.8	3.47	81	37	2.4	5528
21.6.1989	08.20	12.33	(14.00)	N28	E65	1.0	2.05	46	37	2.4	5555
29.9.1989	11.12	11.26	(11.40)	S20	W90	< 15.4	> 8.02	> 1803	90	1.0	5698[1]
03.4.1990	(08.03)	08.27	10.44	N25	E90 (98)	< 13.7	> 14.65	> 628	37	2.4	6007[2]
04.4.1990	13.15	13.21	14.25	N21	E63 (84)	< 7.2	> 10.81	> 341	37	2.4	6007
		13.33					> 10.87				
05.4.1990	13.19	13.44	15.13	N29	E76 (69)	1.0	5.77	129	37	2.4	6007
13.5.1990	12.31	12.49	(13.48)	S17	E90 (70)	1.0	2.58	58	37	2.4	6064
15.5.1990	13.07	13.15	(14.47)	N40	E39	1.0	6.70	149	37	2.4	6063
28.5.1990	(05.01)	05.22	08.51	N22	E41	2.0	1.65	39	37	2.4	6077

(time) = start/end of observation

CMD is taken directly from the map, in parenthesis is the counted value from several days (assuming an average rotation rate of 14°/day)

The size of the burst area is counted from $W_s^2 = W_o^2 - W_a^2$, where W_s is the source size, W_o is the observed half-power beamwidth of the source, and W_a is the antenna beamwidth.

The flux densities are counted with a correction factor $F = a/(1-e^{-a})$ where $a = 0.693(W_s^2/W_a^2)$.

[1] Region already behind the limb, burst presumably coming from this region
[2] Region still behind the limb, burst presumably coming from this region

Table 2. Optical and H_α features happening during measured microwave bursts.

	Active prominences and filaments							H_α flares		
Day	Active prominence	Active dark filament	Bright surge	Dark surge	Arch filament system	Loops	Sudden disappearing filament	Eruptive prominence	Several eruptive centers	Brilliant point/ points
ddmmyy										
20.6.1989	**x		x			x		x (< 90°)	x	
21.6.1989					x				x	x
29.9.1989								**x** (> 90°)		
03.4.1990						x				x
04.4.1990				x		x			x	
05.4.1990	x**								x	x
13.5.1990		x**		x**	x**				x	x
15.5.1990		x		x**		x**	x**		x	x
28.5.1990									x	x

**x microwave event follows
x** microwave event precedes
(< or > 90°), degrees from the central meridian

SIMULTANEOUS Hα AND MICROWAVE OBSERVATIONS OF A LIMB FLARE ON JUNE 20, 1989

Martin Graeter [1] and Therese A. Kucera [2]

[1]Institute of Applied Physics, University of Bern, Switzerland
[2]Department of Astrophysical, Planetary, and Atmospheric Sciences, University of Colorado, USA

Extended abstract. On June 20, 1989 during the Max '91 campaign a large limb flare occurred in active region 5528. It was observed at radio, X-ray, and Hα wavelengths. From the temporal, spectral, and spatial information we get insight into the first seven minutes of flare development since the start of the hard X-ray flare at 14:54 UT. Images in Hα show a blueshifted eruption of a filament which appears later outside the limb as a giant growing prominence. While the filament is erupting large blobs of plasma are seen to move out with speeds of several hundred km/s in the plane of the sky. One of them coincides spatially and temporally with a moving source seen in VLA images (see Fig. 1. at 14:57:36 UT). It is speculated that the moving plasma blob is at the top of a second loop which evolves magnetodynamically. Between the footpoints of the loop system a large Hα kernel develops. Two more eastern subkernels probably form the second ribbon. Later the main kernel develops two links with the off limb loop. Microwave emission sources are seen near both footpoints of the Hα loop at 15:00:01 UT in Fig. 1.

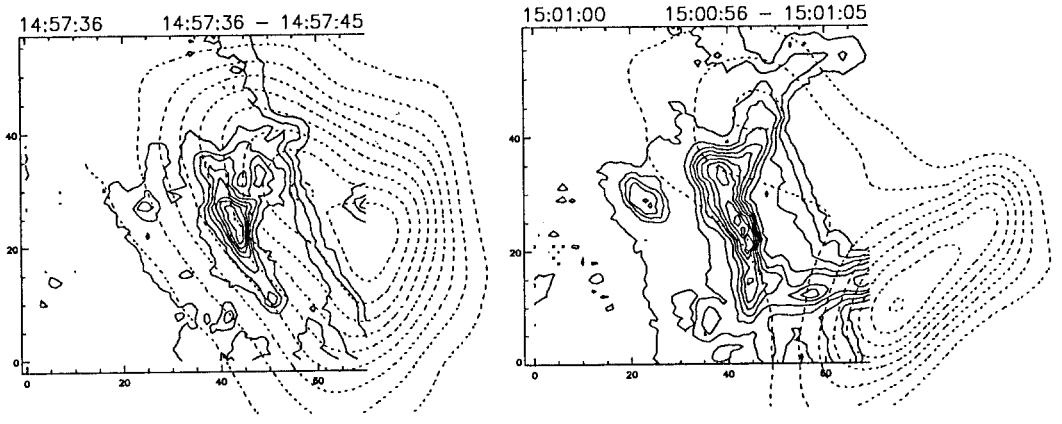

Fig. 1. Isointensity plots of Hα line center (solid lines) and of VLA at 1.4 GHz (dashed lines). Times of the Hα and VLA pictures are given left and right, respectively

NONRESONANT ION–BEAM TURBULENCE IN SOLAR FLARES

Frank Verheest
Instituut voor theoretische mechanika, Universiteit Gent
Krijgslaan 281, B–9000 Gent, Belgium

Special type III radio bursts are attributed to low–energy, super–Alfvénic proton beams. Such beams are unstable against scattering by resonant and nonresonant parallel waves. The latter may dominate and are of two types, with long wavelengths and linear polarization, or else with shorter wavelengths and right/left–hand polarization. Extensions of Fowler's theorem to unstable beam–plasmas indicate higher levels of magnetic field turbulence at shorter wavelengths, up to a sizeable fraction of the flare magnetic field. The beams become sub–Alfvénic before completely travelling down the loop, leading to considerable heating of the flare particles.

1. Introduction

In many astrophysical applications different species making up a plasma can have different equilibrium flow velocities, as in special type III radio bursts with a significantly lower drift than normal, attributed to proton beams at the flare site (Benz & Simnett 1986). These fairly low–energy MeV proton beams are nevertheless super-Alfvénic. Similar low-frequency electromagnetic instabilities occur in the solar wind flow around comets (see *e.g.* Lee 1989).

The linear stability of super–Alfvénic proton beams against scattering by waves in the flare loop coronal plasma has been investigated by Tamres *et al.* (1989) for *resonant* scattering and by Verheest (1990) for *nonresonant* scattering. Under certain conditions the latter may have the highest growth rate (Goldstein & Wong 1987) and is more likely to dominate. We recently developed a method for estimating the saturation levels of such parallel instabilities (Verheest & Lakhina 1991, 1992), based upon an application of Fowler's (1968) theorem for unstable plasmas. There are essentially two types of nonresonant modes. One has long wavelengths and linear polarization, and generalizes the firehose instability. The other one is a shorter–wavelength right/left–hand polarized mode. Both require a relative drift between the bulk and the beam protons which exceeds the local Alfvén speed, and can be triggered by fairly low beam densities.

The theoretical results are recalled in section 2 and applied to the said special type III radio bursts in section 3. In section 4, finally, the conclusions are discussed in the context of other astrophysical applications, as beam instabilities can be viewed as a source of energy transfer from directed energy to plasma turbulence.

2. Theoretical framework

We recall here the essential results from our general papers (Verheest & Lakhina 1991, 1992), directly specialized to a two–beam plasma. Both plasma constituents can in principle have drift velocities parallel to the magnetic field, but for simplicity we use a frame where the main or

2.2. Nonresonant modes: short wavelengths

For wavelengths which are not as long as in the firehose–like case, we take ω small in the sense $\omega \ll |k|U_b + \Omega_i$ (Winske & Leroy 1984, Verheest & Lakhina 1992). Here $k = \mp|k|$ for the right/left–hand polarized modes. Putting now $u = |k|U_b/\Omega_i$ and $M = U_b/V_{Am}$, we approximate (2) as

$$\left[1 - \rho + \frac{\rho}{(1+u)^3}\right]\left(\frac{\omega}{\Omega_i}\right)^2 \pm \rho u \frac{u+2}{(1+u)^2}\left(\frac{\omega}{\Omega_i}\right) + \rho u^2\left[\frac{1}{1+u} - \frac{1-\rho}{\rho M^2}\right] = 0. \tag{7}$$

This quadratic equation can have unstable roots provided its discriminant $\Delta = 4\rho u^2 H(u,\rho)$ is negative, with

$$H(u,\rho) = \rho\frac{\left(1+\frac{u}{2}\right)^2 - 1}{(1+u)^4} - (1-\rho)\left[\frac{1}{1+u} - \frac{1}{M^2(1+u)^3}\right] + \frac{(1-\rho)^2}{\rho M^2}. \tag{8}$$

One sees that

$$H(0,\rho) = (1-\rho)\left(\frac{1}{\rho M^2} - 1\right) \tag{9}$$

is negative, provided initially $\rho M^2 > 1$. On the other hand $H(u,\rho)$ becomes positive for sufficiently large u, and then $H(u,\rho)$ has at least one positive root u_*, with a corresponding range of unstable wavenumbers k. We next suppose that $(1-\rho)^2/\rho M^2$ is small, look for values u_m (and k_m) which maximise the growth rate γ of the unstable modes and get

$$\frac{\mathrm{Re}\,\omega_{\max}}{|k_m|} = \mp\frac{V_{Am}}{M}, \qquad \frac{\gamma_{\max}}{|k_m|} = V_{Am}, \tag{10}$$

almost purely growing modes. The level of turbulence crucially depends on the estimate of the available free energy. First of all, since the instability demands that $\rho M^2 > 1$, an absolute upper bound is $(1-\rho)V_{Am}^2(\rho M^2 - 1)$. This would yield high saturation levels, $|\delta B/B_0| \geq 1$, as found in simulations for shorter–wavelength nonresonant modes (Winske & Leroy 1984). However, to suppose that *all* the available free energy is pumped in the most unstable mode is not quite reasonable and it would be more prudent to assume that the most unstable mode consumes free energy corresponding to its growth rate. This yields

$$\frac{\delta B^2}{B_0^2} \leq \frac{1}{2(1-\rho)}. \tag{11}$$

3. Application to solar flares

We now apply the foregoing results about nonresonant, shorter–wavelength modes, which have higher growth rates, to the special type III radio bursts. Such solar flares have proton beam energies of a couple of MeV, giving beam velocities of 14,000 km/s and more, while only requiring 500 eV electrons for the return current. Furthermore, $m_i V_{Am}^2/2$ is typically in the range of 10 keV, hence $V_{Am} \simeq 1{,}400$ km/s. Since $M \simeq 10$, the threshold number density ratio for the instabilities is about 1 %. Any beam density above this low threshold (compared to the ambient solar flare plasma) will excite the nonresonant Alfvén instabilities discussed here. To fix the ideas we take a low–density beam with *e.g.* $\rho = 0.1$ and find from (10) and (11) that

$$\left|\frac{\mathrm{Re}\,\omega_{\max}}{k_m}\right| \simeq 140 \text{ km/s}, \qquad \frac{\gamma_{\max}}{|k_m|} \simeq 1{,}400 \text{ km/s}, \qquad \frac{\delta B^2}{B_0^2} \simeq 0.55. \tag{12}$$

ambient plasma (with the label m) is at rest. Perpendicular drifts are eliminated by going to a deHoffmann–Teller frame. Both subplasmas or beams are charge and current neutral, the electrons providing the return current.

For wave propagation parallel to $\mathbf{B}_0$ the dispersion law is, following Ichimaru (1973):

$$\omega^2 = c^2k^2 + \frac{\omega_{pm}^2\omega}{\omega \pm \Omega_i} + \frac{\omega_{pb}^2(\omega - kU_b)}{\omega - kU_b \pm \Omega_i}. \tag{1}$$

Here U_b is the beam velocity in the main plasma frame, and $\Omega_b = \Omega_m = \Omega_i$ the proton gyrofrequency. For mode frequencies ω small compared to Ω_i we approximate (1) as

$$(\omega - k\rho U_b)^2 = k^2(1-\rho)(V_{Am}^2 - \rho U_b^2) + \frac{\rho(\omega - kU_b)^3}{\omega - kU_b \pm \Omega_i}, \tag{2}$$

with $\rho = N_b/(N_m + N_b)$ the relative density of the beam and V_{Am} the (reference) Alfvén velocity in the main plasma. We use Fowler's thermodynamics theorem for unstable plasmas (Fowler 1968) in the form

$$\frac{\delta B^2}{2\mu_0} + \frac{\varepsilon_0 \delta E^2}{2} + \frac{1}{2}N_m m_i \delta v_m^2 + \frac{1}{2}N_b m_i \delta v_b^2 \leq \frac{1}{2}(N_m + N_b)m_i F. \tag{3}$$

The left–hand side refers to the fluctuation energies in the magnetic and electric fields and in the plasma and beam particles, whereas the right–hand side expresses the free energy accessible to the instabilities. We compute from Maxwell's equations and the linearized equations of motion the electric field and fluid velocity fluctuations in terms of the magnetic field fluctuations, and perform the same low–frequency approach as in deriving the dispersion law (2). This yields

$$\left\{(1-\rho)V_{Am}^2 + \rho(1-\rho)U_b^2 + \left(\frac{\mathrm{Re}\,\omega}{k} - \rho U_b\right)^2 - \rho\left(\frac{\mathrm{Re}\,\omega}{k} - U_b\right)^2 + (1-\rho)\left(\frac{\mathrm{Im}\,\omega}{k}\right)^2 \right.$$
$$\left. + \rho\frac{|\omega - kU_b|^2}{k^2}\,\frac{\Omega_b^4 + \Omega_b^2|\omega - kU_b|^2}{\left[\Omega_b^2 - (\omega - kU_b)^2\right]\left[\Omega_b^2 - (\omega^* - kU_b)^2\right]}\right\}\frac{\delta B^2}{B_0^2} \leq F. \tag{4}$$

2.1. Nonresonant modes: long wavelengths

If the Doppler–shifted frequency $\omega - kU_b$ for the beam is also small compared to Ω_i, then we are in the long–wavelength, firehose–like limit (Verheest & Lakhina 1991) and get from (2)

$$(\omega - k\rho U_b)^2 = k^2(1-\rho)(V_{Am}^2 - \rho U_b^2). \tag{5}$$

These waves are unstable if $V_{Am}^2 < \rho U_b^2$ and grow to large amplitudes, at the expense of the available free energy. The turbulence thus created causes strong diffusion and scattering of the beam ions, leading to their thermalization (Winske *et al.* 1985). The instability is quenched when the relative streaming ceases to be super–Alfvénic. Full assimilation of the beam ions then has to rely on other mechanisms (Gaffey, Winske & Wu 1988). Since $(1-\rho)(\rho U_b^2 - V_{Am}^2)$ is an effective measure for the normalized free energy F in the unstable regime, we find from (4) the upper bound for the magnetic field fluctuations as

$$\frac{\delta B^2}{B_0^2} \leq \frac{1}{2} - \frac{V_{Am}^2}{2\rho U_b^2} \leq \frac{1}{2}. \tag{6}$$

So the relative streaming between the solar flare plasma and the beam can certainly drive several low–frequency waves unstable. As the unstable waves grow to large amplitudes, inducing large magnetic fluctuations, they take away an appreciable part of the free energy. The beam distribution relaxes to a stable state via the excitation of Alfvén wave turbulence and heating of the main plasma. A crude estimate for the heating follows from (3) and (12) as

$$\frac{\langle \delta v^2 \rangle}{V_{Am}^2} \simeq (1-\rho)\left(\rho M^2 - 1 - \frac{\delta B^2}{B_0^2}\right) \simeq 7.6. \tag{13}$$

One sees that the bulk of the plasma particles could be heated to $70 \sim 80$ keV, and thus beam instabilities can be viewed as an efficient source of energy transfer from directed energy to plasma turbulence. Moreover, the growth rates are large, so that the instabilities grow in much less time than is necessary for the beam to travel through a typical solar flare loop.

4. Conclusions

We have recalled the dispersion law for nonresonant low–frequency electromagnetic waves in a two–beam plasma, determined from it the growth rates in the unstable regime and obtained a theoretical estimate for the magnetic field turbulence levels, by adapting Fowler's thermodynamics theorem.

Although we have considered here only the application to solar flares, the original treatment (Verheest & Lakhina 1991, 1992) given of the low–frequency modes in multispecies beam–plasmas is fully general and can be applied to analogous astrophysical situations. Examples are the pickup by the solar wind of cometary water group ions (Verheest & Lakhina 1991) or Earth's bow shock magnetic turbulence associated with reflected and intermediate ion populations (Verheest & Lakhina 1992).

Acknowledgments. *Discussions with Professor G.S. Lakhina are gratefully recalled, as is a research grant from the National Fund for Scientific Research (Belgium).*

References

Benz A.O. and Simnett G.M. 1986, *Nature* **320**, 508–509

Fowler T.K. 1968, in *Advances in Plasma Physics* (Ed. A. Simon and W.B. Thompson, Wiley) **1**, 201–225

Gaffey J.D. Jr, Winske D. and Wu C.S. 1988, *J. Geophys. Res.* **93**, 5470–5486

Goldstein M.L. and Wong H.K. 1987, *J. Geophys. Res.* **92**, 4695–4700

Ichimaru, S. 1973, *Basic principles of plasma physics* (W.A. Benjamin, Reading, Mass.)

Lee M.A. 1989, in *Plasma Waves and Instabilities at Comets and in Magnetospheres* (Ed. B.T. Tsurutani & H. Oya, Geophys. Monograph Series **53**, Washington) 13–29

Tamres D.H., Melrose D.B. and Canfield R.C. 1989, *Astrophys. J.* **342**, 576–585

Verheest F. 1990, in *Basic plasma processes on the Sun* (Ed. E.R. Priest & V. Krishan, Kluwer, Dordrecht) 383–389

Verheest F. and Lakhina G.S. 1991, *J. Geophys. Res.* **96**, 7905–7910

Verheest F. and Lakhina G.S. 1992, in *Proc. Solar Wind 7 Conf.*, in press

Winske D. and Leroy M.M. 1984, *J. Geophys. Res.* **89**, 2673–2688

Winske D., Wu C.S., Li Y.Y., Mou Z.Z. and Guo S.Y. 1985, *J. Geophys. Res.* **90**, 2713–2726

NONLINEAR EMISSION MECHANISM OF TYPE III SOLAR RADIO BURSTS

Abraham C.-L. Chian[1] and Felipe B. Rizzato[2]

[1]National Institute for Space Research - INPE
P.O. Box 515, 12201 - São José dos Campos, SP, Brazil
[2]Institute of Physics, Federal University of Rio Grande do Sul
P.O. Box 15051, 91500 - Porto Alegre, RS, Brazil

The impulsive phase of eruptive solar flares is characterized by type III radio bursts with a fast frequency drift (Dulk et al. 1985; Goldman and Smith 1986; Benz and Aschwanden 1991). These radio bursts are attributed to electron streams of $E > 10$ KeV that propagate out into the solar wind along an open magnetic field line. Emission can also be from electron streams that propagate down into the dense lower solar atmosphere along a converging closed magnetic field line.

Observations indicate that type III bursts consists of fundamental and harmonic components. A number of theories have been proposed to explain the generation of type III bursts. The commonly accepted scenario that has emerged is as follows (Goldman 1983). As electron streams interact with the solar plasma, Langmuir waves are excited due to a beam-plasma instability. The Langmuir waves then interact with low-frequency density fluctuations to generate fundamental radiation with frequencies near the local plasma frequency. Alternatively, the Langmuir waves can interact with each other to emit harmonic radiation with frequencies near twice the local plasma frequency.

A new emission mechanism of fundamental type III bursts has been suggested recently by Chian and Alves (1988). This mechanism is based on the electromagnetic oscillating two-stream instability (EOTSI) driven by two oppositely propagating Langmuir waves. In the present paper, the Chian and Alves model is improved using the generalized Zakharov equations. Attention is directed toward the influence of the induced ion-acoustic and Langmuir waves on the properties of EOTSI.

The electromagnetic oscillating two-stream instability is operative provided two distributions of Langmuir waves are present in the source region: beam-generated forward Langmuir waves and secondary backward Langmuir waves. Various mechanisms capable of producing such required spectral distribution of Langmuir waves, involving wave-wave coupling or scattering off density irregularities, have been analysed in connection with the harmonic radiation (Goldman 1983). Some of these mechanisms may provide the source of pump waves required for driving EOTSI.

The coupled wave equations (Kuznetsov 1974; Akimoto 1988) that describe the coherent generation of electromagnetic and Langmuir waves by intense Langmuir waves via ponderomotive coupling with ion-acoustic modes are given by the generalized Zakharov equations

$$\left[\partial_t^2 + \omega_p^2 + c^2\, \nabla \times \nabla \times - 3v_{th}^2\, \nabla \left(\nabla \cdot \right)\right] E = - \frac{\omega_p^2}{n_o}\, nE, \tag{1}$$

$$\left[\partial_t^2 - c_s^2\, \Delta\right] n = \frac{\varepsilon_o}{2m_i}\, \Delta \langle E^2 \rangle. \tag{2}$$

In this paper, we examine the decay-type parametric instabilities. In the work by Chian and Alves (1988), the analysis only includes electromagnetic waves in the induced high-frequency modes, apart from the induced low-frequency ion-acoustic waves. Thus, EOTSI was treated as a four-wave process involving two wave triplets. The Chian-Alves model yields an instability that is upconversion ($\omega_T > \omega_o$, where ω_o and ω_T are the frequencies of the pump Langmuir and induced electromagnetic waves, respectively) and purely growing ($\mathrm{Re}(\omega) = 0$). From (1) and (2), it can be seen that in general the instability excites both high-frequency electromagnetic as well as Langmuir waves. Moreover, due to the symmetry of the wavevector kinematics two distinct ion-acoustic waves are excited. In the presence of these induced Langmuir and ion-acoustic waves the behavior of EOTSI is greatly modified.

Consider two Langmuir pumps, $E_o(\pm\, \mathbf{k}_o)$, that propagate oppositely along a longitudinal (x) axis, generating two opposite, Stokes electromagnetic induced modes ($\pm\, \mathbf{k}_T$) emitted along a transverse (y) axis. The coupling between all the modes is provided by low-frequency ion-acoustic fluctuations whose wavevectors are subjected to the conditions $|k_x| \approx |k_o|$ and $|k_y| << |k_o|$ since it is only in this kind of geometry that the electromagnetic modes are not off-resonant. As the consequence of the symmetry of the wavevector kinematics, two symmetrically located ion-acoustic waves ($\pm\, \mathbf{k}$ and $\pm\, \hat{\mathbf{k}} \equiv \pm\, \mathbf{k} \mp 2\mathbf{k}_o$, where $\mathbf{k}_o$ and $\mathbf{k}$ are the wavevectors of the pump Langmuir and induced ion-acoustic waves, respectively) are excited. Depending on the relative phase of these two ion-acoustic modes, the electromagnetic waves can either vanish or be reinforced. Furthermore, from the symmetry of the wavevector kinematics we see that four anti-Stokes Langmuir induced modes ($\pm\, \mathbf{k}_L$ and $\pm\, \hat{\mathbf{k}}_L$, where $\mathbf{k}_L = \mathbf{k}_o + \mathbf{k}$ and $\hat{\mathbf{k}}_L = -\mathbf{k}_o + \mathbf{k}$) can also be generated during the process. These modes, not considered by Chian and Alves (1988), turn out to be of extreme relevance for the dynamics of EOTSI. Thus, the improved model treat EOTSI as an eight-wave process in which two Langmuir pump waves drive two electromagnetic and four Langmuir daughter waves through coupling with ion-acoustic daughter waves.

For the above wave-coupling configuration a Fourier analysis of (1) and (2), assuming the same amplitude and phase for the two counterstreaming Langmuir pump waves, gives the following dispersion relation

$$\omega^2 - \omega_I^2 = - \frac{\omega_P \omega_I^2 W}{8} \left(\frac{2\delta_T}{\delta_T^2 - \omega^2} + \frac{\delta_L}{\delta_L^2 - \omega^2} \right), \qquad (3)$$

where $\delta_T \equiv [c^2(\mathbf{k}-\mathbf{k}_o)^2 - \delta_w]/2\omega_p \approx \omega_T - \omega_o$, $\delta_L \equiv [3v_{th}^2(\mathbf{k}+\mathbf{k}_o)^2 - \delta_w]/2\omega_p \approx 9v_{th}^2 k_o^2 \approx \omega_L - \omega_o$, $\delta_w \equiv \omega_o^2 - \omega_p^2$ and $W \equiv \varepsilon_o E_o^2 / n_o k T_e$.

The dispersion relation (3) has been studied analytically and numerically. The results show that in the presence of the induced Langmuir and second type of ion-acoustic waves, the instability is not always upconversion and purely growing; depending upon the relation between the electromagnetic (δ_T) and electrostic (δ_L) detuning factors, downconversion ($\omega_T < \omega_o$) as well as instabilities with oscillatory ($Re(\omega) \neq o$) ion-acoustic waves are also possible. It is observed that processes occurring in the presence of induced Langmuir waves are much more complex than those occurring in their absence. The basic role of the induced Langmuir waves is to enlarge the range of instability, creating even some new unstable modes.

The properties of EOTSI studied in this paper are in excellent agreement (Chian and Alves 1988) with the solar wind observations of type III bursts of Lin et al. (1986) that present strong evidence of nonlinear wave-wave interactions. Hence, EOTSI may be a likely generation mechanism for the fundamental type III solar radio bursts.

To conclude, we wish to point out that in addition to explain the generation of type III bursts, our theory based on the generalized Zakharov equations (1) and (2) may also account for bulk energization of electrons (Karlicky and Jungwirth 1989; Melrose 1991) during the impulsive phase of eruptive solar flares, by taking into consideration wave-particle interactions between the induced Langmuir waves and the solar plasma.

REFERENCES

Akimoto, K., 1988, Electromagnetic effects on parametric instabilities of Langmuir waves, Phys. Fluids 31, 538-546.

Benz, A.O., and Schwanden, M.J., 1991, Characteristics of the impulsive phase in eruptive flares, this proceedings.

Chian, A.C.-L, and Alves, M.V., 1988, Nonlinear generation of the fundamental radiation of interplanetary type III radiobursts, Astrophys J. 330, L77-L80.

Dulk, G.A., McLean, D.J., and Nelson, G.J., 1985, Solar flares, in D.J. Mclean and N.R. Labrum (eds.) *Solar Physics*, Cambridge U. Press (Cambridge), p.53-87.

Goldman, M.V., 1983, Progress and problems in the theory of type III solar radio emission, Solar Phys. 89, 403-442.

Goldman, M.V., and Smith, D.F., 1986, Solar radio emission, in P.A. Sturrock (ed.) *Physics of the Sun*, Vol.II, Reidel Publishing Co. (Dordrecht), p.325-376.

Karlicky, M., and Jungwirth, K., 1989, Solar Flares and the dynamics of Langmuir waves in current-carrying plasmas, Solar Phys. 124, 319-338.

Kuznetsov, E.A., 1974, The collapse of electromagnetic waves in a plasma, Sov. Phys. JETP 39, 1003-1007.

Lin, R.P., Levedahl, W.K., Lotko, W., Gurnett, D.A., and Scarf, F.L., 1986, Evidence of nonlinear wave-wave interactions in solar type III radio bursts, Astrophys. J. 308, 954-965.

Melrose, D.B., 1991, Particle acceleration in the impulsive phase of solar flares, this proceedings.

A NUMERICAL SIMULATION OF MAGNETICALLY DRIVEN CORONAL MASS EJECTIONS

W. P. Guo[1], J. F. Wang[1], B. X. Liang[1] and S. T. Wu[2]
[1]Department of Space Physics, Wu-Han University
Wu-Han, Hubei, People's Republic of China
[2]Department of Mechanical Engineering and
Center for Space Plasma and Aeronomic Research
The University of Alabama in Huntsville
Huntsville, Alabama 35899 U.S.A.

Abstract Using a quasi-steady, helmet-streamer as the initial corona, we simulate the dynamical evolution of the mass ejection due to magnetic eruption at the base of the streamer. The simulated ejections reproduce some of the observed features of loop-shaped coronal mass ejections. A comparison between the present magnetically driven model and previous thermal driven models will be presented. We show that both the driving mechanism and the initial corona are important in the simulation of CMEs.

I. Introduction

CMEs are complex dynamical phenomena. Magnetic field and plasma flow coupled together make it difficult to analyze their physical behavior theoretically. One approach for studying such phenomena is to utilize the time-dependent, MHD simulation model to study the coronal responses due to finite amplitude perturbations. Mathematically, it is necessary to solve an initial boundary value problem. The early study of this type explored the possibility that loop-like mass ejections could be simulated by the coronal response due to thermal energy release at the base of the corona (e.g. Dryer, *et al.* 1978, Wu *et al.* 1982, 1983). In these simulations they were unable to reproduce some quantitative observed features as pointed out by Sime *et al.* (1984).

Recently, Steinolfson (1988) and Steinolfson and Hundhausen (1988) have taken another approach by emphasizing the role of the initial corona and forms of thermal energy release. They used the heated streamer as the initial atmosphere (Steinolfson, 1988) together with a specific type of thermal energy release (Steinolfson and Hundhausen (1988) and demonstrated that a thermal driving mechanism (or pressure pulse) can simulate many of the observed features of the loopshaped CMEs. However, the type of thermal energy release, in reality, is too arbitrary to exist in the solar atmosphere. They also concluded that CMEs are primarily influenced by the pre-event corona and the driving mechanism does not greatly affect the dynamics. On the other hand, Linker *et al.* (1990) emphasized the importance of the driving mechanism in which they found that the pre-event corona is not the factor to make simulation model successful.

Observations have shown that some CMEs tend to occur over the coronal streamer region (Illing, 1984; Illing and Hundhausen, 1986). In addition , prominences tend to occur near the base of streamers and eruptive prominences are sometimes associated with CMEs. Thus, a large percentage of CMEs may originate or propagate through pre-existing coronal streamers.

Recently, Hu (1990) simulated looplike CMEs by introducing a magnetic pulse at the base of the corona with an initial hydrostatic atmosphere and potential magnetic field of dipole configuration in which the importance of the pre-event corona suggested by Steinolfson and Hundhausen (1988) was ignored. In the present study, we use a quasi- steady coronal streamer without introducing arbitrary distributed heat sources in the pre-event corona. Then, the new magnetic flux emerges from the streamer base, compressing and accelerating the plasma in the corona to form looplike CMEs which show results similar to those obtained by Steinolfson and Hundhausen (1988).

II. Description of the Model and Method of Computations

The theoretical model for the present study assume that the coronal plasma can be represented by a single magnetofluid with negligible dissipative effects (Wu *etal.* 1982)

III. Numerical Results

To establish a pre-event corona (i.e. quasi-steady helmet-streamer) as our initial condition, we solved the set of ideal MHD equations by relaxation method and obtained helmet-streamer (Wang *et al.* 1990) solutions similar to those given by Steinolfson *et al.* (1982) as shown in Figure 1. Then we introduced a disturbance of emerging magnetic flux at the coronal base under the closed field region in the following manner:

$$\vec{B}(R_\odot, \theta, t) = (1 + \alpha t)\vec{B}(R_s, \theta, 0) \qquad (1)$$

with α being $1.02 \times 10^{-3} s^{-1}$ and emerging region has a latitudinal extent of 27° (i.e. $63° \leq \theta \leq 90°$) centered at the equator within the computational domain.

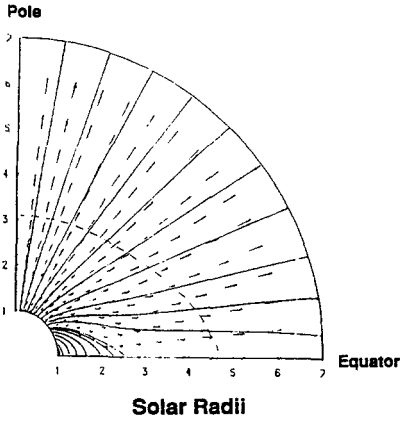

Figure 1. The pre-event coronal structure.

Figure 2 shows the density enhancement; $(\rho(r, \theta, t) - \rho(r, \theta, 0))/\rho(r, \theta, 0)$, and magnetic field lines at 9000 s after introduction of the emerging magnetic flux. The amount of input energy corresponding to this disturbance is $6.7x10^{29} ergs$. For the purpose of demonstrating the importance of the driving mechanism for CMEs , we have performed a related calculation by introducing a thermal disturburance at the coronal base

under the streamer. This thermal disturbance is equivalent to an energy release of $8.4x10^{28} ergs$. The results of density enhancement and magnetic field lines at 9000 s after introduction of the disturbance are presented in Figure 3. From these two cases, we noted that the density enhancement showed a loop-shaped structure with its maximum in the leg of the loop similar to the results obtained by Steinolfson and Hundhausen (1988) for both cases. In addition, there exists a low density cavity between the legs of the loop. These characteristics qualitatively resemble observed loop-shaped CMEs (Sime *et al.* 1984).

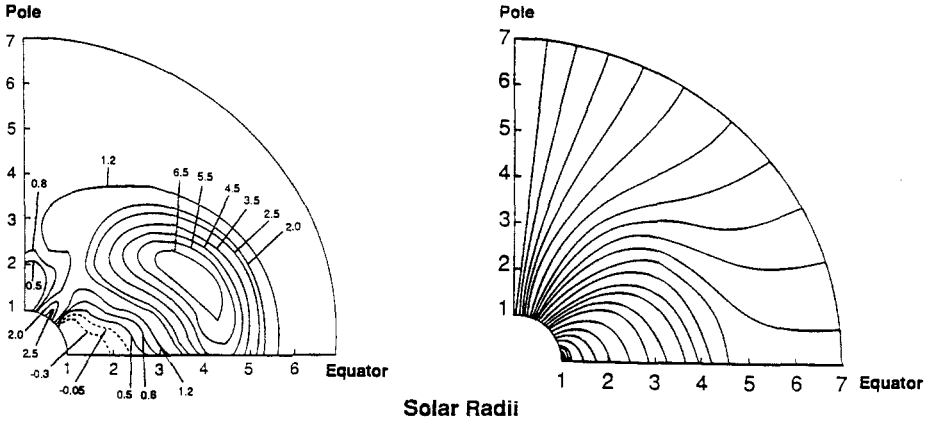

Figure 2. The density enhancement (left) and magnetic field configuration (right) 9000 s after introduction of the emerging flux disturbance corresponds to the pre-event coronal structure shown in Figure 1.

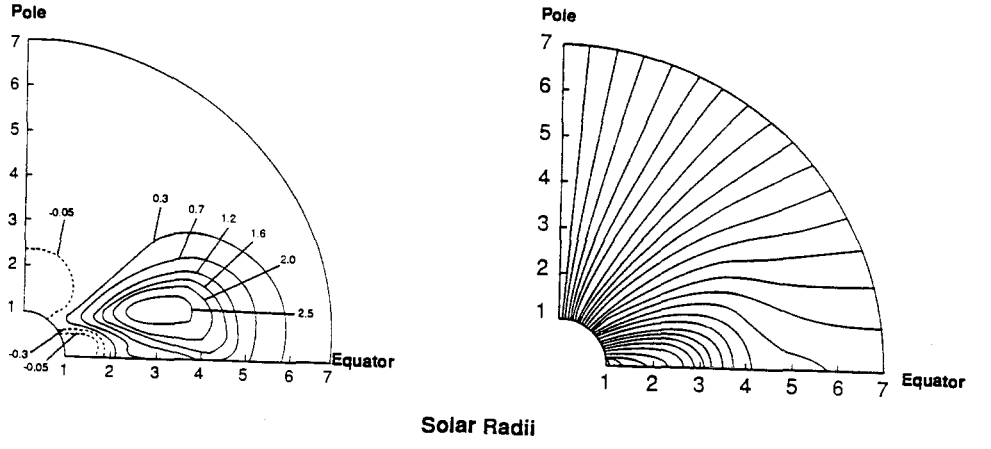

Figure 3. The density enhancement (left) and magnetic field configuration (right) 9000 s after introduction of a thermal pulse of two times stronger than the emerging flux disturbance corresponding to the pre-event coronal structure shown in Figure 1.

IV. Concluding Remarks

Based on the numerial results obtained by the present model, we may conclude:

1. Both pre-event coronal configuration and driving mechanisms are important to simulate the observed characteristics of loop-shaped CMEs.
2. It is not necessary to add an arbitrary heating function as suggested by Steinolfson and Hundhausen to simulate loop-shaped CMEs.
3 The magnetic driving mechanism is a likely candidate to propel non-flare-associated CMEs.

Acknowledgement

We would like to acknowledge Dr. M. Dryer for reading the manuscript and giving valuable suggestions. The work done by S. T. Wu is supported by a NASA grant (NAGW-9) and NOAA contract (50RANR7000104).

References

Dryer, M., S. T. Wu, R. S. Steinolfson, and R. M. Wilson, 1978 , Astrophys . J., *227*, 1059.

Hu, Y. Q., 1990, Chinese J. of Space Sci. *10*, 163.

Illing, R. M. E., 1984, Ap. J., *280*, 399.

Illing, R. M. E., and A. J. Hundhausen, 1986, J. Geophys. Res., *91*,, 10951.

Linker, J. A., G. Van Hoven and D. D. Schnack, 1990, J. Geophys. Res., *95*, 4229.

Sime, D. G., R. M. MacQueen and A. J. Hundhausen, 1984, J. Geophys. Res., *89*, 2113.

Steinolfson, R. S., S. T. Wu, M. Dryer, and E. Tandberg- Hanssen, 1978, Ap. J., *255*, 259.

Steinolfson, R. S., S. T. Suess, and S. T. Wu, 1982, Ap. J., *255*, 730.

Steinolfson, R. S., 1988, J. Geophys. Res., *93*, 14261.

Steinolfson, R., S. and A. J. Hundhausen, 1988, J. Geophys. Res., *93*, 14269.

Wang, J. F., X. Y. Jiang, and D. H. Xiong, 1990, ACTA Geophysica Sinica, *33*, 259.

Wu, S. T., S. Wang, M. Dryer, A. I. Poland, D. G. Sime, C. J. Wolfson, L. E. Orwig and A. Maxwell, 1983, Solar Phys., *85*, 351.

Wu, S. T., Y. Nakagawa, S. M. Han and M. Dryer, 1982, Ap. J., *262*, 369.

CORONAL MASS EJECTIONS: THE LINK BETWEEN SOLAR AND GEOMAGNETIC ACTIVITY

J. T. Gosling, D. J. McComas and J. L. Phillips
Los Alamos National Laboratory
Los Alamos, New Mexico 87545 USA

Using a newly appreciated capability for distinguishing coronal mass ejection events (CMEs) in solar wind data, we have explored the overall effectiveness of CMEs and their associated solar wind disturbances in stimulating geomagnetic activity. Our study was confined to the interval from mid-August 1978 through mid-October 1982, spanning the last solar activity maximum, when the ISEE 3 spacecraft was in orbit about the L1 Lagrange point 240 Re upstream from Earth. We have found that all but one of the 37 largest geomagnetic storms in that era were associated with Earth-passage of CMEs and/or solar wind shock disturbances driven by CMEs. Although CMEs and/or shock disturbances were the primary causes of the most severe geomagnetic disturbances, most minor geomagnetic disturbances were unrelated to these events (see Figure 1). Further, approximately half of all CMEs and half of all shock disturbances driven by CMEs did not produce any substantial geomagnetic activity as they encountered the Earth's magnetosphere. The geomagnetic effectiveness of Earth-directed CMEs and shock wave disturbances driven by CMEs was directly related to the solar wind flow speed, the magnetic field magnitude, and the strength of the southward (GSM) field component associated with the events. The initial outward speed of a CME close to the Sun appears to be the most crucial factor in determining if an earthward-directed event will be effective in exciting a large geomagnetic disturbance.

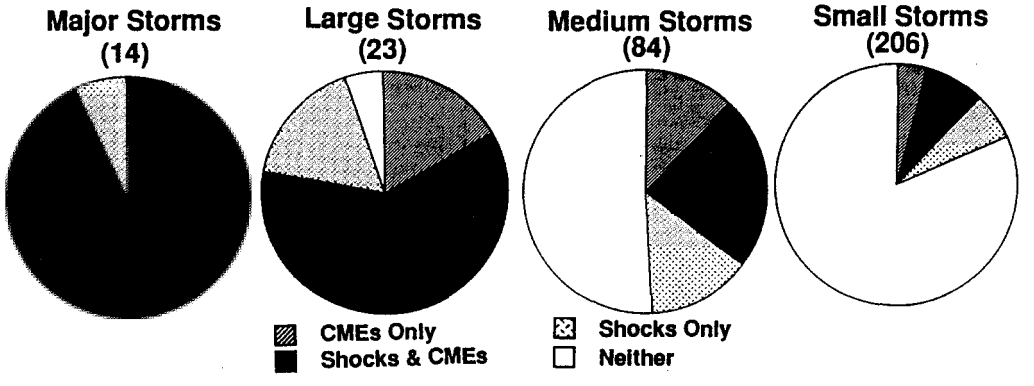

Fig. 1. Pie charts illustrating the association of various geomagnetic storm levels with Earth passage of coronal mass ejection events (CMEs) during the last solar activity maximum. Major, large, medium, and small storms have minimum K_p levels of 8_-, 7_-, 6_-, and 5_- and maximum K_p levels of 9_o, 7_+, 6_+, and 5_+ respectively. The numbers in parentheses indicate the number of storms in each category. Adapted from Gosling et al. [1991].

Gosling, J. T., D. J. McComas, J. L. Phillips, and S. J. Bame, Geomagnetic Activity Associated With Earth Passage of Interplanetary Shock Disturbances and Coronal Mass Ejections, *J. Geophys. Res.*, *96*, 7831, 1991.

A study of geomagnetic variations with periods of four years, six months and 27 days

Alicia L. Clúa de Gonzalez, Walter D. Gonzalez, Severino L. G. Dutra
Instituto Nacional de Pesquisas Espaciais, São José dos Campos, São Paulo, Brazil

Bruce T. Tsurutani
Jet Propulsion Laboratory, California Institute of Technology, Pasadena, California, USA

Abstract

The monthly and daily samples of the *Ap* geomagnetic index for 51 years, in the 1932–1982 interval, were investigated by means of the power spectrum technique. Although in general the results confirm previous findings about possible periodicities in the geomagnetic activity, some aspects are either new or they are now interpreted somewhat differently than other authors have done. The period around 4 years in the monthly *Ap* power spectrum is associated to the dual peak-structure observed in the geomagnetic activity variation (Gonzalez *et al.*, 1990). Several of the peaks shown by the daily *Ap* spectrum are interpreted as harmonics of the six-month period, and others as caused by the solar rotation periodicity, in such a way that the two series of Fourier sequences are considered to be juxtaposed. A strong solar cycle modulation is observed in these series, particularly in that related to the solar rotation period, which almost disappears for the solar maximum phase. Furthermore, a statistic analysis of the geomagnetic storm occurrence has confirmed the findings related to the dual-peak distribution as well to the seasonal variation.

I - Spectrum of the geomagnetic index *Ap*

The power spectrum analysis technique (Jenkins and Watts, 1968) was applied to both the daily and the monthly averages of the *Ap* index. A Hanning-Tukey lag window was used for smoothing and the *window closing* technique allowed for a reasonable choice of the window size (*truncation point*). The spectra, like that seen at Figure 1, have shown that the most relevant periodicity in the geomagnetic activity is indeed that at six months, or seasonal variation. Besides this, and many of its corresponding harmonics, several other peaks show up in the *Ap* spectra, being particularly relevant those around the solar cycle and the solar rotation periods.

Figure 1 shows the power spectrum density (PSD) for the monthly averages of the *Ap* index for a truncation point of 300 months. As seen in this figure, at the low-frequency extreme, the monthly *Ap* spectrum is largely dominated by the solar cycle periodicity that shows up at 10.3 ± 1.1 years, with a confidence level of about 50%. Nevertheless, a peak around 4 years (4.4 ± .2 years) within a 40% level of confidence is present in this spectrum. This possible periodicity in the geomagnetic activity was also observed by Fraser-Smith (1972), Delouis and Mayaud (1975), Currie (1973, 1976) and Kane (1986). This period seems to be associated with the dual-peak structure observed by Gonzalez *et al.* (1990) in the distribution of geomagnetic storms. This refers to the fact, also suggested by other authors, (e.g. Hirshberg, 1973; Crooker *et al.*, 1977; Gosling *et al.*, 1977; Legrand and Symon, 1985, 1989), that during one solar cycle the distribution of geomagnetic storms shows mainly two maxima, one near the solar maximum and the other at the early descending phase of the cycle.

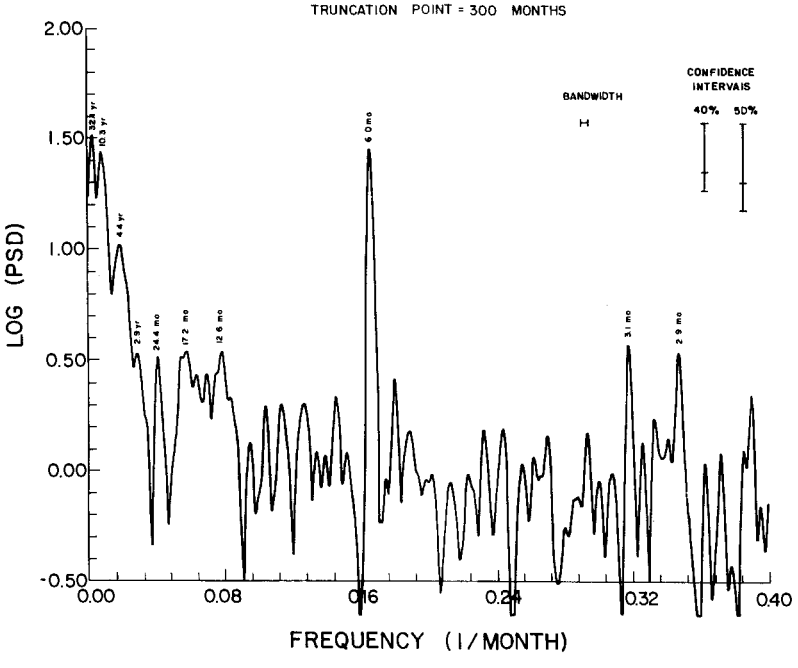

Figure 1. Logarithm of the power spectrum density (PSD) for the monthly averages of the *Ap* index, for the years 1932 through 1982. A Hanning-Tukey lag window with a truncation point of 300 months and a sampling frequency interval of 0.0005 cycles per month were adopted to obtain this spectrum.

Several other peaks are observed at higher frequencies, however the most prominent one is that associated with the well known seasonal variation (see references in Silverman, 1986), shown up at 6.00 ± 0.6 months, with a level of confidence better than 90%.

For the PSD obtained with the daily *Ap* index sample the most prominent peak is also that associated to the six-month period, with a significance level better than 90%. Moreover, many of the other peaks observed in this spectrum seem to correspond,

within the expected error, to harmonics of this periodicity (like those around 90, 60, 45, 30 26 and 22 days). Another important sequence observed in this spectrum is that associated with the solar rotation period, around 27 days. The peak corresponding to its fundamental frequency shows up at 27.2 ± .2 days with a confidence level better than 50%. The lowest harmonics at 13.6 and 7.8 days are well defined at this level but appear side by side with the above mentioned harmonics of the six-month periodicity. On the other hand, the observed intensity distribution for this sequence is about the same of that found for a similar interval in the spectrum of the daily values of the interplanetary magnetic field polarity (Gonzalez and Gonzalez, 1987).

II - Discussion

The six-month period, or seasonal, variation is highly significant (more than 90%) in both the monthly and the daily *Ap* power spectra. However, the subdivision of the data in subsets as small as two-years long has shown the variability of the intensity of the corresponding spectral peak. This variability becomes apparent in Figure 2, that shows the contour lines of the PSD for a truncation point of 200 days and frequencies running from 0 to 0.05 cycles/day, for two-year long samples between 1933 and 1981.

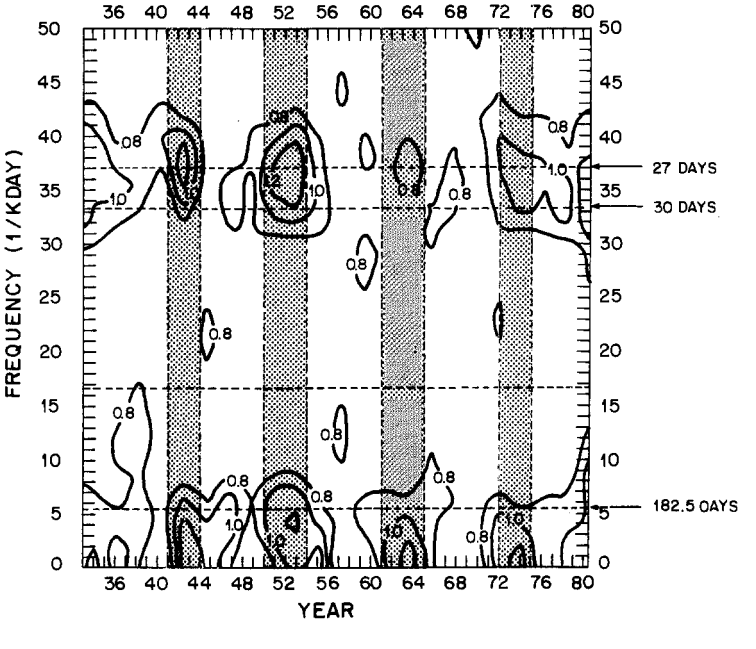

Figure 2. Contour lines of the logarithm of the PSD for two-year running intervals of the daily *Ap* values. The truncation point in the Hanning-Tukey window is 200 days. The vertical dashed lines delimit the intervals corresponding to the descending phase and solar minimum years. The horizontal dashed lines correspond to the indicated periodicities.

As seen in this figure, for years in the late descending phase and solar minima, the spectral power associated with this period is higher than for solar maxima. The amplitude corresponding to the solar rotation periodicity of about 27 days also presents a noticeable solar-cycle modulation, with larger definition during the descending and solar minimum phases, as seen in Figure 2.

The probable periodicity around 4 years observed in the monthly *Ap* spectrum seems to be related to the dual-peak structure in the distribution of geomagnetic storms during one solar cycle. In fact, the statistics analysis of geomagnetic storms with $Ap \geq 50\,\mathrm{nT}$ shows that this distribution presents two peaks around the solar maximum for most of solar cycles, with one of the peaks near the solar maximum and the other about four years later, as established by Gonzalez *et al.* (1990) and previously suggested by other authors.

References

Crooker, N. U., J. Feynman and J. T. Gosling, On the high correlation between long-term averages of solar wind speed and geomagnetic activity, *J. Geophys. Res.*, 82, 1933–1937, 1977.

Currie, R. G., Geomagnetic line spectra — 2 to 70 years, *Astrophys. Space Sci.*, 21, 425–438, 1973.

Currie, R. G., Long period magnetic activity — 2 to 100 years, *Astrophys. Space Sci.*, 39, 251–254, 1976.

Delouis, H. and P. N. Mayaud, Spectral analysis of the geomagnetic activity index *aa* over a 103-year interval, *J. Geophys. Res.*, 80, 4681–4688, 1975.

Fraser-Smith, A. C., Spectrum of the geomagnetic activity index *Ap*, *J. Geophys. Res.*, 77, 4209–4220, 1972.

Gonzalez, A. L. C. and W. D. Gonzalez, Periodicities in the interplanetary magnetic field polarity, *J. Geophys. Res.*, 92, 4357–4375, 1987.

Gonzalez, W. D., A. L. C. Gonzalez and B. T. Tsurutani, Dual-peak cycle distribution of intense geomagnetic storms, *Planet. Space Sci.*, 38, 181–187, 1990.

Gosling, J. T., J. R. Asbridge and S. J. Bane, An unusual aspect of solar wind speed variations during solar cycle 20, *J. Geophys. Res.*, 22, 3311–3314, 1977.

Hirshberg, J., The solar wind cycle, the sunspot cycle and the corona, *Astrophys. Space Sci.*, 20, 473–481, 1973.

Jenkins, G. M. and D. G. Watts, *Spectral Analysis and its Applications*, Holden-Day, San Francisco, California, 1968.

Kane, R. P., Power spectrum analysis of geomagnetic indices, *Proc. Indian Acad. Sci.* (*Earth Planet. Sci.*), 95, 1–12, 1986.

Legrand, J.P. and P. A. Simon, Some solar cycle phenomena related to geomagnetic activity from 1868 to 1980, *Astron. Astrophys.*, 152, 199–204, 1985.

Legrand, J.P. and P. A. Simon, Solar cycle and geomagnetic activity: a review for geophysicists. Part I. The contributions to geomagnetic activity of shock waves and of the solar wind, *Annales Geophys.*, 7, 565–578, 1989.

Silverman, S. M., Annual variation of Aurora and solar wind coupling, *Solar Wind-Magnetosphere Coupling* (Edited by Y. Kamide and J. A. Slavin),643–654, Terra Scientific Company (TERRAPUB), Tokio, 1986.

ATMOSPHERIC MODELS OF FLARE STARS

P.J.D. Mauas[1], A. Falchi[1], and R. Falciani[2]
1 Osservatorio Astrofisico di Arcetri - Italy
2 Dipartimento di Astronomia, Università di Firenze - Italy

Introduction

Comparison between observations of solar and stellar flares shows that they have similar general properties, although many details are different. Observational data on stellar flares, although of lower quality than solar observations, spans a larger range of stellar types, viz. of stellar convective conditions and magnetic situations. Therefore, it is desirable to integrate the physical information derived from solar flares with that obtained from flaring events in different stars in order to improve our understanding of the flare phenomenon.

The great majority of flare stars are dMe objects. Their characteristic spectral features in the visible range are the hydrogen Balmer lines in emission up to H_8 and H_9. These lines are evidence of the existence of a chromosphere and their strength is correlated with stellar flare activity. The spectra of flares on these stars show a strong continuum emission with a characteristic blue color and an enhancement of the hydrogen Balmer lines and of the H and K lines of Ca II. For a complete understanding of stellar flares, a study of the atmospheric structure of dMe stars should be undertaken, together with the modelling of the response of the stellar atmosphere of the flare.

In this work we report preliminary results on the computation of the first semiempirical atmospheric models for the star AD Leo, both in the quiescent and flaring state, based on a full set of spectroscopic observations (very kindly provided by Dr. S.L. Hawley).

The atmospheric models

For the atmospheric modelling we used the program Pandora, kindly provided by Dr. E.H. Avrett. We included in the calculation of the opacities the contribution of a great number of weak atomic and molecular lines, as compiled by Kurucz (1991). Of particular importance for these cool stars is the opacity due to molecules like TiO.

The flare we model was observed by Hawley and Pettersen (1991) on 12 april 1985, during a coordinated multi-wavelength campaign of M dwarf flare observations. It is one of the largest flares ever reported on AD Leo, with a total observed radiative energy output of more than 10^{34} ergs. The observations we model were obtained 915 sec after the flare start, not at the maximum of the continuum emission, but still during the

impulsive phase, that may be considered to change into gradual decay phase around 1500 sec after the flare start.

Figure 1 shows the preliminary atmospheric models obtained. Due to the fact that collisions play only a minor role in the atmosphere of these cool stars, the atmosphere is very far from LTE. This causes problems of convergence of the computed models, which make the whole modelling process very difficult. For this reason, we were not able to complete the modelling of the quiescent high chromosphere, were the Balmer lines are formed. Thus, the model we present here should be considered only as an indication in what respects to the high chromosphere and the location of the transition region. The photosphere, temperature minimum region and low chromosphere, on the other hand, is based on the observed continuum and the very small, if any, emission observed in the Na D, Mg b and Ca I λ 4227 Å lines, and can thus be considered as definitive.

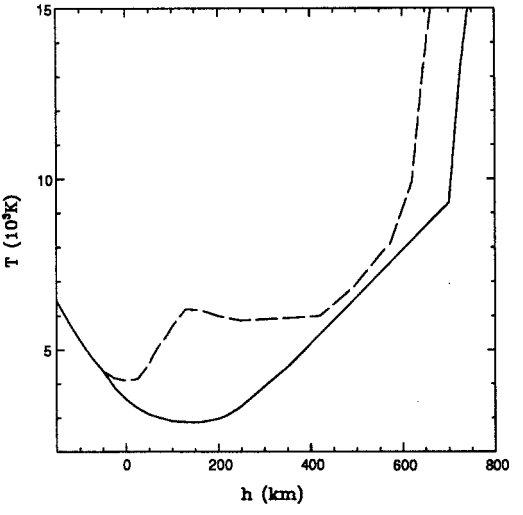

Fig. 1: Our atmospheric models. *Full line*: The quiescent star. *Dashed line*: The flare model.

The flare model, on the other hand, does not present these difficulties, since the much higher temperatures assure a situation much closer to LTE. In this case, the position of the transition region and the structure of the high chromosphere can also be deduced from the observed continuum, which does not present a Balmer jump.

Figure 2 shows a comparison of the observations with the continuum calculations both for the quiet star and the flare. In Figure 2-a note the importance of the inclusion of the molecular opacities in the continuum calculations. The main absorption features

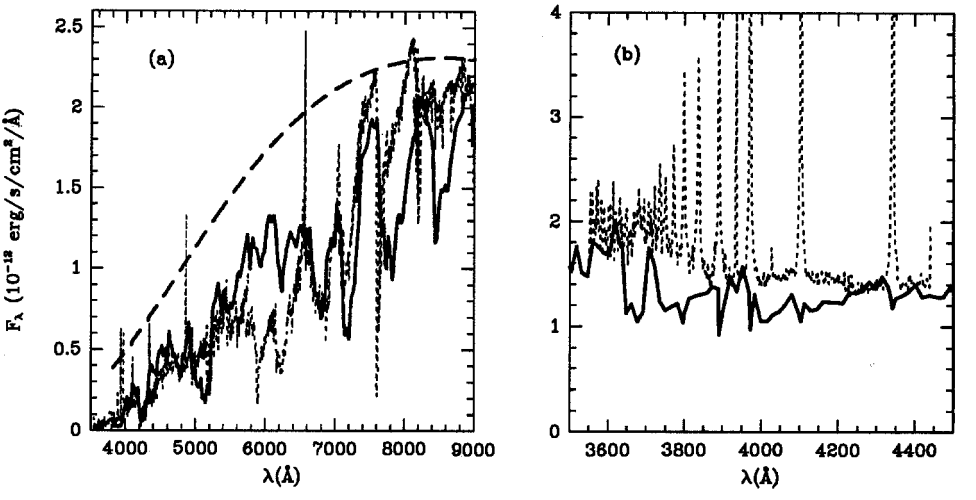

Fig. 2: Comparison of the observations with the continuum calculations. a) quiescent-star model. b) the flare model. *Dotted line*: Observations by Pettersen and Hawley (1989) and Hawley and Pettersen (1991). *Full line*: Present calculations. *Dashed line*: Calculations performed without the opacity due to the weak atomic and molecular lines.

are due to TiO. The difference between the observed and computed spectra at around 6000Å is due to an absorption feature of CaOH not included in the opacity calculations.

For the calculations of the flare spectrum, a 10% filling factor was assumed. Note in Figure 2-b that a jump at the head of the Balmer continuum is not observed, a fact that put constraints on the structure of the high chromosphere, were this jump would be originated. Note also the increase in the observed emission towards the blue, this effect is very hard to model whithout the Balmer jump.

In Figure 3 we compare the computed flux with the observations. Note the fact that we are assuming the same 10% filling factor at all wavelenghts. However, it should be noted that an important fraction of the emission at shorter wavelenghts is formed in the chromosphere, whereas at longer wavelenghts all the radiation comes from the photosphere, and solar observations seem to support a larger filling factor in the chromosphere.

Conclusions

We present preliminary atmospheric models for the flare star AD Leo, both in quiescent state and during a big flare. The models were designed to match the observed continuum flux, and the computations agree quite well with the observations. For the quiescent star, the opacities due to different molecular bands are very important for the calculations of the emitted spectrum.

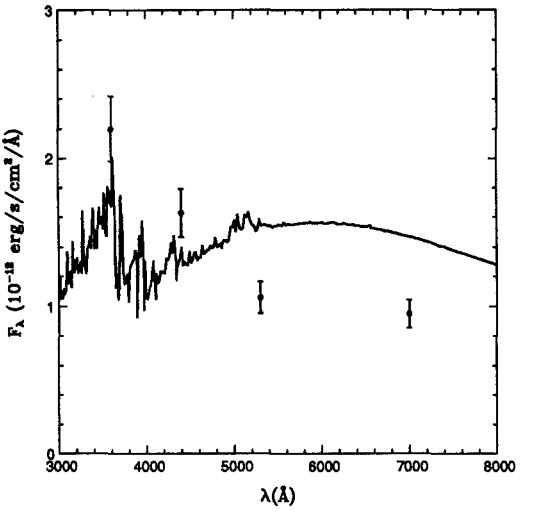

Fig. 3: Comparison of the continuum calculations with the flux observed in the filters U, B, V and R. The error bars represent a 10% estimated error (Hawley and Pettersen 1991).

With respect to the flaring atmosphere, the fact that no Balmer discontinuity was observed places severe constraints on the temperature of the chromosphere, because a hotter chromosphere would produce a much larger emission of the Balmer continuum. This fact implies that the white-light emission has to be formed at photospheric depths.

Even though the agreement between the computed and observed spectrum between 3600 and 4500 Å for the flare atmosphere is quite good, some discrepancies still remain when the comparison is performed between the computed and observed flux in the U, B, V and R filters. This suggests the need to use different filling factors at different heights in the atmosphere, where the radiation at different wavelengths is formed.

References

Hawley, S.L., and Pettersen, B.R. 1991, *Ap. J.*, **378**, 725.

Kurucz, R.L. 1990, *Stellar Atmospheres: Beyond classical Models*, ed. L. Crivellari, I. Hubeny and D.G. Hummer (Dordrecht: Kluwer)

Pettersen, B.R., and Hawley, S.H. 1989, *A. Ap.*, **217**, 187.

SUMMARY
OF THE
COLLOQUIUM

THE EMERGING PICTURE OF ERUPTIVE SOLAR FLARES

P.A. Sturrock
Center for Space Science and Astrophysics
Stanford University, Stanford, CA, U.S.A.

1. Introduction

Since it was impossible to prepare a summary of all the fascinating information that was been presented at this symposium, I undertook the more limited goal of describing the picture of eruptive solar flares that formed in my mind as the result of the presentations at Iguazu. Even this was very difficult, since we heard relevant observational material covering the enormous spectrum from radio waves to gamma rays. Our basic challenge is to deduce from this material the structure of the magnetic field responsible for an eruptive solar flare, and then to understand how the pre-flare state was formed, and how the magnetic-field configuration changes in the course of a flare. This is rather like asking six blind men to describe an elephant, based only upon their contact with part of the elephant. The best that I can do at this time is to recount some of the clues that, with other information yet to be obtained and greater insight yet to be developed, will ultimately lead the determination of the magnetic-field pattern or patterns responsible for eruptive flares.

2. The larger context

In identifying a class of flares called "eruptive solar flares," we are implicitly referring to a classification of flares of which "eruptive flares" represent one class. (In the classification scheme proposed by Bai and Sturrock [1989], "eruptive flares" correspond most closely to their class "gradual GR/P flares.") Hence, to understand eruptive flares, we really need to explore this classification scheme and, in particular, to study the similarities and differences between eruptive flares and the other types. This topic was not addressed during this symposium, but it has been addressed in the past by Priest (1981) and by Svestka (1976, 1986). In addition to understanding the relationship of eruptive flares to other types of flare, we

need to understand the relationship of eruptive flares to related forms of solar activity including filaments, CME's and giant arches. Furthermore, we need to understand the properties of different phases of an eruptive flare: any pre-flare behavior, the impulsive phase, and the late phase that is responsible for post-flare loops.

My goal is to present a picture of eruptive solar flares, as it has emerged from the proceedings of this symposium, in the form of a time sequence of events that involves an eruptive flare. This picture will be outlined in stages in the following sections of this article.

3. Photospheric flows

A solar flare is basically the sudden conversion of magnetic free energy into other forms. The free energy of a magnetic field is usually regarded as the excess energy of a configuration that involves coronal electric currents as compared with the energy of the corresponding field that has the same photospheric flux distribution but is current-free in the corona. However Priest, in describing his "interacting flux model," made the case that magnetic helicity is conserved during reconnection. If this is the case, and if energy release is by reconnection, then a more appropriate estimate of the free energy is the excess energy of the initial field over that of a configuration that has the same photospheric flux distribution and the same magnetic helicity - that is, the corresponding linear force-free field (Woltjer 1958).

The existence of coronal currents implies a stress that may have been present in the magnetic field when it emerged from the photosphere, or may alternatively have been impressed upon the field by photospheric flows. This line of thought suggests that we look to the emergence of magnetic flux in order to understand subsequent solar flares. However, Martin, Livi and Moore, in their presentations, also stressed the importance of "flux cancelation" in leading up to a flare and to related events such as CME's.

As best I understand it, the processes that they are describing can be regarded as a "photospheric trench," analogous to the trenches that exist on the ocean floors on earth. A trench is a location where two plates come together and the material then subsides. When this occurs at the photosphere, flux of opposite polarity will sometimes be brought together. In this situation, we must expect magnetic reconnection to occur. Depending on the height of the reconnection site and the magnetic configuration, photospheric flux will then be dragged down

into the trench and/or pulled out of the photosphere, so that flux appears to have "cancelled" and then disappeared. In general, there will be shearing motion as well as inflow, and the shearing motion has important effects on the evolution of the magnetic topology. Priest (1987) has suggested that all inverse-polarity prominences lie along such trenches.

In her poster paper, Martin discussed the consequences of reconnection at the photosphere-chromosphere interface. Newly reconnected field lines spring into the corona above the polarity inversion zone where cancellation is observed to occur. Martin showed how the result of many such reconnections can lead to the formation of a magnetic rope running along and above the polarity inversion line. Such a configuration can maintain cool plasma at coronal heights, that will then be observed as a filament if viewed on the disk or as a prominence if viewed on the limb. This empirical picture has much in common with theoretical models recently proposed by Van Ballegooijen and Martens (1989), Kuipers (1990) and Ridgway and Priest (1991).

It is important to note that the hydrogen gas that constitutes a filament or prominence is, in this picture, merely a marker of a certain type of magnetic-field configuration. This configuration, that could be referred to as an "extended filament," could extend over much larger regions than the region occupied by the visible filament, as was illustrated in Martin's poster presentation, and as was indeed indicated by Skylab X-ray observations (McIntosh et al. 1976; Webb et al. 1976). If the eruption of such a magnetic-field configuration is responsible for a coronal mass ejection (CME), that configuration may or may not contain cool gas that is recognized as a filament. This would help us understand why a CME may or may not be accompanied by a filament eruption and why, if a filament eruption is involved, it may occupy only a small part of the total region involved in the CME.

4. Magnetic-field eruption

It is clear that the sudden eruption of a magnetic-field configuration can occur if the configuration becomes unstable. However, as Forbes and Priest pointed out in their contributions, it is also possible that the eruption may be attributed to a "loss of equilibrium" (Low 1984; Priest and Forbes 1990; Wolfson and Gould 1985). This concept is based on the consideration of a sequence of field configurations which may be enumerated by a continuous parameter μ that normally represents the degree of stressing of the field (with respect to the

unstressed current-free state). It is possible that a certain class of field configurations exists for $\mu<\mu_c$ but does not exist for $\mu>\mu_c$. Then the critical value μ_c is said to indicate a "loss of equilibrium." However, as Klimchuk and Sturrock (1989) have pointed out, one must be cautious in using this argument. One can apply this argument to a solar problem only if the sequence can be produced by a valid "thought experiment." This is true of some - but not all - of the sequences that have been proposed.

If one is dealing with Hamiltonian systems, a linear series of systems can change from being stable for $\mu<\mu_c$ to unstable for $\mu>\mu_c$. This transition can occur in one of two ways, one representing a nonexplosive onset of instability for which the original series becomes unstable but one or more stable series branch off at the transition point, and the other representing an explosive onset of instability for which the original series becomes unstable but no stable series branches off at the transition point (Sturrock 1966a). In order to explain events such as CMEs or flares, one clearly would be looking for either an explosive onset of instability (rather than a nonexplosive onset), or, as was indicated in the previous paragraph, by a loss of equilibrium.

In the course of discussion arising out of these contributions, it was proposed that the onset of a CME may not be simply an ideal MHD process, but may involve magnetic-field reconnection (Priest 1981). As an analogy, one may consider a tethered hot-air balloon. The configuration may become disturbed in such a way as to put excess strain on one of the tethers, leading it to snap. If this were to occur, there would then be additional strain on the adjacent tethers, so that they, in turn, may also be disrupted. The analogy in the solar model would of course be reconnection of magnetic-field lines.

The eruption of the magnetic-field configuration associated with a photospheric trench may lead to a flare, as we shall discuss in the next section. Alternatively, it may simply lead to disruption of the filament with no other detectable effects in Hα, in which case, as pointed out by Svestka during the meeting, it would be perceived as a "disparition brusque." (However it should be noted that, using more sensitive lines such as HeI at 10830A, a disparition brusque may be accompanied by flare ribbons that can be observed in absorption [Harvey, Sheeley and Harvey 1986]).

Hildner and Webb, in their contributions, pointed out that CME's frequently occur in the vicinity of streamers. When this is the case, the streamer may be disrupted (typically enlarged) before the occurrence of the CME. Priest pointed out that, following the CME, the magnetic field associated with the helmet streamer appears to become open. This

interpretation may of course be invalid: we do not have firm evidence concerning the magnetic-field structure outside the effective radius of the occulting disk of the coronagraph, and we normally have no information at all about the magnetic-field structure below that radius. However, if the interpretation is correct, it is difficult to reconcile with a conjecture made by Aly (1984), that the open-field configuration is the maximum-energy state associated with a given photospheric flux distribution. Aly (1991) and Sturrock (1991) have recently published theorems that substantiate this conjecture. Priest suggested that the initial magnetic-field configuration may possibly not be simply connected, or the final state may not be completely open, and that this may invalidate the applicability of the theorem. Otherwise, it is difficult to understand the fact that an eruption, producing a CME, typically disrupts a helmet streamer and leaves it apparently in an open-field configuration.

As noted before, it is possible that the photospheric trench may extend over a much larger region than the visible filament. In this case, if the eruption of the field configuration associated with the complete trench is responsible for a CME, one can understand why the filament eruption covers only part of the total area involved in the CME.

Although a CME may occur without leading to a flare, many eruptive flares are associated with CMEs. Martin and Livi suggested that it is the slow building up of the magnetic field in filament channels in the corona (in association with the photospheric "flux-cancelation" process) that causes the overlying coronal magnetic field to slowly and concurrently expand outward, setting the stage for the rapid reconnection that is responsible for the impulsive phase of a flare. However Moore, referring to the acceleration in filament motion that typically precedes an eruptive flare, suggested that the eruption of a filament (or of an extended filament) may lead to the rapid stressing of the active-region magnetic field; this rapid stressing may then drive rapid reconnection, a process that Moore regards as the basic energy-release mechanism of the impulsive phase of a flare (Moore et al. 1984; Moore 1988; Priest and Forbes 1990).

5. The Early Phase

There was little discussion of the "early phase" of flares - the phase that precedes the impulsive phase by only a few minutes (Bai and Sturrock 1989) and may be closely related to pre-impulsive-phase mass motion. Evidence for an early phase typically comprises localized

Hα, UV and soft-X-ray brightenings. This phase was referred to by Uchida in the course of his presentation concerning the Japanese spacecraft then named "Solar A," that has since been successfully launched and renamed "Yohkoh." Uchida described the experiments on board the spacecraft: the Soft X-ray Telescope (SXT), the Hard X-Ray Telescope (HXT), the Bragg Crystal Spectrometer (BCS) and the Wide Band Spectrometer (WBS).

Uchida discussed a number of possible targets for the mission, ranging from flares to faint coronal loops, taking into account the sensitivity, spatial resolution, time resolution, etc., of the instruments. However, he particularly stressed the need for studying mass and energy transfer during the "early phase." Uchida pointed to evidence for strong mass flow and localized soft X-ray emission during this phase, and also to evidence for the brightening of coronal loops (Uchida and Shibata 1988). These studies will be facilitated by the high time-resolution of data acquisition and by the capability of retaining and accessing data acquired up to 10 minutes before a flare is "flagged."

The high spatial resolution and wide dynamic range of SXT also offers the exciting prospect of determining whether flare activity is associated with changes in magnetic connectivity, and possibly of seeing the effect of a coronal blast wave on pre-existing coronal structures.

6. The Impulsive Phase and Particle Acceleration

Martens, commenting on Priest's review, pointed out that if the magnetic field is rapidly changing, then, by the induction equation, curl **E** becomes non-zero. The basic requirement of particle acceleration is to develop an electric field (Martens 1988). However, if the quasi-static electric field is to effect particle acceleration, it is necessary that the component of **E** parallel to **B** be non-zero. This is not an automatic consequence of a changing magnetic field. It is well known that if the resistivity is effectively zero, the magnetic field is "frozen" into the plasma, with the consequence that $E_{||} = 0$ except perhaps in the center of a current sheet, where $B = 0$. Hence if the changing magnetic field is to lead to acceleration by a quasi-static electric field, it is necessary that the resistivity should suddenly become significant, due for instance to a velocity-space instability.

Melrose, in his presentation, also discussed the acceleration problem. He pointed out that it is unlikely that a sufficiently large number of electrons can be accelerated by reconnection in a current sheet. This consideration, the rapidity of acceleration, and the fact that in many flares electrons and ions are accelerated rapidly at the same time, all point towards the possible role of current interruption. It may be that the impulsive phase of a flare involves energy release by current interruption rather than by reconnection; alternatively, it may be that current interruption and tearing-mode-type reconnection are different aspects of one complex process responsible for the impulsive phase of a flare.

However, even if reconnection cannot provide the required high number of accelerated electrons, there have been new indications of its role in flare occurrence. Mandrini reported that it is has been possible to estimate from a magnetogram of a solar active region the location of the separatrices, surfaces that separate different field-line connectivities, and of the separator, which is the intersection of the separatrices. The separator is a privileged location for reconnection to occur. Four of the five off-band Hα kernels of a flare observed in this region were located at or near the separatrices and connected by field lines passing near the separator. Taken together with the fact that the flare kernels were associated with strong currents in the preflare state, there appears to be a case for attributing flare activity to current interruption occurring within the context of magnetic reconnection.

Rieger, in his presentation, argued that gamma-ray data, especially data from the SMM satellite, indicate that ions and electrons are accelerated rapidly and almost simultaneously. Rieger concludes that in most flares acceleration occurs as a single process rather than as a sequence of two distinct "steps" as has been proposed by, for instance, de Jager (1969) and Bai and Dennis (1985). Martens also pointed out that the two-step acceleration model faces the problem that high-energy protons are observed from the very onset of a flare (see, for instance, Chupp et al. 1982), leaving very little time for a two-step process to operate. Nevertheless, as Rieger remarked, there is evidence that acceleration occurs in two distinct phases, well separated in time, for some very energetic events.

Benz discussed coherent microwave bursts associated with flares. They are highly fragmented on different levels. (a) Hard X-rays and microwaves have time scales of order 1 s. These are the "elementary flare events" proposed by van Beek et al. (1974) and discussed by Sturrock et al. (1984). Evidence of elementary flare events is also seen in Hα observations (Svestka, Martin and Kopp 1980). (b) Decimeter type III bursts - each indicating an electron beam - have a time scale and repetition rate of order 0.1 s. (c) Narrow-band spikes have the shortest time-scale, of order 0.01 s. The event rates of decimetric type III bursts and spikes

often show a good correlation with the hard X-ray flux (Aschwanden et al. 1990). According to Benz (1985), a constant hard X-ray fluence per burst suggests that the impulsive phase comprises hundreds, sometimes thousands, of sub-events of similar size.

A similar picture emerged from the presentation of Machado who, speaking on behalf of Fishman of Marshall Space Flight Center and his colleagues, presented some of the spectacular high-sensitivity X-ray-burst data currently being acquired by the Burst and Transient Source Experiment (BATSE) on the Gamma-Ray Observatory (GRO) spacecraft. Bursts of small and moderate intensities have shown strikingly well resolved X-ray pulses with durations of order 100 ms. This structure is not as evident in bursts of higher intensities, presumably because the bursts are superimposed.

Correia presented the results of a new observational program aimed at further eludicating the properties of the very rapid mm-wave bursts discovered by the Itapetinga team (Kaufmann et al. 1980; Loran et al. 1985). By using several feeds in conjunction with a single antenna, they are able to track the locations of mm-wave bursts with resolution of order 1 arc sec. The team has found that the locations of a sequence of mm-wave bursts are typically scattered over an area that spans several or tens of arcseconds in extent.

This picture of the flare volume as comprised of many small regions, each of which can act more or less independently but which must also interact in some way, points towards a "firecracker model" or "avalanche model" of the implusive phase of a flare. The latter model has recently been adopted by Lu and Hamilton (1991) who have applied to flares the recent theory of "marginal criticality."

The concept of the impulsive phase of the flare as a collective process, involving many sub-elements, requires that we find a process for coupling these elements. Karlicky, in his presentation, pointed out that Langmuir waves can effectively stimulate energy release in a current-carrying plasma (Karlicky and Jungwirth 1989). If this is the case, it provides a mechanism by which energy-release in a small part of a flux tube may stimulate, through particle acceleration and Langmuir wave generation, energy release along the entire flux tube. Wave processes lead to the spreading of excitation not only along the flux tube but also transverse to the tube, carrying energy across magnetic field lines (Norman and Smith 1978). According to Karlicky, the pre-flare state may comprise many current filaments with currents flowing in both directions, so that the total current can be much smaller than the sum of all of the currents in the flux tubes. In this connection, it is worth noting that if the pre-flare state involves many elementary flux tubes, and if the tubes are all rotated in the same sense,

then current will flow in one direction along every tube but will flow in the opposite direction in the boundary layers between adjacent flux tubes. This picture of the flare region has also been advocated by Haerendel (1987).

Zarro discussed the response of the chromosphere to energy release during the impulsive phase of a flare. It is generally believed that energy deposition on the chromosphere is due mainly to a flux of high-energy electrons, but Zarro pointed out the possible role of high-energy protons, a possibility that has recently been stressed by Martens (1988), Martens and Young (1990), Simnett (1986, 1990), and Simnett and Haines (1990).

Henoux discussed "white light flares" and the intriguing phenomenon of "negative flares," the sudden reduction of white-light emission during a flare. Henoux pointed out that both phenomena may be attributed to a sudden ionization of the solar atmosphere. Sudden energy deposition can heat the chromosphere and lead to increased radiation. On the other hand, the associated increase of ionization in the upper photosphere and temperature-minimum region may lead to increased absorption of photospheric radiation, leading to what is perceived as a "negative flare."

Dennis discussed the relationship between hard X-ray emission and soft X-ray emission during the impulsive phase of a flare. He reminded us of the "Neupert effect," the apparent relationship between the soft X-ray emission and the time integral of the hard X-ray emission (Neupert 1968). This relationship does not hold for all flares, but it does hold for many flares. The normal interpretation of this effect is that hard X-ray emission is associated with electron bombardment of the chromosphere, a process that also heats the chromosphere and hence leads to evaporation, and that soft X-ray emission is due to radiation from the coronal flare plasma that is produced by chromospheric evaporation. However, Dennis pointed out that the Neupert effect can also be produced by other models, for instance the thermal model of Brown et al. (1979), in which a high-temperature plasma (that produces hard X-rays by bremsstrahlung) leads to evaporation of the chromosphere, and hence to soft X-ray emission.

7. The Late Phase

The late phase of eruptive flares was mentioned by Svestka in his introductory talk. He reminded us that the "rising-mound" appearance of limb flares and the two-ribbon

appearance of disk flares can be interpreted in terms of the "CSHKP" (Carmichael-Sturrock-Hirayama-Kopp-Pneuman) model (Carmichael 1964; Sturrock 1966b, 1968; Hirayama 1974; Kopp and Pneuman 1976). The eruption of a filament (or of an "extended filament") distorts the overlying magnetic-field configuration in such a way as to produce a current sheet. Reconnection of this current sheet is responsible for the late phase of an eruptive flare. Electrons accelerated during this phase of reconnection and heat conducted from the reconnection site impinge on the chromosphere, leading to increased Hα and X-ray emission and also to evaporation that in turn leads to soft X-ray emission.

Schmieder discussed the Hα appearance of post-flare loops; these are formed through reconnection in the corona, leading to high-temperature plasma at coronal heights and subsequent cooling to chromospheric temperatures. Some progress has been made in our knowledge of the time development of these structures: their initial temperature exceeds 2×10^7 K and, as the result of chromospheric evaporation, the electron density may be as high as 10^{11} cm^{-3} or 10^{12} cm^{-3}. During the cooling phase, which is the phase that is observed in Hα light, the density may be further enhanced as a result of the downflow of material. Brightenings in the cool Hα loops give the appearance of "coronal rain," but Schmieder has found that the speed of this downflowing material is typically less than the free-fall velocity. This stage of a flare needs further investigation, but the basic physics would seem to be that the hot flare plasma (produced by reconnection-caused heating that leads to chromospheric evaporation) becomes thermally unstable, leading to low-temperature condensations. It is these condensations that are observed through Hα radiation, but their downflow is impeded by the remaining flare plasma.

Poletto, Mandrini and Svestka discussed X-ray observations of giant arches (Svestka 1983) that may perhaps be regarded as part of the late phase of a flare. Krueger described mm-wave observations that indicate large structures on the solar limb that may be related to giant arches. These structures are much larger in dimension than the magnetic-field structures responsible for the late phase of a flare. However, owing to the rather small number of events which have thus far been detected, as well as to their extreme faintness, the observational properties of giant arches are still not well defined and consequently the exact mechanism of their formation or excitation is not well understood. Svestka et al. (1982) and Hick and Priest (1989) have proposed that these structures are the outermost parts of the magnetic-field configuration caused by the CSHKP reconnection process that creates, at a lower level, the post-flare loops. However, another possibility, advocated by Poletto, is that giant arches are due to the interaction of flare-related magnetic structures with more extended pre-existing active-region magnetic-field structures. The supposition is that the flare gives rise to the sudden

disturbance of the active-region magnetic field and that this disturbance precipitates reconnection between the two flux systems where they are in contact. This reconnection leads to a sudden release of energy in the extended loop system that then becomes visible as a "giant arch." Mandrini and Machado suppose that the giant arch is only one specific case of a wider range of possible large-scale coronal structures which need not all be related to eruptive flares. The merits of these different interpretations have recently been discussed by Poletto and Svestka (1990). It is clear that we need more complete data on more cases to determine the exact role played by giant arches in the flare process. An exciting new development at the meeting was the presentation by Svestka and Simberova of a preliminary report of a giant arch that they have found in the Skylab soft X-ray photographs. This event shows much higher spatial resolution than giant arches that have previously been investigated.

8. Concluding Remarks

The overall impression of papers presented at this symposium is that the broad outlines of an eruptive flare have been clarified considerably in recent years. We can now recognize several different stages in the development of such a flare, and we have a superficial understanding of most of the physics involved in these stages. However, much still remains to be understood in greater detail. Without minimizing the importance of CME's, that involve more energy and more mass than flares and occur before flare onset, it seems to me that the greatest challenge concerning flares is that of understanding the mechanisms of energy release during the impulsive phase and of the associated particle acceleration. Machado, in his presentation, pointed out that the locations of X-ray brightenings in some flares correlate very well with the intersections of magnetic separatrices with the chromosphere. Such evidence points towards magnetic reconnection at the separator, as was stressed by Priest. However, the details that would make such a picture convincing are still lacking. Current interruption is a promising alternative, but there is still not a convincing picture of exactly how this occurs during a solar flare. Perhaps both ideas are partly correct and partly in error. If it proves possible to develop a model that involves fast field-line reconnection (Priest and Forbes 1986) and also current-interruption, we may yet obtain a satisfactory model of the impulsive phase of solar flares.

Acknowledgements. This work was supported in part by Lockheed Yohkoh subcontract SE70A3100R, NASA grant NAGW-2265, ONR contract N00014-91-J-1112, and Air Force grant F49620-92-J-0015.

REFERENCES

Aly, J.J. 1984, Ap. J., 283, 349.

Aly, J.J. 1991, Ap. J. (Letters), 375, L61.

Anschwanden, M.J., Benz, A.O., Schwartz, R.A., Lin, R.P., Pelling, R.M., and Stehling, W. 1990, Solar Phys., 130, 39.

Bai, T., and Dennis, B.R. 1985, Ap. J., 292, 699.

Bai, T., and Sturrock, P.A. 1989, Ann. Rev. Astron. Astrophys., 27, 421.

Benz, A.O. 1985, Solar Phys., 96, 357.

Brown, J.C., Melrose, D.B., and Spicer, D.S. 1979, Ap. J., 228, 592.

Carmichael, H . 1964, AAS-NASA Symp. on the Physics of Solar Flares (NASA SP-50), p. 377.

Chupp, E.L., Forrest, D.J., Ryan, J.M., Heslin, J., Reppin, C., Pinkau, K., Kanbach, G., Rieger, E., and Share, G.H. 1982, Ap. J., 263, L95.

de Jager, C. 1969, COSPAR Symposium on Solar Flares and Space Research (eds. C. de Jager and Z. Svestka; Tokyo), p. 1.

Droege, F. 1977, Astron. Astrophys., 57, 285.

Haerendel, G. 1987, Proc. 21st ESLAB Symposium, Bolkesjo, Norway, ESA SP-275, p. 205.

Harvey, K.L., Sheeley, N.R., and Harvey, J.W. 1986, Solar Terrestrial Predictions (eds. P.A. Simon, G. Heckman and M.A. Shea; National Oceanic and Atmospheric Administration, Boulder, CO, and Air Force Geophysical Laboratory, Bedford, MA), p. 198.

Hick, P., and Priest, E.R. 1989, Solar Phys. 122, 111.

Hirayama, T. 1974, Solar Phys., 34, 323.

Karlicky, M., and Jungwirth, K. 1989, Solar Phys., 124, 319.

Kaufmann, P., Strauss, F.M., Opher, R., and Laporte, C. 1980, Astron. Astrophys., 87, 58.

Klimchuk J.A., and Sturrock P.A. 1989, Ap. J., 345, 1034.

Kopp, R.A., and Pneuman, G. 1976, Solar Phys., 50, 85.

Kuipers, J. 1990, Plasma Phenomena in the Solar Atmosphere (eds. M.A. Dubois, F. Bely-Dubau and D. Gresillon; Les Editions de Physique, Les Ulis, France), p. 227.

Loran, J.M., Brown, J.C., Correia, E., and Kaufmann, P. 1985, Solar Phys., 97, 363.

Low, B.C. 1984, Ap. J., 286, 772.

Lu, E.T., and Hamilton, R.J. 1991, Ap. J. (Letters), 380, L89.

Martens, P.C.H. 1988, Ap. J. (Letters), 330, L131.

Martens, P.C.H., and Young, A. 1990, Ap. J. Suppl., 73, 333.

McIntosh, P.S., Krieger, A.S., Nolte, J.T., and Vaiana, G. 1976, Solar Phys., 49, 57.

Moore, R.L. 1988, Ap. J., 324, 1132.

Moore, R.L., Hurford, G.J., Jones, H.P., and Kane, S.R. 1984, Ap. J., 276, 379.

Norman, C.A., and Smith, R.A. 1978, Astron. Astrophys., 68, 145.

Neupert, W.M. 1968, Ap. J. (Letters), 153, L59.

Poletto, G., and Svestka, Z. 1990, Solar Phys., 129, 363.

Priest, E.R. (ed.) 1981, Solar Flare Magnetohydrodynamics (New York: Gordon and Breach).

Priest, E.R. 1987, The Role of Fine-Scale Magnetic Fields on the Structure of the Solar Atmosphere (eds. E. Schroeter, M. Vasquez and A. Wyller; Cambridge University Press), p. 297.

Priest, E.R., and Forbes, T.G. 1986, J. Geophys. Res., 91, 5579.

Priest, E.R., and Forbes, T.G. 1990, Solar Phys., 126, 319.

Ridgway, S.T., and Priest, E.R. 1991, Solar Phys. (submitted).

Simnett, G.M. 1986, Solar Phys., 106, 165.

Simnett, G.M. 1990, Memorie della Societa Astronomica Italiana (in press).

Simnett, G.M., and Haines, M.G. 1990, Solar Phys., 130, 253.

Sturrock, P.A. 1966a, Phys. Rev. Letters, 16, 270.

Sturrock, P.A. 1966b, Nature, 211, 695.

Sturrock, P.A. 1968, IAU Symp. No. 35, Structure and Development of Solar Active Regions (ed. K.O. Kiepenheuer; Dordrecht, Reidel), p. 471.

Sturrock, P.A. 1991, Ap. J., 380, 655.

Sturrock, P.A., Kaufmann, P., Moore, R.L., and Smith, D.F. 1984, Solar Phys., 94, 341.

Svestka, Z. 1976, Solar Flares (Dordrecht-Holland: Reidel).

Svestka, Z. 1983, Space Sci. Rev., 35, 259.

Svestka, Z. 1984, Solar Phys., 94, 171.

Svestka, Z. 1986, Proc. NSO/SMM Symposium on The Lower Atmosphere of Solar Flares (ed. D.F. Neidig; National Solar Observatory, Sacramento Peak), p. 332.

Svestka, A., Martin, S.F., and Kopp, R.A. 1980, IAU Symp. No. 93, Solar and Interplanetary Dynamics (eds. M. Dryer and E. Tandberg-Hanssen), p. 217.

Uchida, Y., and Shibata, K. 1988, Solar Phys., 116, 291.

Van Ballegooijen, A., and Martens, P. 1989, Ap. J., 343, 971.

Van Beek, H.F., de Feiter, L.D., and de Jager, C. 1974, Space Research, 14, 30.

Webb, D.F., Krieger, A.S., and Rust, D.M. 1976, Solar Phys., 48, 159.

Wolfson, R., and Gould, S.A. 1985, Ap. J., 296, 287.

Woltjer, L. 1958, Proc. Nat. Acad. Sci., 44, 489.